CARDIFF
UNIVERSITY
PRIFYSGOL
CAERDYDD

THE GEOCHEMISTRY AND PETROGENESIS OF THE EARLY PROTEROZOIC MATACHEWAN LARGE IGNEOUS PROVINCE

Thomas Jake Raimund Ciborowski

Submitted in partial fulfilment of the requirements for the degree of PhD.

March 2013

What is all your studying worth, all your learning,
all your knowledge, if it doesn't lead to wisdom?

Iain M. Banks

Declaration

This work has not previously been accepted in substance for any degree and is not concurrently submitted in candidature for any degree.

Signed ……………………………………………………………………… (candidate)

Date ………………………

Statement 1

This thesis is being submitted in partial fulfilment of the requirements for the degree of PhD.

Signed ……………………………………………………………………… (candidate)

Date ………………………

Statement 2

This thesis is the result of my own independent work/investigation, except where otherwise stated.

Other sources are acknowledged by explicit references.

Signed ……………………………………………………………………… (candidate)

Date ………………………

Statement 3

I hereby give consent for my thesis, if accepted, to be available for photocopying and for inter-library loan, and for the title and summary to be made available to outside organisations.

Signed ……………………………………………………………………… (candidate)

Date ………………………

Statement 4

I hereby give consent of my thesis, if accepted, to be available for photocopying and for inter-library loans after expiry of a bar on access previously approved by the Graduate Development Committee.

Signed ……………………………………………………………………… (candidate)

Date ………………………

ABSTRACT

The Matachewan Large Igneous Province (LIP) is interpreted to have formed during mantle plume-induced continental break-up during the early Proterozoic. When the Matachewan LIP is reconstructed to its original configuration, the dyke swarms, layered intrusions and flood basalt provinces emplaced over the lifetime of the province comprise one of the largest magmatic provinces recognised in the geological record. New geochemical data allow, for the first time, the Matachewan LIP to be treated as a single, coherent entity.

The major and trace element data presented here show that Matachewan LIP suites share a common tholeiitic composition and trace element geochemistry characterised by enrichment in the most incompatible elements and depletion in the less incompatible elements. This signature, ubiquitous in early Proterozoic continental magmatic rocks, may indicate that the Matachewan LIP formed through contamination or mixing of its primary magmas with crustal material or that the early Proterozoic mantle had a fundamentally different composition to the modern mantle.

Aside from the radiating geometry of the dyke swarms, a plume origin for the Matachewan LIP is implied by the geochemistry of some of the suites, used here to constrain the potential temperature of the magmatism. Comparison of these potential temperatures with the temperature of the early Proterozoic upper mantle, shows that the province is the product of anomalously hot magmatism as predicted by mantle plume theory. Geochemical data from coeval intrusions suggest that the plume head was compositionally heterogeneous and sampled material from both depleted and enriched mantle. Sr-Nd-Pb isotopic data show that this source heterogeneity dictates the Ni-Cu-PGE potential of the related intrusions.

The enormity of the Matachewan LIP cannot be overstated and its potential impact on the early Proterozoic global environment was likely immense – it may even have been the trigger to the irreversible oxygenation of our planet.

ACKNOWLEDGEMENTS

This project represents three and a half years of work made possible only through the assistance of a great number of people to whom I am utterly indebted.

I firstly wish to thank my supervisors, Andrew Kerr, Iain McDonald and Richard Ernst who advised and helped me significantly these last few years. Andrew has been an infallible supervisor who has always been on hand to answer my questions and guide me along the way. Iain's expert supervision on all things Ni-Cu-PGE was invaluable and his help in understanding the upsettingly small amounts of mineralisation in the Blue Draw Metagabbro was instrumental in producing some of the more interesting parts of this study. I thank Richard for introducing me to the Matachewan Large Igneous Province and for his help and hospitality during the 2010 field season. I also cannot overstate my gratitude to Matthew Minifie. If the furtherance of science is achieved by standing on the shoulders of giants, Matt is a colossus. Without his contribution to understanding Large Igneous Provinces, or the hours of discussion we had on the matter, I'd have never finished.

I owe a debt of gratitude to Ley Wooley, Pete Fisher, Tony Oldroyd, Lawrence Badham and Ian Millar for their help in analysing my samples in such an efficient manner. I also owe thanks to Mike Easton, Dick James, Bill Church, Steve Harlan, Ken Buchan, Pete Dahl, Jon Hronsky, Ming Zhang, Bill Griffin and Ulf Söderlund for their assistance in the acquisition of my data.

I'd also like to thank my PhD colleagues at Cardiff. You have been the finest group of people I could hope to have met and spent the last three and a half years with. In particular, I thank Joe Orme whose sense of humour, disposition and counsel made the write-up attrition possible.

My mother, my father and my sister always have and forever will be inspirational to me. Their unending support for me in whatever I do is moving and it is to them that I dedicate this work. Finally, from the bottom of my heart, I thank Tracy for her patience, understanding, time and effort.

CONTENTS

1. INTRODUCTION

1.1. Project Rationale

Large igneous provinces (LIPs) consist of large volumes (>1.3 Mkm^3) of predominantly mafic-ultramafic magmatism emplaced during short (1-5 My) periods of activity over a maximum lifespan of ~50 My by processes unrelated to ‘normal’ spreading or subduction (Coffin and Eldholm 1991; 1994; Bryan and Ernst 2008). LIPs are preserved throughout the geologic record and their study has been used to understand large-scale mantle processes and also constrain pre-Phanerozoic palaeocontinental reconstructions (Ernst and Buchan 2004; Coffin and Eldholm 2005; Neal et al. 2008).

Such mafic-ultramafic magmatism occurred on the Superior, Karelia, Kola, Hearne and Wyoming cratons during the early Proterozoic. When these cratons are reconstructed as part of the supercraton Superia, the individual igneous suites of the magmatic event are restored to their inferred primary distribution (Bleeker 2003; Ernst and Bleeker 2010). This reconstructed ~2.48 Ga Matachewan LIP includes radiating dyke swarms, suites of layered intrusions, sill complexes and flood basalt provinces, the exact anatomy of which are still debated (Heaman 1997; Dahl et al. 2006; Van Boening and Nabelek 2008; Söderlund et al. 2010). The layered intrusions are of particular interest because of their economic potential for Ni-Cu-platinum group element (PGE) sulphide mineralisation (James et al. 2002; Iljina and Hanski 2005).

Prior to this study, many of the individual igneous suites were poorly-known (particularly in terms of their geochemistry), no attempt had been made to study the Matachewan LIP as a single entity, and no coherent geochemical dataset existed for the province. Thus, this project has collected and compiled existing geochemical, isotopic, and other pertinent data for the reconstructed magmatic system, in order to understand: the nature and origin of the mantle sources, the anatomy of the magmatic plumbing system within the lithosphere; the processes and potential for concentrating Ni-Cu-PGE into particular regions within the LIP; and how the emplacement of the LIP may have affected the global environment during the Archaean-Proterozoic transition.

1.2. Aims

This thesis is the first to study the geochemistry of the Matachewan LIP as a single, coherent entity. The elemental data obtained at Cardiff and the isotopic data analysed at the NERC Isotope Geosciences Laboratories at Keyworth compliment already-published data on the Matachewan LIP and together are used to:

- Produce a coherent and comprehensive dataset for each of the igneous suites thought to be part of the LIP.
- Determine whether the LIP primary magmas are the product of melting of an anomalously hot mantle plume source region.
- Investigate the nature of the mantle source regions from which the LIP primary magmas were derived.
- Determine how the primary magmas of the LIP were modified by interaction with other material prior to their emplacement in the crust.
- Understand the factors which control Ni-Cu-PGE mineralisation within the province and establish whether future exploration for such mineralisation can be better directed using geochemistry.
- Investigate how the LIP may have affected the environment during the Archaean-Palaeoproterozoic transition.
- Produce a synthesis which marries the conclusions of this study into a petrogenetic model for the entire Matachewan LIP.

This project represents an excellent opportunity to investigate, in detail, the mantle sources and magmatic plumbing systems of a LIP in 3D and is likely to have wider implications for our understanding of LIP petrogenesis, large-scale mantle dynamics, the formation of magmatic Ni-Cu-PGE mineralisation, and the ability of igneous activity to effect whole-scale change in Earth’s atmosphere.

1.3. Thesis Structure

This thesis is split into six chapters. Following this introduction, Chapter 2 describes LIPs in terms of their internal anatomy and potential petrogenetic mechanisms. Chapter 2 then goes on to explain how previous studies have, in turn, modified the Matachewan LIP reconstruction before summarising our current understanding of the reconstruction. Then, each of the igneous suites thought to be part of the Matachewan LIP are described in terms of their geology, age, Ni-Cu-PGE mineralisation and postulated tectonic settings. Chapter 3 summarises how, and from where, samples were collected and where possible, describes the main petrographic features of each of the suites. Chapter 4 is the main results chapter and presents the major, trace and platinum-group element data for each of the suites as well as the Sr-Nd-Hf-Pb isotopic data analysed by this study. Chapter 5 discusses the geochemical data and attempts to understand the evolution of each of the igneous suites using various petrogenetic models and whether the geochemistry of each of the suites is consistent with their proposed derivation from a mantle plume. The potential of the individual suites to host Ni-Cu-PGE mineralisation is discussed as are the effects the emplacement of the Matachewan LIP may have had on the early Palaeoproterozoic environment. Finally, a brief summary of the project is presented in Chapter 6 which highlights the main conclusions. Additional sample information, analytical methods, geochemical data and quality control information are presented in the electronic appendices at the end of the thesis.

2. GEOLOGICAL OVERVIEW

2.1. Large Igneous Provinces

Large Igneous Provinces (LIPs) were first defined as large areas (>0.16 Mkm^2 area, >1.3 Mkm^3 volume) of mafic magmatism emplaced rapidly into an intraplate setting by processes not connected with 'normal' spreading or subduction (Coffin and Eldholm 1991; 1994). This original definition of LIPs resulted in the inclusion of flood basalts, dyke swarms, submarine ridges, seamount chains, oceanic plateaus, ocean basin flood basalts and volcanic rifted margins and based on this definition, ~120 different Phanerozoic-age LIPS were identified (Coffin and Eldholm 2005) **(Fig. 2.1)**.

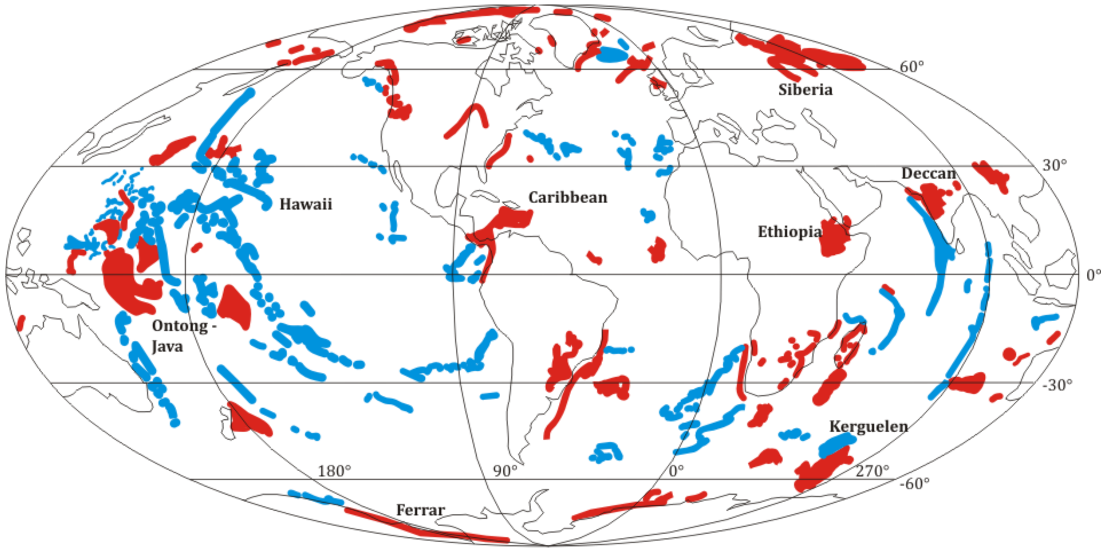

Fig. 2.1. Global map of Phanerozoic LIPs. Red – LIPS associated with mantle plume heads. Blue – LIPs associated with mantle plume tails. Modified from Neal et al. (2008).

Sheth (2007) proposed expanding and changing the definition of LIPs to any igneous province with an areal extent >50,000 km^2. This change in definition would reclassify many other igneous formations as LIPs including predominantly andesitic active island arcs, active continental margins and anorogenic granitic batholiths. The most recent definition for LIPs was proposed by Bryan and Ernst (2008) who disagreed with a broadening of the definition as proposed by Sheth (2007) and instead proposed a more specific criteria for LIPs as *"magmatic provinces with areal extents >0.1 Mkm^2, igneous volumes >0.1Mkm^3, maximum life spans of ~50 million years that have intraplate tectonic settings, or geochemical affinities, and are* *characterised by igneous pulse(s) of short duration (~1-5 million years) during which time, a large proportion (>75%) of the total igneous volume has been emplaced”*.

Bryan and Ernst (2008) maintain that the LIP definition proposed by Sheth (2007) could be applied to such a large range of igneous provinces that the term ‘LIP’ would no longer carry any genetic significance. That said, considerable debate exists as to the processes responsible for LIP formation (Foulger and Jurdy 2007). However, some variation on the mantle plume model is currently favoured by the majority of workers for most LIPs [e.g., Campbell and Griffiths (1990); Coffin and Eldholm (1994); Ernst and Bleeker (2010), Timm et al. (2011)].

Coffin and Eldholm (1994) subdivided individual LIPs into three parts: the extrusive zone, the middle crust zone and the lower crustal body **(Fig. 2.2)**. The extrusive zone is dominated by basaltic flows, with occasional felsic members associated with the early and late stages of LIP formation. The flows can be extremely large, extending laterally for thousands of kilometres and can be tens of kilometres thick (Ernst 2007). The Ontong Java is the largest known igneous province and the total igneous volume for the plateau is estimated to be 59-77 Mkm^3 (Kerr and Mahoney 2007). Typically, erosion has removed much of the extrusive zone in older LIPs, though remnants are occasionally preserved within intracratonic basin successions [e.g., Sandeman and Ryan (2008)]. The middle crust zone contains the ‘plumbing system’ for the extrusive zone in the form of dykes, sills and layered intrusions. These plumbing systems are only directly observed in LIPs sufficiently old to have had the extrusive cover eroded or to have been dissected by later tectonic events. The most easily recognised features of these plumbing systems are the dykes which form linear dyke sets or massive radiating swarms (Ernst and Buchan 2001). The lower crustal body of LIPs is rarely exposed, but is inferred from P-wave velocities of 7.0-7.6 km s^{-1} at the base of the crust beneath more recent LIPs which suggests the presence of an ultramafic underplated layer beneath these systems (Coffin and Eldholm 2005).

There is considerable debate on the mechanisms of continental breakup and the formation of LIPs. Currently, the majority opinion favours a plume model for the emplacement of LIPs, and is even described as ‘endemic’ by Jones et al. (2002).

However, other processes for LIP formation have also been proposed, including mantle delamination (Anderson 2000; McHone 2000; Anderson 2005; Elkins-Tanton 2005), edge-driven convection (King and Anderson 1995; 1998; King and Ritsema 2000; King 2007), bolide impact (Jones et al. 2002; Ingle and Coffin 2004; Jones 2005) and mantle insulation (Anderson 1982; Doblas et al. 2002; Coltice et al. 2007; 2009).

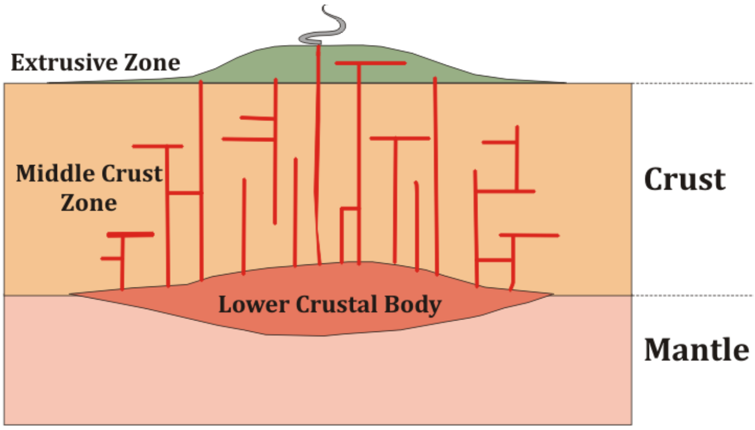

Fig. 2.2. Schematic cross-section through a continental LIP. Modified from Coffin and Eldholm (2005).

2.2. Matachewan Large Igneous Province

The Matachewan LIP is a proposed reconstruction of coeval igneous rocks on five separate Archaean cratonic blocks into a single, cogenetic magmatic system formed by an incident mantle plume beneath the supercontinent ‘Superia’ at ~2.48 Ga (Heaman 1997). The most recent iteration of the Matachewan LIP links ~10 magmatic suites spread across the Superior, Wyoming, Hearne, Karelia and Zimbabwe cratons (Söderlund et al. 2010). Fig. 2.33 at the end of this chapter shows the present day locations of the cratons which made up Superia as well as the locations of the dyke swarms, layered intrusions and flood basalt provinces which comprise the Matachewan LIP. To understand the Matachewan LIP model and how various igneous rocks have come to be included in the reconstruction, we need to understand how the model itself has been developed.

Ascribing the original idea of the Matachewan LIP to a single author or work is problematic as tentative correlations involving rocks associated with the Matachewan LIP have been proposed for decades (Blackwelder 1926; Young 1988; Patterson and Heaman 1991). However, the first work to study the question in real detail following the pioneering work of Williams et al. (1991) is that of Roscoe and Card (1993) who produced and correlated detailed stratigraphy for the Huronian Supergroup of the Superior craton with the Snowy Pass Supergroup of the Wyoming craton **(Fig. 2.3)**. They suggested that these rocks were deposited in a common, rift-related intracratonic basin formed during the break-up of an Archaean-Early Proterozoic supercontinent (Kenorland) of which the Superior and Wyoming cratons were a part. Aspler and Chiarenzelli (1998) also supported a Snowy Pass-Huronian link as part of the Kenorland supercontinent, but unlike Roscoe and Card (1993), they reinterpreted the Huronian and Snowy Pass supergroups as contemporaneous rifted passive margin sequences deposited along the southern margin of the Kenorland supercontinent.

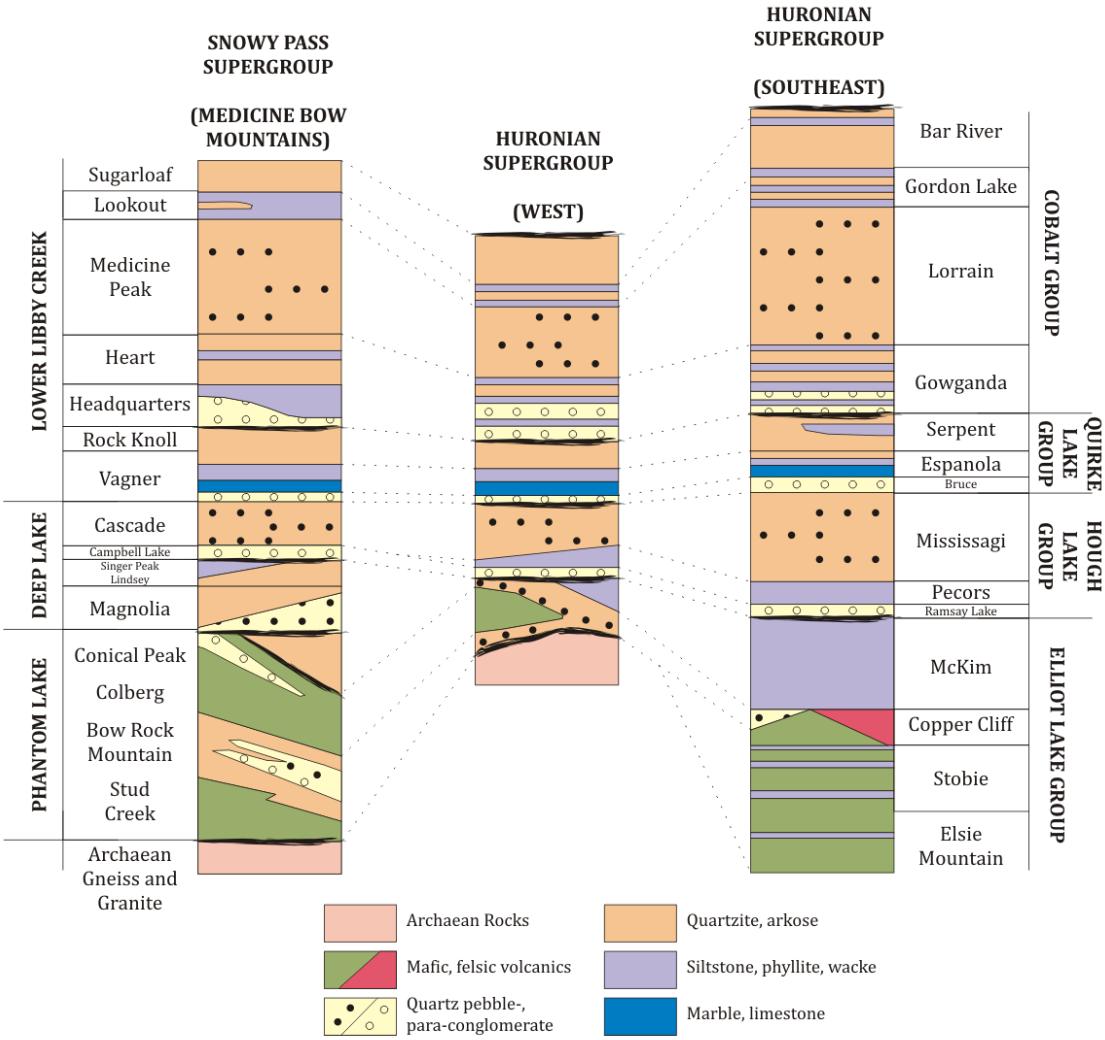

Fig. 2.3. Comparative stratigraphy of the Huronian Supergroup and Snowy Pass Supergroup. Modified from Roscoe and Card (1993).

Heaman (1997) extended Roscoe and Card's (1993) reconstruction to include the Karelia craton by interpreting the coeval U-Pb ages of the Matachewan radiating dyke swarm (Superior craton) with the Sumi-Sariola-Strelna group volcanics (Karelia craton) as indication of a cogenetic source for the magmatism on the two cratons at ~2.47 Ga **(Fig. 2.4)**. It was also in this work that a mantle plume was first suggested as a mechanism for the break-up of the supercontinent Kenorland made up of the Wyoming, Superior and Karelia cratons and the formation of the rocks discussed thus far.

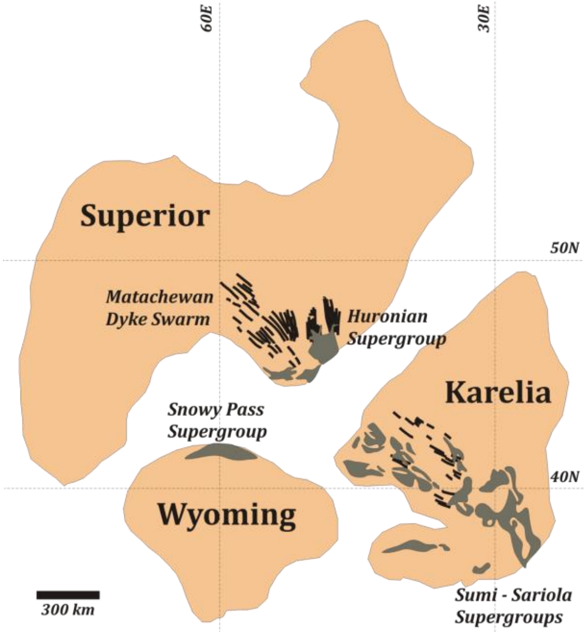

Fig. 2.4. ~2.45Ga Superior-Wyoming-Karelia reconstruction. Modified from Heaman (1997).

After noting striking similarities in the tectonic history of the Superior and Karelia cratons, Vogel et al. (1998b) compared the intrusion history and geochemistry of the coeval layered intrusions found on both cratons. They found that the igneous history of the two cratons remained similar until approximately ~2.20 Ga following which, coeval intrusions do not occur on both cratons **(Fig. 2.5)**. Geochemical data for parental magmas of the ~2.45 Ga East Bull Lake Suite of layered intrusions (Superior craton) and Fennoscandian intrusions (Karelia craton) and suggest that the magmas can be related to each other by varying degrees of partial melting, contamination and fractional crystallisation of a common source (Vogel et al. 1998b). This may be further evidence genetically linking the East Bull Lake Intrusive Suite to the Fennoscandian intrusions, hence linking the Superior craton with the Karelia cratons into an Archaean-Early Proterozoic ancestral supercraton which began to rift at ~2.5Ga (Vogel et al. 1998b).

The potential ~2.5 Ga link between the Superior, Wyoming and Karelia cratons was further strengthened by Ojakangas et al. (2001) who correlated glaciogenic deposits, a palaeosol horizon and carbonate sequences with high ^{13}C values between the Huronian Supergroup (Superior craton), Sariolan Formation (Karelia craton) and Snowy Pass Supergroup (Wyoming craton).

Bleeker (2003) suggested that early-earth continental reconstructions should be approached by first grouping the ~35 Archaean cratons currently recognised into 'clans' which should be defined by similar tectonic histories, periods of mafic magmatism and common key stratigraphic markers. Using this method, Bleeker (2003) defined 3-4 craton clans which existed during the Archaean – Early Proterozoic, the inference being that these clans existed as individual continents separated by intervening ocean with each continent experiencing a common geologic history prior to continental rifting and tectonic dispersal into the ~35 cratonic fragments recognised today. The 'Superia' clan (made up of the Superior, Hearne and Karelia cratons) are grouped together based on coeval 2.47-2.45 Ga mafic dyke swarms, 2.4-2.2 Ga glaciogenic sedimentary sequences and a similar cratonisation age (2.68-2.63 Ga) for the three cratons. Bleeker (2003) noted that the constraints on these groups may be greatly improved with further study and that the current ambiguity allows certain cratons such as the Wyoming to be tentatively grouped into more than one clan. Bleeker (2003) suggested that this may indicate that rather than the existence of several separate cratons, the craton clans may have formed parts of a sprawling Kenorland-like supercontinent with the more ambiguous cratons such as the Wyoming occupying intermediate positions between the clan cores.

Bleeker (2004) strengthened his earlier 'Superia' reconstruction involving the Superior, Hearne and Karelia cratons by comparing the Kaminak dyke swarm (Hearne craton) with the Matachewan dyke swarm (Superior craton). Bleeker (2004) suggested that the essentially identical age of the two swarms (~2.45 Ga), the presence of characteristic plagioclase megacrysts and earlier palaeomagnetic studies (Christie et al. 1975) show that the cratons were sutured together prior to 2.45 Ga and that the arrival of a mantle plume head initiated rifting of the 'Superia' supercontinent and concomitant emplacement of the Matachewan and Kaminak dyke swarms **(Fig. 2.6)**.

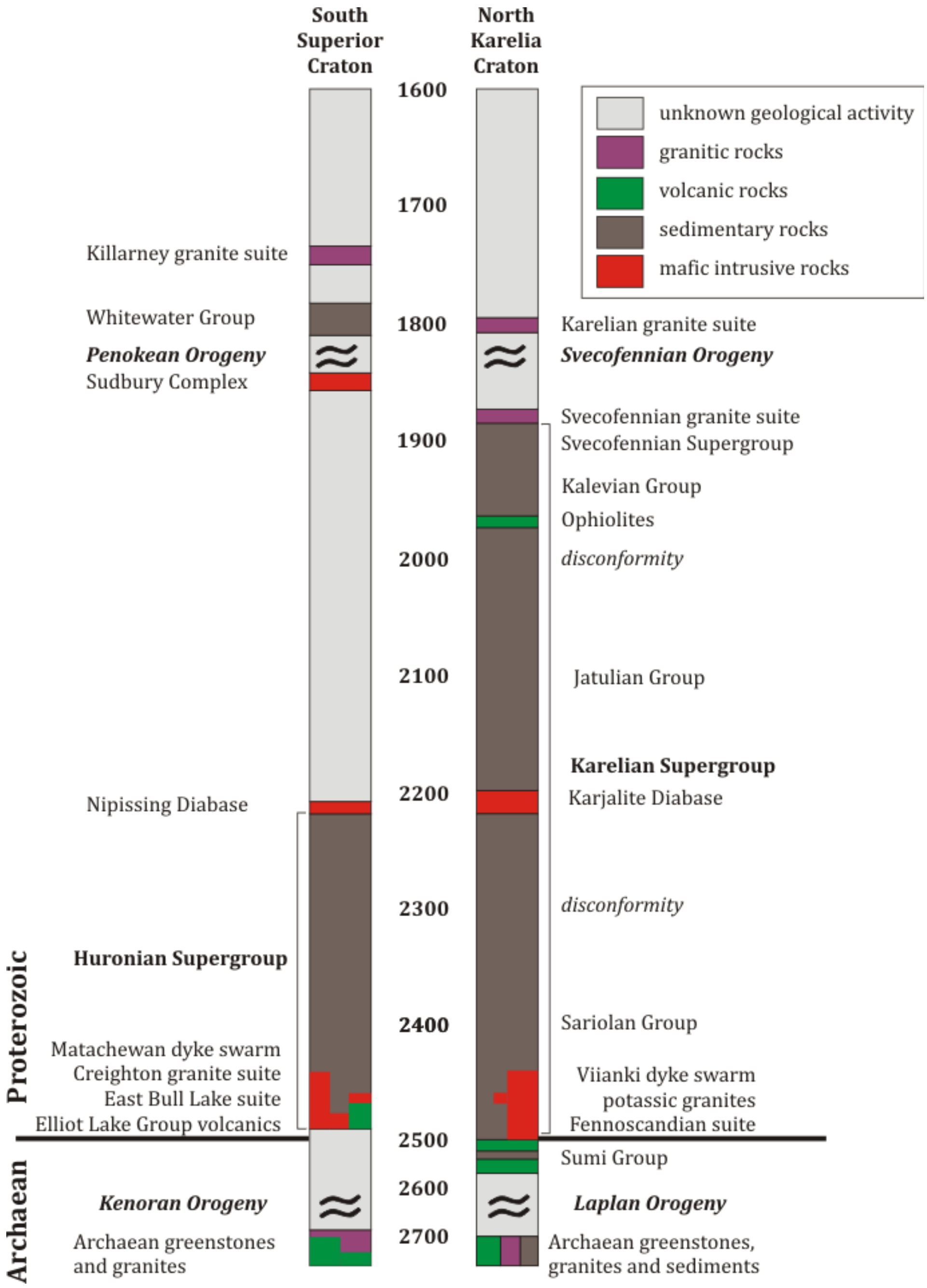

Fig. 2.5. Comparative geological histories for the Superior and Karelia cratons. Modified from Vogel et al. (1998b).

An earlier palaeomagnetic study of a quartz diorite from the Wind River Range of the Wyoming craton (Harlan et al. 2003) showed that at 2.2 Ga, the Wyoming and Superior cratons were close neighbours. Harlan (2005) suggested that it is possible that this proximity persisted back to at least ~2.5 Ga. The reasoning behind this supposition was that Harlan (2005) suspected that the Leopard Dykes (so called for their ubiquitous plagioclase megacrysts) of the Wyoming craton are Palaeoproterozoic in age and may be cogenetic with the similarly textured

Matachewan and Kaminak dyke swarms of the Superior and Hearne cratons. Harlan (2005) noted, however, that a reliable age for the Leopard dyke swarm did not yet exist and that palaeomagnetic data for the Leopard swarm was limited, leaving any such reconstruction involving the Leopard dykes speculative.

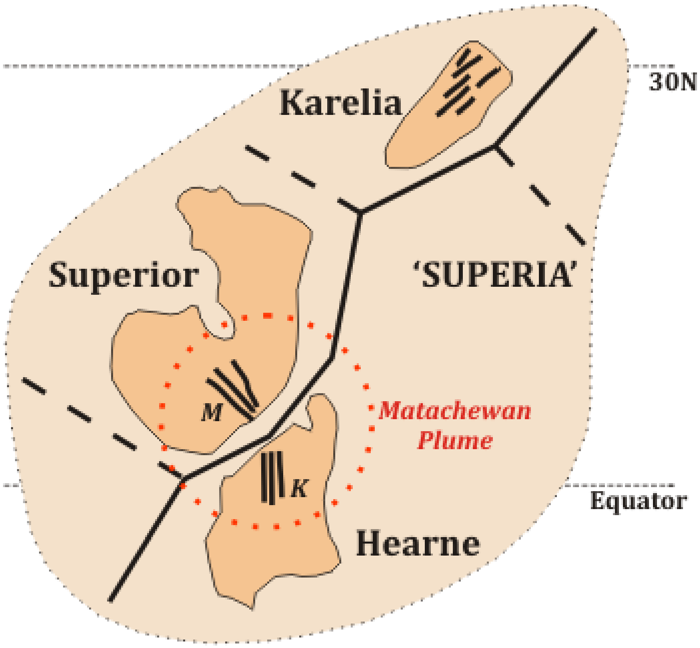

Fig. 2.6. ~2.45Ga Superior-Hearne-Karelia reconstruction. Modified from Bleeker (2004).

Dahl et al. (2006) strengthened a ~2.5 Ga Superior–Wyoming correlation following U-Pb dating of pristine magmatic titanite from the Blue Draw Metagabbro, a 1 km thick layered mafic sill exposed in the Black Hills Laramide uplift in eastern Wyoming craton. Dahl et al. (2006) showed the Blue Draw Metagabbro (and potentially other Proterozoic mafic bodies exposed in the Black Hills uplift, which lack definitive age data) was intruded into the Boxelder Creek Quartzite host rock at ~2.48 Ga. This age is identical to the similarly-sized mafic intrusions of the East Bull Lake Intrusive Suite on the Superior craton (Krogh et al. 1984). Dahl et al. (2006) use this indistinguishable age of the Blue Draw and East Bull Lake Intrusive Suite along with similarities between the Boxelder Creek Quartzite, Magnolia Sandstone (Snowy Pass Supergroup, Wyoming craton) and Livingstone Creek Sandstone (Huronian Supergroup, Superior craton) to produce a supercontinent reconstruction for ~2.5 Ga which includes the Wyoming, Superior and Karelia cratons **(Fig. 2.7)**.

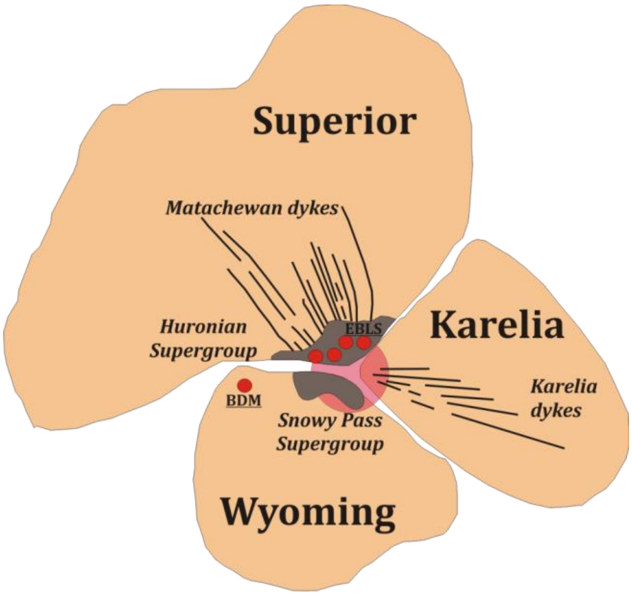

Fig. 2.7. ~2.48Ga Superior-Wyoming-Karelia reconstruction. Modified from Dahl et al. (2006).

In an attempt to better constrain ancient continental reconstructions, Ernst et al. (2008) first proposed the use of craton ‘magmatic barcodes’. In essence, the ‘barcode’ is a high resolution U-Pb geochronological record of magmatism not related to normal spreading or subduction preserved within a craton **(Fig. 2.8)**. Ernst et al. (2008) proposed that temporal matching of the ‘barcodes’ for different cratons provides the most robust method for reconstructing ancient continents. They presented such ‘barcodes’ for the Superior, Hearne and Karelia cratons and showed that at various points between 2.66 and 2.10 Ga, similar styles of igneous activity in the form of dyke swarms, layered intrusions and flood basalt volcanism is recorded on the cratons. For comparison, Ernst et al. (2008) provided a ‘bar-code’ for the Slave craton which shows a relatively poor match with the other three. Using this approach Ernst et al. (2008) suggested that the Superior, Hearne and Karelia cratons were adjacent pieces of crust within an ancestral supercontinent (Superia) during the late-Archaean and Palaeoproterozoic until Superia rifted sometime after 2.2 Ga.

Ernst and Bleeker (2010) proposed a ~2.5-2.45 Ga supercontinent reconstruction which took account of the work discussed above. The reconstruction genetically links volcano-sedimentary sequences, layered intrusions and mafic dyke swarms on the Wyoming, Superior, Karelia and Hearne cratons and interprets these rocks to have formed during rifting of this supercontinent, beginning at ~2.5 Ga and ending finally at ~2.2 Ga. Crucially, the reconstruction reassembles the mafic dyke swarms preserved on the four constituent cratons into one, giant radiating swarm, thought to define a mantle-plume locus which drove the rifting event. Söderlund et al. (2010) modified Ernst and Bleeker's (2010) reconstruction by including the Zimbabwe craton based on ages of three mafic dyke swarms preserved on the craton which overlap ages recorded for intrusions included in the 'Superia' reconstruction.

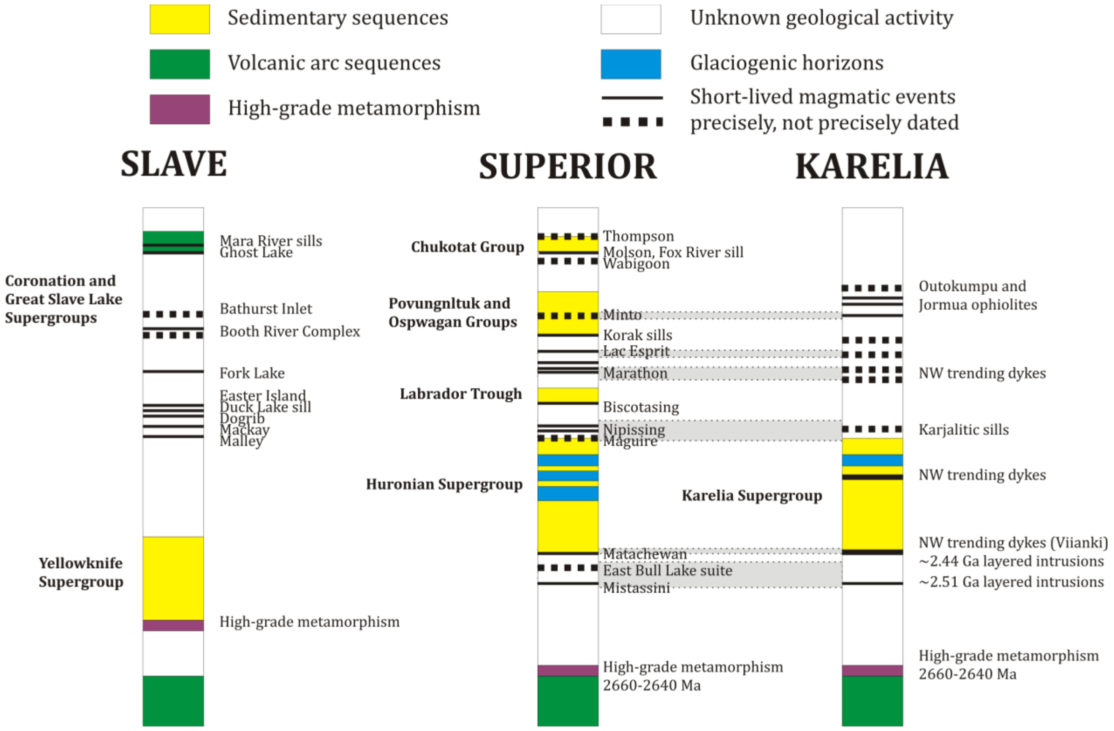

Fig. 2.8. Comparative geological histories for the Slave, Superior and Karelia cratons. Modified from Ernst et al. (2008).

The above paragraphs summarise the work which has contributed to the development of the Matachewan LIP reconstruction into its most recent iteration **(Fig. 2.9)**. The following sections review the current understanding of each of the individual Matachewan LIP formations.

2.2.1. Matachewan Dyke Swarm

2.2.1.1. Geology

The Matachewan dyke swarm is made up of thousands of north-northwest trending dykes which crop out over an area of 300,000 km^2 in southern Ontario and south western Quebec. The dykes are sub-vertical and can be up to ~60 m wide, though the majority have diameters of ~10-20 m (Bates and Halls 1990; Nelson et al. 1990; Heaman 1997). The dykes are Fe-rich quartz tholeiites and are primarily composed of plagioclase and pyroxene with lesser amounts of amphibole, quartz, Fe-Ti oxides and apatite and preserve relict intergranular-subophitic textures (Bates and Halls 1990; Nelson et al. 1990; Siddorn 1999). Locally, the Matachewan dykes contain distinctive plagioclase megacrysts which can be up to ~20 cm in length which are known to occur in planar zones, parallel to the dyke margins (Halls 1991; Siddorn 1999). Metamorphic mineral assemblages of epidote, sericite, amphibole and chlorite observed in the Matachewan dykes (Nelson et al. 1990) suggest that metamorphism of the Matachewan dyke swarm reached a maximum of lower greenschist facies (Halls 1991).

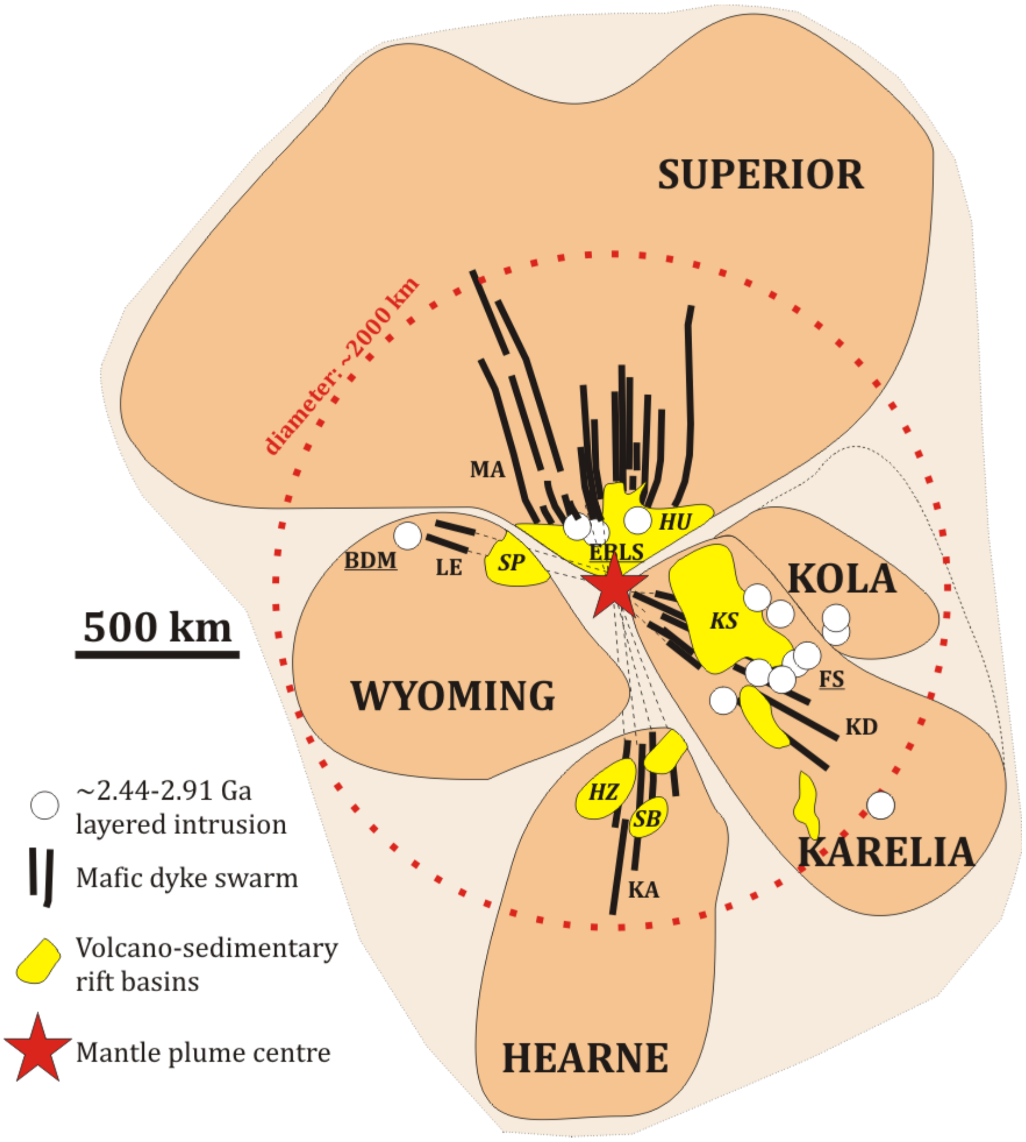

Fig. 2.9. ~2.48Ga Superior-Wyoming-Karelia-Hearne reconstruction. Modified from Ernst et al. (2008) and Söderlund et al. (2010).

Individual Matachewan dykes can be followed in outcrop over tens of kilometres (Phinney and Halls 2001) while high resolution aeromagnetic data (West and Ernst 1991) allows single dykes to be traced in the subsurface for hundreds of kilometres, and reveals that they transcend tectonic boundaries between the east-west trending Archaean granite-greenstone and metasedimentary terranes which make up the Superior craton **(Fig. 2.10)**.

Several workers (Bates and Halls 1990; West and Ernst 1991; Zhang 1999) have divided the Matachewan dyke swarm into three sub-swarms, characterised by slight changes in modal dyke orientation and delineated by intervening areas with a low density of dykes. The literature is virtually unanimous [with the exception of McHone et al. (2005)] in its interpretation of these sub-swarms as being part of a single fanning system with an arc angle of between ~40-60° which radiates from a focus somewhere near Sudbury, Ontario [e.g., (Ernst et al. 1995; Park et al. 1995; Zhang 1999; Phinney and Halls 2001; Halls et al. 2005; Halls et al. 2007)].

2.2.1.2. Age

Heaman (1997) dated four Matachewan dyke samples. Two samples were collected from both sides of the Kapuskasing structural zone. U-Pb analysis of six baddeleyite and three zircon grains from the two samples collected from west of the Kapuskasing structural zone yielded a relatively precise upper intercept age of $2445.8^{+2.9}_{-2.6}$ Ma. U-Pb analysis of four baddeleyite grains from the two samples collected from east of the Kapuskasing structural zone resulted in a much more imprecise upper intercept age of 2473^{+16}_{-9} Ma.

Heaman (1997) interpreted these dates as showing that the Matachewan dyke swarm is a composite swarm made up of the ~2.45 Ga Hearst and ~2.47 Ga Matachewan sub-swarms, which together constitute the Matachewan igneous event which spans ~30 My from ~2.48-2.45Ga. However, Heaman (1997) concluded that not enough age data exists to determine if the Matachewan and Hearst swarms are formed by separate magmatic pulses, or if the ~2.45Ga age of the Hearst swarms represents the end of a continuous magmatic event which started at ~2.47Ga. Halls et al. (2005) also dated a Matachewan dyke from west of the Kapuskasing (U-Pb baddeleyite) to give a discordant age of 2459 ± 5 Ma for the Matachewan swarm which falls within the range determined by Heaman (1997).

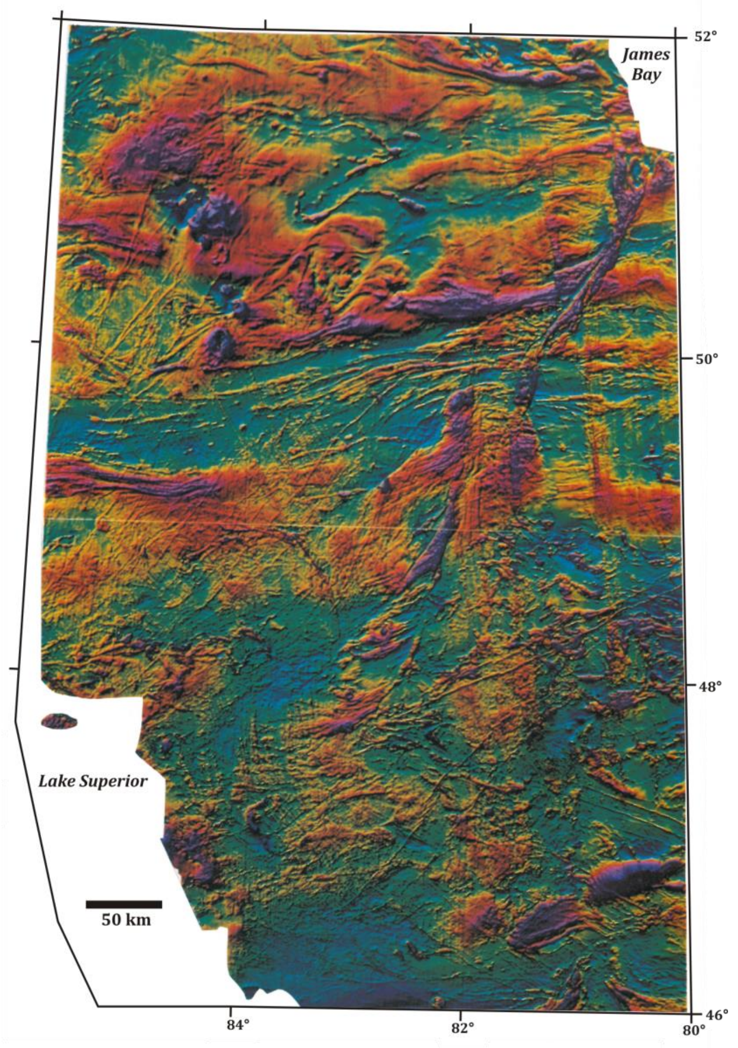

Fig. 2.10. Aeromagnetic image of southwest Ontario. Linear features with a N-S or NW-SE strike are Matachewan dykes. Modified from West and Ernst (1991).

Since the work of Heaman (1997), the 'Hearst' swarm has been largely dropped from the nomenclature and the 2.45-2.47 Ga Hearst-Matachewan swarm (Heaman (1997) is now more commonly referred to as the ~2.45 Ga Matachewan dyke swarm (Halls and Davis 2004; Halls et al. 2005; Halls 2009)

2.2.1.3. Tectonic Setting

By far, the most widely accepted view regarding the petrogenesis of the Matachewan dyke swarm is that the swarm is a product of mantle plume-induced magmatism during rifting of an Archaean supercontinent [e.g., (Ernst et al. 1995; Phinney and

Halls 2001; Ernst and Buchan 2002; Bleeker 2004; Söderlund et al. 2010)]. The most definitive evidence for a mantle plume origin for the Matachewan dyke swarm is the swarm's apparent radiating geometry which defines a fanning system with an arc angle of ~40-60° [e.g., (Ernst et al. 1995; Park et al. 1995; Zhang 1999; Phinney and Halls 2001; Halls et al. 2005; Halls et al. 2007)]. It is argued that the intrusion of a dyke swarm with radiating geometry like that exhibited by the Matachewan swarm can only be adequately explained by intrusion of magma into crust which is subject to a radial stress regime related to crustal doming directly above the buoyant head of a mantle plume (Ernst and Buchan 2001; Phinney and Halls 2001; Ernst and Bleeker 2010). The location of the plume head is thought to be defined by the apparent focus of radiating dyke swarms **(Fig. 2.11)**, which in the case of the Matachewan dyke swarm, is close to Sudbury, Ontario.

Heaman (1997) argued that the sheer volume of magma injected into the crust over such a relatively short time frame, (from the Matachewan dyke swarm along with those preserved on other cratons as part of a larger LIP) can only be delivered by the melting of a mantle plume head beneath the lithosphere. Ernst et al. (1995) also contend that the presence of more voluminous magmatism in the form of layered intrusions (East Bull Lake suite) and continental flood basalts (Huronian Supergroup) near the focus of the Matachewan dyke swarm and absence in more distal parts of the swarm is also compatible with the variable volumes of melt expected to produced by different regions of a melting mantle-plume head.

Despite the near unanimity of opinion regarding the radiating geometry (and hence, inferred mantle plume origin) of the Matachewan dyke swarm, McHone et al. (2005) argue that the Matachewan dyke swarm does not in fact radiate from a focal point and propose instead, most of the Matachewan dykes are subparallel. Alternatively, McHone et al. (2005) suggested that the fanning observed by other authors is more likely to be 'sweeps and curves' in dyke geometry caused by pre-existing tectonic fabrics and hence not related to any mantle plume.

Several studies have investigated the geochemistry of the Matachewan dyke swarm [e.g., (Nelson et al. 1990; Smith et al. 1992; Phinney and Halls 2001; Halls et al. 2005)], though the majority are concerned with the evolution of the Matachewan magmas following their extraction from the mantle. Phinney and Halls (2001) conducted the only study which attempted to understand the tectonic setting of the Matachewan dyke swarm using geochemistry. In their discussion, Phinney and Halls (2001) suggest that Hf/Zr ratios in the dykes decrease with increasing distance from the dykes' focus near Sudbury [Figure 15 in Phinney and Halls (2001)]. Variable degrees of fractional crystallisation were considered unlikely to account for this trend due to the relatively high speed of magma flow observed in similar dykes. Phinney and Halls (2001) also ruled out contamination of the magmas by crustal material during lateral movement of the dyke magmas through the crust. Instead, Phinney and Halls (2001) suggest that the systematic change in Hf/Zr ratios observed in the Matachewan dyke swam reflects primary compositional heterogeneities in the mantle plume head.

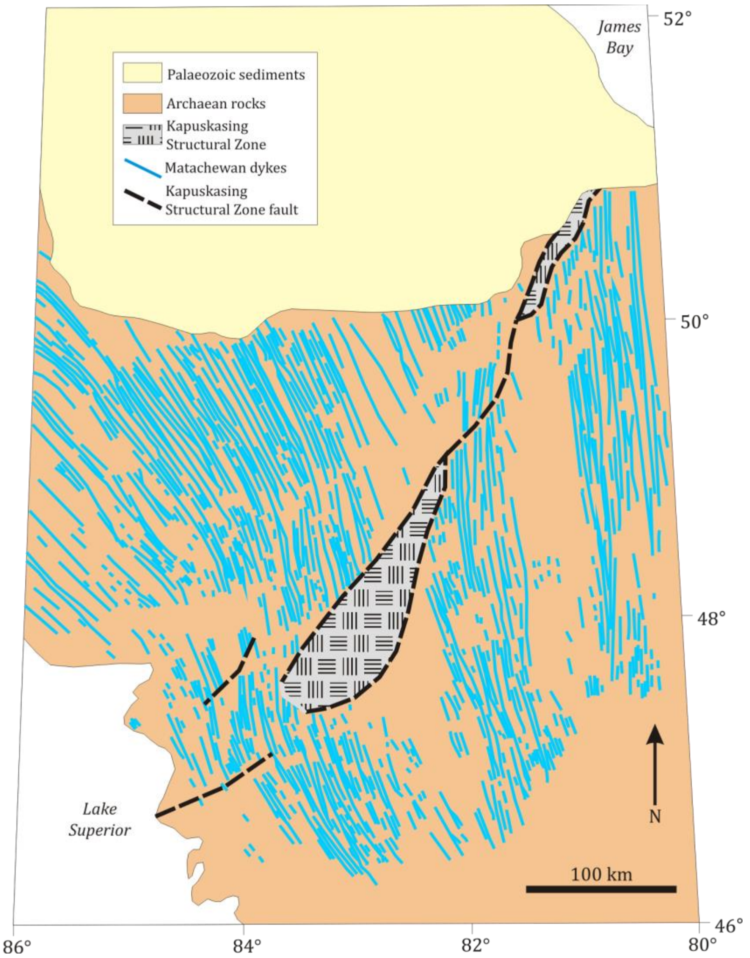

Fig. 2.11. Simplified geological map of southwest Ontario showing the change in trend of Matachewan dykes across the province. Modified from Bates and Halls (1990).

However, it is my opinion that the trend of decreasing Hf/Zr ratios with increased distance from the focus of the Matachewan dyke swarm as observed by Phinney and Halls (2001) is not statistically significant and instead, the Hf/Zr ratios in the Matachewan dykes show no relationship with distance from focus and hence, cannot be used as evidence for a mantle plume setting.

2.2.1.4. Ni-Cu-PGE Mineralisation

Despite being investigated as potential parental magmas of the Ni-Cu-PGE-bearing East Bull Lake Suite of layered intrusions (Vogel et al. 1999), no mineralisation has been reported in the Matachewan dyke swarm and swarm is not the focus of any current or historic exploration programme.

2.2.2. East Bull Lake Suite

2.2.2.1. Geology

East Bull Lake Intrusion

The East Bull Lake intrusion is a texturally and mineralogically layered gabbro-anorthosite intrusion, in Archaean host rocks ~50 km west of Sudbury, Ontario. The East Bull Lake intrusion **(Fig. 2.12)** has an areal extent of ~43 km^2, records a minimum stratigraphic thickness of 800 m (James et al. 2002) and intrudes the Archaean Whiskey Lake greenstone belt, Algoman granitic suite and the Parisien Lake syenite (Peck et al. 1991).

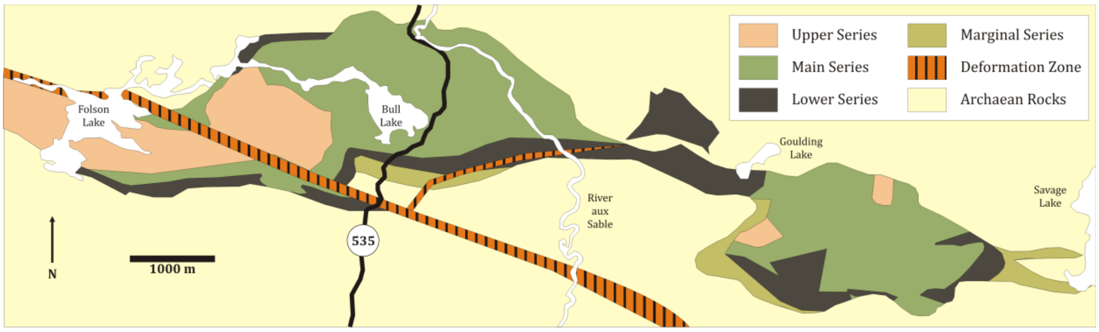

Fig. 2.12. Geological map of the East Bull Lake intrusion. Modified from James et al. (2002).

Stratigraphy

The four series (Marginal, Lower, Main and Upper) which make up the stratigraphy of the East Bull Lake intrusion **(Fig. 2.13)** are described elsewhere in the literature [e.g., (Peck et al. 1991; Peck and James 1992; Peck et al. 1995; James et al. 2002)) and the detailed summaries presented below are largely taken from these studies unless otherwise cited.

Marginal Series

The Marginal Series is made up of the Border and Gabbronorite zones. The Border Zone represents a transitional zone between the country rock and the intrusion and is comprised of a breccia zone several tens of meters thick which contains xenoliths of Archaean tonalitic and granitic basement country rock intruded by, and enclosed in, gabbroic and anothorsite veins (Peck and James 1992). The xenoliths are commonly hornfels and some show evidence of in-situ melting (Peck et al. 1995). Where this melting is observed, adjacent vein material contains 3-4% quartz and/or patchy granophyric-textured leucotonalite and leucogranite (James et al. 2002). The vein to xenolith ratio in the Border Zone increases both laterally towards the intrusion and stratigraphically upwards. The vein orientation in the Border Zone varies but they strike predominantly at right-angles to the layering in the intrusion. The composition of the veins ranges from anorthosite to melanogabbronorite but is mostly leucogabbronorite-gabbronorite. Peck and James (1992) note that anorthositic veins appear to crosscut gabbroic veins, which suggests that at least two magma pulses formed the East Bull Lake intrusion. The Border Zone also contains small bodies of plagioclase-rich cumulates, similar to those found more abundantly in the Anorthosite Zone, higher up in the stratigraphy. These plagioclase-rich cumulates are present in the Border Zone as small, variably-textured gabbronorite bodies which cut across stratigraphic boundaries near the base of the intrusion (Peck et al. 1995).

The Border Zone is overlain by the variable thickness (1-50 m), texturally and modally layered Gabbronorite Zone. The Gabbronorite Zone is interpreted by Chubb (1994) and Peck et al. (1995) as being a dyke-like body which intruded into the East Bull Lake intrusion at some point after the formation of the overlying cumulate rocks of the Lower Series. This is evidenced by the fact that; firstly, gabbroic veins of a very similar composition to the Gabbronorite Zone rocks intrude into the overlying Lower Series, secondly, the Gabbronorite Zone is locally observed to contain fragments of the overlying Inclusion-Bearing Zone and, thirdly, that grain size in the Gabbronorite Zone decreases from the centre of the zone outwards.

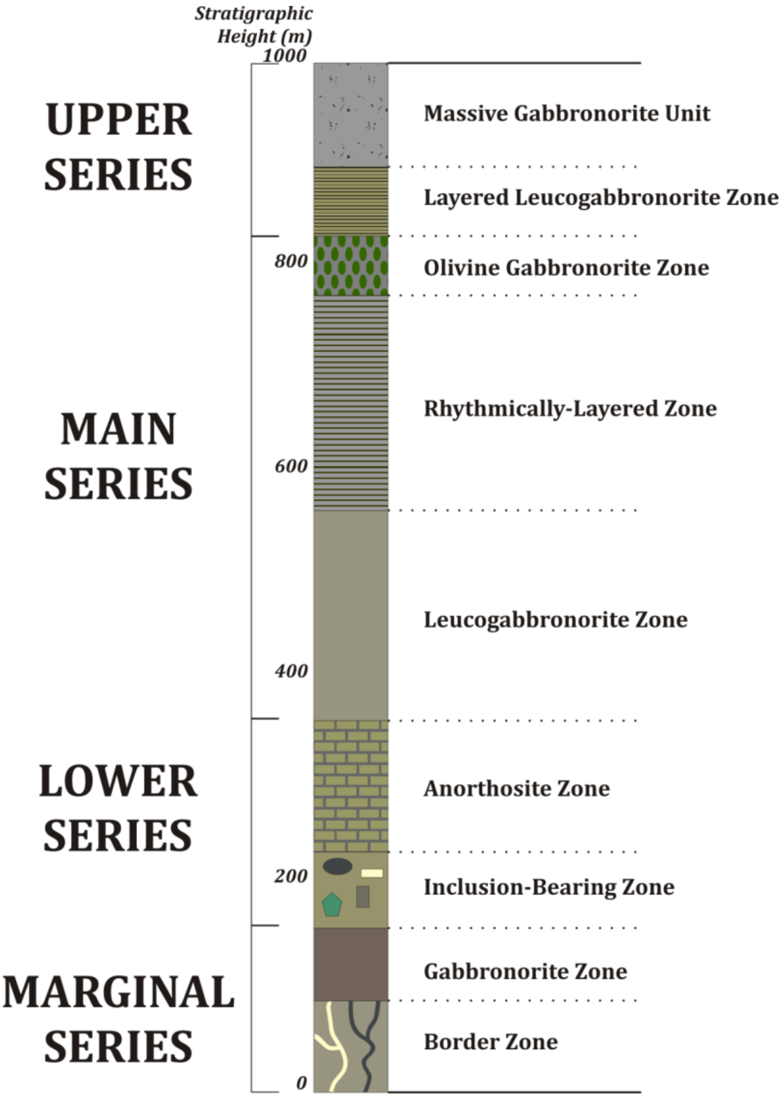

Fig. 2.13. Stratigraphy of the East Bull Lake intrusion. Modified from James et al. (2002).

Lower Series

The Lower Series is made up of the Inclusion-Bearing Zone and the Anorthosite Zone. The ~65 m thick Inclusion-Bearing Zone is further subdivided into the Inclusion-Bearing Gabbronorite and Inclusion-Bearing Leucogabbronorite units by Peck et al. (1995). The two units are petrologically and texturally similar and are distinguished by the presence of anorthosite nodules in the Leucogabbronorite unit but not in the Gabbronorite unit. The Inclusion-Bearing Zone is dominantly made up of a medium-coarse grained gabbronorite-leucogabbronorite matrix and up to 15% heterolithic inclusions (Peck et al. 1995). The inclusions consist of basement xenoliths, anorthosite, leucogabbro autoliths and discontinuous, podiform pyroxenite and melagabbro bands and pods (James et al. 2002).

The Anorthosite Zone is made up of coarse grained anorthosite and leucogabbronorite which are locally cut by cross-cutting gabbroic vein networks (James et al. 2002). A notable feature of the Anorthosite Zone is the local presence of irregular, cm-m scale pyroxenite bodies. These pyroxenite bodies are both geochemically and petrographically similar to the pyroxenite bodies found within the Inclusion-Bearing Zone (Peck et al. 1995).

The Main Series

The Main Series is made up of the Leucogabbronorite Zone at the base of the series, followed by the Rhythmically Layered Zone and the Olivine Gabbronorite Zone at the top of the series. The igneous layering observed in the Main Series becomes increasingly more developed upwards through the Series and is characterised by centimetre-metre scale layers of leucogabbronoritic and gabbronoritic rocks. Layering in the Leucogabbronorite Zone is due to variations in the amount of plagioclase and pyroxene, while layering in the Rhythmically Layered Zone is caused by variations in modal amounts of olivine and plagioclase. Throughout the Main Series, rocks become more plagioclase-rich with increasing stratigraphic height (James et al. 2002).

The Leucogabbronorite Zone is up to 400m thick and is made up of gradational subzones of anorthositic gabbronorite, gabbroic anorthosite and anorthosite which are characterised by the presence of coarse grained-pegmatitic, modally-layered leucogabbronorite and anorthosite mesocumulates (Peck et al. 1991). The rocks of the Leucogabbronorite Zone are composed of cumulus plagioclase and orthopyroxene and post-cumulus clinopyroxene and titanomagnetite (James et al. 2002). The Rhythmically Layered Zone is up to 150m thick and is made up of alternating leucogabbronorite and gabbronorite layers 1-2m thick which commonly show poikilitic textures (Peck et al. 1991). Finer scale layering is also observed and this is picked out by modal variations in the amounts of olivine and plagioclase in the rock. The rocks of the Rhythmically Layered Zone are composed of cumulus plagioclase, orthopyroxene and olivine with postcumulus clinopyroxene and magnetite (James et al. 2002). The Olivine Gabbronorite Zone at the top of the Main Series is a 50-70 m thick, fault bounded zone composed of centimetre-scale layers of dominantly olivine gabbronorite with lesser gabbronorite, norite, peridotite and troctolite (James et al. 2002).

Upper Series

The Upper Series contains the most petrologically evolved rocks found in the East Bull Lake intrusion and is comprised of the Layered Gabbronorite Zone and the Massive Gabbronorite Zone. The ~80 m thick Layered Gabbronorite Zone is made up of planar-disrupted, irregular, texturally and modally varying layers of alternating gabbro, leucogabbro and subordinate melanogabbro (James et al. 2002). The rocks are composed of cumulus plagioclase and post cumulus clinopyroxene and titanomagnetite (Peck et al. 1991). The Massive Gabbronorite unit is made up of planar, fine-medium grained gabbronorite and ferrogabbronorite (Peck et al. 1995).

Agnew Intrusion

The Agnew intrusion is a texturally and mineralogically layered gabbronoritic intrusion, preserved between the granitic-gneissic rocks of the Archaean Ramsay-Algoma granitoid suite and the Palaeoproterozoic Huronian Supergroup, approximately 70 km west of Sudbury, Ontario **(Fig. 2.14)**. The Agnew intrusion has an areal extent of ~50 km^2 and records a minimum stratigraphic thickness of 2100 m. Intrusive contacts between the Agnew intrusion and Ramsay-Algoma granitoids are obscured by psuedotachylitic breccias associated with the ~1.85 Ga Sudbury event and younger sills which have intruded along the footwall contact (Vogel et al. 1999). The upper contact of the Agnew intrusion and overlying Huronian Supergroup rocks is preserved on the eastern side of the intrusion where it is observed to be a disconformable and locally unconformable contact (James et al. 2002).

Stratigraphy

The stratigraphy of the Agnew intrusion **(Fig. 2.15)** is described in detail in a Ph.D. thesis (Vogel 1996) and summarised elsewhere (Vogel et al. 1998a; Vogel et al. 1999; James et al. 2002; Easton et al. 2010). This previous work has subdivided the stratigraphy of the Agnew intrusion into three series (Marginal, Lower and Upper) which are thought to be correlative with the Lower, Main and Upper series of the East Bull Lake intrusion respectively (James et al. 2002).

Marginal Series

The Marginal Series is ~200 m thick and is comprised of the Marginal Gabbronorite Zone and the Marginal Leucogabbronorite Zone. The Marginal Gabbronorite Zone is found at the base of the Agnew intrusion and is composed of a ~200 m thickness of massive, medium grained, olivine-gabbronorite which shows chilled contacts and is associated with younger dykes which cut the whole stratigraphy (James et al. 2002). Vogel et al. (1999) interprets the Marginal Gabbronorite Zone as being a product of a later magma pulse which intruded along the base of the Agnew intrusion.

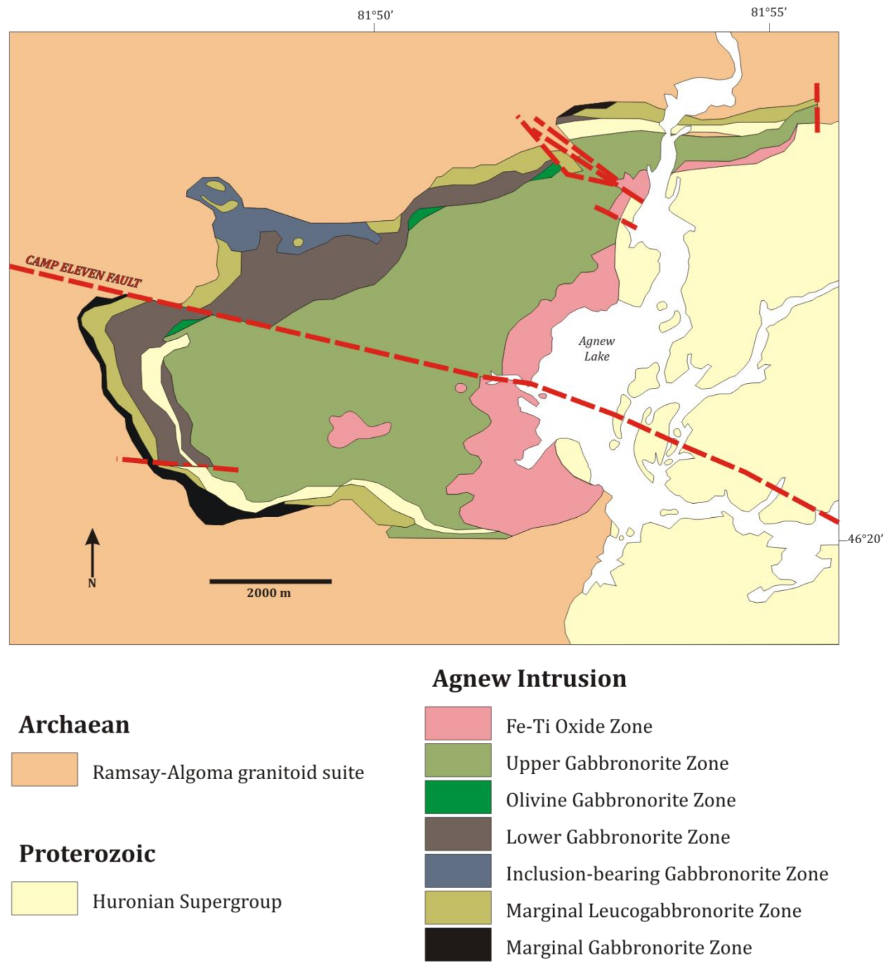

Fig. 2.14. Geological map of the Agnew intrusion. Modified from Vogel et al. (1999).

The Marginal Leucogabbronorite Zone is the lowest part of the Agnew intrusion proper and is subdivided into three units (James et al. 2002); the Varitextured Unit (present in the south and west), the Mottled Unit (present in the north) and the Nodular Unit (present in the northwest). As the name suggests, the Varitextured Unit is variable both in texture and composition. The unit generally grades from melanocratic at the base to leucocratic-granophyric at the top. The variability in texture of the unit manifests itself as grain size variations from medium-grained to pegmatitic over metre-scale areas of outcrop (Vogel 1996). The Varitextured Unit also contains xenoliths which range in composition from granitic (interpreted to be derived from underlying Archaean host rocks) to ultramafic, which are similar in character to the mafic inclusions preserved in the Inclusion-Bearing Zone in the East Bull Lake intrusion (Peck et al. 1995; Vogel et al. 1998a). The Mottled Unit is similar to the underlying Varitextured Unit in that it ranges in composition from melanocratic at the base to leucocratic higher up, with granophyre occurring locally at the top of the unit. This unit also contains large (up to 10 cm) amphibolitised orthopyroxene oikocrysts which occur in an anorthositic groundmass and can account for up to ~70% of the rock volume (Easton et al. 2010). The Nodular unit is limited to the upper part of the Marginal Leucogabbronorite Zone in the northwest part of the intrusion, where it is exposed as a <50 m thick horizon of homogenous lenses of densely-packed, equidimensional plagioclase nodules held within a gabbronorite-pyroxenite matrix. The nodules are made up of aggregates of plagioclase crystals up to 1cm in length and account for 70-90% of an outcrop. Vogel (1996) notes that the plagioclase aggregates in the Nodule unit are similar to the anorthosite xenoliths in the Inclusion-Bearing unit of the East Bull Lake intrusion.

Lower Series

The ~800 m thick Lower Series is made up of the Inclusion-bearing Zone and the Lower Gabbronorite Zone. The ~180 m thick Inclusion-bearing Zone is a texturally and compositionally complex unit which ranges in composition from pyroxenite-gabbronorite-anorthosite and in grain size from medium grained to pegmatitic which the two seemingly unrelated (Vogel 1996). The inclusions present in the Zone are dominated by aggregates of plagioclase, similar to those observed in the underlying nodular unit. Other, less volumetrically significant inclusions include partially melted xenoliths derived from the Archaean footwall and also melanogabbronorite pods similar to those observed in the underlying Varitextured unit (Easton et al. 2010).

The Inclusion-Bearing Zone grades into the overlying Lower Gabbronoritic Zone which itself signifies the first appearance of centimetre-scale modal layering in the Agnew intrusion. Above a ~225m thick basal massive unit, the layering in the Lower

Gabbronorite Zone is defined by laterally restricted, alternating 3 cm - 1.5 m thick bands of coarse grained and equigranular gabbronoritic-leucogabbronoritic rock which show gradational to sharp modal changes (Vogel 1996).

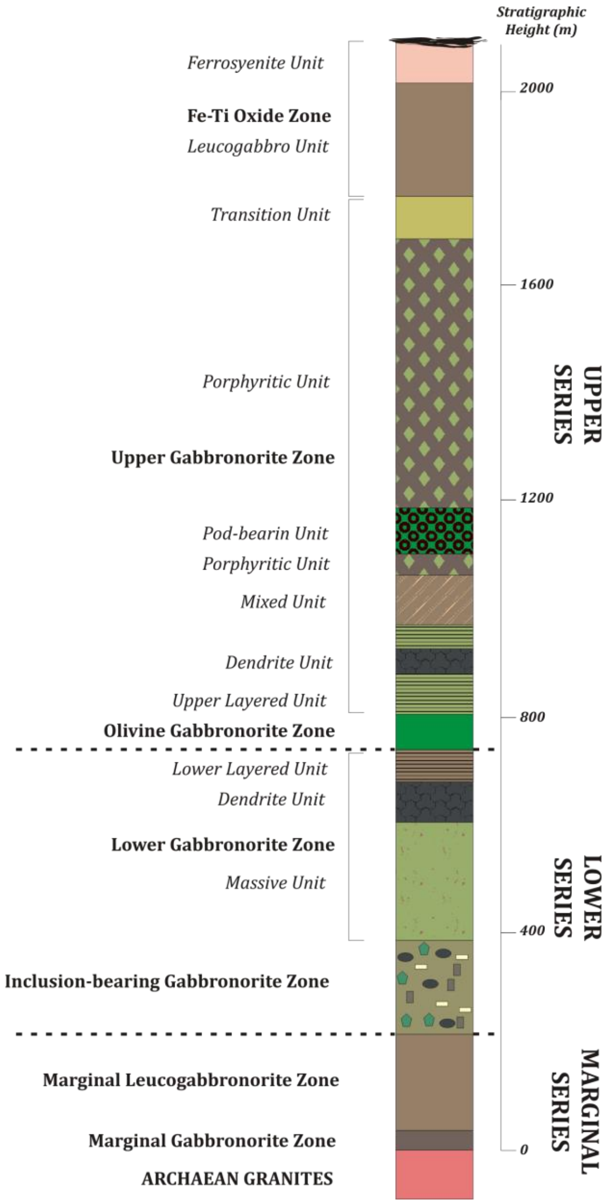

Fig. 2.15. Stratigraphy of the Agnew intrusion. Modified from Vogel et al. (1999).

<u>Upper Series</u>

The Upper Series is subdivided into the Olivine Gabbronorite, Upper Gabbronorite and Fe-Ti Oxide Zones (Vogel et al. 1999). The Olivine Gabbronoite Zone at the base of the Upper Series is exposed as a ~50m thick well-layered unit of centimetre-metre scale bands of olivine gabbronorite, leucogabbronorite and olivine melanogabbronorite. The Upper Gabbronorite zone accounts for the majority of the

Upper Series rocks and at its base records a complicated stratigraphy of layered gabbronorites and leucogabbronorites which locally preserve dendritic textures and is Inclusion-Bearing (Easton et al. 2010).

The thickest unit of the Upper Series, and the Agnew intrusion as a whole, is the ~500 m thick Porphyritic Unit. This unit is characterised by medium grained gabbronorites which contain variable amounts (up to 70%) of 1-4 cm wide plagioclase phenocrysts and glomerophenocrysts (Vogel 1996). The layering in the Porphyritic Unit is defined by centimetre-metre scale layers of plagioclase-porphyritic rocks and intervening equigranular gabbronoritic rocks. Near the base of the Porphyritic Unit, slumping and magmatic deformation within the crystal pile has formed the Pod-bearing Unit, indicated by <1m diameter, rounded pods of porphyritic leucogabbronorite and granophyre within a porphyritic gabbronorite matrix (Vogel et al. 1999). The Transition Unit is found at the top of the Upper Gabbronorite Zone and forms a layered sequence of gabbronorite and leucogabbronorites.

The upper most zone of the Agnew Intrusion is made up of the Fe-Ti Oxide Zone which is 200-400m thick and shows evidence of erosion prior to the deposition of overlying strata (Vogel et al. 1999). The zone is made up of the Leucogabbronorite Unit and the Ferrosyenite Unit and marks the first occurrence of titanomagnetite in the Agnew intrusion. The Leucogabbronorite Unit is made up of massive, coarse grained, pyroxene-normative leucogabbro with large (2-3cm) titanomagnetite masses. The Ferrosyenite Unit grades upwards from dark ferrosyenite at the base to light alkali-feldspar granite near the unconformity between the Agnew intrusion and overlying sediments.

River Valley

The River Valley intrusion is a texturally and mineralogically layered gabbronoritic intrusion, preserved between the Red Cedar Lake and Pardo granitic-gneissic rocks and the Palaeoproterozoic Huronian Supergroup (Easton 2007). The River Valley intrusion crops out approximately 65 km east-northeast of Sudbury, Ontario and has an areal extent of ~200 km^2 which records a minimum stratigraphic thickness of 1000 m **(Fig. 2.16)**. The intrusion has been significantly deformed during the

Grenville orogeny and intrusive contacts between the top of the intrusion and overlying Huronian Supergroup rocks have been obscured and are commonly thrust-bounded (James et al. 2002). Intrusive contacts between the Agnew intrusion and Red Cedar Lake gneisses and granitoids, however, are defined by a fine-medium grained gabbro which may be a chilled margin of the intrusion (James et al. 2002).

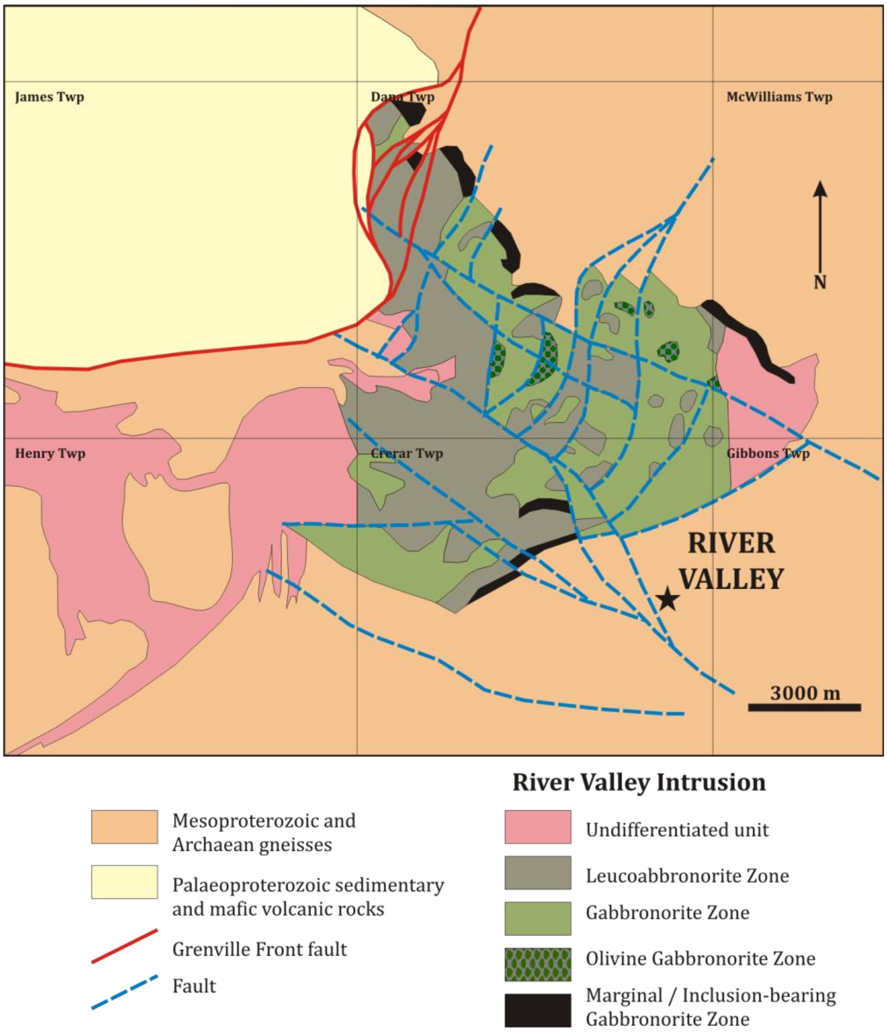

Fig. 2.16. Geological map of the River Valley intrusion. Modified from James et al. (2002).

Stratigraphy

The deformation of the River Valley intrusion during the Grenville orogeny means that the stratigraphy of the River Valley intrusion is much harder to interpret than other intrusions in the suite. However, the northern half of the intrusion has been mapped by (Easton and Hrominchuk 1999; Hrominchuk 1999; Hrominchuk 2000) and these interpretations have been refined and summarised by James et al. (2002) and Easton (2003). Unlike the East Bull Lake and Agnew intrusions, separate series of rocks have not been delineated in the River Valley intrusion and instead, the intrusion has been subdivided into five lithological zones, namely, the Marginal Zone, Inclusion-bearing Zone, Olivine Gabbronorite Zone, Gabbronorite Zone and Leucogabbronorite Zone **(Fig. 2.17)**.

The Marginal Zone rocks immediately adjacent to the contact are chaotic mixtures of fragmented inclusions of footwall rocks set in a fine-medium grained gabbronorite matrix (Hrominchuk 2000). The country rock fragments are commonly alkali feldspar granites and quartz feldspathic or amphibolitic gneisses and the gabbronorite matrix is composed of cumulus plagioclase and orthopyroxene with lesser amounts of clinopyroxene and accessory magnetite, quartz, biotite and sulphides (Easton 2003). Alteration of the gabbronoritic matrix is characterised by replacements of pyroxene and plagioclase by amphibole and epidote respectively. The ~170 m thick Marginal Zone grades into the overlying Inclusion-bearing Zone, the contact between the two being defined by the first occurrence of mafic-ultra mafic autoliths inclusions within the rock (Easton and Hrominchuk 1999). The matrix of the Inclusion-bearing Zone is composed of fine-medium grained gabbro-gabbronorite. The contact between the Inclusion-bearing Zone and the overlying Olivine Gabbronorite Zone is sharp and erodes downwards into the Inclusion-bearing Zone (James et al. 2002). The Olivine gabbronorite Zone grades upwards from olivine-rich cumulates at the base of the zone into troctolites and gabbronorites at the top of the zone in a series of 0.3-1.5 m thick layers. The Gabbronorite Zone is an approximately 200 m thick zone of alternating metre-thick layers of norite, gabbronorite and leucogabbronorite, which themselves record fractionation from norites at the base of a layer to gabbronorites at the top (Easton 2003). The Leucogabbronorite Zone accounts for the uppermost ~200m of the intrusion and is composed of non-layered, massive, medium-coarse grained leucogabbronorites and anorthosites.

2.2.2.2. Age

East Bull Lake Intrusion

Krogh et al. (1984) reports the most widely cited age for the East Bull Lake intrusion of 2480_{+10}^{-5} Ma. This age is obtained from U-Pb TIMS analysis of two fractions of baddeleyite and one fraction of zircon obtained from an olivine gabbro from near the top of the intrusion. This age supersedes a whole-rock Sm-Nd age of 2472 Ma (McCrank et al. 1989) which is associated with a large (±76 Ma) error.

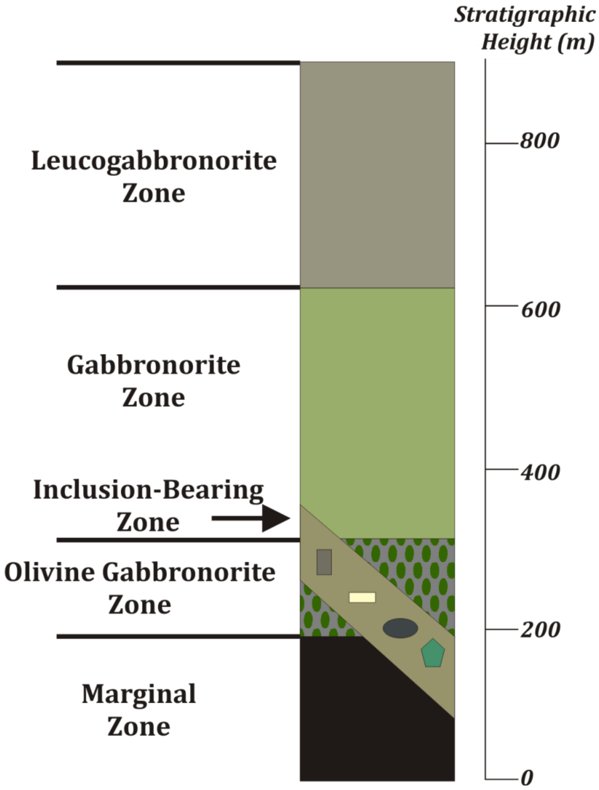

Fig. 2.17. Stratigraphy of the River Valley intrusion. Modified from James et al. (2002).

Agnew Intrusion

The only age supplied in the literature for the Agnew Lake intrusion is presented by Krogh et al. (1984) who dates the intrusion as 2491±5 Ma. This age is obtained from U-Pb TIMS analysis of three zircon fractions obtained from a massive, medium grained alkali feldspar granite from the top of the intrusion.

River Valley Intrusion

The most widely cited age for the River Valley intrusions is reported as unpublished data from Larry Heaman by Easton et al. (1999). The age of 2476^{+2}_{-1}Ma was obtained by U-Pb TIMS analysis of baddeleyite and zircon fractions from the layered gabbronorite unit from the centre of the intrusion. This U-Pb age supercedes several other ages reported by Ashwal and Wooden (1989) who used whole-rock Pb-Pb, Sm-Nd and Rb-Sr methods to obtain ages that range between 1960-2562 Ma which are associated with ±68-165 Ma errors.

2.2.2.3. Tectonic Setting

The most widely accepted view regarding the tectonic setting of the East Bull Lake suite is that the intrusions were emplaced during mantle plume-driven continental break-up as part of a ‘rifting suite’ which includes the Matachewan dyke swarm and Huronian Supergroup volcanics (Vogel et al. 1998a; James et al. 2002; Easton et al. 2010). Much of this interpretation is based on the broadly coeval nature of the East Bull Lake suite, Huronian continental flood basalts and radiating Matachewan dykes, the timing, field relationships and inferred igneous volumes of which are argued to be only adequately explained by mantle-plume magmatism (Heaman 1997; Ernst and Buchan 2001; James et al. 2002).

Vogel et al. (1998a) studied the East Bull Lake suite in terms of its parental melt geochemistry and magmatic sources. They noted that the East Bull Lake suite parental melts are characterised by trace-element chemistry usually associated with subduction-modified sub-continental lithospheric magmas more commonly found in volcanic arc environments. Vogel et al. (1998a) notes, however that the chemical signature recorded by the East Bull Lake suite is shared by most >2 Ga Archaean greenstone volcanic rocks and dyke swarms, which may indicate that the Archaean-Palaeoproterozoic mantle differed both in composition and structure from the modern mantle. As an alternative to a transient mantle composition, Vogel et al. (1999) suggest that the intra-continental Archaean-Palaeoproterozoic magmatism (including that which formed the East Bull Lake suite) may have been driven by thermal plumes, which rather than providing magma, provided heat to promote melting in shallower mantle rocks which had already been compositionally modified by subduction processes.

2.2.2.4. Ni-Cu-PGE Mineralisation

East Bull Lake Intrusion

The ‘contact-type’ Ni-Cu-PGE mineralisation observed in the East Bull Lake intrusion is described in detail by (Chubb 1994; Peck et al. 1995; Peck et al. 2001; James et al. 2002). PGE-enriched, disseminated sulphide mineralisation is observed near the base of the intrusion in the Marginal and Lower series rocks (Easton et al. 2010) with the most abundant and economically interesting mineralisation hosted in the Inclusion-Bearing Zone within a few tens of metres of the footwall contact of the intrusion.

In the Inclusion-Bearing Zone, the sulphide mineralisation occurs as 0.5-5 cm irregularly shaped ‘blebby’ (and probably recrystallised) aggregates of pyrrhotite (with locally abundant pyrite), chalcopyrite and minor pentlandite (Peck et al. 2001; James et al. 2002). The mineralisation is predominantly disseminated through the gabbronoritic-leucogabbronoritic matrix, but also to a lesser extent within the pyroxenite and melagabbronorite pods in present in the zone (James et al. 2002). PGE abundances show strong correlations with other chalcophile elements indicating that PGE concentration is partially controlled by the amount of sulphide present in the rock (Peck et al. 2001). In the Inclusion-Bearing Zone, PGMs occur in, or proximal to, sulphides as Pd-Be-Te minerals and sperrylite.

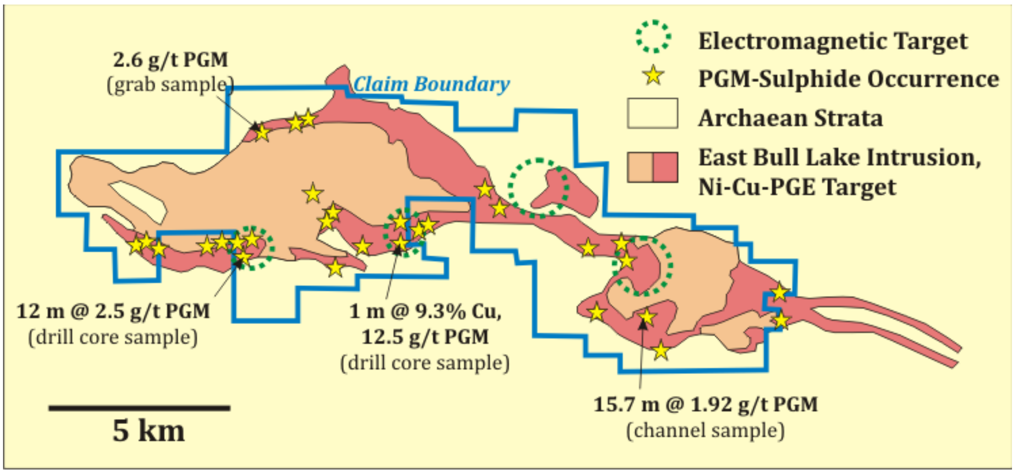

Fig. 2.18. Map showing notable Ni-Cu-PGE mineralisation in the East Bull Lake intrusion. Modified from Mustang Minerals Press Release (2008).

Drilling has demonstrated that despite the ‘nuggety’ dissemination of sulphide mineralisation, sulphides account for, on average, 0.5-2% of the Inclusion-Bearing Zone and grade between 100 ppb - ~11 ppm Pt+Pd+Au (Peck et al. 2001). The sulphides themselves are characterised by Cu/Ni and Pd/Pt values of 0.6-4.8 and 1.6-4.3 respectively (James et al. 2002).

Peck et al. (2001) argues that the contact-type of mineralisation observed in the East Bull Lake intrusion is the product of a two-stage fractionation process. The initial magma to fill the East Bull Lake chamber reached sulphur saturation (while retaining its chalcophile element budget) during its ascent from a deeper, fractionating magma chamber. Once inside the East Bull Lake magma chamber, the dense immiscible sulphide liquid began to accumulate at the margins of the intrusion. Repeated injections of metal-bearing silicate melt into the intrusion and subsequent turbulent convection led to interaction between the immiscible sulphide liquid and large quantities of silicate melt, thus enriching the PGE tenor of the mineralisation to the levels observed in the intrusion.

Agnew Intrusion

The types of Ni-Cu-PGE mineralisation observed in the East Bull Lake intrusion are described in detail by Vogel (1996), Vogel et al. (1999) and James et al. (2002). Like the East Bull Lake intrusion, the most impressive Ni-Cu-PGE mineralisation found in the Agnew intrusion is hosted as ‘contact-type’ disseminated sulphides within the gabbronoritic matrix of inclusion-bearing rocks close to the margins of the intrusion (James et al. 2002). In these units, the sulphide mineralisation manifests itself as fine grained disseminations or coarse grained (up to 3 cm) blebs composed of chalcopyrite and pyrrhotite and lesser pentlandite (Vogel 1996). Sulphide mineralisation is variable in abundance throughout the intrusion-bearing units, but is estimated by James et al. (2002) to average around 0.5-2 %. The sulphides themselves are characterised by Cu/Ni and Pd/Pt values of 0.2-20 and 1-3 respectively (Vogel 1996). A second zone of mineralisation occurs within the Fe-Ti Oxide Zone near the top of the intrusion at the boundary between the Leucogabbro and Ferrosyenite units. In this zone, sulphides form fine grained disseminations which account for 1-2 % of the rock volume and are dominated by chalcopyrite and pyrrhotite (James et al. 2002).

James et al. (2002) argue that the similarities in texture and lithology between the mineralised marginal rocks in the East Bull Lake and Agnew intrusions suggest that Peck et al.’s (2001) model of enrichment of an immiscible sulphide melt by interaction with repeated injections of silicate magma for the East Bull Lake intrusion also applies to the Agnew intrusion. Alternatively, Vogel (1999) argues that the Agnew magma was intruded as a sulphur-undersaturated magma which was contaminated by host rocks close to the margin of the intrusion, and through this contamination, reached sulphur saturation and precipitated Ni-Cu-PGE bearing sulphides. Regarding the upper zone of mineralisation, James et al. (2002) argues that this mineralisation formed during closed-system fractionation of sulphur-undersaturated magma pulses which underwent fractional crystallisation and produced an immiscible sulphide melt, which itself crystallised to form a ‘reef’ of disseminated sulphide on top of the crystal pile near the top of the intrusion.

River Valley Intrusion

Ni-Cu-PGE mineralisation preserved in the River Valley intrusion is described by James et al. (2002) and Easton (2003). Mineralisation in the River Valley intrusion is similar to that observed in the other East Bull Lake suite intrusions in that the bulk of the mineralisation occurs as disseminated-blebby aggregates of chalcopyrite + pyrrhotite hosted in inclusion-bearing rocks (Marginal and Inclusion-bearing Zones) within a few tens of metres of the basal contact (James et al. 2002).

The mineralisation within the Marginal and Inclusion-bearing Zones is variable, with disseminated sulphides primarily hosted in the gabbroic-gabbronoritic matrix becoming more blebby-massive with increasing proximity to included fragments of country rock (Easton and Hrominchuk 1999; Hrominchuk 1999; Hrominchuk 2000). The sulphides in the mineralised parts of the intrusion are characterised by Cu/Ni and Pt/Pd radios of 2 and 0.4 respectively and contain up to 0.5 g/t Pt+Pd+Au (James et al. 2002).

Hrominchuk (2000) suggested that local contamination of the River Valley magma caused by assimilation of country rock fragments caused the magma to become locally saturated in sulphur and precipitate Ni-Cu-PGE bearing sulphides. This interpretation was based on observations which show that the most abundant mineralisation occurs in rocks which show good evidence of crustal contamination (resorbed fragments, blue-quartz eyes and elevated Ti, U, Na, Zr, Y and LREE contents) whereas mineralisation is weak or absent in rocks which lack such evidence of contamination (Hrominchuk (2000).

Summary

The marginal zones of the East Bull Lake Intrusive suite have been the subject of sustained exploration for Ni-Cu-PGE mineralisation for the last two decades following initial work on the intrusions by the Ontario Geological Survey (Peck et al. 1991; Peck and James 1992; Peck et al. 1995). Active exploration is currently underway on the East Bull Lake **(Fig. 2.18)** and River Valley intrusions which have been shown to contain significant mineralized zones, which in the case of River Valley, contain inferred resources of 35.9 Mt grading at 0.53 g/t Pd+Pt+Au, 0.06 wt.% Cu and 0.03 wt.% Ni (Pacific North West Capital Corp. News Release, 1/5/2012).

2.2.3. Thessalon Formation

2.2.3.1. Geology

The Huronian Supergroup is a 5-12 km thick volcanic-sedimentary succession which sits unconformably on the Archaean basement rocks of the southern Superior Province. The Huronian crops out discontinuously west from the east shore of Lake Superior, through Sudbury, to Lake Timiskaming **(Fig. 2.19)**.

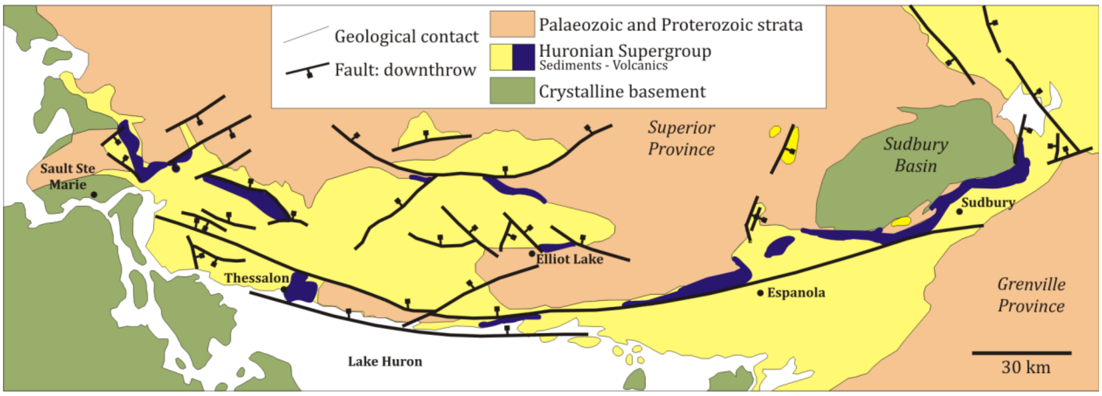

Fig. 2.19. Geological map showing the extent of the Huronian Supergroup in southern Ontario. Modified from Jolly et al. (1992).

The Huronian Supergroup is subdivided into four lithostratigraphic formations **(Fig. 2.20)**; which from the base, include the Elliot Lake, Hough Lake, Quirke Lake and Cobalt Groups (Bennett et al. 1991; Jackson 2001). The Elliot Lake Group is of interest to the current study as it contains the only ~2.45Ga volcanic rocks preserved within the supergroup (Krogh et al. 1984) which are also linked to continental breakup of Superia and the formation of the Superia LIP (Heaman 1997; Easton et al. 2010; Ernst and Bleeker 2010). The Elliot Lake group is subdivided into the Livingstone Creek, Thessalon, Matinenda and McKim Formations (Bennett et al.

1991) and the volcanic rocks of interest form part of the 330-1200 m thick Thessalon Formation.

The Thessalon Formation volcanics are predominantly composed of fine-medium grained basaltic, basaltic-andesitic, andesitic and subordinated rhyolitic flows, the more mafic members being commonly porphyritic and/or amygdular, the amygdales having been infilled with chlorite+quartz+epidote (Jolly 1987a; Bennett et al. 1991). Maximum greenschist facies metamorphism has altered the mafic rocks' primary groundmass mineralogy to chlorite-albite-epidote-actinolite assemblages, while alteration of augite and plagioclase phenocrysts is limited to crystal margins (Jolly 1987a; Jolly 1987b). Opaque phases have largely been replaced by haematite and sphene, though some primary titanomagnetite is preserved in the cores of large masses of the mineral (Jolly 1987a). Bennett et al. (1991) presents evidence of both ashfall tuffs and pillow basalts within the Thessalon Formation, indicating that eruptions occurred both subaerially and subaqueously during deposition of the formation.

2.2.3.2. Age

The eruptive age of the Elliot Lake Group is bracketed by the 2491±5 Ma Agnew intrusion which the group unconformably overlies (Krogh et al. 1984; Vogel et al. 1999) and the $2450^{+25}/_{-10}$ Ma Copper Cliff Rhyolite which lies conformably at the top of the Elliot Lake Group volcanic rocks (Krogh et al. 1984). The age of the Copper Cliff Rhyolite was obtained by U-Pb analysis of five zircon samples, two of which were obtained from cracked and abraded grains (Krogh et al. 1984). The cracked grains define a maximum age of 2475 Ma, while the uncracked grains define an age of $2444^{+8}/_{-4}$ Ma. Taken together, Krogh et al. (1984) suggest that the best age estimate for the Copper Cliff Rhyolite is $2450^{+25}/_{-10}$ Ma. The age of the mafic rocks of the Eliot Lake Group is further bracketed by the 2477±9 Ma Murray Pluton which intrudes the base of the group near Sudbury (Bennett et al. 1991; Krogh et al. 1996).

The contact relationships between the dated intrusions and the mafic volcanic rocks of the Elliot Lake Group as described above, bracket the eruption of the mafic volcanic rocks between 2491±5 Ma and 2477±9 Ma.

2.2.3.3. Tectonic Setting

The Huronian Supergroup has long been interpreted to represent prolonged sedimentation in an extending Archaean basin (Dietz and Holden 1966; Bennett et al. 1991; Roscoe and Card 1993; Bekker et al. 2005). The Thessalon Formation volcanic rocks in the Elliot Lake Group at the base of the Huronian Supergroup are thought to be the result of the initial rifting event (Phinney and Halls 2001; Ernst and Bleeker 2010). More recently, a mantle plume has become the most favoured mechanism for driving the rifting event which led to the deposition of the Huronian Supergroup (Heaman 1997; Ernst and Buchan 2001).

Jolly (1987a; 1987b) and Jolly et al. (1992) studied the geochemistry of the Thessalon volcanics and noted that their trace element chemistry is characterised by LILE and LREE enrichments relative to depletions in the HREE and other HFSE – a signature more commonly associated with subduction zone magmas. Jolly et al. (1992) argues that the chemistry recorded by the Thessalon volcanics cannot be due to contamination of the most primitive Huronian samples with continental crust and is instead more likely to have been inherited from an upper mantle source which had been modified by subduction processes, probably during accretion and cratonisation of the Superior craton during the Archaean.

2.2.3.4. Ni-Cu-PGE Mineralisation

Large scale Ni-Cu-PGE sulphide mineralisation has not been observed in the Thessalon Formation and the volcanic rocks are not the subject the of any past or present exploration projects. Chalcopyrite mineralisation is observed locally within amygdales (Stupavsky and Symons 1983), but is most likely a post-eruption hydrothermal phenomenon rather than a primary magmatic one.

2.2.4. Blue Draw Metagabbro

2.2.4.1. Geology

The Blue Draw Metagabbro (BDM) is an 800 m thick (~6 km^2 outcrop area) layered amphibolite sill which crops out in the Black Hills uplift, South Dakota, immediately west of Nemo township.

The ~7000 km^2 Black Hills Uplift **(Fig. 2.21)** lies along the eastern margin of the Wyoming Province and is one of only a few areas which expose the Precambrian basement of the province. The rocks preserved in the Black Hills were uplifted during the ~75-35 Ma Laramide Orogen and expose a complex sequence of basal metaconglomerates and quartzites which are overlain by quartzites, graywackes, iron formations, metavolcanics, gabbros, schists, phyllites and slates which have been deformed during at least three to five separate events (Redden et al. 1990; Hill 2006).

The BDM intrudes the Boxelder Creek Quartzite which is the oldest recognised sedimentary sequence to have been deposited on the ~2.6 Ga Little Elk Terrane. The ~3300 m thick Boxelder Creek Quartzite is composed of a basal assemblage of taconite-bearing and chloritic conglomerates, laterally changing to phyllites and dolomitic marbles which are overlain by granular quartzites, iron formations and fluvially deposited metaconglomerates (Lee 1996; Hill 2006).

Stratigraphy

Initial work on the BDM by Woo (1952) described the intrusion as a 1 km thick layered sill which exposes a fractionated sequence of serpentinite at the base which grades into hornblendite, plagioclase gabbro-diorite, biotite granodiorite and discontinuous dioritic pegmatite **(Fig. 2.22)**. The margins of the intrusion are concordant with bedding in the Boxelder Creek Quartzite which, in the study area, dips 70-80° towards the northwest. A series of dominantly NW-SE trending faults have removed the side-wall contacts of the intrusion and have otherwise dismembered the BDM such that slivers of metamorphosed gabbro thought to be correlative with the BDM crop out at several locations throughout the area (Dahl et al. 2006).

Based on metamorphic mineral assemblages, Maranate (1979) divided the BDM into a ~130 m thick Serpentinite unit which is successively overlain by the ~100 m thick Lower Hornblendite unit and the ~250 m thick Amphibolite which is separated into Lower and Upper units by the ~50 m thick Upper Hornblendite unit which crops out discontinuously at ~380 m from the base of the intrusion. The Upper Amphibolite unit is overlain by a ~60 m thick Border Zone of biotite- and quartz-rich rocks which, close to the margin of the intrusion, contain xenoliths of the Boxelder Creek

Quartzite **(Fig. 2.22)**. This study will use an updated stratigraphic nomenclature which is described in later chapters.

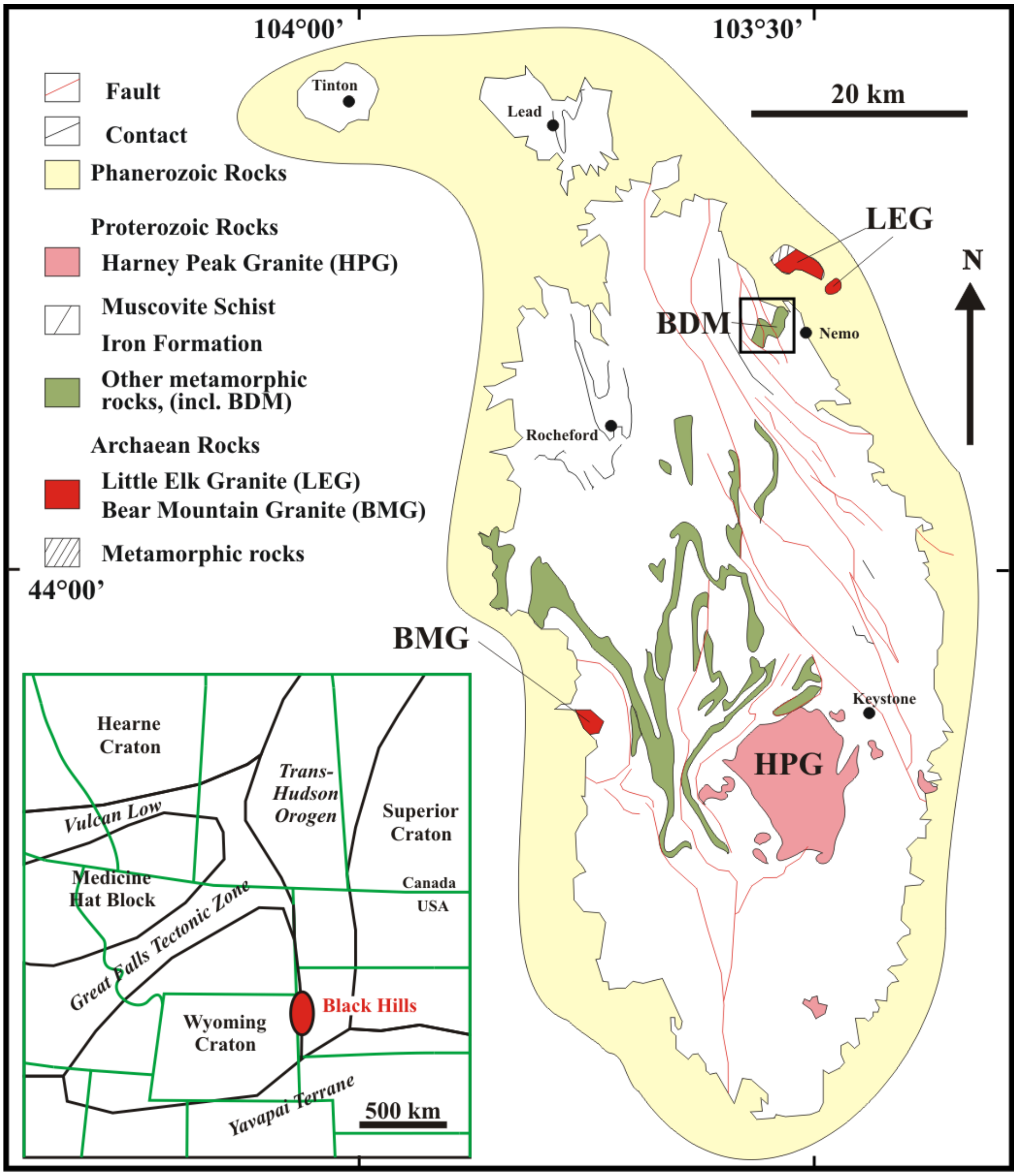

Fig. 2.21. Geological map of the Black Hills Uplift showing the location of the Blue Draw Metagabbro (BDM). Modified from Dahl et al. (2006).

2.2.4.2. Age

The BDM is one of several Archaean-Palaeoproterozoic metamorphosed mafic intrusions preserved within the Black Hills, but is significant in that it is the only one for which a reliable date has been obtained. The best age estimate for the intrusion of the BDM is a ^{207}Pb/^{206}Pb titanite age of 2480±6 Ma from a dioritic pegmatite near the stratigraphic top of the sill (Dahl et al. 2006). This age supersedes previous work by Redden et al. (1990) who interpreted the BDM to have been intruded 2170±100 Ma based on a highly discordant array of U-Pb zircon data from the same dioritic pegmatite.

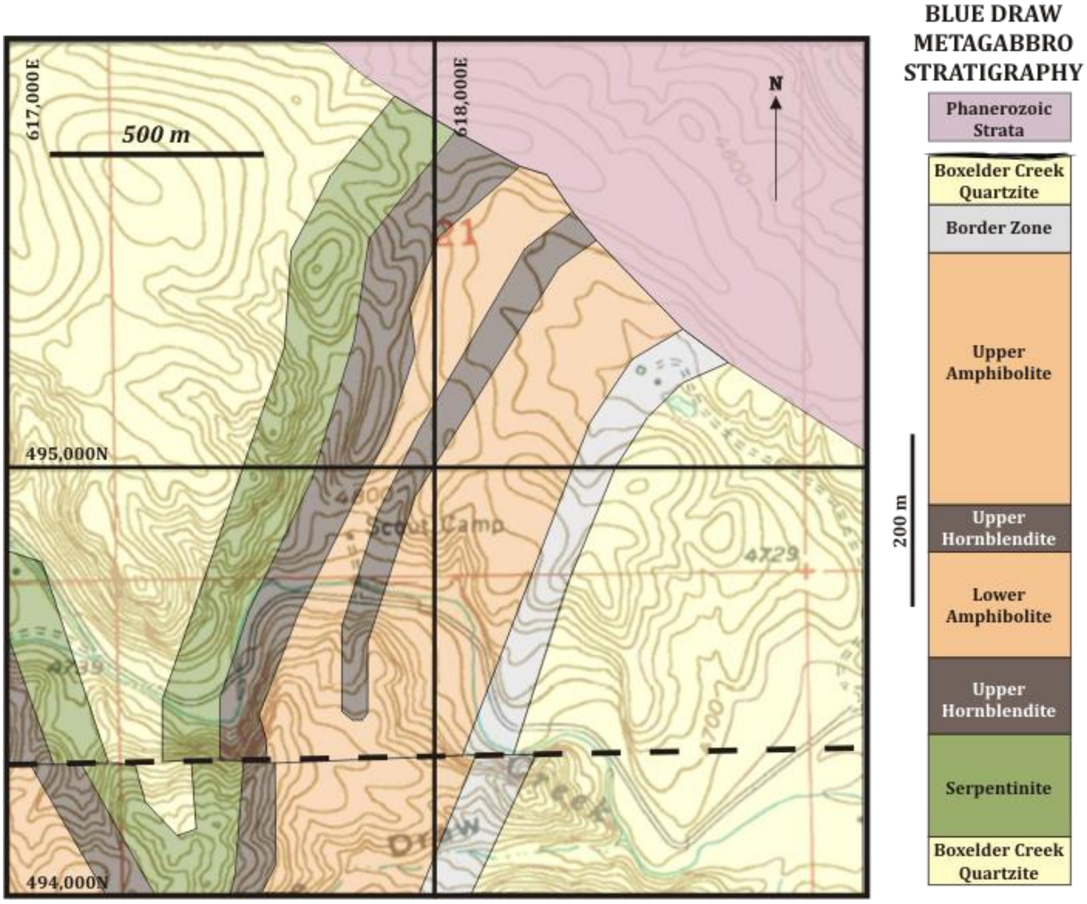

Fig. 2.22. Geological map and stratigraphy of the Blue Draw Metagabbro. Modified from Maranate (1979).

2.2.4.3. Tectonic setting

Two tectonic settings for the BDM are proposed in the literature. The majority opinion favours an intra-continental rift setting, within which, magmatism and rifting developed in response to an incident mantle plume beneath an Archaean supercontinent of which the Wyoming province and Superior craton were a part. This intra-continental rift setting is inferred from both overlapping age data from intrusions on the Superior and Wyoming (Dahl et al. 2006) and stratigraphic correlations between the rifted margin sediments which host the BDM, and other units preserved on the Superior craton and Wyoming Province (Roscoe and Card 1993). The Boxelder Creek Quartzite, along with correlative units in the Huronian

Supergroup (Superior Province) and Snowy Pass Supergroup (Wyoming Province) have been interpreted to have formed in an intracratonic rift environment between ~2.55-2.48 Ga in response to mantle-plume-driven continental break-up (Roscoe and Card 1993; Heaman 1997; James et al. 2002).

Conversely, Van Boening and Nabelek (2008) interpreted the BDM to be a product of an episode of subduction-related continental arc magmatism which persisted along the eastern margin of the Wyoming Province between at least ~2.56-2.48 Ga. They base this interpretation on geochemical similarities between the BDM and the ~2.56 Ga arc-related, calc-alkaline Little Elk Granite. Van Boening and Nabelek (2008) also dismiss the possibility of a genetic link between the BDM and the East Bull Lake suite of layered intrusions on the Superior craton as postulated by others (Dahl et al. 2006; Söderlund et al. 2010) based on differences in trace element chemistry of the two suites and the consistency of BDM samples plotting in Calc-alkaline basalt fields on tectonic discrimination diagrams.

2.2.4.4. Ni-Cu-PGE Mineralisation

Despite the potential cogenetic origin and well documented similarities between the significantly mineralised East Bull Lake suite and BDM, the latter has not previously been explored for Ni-Cu-PGE mineralisation.

2.2.5. Leopard Dyke Swarm

2.2.5.1. Geology

The Leopard dyke swarm is made up of numerous of E-NE trending dykes which intrude the crystalline Archaean basement rocks of the Wyoming craton (Harlan 2005). The Leopard dykes exhibit a similar preservation style to the Blue Draw Metagabbro in that the dykes are exposed in tectonic uplifts (namely the Bighorn Mountains and the Beartooth Mountains) of the craton which were exhumed during the ~75 Ma Laramide orogeny. The Bighorn Mountains and Beartooth Mountains tectonic uplifts which expose the Leopard dykes are laterally separated by ~150 km of Phanerozoic cover sequences, indicating that the Leopard dyke swarm intrudes an area of at least 20,000 km^2 in the subsurface.

In outcrop, the Leopard dykes generally strike 080°, are vertical or dip steeply to the south and can be traced along strike for up to five kilometres (Heimlich and Manzer 1972). The dykes pinch and swell along strike but are usually ~15 m thick. The texture and modal mineral compositions of the dykes vary both along strike and across the width of the dykes. The texture of non-porphyritic dyke margins and the groundmass more phenocryst-dominated part of the dykes varies from ophitic-subophitic to xenomorphic granular (Heimlich and Manzer 1972). The mineralogy of these non-porphyritic dyke rocks is dominated by altered plagioclase and clinopyroxene with trace amounts of orthopyroxene and opaque phases. The plagioclase in the groundmass accounts for ~48-54% of the rock volume and forms anhedral-subhedral, lath-shaped crystals which have been variably saussuritised. The clinopyroxene in the groundmass occurs primarily as augite with lesser amounts of pigeonite and accounts for 40-45% of the rock volume. The clinopyroxene forms anhedral-subhedral, equant crystals which vary from fresh to totally-replaced by radiating aggregates of acicular actinolite and hornblende. In phenocryst-dominated samples, plagioclase phenocrysts can account for up to 65% of the rock volume and form euhedral-subhedral crystals which are usually ~8 cm in diameter, but can be up to ~20 cm. Similar to the plagioclase in the groundmass, the plagioclase phenocrysts are also variably saussuritised and often shown an increase in alteration intensity towards the centre of the phenocryst (Heimlich and Manzer 1972).

Prior to this work, relatively little was known about the geochemistry of the Leopard dykes. Heimlich and Manzer (1972) provide the only geochemical data for the swarm and report major element analyses for four samples taken from two Leopard dykes. This limited geochemical data suggest that the Leopard dykes are tholeiitic in composition.

2.2.5.2. Age

The only absolute age reported for the Leopard dyke swarm comes from whole-rock Rb-Sr and K-Ar dates obtained from six Leopard dykes exposed in the Beartooth Mountains (Larson et al. 1973). These six samples all yield Rb-Sr ages of 2.55 Ga, but highly variable (1.69-2.16 Ga) K-Ar ages. Larson et al. (1973) reports these ages as personally communicated data without any extra information regarding the dating work and any potential caveats associated with the analysis. Moreover, the Rb-Sr and

K-Ar dating methods are known to be significantly affected by even low-intensity alteration (Graham et al. 1993). For these reasons, Harlan (2005) suggests that the Leopard dykes lack any sort of robust geochronological control and can only be assumed to be Palaeoproterozoic based on currently exposed field relationships.

U-Pb dating of mafic dyke material from the Wyoming craton (including the Leopard dykes) is currently being undertaken at the University of Wyoming (Richard Ernst, personal communication 2012). The result of this work should resolve key questions regarding episodes of mafic magmatism and supercontinent cycles, which have affected the Wyoming craton.

2.2.5.3. Tectonic Setting

Given the paucity of modern and in-depth studies regarding the Leopard dykes, no concerted attempt has been made to understand the tectonic setting of the swarm. However, based on similar appearances **(Fig. 2.23)** and overlapping palaeomagnetic pole directions (Larson et al. 1973), Heaman (1997) speculated that the Leopard dykes are coeval and cogenetic with the Matachewan dyke swarm on the Superior craton and represent a fragment of a giant radiating swarm which was intruded during mantle-plume induced rifting of an Archaean supercontinent.

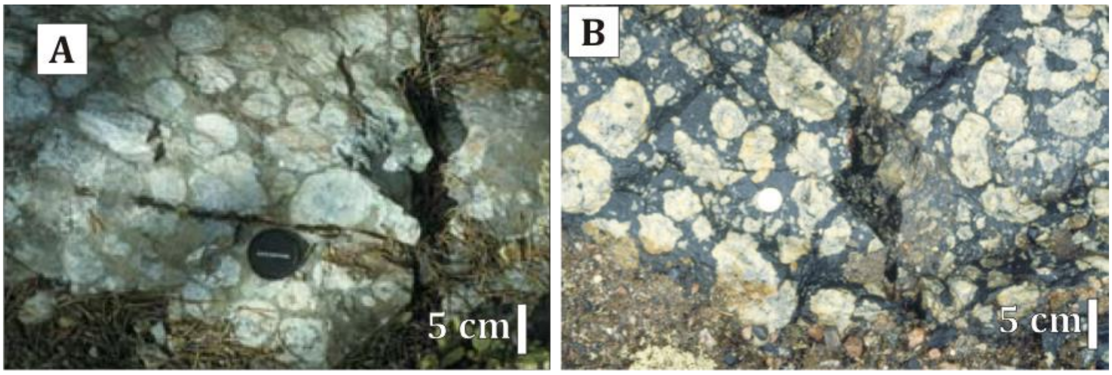

Fig. 2.23. Photographs of (A) Leopard dykes and (B) Matachewan dykes, both showing ubiquitous plagioclase megacrysts. Photo A taken from Harlan (2005) and B taken from Bleeker (2004).

2.2.5.4. Ni-Cu-PGE Mineralisation

Ni-Cu-PGE sulphide mineralisation has not been observed in the Leopard dyke swarm and the swarm is not the subject the of any past or present exploration projects. The Blue Draw Metagabbro is the only ~2.45-2.5 Ga layered intrusion identified on the Wyoming craton, which has been speculatively linked with the Leopard dyke swarm (Heaman 1997; Harlan 2005; Ernst and Bleeker 2010).

2.2.6. Kaminak Dyke Swarm

2.2.6.1. Geology

The Kaminak dyke swarm **(Fig. 2.24)** is made up of hundreds of north-northeast trending dykes which crop out over an area of 20,000 km^2 in southern Nunavut, approximately 100 km west of Hudson Bay (Buchan and Ernst 2004).

The Kaminak dykes are Fe-rich quartz tholeiites and are predominantly composed of plagioclase and clinopyroxene with minor amounts of olivine and Fe-Ti oxides (Christie et al. 1975; Sandeman and Ryan 2008). The dykes range in texture from aphyric to plagioclase porphyritic and locally, the dykes can contain abundant megacrysts (~10 cm wide) of plagioclase (Bleeker 2004). the dykes are highly variable in their extent of alteration, with unaltered dykes preserving ophitic textures, while more pervasive alteration in the dykes is characterised by saussuritization of feldspar, uralitisation of pyroxene replacement of olivine to serpentine (Christie et al. 1975; Sandeman and Ryan 2008).

The metamorphic mineral assemblages of epidote, sericite, amphibole and chlorite observed in the Kaminak dykes suggest that metamorphism of the bulk of the Kaminak dyke swarm reached a maximum of lower greenschist facies. However, metamorphic grade of the Kaminak dykes increases towards the north, where at maximum, the Kaminak dykes have been metamorphosed to large boudins of amphibolite within country rocks of migmatitic gneiss (Christie et al. 1975).

The Kaminak dykes are generally vertical and vary from ~1-40 m in thickness. The dykes tend to form resistant ridges which can be traced over tens of kilometres before being truncated by younger faults (Christie et al. 1975; Sandeman and Ryan 2008). The N-NE trend of the dykes bisects the dominant tectonic boundaries between the Archean supracrustal and granitoid rocks which make up the hosting Ennadai-Rankin greenstone belt (Aspler et al. 2000). The trends of the Kaminak dykes have been described as radiating, with an arc angle of ~40° by Ernst and Bleeker (2010) and as a linear array (Sandeman and Ryan 2008).

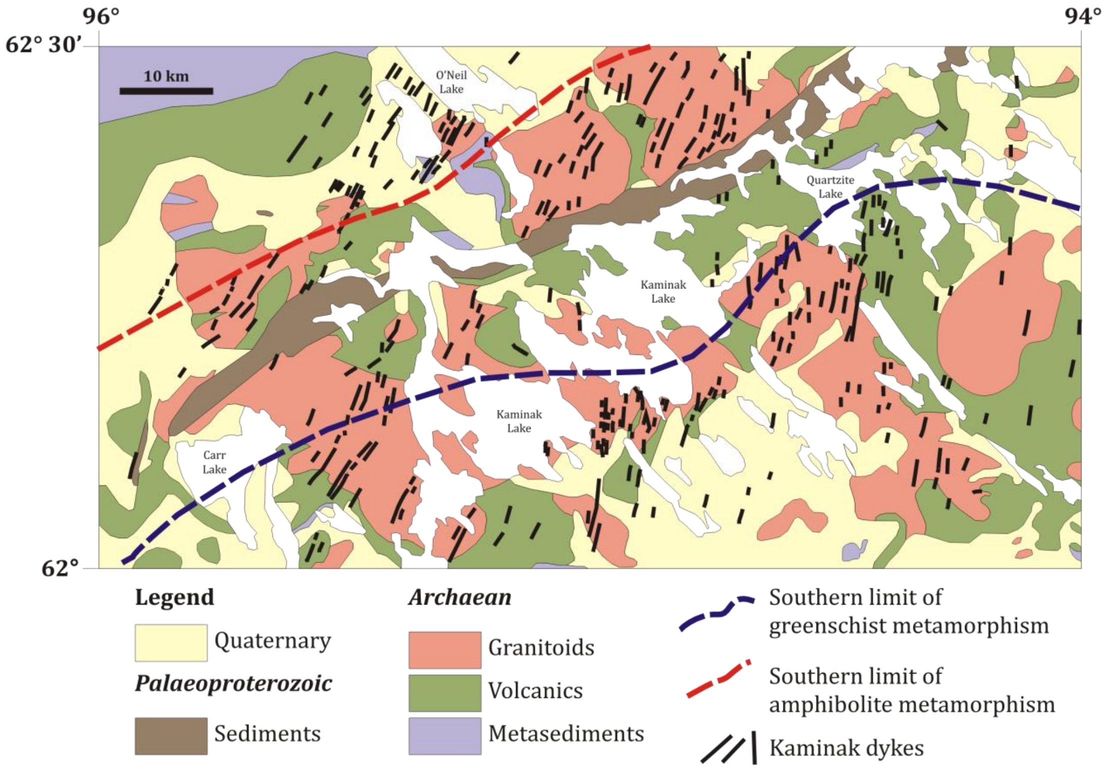

Fig. 2.24. Geological map showing locations of the Kaminak dykes. Modified from Sandeman and Ryan (2008).

Based on observed field relationships and geochemical similarities, the Kaminak dyke swarms have been interpreted to be feeders to the continental tholeiitic basalts of the Spi Group which crop out in the core of a syncline, preserved in the modern day Spi basin (Sandeman and Ryan 2008).

2.2.6.2. Age

The most widely cited age of the Kaminak dyke swarm is a U-Pb date from magmatic baddeleyite of 2450 ± 2 Ma (Heaman 1994). This age supersedes previous variable K-Ar whole-rock ages which have errors on the magnitude of ±100 million years (see summary in Christie et al. (1975)). A second Kaminak dyke dated by U-Pb analysis of magmatic baddeleyite yielded an age of 2498 ±2 Ma (Heaman 2004). These two ages led Ernst and Bleeker (2010) to suggest that the Kaminak dyke swarm is a composite swarm made up of two pulses of magmatism, which were emplaced approximately 50 million years apart.

Heaman's (1994; 2004) two widely cited U-Pb ages (Aspler et al. 2002; Sandeman and Ryan 2008; Ernst and Bleeker 2010) are reported in single page conference abstracts and not in a more extensive work. Hence, it is difficult to fully determine the context of the reported dates or understand any potentially associated caveats with the analysis.

2.2.6.3. Tectonic Setting

Buchan and Ernst (2004) and Ernst and Bleeker (2010) propose that the trend of the Kaminak dykes define a radiating pattern with an arc angle of 40°, which indicates a focal point just to the south of Chesterfield Inlet. Further to this, Bleeker (2003) and Ernst and Bleeker (2010) suggest a genetic link between the Kaminak dyke swarm and the Matachewan dyke swarm on the Superior craton based on overlapping U-Pb ages and existing palaeomagnetic data from the dyke swarms which allow the Superior and Hearne cratons to be adjacent at ~2.5 Ga. The interpretation of the Kaminak dykes as a radiating swarm in its own right or as a now dismembered part of a much larger swarm including the Matachewan dykes, has led previous authors to interpret the Kaminak dyke swarm as a product of mantle-plume induced magmatism during rifting of an Archaean supercontinent **(Fig. 2.25)** (Bleeker and Ernst 2006; Ernst and Bleeker 2010; Söderlund et al. 2010).

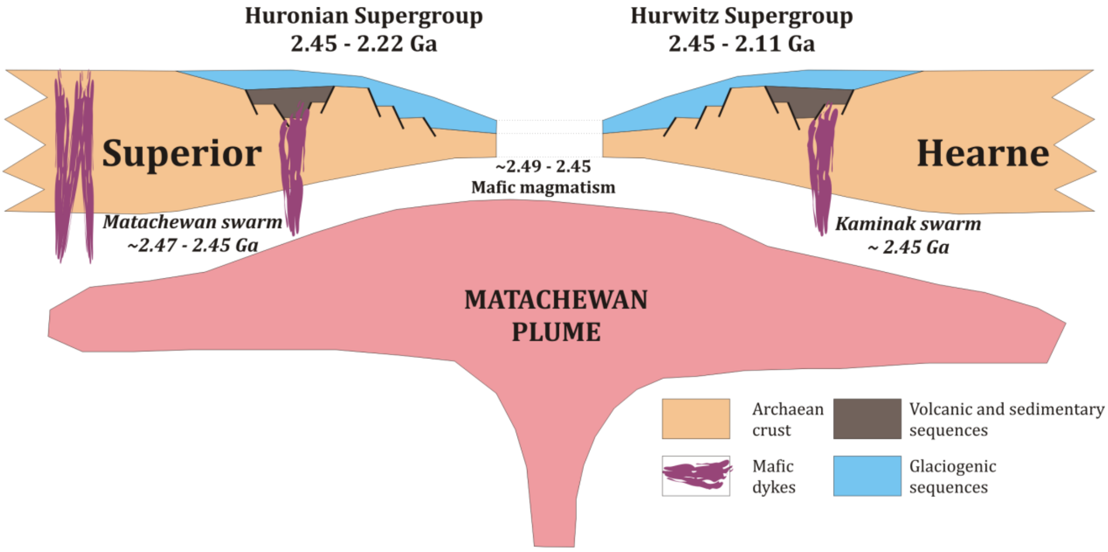

Fig. 2.25. Mantle plume model for the formation of the Matachewan and Kaminak dykes swarms and Huron and Hurwitz Supergroups. Modified from Bleeker (2004).

Sandeman and Ryan (2008) carried out the only geochemical study of the Kaminak dykes aimed at understanding the swarm in terms of its mantle source and tectonic setting. In their study, Sandeman and Ryan (2008) argue that the trace element chemistry of the Kaminak dykes (characterised by enrichments in the large ion lithophile and light rare earth elements relative to the heavy rare earth elements and significant depletions in the high field strength elements) show that the parent magmas of the Kaminak dykes are the result of mixtures between subduction-modified sub-continental lithospheric mantle and depleted MORB mantle. Sandeman and Ryan (2008) contend that while the geochemistry of the Kaminak dykes does not indicate any material input from a mantle plume, this may be explained by the Kaminak dyke swarm having occupied a distal position relative to the plume head at ~2.45 Ga.

2.2.6.4. Ni-Cu-PGE Mineralisation

Ni-Cu-PGE sulphide mineralisation has not been observed in the Kaminak dyke swarm and the swarm is not the subject the of any past or present exploration projects. No layered intrusions coeval with the Kaminak dyke swarm have been identified on the Hearne craton.

2.2.7. Viianki Dyke Swarm

2.2.7.1. Geology

Mafic dyke swarms preserved on the Karelia craton are poorly defined. The age spectrum of 2.4-2.5 Ga events recorded on the craton is in the process of being evaluated (Kulikov et al. 2010). Preliminary analysis of the ages of Palaeoproterozoic mafic dykes preserved on the Karelia craton indicates that the craton experienced at least 3-4 mafic igneous events between 2.4-2.5 Ga which broadly overlap the ages of mafic dykes preserved on the other cratons studied in this work. Unlike the events on other cratons, very few attempts have been made to delineate the dated Karelia dykes into separate swarms which share a consistent trend, appearance, mineralogy and chemistry.

One of the few Palaeoproterozoic swarms to be identified is the Viianki dyke swarm **(Fig. 2.26)**, which has been identified as the likely feeder to the ~2.44 Ga layered mafic intrusions on the craton (Vogel et al. 1998b). Vogel et al. (1998b) characterised the Viianki swarm as a northwest trending swarm of tholeiitic basalts and andesites. The Viianki dykes are likely to be equivalent to the Karelia dykes described by Mertanen et al. (1999) based on the similar ages, trends and geographic locations of dykes reported by the two sets of workers. Mertanen et al. (1999) describes the Karelia dykes as northwest trending and subvertical, ranging in thickness from 6 cm - 200 m with compositions which range from Fe-tholeiitic and tholeiitic to calc-alkaline. Neither of the two studies describe the mineralogy of the dykes in detail, but Mertanen et al. (1999) notes that the dykes are generally unaltered and fresh.

While the work of Vogel et al. (1998b) and Mertanen et al. (1999) represent two of the very few attempts at identifying unique swarms on the Karelia craton, the existence of other Palaeoproterozoic dyke swarms on the craton is extremely likely. U-Pb and other dating methods have shown that mafic dykes were intruded into the Karelia craton throughout much of the Proterozoic and doubtless, following more work on both dated and currently undated dykes, more mafic dyke swarms will be identified. As such dating work is beyond the scope of the current study, the following discussion will primarily focus on the Karelia/Viianki dyke swarm as defined by Mertanen et al. (1999) and Vogel et al. (1998b) This swarm will henceforth be referred to as the Viianki dyke swarm, so as to avoid any confusion with other dyke swarms preserved on the Karelia craton.

2.2.7.2. Age

Vogel et al. (1998b) estimate the age of the Viianki dykes as ca. 2440 Ma. Vogel et al. (1998b) does not report a direct date for the Viianki dykes, but rather suggests that the Viianki dykes provide the most likely parental magmas for some of the Palaeoproterozoic layered intrusions on the Karelia craton including Kemi, Koitelainen, Akanvaara, Burakovsky and Tornia, which range in age from 2433±8 Ma – 2449±2 Ma (see summary in Vogel et al. (1998b) and Lauri et al. (2012)). When describing the Karelia dykes (thought to be equivalent to the Viianki dykes), Mertanen et al. (1999) reports a U-Pb baddeleyite age of 2446±5 Ma and several Sm-Nd ages with much larger errors of between 2422±35 Ma – 2476±30 Ma.

2.2.7.3. Tectonic Setting

Vogel et al. (1998b) studied the geochemistry of the Viianki dykes and their proposed analogues on the Superior Craton and found that the two sets of magmas could be petrogenetically related to each other through different degrees of crustal contamination of a common magma, or, through differing degree of partial melting of a common mantle source. Vogel et al. (1998b) also notes that the chemical signature recorded by the Viianki dykes is consistent with the magma derivation from an upper mantle source, which had experienced removal of MORB during the Archaean and subsequent enrichment by subduction fluids; and does not indicate any input of material from a mantle plume.

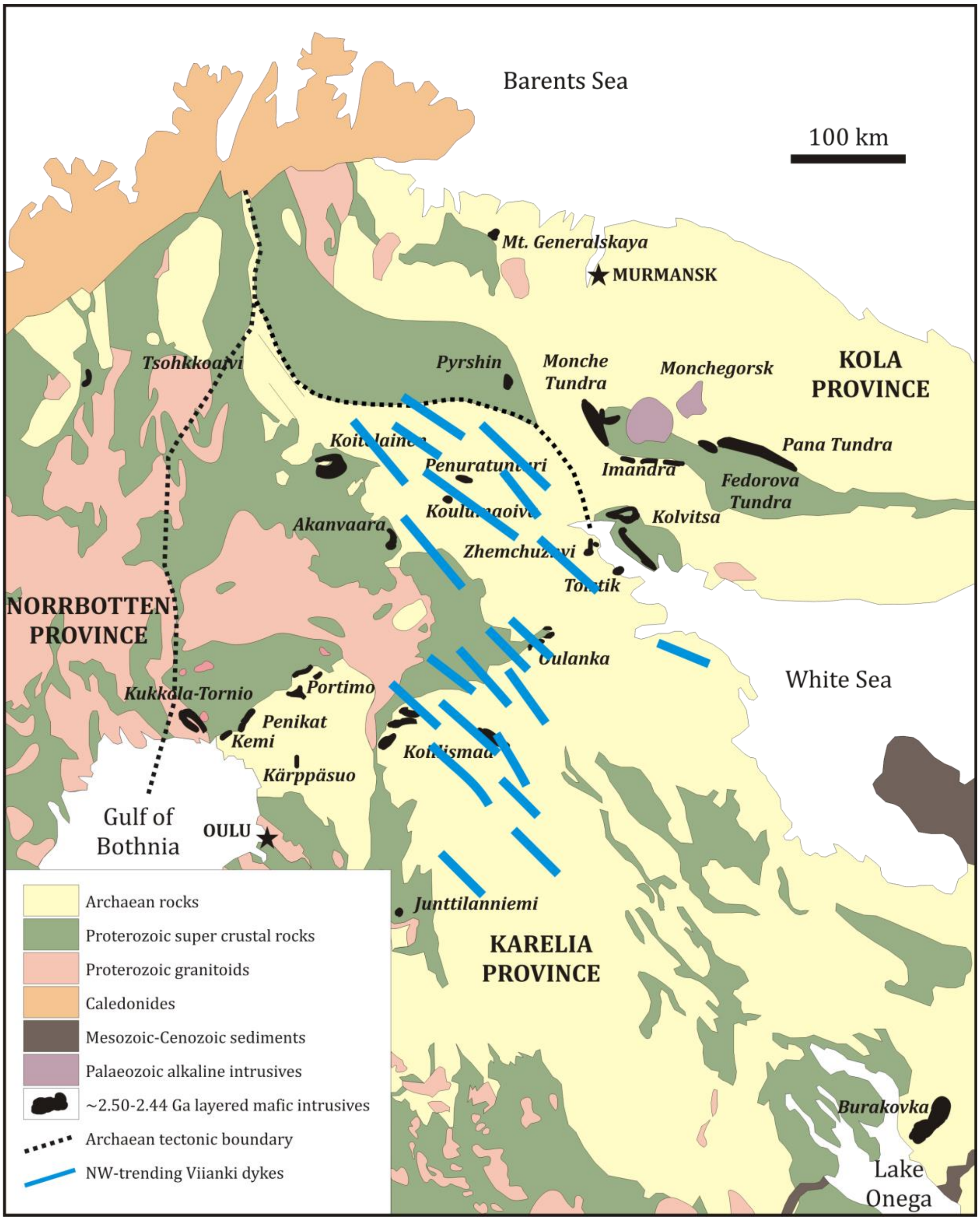

Fig. 2.26. Geological map showing the extent of the Viianki dyke swarm. Dyke traces are schematic after Vogel et al. (1998b) and Kulikov et al. (2010).

Mertanen et al. (1999) dispute earlier continental reconstructions (Heaman 1997) which place Karelia to the south of the Superior craton at ~2.45 Ga and which interpret the coeval magmatism on the two cratons as the product of a mantle plume. Mertanen et al. (1999) instead argue that the palaeomagnetism of the Viianki dykes does not allow for the dykes to be the southward continuation of the Matachewan swarm as suggested by others (Buchan and Ernst 2004; Ernst and Buchan 2004; Söderlund et al. 2010) as available palaeomagnetic data for the Karelia craton places the craton to the north and east of the Superior Craton at ~2.45 Ga. Mertanen et al. (1999) argue that such a reconstruction [as permitted by palaeomagnetic data (Bates and Halls 1990)] produces a Matachewan-Viianki dyke architecture which is incompatible with the two swarms having originated from the same point-source.

Bleeker (2003) suggests that the palaeomagnetic data used by Mertanen et al. (1999) is complex and largely uncertain and that allowing the palaeomagnetic data to dictate the ~2.45 Ga Superior-Karelia reconstruction dismisses far more robust geological data. Instead, the reconstruction provided by Bleeker et al. (2008) places the Karelia craton to the south of the Superior craton and interprets the Viianki dyke swarm to be the southward extension of the Matachewan dyke swarm and the whole Viianki-Matachewan composite swarm to have been intruded during mantle-plume induced continental rifting.

2.2.7.4. Ni-Cu-PGE mineralisation

The Viianki dykes are not known to host any Ni-Cu-PGE mineralisation. However, Vogel et al. (1998b) use geochemistry to show that the Viianki dykes are the most likely candidates to have fed some of the ~2.45 Ga mafic layered intrusions on the Karelia craton which themselves are known to host significant quantities of chromite and PGE-enriched base metal sulphides (Iljina and Hanski 2005).

2.2.8. Seidorechka Formation

2.2.8.1. Geology

Reconstructions involving the Huronian and Karelia Supergroups involve correlations of; ~2.45 Ga volcanic rocks, carbonates with C-isotope anomalies, carbon-rich units, glaciogenic horizon, palaeosols and other characteristic sedimentary units preserved within the two supergroups (Ojakangas et al. 2001). The rocks of interest to this current study constitute part of the Seidorechka Formation near the base of the Sumi Group (Melezhik 2006).

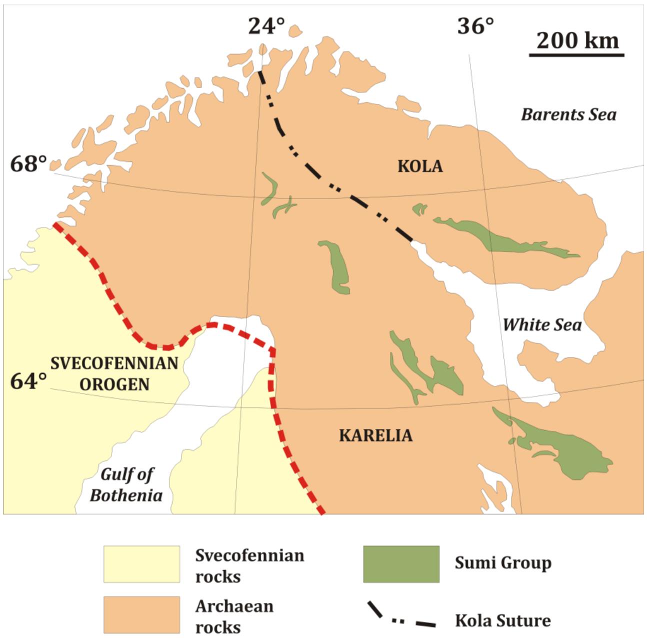

Fig. 2.27. Geological map showing the extent of the Sumi Group. Modified after Melezhik (2006).

The Sumi Group is preserved in several basins adjacent to the White Sea in northwest Russia and northern Finland **(Fig. 2.27)**. The Seidorechka Formation **(Fig. 2.28)** is ~3000 m thick and composed of amygdaloidal komatiitic, basaltic and basaltic-andesitic flows at the base, and dacitic-rhyolitic flows at the top (Melezhik and Sturt 1994; Puchtel et al. 1997). Individual flows can be up to ~150 m thick, the larger of which preserve primary magmatic stratigraphy (Puchtel et al. 1996). The Seidorechka Formation rocks are variably well preserved and metamorphic grade does not exceed lower greenschist facies (Chashchin 2008; Puchtel et al. 1997). Based on the distribution of current exposures, the original areal extent of the Seidorechka Formation has been estimated to be between 100,000-700,000 km^2 (Heaman 1997; Melezhik 2006).

2.2.8.2. Age

The most widely cited age of eruption of the Seidorechka Formation (Amelin et al. 1995) of 2442.2±1.7 Ma was obtained through U-Pb analysis of baddeleyite from a felsic subvolcanic unit from within the formation. Puchtel et al. (1997) report a U-Pb age of 2437±3 Ma which was obtained through U-Pb analysis of zircon from a dacitic lava flow. Chashchin et al. (2008) also present U-Pb analysis of primary magmatic zircons from Seidorechka rocks and interpret an age of 2444±8 Ma as the eruption age of the formation. A summary of much of the dating work on the Sumi Group volcanic rocks is presented by Hanski et al. (2001). The most precise U-Pb dates summarised by Hanski et al. (2001) indicate that the Seidorechka Formation was erupted at ~2.44 Ga.

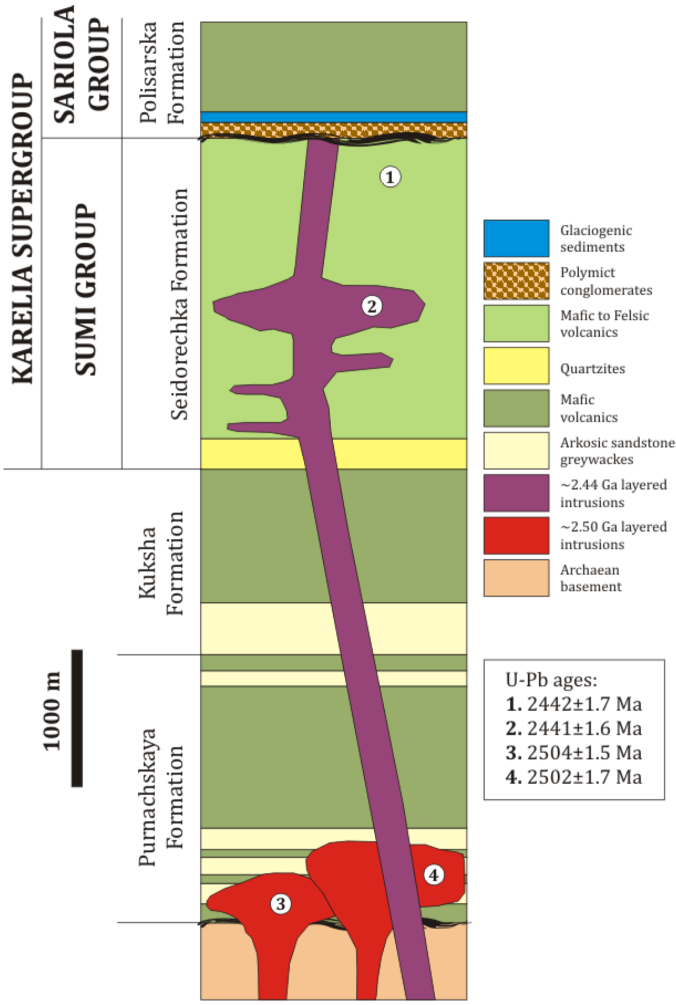

Fig. 2.28. Stratigraphy of the Karelia Supergroup. Modified from Melezhik (2006).

2.2.8.3. Tectonic Setting

Heaman (1997) interprets the similarities between the Huronian and Karelia Supergroups as evidence that the two were deposited adjacently in a single, continuous basin which formed in response to mantle plume-induced continental rifting. Heaman (1997) primarily uses the overlapping ages of basaltic flows preserved within the two Supergroups to infer the existence of an enormous continental flood basalt province which erupted at ~2.44 Ga. Heaman (1997) argues that the sheer volume of magma erupted during this ~2.44 Ga event can only be adequately explained by mantle plume-induced magmatism. This reasoning is also favoured by Kulikov et al. (2010).

Puchtel et al. (1997) studied chilled margins of individual flows in the Seidorechka Formation and found that the primary magmas contained 12.8-15.5 wt.% MgO. Puchtel et al. (1997) uses these MgO contents to infer a mantle potential temperature of 1530-1630 °C for the source of the Seidorechka Formation. Puchtel et al. (1997) argues that these temperatures are much higher than the estimated temperature of the ambient mantle at the time of eruption of the Seidorechka Formation [1480 °C (Richter 1988; Herzberg 1995)] and can only be explained by the existence of a thermal anomaly (mantle plume) at the base of the Karelia Craton at ~2.45 Ga.

2.2.8.4. Ni-Cu-PGE Mineralisation

Ni-Cu-PGE sulphide mineralisation has not been observed in the Seidorechka Formation and the Formation is not the subject the of any past or present exploration projects. Several well-mineralised layered intrusions coeval with the Seidorechka Formation have been identified on the Karelia craton.

2.2.9. Fennoscandian Suite

2.2.9.1. Geology

The Fennoscandian suite of layered intrusions included in Matachewan Large Igneous Province reconstructions is made up of ~20 individual intrusions which crop out in northern Finland and northwest Russia **(Fig. 2.29)**. Summarising of the plethora of work on each of the intrusion is beyond the scope of this study and the following overview will be based on work which considers the Fennoscandian intrusions as a group or groups.

The Matachewan-age layered intrusions are preserved in two discontinuous belts which transect the Karelia craton (Iljina and Hanski 2005). The east-west trending Tornio-Näränkävaara Belt crosses Sweden, Finland and Russia between the tip of the Gulf of Bothnia to the White Sea and includes the Kukkola-Torni, Kemi, Penikat, Portimo and Kollismaa intrusions. The second belt trends northwest-southeast across

Finland between Kasivarsi and Lake Onega and includes the Tsohkkoaivi, Koitelainen, Keivitsa, Akanvaara, Oulanka and Burakovka intrusions.

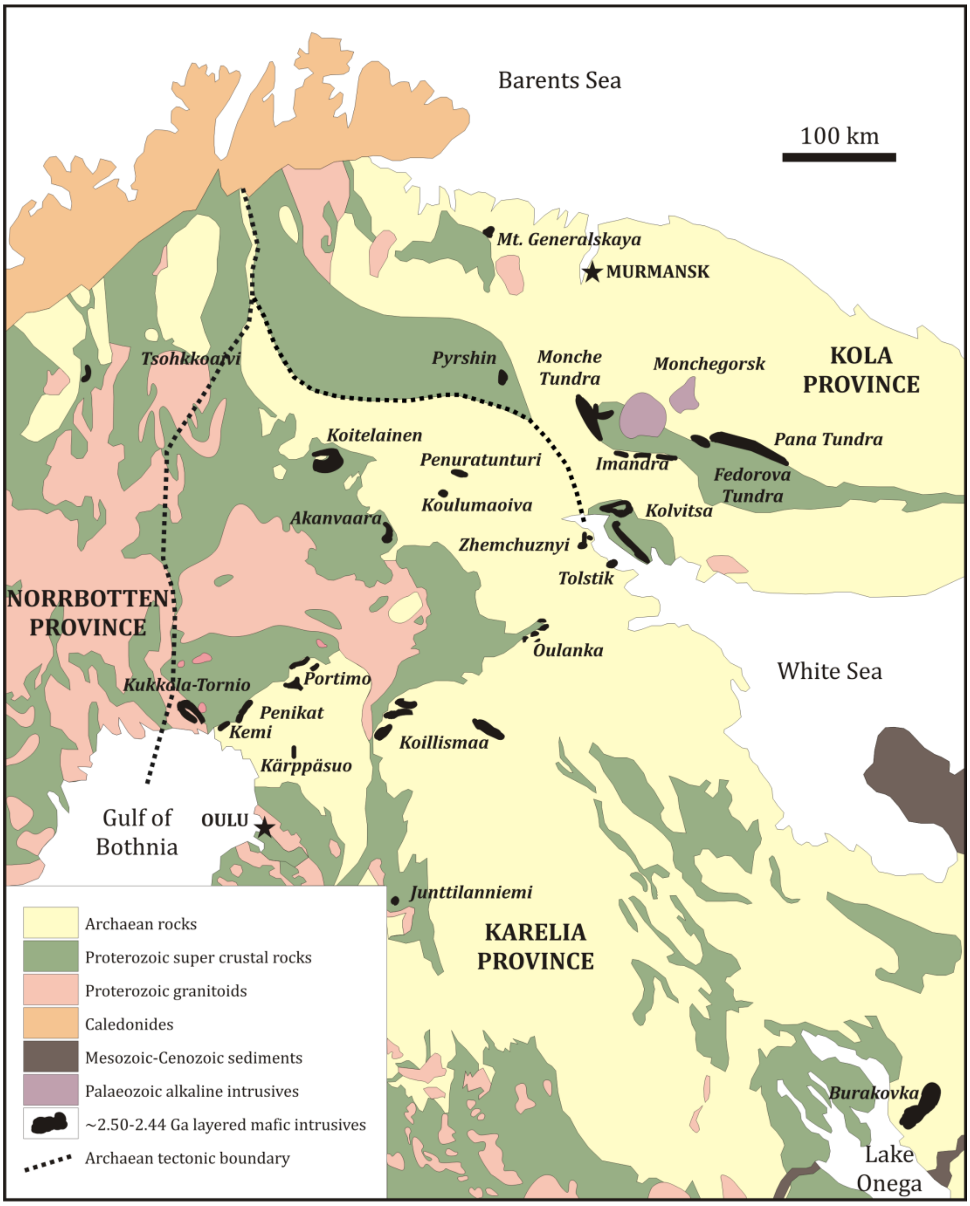

Fig. 2.29. Geological map showing the extent of the ~2.5-2.44 Ga Fennoscandian intrusions. Modified after Lauri et al. (2012).

The rocks which form the footwalls to the intrusions are late Archaean tonalitic gneisses and early Palaeoproterozoic greenstone belts (Alapieti et al. 1990). Few of the intrusions, including the Oulanka complex and Burakoyka are entirely hosted by the Archaean basement rocks, but most of the intrusions are located along the contact between these rocks and the unconformably overlying Proterozoic volcanic-sedimentary Sumi, Sariola and Strelna groups (Weihed et al. 2005).

Vogel et al. (1998b) subdivide the Fennoscandian intrusions into two groups which differ in their chromite contents and proportions of mafic-ultramafic rocks. Vogel et al. (1998b) define a Cr-poor group of intrusions (including the Oulanka Kollismaa and Portimo intrusions) which lack chromite and a Cr-rich group of intrusions (including the Kukkola/Tornio, Kemi and Koitelainen intrusions) which contain numerous chromite seams. Both types of intrusions are made up of a marginal series, a layered series and a granophyric unit which caps the intrusions **(Fig. 2.30)**. The marginal series of both sets of intrusions are composed of a reversely graded sequence of gabbronorite and peridotite. The base of the overlying layered series in both sets of intrusions is composed of a basal ultramafic unit which grades into layers of gabbros and leucogabbros, the difference between the Cr-poor and Cr-bearing groups of intrusions is that in the Cr-poor intrusions, the proportion of ultramafic-mafic rocks is ~ 1:20, where as in the Cr-bearing intrusions, this proportion is closer to parity. Members of both types of intrusions preserve a granophyric cap, which in some of the intrusions is interpreted to have been eroded.

Alapieti (2005b) divides these Fennoscandian intrusions differently to Vogel et al. (1998b) and instead, delineates three types; ultramafic-mafic, mafic and intermediate 'megacyclic' based on the petrology of the intrusions. The ultramafic-mafic type of intrusions (which include the Kukkola-Tornio, Kemi and Burakovka intrusion) are defined by a thick ultramafic sequence at the base which are overlain by mafic and anorthositic cumulate rocks. The mafic type of intrusion (including the Kollismaa, Koitelainen and Akanvaara intrusions) are characterised by a much thinner (occasionally missing) basal ultramafic sequence relative to overlying plagioclase-rich cumulate rocks. The layered series of the intermediate 'megacyclic' intrusions (including the Penikat and Portimo intrusions) are composed of distinct megacyclic units which grade from ultramafic basal sequences upwards into gabbros and anorthosites.

2.2.9.2. Age

The Fennoscandian suite has been dated by several groups, [e.g., (Amelin et al. 1995; Puchtel et al. 1997; Bayanova et al. 2009)] and these dates are summarised by Lauri et al. (2012) who compile 20 ages (mostly U-Pb analyses of magmatic zircons) from each of the intrusions. The age range defined by these analyses suggests that the

Fennoscandian suite were intruded between ~2424-2470 Ma, with the majority being emplaced between ~2440-2442 Ma.

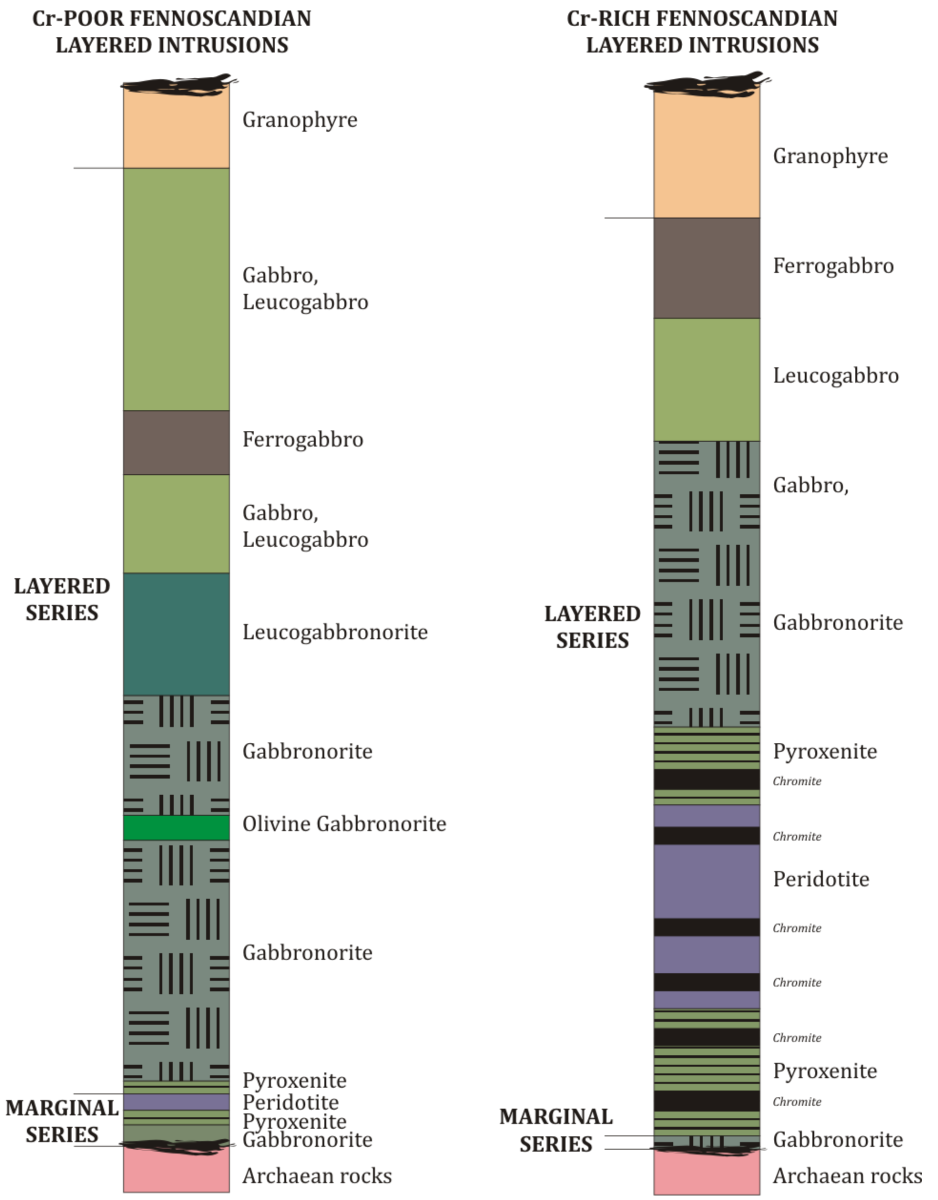

Fig. 2.30. Comparative stratigraphies of ~2.5-2.44 Ga Cr-poor and Cr-bearing Fennoscandian intrusions. Modified from Vogel et al. (1998b).

2.2.9.3. Tectonic setting

Most previous work concludes that the Fennoscandian intrusions are the product of mantle plume magmatism. In addition to overlapping U-Pb ages between the Fennoscandian intrusions and magmatism on other cratons (Heaman 1997; Ernst 2007; Söderlund et al. 2010), other studies cite geological and geochemical evidence in support of a mantle plume origin.

Amelin et al. (1995) argue that the deep levels of erosion of Archaean rocks, faulting, vertical block movements and the presence of poorly sorted sedimentary units [interpreted to be graben fill sequences (Gorbunov et al. 1985)] beneath the flood basalts of the Sumi, Sariola and Strelna Groups is strong evidence of large amounts of crustal uplift prior to ~2.45 Ga- a phenomenon predicted to occur above a buoyant mantle plume head (Campbell 2007). Amelin et al. (1995) also argue that the ~60 million year time gap between the ~2.44 Ga Fennoscandian intrusions and ~2.5 Ga mafic magmatism recorded in the north of the craton is characteristic of other plume-related suites. Amelin et al. (1995) also argue that the MgO contents of some of the ~2.44 Ga flood basalts and estimated parent melts for the layered intrusions lie within the range expected for magmas formed during mantle-plume induced mantle melting.

Weihed et al. (2005) argues that the temporal association of layered intrusions, flood basalts and dyke swarms is also evidence of mantle plume magmatism. Bayanova et al. (2009) estimate the ~2.44 Ga magmatism described by Weihed et al. (2005) to cover an area of >200,000 km^2 and argue that the volume of magmatism along with its homogenous and enriched isotopic chemistry can only be explained by mantle plume-induced magmatism.

2.2.9.4. Ni-Cu-PGE Mineralisation

Alapieti (2005b; 2005a) and Iljina (2007) summarise the Ni-Cu-PGE mineralisation contained in the ~2.44 Ga Fennoscandian intrusions into two main types. The first type is characterised by disseminated-massive sulphides mineralisation preserved within the marginal series rocks, similar in form to the ‘contact-type’ mineralisation observed in the East Bull Lake suite. This mineralisation occurs as relatively thin (~30 m thick) zones of fine-grained disseminated sulphides as well as massive, tabular horizons with thickness between 20 cm – 15 m (Alapieti 2005a). Sulphide mineralogy in the Marginal Series is dominated by pyrrhotite with lesser amounts of chalcopyrite and pentlandite, which usually contains ~2 ppm Pt+Pd+Au, though in the Ahmavaara intrusion from within the Portimo complex, PGE concentrations can be up to >10 ppm (Iljina 2007).

The second type of mineralisation observed in the Fennoscandian intrusions is preserved as reefs within the poikilitic plagioclase-orthopyroxene cumulates of Layered Series (Alapieti 2005a). The reefs are generally ~50 cm thick but can be up to 20 m thick and are variable in mineralogy and can be dominated by bornite and chalcopyrite or can be sulphide-poor (Iljina 2007). The reefs form laterally extensive horizons which can be traced over the entire strike of some intrusions (~23 km in the case of the Penikat intrusion) and can contain up to ~20 ppm PGE (Iljina 2007).

Arguably, the ~2.44Ga Fennoscandian intrusions are the most attractive Ni-Cu-PGE targets from the Matachewan Large Igneous Province due to their number, documented occurrences and history of active mining. Saltikoff et al. (2006) presents a detailed history of mining in Finland. Notable examples include the Penikat intrusion, within which a number of PGE-bearing reefs have been identified, one of which, the Sompujarvi reef has been mined, producing 1265 tonnes of ore grading at 10 g/t Pt and 20 g/t Pd while other reefs at Penikat have been estimated to contained insitu resources of ~2340 t Pt and 2490 t Pd (Saltikoff et al. 2006). Exploration of the Suhanko intrusions of the Portimo complex has delineated three separate zones of contact-type mineralisation, the most impressive being the 99.8 Mt Ahmavaara deposit which contains estimated resources grading at 0.23 g/t Pt, 1.1 g/t Pd and 0.14 g/t Au (Outokumpu Oy & GoldFields Ltd. Press Release. 2002).

These deposits as well as others preserved within the Fennoscandian intrusions including the Koitelainen, Kollismaa, Kemi and Narkaus are actively being explored to further define the Ni-Cu-PGE potential of the ~2.44 Ga Fennoscandian intrusions.

2.3. Summary

This geological overview has reviewed Large Igneous Provinces in terms of their general geology and proposed mechanisms of formation. The evolution of the Matachewan Large Igneous Province has also been reviewed. Each work which has, in some way, contributed to our understanding of the Matachewan Large Igneous Province has been presented and the observations, interpretations and conclusions have been described. Although the most widely accepted mechanism for the formation of the Matachewan Large Igneous Province is the impingement of a mantle plume beneath an Archaean supercontinent, it is not universally accepted.

Volcanic arcs, failed rifts and normal continental and ocean spreading have all been suggested to have formed different component igneous packages of the proposed Matachewan LIP.

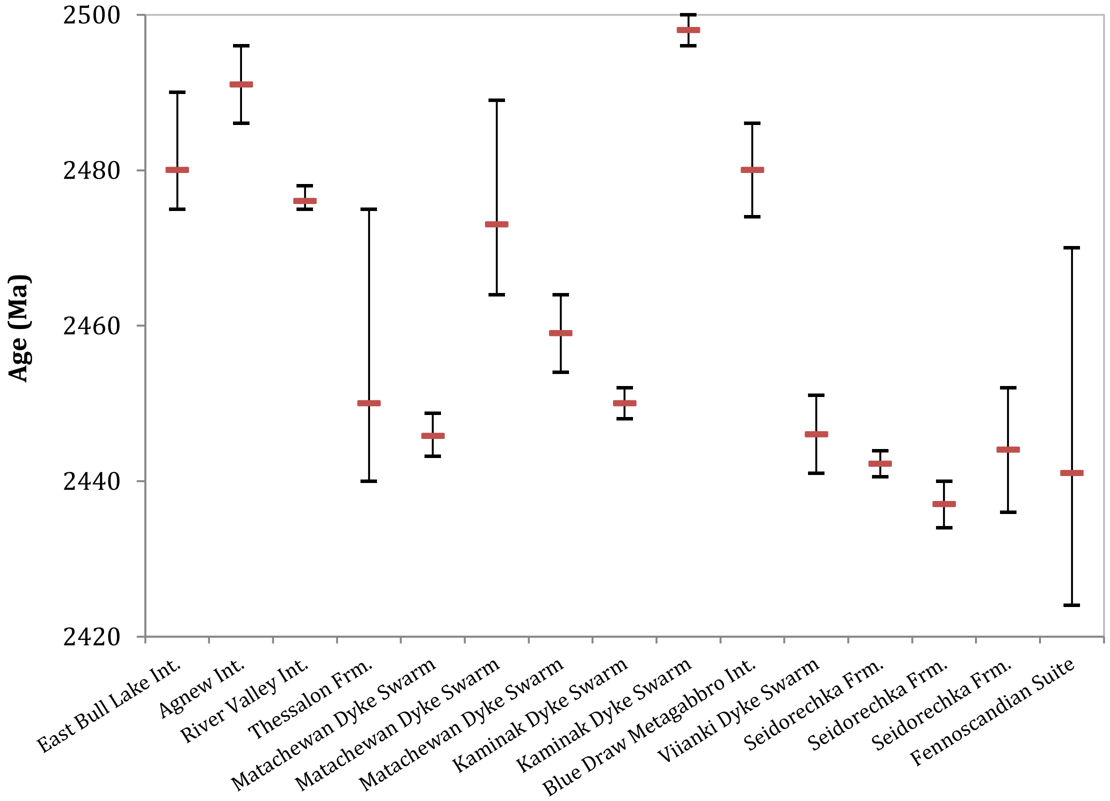

Fig. 2.31. Diagram showing the age ranges for dated Matachewan LIP rocks. See text for data sources.

Thus far, geochronology work has been key to the evolution of the Matachewan LIP model. A number of different methods (U-Pb, K-Ar, Rb-Sr, Pb-Pb) have been used to date Matachewan Large Igneous Province rocks, with the most precise ages resulting from U-Pb analyses of magmatic baddeleyite. The array of ages recorded by the Matachewan Large Igneous Province rocks is presented in **Figure 2.31**. The ages recorded define a period of mafic magmatism which ranges in age between ~2498-2441 Ma. **Figure 2.32** shows that bulk of the magmatic activity peaks at end of the province’s life and is predominantly located on the Karelia craton. If the layered intrusions on the Superior and Karelia cratons are grouped together, the Matachewan Large Igneous Province magmatism appears more bimodal in character defined by an early pulse at ~2.48 Ga recorded by the East Bull Lake Suite and Blue

Draw Metagabbro, and a younger pulse at ~2.44-2.46 Ga defined by the Fennoscandian intrusions and dyke swarms and flood basalts preserved on each of the cratons.

This review has also summarised work which shows that some of the magmatic rocks of the Matachewan Large Igneous Province are economically important in terms of Ni-Cu-PGE mineralisation. The most spectacular occurrences and active mining are limited to the ~2.44 Ga Fennoscandian intrusions. The ~2.48 Ga East Bull Lake suite intrusions are also mineralised to a lesser extent and despite decades of exploration, have yet to be mined. Ni-Cu-PGE mineralisation has never been reported in the ~2.48 Blue Draw Metagabbro.

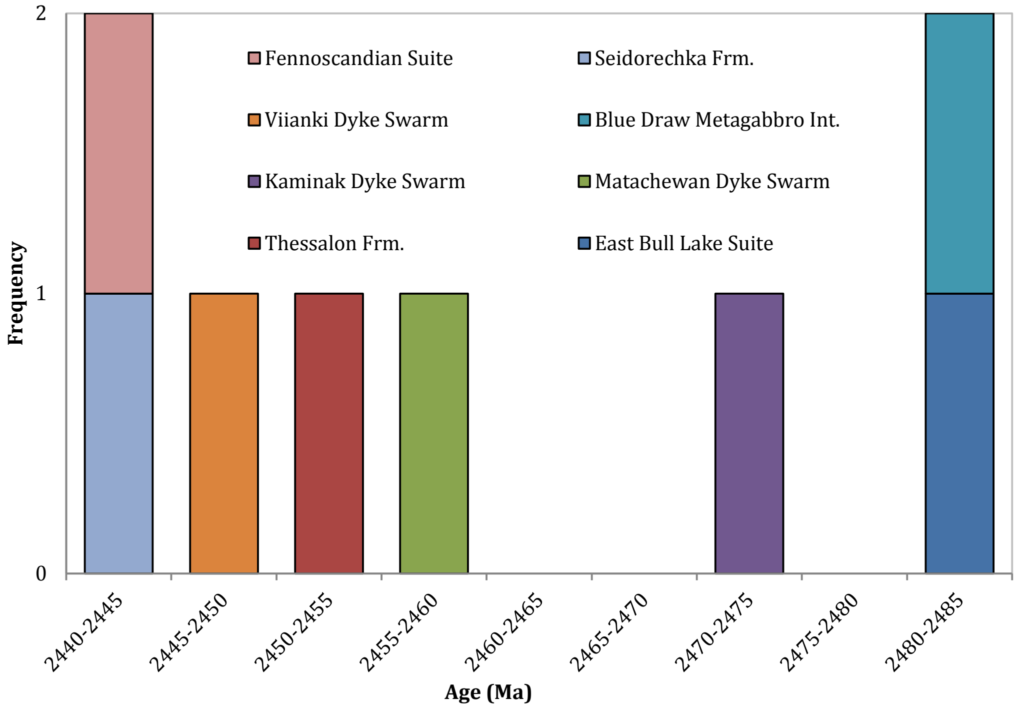

Fig. 2.32. Histogram showing distribution of ages of Matachewan LIP rocks. Suites with more than one reported age are averaged. The East Bull Lake Suite and Fennoscandian intrusions are treated as groups with defined by an average age. See text for data sources.

Fig. 2.33. Satellite image showing the present day positions of the cratons which make up the reconstructed Archaean supercontinent, Superia. Also shown are the locations of the dyke swarms, layered intrusions and flood basalt provinces sampled as part of this project. The Matachewan Dyke Swarm, East Bull Lake Suite and Huronian Supergroup are preserved on the Superior craton; The Kaminak Dyke Swarm is preserved on the Hearne craton; the Leopard Dyke Swarm and Blue Draw Metagabbro are preserved on the Wyoming craton, and; the Viianki Dyke Swarm, Fennsoscandian Suite and Sumi Supergroup are preserved on the Kola and Karelia cratons.

3. SAMPLE COLLECTION AND PETROGRAPHY

3.1. Introduction

Rock samples used in this study were collected between 2010 and 2011. Independent fieldwork was conducted to sample many of the North American Matachewan LIP rocks. However, constraints of time and expense mean that many of the samples in more remote regions were obtained by sampling archived collections at the Geological Survey of Canada (GSC) in Ottawa or were provided by workers who had studied the formations previously. Details on how and where rock samples were collected are given in the sections below, as are descriptions of their petrographic features. Data for those suites for which no material could be analysed is taken from previous studies. The locations for the samples used in the study are presented in **Appendix A**.

3.2. Matachewan Dyke Swarm

3.2.1. Sample Collection

Seventy powdered samples from Matachewan dyke outcrops across south western Ontario were collected for this study. These samples were originally collected by William Phinney, Henry Halls, Ken Buchan and Walter Fahrig during previous investigations of the Matachewan dykes and were stored in the GSC archives. These powders were augmented by seven rock samples collected from outcrops of Matachewan dykes near Sudbury, Ontario during fieldwork in 2010. A map showing the locations of the Matachewan dykes studied in this project is shown in **Fig. 3.1**.

The seven rock samples collected during this study were sampled from fine grained chilled margins and the medium grained interiors of thicker Matachewan dykes. Owing to the dense and often swampy vegetation in southern Ontario, most of the Matachewan dykes sampled were sourced from road cuts or blasted exposures. In outcrop, the Matachewan dykes are dark green in colour and vary in their appearance from plagioclase porphyritic to aphyric. Where observed, phenocrysts in the plagioclase-phyric dykes range in size up to ~5 cm and are either made up of single, euhedral lath-shaped crystals or are glomerocrysts. In the study area, Matachewan dykes are observed to cut the Archaean Whiskey Lake greenstone belt rocks of the

Wawa-Abitibi Terrane, the East Bull Lake suite of intrusions and the volcanic formations at the base of the Huronian Supergroup **(Fig 3.2)**.

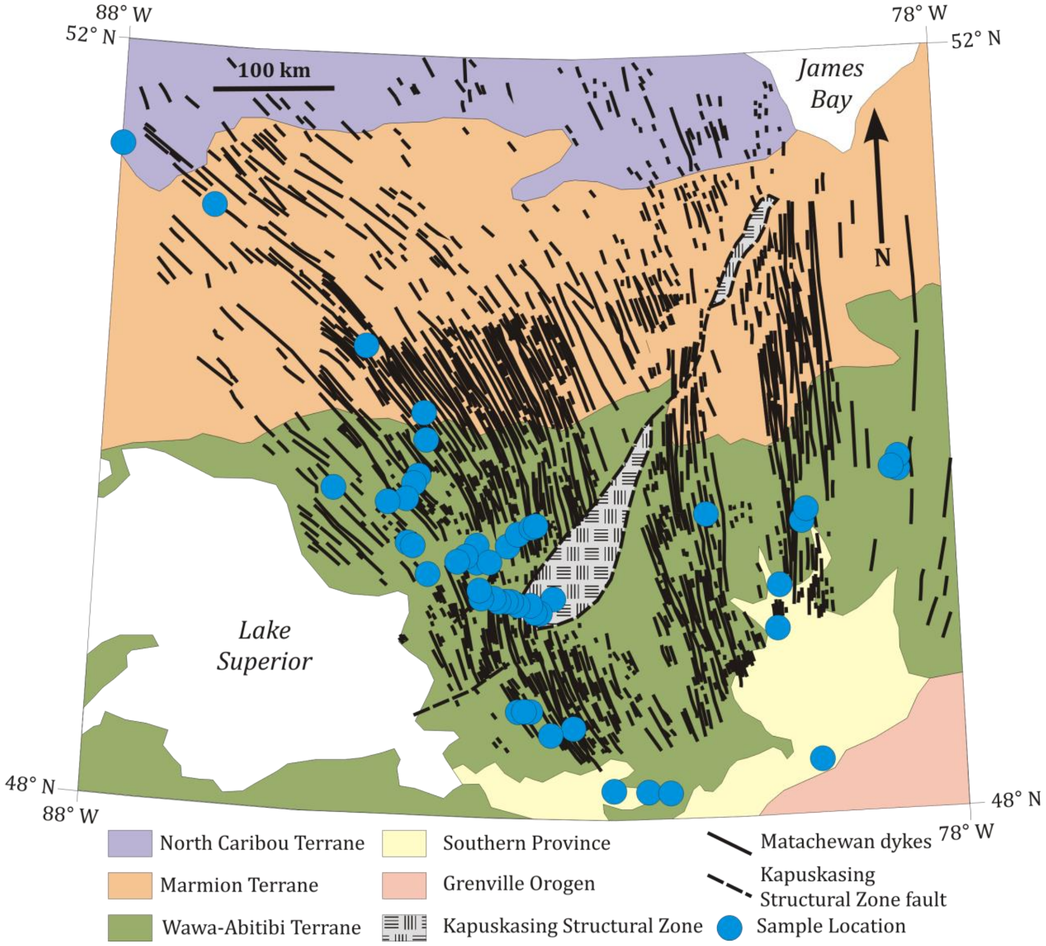

Fig. 3.1. Map showing the sample locations of Matachewan dykes studied in this project. Map compiled after Bates and Halls (1990), Tomlinson et al. (2004) and Buchan et al. (2007).

3.2.2. Petrography

Fine grained Matachewan dykes are equigranular with intergranular textures. The dyke mineralogy is dominated by plagioclase and clinopyroxene which occur in roughly equal proportions and trace amounts of quartz and opaque oxide phases **(Fig. 3.3A)**. Clinopyroxene constitutes ~50% of the mineralogy and forms elongate, subhedral prisms. The clinopyroxene is variably altered, typically being replaced by fine grained acicular actinolite, fine grained hornblende and fine grained opaque phases- all of which give the pyroxene a very mottled appearance **(Fig. 3.3B)**. The fine grained plagioclase comprises ~ 50% of the fine grained Matachewan dykes and generally formed elongate, subhedral laths. The plagioclase is variably altered with some crystals retaining good quality twins while most are slightly-moderately repl-

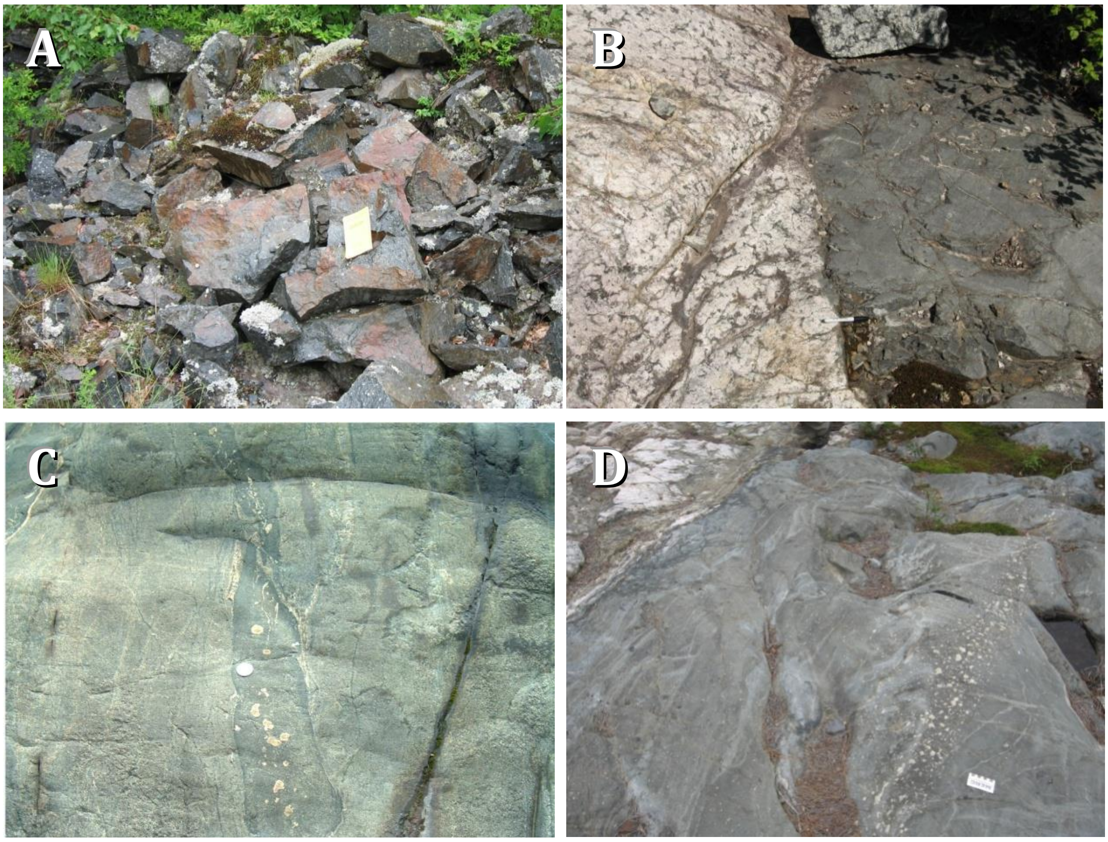

Fig. 3.2. Photographs of exposures of Matachewan dykes. **A)** Blasted outcrop of Matachewan dyke rocks on Highway 533, corresponds to geochemistry sample MA001; **B)** Fine-grained Matachewan dyke cutting the Nodular Anorthosite unit of the Agnew Intrusion; **C)** Plagioclase-megacrystic Matachewan dyke cutting Huronian Supergroup rocks near the Clarabelle Mine, North Sudbury; **D)** Plagioclase-phyric Matachewan dyke cutting the Leucogabbronorite zone (top left) of the River Valley Intrusion.

aced by very fine grained quartz, sericite and epidote which give the plagioclase crystals a very dusty appearance. Opaque phases represent ~5% of the fine grained Matachewan dykes, the vast majority of which are associated with altered clinopyroxene, occurring as fine grained amorphous masses within the crystals, adjacent to the pervasive amphibole alteration **(Fig. 3.3B)**. Opaque phases are largely absent from elsewhere in the Matachewan dykes which suggests that the opaque phases are an alteration product of the clinopyroxene. Quartz occurs in very minor amounts in the fine grained dykes and where present, occurs as fine grained aggregates or single crystals unevenly disseminated through the rock. Individual crystals form subhedral crystals with a crude hexagon-shaped cross-section and have a dusty appearance due to the large amount of inclusions. The fine grained dykes are not totally aphanitic as some samples contain larger (up to 5 mm) plagioclase crystals which form euhedral elongate laths. These laths are significantly more altered than the groundmass plagioclase and have a mottled appearance caused by fine grained

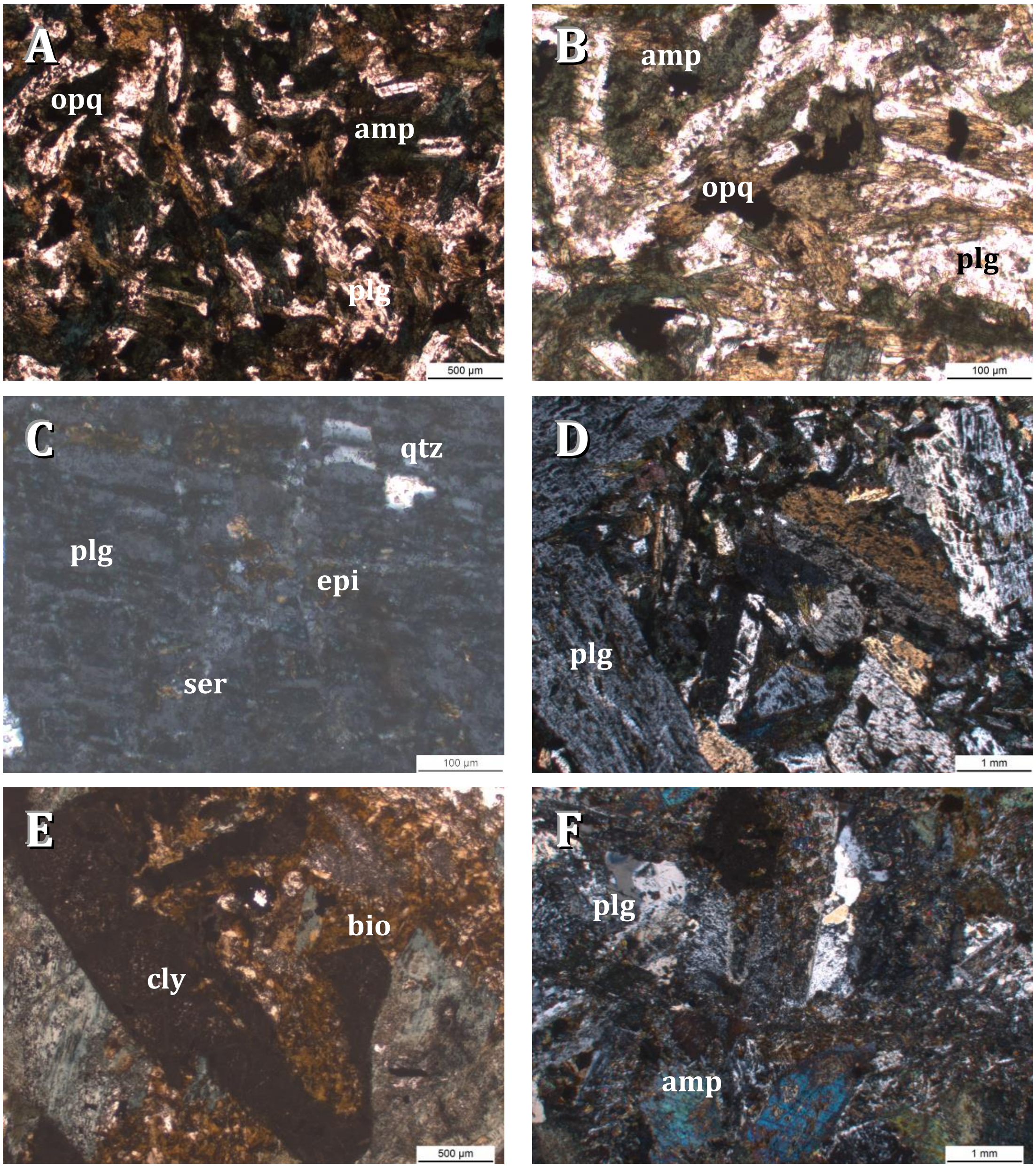

Fig. 3.3. Photomicrographs of the Matachewan dyke swarm. **A)** Plane-polarised light (PPL) photomicrograph of typical texture and mineralogy of aphynitic Matachewan dykes; **B)** PPL view of alteration of pyroxene to green amphibole and opaque material; **C)** Cross-polarised light (XPL) photomicrograph of alteration of plagioclase to fine grained sericite, quartz and epidote; **D)** XPL view of plagioclase phenocrysts in porphyritic Matachewan dykes; **E)** PPL view of advanced biotite and clay alteration of clinopyroxene in medium-grained, equigranular Matachewan dykes; **F)** XPL view of typical texture and mineralogy of medium-grained, equigranular Matachewan dykes.

alteration assemblages of quartz, sericite and epidote **(Fig. 3.3C)**. Where observed, these large plagioclase crystals occur as either single crystals or ‘clumps’ of several crystals **(Fig. 3.3D)**. The presence of these very large plagioclase phenocrysts suggests that they formed during fractional crystallisation of a magma stored in a deeper chamber and were incorporated into the dyke magma during periodic tapping of the chamber.

The medium grained sampled Matachewan dykes have a similar mineralogy to the fine grained samples in that they are dominated by altered pyroxene and plagioclase with lesser amounts of quartz and opaque phases. The clinopyroxene in medium grained Matachewan dykes accounts for ~60% of the rock volume and forms subhedral, elongate crystals which are far more altered than the clinopyroxene in the fine grained dykes and contain fine grained biotite and clay as alteration products **(Fig. 3.3E)**.

There is markedly less plagioclase in the medium grained dykes than in the fine grained dykes (~40%) and in the medium grained dykes, the plagioclase is significantly more altered to fine grained quartz, sericite and epidote **(Fig. 3.3F)**. Quartz is more abundant (up to ~3%) in the medium grained dykes and forms polycrystalline aggregates of anhedral crystals which have indefinite grain boundaries. There is also significantly less opaque material in the medium grained dykes, which, like in the fine grained dykes is concentrated within altered pyroxene crystals. The alteration described above suggests that the Matachewan dykes (at least those which have been examined) have only experienced low grade metamorphism which likely did not exceed greenschist facies.

3.3. East Bull Lake Suite

3.3.1. Sample Collection

Seven, eight and fourteen samples were collected from the East Bull Lake, Agnew and River Valley intrusions respectively during a fieldtrip as part of the 11th International Platinum Symposium, held in Sudbury in June 2010. Six samples were also collected from the Gerow Township intrusion which has been interpreted, based on petrography and limited geochemistry (Easton et al. 2010), to be another, previously unknown, East Bull Lake suite intrusion. Continuous exposures of East Bull Lake suite rocks are scarce, with the most impressive exposures found in man-made excavations. Aside from such areas, the most common exposures are variably large ‘whale-back’ type exposures in the hummocky high ground around the numerous lakes in the area. These exposures vary greatly in size, and can be up to 10s of m^2. Photographs of exposures of East Bull Lake suite rocks are shown in **Fig. 3.4**.

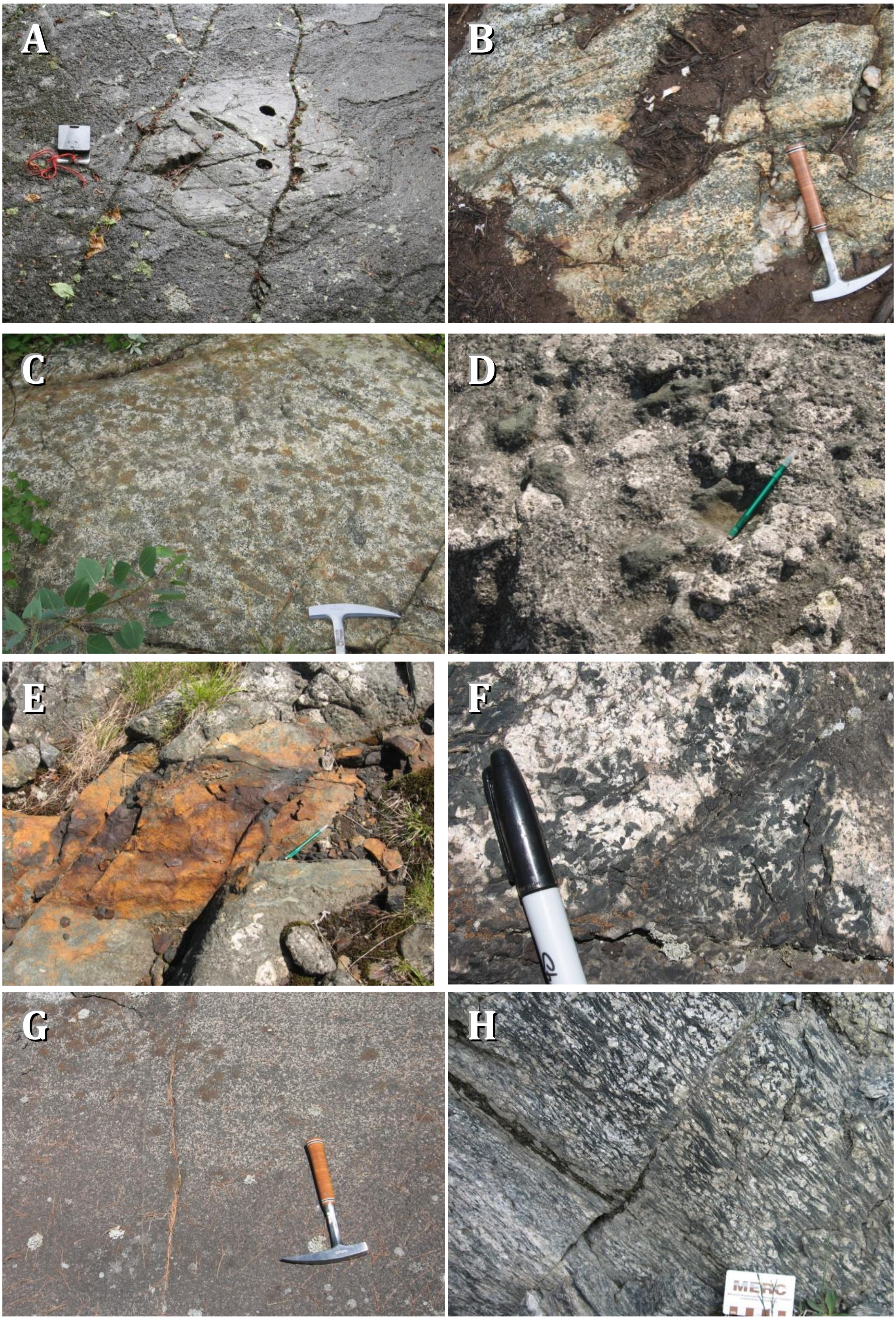
A
B
C
D
E
F
G
H
MERC

Fig. 3.4. Photographs of outcrops of East Bull Lake suite intrusions. **A)** Pyroxenite xenolith in gabbronoritic matrix from the inclusion-bearing zone of the East Bull Lake Intrusion; **B)** Centimetre-scale layering of leucogabbronorite and gabbronorite in the Gerow Intrusion; **C)** Disseminated sulphide mineralisation in massive gabbronorite in the Gerow Intrusion; **D)** Nodular anorthosite from the inclusion-bearing gabbronorite zone of the Agnew Intrusion. Note the dark green pyroxenite fragments; **E)** Sulphide burn in the nodular anorthosite unit, Agnew Intrusion; **F)** Dendrite unit in the Upper Gabbronorite Zone, Agnew Intrusion; **G)** Centimetre-scale layering of gabbronorite in the East Bull Lake Intrusion; **H)** Mylonitized anorthosite from the River Valley Intrusion; **I)** Mafic xenoliths in gabbronoritic matrix from an unmineralised section of the Inclusion-Bearing Zone; **J)** Mineralised xenolith of layered leucogabbronorite in gabbroic matrix from the Inclusion-Bearing Zone, River Valley Intrusion; **K)** Unmineralised mafic xenoliths in mineralised gabbronoritic matrix from the Inclusion-bearing Zone, River Valley Intrusion; **L)** Close-up of nodular anorthosite, showing closely packed plagioclase glomerophenocrysts with interstitial pyroxenitic matrix from a quarry in the Agnew Intrusion.

3.3.2. Petrography

Stratigraphic subdivision of much of the East Bull Lake suite of intrusions relies on quite subtle variations in mineralogy and layering scale. For example, above the Marginal Series rocks, the East Bull Lake suite intrusions are subdivided into units such as massive gabbronorite, layered gabbronorite, rhythmically layered gabbronorite, vari-textured gabbronorite and leucogabbronorite **(Fig. 2.13)**. To avoid repetition, petrographic descriptions of East Bull Lake suite rocks provided here are limited to the main rock types observed in the intrusion.

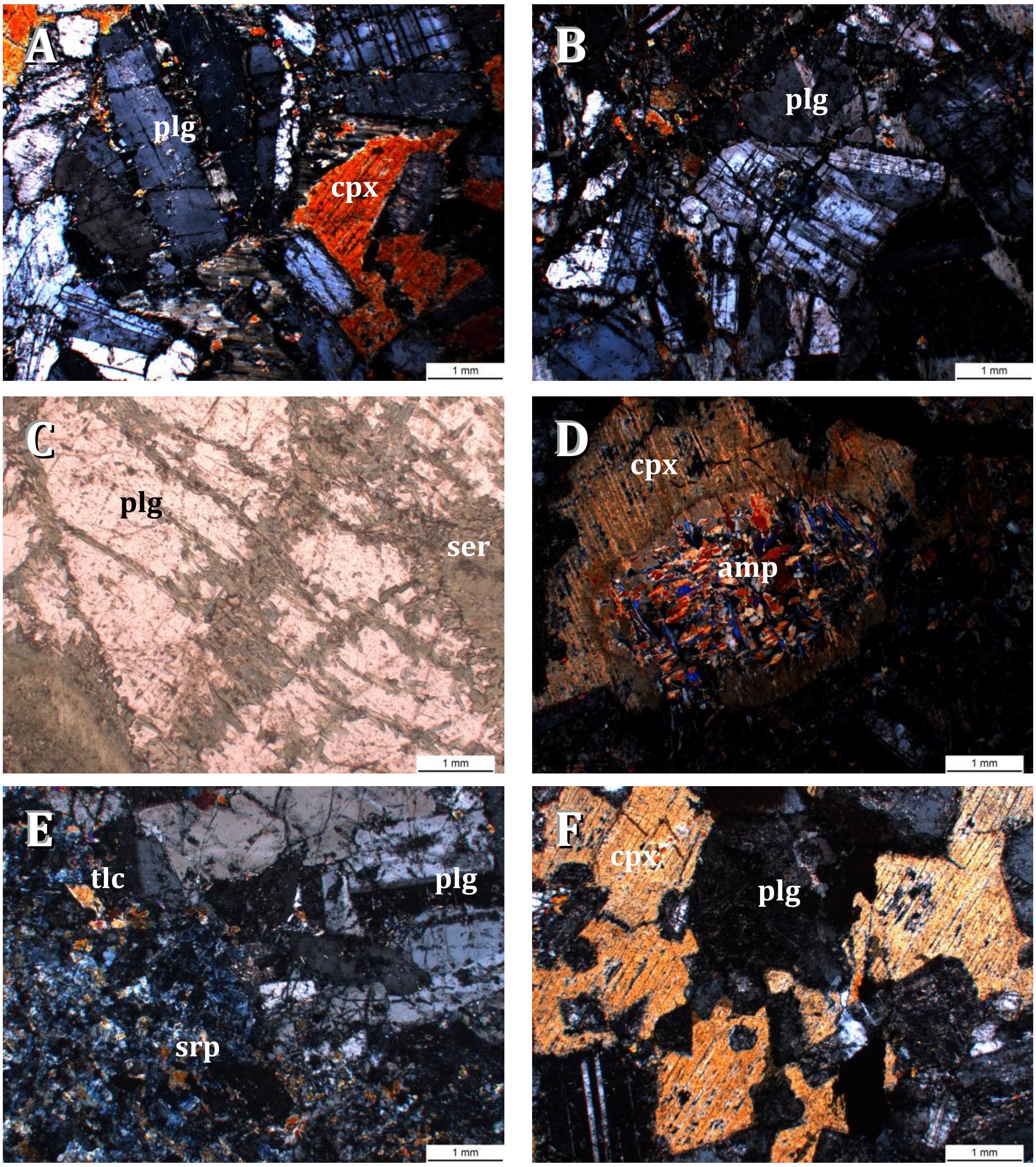

Fig. 3.5. Photomicrographs of the East Bull Lake suite gabbronoritic rocks. **A)** XPL view of typical texture in gabbronoritic rocks; **B)** XPL view of anhedral medium grained plagioclase crystals in more plagioclase-phyric gabbronoritic rocks; **C)** PPL view of pervasive fractures of pale green mica within plagioclase crystals in the gabbronoritic rocks; **D)** XPL view of typical alteration of clinopyroxene to fine-grained aggregates of amphibole in crystal interiors; **E)** XPL view of typical alteration of olivine to fine grained sericite, talc and Fe-oxides in more olivine-phyric gabbronoritic rocks; **F)** XPL view of ophitic textured gabbronoritic rocks.

Gabbronoritic rocks

The East Bull Lake Suite gabbronorites are predominantly composed of randomly aligned medium-coarse grained cumulus plagioclase with varying amounts of cumulus orthopyroxene and olivine set within intercumulus clinopyroxene **(Fig. 3.5A)**. The gabbronoritic samples collected during this study range in mineralogy between gabbronorite, olivine gabbronorite and leucogabbronorite with leucogabbronoritic samples the most common. The plagioclase in the gabbronorite rocks forms euhedral elongate laths (<5 mm in length) in cases where single crystals are preserved in the interstitial clinopyroxene oikocrysts, or, as intergrown, anhedral, amorphous crystals in more plagioclase-phyric samples where growth of adjacent plagioclase crystals has impeded euhedral crystal formation **(Fig. 3.5B)**. Alteration of the plagioclase in the gabbronoritic rocks is significant and dominated by either very fine grained replacements by sericite and quartz, or replacement by pale green mica (possibly phengite) along pervasive fracture networks **(Fig. 3.5C)**. The next most dominant phase in the gabbronoritic rocks is orthopyroxene, which forms subhedral-euhedral prisms up to ~6 mm in length. The orthopyroxene is significantly altered to very fine grained acicular actinolite and green tremolite at crystal margins and fine grained aggregates of hornblende in crystal interiors **(Fig. 3.5D)**. Primary olivine is not observed in thin section but remnants can be inferred from fine grained assemblages of talc, serpentine and iron oxides which appear to have pseudomorphed euhedral olivine **(Fig. 3.5E)**. Clinopyroxene in the gabbronoritic rocks appears to be a post cumulus phase as it commonly forms anhedral oikocrysts which enclose euhedral plagioclase crystals in locally ophitic-textured samples **(Fig. 3.5F)**. The clinopyroxene is generally better preserved than the orthopyroxene in the gabbronoritic rocks and is only slightly replaced by very fine grained (occasionally acicular) crystals of amphibole, giving the clinopyroxene a dusty appearance.

Anorthositic rocks

Anorthositic rocks in the East Bull Lake suite are primarily composed of randomly orientated, coarse grained, inequigranular plagioclase with lesser amounts of orthopyroxene and intercumulus clinopyroxene **(Fig. 3.6A)**. The plagioclase ranges in habit from anhedral to subhedral and is generally well preserved with alteration limited to very fine grained replacements of quartz and sericite **(Fig. 3.6B)**. Some of the plagioclase crystals are rimmed with very fine grained acicular actinolite and tremolite which appears to have grown over plagioclase crystal boundaries **(Fig. 3.6C)**. This amphibole material is likely derived from alteration of orthopyroxene as evidenced by occasional phenocrysts of primary orthopyroxene which show alteration to similar looking material **(Fig. 3.6D)**. This same very fine grained acicular amphibole material fills randomly orientated, mm-scale fracture networks within the cumulus plagioclase **(Fig. 3.6E)**. This texture suggests that the anorthositic rocks of the East Bull Lake suite formed as cumulates of mostly plagioclase (and minor orthopyroxene) set in an intercumulus matrix of clinopyroxene, before being intruded by a second pulse of mafic magma which form the pyroxenitic (now altered to amphibole) vein material.

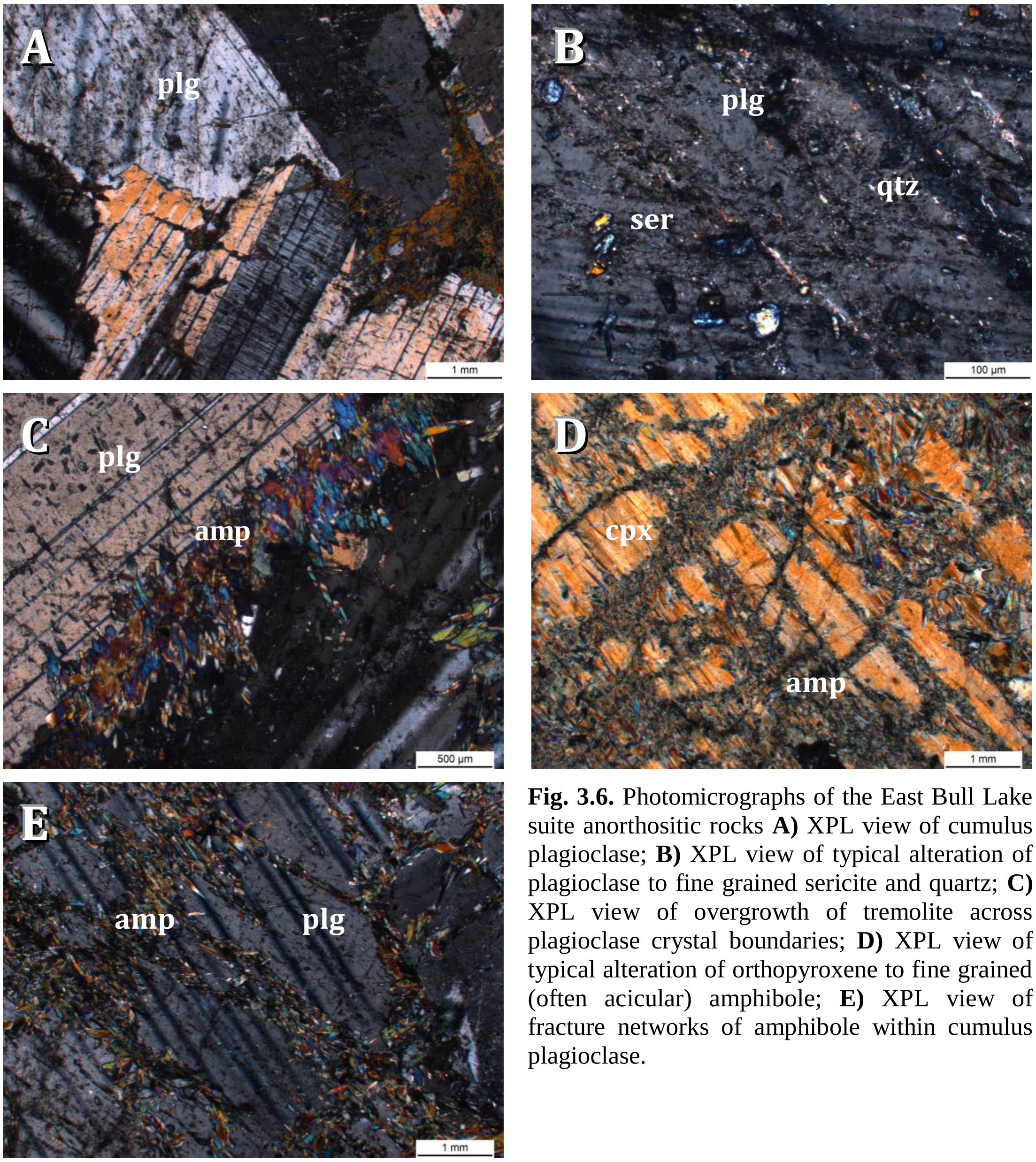

Fig. 3.6. Photomicrographs of the East Bull Lake suite anorthositic rocks **A)** XPL view of cumulus plagioclase; **B)** XPL view of typical alteration of plagioclase to fine grained sericite and quartz; **C)** XPL view of overgrowth of tremolite across plagioclase crystal boundaries; **D)** XPL view of typical alteration of orthopyroxene to fine grained (often acicular) amphibole; **E)** XPL view of fracture networks of amphibole within cumulus plagioclase.

Inclusion-Bearing rocks

The matrix of the Inclusion-Bearing rocks is gabbronoritic-leucogabbronoritic in composition and contains varying amounts of plagioclase, clinopyroxene and orthopyroxene **(Fig. 3.7A)**. The matrix is largely equigranular and ranges in size from medium-coarse grained. In the majority of samples studied, the dominant mineral is plagioclase (up to ~70% in some samples) which forms euhedral, elongate, inter-locking prisms with adcumulate texture **(Fig. 3.7B)**. The plagioclase is moderately well preserved in the matrix with alteration limited to very fine grained, disseminated replacements of quartz and sericite. Clinopyroxene and orthopyroxene occur in approximately equal proportions and form subhedral crystals which are heavily altered to fine grained, occasionally acicular amphibole **(Fig. 3.7C)**. The sulphide content of the gabbronoritic matrix of the inclusion-bearing rocks is highly variable and in the samples studied ranges from non-existent up to ~5%. In sulphide-bearing samples the sulphides form very fine grained, anhedral crystals which are evenly disseminated through the matrix **(Fig. 3.7D)**.

The pyroxenite pods in the Inclusion-Bearing zone are primarily composed of large, equant megacrysts of orthopyroxene set within a finer grained groundmass of amphibole, orthopyroxene and clinopyroxene **(Fig. 3.7E)**. In hand specimen, the orthopyroxene megacrysts can be up to ~5 cm in length and form elongate, euhedral prisms which account for ~50% of the rock **(Fig. 3.7F)**. In thin section, the orthopyroxene megacrysts are generally well preserved, although embayments along the grain boundaries are filled with fine grained amphibole suggesting that alteration has affected the margins of the orthopyroxene **(Fig. 3.7G)**. The interiors of the orthopyroxene megacrysts are generally well preserved, although, minor alteration to amphibole is manifested as fine grained amorphous blebs which are disseminated through the crystals, or as elongate replacements concentrated along cleavage planes **(Fig. 3.7H)**. The orthopyroxene megacrysts also contain very fine grained inclusions of opaque material which ranges in habit from anhedral blebs to euhedral, equant crystals with a rectangular-diamond shaped cross section **(Fig. 3.7I)**. Amphibole constitutes approximately 60% of the groundmass of the pyroxenite pods and occurs in two distinct forms. The most abundant form of amphibole is preserved as euhedral, elongate laths with equant, diamond shaped cross-sections **(Fig. 3.7J)**. The second form of amphibole occurs as anhedral masses, characterised by a pervasive and randomly aligned opaque fracture network **(Fig. 3.7K and L)** which does not penetrate into the other type of amphibole or the orthopyroxene megacrysts. Occasionally, this ‘fractured’ type of amphibole is observed to replace remnants of clinopyroxene **(Fig. 3.7M)** which suggests that this type of amphibole is secondary.

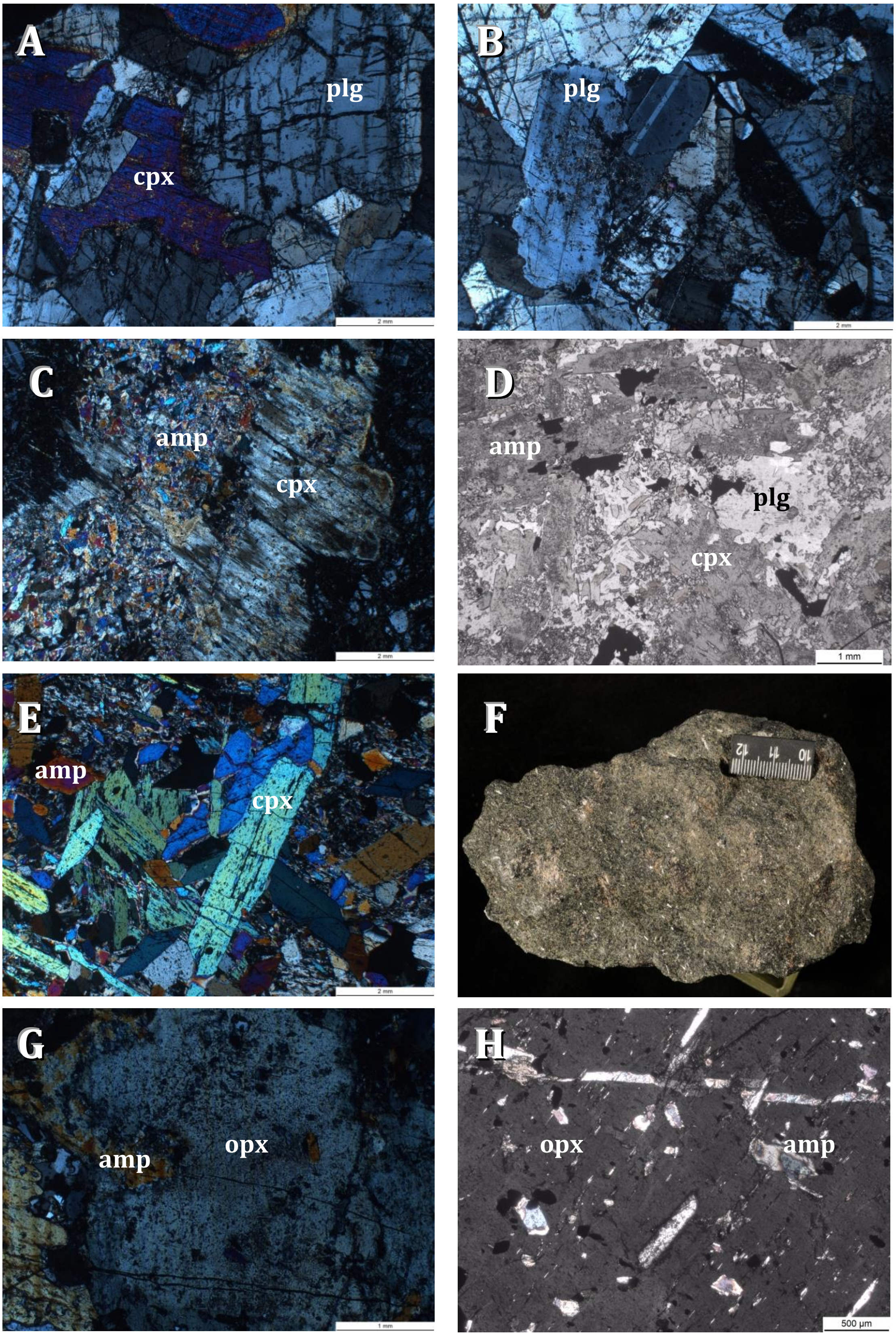
A
plg
cpx
2 mm
B
plg
2 mm
C
amp
cpx
2 mm
D
amp
plg
cpx
1 mm
E
amp
cpx
2 mm
F
10
11
12
G
amp
opx
1 mm
H
opx
amp
500 µm

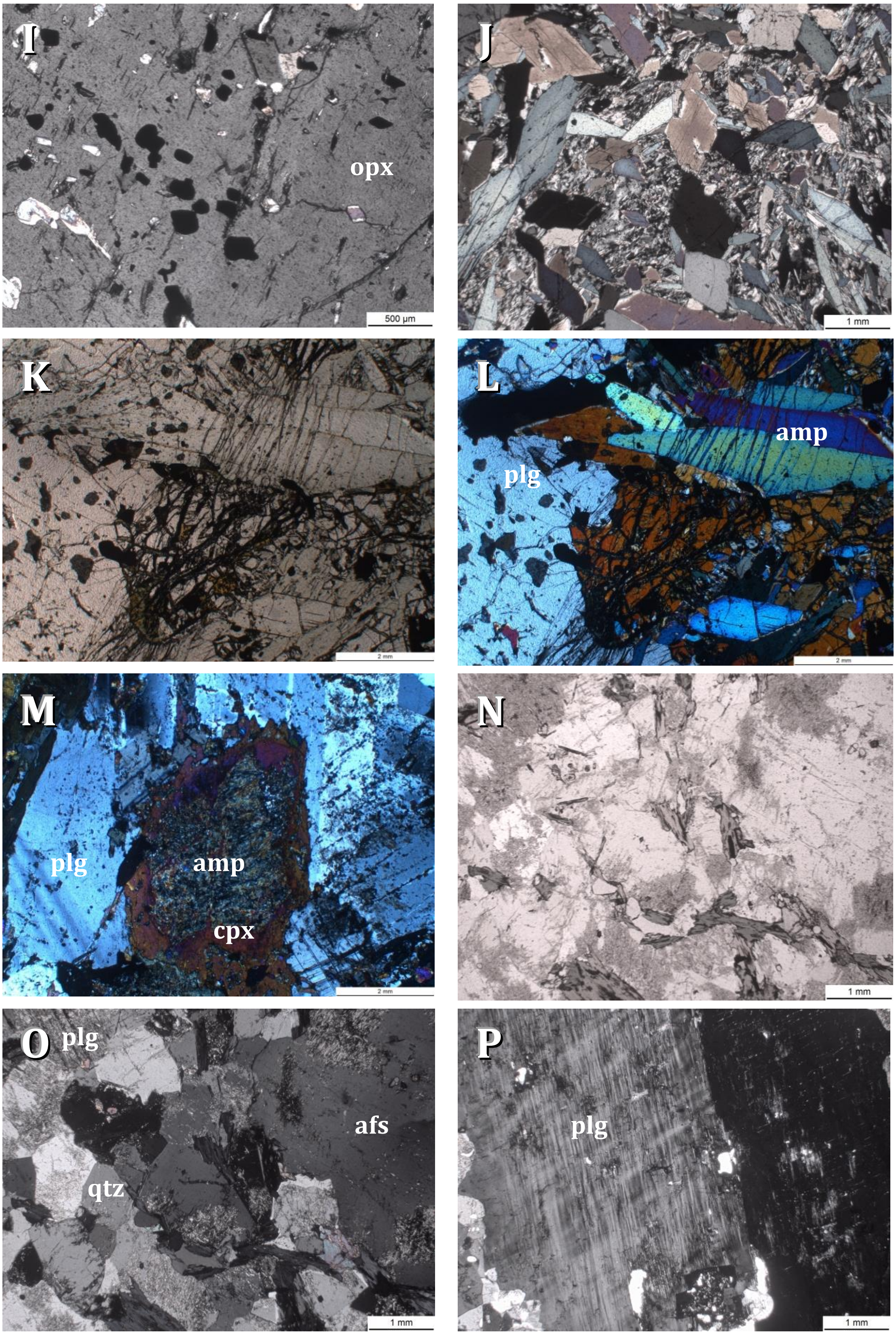
I
opx
500 µm
J
1 mm
K
2 mm
L
amp
plg
2 mm
M
plg
amp
cpx
2 mm
N
1 mm
O
plg
afs
qtz
1 mm
P
plg
1 mm

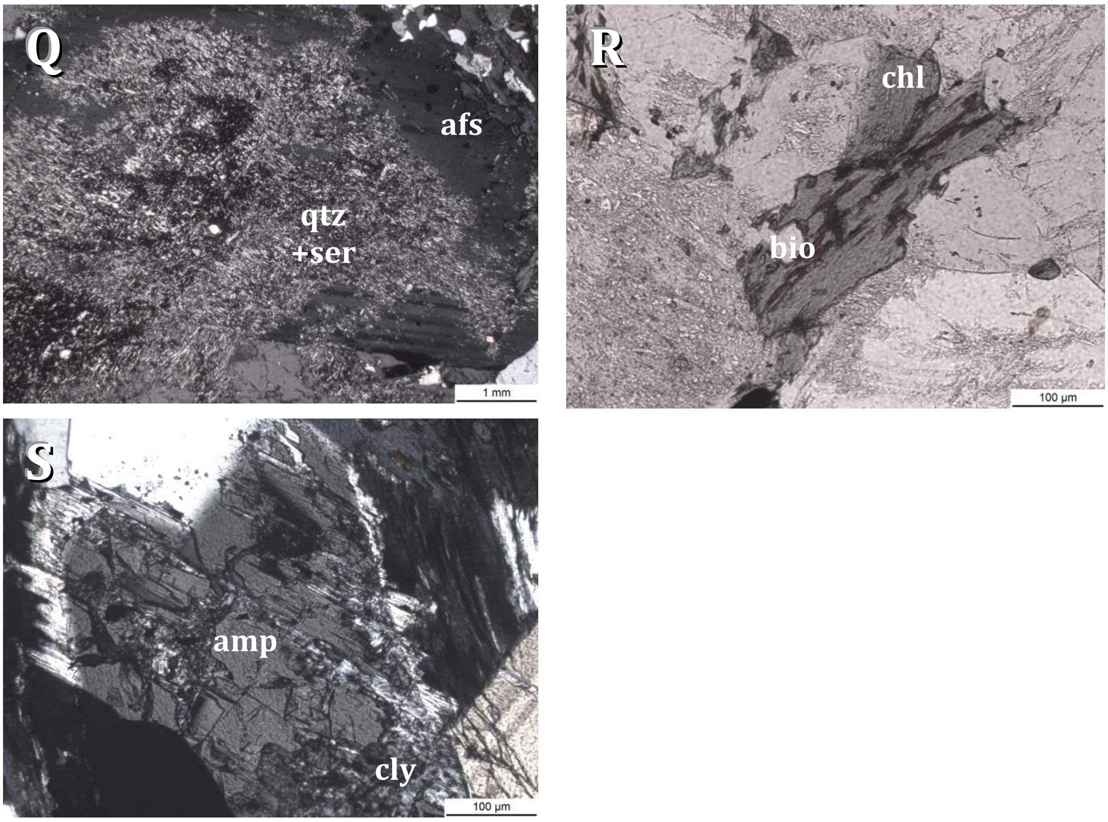

Fig. 3.7. Photomicrographs of the East Bull Lake suite Inclusion-Bearing unit: **A)** XPL view of typical texture and composition of gabbronoritic matrix of inclusion-bearing rocks; **B)** XPL view of adcumulate texture in plagioclase from the gabbronoritic matrix; **C)** XPL view of fine-grained acicular replacements of amphibole after clinopyroxene in the gabbronoritic matrix; **D)** PPL view of gabbronoritic matrix showing the anhedral and disseminated nature of the sulphides (opaques); **E)** XPL view of typical texture and composition of pyroxene inclusions; **F)** Photograph of pyroxene inclusion in hand-sample. Reflective laths are cleavage-plane sections of orthopyroxene; **G)** XPL view of alteration of orthopyroxene megacrysts to fine grained amphibole along crystal margins; **H)** XPL view of fine grained alteration of orthopyroxene within the megacrysts; **I)** XPL view of very fine grained inclusions of opaque minerals within orthpyroxene megacrysts; **J)** XPL view of typical texture and composition of the matrix of the pyroxenite inclusions; **K)** PPL view of 'fractured' amphibole; **L)** XPL view of **K**; **M)** XPL view showing alteration of clinopyroxene to 'fractured' amphibole; **N)** PPL view of typical texture and composition of the granitic inclusions; **O)** XPL view of **N**; **P)** XPL view of orthoclase phenocryst showing both Carlsbad and polysynthetic twinning; **Q)** XPL view of very fine grained sericite and quartz alteration of orthoclase; **R)** PPL view of chlorite crystal with irregular margins and inclusions of biotite; **S)** XPL view showing alteration of amphibole to fine grained clay minerals.

The granitic xenoliths are predominantly composed of orthoclase, quartz, chlorite, amphibole and biotite **(Fig. 3.7N and O)**. The granitic inclusions have an inequigranular texture with orthoclase phenocrysts forming subhedral, elongate prisms (<5mm in length) which display both Carlsbad and polysynthetic twins **(Fig. 3.7P)**. These orthoclase phenocrysts are altered to fine grained sericite, concentrated within crystal interiors **(Fig. 3.7Q)**. The finer groundmass is composed of subhedral, equant orthoclase which shows similar twins and alteration as the phenocrysts. Fine grained orthoclase makes up ~60% of the groundmass. Quartz accounts for ~20%

and forms anhedral crystals. Chlorite comprises ~15% of the groundmass and forms elongate laths which have irregular crystal margins with adjacent orthoclase crystals **(Fig. 3.7R)**. Amphibole accounts for ~5% of the groundmass and displays strong, green pleochroism. The amphibole is significantly altered to fine grained clay and quartz **(Fig. 3.7S)**. Biotite occurs in trace amounts in the granitic inclusions and forms, thin elongate crystals which are partially altered to chlorite.

Gabbroic and anorthositic xenoliths are also present (see **Fig. 3.4J** and **3.4K**). In thin section, these inclusions are indistinguishable from similar lithologies higher up.

3.4. Blue Draw Metagabbro

3.4.1. Sample Collection

Ninety-six samples of the Blue Draw Metagabbro and surrounding rocks were collected. Ninety of the samples are from the Blue Draw itself while the remaining six samples were collected from the Boxelder Creek Quartzite host rock from either side of the intrusion. All of the samples were collected along traverses oriented perpendicular to the dominant strike of the igneous layering from the least-deformed north eastern half of the intrusion, approximately 2 km west of the town of Nemo. Traverses were selected by studying the outcrop map of Maranate (1979) and choosing areas which provided the most extensive and continuous outcrop. A sample spacing of five metres was used along the traverses such that chemostratigraphic profiles through the intrusion could be constructed (see Chapter 3). Access into the area is provided by Forestry Road 140 which runs parallel to Boxelder Creek from Nemo. Exposure in the valley floor is minimal **(Fig. 3.8)**, but steep faced ridges which mark the higher ground have less dense coniferous vegetation and in places, continuous exposure can be followed for up to 100m. A map showing the sample locations is shown in **Fig. 3.9**.

3.4.2. Petrography

The stratigraphic nomenclature used in this study divides the BDM into a ~130 m thick peridotite unit which is successively overlain by the ~100 m thick lower olivine melagabbronorite unit and the ~250 m thick gabbronorite unit which is separated into lower and upper units by the ~50 m thick melagabbronorite unit which crops out discontinuously at ~380 m from the base of the intrusion. The upper gabbronorite unit is overlain by a ~60 m thick quartz gabbronorite unit which, close to the margin of the intrusion, contains xenoliths of the Boxelder Creek Quartzite. This nomenclature is modified after the work of Maranate (1979) and is explained in Chapter 3.

Fig. 3.8. Photographs of Blue Draw Metagabbro exposures. **A)** Typical exposure in the area is limited to blocky sub-crop on higher ground; **B)** Steep-sided cliffs exposure up to ~100 m of igneous stratigraphy; **C)** Road-side exposure adjacent to Forest Road 140; **D)** Cliff-face showing primary metre-scale igneous layering in the Upper Gabbronorite unit. Layering is dipping steeply to the west (Photograph taken facing northeast); **E)** Malachite staining observed in outcrop in Quartz Gabbronorite unit (equivalent of geochemistry sample BD070); **F)** Sigmoidal stress fracture in Boxelder Creek Quartzite ~1 km south of the Blue Draw Metagabbro.

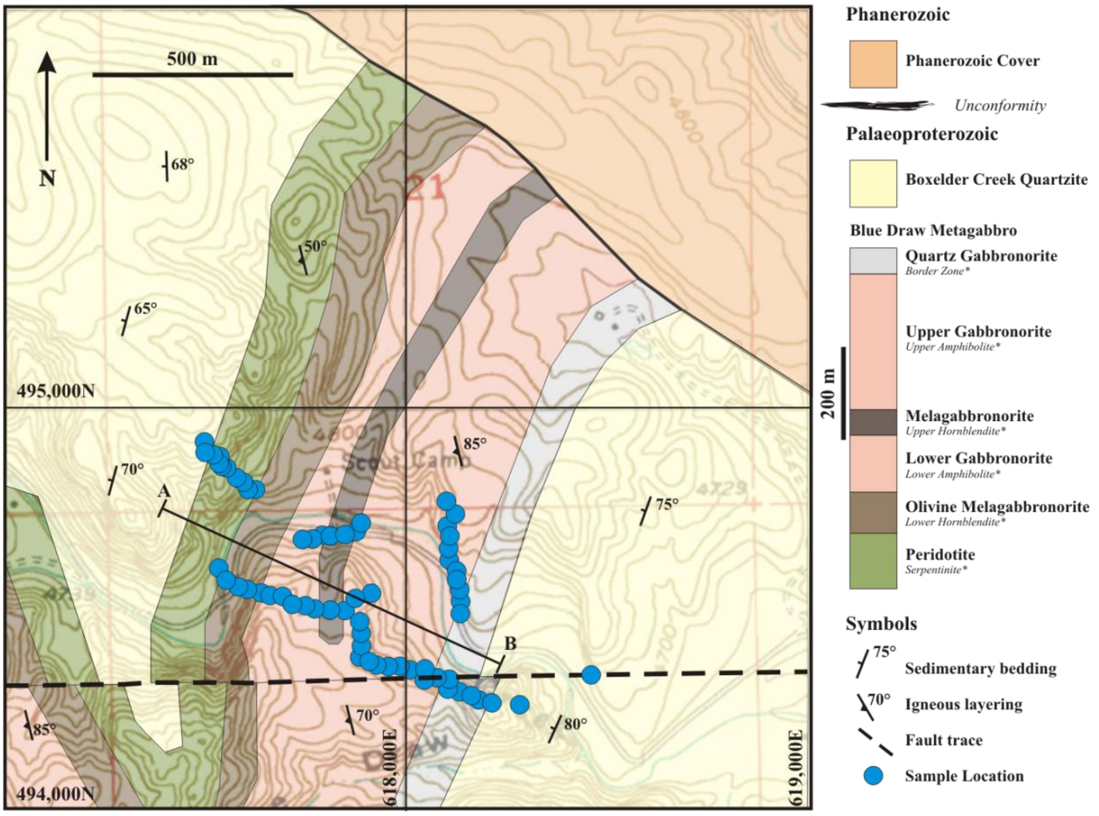

Fig. 3.9. Map showing sample locations of Blue Draw Metagabbro rocks studied in this project. Geology modified after Maranate (1979).

Peridotite unit

The peridotite unit at the base of the intrusion is dominated by serpentinised olivine (~90%) and chrome spinel (~10%) though some samples can contain up to ~40% altered pyroxene. The unit ranges from equigranular nearer the base, with samples showing cumulate textures, to porphyritic, in which megacrysts of serpentinised olivine are enclosed by finer grained crystals of the same material **(Fig. 3.10A** and **B)**. Serpentinisation of the olivine in this unit is complete and forms radial to randomly aligned masses of very fine grained crystals of serpentine which pseudomorph the primary olivine crystals and largely preserve primary igneous textures **(Fig. 3.10C)**.

Towards the top of the peridotite unit, serpentinised olivine occurs as both a megacryst phase and groundmass phase. In the megacrysts, talc and magnesite alteration is aligned in bands across the megacrysts giving them an apparent fabric which is not shared with the groundmass.

In the intrusion as a whole, chrome spinel is most abundant in the peridotite unit where it occurs as fine grained euhedral-subhedral prismatic crystals which are disseminated evenly through the rock. Where the peridotite unit is megacrystic, chrome spinel is present both as inclusions in the serpentinised olivine megacrysts and disseminated through the groundmass. The grain boundaries of chrome spinel crystals in the equigranular serpentinites are irregular and show evidence of alteration and recrystallisation. This effect is less visible in spinel crystals included in serpentinised olivine megacrysts.

Olivine melagabbronorite unit

The olivine melagabbronorite unit is composed primarily of altered pyroxene and plagioclase **(Fig. 3.10D)**. At the base of the unit, altered pyroxene accounts for ~80% of the rock volume, while altered plagioclase and very minor amounts of serpentinised olivine accounts for the rest. At the top of the unit, altered clinopyroxene decreases to <50% of the rock volume and altered plagioclase becomes dominant. The altered pyroxenes in the olivine melagabbronorite unit are primarily clinopyroxene (which, in less altered samples, preserve primary, euhedral lath-shaped habits) with lesser amounts of orthopyroxene. The alteration of the pyroxenes manifests itself as either fine grained cross-cutting bladed crystals of amphibole and patchy calcite in pyroxene interiors and grain boundaries **(Fig. 3.10E)**, to total pseudomorphic replacements. The alteration of the plagioclase is similar to that observed elsewhere in the intrusion and is dominated by very fine grained replacements of sericite and quartz **(Fig. 3.10F)**.

Lower gabbronorite unit

The lower gabbronorite unit **(Fig. 3.10G)** is predominantly (50-60%) composed of plagioclase showing moderate-advanced sericite alteration. Approximately 35% of the rock is made up of altered pyroxenes, dominated by pale green clinopyroxene which shows moderate-advanced alteration to amphibole, biotite, calcite and quartz **(Fig. 3.10H)**. The biotite alteration primarily occurs at grain boundaries where it pseudomorphically replaces the pyroxene while the quartz occurs as amorphous patches in the middle of crystals. Trace amounts of magnetite showing partial alteration to secondary iron oxides (likely haematite) are present **(Fig. 3.10I)**.

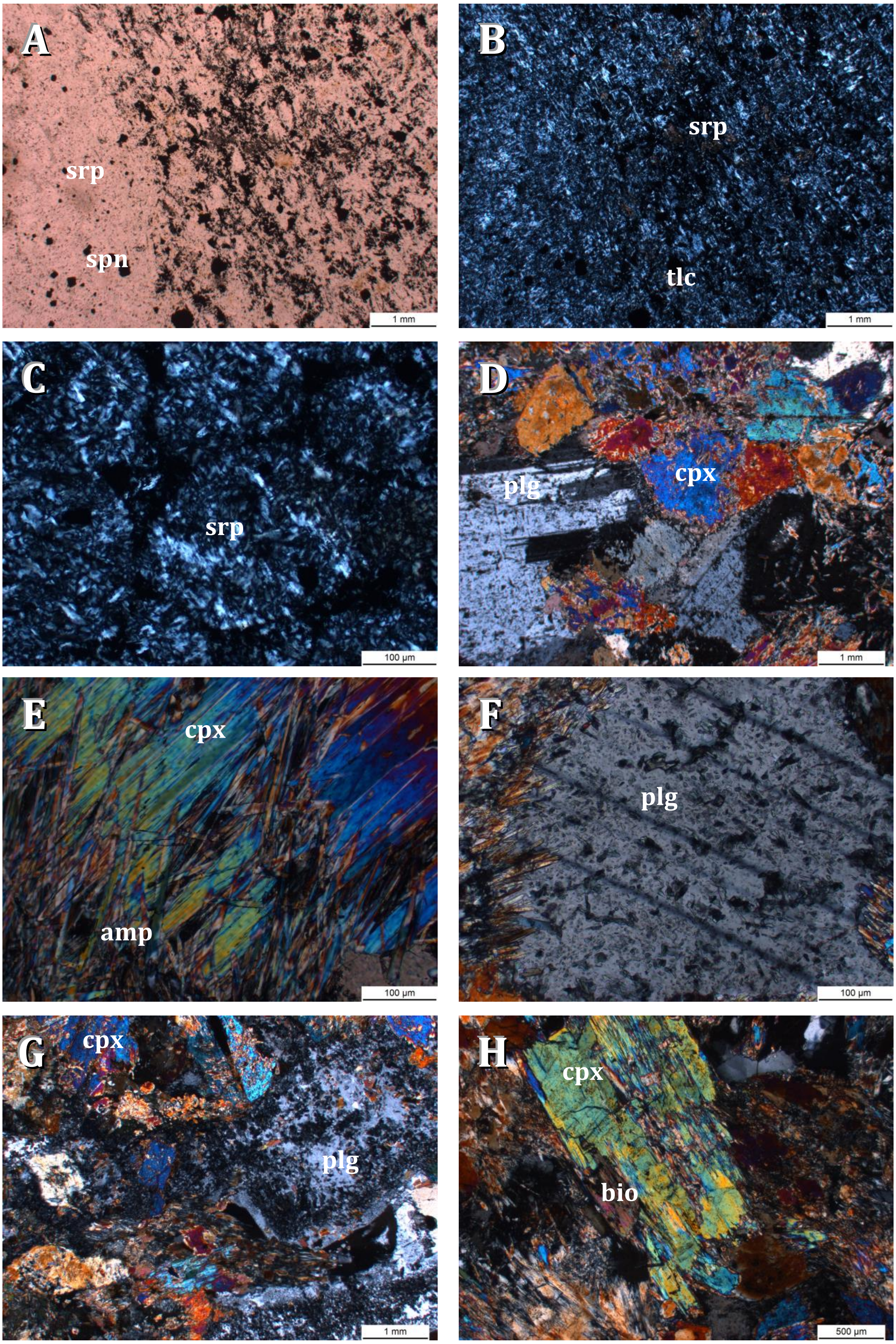
A
srp
spn
1 mm
B
srp
tlc
1 mm
C
srp
100 µm
D
plg
cpx
1 mm
E
cpx
amp
100 µm
F
plg
100 µm
G
cpx
plg
1 mm
H
cpx
bio
500 µm

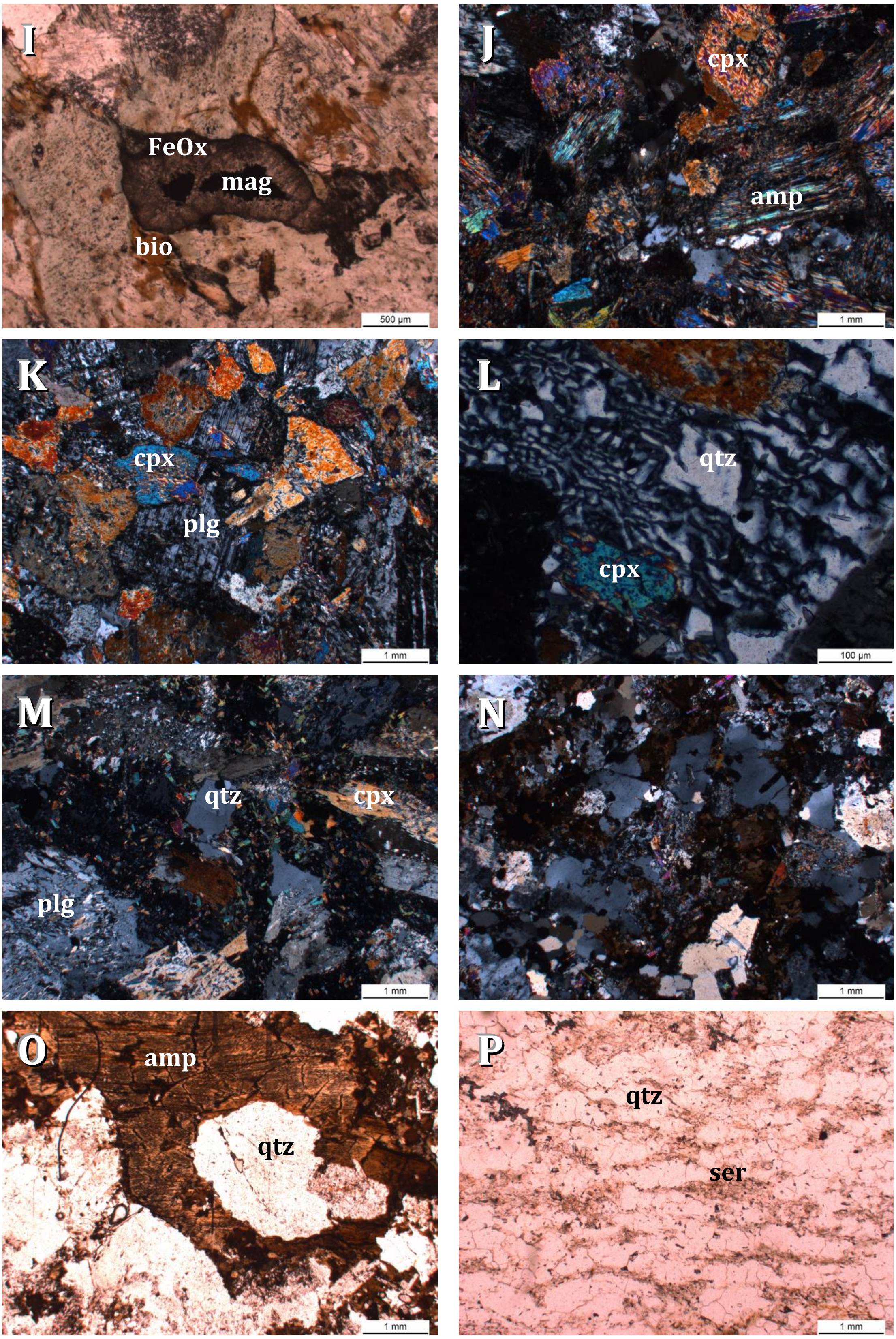
I
FeOx
mag
bio
500 µm
J
cpx
amp
1 mm
K
cpx
plg
1 mm
L
qtz
cpx
100 µm
M
qtz
cpx
plg
1 mm
N
1 mm
O
amp
qtz
1 mm
P
qtz
ser
1 mm

Fig. 3.10. Photomicrographs of the Blue Draw Metagabbro. **A)** PPL view of typical texture in the Peridotite unit showing megacrystic olivine to the left and finer grained olivine to the right of the image; **B)** XPL view of view in **A**; **C)** XPL view of typical alteration of olivine in peridotite unit; **D)** XPL view of typical texture and mineralogy of the olivine melagabbronorite unit; **E)** XPL view of typical alteration of clinopyroxene to fine grained, acicular amphibole; **F)** XPL view of typical alteration of plagioclase to fine grained quartz, sericite and epidote; **G)** XPL view of typical texture and mineralogy of the lower gabbronorite unit; **H)** XPL view of typical alteration of clinopyroxene to biotite, calcite and amphibole in the lower gabbronorite unit; **I)** PPL view of alteration of magnetite to secondary Fe oxides in the lower gabbronorite unit; **J)** XPL view of typical texture and mineralogy of the melagabbronorite unit; **K)** XPL view of typical texture and mineralogy of the upper gabbronorite unit; **L)** XPL view of granophyric quartz in the upper gabbronorite unit; **M)** XPL view of typical texture and mineralogy of the rocks near the top of the upper gabbronorite unit, note the decrease in abundance of clinopyroxene in comparison to **K** which is from nearer the base of the unit; **N)** XPL view of typical texture and mineralogy of the quartz gabbronorite unit; **O)** PPL view of interstitial nature of amphibole in the quartz gabbronorite unit; **P)** PPL view of typical texture and mineralogy of the Boxelder Creek Quartzite. Microscopic-scale layering is identified by the bands of micaceous material which are aligned to the horizontal in this image.

Melagabbronorite unit

The melagabbronorite unit is similar in mineralogy to the olivine melagabbronorite unit in that it is dominated by altered clinopyroxene (60-80%) with lesser amounts of moderately sericitised plagioclase, serpentinised olivine and contains trace amounts (<2%) of an opaque phase, potentially chromite or magnetite which has been altered to secondary iron oxide phases along grain boundaries **(Fig. 3.10J)**.

Upper gabbronorite unit

The rocks at the base of the upper gabbronorite **(Fig. 3.10K)** are predominantly made up of variably sericitised plagioclase (~55%). Approximately 40% of the rock is composed of altered pyroxene with clinopyroxene being dominant. The pyroxenes are moderately to completely altered to amphibole and calcite. Some samples contain minor amounts (<5%) of quartz which occasionally displays granophyric texture **(Fig. 3.10L)**. Trace amounts of fine grained, euhedral, partially oxidised magnetite are also present.

Towards the top of the upper gabbronorite unit, partially sericitised plagioclase and quartz become more abundant and collectively constitute approximately 60-70% of the rock volume **(Fig. 3.10M)**. In the uppermost samples from the upper gabbronorite unit, biotite (with minor amounts of chlorite), which can constitute up to 20% of the rock, occurs as fine grained aggregates of randomly aligned minerals that form networks around larger (usually plagioclase) crystals. Clinopyroxene is largely absent from the rocks near the top of the upper gabbronorite unit, but orthopyroxene remains, constituting ~10% of the rock volume and is moderately–completely altered to green amphibole, biotite, calcite and quartz.

Quartz gabbronorite unit

The quartz gabbronorite unit of the intrusion is composed of silicic rocks which become extremely quartz-rich at the top of the zone **(Fig. 3.10N)**. In the quartz gabbronorite unit, quartz occurs both as a primary phase and as fine grained inclusions in sericitised plagioclase crystals. Primary quartz occurs as granular masses of fine grained equant crystals which exhibit irregular grain boundaries both within the masses and with adjacent plagioclase which occurs in minor amounts and is weakly to moderately sericitised. Biotite (and minor chlorite) is the most common mica in the quartz gabbronorite unit and occurs as very fine grained granular masses of randomly aligned euhedral laths. Muscovite is also present in this unit but in minor amounts and is intergrown with biotite. Iron-rich amphibole (hornblende) is also present in minor amounts and forms anhedral crystals which fill the space between the abundant quartz **(Fig. 3.10O)**. The grain boundaries of the hornblende are altered to biotite with minor muscovite.

Boxelder Creek Quartzite

The Boxelder Creek Quartzite is made up almost entirely of poorly sorted, fine-medium grained, sub-rounded quartz with minor amounts of muscovite. Microscopic layering of the Boxelder Creek Quartzite is preserved and defined by interlaying of more micaceous bands within the quartzite **(Fig. 3.10P)**. In hand specimen, samples from the Boxelder Creek Quartzite appear more psammitic than as true quartzites.

Summary

In summary, the BDM records a primary igneous stratigraphy which shows a general evolution from mafic cumulates rich in olivine and pyroxene at the base to more evolved, mafic mineral-poor, feldspar-rich rocks with increasing stratigraphic height. This general trend is interrupted at the base of the melagabbronorite unit which contains a much greater proportion of mafic minerals than the underlying lower gabbronorite unit, which may suggest that the BDM was recharged during fractionation. The likelihood of this is explored later (see chapter 4). At the uppermost levels of the intrusion, the rocks are extremely evolved and contain high percentages of primary quartz and mica. At the lowest levels of the intrusion, serpentinised olivine is present in two size populations **(Fig. 3.10A** and **B)** which suggests that the BDM parental magma was intruded as a melt + olivine crystal mixture. Following crystallisation, the dominant primary magmatic minerals in the intrusion were olivine, pyroxene and plagioclase. These have subsequently been moderately-completely replaced by serpentine, amphibole, calcite, sericite and quartz which is characteristic of greenschist-amphibolite facies metamorphism.

3.5. Leopard Dyke Swarm

3.5.1. Sample Collection

Stephen Harlan (George Mason University) provided 20 Leopard dyke samples which he collected from the Leopard dykes that crop out in the Bighorn National Forest, Wyoming. The samples provided are the remains of palaeomagnetic cores collected prior to 2005 by Professor Harlan as part of a previous study (Harlan 2005). **Fig. 3.11** shows the location of the sampled Leopard dykes.

3.5.2. Petrography

The Leopard dykes are predominantly fine grained and porphyritic. The proportion of phenocrysts is variable between samples, with some samples containing no phenocrysts while others can contain up to 60% rock volume of phenocrysts. The phenocrysts form euhedral, elongate prisms which, in the samples studied, are up to 3 cm in length **(Fig. 3.12A)** but have been reported to be up to 20 cm in length (Heimlich and Manzer 1972).

Alteration of the plagioclase phenocrysts is variable and patchy **(Fig. 3.12B)**. In less altered regions of the phenocrysts, the plagioclase retains its characteristic twinning, while in other more altered regions, the plagioclase is entirely replaced by very fine grained masses of sericite, quartz, zoisite and other clay minerals. This alteration is commonly localised along crystal cleavages, but also forms randomly aligned networks and aggregates within the crystal. The crystal margins of the phenocrysts are not sharp with the groundmass and appear to be altered to ultra fine grained sericite and quartz.

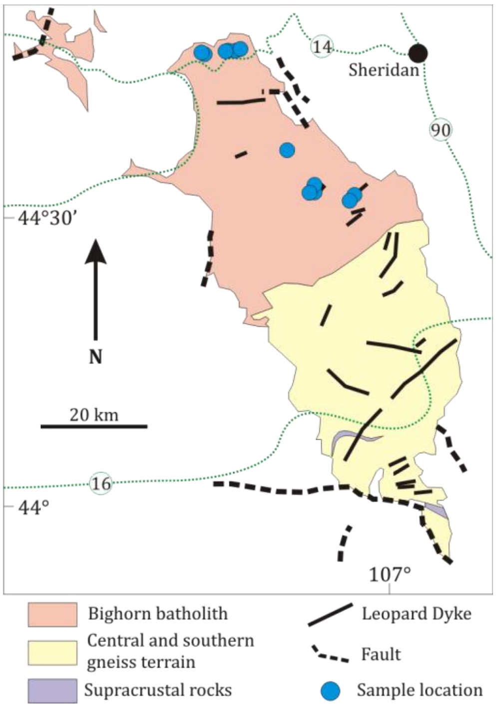

Fig. 3.11. Map showing sample locations of Leopard dykes studied in this project. Geology modified after Frost and Fanning (2006).

The groundmass of the Leopard dykes is composed of approximately equal proportions of plagioclase and clinopyroxene and trace amounts of magnetite and altered olivine **(Fig. 3.12C)**. The plagioclase in the groundmass forms randomly aligned, euhedral, elongate laths which are typically much less altered than the plagioclase phenocrysts. The clinopyroxene forms both euhedral, elongate prisms and stubby, anhedral crystals which appear to have filled the space between the groundmass plagioclase crystals. The clinopyroxene is variably altered to very fine grained aggregates of fibrous green actinolite and brown hornblende. This alteration is commonly concentrated along crystal cleavages and grain boundaries **(Fig. 3.12D)**. The magnetite in the groundmass constitutes ~1% of the rock and forms euhedral rhombic and octahedral crystals which occur as individual crystals within the groundmass or as aggregates of crystals **(Fig. 3.12E)** The olivine content of the Leopard dykes is variable with some dykes containing up to ~5% olivine, while in some samples, olivine (or its pseudomorphs) is not observed. Primary olivine is rarely preserved and is instead, usually totally altered to assemblages of very fine grained serpentine and iddingsite. The alteration of the olivine crystals is commonly observed to radiate out from the altered olivine crystals and is localised along fissures within the hosting plagioclase crystals **(Fig. 3.12F)**. The alteration described above suggests that the Leopard dykes have only experienced low grade metamorphism which likely did not exceed greenschist facies. The presence of very large plagioclase phenocrysts suggests that they formed during fractional crystallisation of a magma stored in a deeper chamber and were incorporated into the dyke magma during periodic tapping of the chamber.

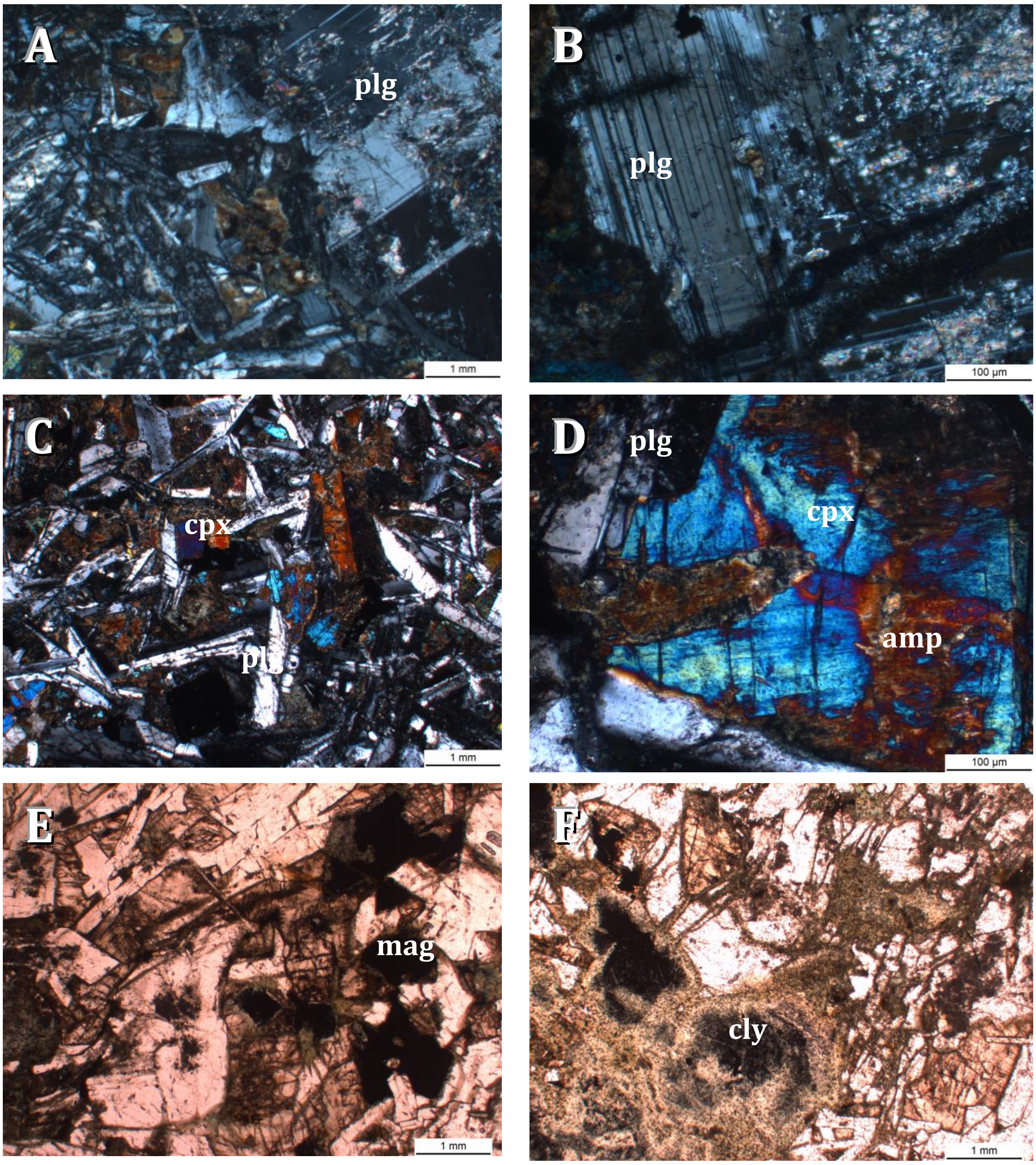

Fig. 3.12. Photomicrographs of the Leopard dyke swarm. **A)** XPL view of typical texture and mineralogy of plagioclase-porphyritic Leopard dykes; **B)** XPL view of alteration of plagioclase phenocrysts to fine grained sericite and quartz; **C)** XPL view of typical texture and mineralogy of the groundmass of the Leopard dykes; **D)** XPL view of typical alteration of clinopyroxene to fine grained amphibole; **E)** XPL view showing the disseminated and aggregate nature of magnetite in the Leopard dykes; **F)** XPL view of alteration of olivine to iddingsite pseudomorphs. Note the chloritic fracture material radiating from the altered olivine.

3.6. Kaminak Dyke Swarm

3.6.1. Sample Collection

Fifty-seven powdered samples of Kaminak dykes were collected for this study. These samples were originally collected by Hamish Sandeman, Walter Fahrig and Anthony LeCheminant and are stored at the GSC archives. Several rock samples of the Kaminak dykes are also stored at the GSC archives and are described below. A map showing the locations of the Kaminak dykes studied in this project is shown in **Fig. 3.13**.

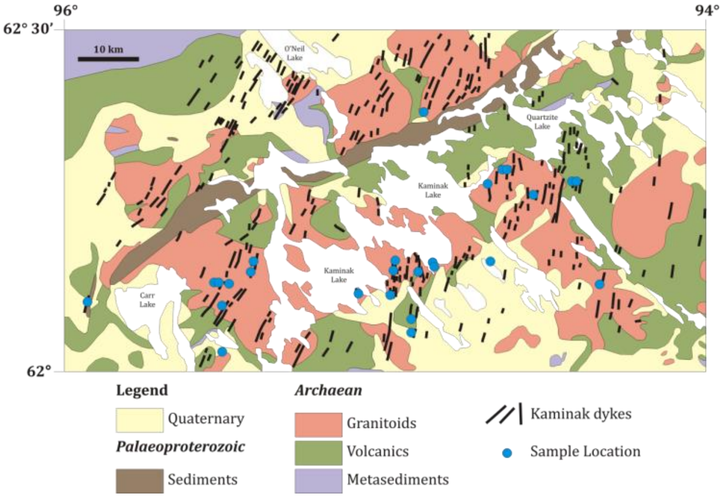

Fig. 3.13. Map showing sample locations of Kaminak dykes studied in this project. Geology modified after Sandeman and Ryan (2008).

3.6.2. Petrography

The Kaminak dykes sampled range from aphyric to plagioclase porphyritic. The dykes display ophitic-equigranular textures and are composed of fine grained plagioclase and clinopyroxene with trace amounts of opaque phases. Where observed, the plagioclase phenocrysts form euhedral, elongate laths (up to 5 mm) and have been significantly altered to quartz, sericite and epidote giving the phenocrystic plagioclase a very regular and speckled appearance **(Fig. 3.14A)**. The plagioclase in the groundmass is typically less altered than the phenocrysts and forms fine grained, euhedral laths which are intergrown with euhedral-elongate prisms of clinopyroxene. The groundmass is moderately altered and characterised by fine grained replacements of the clinopyroxene by amphibole and replacements of the plagioclase with fine grained quartz and sericite, giving the plagioclase a dusty appearance **(Fig. 3.14B)**. Opaque phases account for ~2% of the groundmass and form fine grained, anhedral blebs which are disseminated through the rock. Olivine is not observed in the Kaminak dykes sampled.

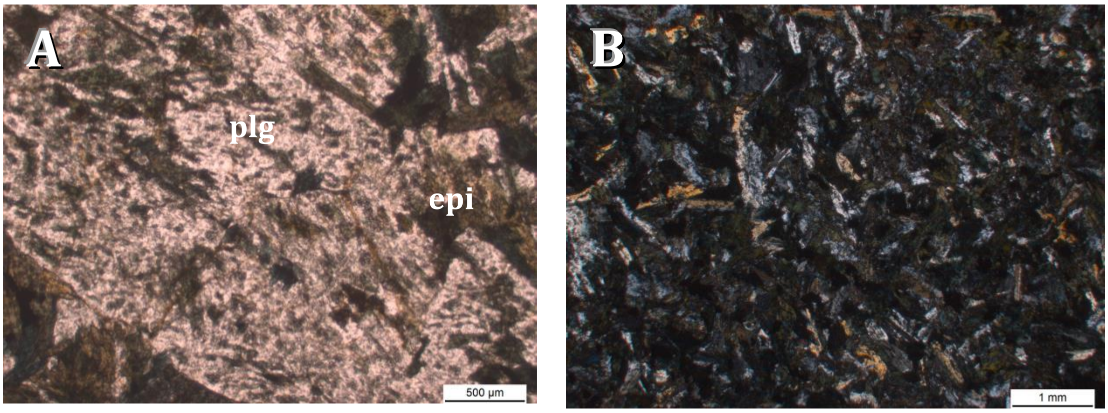

Fig. 3.14. Photomicrographs of the Kaminak dyke swarm. **A)** PPL view of typical alteration in plagioclase phenocrysts to fine grained quartz, sericite and epidote; **B)** XPL view of typical texture and mineralogy of groundmass of Kaminak dykes.

3.7. Non-sampled Matachewan LIP Suites

This study was unable to obtain material from the Thessalon Formation volcanics of the Huronian Supergroup, the Viianki dyke swarm or the Seidorechka Formation of the Karelia Supergroup. Instead, this study uses previously published data with which it compares the other Matachewan LIP suites.

3.7.1. Thessalon Formation

The data for the Thessalon Formation used by this study comes from 79 basalts-basaltic andesites analysed by Kirsty Tomlinson as part of her Ph.D. thesis on Precambrian Greenstone belts in Canada (Tomlinson 1996). The majority of samples collected come from along the north shore and islands of Lake Huron and various roads either side of Highway 17 **(Fig. 3.15)**.

The lavas of the Thessalon Formation are mostly fine grained and aphanitic and have been metamorphosed to predominantly lower greenschist facies (Tomlinson 1996). Primary mineralogy consisting of varying amounts of olivine, clinopyroxene and plagioclase is only preserved in the coarsest flows while more altered samples are characterised by alteration assemblages of albite, actinolite, epidote, chlorite ± stilpnomelane ± biotite ± sphene ± tremolite ± quartz (Jolly 1992; Tomlinson 1996).

3.7.2. Viianki Dyke Swarm

The data for the Viianki dyke swarm of Finland and northeast Russia used by this study comes from 6 analyses published in the literature (Vogel et al. 1998). The data presented by Vogel et al. (1998) are a representative suite of analyses of hundreds of Viianki dyke samples. The expansive dataset is published in diagrammatic form by Vuollo and Huhma (2005) but is otherwise not publically available as the data is currently under further study (J. Vuollo pers. Comm. 2012). The 6 samples presented by Vogel et al. (1998) were collected from Viianki dykes interpreted to have fed to some of the 2.44-2.50 Ga Fennoscandian layered intrusions, namely, the Penikat, Koillismaa and Oulanka intrusions **(Fig. 3.16)**.

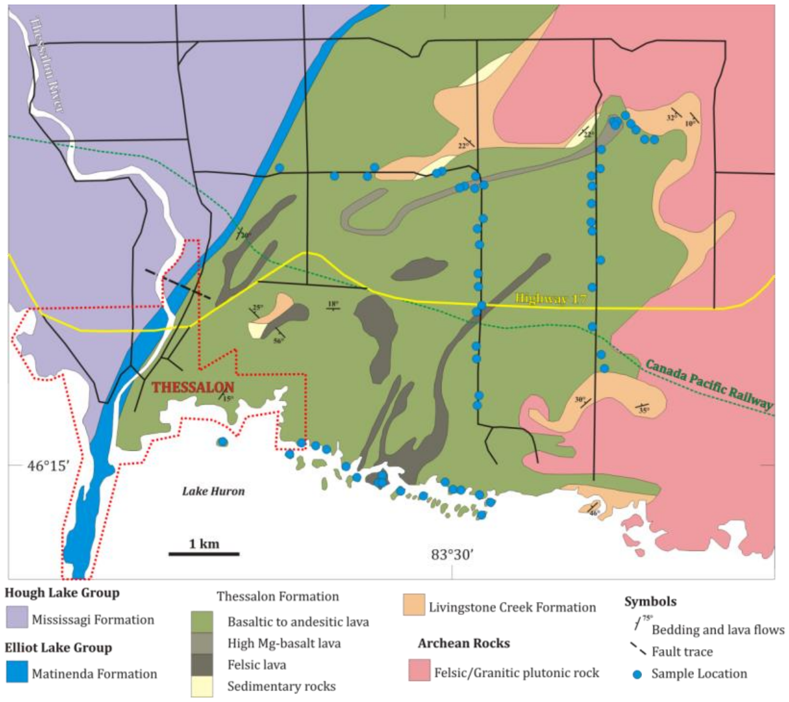

Fig. 3.15. Geologic map of the area around Thessalon, Ontario showing the sample locations of Tomlinson (1996). Modified after Tomlinson (1996) and Ontario Geological Survey Map 2544.

Vuollo and Huhma (2005) indentified boninitic-noritic, gabbronoritic and tholeiitic types of Viianki dykes. The mineralogy of these three subgroups is dominated by plagioclase, clinopyroxene and orthopyroxene with minor amounts (<5%) of olivine and trace amounts of quartz, chromite and Fe-Ti-V oxides. Alteration in the Viianki dykes is variable, with pristine dykes with cumulus texture and primary mineralogy preserved along the Finnish-Russian border and more altered dykes to the west. Where alteration is observed in the Viianki dykes, primary pyroxene and olivine have been replaced by fine grained amphibole and serpentine. Vuollo and Huhma (2005) provide photomicrographs of Viianki dyke samples which are shown in **Fig. 3.17**.

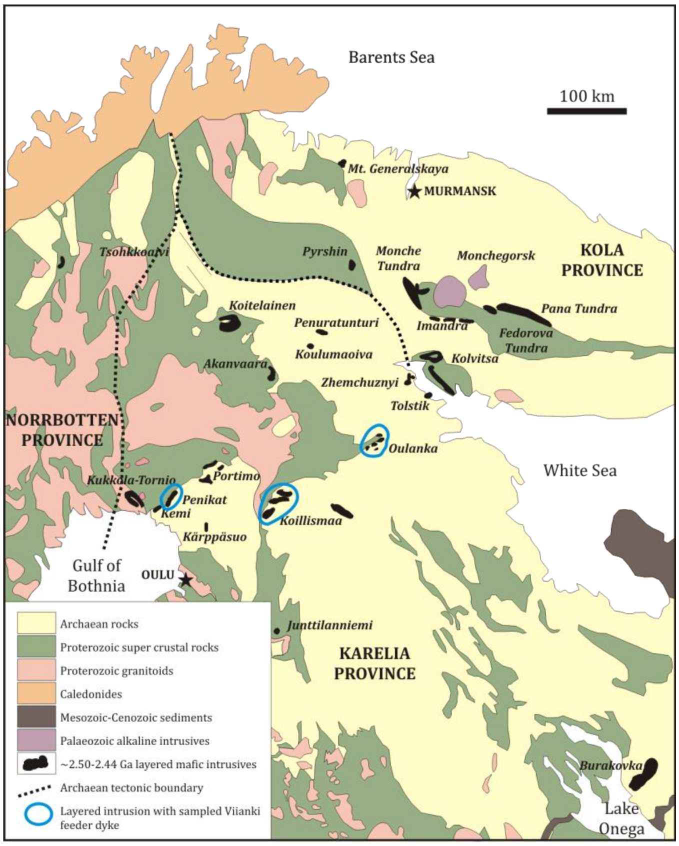

Fig. 3.16. Geological map showing the extent of the ~2.51-2.44 Ga Fennoscandian intrusions and those intrusions for which Viianki feeder dykes are discussed in this study. Modified after Lauri et al. (2012).

3.7.3. Seidorechka Formation

The data for the Seidorechka Formation of northeast Russia used by this study comes from 41 major element analyses (Chashchin et al. 2008) and 13 major and trace element analyses (Mints et al. 1996) published in the literature. These samples were collected from komatiitic-rhyolitic Seidorechka Formation flows preserved in the extreme west of the Imandra-Varzuga rift zone of the Kola Peninsula **(Fig. 3.18)**. Unfortunately, precise sample location information is not provided by Chashchin et al. (2008) or Mints et al. (1996) and instead the two studies define a sample area between 67.48N, 33.50E and 67.90N, 32.90E which is centred on Imandra Lake, approximately 20 km northwest of the town of Apatity.

Little information regarding the petrography of the Seidorechka Formation is given in the literature: Chashchin et al. (2008) notes that metamorphism in the Imandra-Varzuga rift zone-hosted Seidorechka Formation rocks did not exceed lower greenschist facies while Puchtel et al. (1997), who studied equivalent rocks preserved in the Vetreny Poyas belt (approximately 500 km southeast of the Imandra-Varzuga rift zone), states that alteration of the Seidorechka Formation is minimal and metamorphism likely did not exceed prehnite-pumpellyite facies.

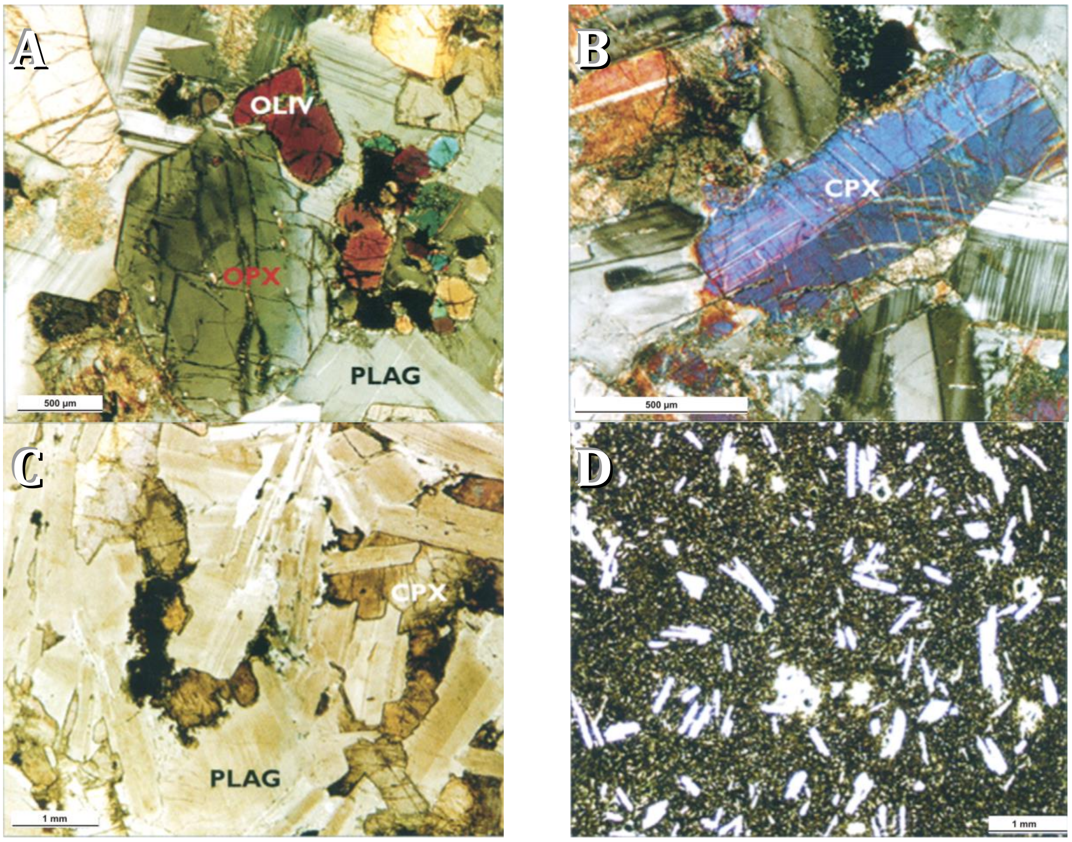

Fig. 3.17. Photomicrographs of Viianki dykes modified from Vuolla and Huhma (2005). **A)** XPL view of cumulus texture in unaltered boninitic-noritic Viianki dyke; **B)** XPL view of typical cumulus texture and mineralogy of pristine gabbronoritic Viianki dyke; **C)** PPL view of unaltered tholeiitic Viianki dyke; **D)** XPL view of fine grained, inequigranular tholeiitic Viianki dyke with elongate plagioclase laths.

3.8. Summary

This chapter has presented how and from where the samples used in this study were collected **(Table 3.1)**. In total, 424 individual samples will be discussed in the following chapters. Of these, 139 were collected by previous workers and were analysed prior to 1998 (Mints et al. 1996; Tomlinson 1996; Vogel et al. 1998; Chashchin et al. 2008). The veracity of this older data is discussed in Chapter 4.

Petrographic study of the samples collected has shown that metamorphism of the Matachewan LIP suites rarely exceeds greenschist facies and preserves much of the primary mineralogy. In the East Bull Lake Suite (the one Matachewan LIP suite where metamorphism reaches amphibolite facies), metamorphism has only affected the River Valley intrusion, while the other three East Bull Lake Suite intrusions studied have only been metamorphosed to greenschist facies. The relatively low metamorphic grade of the Matachewan LIP suites may mean that the geochemistry recorded by the rocks is, in many cases, close to primary (see Chapter 4).

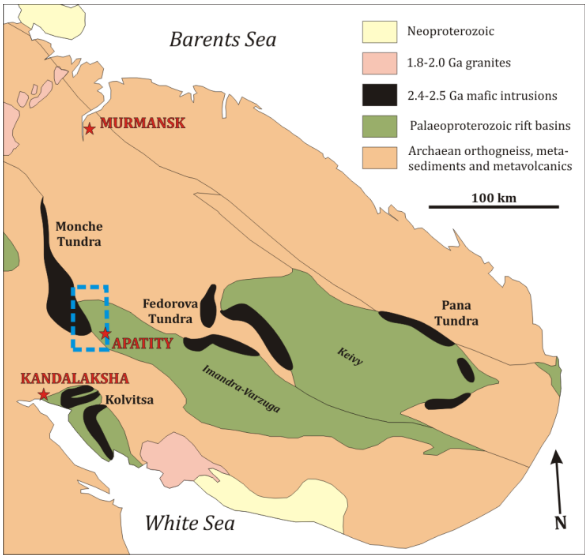

Fig. 3.18. Geologic map of the Kola Peninsula, Russia showing the sample area (dashed rectangle) of Chashchin et al. (2008) and Mints et al. (1996). Map modified after Timmerman and Daly (1995).

Suite	Samples	Metamorph. grade	New data?	Alteration assemblage	Igneous mins. Preserved (%)	Ref.
Matachewan dyke swarm	77	Greenschist	✓	Amp+Qtz+Ser+Epi	60%	-
East Bull Lake Suite	35	Amphibolite	✓	Amp+Qtz+Ser+Tlc +Epi+Chl	50%	-
Thessalon Formation	79	Greenschist	×	Amp+Qtz+Bio+Cly +Epi+Chl	-	1
Blue Draw Metagabbro	96	Greenschist	✓	Srp+Tlc+Amp+Cal +Bio+Qtz+Ser	0 – 40%	-
Leopard dyke swarm	20	Greenschist	✓	Srp+Amp+Cly+Qtz +Ser	40%	-
Kaminak dyke swarm	57	Greenschist	✓	Qtz+Ser+Epi+Amp	60%	-
Seidorechka Formation	54	Greenschist	×	-	-	2, 3
Viianki dyke swarm / Fennoscandian Suite	6	Greenschist	×	Qtz+Srp+Epi+Amp	? – 100%	4

Table 3.1. Summary information for the samples collected for this study showing the characteristic alteration assemblages and amounts of primary mineralogy preserved, on average, in each suite. Refs: 1 - Tomlinson (1996), 2 - Mints et al. (1996), 3 - Chashchin et al. (2008), 4 - Vogel et al. (1998). Mineral abbreviations: Qtz – Quartz, Amp – Amphibole, Ser – Sericite, Epi – Epidote, Srp – Serpentine, Cly – Clays, Bio – Biotite, Tlc – Talc, Chl – Chlorite.

4. RESULTS

4.1. Introduction

In the following sections, the whole-rock elemental and isotopic data for each of the magmatic suites studied in this project is presented with a summary given at the end **(Table 4.2)**. Laboratory methods are detailed in **Appendix B**. All data can be found in **Appendices C** and **D**. In this study, total iron is referred to as $Fe_2O_3^{(T)}$. $FeO^{(EST)}$ and $Fe_2O_3^{(EST)}$ are calculated using **Equation 4.1** and Mg-*number* (Mg#) is calculated using **Equation 4.1** (Gill 2011). All the major element concentrations presented in this thesis have been recalculated on an anhydrous basis.

$$\mathrm{FeO}^{(\mathrm{T})} = \mathrm{Fe_2O_3}^{(\mathrm{T})} \times 0.8998$$
$$\mathrm{FeO}^{(\mathrm{EST})} = 0.9 \times \mathrm{FeO}^{(\mathrm{T})}$$
$$\mathrm{Fe_2O_3}^{(\mathrm{EST})} = \left(\mathrm{FeO}^{(\mathrm{T})} - \mathrm{FeO}^{(\mathrm{EST})}\right) \times 1.11$$

Equation 4.1

$$\mathrm{Mg\#} = 100 \times \left(\frac{\mathrm{MgO}}{\mathrm{MgO} + \mathrm{FeO}^{(\mathrm{T})}}\right)$$

Equation 4.2

The major and trace element geochemistry of each suite of rocks will be described and the effects of secondary alteration and element mobility will be assessed by plotting each element against Zr. Elements which show good correlation with Zr are assumed to relatively immobile. Elements which show non-systematic scatter that cannot be explained by a petrogenetic mechanism are interpreted as having been remobilised and will not be used to assess the petrogenesis of the given suite.

Major and trace element concentrations are plotted against different fractionation indexes in order to assess the crystallisation history of the magmatic rocks. Major and trace element concentrations will also be used to classify the rocks in terms of rock type and volcanic series. Plots of trace element ratios, as well as chondrite- and Primitive Mantle- normalised diagrams are used to interpret the source composition and tectonic setting for each of the magmatic suites. REE data will also be used to estimate the extent of processes such as fractional crystallisation and crustal contamination. Trace element anomalies on chondrite- or Primitive Mantle-normalised diagrams are manifested as significant enrichments or depletions in the normalised concentration of an element relative to the adjacent elements on the diagram. The size and nature of these anomalies can be important indicators of petrological processes (Briqueu et al. 1984) and in this study, are quantified using **Equation 4.3** which uses Nb as an example. Isotopic data from some of the layered intrusions are also used to fingerprint the mantle source-regions important for the Ni-Cu-PGE mineralisation preserved within the Matachewan LIP.

$$\frac{\mathrm{Nb}}{\mathrm{Nb}^{*}} = \frac{\mathrm{Nb}}{0.5\ \times (\mathrm{Th} + \mathrm{La})}$$

Equation 4.3

Note: chemical symbols refer to chondrite- or Primitive Mantle normalised abundances. Ti/Ti* and Eu/Eu* are calculated using the elements Gd and Sm

4.2. Alteration and Element Mobility

Before the elemental and isotopic data can be used to interpret the petrogenesis of each of the magmatic suites, the data must be assessed in terms of secondary alteration and element mobility. Sub-solidus element mobility is driven by weathering, diagenesis, metamorphism, or through interactions with hydrothermal fluids and can alter the geochemistry of a rock. Without being properly understood, the geochemical changes caused by secondary alteration and element mobilisation can potentially lead to incorrect interpretations being made about the rock.

The ability of an element to be remobilised during secondary alteration is related to its ionic potential (charge/radius). Elements of low ionic potential (< 0.03 pm^{-1}) tend to enter solution as hydrated cations while elements with high ionic potential (> 0.10 pm^{-1}) are removed in solution as hydrated oxyanions [e.g., (Pearce 1996; Hastie et al. 2007)]. The most immobile elements are those with intermediate ionic potentials (0.03 – 0.10 pm^{-1}) which tend to remain in the solid product during alteration (Pearce 1996). Such elements include the REE (excluding Eu and La), Zr, Hf, Nb, Ta, Y, Ti, Cr, Th, Sc and Ga (Hastie et al. 2007). Pearce (1996) suggested that the immobile behaviour exhibited by elements with intermediate ionic potential reduces as metamorphic conditions approach upper amphibolite-granulite facies. As most of the rocks which constitute the Matachewan LIP have not experienced more than greenschist facies metamorphism [e.g., Jolly 1987a; Redden et al. 1990; Sandeman and Ryan 2008), it could potentially be assumed that the effects of secondary remobilisation are negligible. However, the behaviour described above is not definitive and studies have shown that secondary remobilisation of the elements listed can occur at less extreme conditions than amphibolite-granulite facies metamorphism, particularly in the presence of carbonate-, halide- or hydrogen sulphide-bearing solutions [e.g., Giere 1993; de Hoog and Van Bergen 2000; Fadda et al. 2012) .

As the majority of the rocks studied in this project have undergone at least greenschist facies metamorphism, show petrographic evidence of alteration and have not-insignificant LOI values, sub-solidus element mobility must be assessed. To do this, each element is plotted against Zr following the method used by Cann (1970). Zr is incompatible during basalt fractionation and is considered to be immobile at low degrees of metamorphism (Pearce 1996). Therefore, when another incompatible element from a cogenetic suite of rocks is plotted against Zr, there should be a linear correlation between the two elements. If secondary remobilisation has affected either of the elements in question, we would expect to see a large degree of scatter. However, a loss of correlation between two incompatible and (usually) immobile elements may not necessarily mean that the element(s) have been affected by secondary remobilisation as differing degrees of contamination or partial melting or a heterogeneous mantle source can also disturb the expected, linear correlation.

To quantify the significance of any correlation, the square of the product moment correlation coefficient (R) is calculated **(Equation 4.4)** which reveals how much of the variation in the Y variable is due to the X variable in percentage terms. R^2 defines the strength of a correlation and R^2 values approaching 1 indicate a good correlation while R^2 values close to 0 indicate no correlation. For this current study, elements which have $R^2 \geq 0.75$ will be referred to as having a good correlation with Zr, while elements with an $0.75 > R^2 \geq 0.5$ will be referred to as having a moderate correlation with Zr. Elements with an $R^2 < 0.5$, will be referred to as having a poor correlation with Zr. Such elements, whose scatter cannot be explained by a petrogenetic mechanism, are inferred to have been remobilised by sub-solidus fluids. These mobile elements will not be used to assess petrogenetic processes.

$$R = \frac{\Sigma_{i=1}^{n}(X_i - \overline{X})(Y_i - \overline{Y})}{\left(\sqrt{\Sigma_{i=1}^{n}(X_i - \overline{X})^2}\right)\left(\sqrt{\Sigma_{i=1}^{n}(Y_i - \overline{Y})^2}\right)}$$

Equation 4.4

This approach works well for rocks which have not experienced in-situ fractionation but not so well for rocks which have such as layered intrusions. This is because in fractionating systems, an elements partition coefficient varies depending on the mineral phase fractionating from the melt at a given time. For example, Zr is incompatible in both olivine and pyroxene while Sc is incompatible in olivine but compatible in pyroxene (Adam and Green 2006). This means that during olivine fractionation, both Zr and Sc are concentrated in the residual melt, hence, the correlation between Zr and Sc upwards through an olivine cumulate pile is positive. However, during fractionation of clinopyroxene, Sc is concentrated in the pyroxene while Zr is concentrated in the residual melt, hence, the correlation between Zr and Sc upwards through a clinopyroxene cumulate pile is negative. The result of this is that when samples from a stratified igneous intrusion are plotted together, selectively compatible elements (such as Sc) produce curves rather than linear correlations when plotted against Zr. In such cases, element mobility will be determined by examining the correlation between entirely incompatible elements (LILE, HFSE, La and Ce) and Zr (which are expected to be linear), and extrapolating the findings from these elements to other more variably compatible elements which have a similar potential for remobilisation.

4.3. Matachewan Dyke Swarm

4.3.1. Alteration and Element Mobility

The LOI for the Matachewan dykes range from -0.58 to 2.80 wt.% (sample FA62-077-01 falls out of this range with an anomalously high LOI of 5.32 wt.%). These LOI values are relatively low and may suggest that the Matachewan dykes have experienced little alteration. However, previous studies (Nelson et al. 1990; Halls 1991) have documented alteration mineral assemblages of epidote, sericite, amphibole and chlorite – indicative of greenschist facies metamorphism. Petrographic work presented in Chapter 3 confirms the presence of this alteration **(Fig. 3.3)**. In order to asses if this alteration has caused secondary remobilisation, each element is plotted against Zr which is regarded to be immobile under greenschist facies metamorphic conditions (Pearce 1996). A subset of these graphs is shown in **Fig. 4.1**. Examination of these graphs shows that the Matachewan dykes can be delineated into two sub-groups based on differences in trace element chemistry with the Group 1 dykes far more numerous than the Group 2 dykes. The Group 1 dykes are depleted in LREE relative to the Group 2 dykes at the same Zr concentration while also being enriched in HREE relative to the Group 2 for samples with the same Zr concentration. This grouping is also observed on plots of Zr vs. Sc, Y and Sr.

For the Group 1 dykes, the elements which show a good correlation with Zr ($R^2 > 0.75$) include, Hf, the REE (excluding Eu) Nb, Y and TiO_2. The elements which show a moderate correlation with Zr ($0.5 < R^2 < 0.75$) include Fe_2O_3, P_2O_5, Eu and Ta. The elements which show a poor correlation with Zr ($R^2 < 0.5$) include SiO_2, Al_2O_3, MnO, MgO, CaO, Na_2O, K_2O, Sc, V, Cr, Ni, Cu, Zn, Sr, Ba, Ga, Rb, Mo, Sn, Cs, Pb, Th and U. These correlations suggest that secondary element remobilisation of the Group 1 Matachewan dykes has affected the majority of the major elements, LILE, transition elements and some of the HFSE elements (U and Th). The potential mobility of Th is interesting as the HFSE are thought to be immobile under metamorphic conditions experienced by the Matachewan dykes (Pearce 1996). Instead this poor correlation between Th and Zr may be the result of contamination of the Group 1 parent magma by heterogeneous crust (Plank 2005).

For the Group 2 dykes, the elements which show a good correlation with Zr ($R^2 > 0.75$) include, Hf, Nb, Nd, Sm, Gd, Tb and Dy. The elements which show a moderate correlation with Zr ($0.5 < R^2 < 0.75$) include P_2O_5, Na_2O, Sr, Y, Ce, Pr, Ho, Er, Tm, Yb, Lu, Ta and Th. The elements which show a poor correlation with Zr ($R^2 < 0.5$) include SiO_2, TiO_2, Al_2O_3, Fe_2O_3, MnO, MgO, CaO, K_2O, Sc, V, Cr, Ni, Cu, Zn, Rb, Mo, Sn, Cs, La, Eu, Pb and U. These correlations indicate that secondary element remobilisation of the Group 2 Matachewan dykes has affected the major elements,

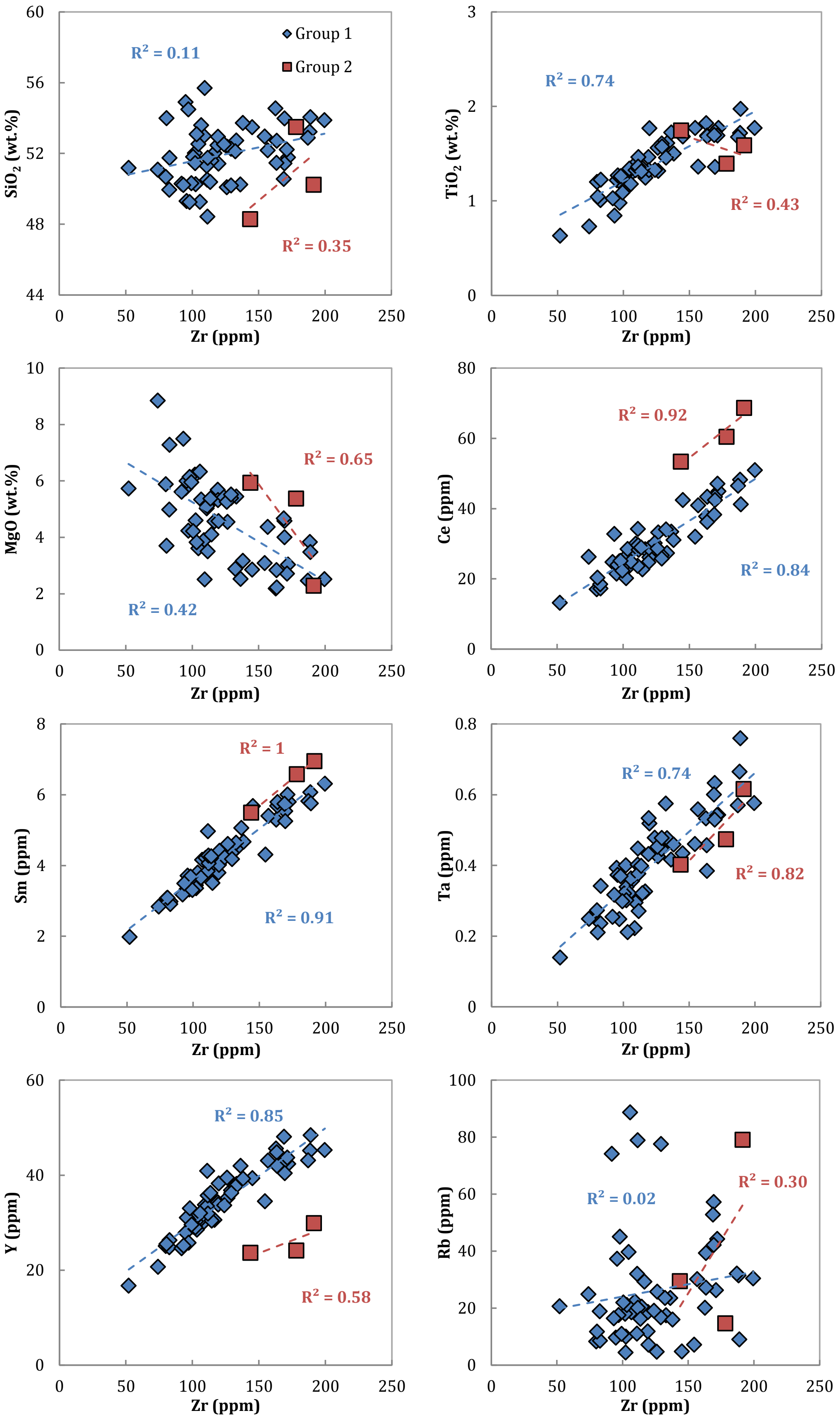

Fig. 4.1. Bivariate diagrams of selected elements vs. Zr for the Matachewan dyke swarm samples.

LILE, transition elements and LFSE. The LREE and HREE have been moderately affected, while the other HFSE are largely unaffected. However, the correlations are based on three analyses and may not be statistically valid.

Alteration of the Matachewan dykes appears to have affected the two subgroups differently. Typically, the Group 2 dykes display poorer correlations between the REE and Zr than the Group 1 dykes which may suggest that the Group 2 dykes have experienced more advanced alteration. However, this poorer correlation is not entirely universal among the other elements as the Group 2 dykes show better correlations between Zr and Na_2O, Sr and Th than the Group 1 dykes.

4.3.2. Classification

On the TAS diagram **(Fig. 4.2)** the majority of the Group 1 dykes form a tight cluster in the tholeiitic basalt and basaltic andesite fields. Three Group 1 dykes plot inside the trachybasalt field, just within the alkaline series while one sample plots as a tholeiitic basaltic trachyandesite. The Group 2 dykes are far more spread out on the TAS diagram. Half of the Group 2 dykes plot as tholeiitic basaltic andesites while one sample each plot in the basalt, basaltic trachyandesite and dacite fields.

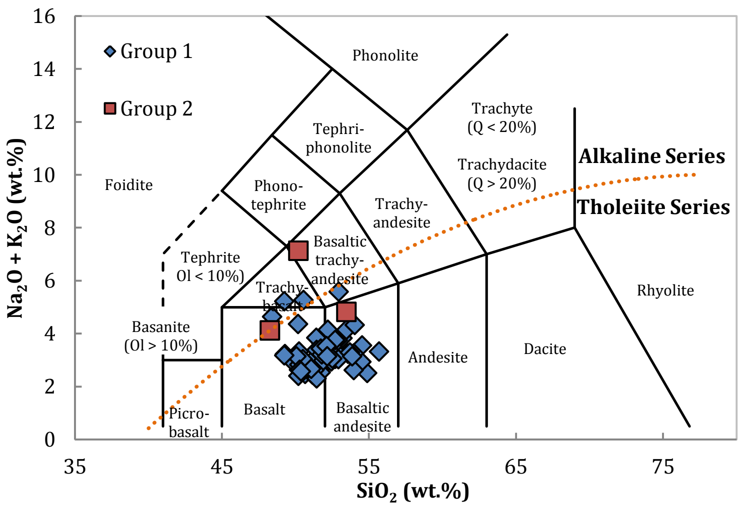

Fig. 4.2. Total alkali vs. SiO_2 (TAS) diagram for the Matachewan dyke swarms samples. Field boundaries defined by Le Maitre et al. (1989).

As the TAS diagram relies on the oxides of Na and K (two elements which have been shown to have been remobilised in the Matachewan dykes) to classify igneous rocks, its applicability to the Matachewan dykes is questionable. The Zr/Ti vs.

Nb/Yb diagram is more useful as the elements used in the classification have been shown to be immobile during greenschist facies metamorphism. On this diagram **(Fig. 4.3)**, Group 1 dykes plot as a tight cluster which straddles the basalt-basaltic andesite boundary. Group 2 dykes plot just to the right of the Group 1 cluster and also straddle the basalt-basaltic andesite boundary.

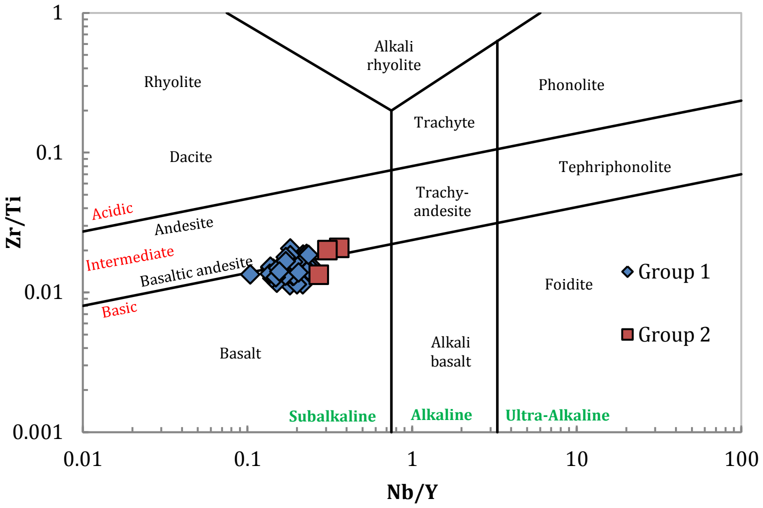

Fig 4.3. Zr/Ti vs. Nb/Y diagram for the Matachewan dyke swarm. Fields from Pearce (1996).

4.3.3. Major Element Variation

The Group 1 dykes range in MgO, TiO_2 and Fe_2O_3 between 2.2-8.8, 0.6-2.0 and 11.0-18.2 wt.% respectively. These values correspond to a range in Mg# of 12-45. SiO_2 in the Group 1 dykes ranges from 48.4-55.7 wt.% while total alkalis range from 2.3-5.6 wt.%. The Group 2 dykes range in MgO, TiO_2 and Fe_2O_3 between 2.0-5.9, 1.1-1.7 and 10.0-14.6 wt.% respectively. These values correspond to a range in Mg# of 18-32. SiO_2 in the Group 2 dykes ranges from 48.3-64.1 wt.% while total alkalis range from 4.1-7.1 wt.%.

The major elements in the Group 1 display poor linear correlations ($R^2 < 0.5$) with MgO **(Fig. 4.4)** and may be further evidence of the major elements having undergone sub-solidus mobility. Given that the correlations are poor, positive correlations exist between MgO and SiO_2, TiO_2, Fe_2O_3, Na_2O and P_2O_5 while negative correlations exist between MgO and Al_2O_3 and CaO. In the Group 2 dykes, all of the major elements except Fe_2O_3 show poor linear correlations with MgO which, like the Group 1 dykes, confirms the suspicions raised by **Fig. 4.1** that these elements have been mobilised. Although the correlations are poor for Group 2 dykes, SiO_2 shows a negative correlation with MgO while TiO_2, Al_2O_3, Na_2O and Fe_2O_3 show positive correlations. The remaining major elements show no obvious correlation with MgO.

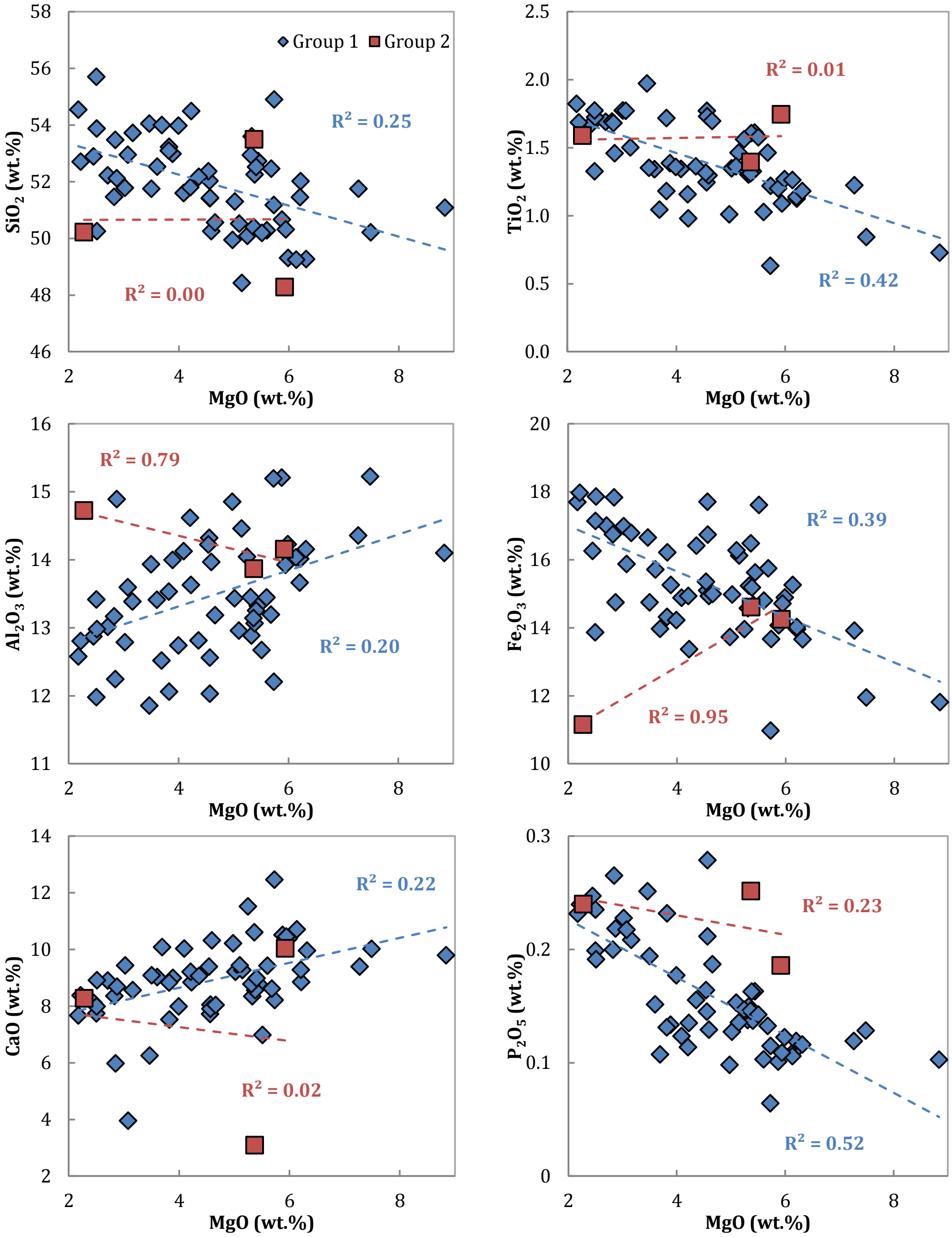

Fig. 4.4. Bivariate diagrams of selected major elements vs. MgO for the Matachewan dyke swarm samples.

4.3.4. Trace Element Variation

In the Group 1 dykes, trace elements which are compatible during fractionation of mafic melts either show; no obvious correlation with MgO, as is the case with Co

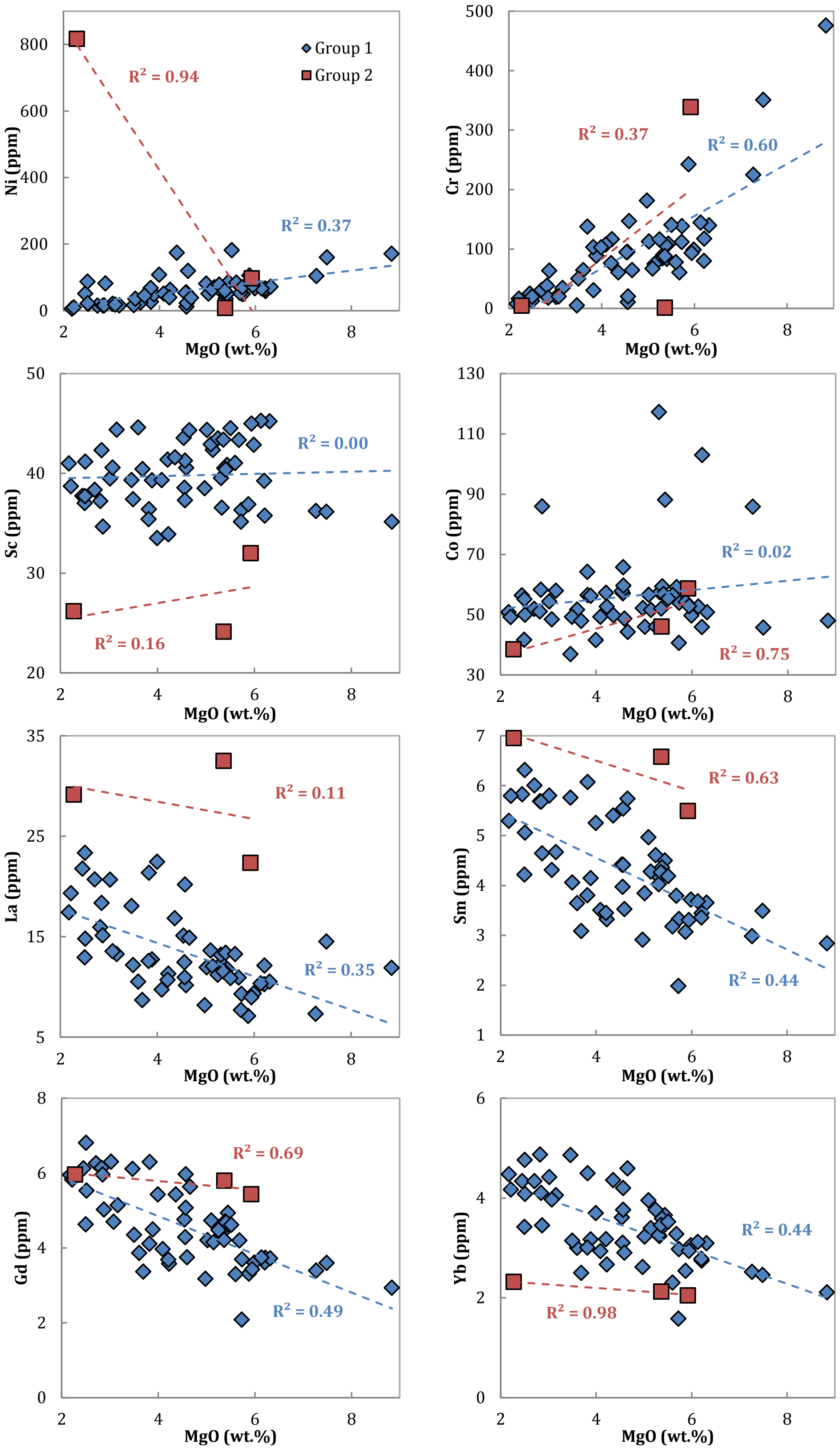

Fig. 4.5. Bivariate diagrams of trace elements vs. MgO for the Matachewan dyke swarm samples.

and Sc; a poor-moderate positive correlation, as is the case with Ni and Cr (which range between 5-817 ppm and 5-182 ppm respectively), or; in the case of V, a very poorly negative correlation. Incompatible elements (including La, Sm, Gd and Yb) show poor (R^2 = 0.37-0.44) negative correlations with MgO **(Fig. 4.5)**. In the Group 2 dykes, Ni ranges in concentration between 8-817 ppm and shows a good negative correlation with MgO (R^2 = 0.94). However, one sample contains 817 ppm Ni which is higher than the most mineralised sample from the East Bull Lake Suite **(Fig. 4.15)** suggesting that this analysis is erroneous. Unfortunately, this sample was collected as a powder and so petrography cannot be used to explain this high Ni. V, Sc, Cr and Co show poor-good positive correlation with MgO; La, Sm, Gd and Yb all show very poor (R^2 < 0.16) negative correlations with MgO **(Fig. 4.5)**.

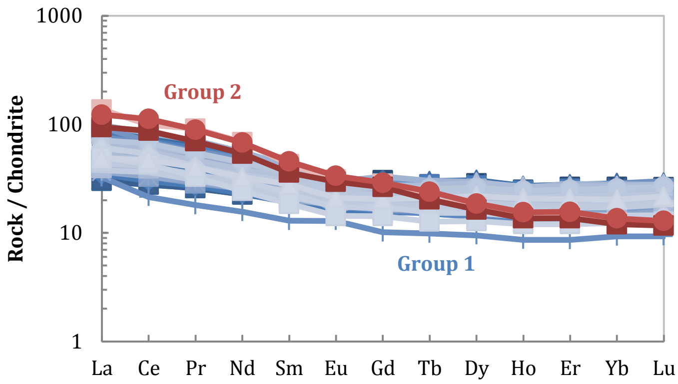

Fig. 4.6. Chondrite-normalised REE diagrams for the Matachewan dykes. Normalising values from McDonough and Sun (1995).

Chondrite-normalised REE patterns for the Group 1 dykes **(Fig. 4.6)** show sub-parallel trends with REE concentrations ~16-56× chondritic values. The Group 1 dykes are enriched in LREE $(La/Sm)_N$ = 2.03 relative to the HREE which have relatively flat patterns $(Gd/Yb)_N$ = 1.12. The Group 1 dykes have variably negative Eu anomalies. Sixty-five of the seventy Group 1 dykes sampled record Eu/Eu* between 0.8-1.0, four samples have significantly more negative anomalies (the lowest recording Eu/Eu* = 0.55) while a single sample (MA002) records a positive Eu anomaly of Eu/Eu* = 1.12. The Chondrite-normalise REE pattern displayed by the Group 1 dykes is best approximated in slope by the E-MORB reservoir. Chondrite-normalised REE patterns for the Group 2 dykes show sub-parallel trends with REE concentrations ~46-64× chondritic values. The Group 2 dykes are enriched in LREE $(La/Sm)_N$ = 3.10 relative to the HREE which have somewhat steep patterns

$(Gd/Yb)_N$ = 2.29. The Group 2 dykes have variably negative Eu anomalies. Five of the six Group 2 samples record Eu/Eu* values between 0.87-0.98 while one sample (RL12-3-1) records a significantly more negative anomaly (Eu/Eu* = 0.68). The Chondrite-normalised REE pattern displayed by the Group 2 dykes is best approximated in slope by the OIB reservoir (Sun and McDonough 1989).

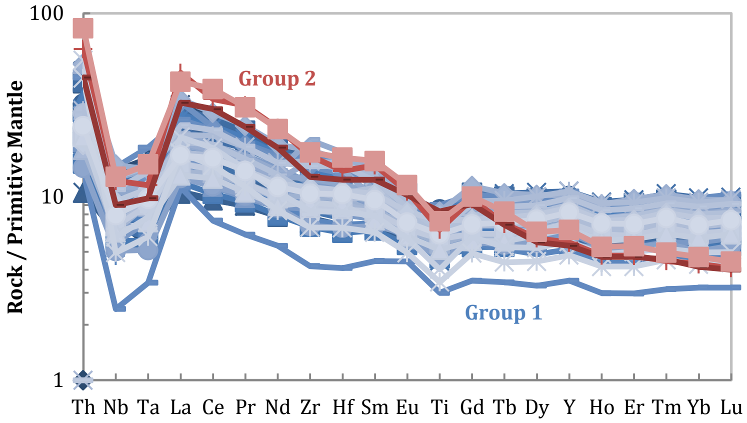

Fig. 4.7. Primitive Mantle-normalised multi-element diagrams for the Matachewan dykes. Normalising values from McDonough and Sun (1995).

On Primitive Mantle-normalised multi-element plots **(Fig. 4.7)**, the Group 1 dykes show sub-parallel trends with trace element concentrations 3-9x that of the Primitive Mantle. As in **Fig. 4.6**, the Group 1 dykes show enrichment in the most incompatible elements relative to the less incompatible elements. All of the Group 1 dykes show significant negative Nb anomalies (Nb/Nb* range = 0.16-0.75, average = 0.40) and negative Ti anomalies (Ti/Ti* range = 0.56-0.93, average = 0.74). The Group 2 dykes also record negative Nb and Ti anomalies, but are much more negative than those observed in the Group 1 dykes (Nb/Nb* range = 0.14-0.23, average = 0.2. Ti/Ti* range = 0.52-0.93, average = 0.60).

On an Nb/Y vs. Zr/Y diagram **(Fig. 4.8)**, Group 1 dykes straddle the boundary between plume and non-plume sources plotting in overlapping areas of the oceanic plate basalt, volcanic arc and normal mid-ocean ridge basalt fields. Group 1 dykes form a trend between the Primitive Mantle and enriched component end-members of Condie (2005). On the same diagram, Group 2 dykes plot in the volcanic arc basalt field close to the enriched component end-member. On a Zr/Nb vs. Nb/Th diagram **(Fig. 4.9)**, the majority of Group 1 dykes plot within the overlapping area of the volcanic arc and oceanic plateau basalt fields and define a trend of decreasing Zr/Nb with increasing Nb/Th. On the same diagram, Group 2 dykes plot in the volcanic arc basalt field, clustered close to the enriched component end-member.

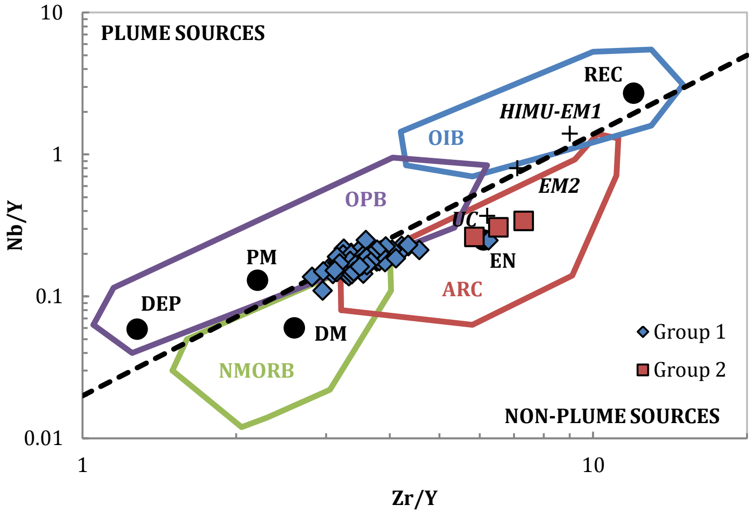

Fig. 4.8. Nb/Y vs. Zr/Y diagram for the Matachewan dyke swarm samples. Field boundaries and end-member compositions from Condie (2005). Abbreviations: UC = upper continental crust, PM = Primitive Mantle, DM = shallow depleted mantle, HIMU = high mu (U/Pb) source, EM1 and EM2 = enriched mantle sources, ARC = arc related basalts, NMORB = normal mid-ocean ridge basalt, OPB = oceanic plateau basalt, OIB = oceanic island basalt, DEP = deep depleted mantle, EN = enriched component, REC = recycled component.

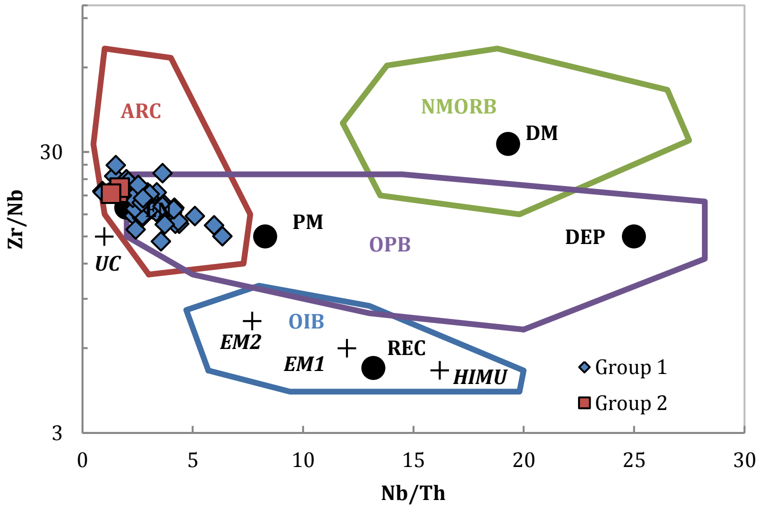

Fig. 4.9. Zr/Nb vs. Nb/Th diagram for the Matachewan dyke swarm samples. Field boundaries and end-member compositions estimated from Condie (2005). Abbreviations as in **Fig. 4.8**.

4.4. East Bull Lake Suite

4.4.1. Alteration and Element Mobility

The highest LOI value recorded by the studied East Bull Lake suite rocks is 6.61 wt.% which confirms that alteration of the East Bull Lake Suite is relatively advanced. The alteration of the East Bull Lake Suite rocks, as observed in thin section, is characterised by fine grained replacement of talc, chlorite and iron oxides (after olivine), sericite and quartz (after plagioclase) and fine grained and acicular amphibole after pyroxene **(Fig. 3.5)**. This alteration assemblage suggests that the East Bull Lake Suite rocks have undergone greenschist-lower amphibolites facies metamorphism, which is in agreement with the findings of James et al. (2002). To determine if this alteration has affected the geochemistry of the East Bull Lake Suite intrusions, each element is plotted against Zr as before. A subset of these graphs is shown in **(Fig. 4.10)**.

The East Bull Lake and Agnew intrusions record very similar correlations of elements with Zr, i.e., for both intrusions, there are significant correlations ($R^2 > 0.75$) between Zr and the REE, HFSE, TiO_2 and P_2O_5 while the remaining major, large ion lithophile and compatible trace elements show poor correlations with Zr. The Gerow intrusion also records good correlations between Zr and the HFSE and REE as well as Cs and Cr while also having moderate correlations ($0.75 > R^2 > 0.5$) between Zr and TiO_2, Fe_2O_3, MgO, K_2O, Ga and Rb. Most elements in the River Valley intrusion show poor correlations with Zr. The only elements with good correlations with Zr in the River Valley samples are Hf, Ta and Th while a moderate correlation is observed between Zr, and U, Nb, La, Ce, Pr and Nd.

The correlations described above indicate that the wholly incompatible REE and HFSE have not been significantly remobilised in the East Bull Lake, Agnew and Gerow intrusions during post-intrusion greenschist facies metamorphism. The poor correlation between Zr and these same elements in the River Valley intrusion suggests that the latter has experienced more intense alteration than the other East Bull Lake Suite intrusions. This is a plausible hypothesis as, unlike the other East Bull Lake suite intrusions, the River Valley intrusion is preserved within the Mesoproterozoic Grenville Front Tectonic Zone where metamorphic grade reaches (at least) granulite facies (Martignole and Martelat 2005). As immobile behaviour of the REE and HFSE is expected to cease at metamorphic conditions above lower amphibolite facies (Pearce 1996), the scatter observed in plots involving these elements for River Valley rocks may reflect their more intense history of metamorphism relative to the other East Bull Lake Suite intrusions. The poor correlations observed between most of the major elements and Zr in each of the intrusions may suggest that these elements have been remobilised. However, the poor

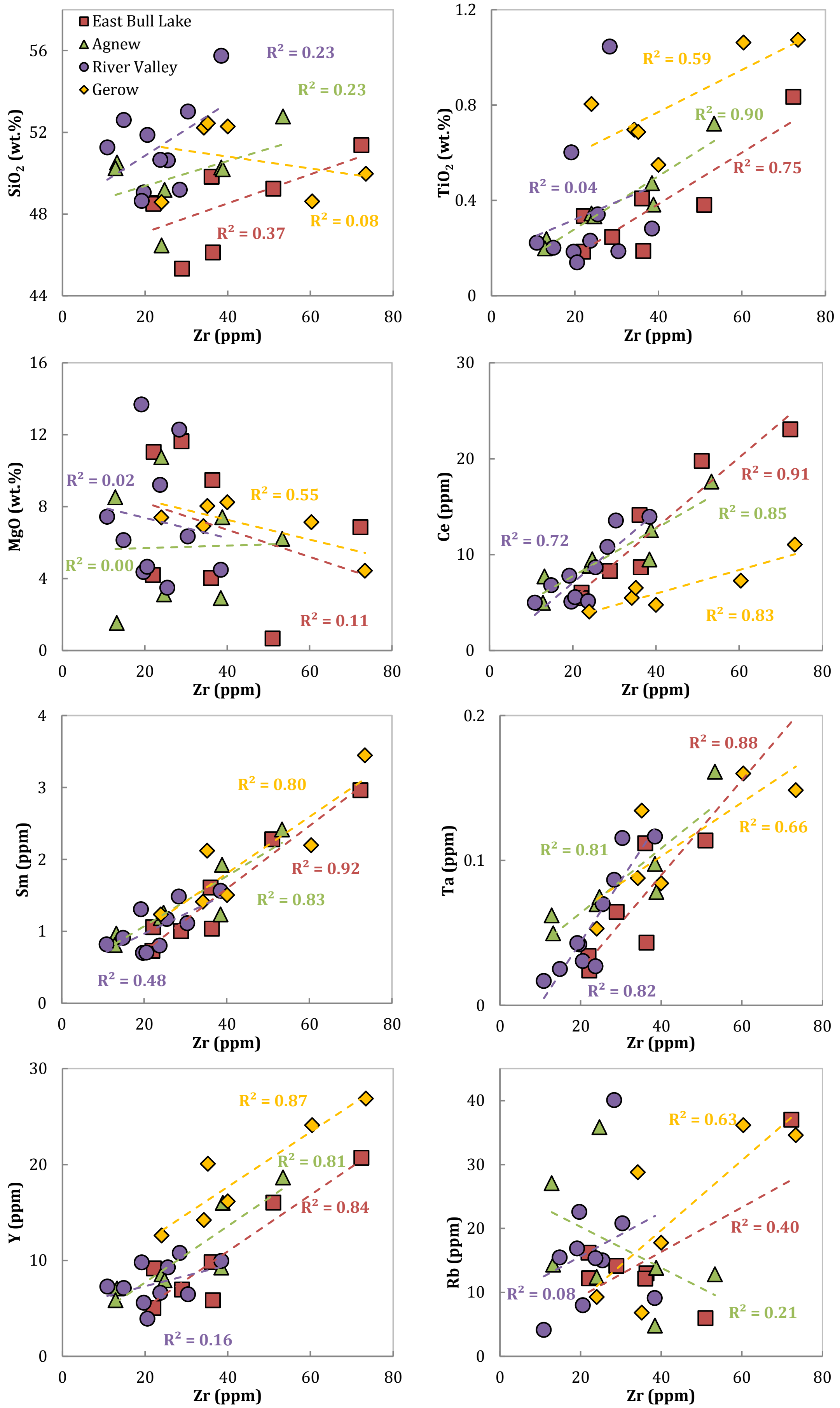

Fig. 4.10. Bivariate diagrams of selected elements vs. Zr for the East Bull Lake Suite intrusions.

correlation may also be the result of the cumulate nature of the some of the layered rocks in the intrusion **(Fig. 3.4)**.

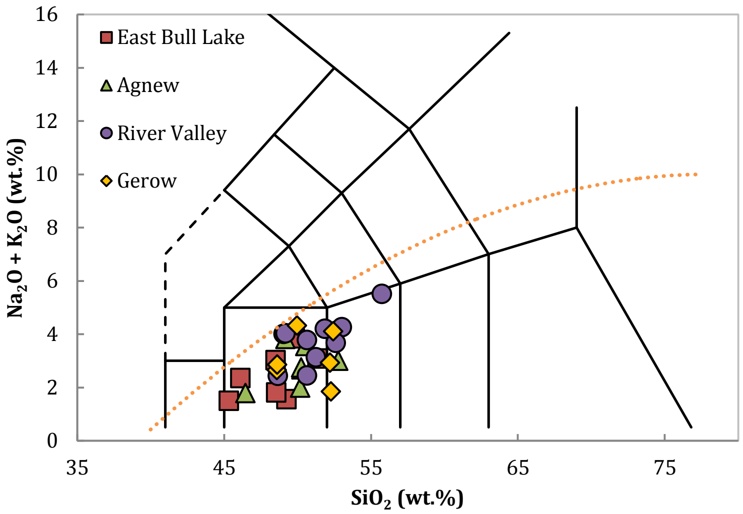

Fig. 4.11. Total alkali vs. SiO$_2$ (TAS) diagram for samples from the East Bull Lake Suite of intrusions. Field boundaries defined by Le Maitre et al. (1989). Field names are shown in **Fig. 4.2**.

4.4.2. Classification

The total alkali vs. silica (TAS) diagram **(Fig. 4.11)** classifies the majority of the East Bull Lake suite samples collected for this study as tholeiitic basalts and basaltic andesites. The Zr/Ti vs. Nb/Y diagram **(Fig. 4.12)** makes the same general distinction.

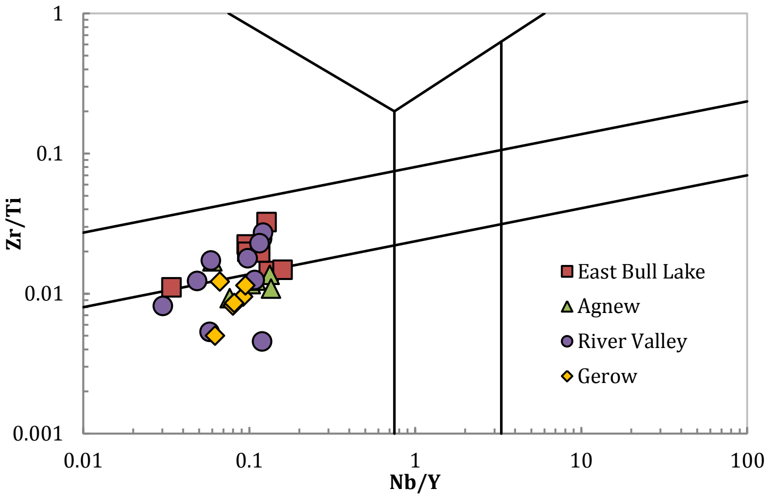

Fig. 4.12. Zr/Ti vs. Nb/Y diagram for the East Bull Lake Suite intrusion samples.

The East Bull Lake suite samples can also be classified using CIPW normative compositions plotted on the IUGS plagioclase-olivine-pyroxene ternary diagram **(Fig. 4.13)**. All of the studied samples plot in the gabbronorite and olivine gabbronorite fields. Using this classification, the East Bull Lake suite rocks can be subdivided into mela-, leuco-, olivine gabbronorites and leuco- gabbronorites. Subdividing the rocks based on lithology may prove useful in characterising the mineralisation potential of different units within the intrusions.

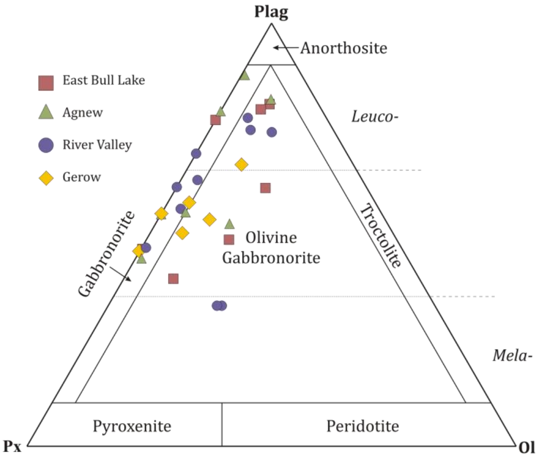

Fig. 4.13. Classification of the rocks from the East Bull Lake Suite intrusions based on CIPW norm calculations and IUGS classification. Fields taken from Le Maitre (2002) and Barnes and Gomwe (2011).

4.4.3. Major Element Variation

The East Bull Lake, Agnew, River Valley and Gerow intrusion samples range in MgO contents between 0.65-11.62 wt.%, 1.51-10.73 wt.%, 3.48-13.67 wt.% and 4.41-8.23 wt.% respectively, Fe_2O_3 contents between 4.45-14.41 wt.%, 4.30-13.65 wt.%, 4.79-13.89 wt.% and 10.50-13.62 wt.% respectively and in TiO_2 contents between 0.18-0.83 wt.%, 0.20-0.72 wt.%, 0.14-1.05 wt.% and 0.55-1.07 wt.% respectively. These ranges correspond to Mg# of 10.87-51.07 in East Bull Lake, 28.11-51.49 in Agnew, 40.98-60.10 in River Valley and 27.58-46.57 in Gerow respectively. SiO_2 contents in the East Bull Lake, Agnew, River Valley and Gerow intrusions range from 45.32-51.37 wt.%, 46.46-52.77 wt.%, 48.64-55.74 wt.% and 48.58-52.43 wt.% respectively while total alkali content ranges between 1.49-3.84 wt.%, 1.78-3.82 wt.%, 2.43-5.51 wt.% and 1.85-4.32 wt.% respectively.

Samples from the three main East Bull Lake Suite intrusions (East Bull Lake, Agnew and River Valley) show poorly negative ($R^2 < 0.33$) linear correlations between SiO_2 and MgO, moderate-good negative ($0.65 < R^2 < 0.90$) correlations between Al_2O_3 and MgO, moderately positive ($R^2 \sim 0.69$) correlations between Fe_2O_3 and MgO and

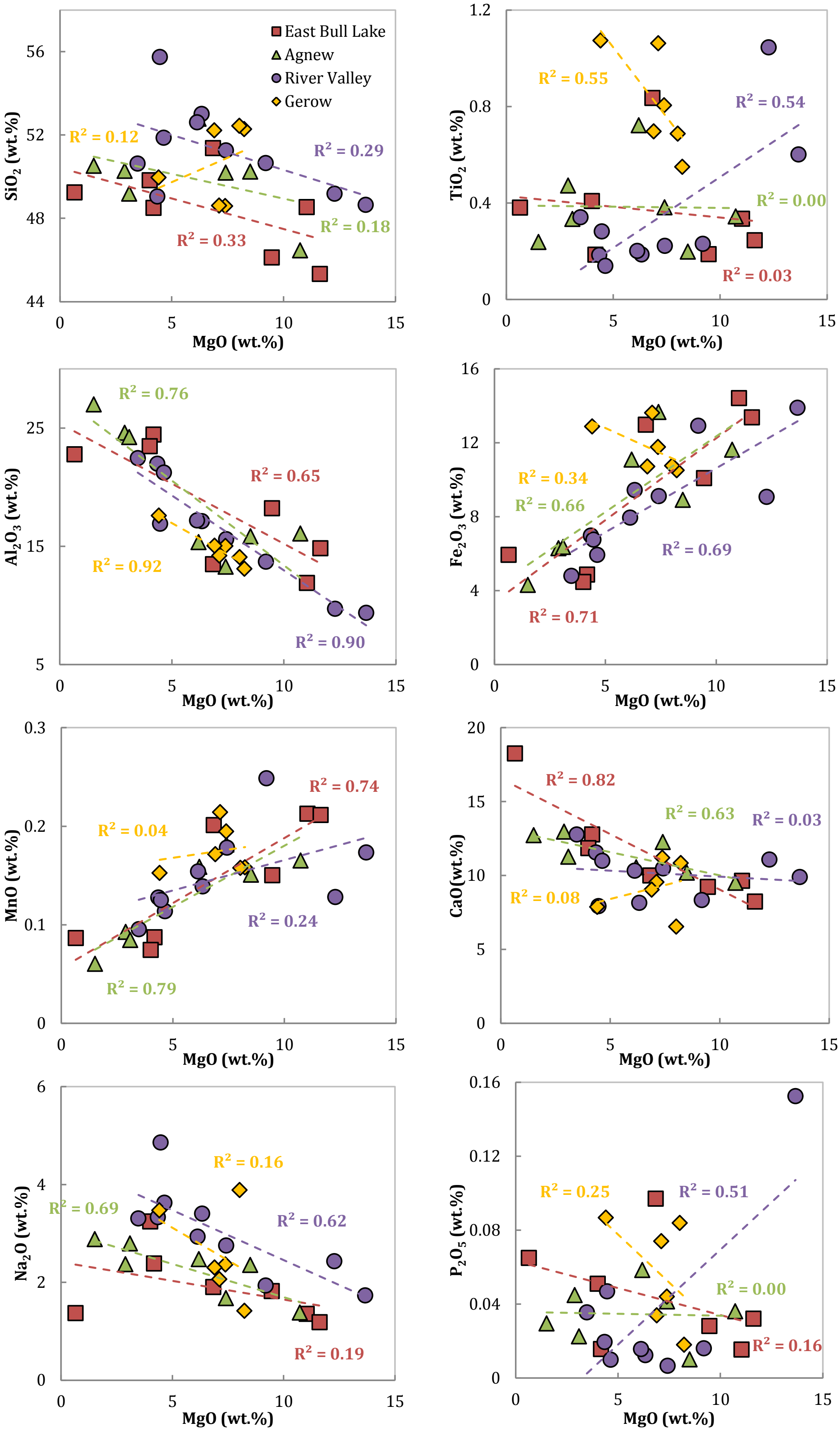

Fig. 4.14. Bivariate diagrams of selected major elements vs. MgO for the East Bull Lake Suite.

moderate-good negative ($0.62 < R^2 < 0.84$) correlations between Na_2O and MgO. The East Bull Lake and Agnew intrusions show moderate-good linear correlations between MgO and MnO and CaO, which are positive and negative respectively. Other major element oxides which are incompatible during basaltic magma fractionation (TiO_2, P_2O_5 and K_2O) generally show poor or no correlation with MgO in the East Bull Lake Suite intrusions **(Fig. 4.14)**.

4.4.4. Trace Element Variation

The East Bull Lake, Agnew, River Valley and Gerow intrusions vary in Ni content between 27-450 ppm, 39-400 ppm, 41-709 ppm and 35-240 ppm respectively as well as varying in Cr content between 10-412 ppm, 15-198 ppm, 51-604 ppm and 8-427 ppm respectively. Correlations between MgO and the compatible trace elements; Ni, Cr, Sc and Co are variable in the four intrusions but are generally moderately positive **(Fig. 4.15)** indicating that fractional crystallisation in the East Bull Lake Suite is controlled to an extent by fractionation of olivine, chrome-spinel and clinopyroxene. Elements which are incompatible during basaltic fractionation (La, Sm, Yb and Nb) show either poor or no correlation with MgO.

Fig. 4.16 shows chondrite-normalised REE profiles for the four different East Bull Lake Suite intrusions. Total abundance of REE in the samples studied of each of the East Bull Lake, Agnew, River Valley and Gerow intrusions range from 7-26, 7-20, 6-15 and 7-20 × chondritic values respectively. The East Bull Lake, Agnew and River Valley intrusions show similar concave-up patterns of LREE enrichment relative to the HREE with $Ce/Sm_{(N)}$ ranging between 1.42-3.05 and $Gd/Yb_{(N)}$ ranging between 0.87-1.39 (Ce is used in lieu of La in this case as the La analysis in some of the Gerow samples appears to have been remobilised). These three intrusions also record variable Eu anomalies ($Eu/Eu^* = 0.71-1.96$) which are poorly correlated with total REE abundance **(Fig. 4.17)**. The Chondrite-normalised REE chemistry of the East Bull Lake, River Valley and Agnew intrusions are best approximated by E-MORB (Sun and McDonough 1989).

The REE chemistry of the Gerow intrusion differs markedly from the other three East Bull Lake suite intrusions studied in that the former displays much flatter chondrite-normalised REE patterns with ranges in $Ce/Sm_{(N)}$ of 0.77-0.97 and Gd/Yb

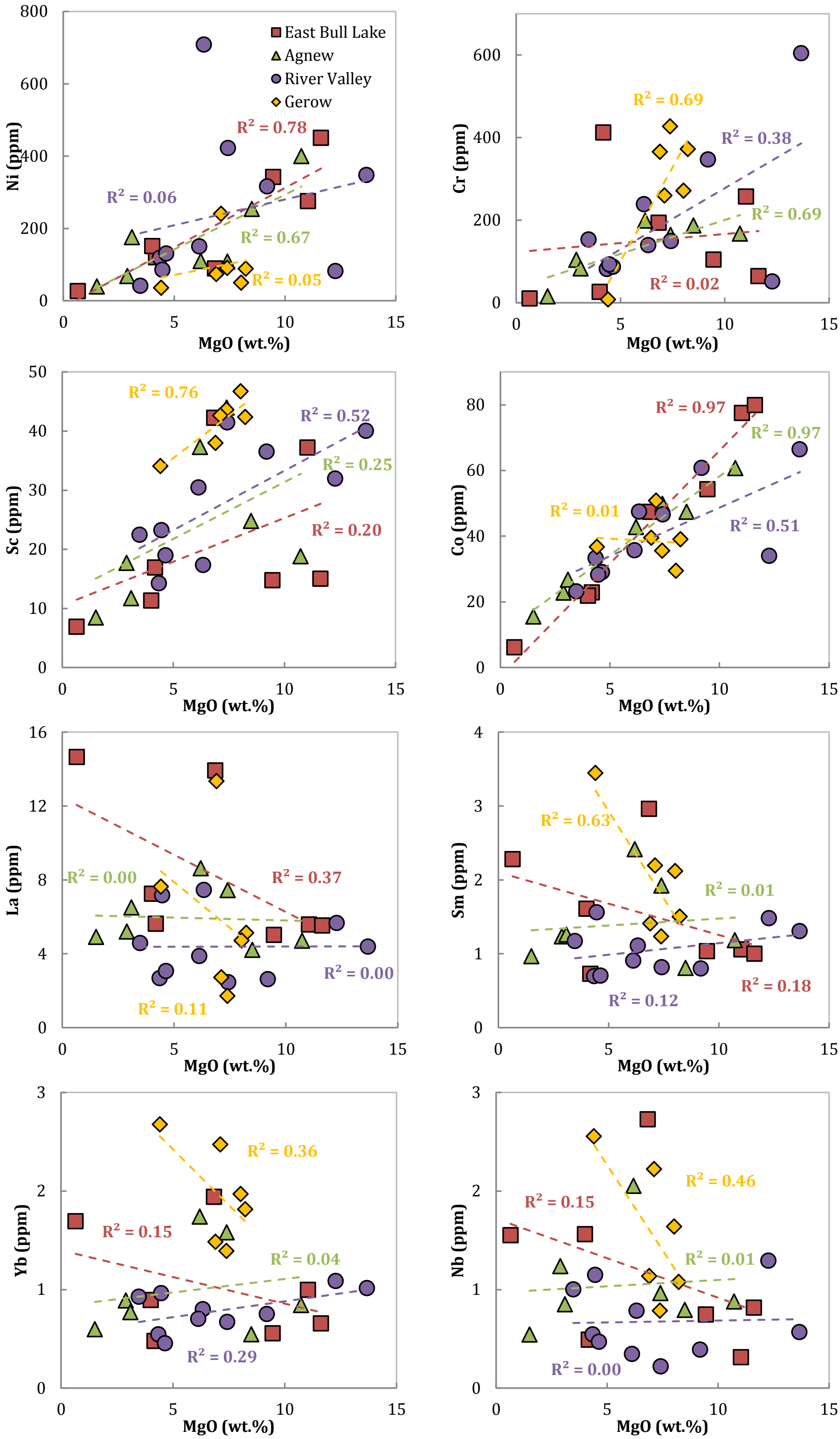

Fig. 4.15. Bivariate diagrams of selected trace elements vs. MgO for the East Bull Lake Suite.

(N) of 0.83-1.11. This chondrite-normalised REE chemistry is best approximated by the N-MORB reservoir. The differences between the three principal East Bull Lake Suite intrusions and the Gerow intrusion may indicate that the latter formed from a fundamentally different magma than the others, or that if all four intrusions share a common parent magma, the East Bull Lake, River Valley and Agnew intrusions have undergone significantly more crustal contamination than the Gerow intrusion. U-Pb age dating of the Gerow intrusion should be conducted to determine whether this intrusion is coeval and potentially cogenetic with the other three principal East Bull Lake suite intrusions.

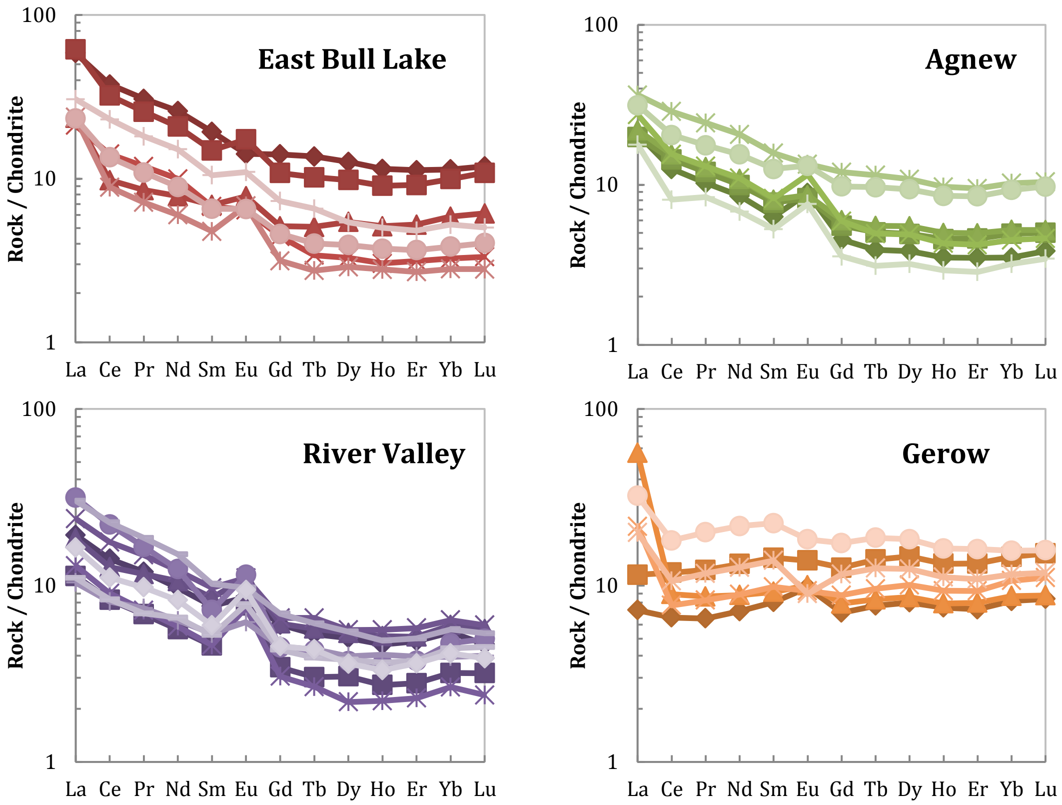

Fig. 4.16. Chondrite-normalised REE diagrams for individual East Bull Lake Suite intrusions. Normalising values from McDonough and Sun (1995).

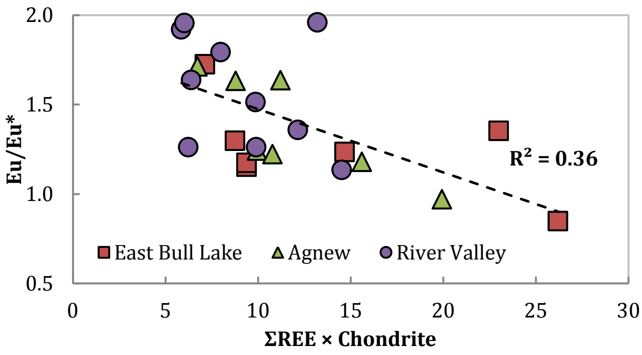

Fig. 4.17. Bivariate diagram showing Eu/Eu* vs. ΣREE × Chondrite in the East Bull Lake, Agnew and River Valley intrusions.

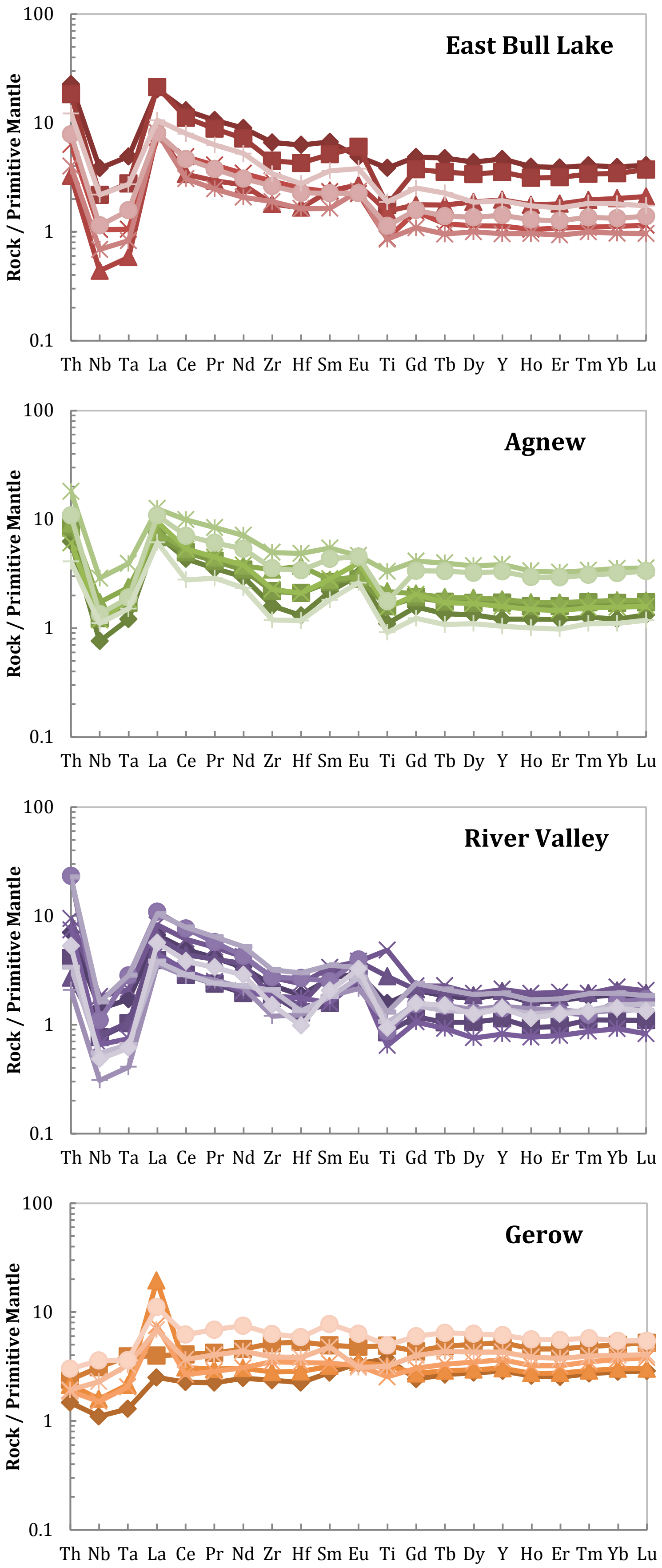

Fig. 4.18. Primitive Mantle-normalised multi-element diagrams for the East Bull Lake Suite intrusions. Normalising values from McDonough and Sun (1995).

On primitive-mantle normalised diagrams **(Fig. 4.18)** the East Bull Lake, Agnew and River Valley intrusions show similar patterns of enrichment in the most incompatible elements relative to the less incompatible elements. These three intrusions also show consistently negative Nb-Ta anomalies (Nb/Nb* = 0.06-0.22), variable (but usually slightly negative) Zr-Hf anomalies (Zr/Zr* = 0.53-1.07, average = 0.80) and consistently negative Ti anomalies (Ti/Ti* = 0.40-1.72, average = 0.66). On the same diagrams, the Gerow intrusion shows very different patterns to the other three intrusions, in that the Gerow samples are depleted in the most incompatible elements relative to the least incompatible elements. When separated into rock type, rather than intrusion, it appears that the anomalies described above are not obviously related to a specific lithology or stratigraphic horizon within the intrusions **(Fig. 4.19)**. The Gerow samples also record no (or occasionally slightly negative) Nb-Ta anomalies ($Th/Nb_{(N)}$ = 1.35-0.77, average = 1.06), positive La anomalies – potentially caused by mobilisation of La, variable Zr-Hf anomalies (Zr/Zr* = 0.83-1.09, average = 0.94) and variable Ti anomalies (Ti/Ti* = 0.72-1.43, average = 0.97).

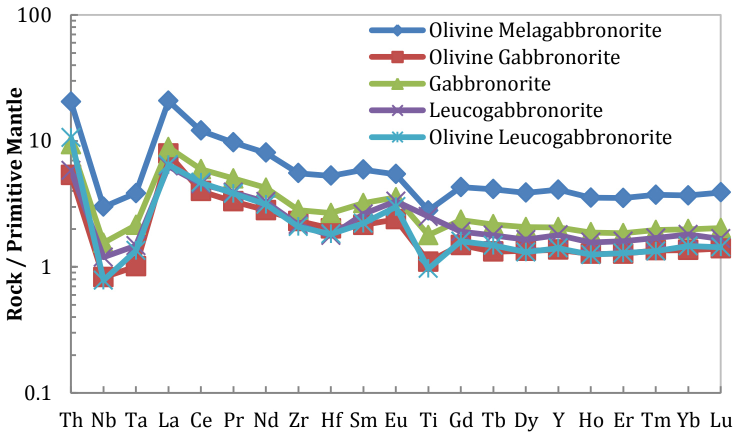

Fig. 4.19. Primitive Mantle-normalised multi-element diagram for average values for each of the lithologies which make up the East Bull Lake Suite intrusions (See **Fig. 4.13**). Normalising values from McDonough and Sun (1995).

On a Zr/Nb vs. Nb/Th diagram **(Fig. 4.20)**, the East Bull Lake, Agnew and River Valley samples all plot in the arc field while the Gerow intrusion samples plot largely between the arc and N-MORB fields. On the Zr/Nb vs. Zr/Y diagram **(Fig. 4.21)**, all of the East Bull Lake Suite samples plot on an array of increasing Nb/Y with increasing Zr/Y just inside the non-plume source area of the graph and within the NMORB and volcanic arc basalt fields.

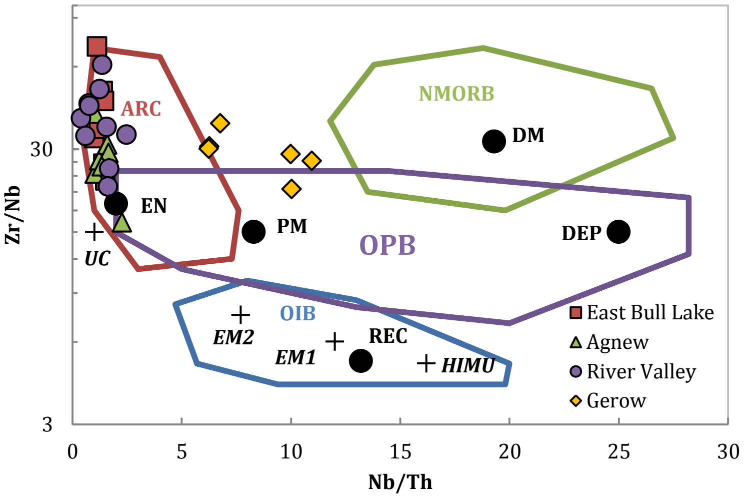

Fig. 4.20. Zr/Nb vs. Nb/Th diagram for the East Bull Lake Suite intrusions. Field boundaries and end-member compositions from Condie (2005). Abbreviations as in **Fig. 4.8**.

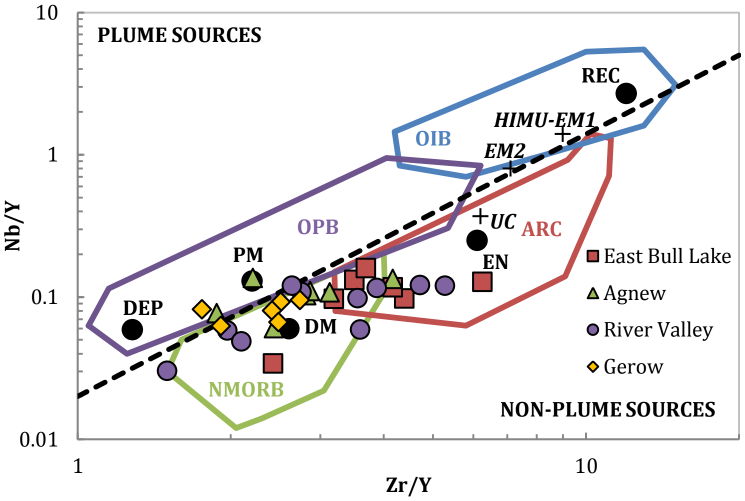

Fig. 4.21. Nb/Y vs. Zr/Y diagram for the East Bull Lake Suite intrusions. Field boundaries and end-member compositions from Condie (2005). Abbreviations as in **Fig. 4.8**.

4.4.5. Platinum-Group Elements

Fig. 4.22 shows chondrite-normalised PGE data for each of the three principal East Bull Lake Suite intrusions. **Fig. 4.22** shows that in general, the East Bull Lake suite intrusions are enriched in the Palladium Group PGE (PPGE) relative to the Iridium Group PGE (IPGE) with the East Bull Lake, Agnew and River Valley intrusions recording average Ir/Pt$_{(N)}$ of 0.20, 0.08 and 0.04 respectively. Rocks from the unmineralised zones of the three intrusions commonly contain low abundances of PGE and record a range of ΣPGE of between 0.003-0.03 × chondritic values. Specifically, unmineralised rocks of the East Bull Lake intrusion contain ΣPGE abundances of between 11-18 ppb, while unmineralised rocks of the Agnew and River Valley intrusions contain ΣPGE abundances of between 21-61 ppb and 46-101 ppb respectively. The samples with the highest PGE contents (RV014 and RV015) are sampled from the mineralised gabbronorite matrix of the inclusion-bearing zone of the River Valley intrusion and contain 2892 ppb and 980 ppb total PGE respectively. Sample AG007 comes from the equivalent zone in the Agnew intrusion but contains 61 ppb ΣPGE, which is within the range recorded by unmineralised East Bull Lake Suite rocks. These results may demonstrate the heterogeneity of the 'blebby' mineralisation observed in the inclusion-bearing zone (Peck et al. 2001; James et al. 2002).

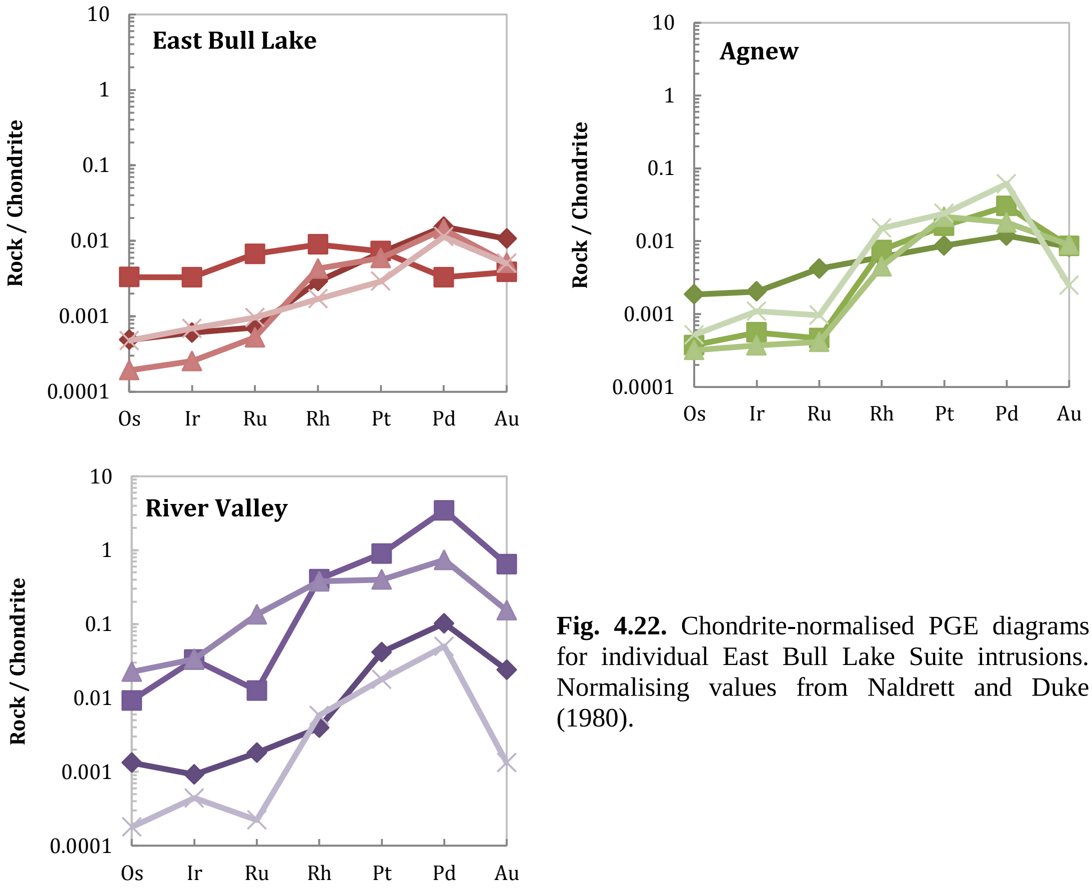

Fig. 4.22. Chondrite-normalised PGE diagrams for individual East Bull Lake Suite intrusions. Normalising values from Naldrett and Duke (1980).

When the East Bull Lake Suite samples are divided into rock type as calculated using the CIPW norm **(Fig. 4.13)**, rather than intrusion, it would appear that gabbronoritic rocks are the most prospective **(Fig. 4.23)**. However, the data for the gabbronoritic rocks of the East Bull Lake suite are skewed by the two mineralised samples which have gabbronoritic compositions. When these samples are removed, the remaining gabbronoritic rocks contain similar PGE abundance to other unmineralised East Bull

Lake Suite lithologies, which indicates that lithology is not a totally useful indicator of degree of mineralisation in the East Bull Lake Suite.

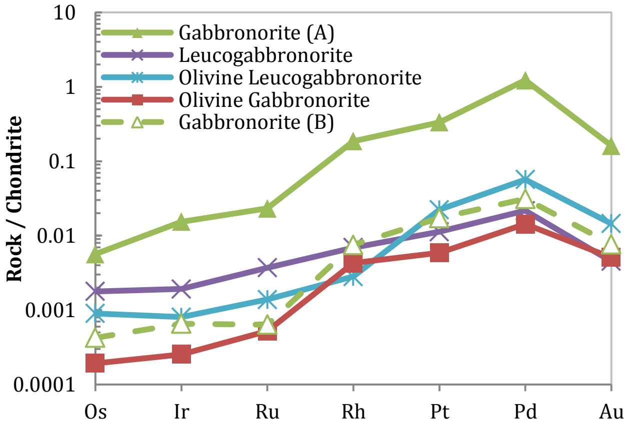

Fig. 4.23. Chondrite-normalised PGE diagrams for average values for each of the lithologies which make up the East Bull Lake Suite intrusions (See **Fig. 4.13**). Gabbronorite (A) = Average Gabbronorite including mineralised samples and (B) = Average Gabbronorite not including mineralised samples. Normalising values from Naldrett and Duke (1980)

4.5. Thessalon Formation

4.5.1. Alteration and Element Mobility

Due to constraints of time and expense, only a few samples were collected from the Thessalon Formation volcanics of the Huronian Supergroup and made into thin-sections. Instead, this study uses the data of Kirsty Tomlinson who collected 84 samples related from the Thessalon Formation of the Huronian Supergroup as part of her Ph.D. thesis on early Precambrian Greenstone Belts (Tomlinson 1996). The data presented here includes 78 samples of Thessalon Formation basalts and basaltic andesites from Tomlinson (1996) which can be found in full in **Appendix C**.

The LOI for the Thessalon Formation volcanics range from 1.0 to 6.7 wt.%. Some of these LOI values are relatively high and may suggest that the Thessalon Formation rocks have experienced little alteration. However, previous studies (Jolly 1987a; Tomlinson 1996) have documented alteration assemblages indicative of greenschist facies metamorphism in all but the coarsest flows of the Thessalon Formation. A subset of element vs. Zr graphs is shown in **Fig. 4.2**. Examination of these graphs shows that the Thessalon Formation volcanics have a quite complex geochemistry and that, based on trace and major element relationships, the volcanic rocks can be divided into at least four separate groups. The distinction between Group 1 and Group 2 volcanics is not immediately obvious on plots of major elements vs. Zr, but does become apparent with plots of the MREE and HREE vs. Zr. On these plots, Group 2 volcanics display correlations with much steeper gradients than Group 1 volcanics do. Group 3 volcanics have much higher concentrations of MgO, Ni and Cr and also have much lower concentrations of Al_2O_3 relative to the other Thessalon samples which have similar Zr contents. Group 4 volcanics have much higher Th and U contents than other Thessalon samples with similar Zr contents.

Group 1 volcanics show good correlations between Zr and Nb and Hf only. Moderately strong correlations are observed between Zr and Ce, Pr, Nd, Yb, Lu, Th and U while there are weak correlations between Zr and the remaining elements.

For Group 2 volcanics, the elements which show a poor correlation with Zr include the major, LIL, and compatible trace elements, Eu, Ta, Th and U. Elements which show a moderate correlation with Zr include Y, Er, Tm, Yb, Lu and Hf. The REE (La, Ce, Pr, Nd, Sm, Gd, Tb, Dy and Ho) are the only elements to show a good, linear positive correlation with Zr. Group 3 samples exhibit poor correlations between Zr and the major elements, Sc, Cr, Zn, V, Ba, and the MREE-HREE, moderately good correlations between Zr and the LREE, K_2O, P_2O_5, Rb, Cs, Yb and Ta and good correlations between Zr and Ni, Nb, Th, U, Sr and Y. However, as only three Group 3 samples have trace element data, the R^2 values recorded above for the trace elements cannot be used with confidence as, with such a small population size, the product moment correlation coefficient becomes less robust as it can be affected by anomalous samples. Group 4 volcanics contain a very narrow range of Zr (5 ppm) relative to the other trace elements and all elements record a poor correlation with Zr.

The correlations described above are interesting for two reasons. Firstly, it is not uncommon for elements which are considered to be immobile under greenschist facies metamorphism (Pearce 1996; Hastie et al. 2007) to record poor correlations with Zr in the Thessalon Formation rocks, despite them having experienced relatively low degrees of metamorphism (Mossman and Harron 1983). Secondly and perhaps more surprisingly is the fact that the strength of the correlations is not uniform between the different groups despite the groups belonging to the same volcanic formation and thus sharing a common tectonic and metamorphic history. Potential reasons behind the different geochemistry preserved by the Thessalon Formation volcanic rocks are explored later in the thesis.

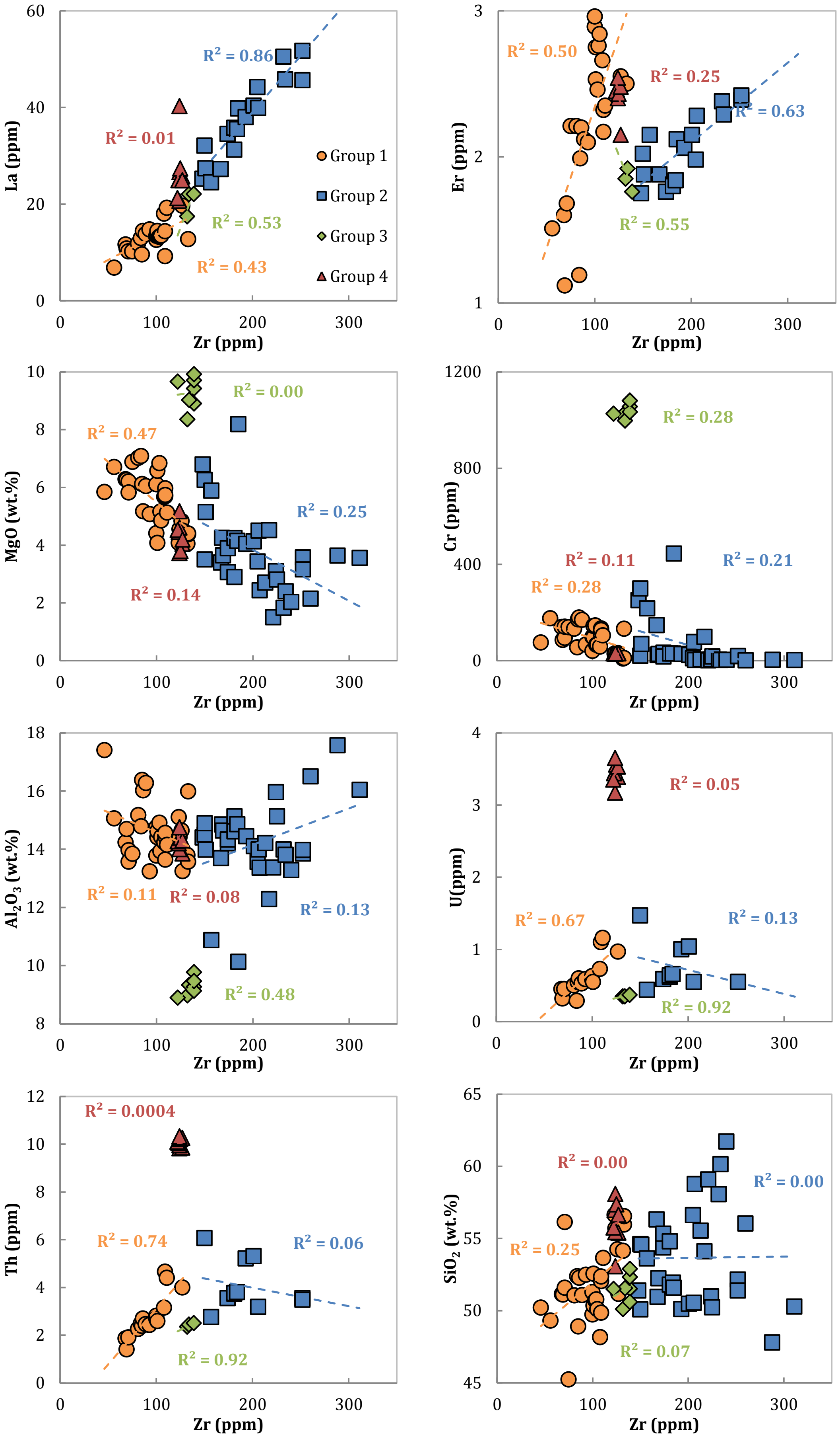

Fig. 4.24. Bivariate diagrams of selected elements vs. Zr for the Thessalon Formation samples.

4.5.2. Classification

On the TAS diagram **(Fig. 4.25)**, the majority of the Group 1 Thessalon volcanics plot as tholeiitic basalts-andesites, while approximately 30% of Group 1 samples plot within the alkaline series as trachybasalts-trachyandesites. The majority of the Group 2 volcanic rocks plot as tholeiitic basalts and fewer basaltic andesites and trachyandesites. The Group 3 samples form a fairly tight cluster which straddles the tholeiitic basalt-basaltic andesite transition. The Group 4 samples form a diffuse scatter in the tholeiitic basaltic andesite, andesite, basaltic trachyandesite and trachyandesite fields.

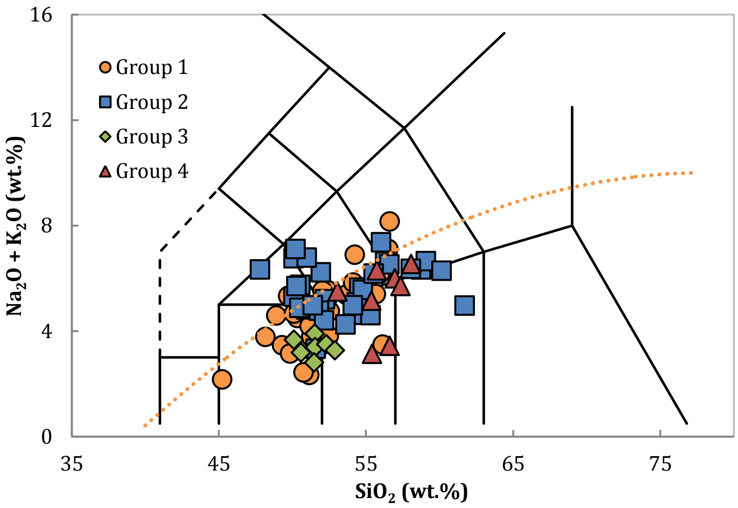

Fig. 4.25. Total alkali vs. SiO_2 (TAS) diagram for the Thessalon Formation samples. Field boundaries and names as in **Fig. 4.2**.

The poor correlation of Na_2O, K_2O and SiO_2 with Zr observed in the Thessalon volcanic groups suggests that these elements may have been remobilised. Therefore, the Zr/Ti vs. Nb/Y diagram may be of more use in classifying the Thessalon Formation rocks. On this diagram **(Fig. 4.26)**, the majority of Group 2 samples plot as a fairly tight cluster in the subalkaline basalt and basaltic andesite fields. The Group 1 samples also lie within the subalkaline basalt and basaltic andesite fields but plot separately from Group 2 samples and typically record lower Nb/Y ratios. Three Group 3 samples form a very tight cluster in the subalkaline basalt field while Group 4 samples plot as a tight cluster on the transition between subalkaline basaltic andesite-andesite.

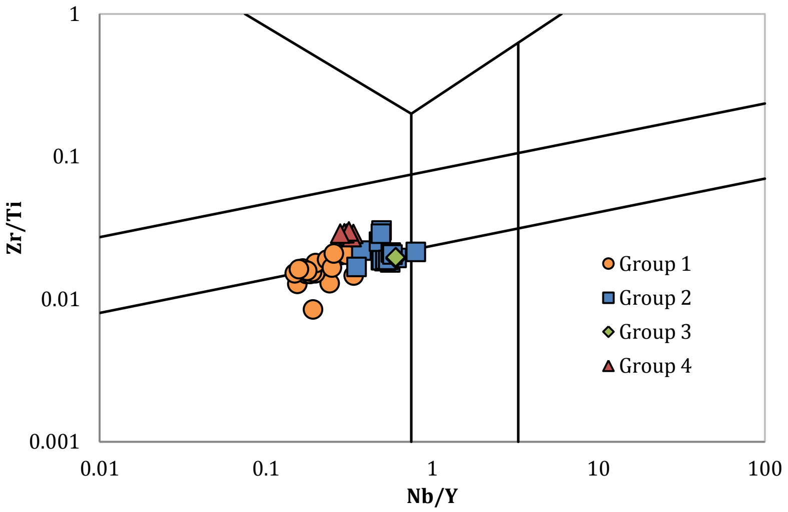

Fig 4.26. Zr/Ti vs. Nb/Y diagram for the Thessalon Formation volcanic rock. Field boundaries defined by Pearce (1996).

4.5.3. Major Element Variation

Group 1 volcanics range in MgO, TiO_2 and Fe_2O_3 between 4.1-7.1, 0.6-1.5 and 10.1-17.0 wt.% respectively. These values correspond to a range in Mg# of 25-43. SiO_2 in Group 1 volcanics ranges from 45.2-56.6 wt.% while total alkalis range from 2.2-8.2 wt.%. Group 2 volcanics range in MgO, TiO_2 and Fe_2O_3 between 1.5-8.2, 1.1-2.0 and 10.2-16.7 wt.% respectively. These values correspond to a range in Mg# of 14-38. SiO_2 in Group 2 volcanics ranges from 47.8-61.7 wt.% while total alkalis range from 3.3-7.4 wt.%. The Group 3 volcanics range in MgO, TiO_2 and Fe_2O_3 between 8.4-9.9, 1.1-1.3 and 12.5-14.6 wt.% respectively. These values correspond to a range in Mg# of 41.2-46.4. SiO_2 in Group 3 volcanics ranges from 50.1-52.9 wt.% while total alkalis range from 2.8-3.9 wt.%. Group 4 volcanics range in MgO, TiO_2 and Fe_2O_3 between 3.7-5.2, 0.7-0.7 and 9.7-13.3 wt.% respectively. These values correspond to a range in Mg# of 28-32. SiO_2 in Group 4 volcanics ranges from 53.1-58.1 wt.% while total alkalis range from 3.1-6.5 wt.%.

All of the major elements in Group 1 and 2 volcanics have weak correlations with MgO **(Fig. 4.27)**, which may be further evidence that MgO (and the other major elements) has been remobilised in the Thessalon Formation. Although the correlations are weak, Group 1 and 2 volcanics show negative correlations between MgO and SiO_2, TiO_2, Na_2O, K_2O and P_2O_5 while also showing positive correlations between MgO, Fe_2O_3 and CaO. These correlations may suggest that the evolution of Group 1 and 2 Thessalon volcanics was controlled by the fractionation and removal

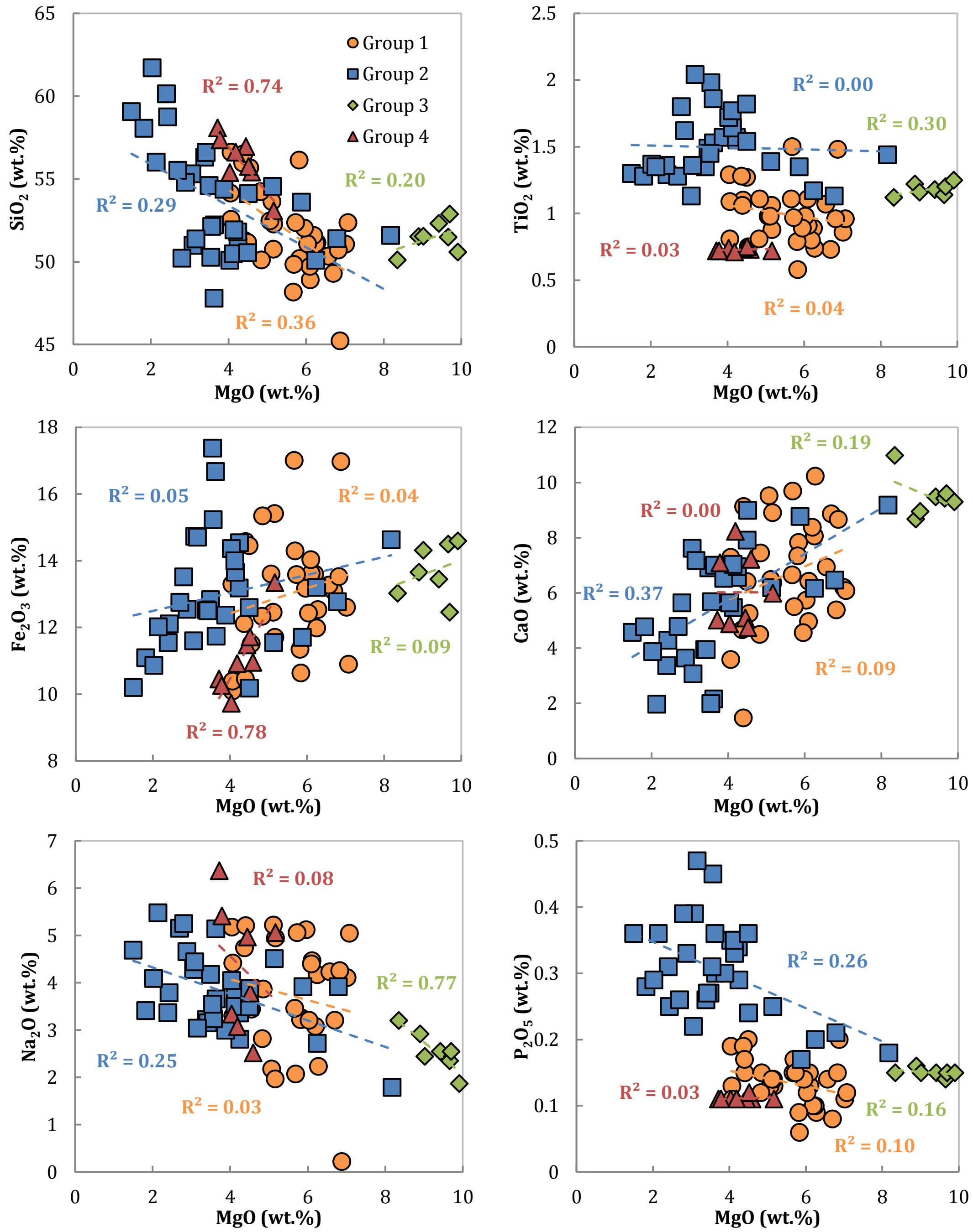

Fig. 4.27. Bivariate diagrams of selected major elements vs. MgO for the Thessalon Formation.

of Mg, Fe and Ca bearing minerals in a deeper magma chamber. Group 3 and 4 volcanics typically show very weak correlations with MgO and trends are not immediately obvious for the majority of the major elements although Group 4 volcanics show significant negative linear correlations between MgO, SiO_2 and Fe_2O_3, similar to those observed in Group 1 and 2 samples.

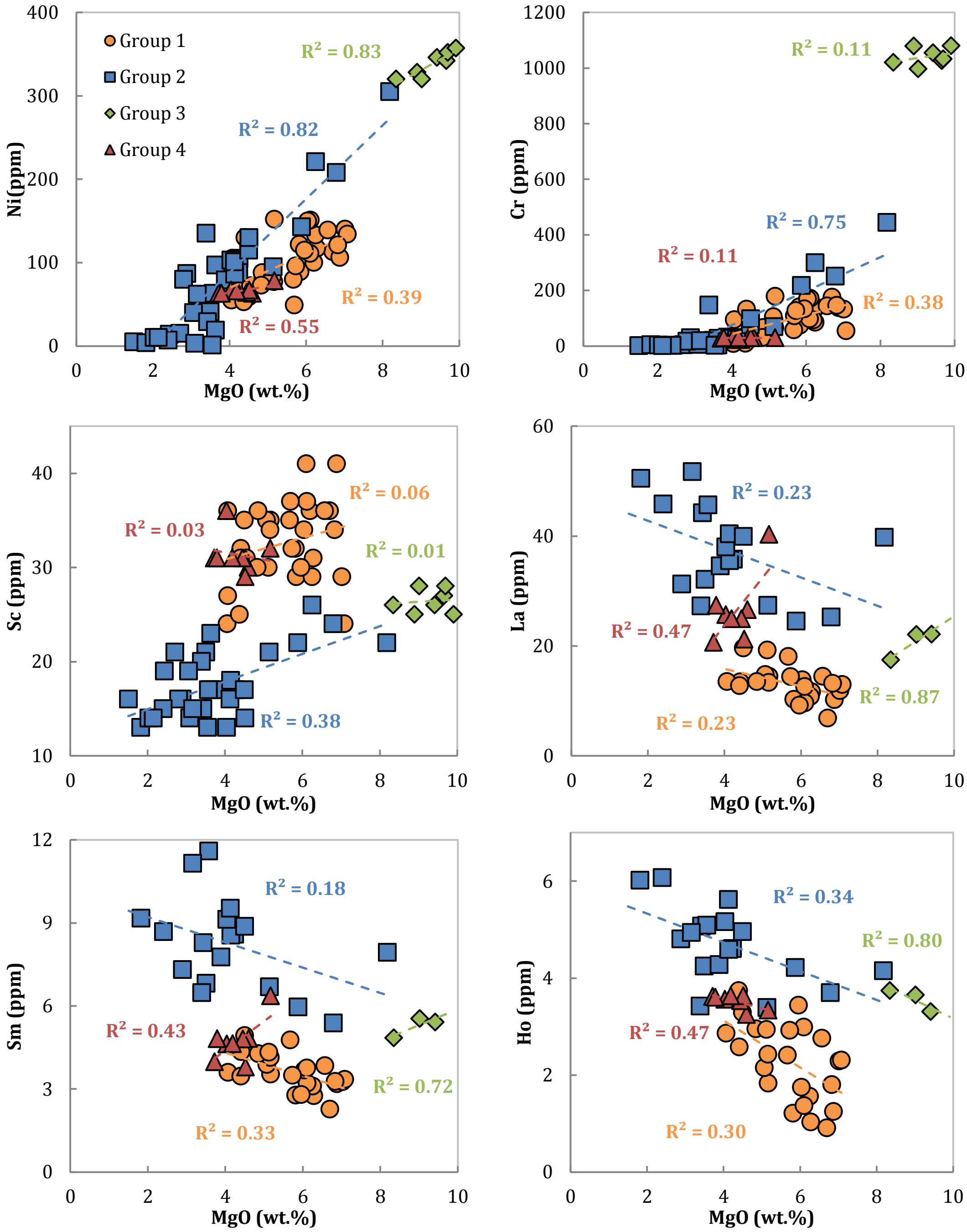

Fig. 4.28. Bivariate diagrams of trace elements vs. MgO for the Thessalon Formation samples.

4.5.4. Trace Element Variation

In the Thessalon Formation volcanic groups, the elements which are compatible during basaltic fractionation show variable negative correlations with MgO **(Fig. 4.28)**. Group 2 volcanics contain the largest ranges in Cr and Ni of all of the groups (1-444 ppm Cr and 1-205 ppm Ni) and encompass the smaller ranges observed in the Group 1 and 4 volcanics. Group 3 samples contain much greater concentrations of Ni (320-357 ppm) and Cr (997-1080 ppm) than the other groups and also show strong negative linear correlations between these elements and MgO. Weak linear negative correlations are observed between MgO and the incompatible trace elements in the Group 1 and 2 Thessalon volcanics. Interestingly, Group 3 and 4 samples record positive correlations between MgO and some of the incompatible trace elements, however, these correlations may be erroneous due to the relatively small population size of these two groups.

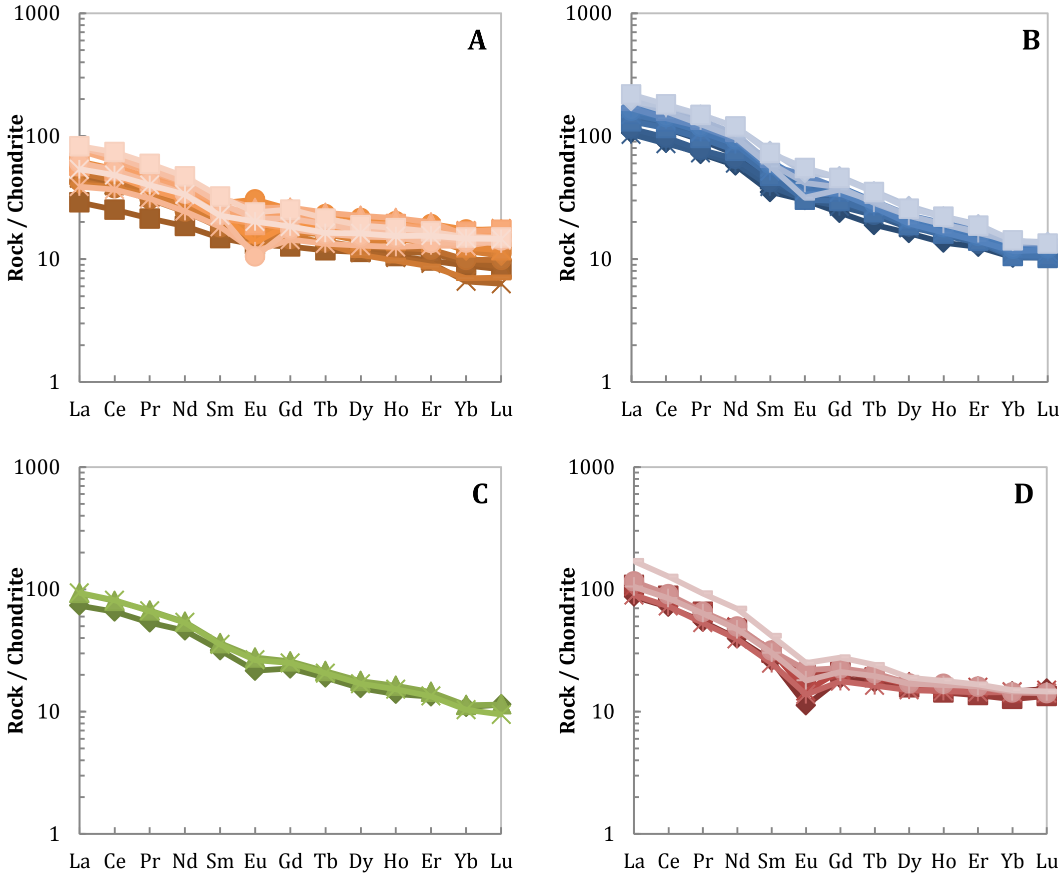

Fig. 4.29. Chondrite-normalised REE diagrams for (A) Group 1, (B) Group 2, (C) Group 3 and (D) Group 4 of the Thessalon Formation. Normalising values from McDonough and Sun (1995).

Chondrite-normalised REE diagrams for the Thessalon Formation **(Fig. 4.29)** show that the four groups are characterised by LREE enrichment relative to the HREE with variable (commonly negative) Eu anomalies. The degree of LREE enrichment varies between the groups with Group 2 volcanics being most enriched [$(La/Yb)_N$ = 13.07], much greater than that recorded by Group 1 volcanics (mean $(La/Yb)_N$ = 4.37). Group 3 and Group 4 volcanics show similar levels of LREE enrichment, with average $(La/Yb)_N$ values of 8.00 and 7.83 respectively. Group 2 volcanics also record the steepest HREE slopes (mean $(Gd/Yb)_N$ = 2.88), almost twice as steep as those of

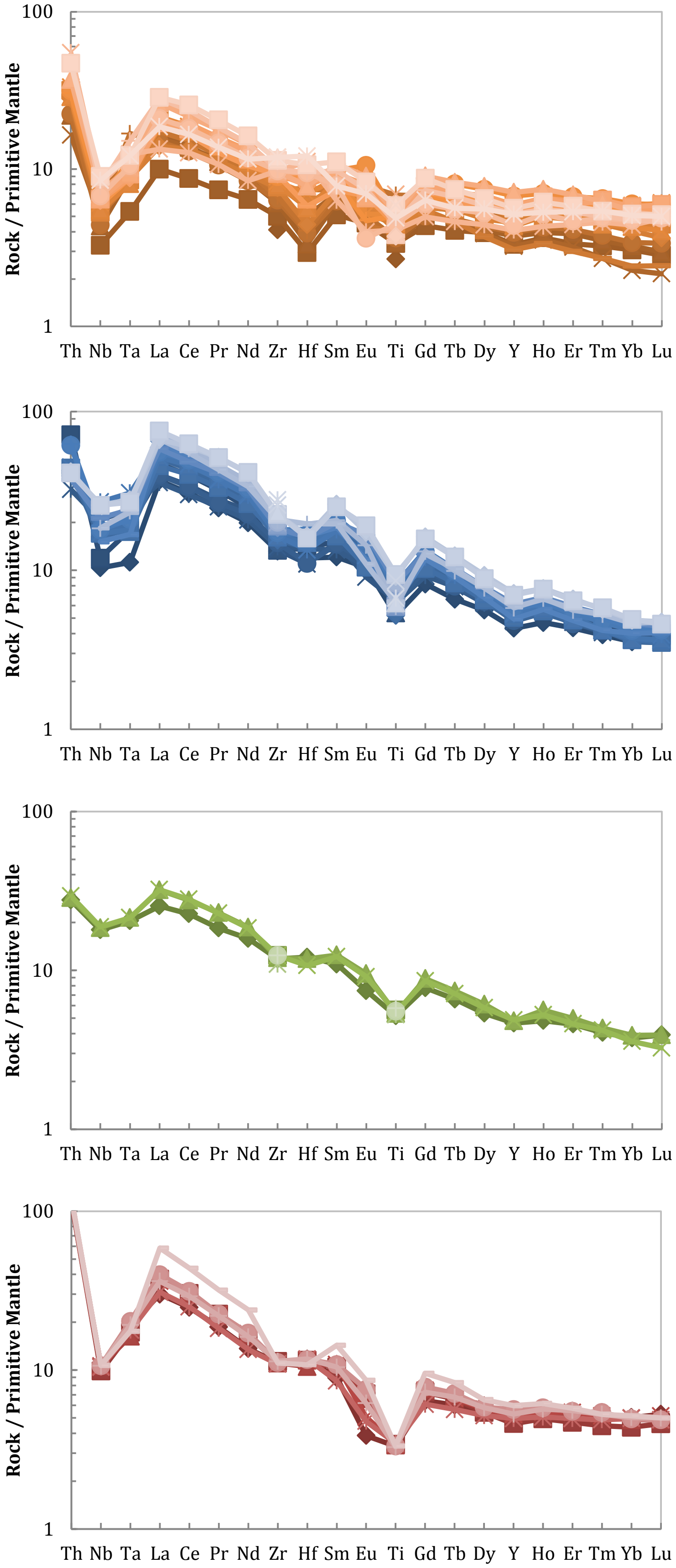

Fig. 4.30. Primitive Mantle-normalised multi-element diagrams for the Thessalon Formation. (A) Group 1, (B) Group 2, (C) Group 3 and (D) Group 4. Normalising values from McDonough and Sun (1995).

Groups 1 and 4 which have $(Gd/Yb)_N$ of 1.47 and 1.51 respectively. The Group 3 volcanics have an average $(Gd/Yb)_N$ of 2.25, intermediate between the other groups. All of Group 3 and 4 samples show Eu anomalies of between Eu/Eu* = 0.50-0.89. Group 1 and 2 samples show variable ranges in Eu/Eu* of 0.52-1.13 and 0.67-1.02 respectively. These ranges in Eu/Eu* may indicate that the Group 3 and 4 volcanics experienced plagioclase fractionation while the Group 1 and 2 lavas may have undergone plagioclase fractionation and removal/accumulation.

On Primitive Mantle-normalised multi-element plots (**Fig. 4.30**), the Thessalon Formation rocks all have similar patterns of incompatible element enrichment and negative anomalies in Nb-Ta, Ti, Y and Zr-Hf. The largest Nb-Ta (Nb/Nb* = 0.2) and Ti (Ti/Ti* = 0.4) anomalies are observed in Group 4 volcanics. The smallest Nb-Ta anomalies are recorded by Group 3 volcanics (Nb/Nb* = 0.7) and it is this group which is the only one that has $(Th/La)_N$ ratios less than 1. All samples from Groups 2, 3 and 4 have negative Zr-Hf anomalies between (Zr/Zr*) = 0.6-1.0. All but one of Group 1 samples show similarly large, negative Zr-Hf anomalies while, the one sample which does not, shows a positive Zr-Hf anomaly of (Zr/Zr*) = 1.3.

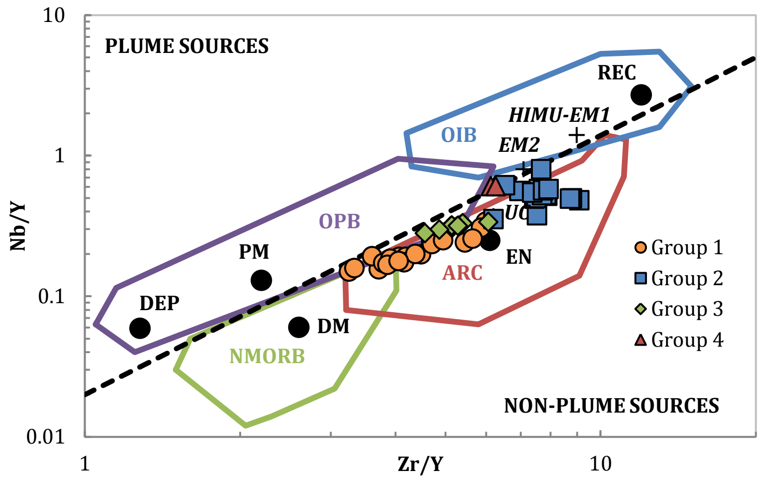

Fig. 4.31. Nb/Y vs. Zr/Y diagram for the Thessalon Formation samples. Field boundaries and end-member compositions from Condie (2005). Abbreviations as in **Fig. 4.8.**

On the Nb/Y vs. Zr/Y diagram **(Fig. 4.31)**, the Thessalon Formation samples plot on an array of increasing Nb/Y and Zr/Y within the non-plume sources area of the diagram. Group 1 samples plot on a trend which crosses the NMORB and volcanic arc basalt fields. Group 2 samples produce a fairly diffuse scatter almost entirely within the volcanic arc basalt field. The Group 3 samples define a trend in the overlapping portions of the oceanic plateau and volcanic arc basalts while Group 4 samples plot in a tight cluster in the space between the oceanic plateau, ocean island and volcanic arc basalt fields. On the Zr/Nb vs. Nb/Th diagram **(Fig. 4.32)**, the Group 1 Thessalon volcanics form a moderately tight cluster within the volcanic arc basalt field, very close to the enriched component end-member. The majority of Group 2 samples plot within the overlapping portions of the volcanic arc and oceanic plateau basalt fields. The Group 3 samples fall in the space between the volcanic arc, oceanic plateau and ocean island basalt fields while the Group 4 samples fall just to the left of the volcanic arc basalt field and very close to the composition of the upper continental crust.

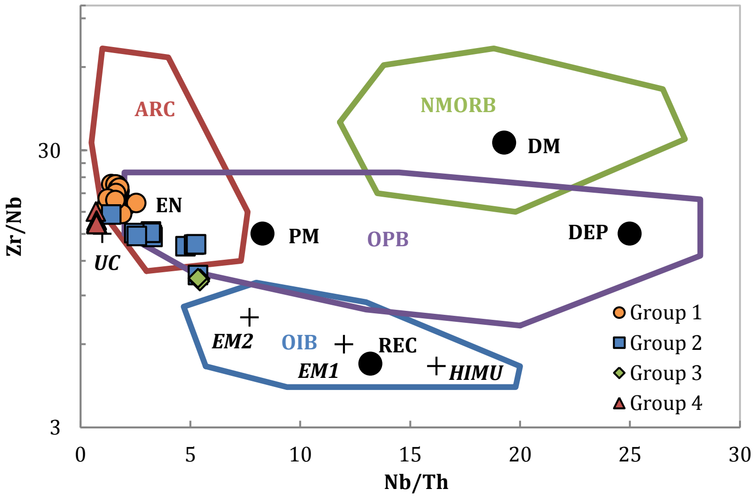

Fig. 4.32. Zr/Nb vs. Nb/Th diagram for the Thessalon Formation samples. Field boundaries and end-member compositions from Condie (2005). Abbreviations as in **Fig. 4.8**.

4.6. Blue Draw Metagabbro

4.6.1. Alteration and Element Mobility

Rocks from the BDM range in LOI values between 0.51-12.40 wt.%. These values may suggest that alteration of the BDM is variable and is potentially quite significant. The alteration observed in thin section (see chapter 3) is characterised by extensive alteration of clinopyroxene to amphibole and calcite, serpentinization of olivine and replacement of plagioclase by fine grained sericite and quartz. This observed alteration is in agreement with the findings of Redden et al. (1990) and Van Boening and Nabelek (2008) who suggested that post-crystallization metamorphic events do not appear to have exceeded greenschist facies conditions in the BDM. To

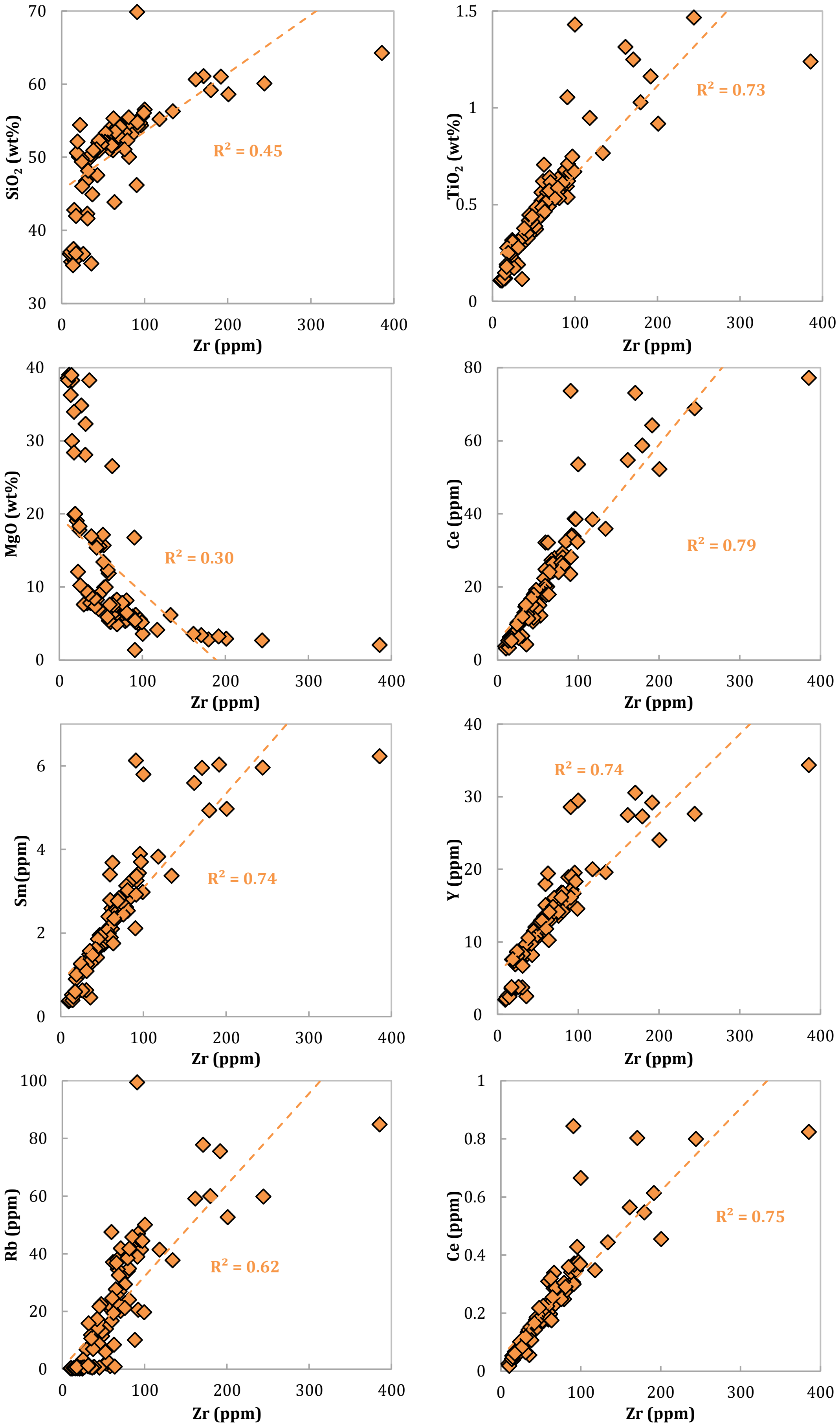

Fig. 4.33. Bivariate diagrams of trace elements vs. Zr for the Blue Draw Metagabbro.

determine if this alteration has affected the chemistry of the BDM, each element is plotted against Zr. A subset of these graphs is shown in **(Fig. 4.33)**.

The elements which show strong correlations with Zr ($R^2 > 0.75$) include the REE (excluding La and Eu), the HFSE; Ta, Hf, Nb, Y and U and TiO_2, and P_2O_5. The elements which show a moderate correlation with Zr ($0.75 > R^2 > 0.5$) include La, Eu, Ba, Cs, K_2O and Rb. Elements with a poor correlation with Zr ($R^2 < 0.5$) include the compatible trace elements; Sc, V, Ni, Co and Cr, the major elements; SiO_2, CaO, MgO, Al_2O_3, Fe_2O_3 and Na_2O, as well as Cu. Pb, Zn, Sr and Cu.

These correlations indicate that the incompatible HFSE and REE have not been significantly remobilised during greenschist metamorphism of the BDM while the incompatible LILE have been mobilised. The relatively low R^2 values exhibited by the most of the major elements and compatible trace elements may suggest that extensive secondary remobilisation of these elements has occurred. However, it is apparent from the trends observed that the data for these elements are not scattered and instead, largely plot as curves and occasionally with separate clusters of data. These trends are likely the result of fractional crystallisation and cumulate nature of some of the BDM rocks.

4.6.2. Classification

Maranate (1979) produced the first map of the BDM **(Fig 2.22)** and based on metamorphic mineral assemblages, divided the BDM into a ~130 m thick serpentinite unit which is successively overlain by a ~100 m thick lower hornblendite unit and a ~250 m thick amphibolite which is separated into lower and upper units by a ~50 m thick upper hornblendite unit which crops out discontinuously at ~380 m from the base of the intrusion. The upper amphibolite unit is overlain by a ~60 m thick border zone of biotite- and quartz-rich rocks which, close to the margin of the intrusion, contain xenoliths of the Boxelder Creek Quartzite.

The stratigraphic nomenclature proposed by Maranate (1979) described above is unsuitable, partly because the metamorphic terms used to describe the lithologies are at odds with the igneous nature of the BDM. Furthermore, the slight differences in modal mineral abundances between rocks classed as amphibolites and others which are classed as hornblendites (the latter being more melanocratic) do not adequately reflect the lithological variation within the intrusion. Thus one of the aims of this current study is to produce a new stratigraphic nomenclature for the BDM intrusion.

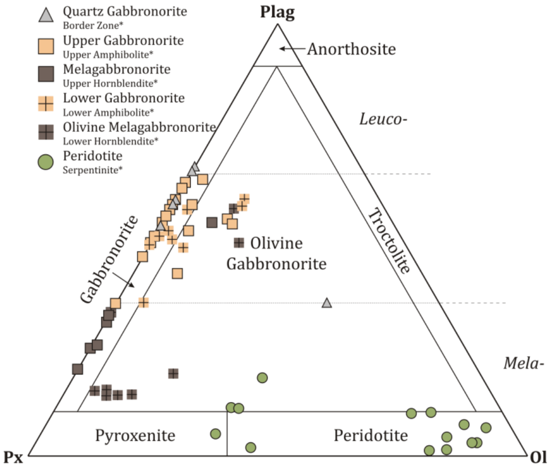

Fig. 4.34. Classification of the rocks from the Blue Draw Metagabbro. * denotes stratigraphic unit mapped by Maranate (1979). Fields taken from Le Maitre (2002) and Barnes and Gomwe (2011).

To do this, CIPW normative mineralogies for samples from the stratigraphic units mapped by Maranate (1979) were calculated and classified using the IUGS plagioclase-olivine-pyroxene classification scheme (Le Maitre 2002). This classification allows new lithological names for the different units of the BDM to be assigned **(Fig. 4.34)**. Most samples from the rock units described by Maranate (1979) fall within discrete areas within the IUGS plagioclase-olivine-pyroxene classification scheme. Using this classification, the serpentinite, lower hornblendite, lower amphibolite, upper hornblendite, upper amphibolite and border zone units of Maranate (1979) have been reclassified into the peridotite, olivine melagabbronorite, lower gabbronorite, melagabbronorite, upper gabbronorite and quartz gabbronorite units respectively.

The total alkali vs. silica (TAS) diagram classifies the BDM samples as a continuum of tholeiitic gabbros, diorites and granodiorites **(Fig. 4.35)**. Further, the continuum defined by the analyses also broadly reflects the igneous stratigraphy in the intrusion, in that the peridotite unit and olivine melagabbronorite unit from near the base of the intrusion plot as gabbros, while the upper gabbronorite unit and quartz gabbronorite unit rocks from near the top of the intrusion plot as diorites and granodiorites. This trend is likely to be an effect of fractional crystallisation of the BDM parent magma.

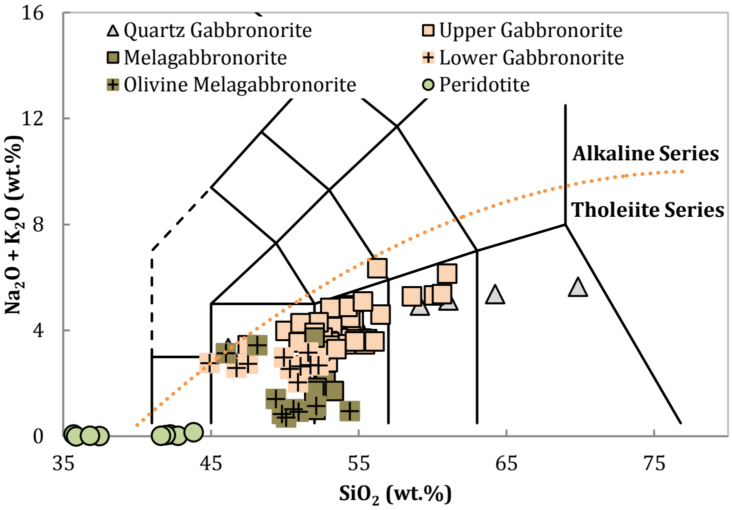

Fig. 4.35. Total alkali vs. SiO$_2$ (TAS) diagram for the Blue Draw Metagabbro samples. Field boundaries defined by Le Maitre et al. (1989). Field names are shown in **Fig. 4.2**.

The TAS diagram relies on Na and K to classify igneous rocks, consequently the applicability of the TAS diagram for classifying BDM rocks is questionable, as these elements have been remobilised in the intrusion. Instead, the Zr/Ti vs. Nb/Y (Pearce 1996) diagram **(Fig. 4.36)** is more useful. On this diagram the majority of the BDM rocks plot in a cluster which overlaps the subalkaline basaltic and basaltic andesite fields. There does not appear to be a trend associated with stratigraphic height in these data as the different stratigraphic units largely overlap in Zr/Ti-Nb/Y space.

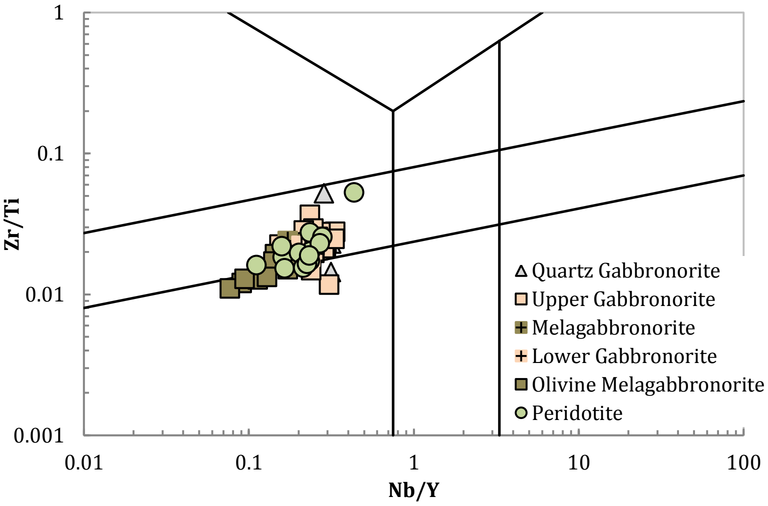

Fig. 4.36. Zr/Ti vs. Nb/Y diagram for the Blue Draw Metagabbro samples.

4.6.3. Major Element Variation

The BDM ranges in MgO, Fe_2O_3 and TiO_2 from 1.4-39.0 wt.%, 6.7-13.4 wt.% and 0.11-1.47 wt.% respectively. These ranges correspond to a range in Mg# of 17-80. SiO_2 in the BDM ranges from 35.2-69.8 wt.% while total alkalis range from 0-6.4 wt.%.

In the BDM, none of the major element oxides exhibit a simple linear correlation with MgO **(Fig. 4.37)**. The incompatible major element oxides (P_2O_5, TiO_2, Na_2O, and K_2O) share a common variation with MgO and are characterised by very low abundances in the MgO rich peridotite unit. Above the peridotite unit (in rocks with MgO < 25 wt.%), P_2O_5, TiO_2, Na_2O, and K_2O record a negative correlation with MgO, defined by linear increases in incompatible element concentrations with decreasing MgO contents. The slope of this negative correlation changes in rocks where MgO <7 wt.% where it becomes far steeper as rocks become more enriched in P_2O_5, TiO_2, Na_2O, and K_2O over a smaller MgO range (~7.0-1.4 wt.%) than observed in rocks with higher MgO contents.

For the remaining major element oxides (SiO_2, Fe_2O_3, CaO, Al_2O_3 and MnO) the stratigraphic units of the BDM define broad clusters in MgO vs. major element oxide space. In the case of CaO, the samples from the peridotite unit plot as a diffuse grouping with low (0-2 wt.%) CaO contents but very high (28-39 wt.%) MgO. The samples from the melagabbronorite and olivine melagabbronorite units plot as a second diffuse grouping between ~10-20 wt.% MgO and contain ~8-14 wt.% CaO. The upper and lower gabbronorite units and quartz gabbronorite unit rocks define a positive linear trend of increasing CaO with increasing MgO between ~1.4 wt.% CaO and ~1.3 wt.% MgO in the quartz gabbronorite unit to ~9 wt.% MgO and 13.3 wt.% CaO at the base of the lower gabbronorite unit. These diffuse groupings are also apparent in MgO vs. MnO space.

The BDM defines scattered, negative linear correlations in terms of SiO_2 and Al_2O_3 vs. MgO such that the peridotite unit contains the highest MgO contents and lowest SiO_2 and Al_2O_3 contents (35-44 wt.% SiO_2 and 2-6 wt.% Al_2O_3) while the upper and lower gabbronorite units contain the highest SiO_2 and Al_2O_3 contents (≥70 wt.% and ≥9 wt.% respectively) but lowest MgO contents (generally > 10 wt.%). The mela-

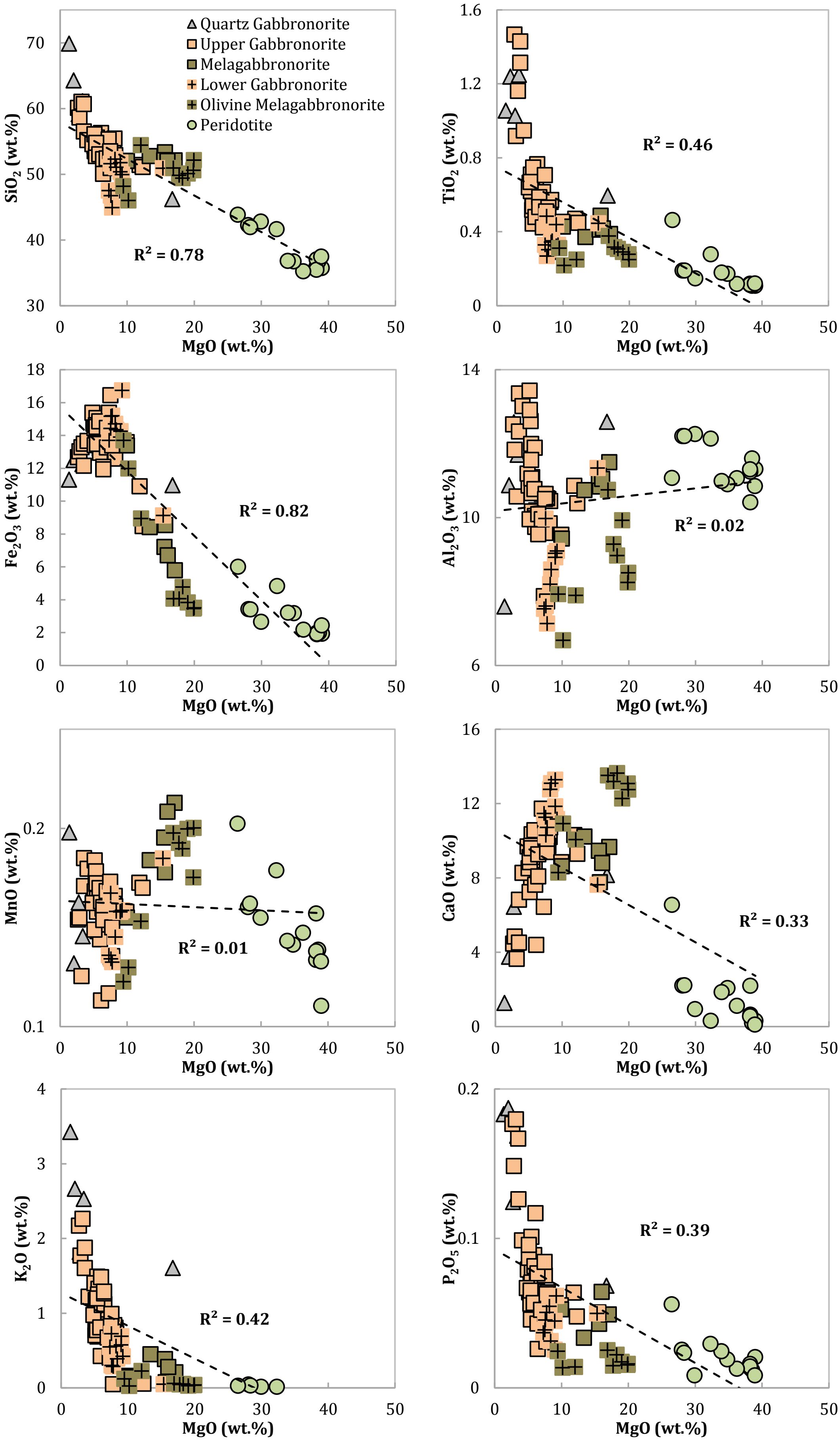

Fig. 4.37. Bivariate diagrams of selected major elements vs. MgO for the Blue Draw Metagabbro.

gabbronorite and olivine melagabbronorite units contain SiO_2, Al_2O_3 and MgO intermediate between the peridotite unit and the upper and lower gabbronorites.

4.6.4. Trace Element Variation

The BDM ranges in Ni and Cr between 6-1376 and 16-3131 ppm respectively. Ni, Cr and Co define good ($R^2 > 0.75$) linear positive correlations with MgO **(Fig. 4.38)**. Sc defines a poor ($R^2 = 0.25$) linear correlation with MgO for the whole intrusion as the data fall on two separate trends: The first trend is defined by the samples from the peridotite unit which show a negative linear correlation between Sc and MgO while the second trend comprises samples from the rest of the stratigraphy (MgO < 20 wt.%) which show a sublinear positive correlation between Sc and MgO. La, Sm, Yb and Nb vs. MgO graphs define curved negative correlations between MgO and the incompatible trace elements. The inflection point for the curves occurs at ~7 wt.% MgO where rocks with MgO > 7 wt.% define a much less steep gradient than rocks where MgO < 7 wt.%.

Fig. 4.39 shows average chondrite-normalised REE patterns for the different stratigraphic units in the BDM with salient features from the whole data set shown in **Table 2**. Total abundance of REE is linked to stratigraphic height with the lowermost peridotite unit containing ∑REE 6.5 times chondritic values increasing with each stratigraphic unit to the most evolved rocks of the Border Zone which have ∑REE of 53 times chondritic values. All BDM rocks have a concave-up pattern of light-REE (LREE) enrichment with a range in $(La/Yb)_N$ of 2.4-13.0. Each stratigraphic unit in the intrusion has a sub-parallel REE pattern with slight differences in slope being explained by differences in modal mineral compositions. For example, the peridotite unit at the base of the intrusion is dominated (~90 vol.%) by altered olivine and has an average $(La/Yb)_N$ ratio of 6.6 while the immediately overlying olivine melagabbronorite unit which is dominated by altered clinopyroxene and subordinate amounts of altered plagioclase has an average $(La/Yb)_N$ ratio of 3.8. The difference in $(La/Yb)_N$ ratios between these two units may be explained by the greater compatibility of the heavy-REE (HREE) relative to the LREE in clinopyroxene compared to olivine (Bédard 2005; 2007) thus giving the pyroxene dominated olivine melagabbronorite unit a lower $(La/Yb)_N$ ratio than the olivine-dominated peridotite unit.

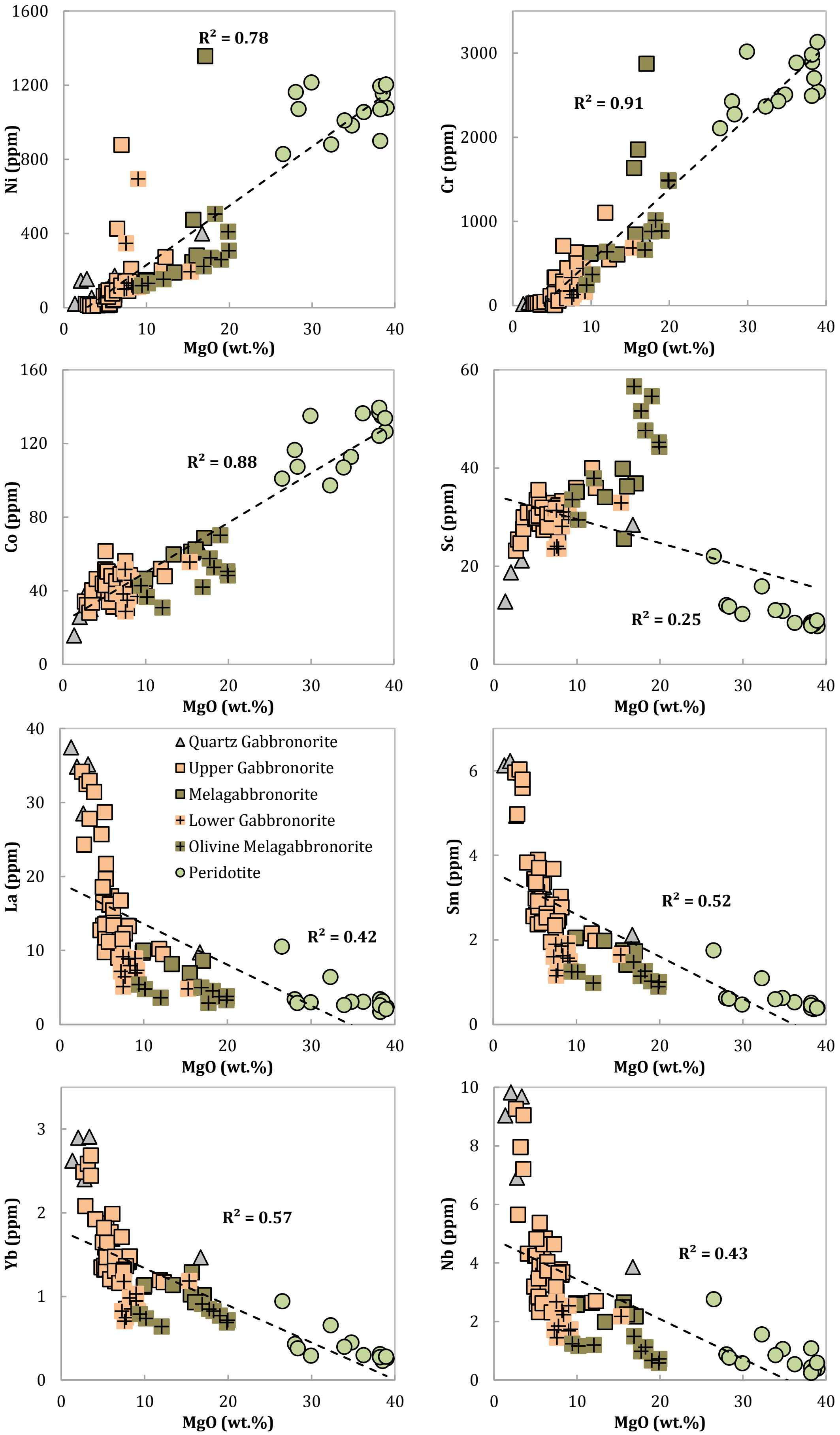

Fig. 4.38. Bivariate diagrams of selected trace elements vs. MgO for the Blue Draw Metagabbro.

Consistent Eu anomalies are observed in the lower gabbronorite unit and quartz gabbronorite unit. The anomaly in the lower gabbronorite unit is slightly positive (Eu/Eu* = 1.1) [Eu/Eu* = $Eu_N/((Sm_N + Gd_N)/2)$] which likely reflects an accumulation of plagioclase in the unit after the crystallisation and removal of olivine and clinopyroxene to form the underlying peridotite and olivine melagabbronorite units. The quartz gabbronorite unit is the only unit in the BDM with a sizeable negative Eu anomaly (Eu/Eu* = 0.7) and this is most likely due to plagioclase fractionation. Primitive Mantle normalised multi-element profiles **(Fig. 4.40)** also reveal that all the BDM rocks have pronounced negative anomalies in Nb, Ta and Ti.

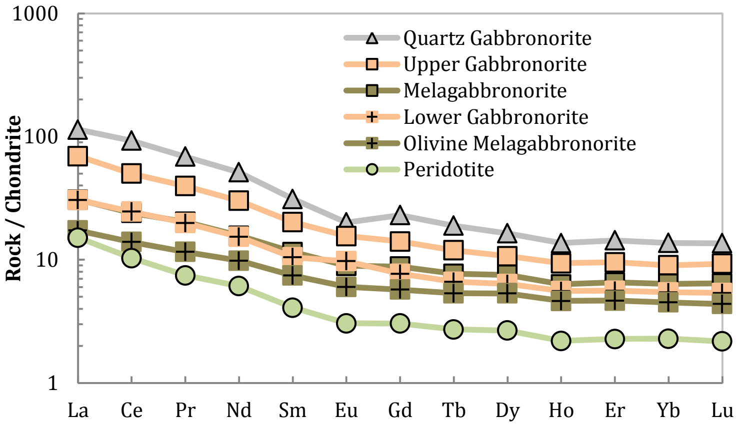

Fig. 4.39. Chondrite-normalised REE diagram for average values for each stratigraphic unit of the Blue Draw Metagabbro. Normalising values from McDonough and Sun (1995).

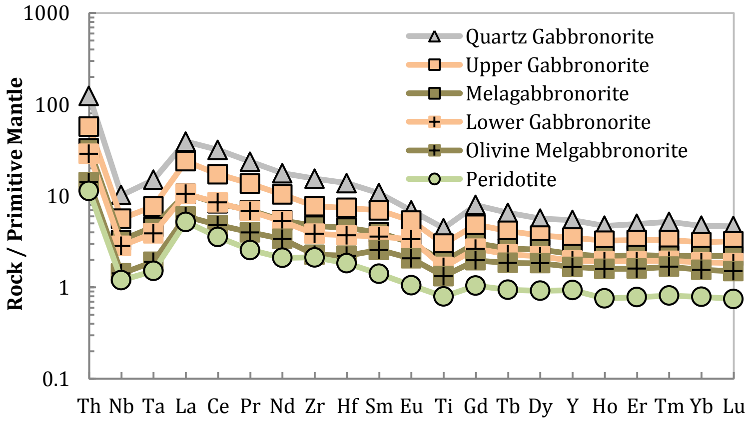

Fig. 4.40. Primitive Mantle-normalised multi-element diagram for average values for each stratigraphic unit of the Blue Draw Metagabbro. Normalising values from McDonough and Sun (1995).

On a Zr/Nb vs. Nb/Th diagram **(Fig. 4.41)**, the majority of the Blue Draw Metagabbro samples all plot along the far left boundary of the volcanic arc basalt field of Condie (2005). On a Zr/Nb vs. Zr/Y diagram **(Fig. 4.42)**, the majority of the Blue Draw Metagabbro samples plot on an array of increasing Nb/Y with increasing Zr/Y just inside the non-plume source field of the graph and within the NMORB and volcanic arc basalt fields. Four samples plot just within the plume source area of the graph, within the oceanic plateau basalt field.

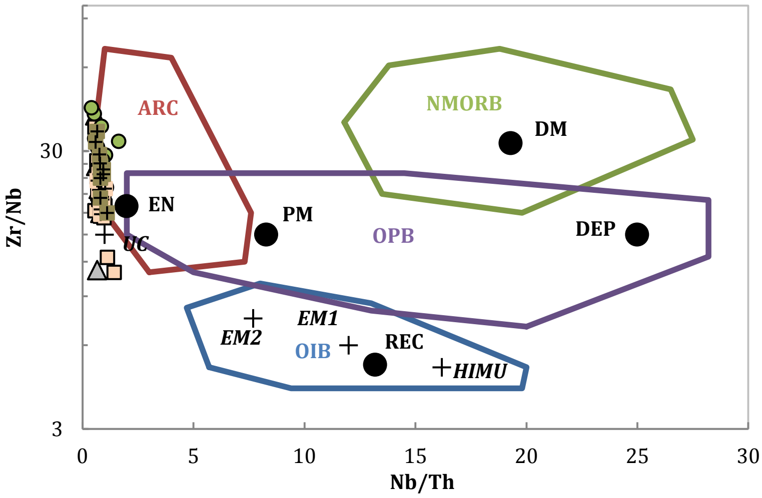

Fig. 4.41. Zr/Nb vs. Nb/Th diagram for the Blue Draw Metagabbro. Field boundaries and end-member compositions from Condie (2005). Abbreviations as in **Fig. 4.8**. Lithological symbols as in **Fig. 4.34**.

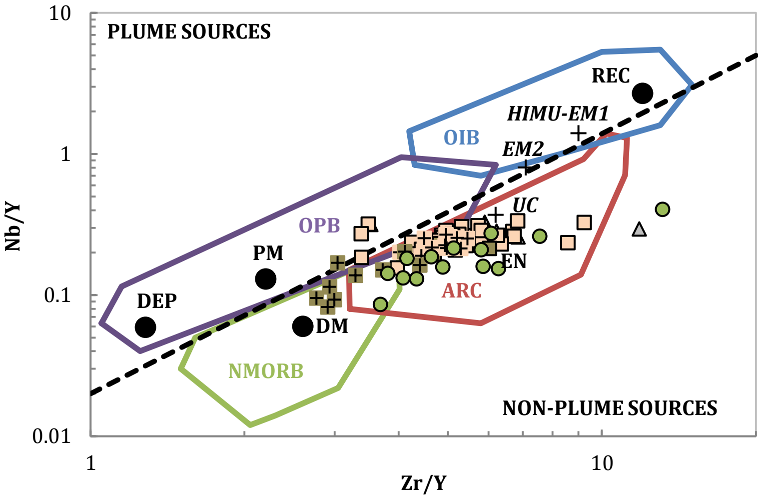

Fig. 4.42. Nb/Y vs. Zr/Y diagram for the Blue Draw Metagabbro. Field boundaries and end-member compositions from Condie (2005). Abbreviations as in **Fig. 4.8**. Lithological symbols as in **Fig. 4.34**.

4.6.5. Geochemical Trends with Stratigraphic Height

Representative major and trace elements are plotted against stratigraphic height in **Fig. 4.43**. This approach is made possible by the sampling strategy shown in **Fig. 3.10**. A series of strike-normal traverses permitted collection of samples from throughout the stratigraphy of the intrusion. By projecting the sample locations along strike to the cross section line, chemostratigraphic profiles for the Blue Draw intrusion can be constructed. These chemostratigraphic profiles demonstrate geochemical trends through the intrusion and help define the mineralisation potential of the intrusion.

4.6.5.1. Major Element Oxides

SiO_2

In the peridotite unit at the base of the intrusion, SiO_2 concentration is constant at ~37 wt.%. SiO_2 concentration jumps to ~50 wt.% at the base of the olivine melagabbronorite unit (125m) where it remains fairly constantly throughout the olivine melagabbronorite and lower gabbronorite units. Above the lower gabbronorite unit, SiO_2 begins to increase in concentration with increasing stratigraphic height, trending from ~52 wt.% at the base of the melagabbronorite unit to ~55 wt.% at the top of the upper gabbronorite unit (~700m). Between 700m and the top of the quartz gabbronorite unit at ~770m, SiO_2 concentration increases with stratigraphic height at a rate far higher than observed lower in the intrusion to reach ~70 wt.% at the top of the intrusion.

TiO_2

Just above the footwall contact of the intrusion, the peridotite unit contains ~0.1 wt.% TiO_2 which remains constant throughout the unit. At the base of the olivine melagabbronorite unit, TiO_2 concentration jumps to ~0.3 wt.% and begins to increase linearly with increasing stratigraphic height throughout the stratigraphy to reach ~0.7 wt.% at ~700m. Above this height, TiO_2 increases in concentration dramatically to reach ~1.5 wt.% at the top of the Upper Gabbronorite unit (~715m). The Quartz Gabbronorite unit rocks do not record a systematic change in TiO_2 concentration with stratigraphic height and averages at ~1 wt.% for the whole zone.

Al_2O_3

At the base of the intrusion, the peridotite unit contains ~6 wt.% Al_2O_3 which decreases with stratigraphic height to reach ~1.9 wt.% at 75m where it remains constant for the rest of the Peridotite unit. At the base of the Olivine Melagabbronorite unit, Al_2O_3 concentration jumps to ~3.5 wt.% and increases rapidly to reach ~14 wt.% at the top of the Olivine Melagabbronorite unit. This increase continues through the Lower Gabbronorite unit to reach ~14.5 wt.% at the top of the unit. At the base of the Melagabbronorite unit, two trends in Al_2O_3 concentration can be seen: The first trend shows a sharp decrease in Al_2O_3 concentration to ~6 wt.% at the base of the Melagabbronorite unit before concentration increases again with stratigraphic height to reach ~14 wt.% at ~600m. The second trend shows that Al_2O_3 concentration remains largely constant throughout the Melagabbronorite unit and lower half of the Upper Gabbronorite unit at ~13.5 wt.%. At ~600m, Al_2O_3 concentration increases to ~17 wt.% before decreasing with stratigraphic height to reach ~11 wt.% at the top of the intrusion.

Fe_2O_3

At the base of the intrusion, the Peridotite unit contains, on average, ~11 wt.% Fe_2O_3. At the base of the Olivine Melagabbronorite unit, Fe_2O_3 concentration drops fairly sharply to ~8 wt.% where it remains throughout the Olivine Melagabbronorite and Lower Gabbronorite units. At the base of the Melagabbronorite unit, Fe_2O_3 concentration increases to ~11 wt.% and remains constant, without showing any discernable relationship with stratigraphic height until ~600m, at which point, the Upper Gabbronorite unit records a wide range in Fe_2O_3 concentration of between ~10-14 wt.%.

MnO

MnO concentration remains largely constant throughout the intrusion at ~0.16 wt.% and does not show systematic changes with stratigraphic height. However, the highest MnO concentrations in the intrusion are associated with the lowermost parts of the Upper and Olivine Melagabbronorite units.

MgO

At the base of the Peridotite unit, MgO concentration is ~30 wt.% which increases to ~38 wt.% half way up the unit and remains constant throughout the rest of the unit. At the base of the Olivine Melagabbronorite unit, MgO concentration drops dramatically to ~20 wt.% where it continues to fall with increasing stratigraphic height to reach ~9 wt.% at the base of the Lower Gabbronorite unit, throughout which MgO concentration remains largely constant between ~8-9 wt.%. At the base of the Olivine Melagabbronorite unit, MgO concentration increases sharply to ~17 wt.% before decreasing steadily with stratigraphic height to reach ~1.4 wt.% at the top of the intrusion.

CaO

In the Peridotite unit, CaO concentrations are scattered around ~1 wt.%. At the base of the Olivine Melagabbronorite unit, CaO concentration sharply increases to ~13 wt.% before falling rapidly again to reach ~8 wt.% at the top of the unit. CaO concentration jumps to ~1 wt.% at the base of the Lower Gabbronorite unit before decreasing with stratigraphic height to reach ~8 wt.% at the base of the Upper Gabbronorite unit. At ~500m, CaO begins to decrease from ~11 wt.% to reach ~1.3 wt.% at the top of the intrusion.

K_2O

Throughout the Peridotite unit, K_2O concentration remains largely close to detection limit. At the base of the Olivine Melagabbronorite unit, K_2O concentration begins to increase with stratigraphic height to reach ~0.7 wt.% at the top of the Lower Gabbronorite unit. At the base of the Melagabbronorite unit, K_2O concentration drops sharply to close to detection limit before increasing again with stratigraphic height to reach ~3.4 wt.% at the top of the intrusion.

P_2O_5

The Peridotite unit contains ~0.02 wt.% P_2O_5 which increases with stratigraphic height to ~0.08 wt.% at ~700m. Above ~700m, P_2O_5 increases with stratigraphic height at a much greater rate than that observed lower in the intrusion to reach ~0.2 wt.% at the top of the Quartz Gabbronorite unit at ~770m.

Major element oxide summary

Stratigraphic geochemical profiles for the major elements show that generally the BDM trends from Mg- and Fe-rich rocks at the base of the intrusion to more Si- and Al-rich rocks at the top. Throughout the Peridotite unit, SiO_2, MgO and Fe_2O_3 concentrations remain largely constant at ~37 wt.%, 38 wt.% and 11 wt.% respectively. At the base of the Olivine Melagabbronorite unit (~125 m), the SiO_2 concentration increases to ~52 wt.% and remains constant until ~700 m, at which point SiO_2 increases with stratigraphic height to ~70 wt.% at the top of the intrusion. Conversely to SiO_2, MgO begins to decrease in concentration above the Peridotite unit to reach ~1 wt.% at the top of the intrusion. This decrease in MgO is mirrored by CaO and a concomitant increase in Al_2O_3.

These general trends described above are interrupted by a partial resetting of compositions at the base of the Melagabbronorite unit (~370 m) where whole-rock composition become more basic before evolving to more acidic compositions with increasing stratigraphic height.

4.6.5.2. REE and HFSE

Stratigraphic geochemical profiles for the REE and HFSE show similar trends through the BDM. REE and HFSE concentrations are lowest in the peridotite unit at the base of the intrusion and remain constantly low throughout the unit. At the base of the olivine melagabbronorite unit (~125 m), REE and HFSE concentrations begin to increase with stratigraphic height. This increase is perturbed at ~300 m by a sharp fall in REE and HFSE concentrations after which, concentrations begin to increase again at a similar rate to that observed between 125-300 m. This increase in REE and HFSE concentration with stratigraphic height continues uniformly until ~700 m, at which point, the rate of REE and HFSE concentration increase becomes an order of magnitude higher than that observed lower in the intrusion.

4.6.5.3. Compatible Trace Elements

Compatible trace element (Ni, Co, Cr, Sc and V) concentrations in the BDM appear linked to modal mineral proportions in the rock. Stratigraphic geochemical profiles for these elements define two often complimentary trends in the BDM. The first trend is defined by Ni, Co and Cr, the highest concentrations of which are recorded in the peridotite unit at the base of the intrusion. At the base of the olivine melagabbronorite unit (~125 m), concentrations of Ni, Co and Cr decrease exponentially with stratigraphic height before stabilising at low levels which remain low through the lower gabbronorite unit until they peak again at the base of the melagabbronorite unit at ~380 m. Following this peak at ~380 m, concentrations of Ni, Co and Cr decrease rapidly in a similar way to that observed in the olivine melagabbronorite and lower gabbronorite units.

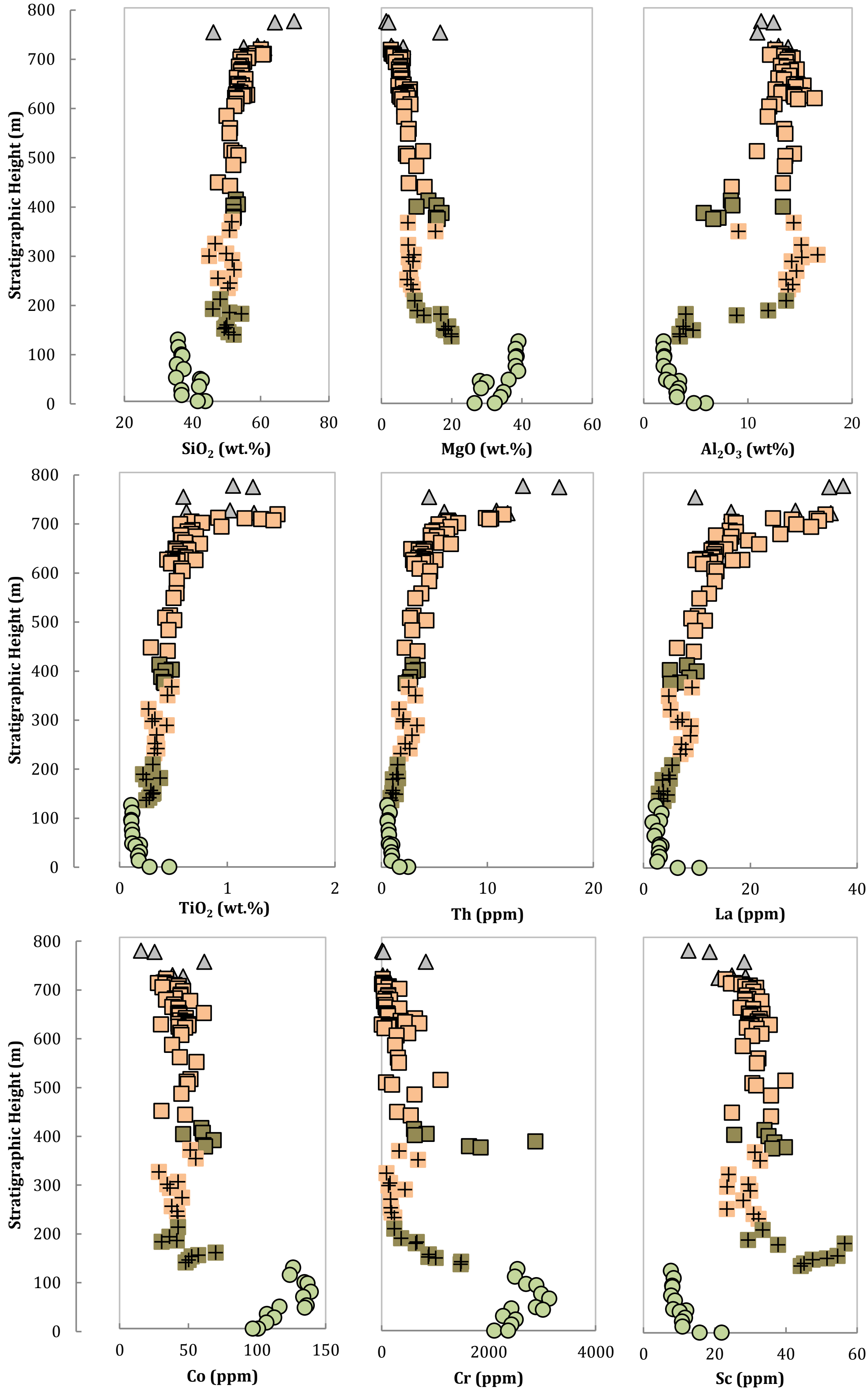

Fig. 4.43. Chemostratigraphic profiles through the Blue Draw Metagabbro for selected major and trace elements. Lithological symbols are the same as in **Fig. 4.34**.

The second trend is defined by Sc and V, the lowest concentrations of which are recorded in the peridotite unit. Concentrations of Sc and V peak at the base of the olivine melagabbronorite unit before decreasing rapidly in a similar manner to Ni, Co and Cr. Concentrations in Sc and V peak again at the base of the melagabbronorite unit before either decreasing with increasing stratigraphic height (Sc) or showing no readily discernable trend with increasing stratigraphic height (V).

4.6.5.4. Platinum-Group Elements

The PGE can be split into two subgroups (IPGE: Ru, Os, Ir; and PPGE: Pd, Pt, Rh, Au) based on their differing behaviour during fractionation (Barnes et al. 1985). These groupings are reflected in the PGE depth profiles for the BDM **(Fig. 4.44)** in that the IPGEs (Ir and Ru) show similar trends to each other and which are different to those of the PPGEs.

The IPGEs record their highest concentrations in the peridotite unit (up to ~6 ppb Ru and ~1.5 ppb Ir) and decrease rapidly above the peridotite unit, levelling off at ~0.3 ppb Ru and ~0.1 ppb Ir between 200-400 m. A second Ir-Ru peak is observed in two samples between ~400-500 m, above which IPGE concentrations in the BDM decrease towards detection limit with increasing stratigraphic height. In contrast, the PPGEs (Pt, Pd and Au) from the peridotite unit record some of the lowest concentrations in the intrusion (~2.5 ppb Pt, 2.7 ppb Pd and 0.5 ppb Au). Above the peridotite, PPGE concentrations remain scattered, but low, throughout the intrusion until ~650-700 m where the Pt, Pd and Au concentrations spike up to ~14 ppb, ~60 ppb and ~3 ppb respectively. Above this zone, PPGE concentrations decrease towards detection limit with increased stratigraphic height. Rhodium shows intermediate behaviour between the IPGE and other PPGE in the BDM in that it is relatively abundant in the peridotite unit (similar to the IPGE) but also has a spike in concentration at ~650-700 m (similar to the PPGE).

The shape of chondrite-normalised PGE patterns in BDM rocks changes with stratigraphic height **(Fig. 4.45)**. The peridotite unit has relatively flat PGE patterns [$(Ir/Pt)_N = 1$] while the upper gabbronorite unit and quartz gabbronorite unit rocks show more fractionated patterns [$(Ir/Pt)_N = 0.1$]. All BDM samples show a marked depletion in Ni and Cu relative to Ir and Pt respectively.

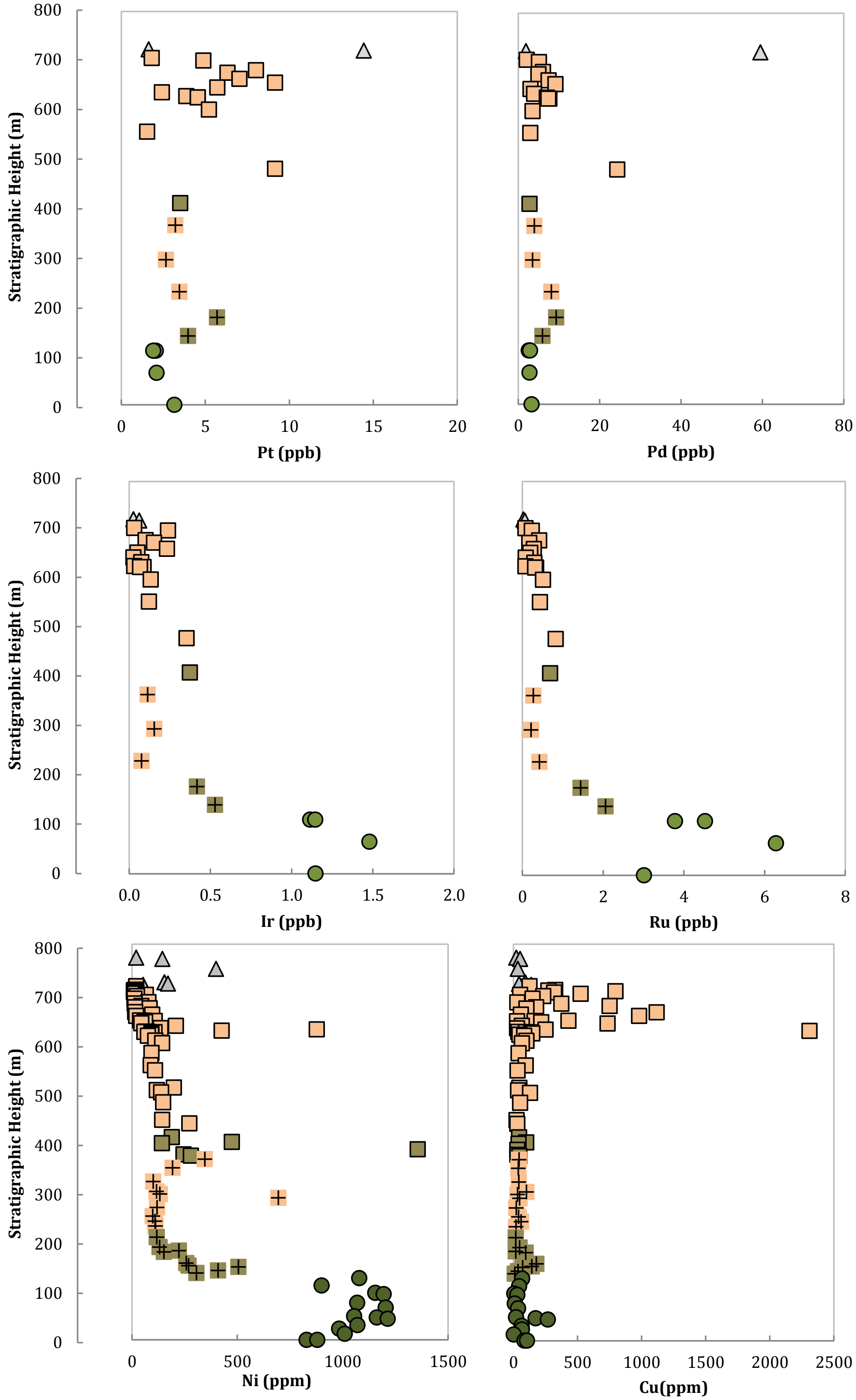

Fig. 4.44. Chalcophile element chemostratigraphic profiles through the Blue Draw Metagabbro. Lithological symbols are the same as in **Fig. 4.34**.

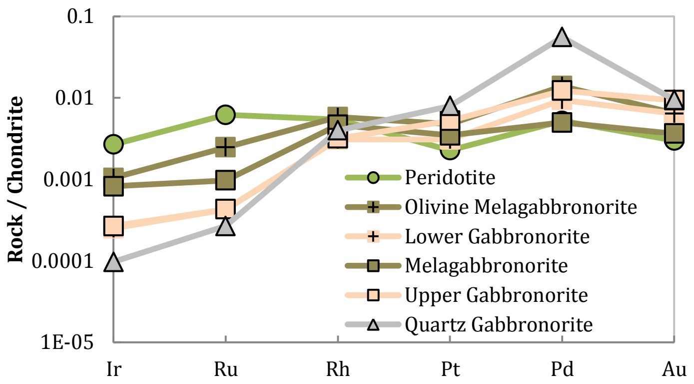

Fig. 4.45. Chondrite-normalised PGE diagrams for average values for each of the stratigraphic units of the Blue Draw Metagabbro. Normalising values from Naldrett and Duke (1980)

4.7. Leopard Dyke Swarm

4.7.1. Alteration and Element Mobility

The LOI values of the studied Kaminak samples range from 0.03-3.10 wt.%. These values are quite low, which may suggest that little alteration of the dykes has occurred. However, petrographic study of the Leopard dykes (see Chapter 3) has shown that the primary mineralogy of plagioclase, clinopyroxene and olivine has been variably altered to sericite, quartz, amphibole, chlorite and iron oxides. To assess if this alteration caused secondary element remobilisation, each element has been plotted against Zr. Representative graphs are shown in **(Fig. 4.46)**. Examination of these graphs shows that the Leopard dykes can be sub-divided into two groups based on differences in major and trace element geochemistry with the Group 2 dykes being far more evolved (higher SiO_2, lower MgO and higher incompatible element concentrations) than the more numerous Group 1 dykes.

For Group 1 dykes, the elements which show good correlations with Zr ($R^2 > 0.75$) include the REE, TiO_2, MgO, P_2O_5, Al_2O_3, Fe_2O_3, MnO, V, Sc, Co, Cu, and the HFSE; Ta, Hf, Nb, Y and U. The elements which show a moderate correlation with Zr ($0.75 > R^2 > 0.5$) include SiO_2, CaO, Zn and Sr. Elements which show a poor correlation with Zr include the LILE, Pb, Ni, Ga and Th. The poor correlation of Th is interesting given the good correlations with Zr displayed by the other HFSE, especially given the findings from other studies which have shown Th to be immobile under greenschist facies metamorphism [e.g., Pearce 1996). The correlations described above indicate that significant secondary elemental remobilis-

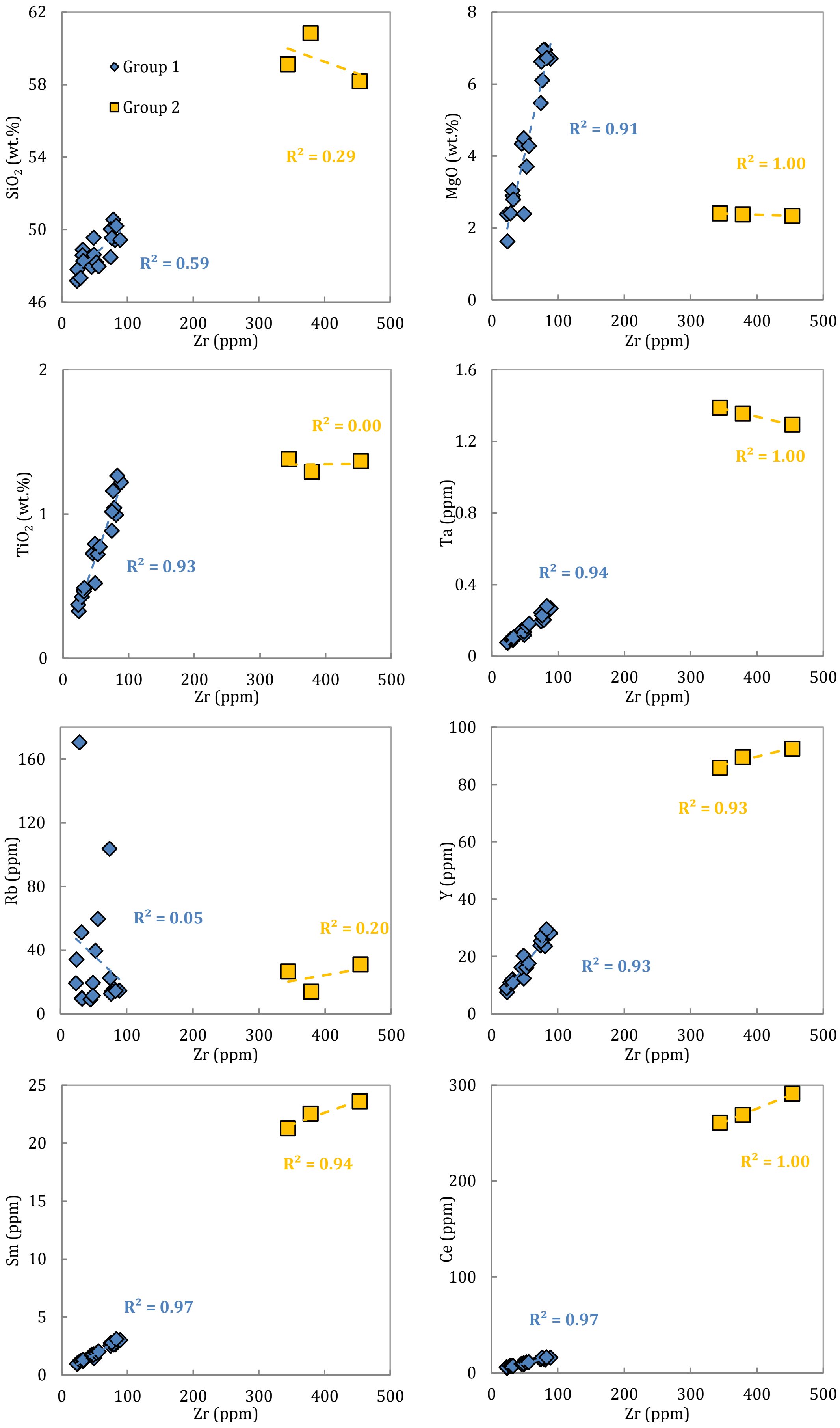

Fig. 4.46. Bivariate diagrams of selected trace elements vs. MgO for the Leopard Dyke Swarm.

ation of the Group 1 Leopard dykes is largely limited to the LILE, Ni, Ga, Pb and Th. The remaining major and trace element (including the REE and HFSE) concentrations of the Group 1 Leopard dykes are likely to closely represent primary compositions.

For Group 2 Leopard dykes, the elements which show good correlations with Zr ($R^2 > 0.75$) include the REE (except La and Eu), Al_2O_3, P_2O_5, Cr, Tm, Th and Pb. The elements which show a moderate correlation with Zr ($0.75 > R^2 > 0.5$) include CaO, MnO, Nb, Eu and U. Elements which show poor correlation with Zr include SiO_2, TiO_2, MgO, Fe_2O_3, the LILE, Sc, V, Co, Ni, Zn and Cu. The poor correlation of TiO_2 is interesting given the strong correlations with Zr displayed by the other HFSE and findings from other studies which have shown Ti to be immobile under greenschist facies metamorphism (Pearce 1996). The correlations described above indicate that significant secondary elemental remobilisation of Group 2 Leopard dykes is largely limited to the LILE, compatible trace elements and some of the major elements (SiO_2, TiO_2, MgO, Fe_2O_3). The remaining major and trace element concentrations recorded by Group 2 Leopard dykes may potentially represent primary compositions. However, as only three Group 2 Leopard dykes were analysed by this study, the R^2 values recorded above cannot be used with total confidence as, with such a small population size, the product moment correlation coefficient is liable to being affected by anomalous samples. That said, the R^2 values for Group 2 dykes fit the general trends expected for greenschist metamorphism, i.e., good correlations for the more immobile REE and HFSE and poor correlations for the more mobile, LIL, major and compatible trace elements.

4.7.2. Classification

On the TAS diagram, all but two Group 1 Leopard dyke swarm samples plot as a tight cluster in the tholeiitic basalt field. The remaining two samples plot as an alkaline basalt and an alkaline trachybasalt **(Fig. 4.47)**. The Group 2 Leopard dykes all plot in the tholeiitic andesite field.

As Na and K have been shown to have been remobilised in the Leopard dyke swarm, the applicability of the TAS diagram is questionable. Instead, the Zr/Ti vs. Nb/Yb diagram **(Fig. 4.48)** is more useful. On this diagram, the Group 1 Leopard dyke swarm plots as a tight cluster of sub-alkaline basalts near to the basalt-andesite transition while the Group 2 Leopard dykes plot just below the andesite-dacite transition, within the subalkaline andesite field.

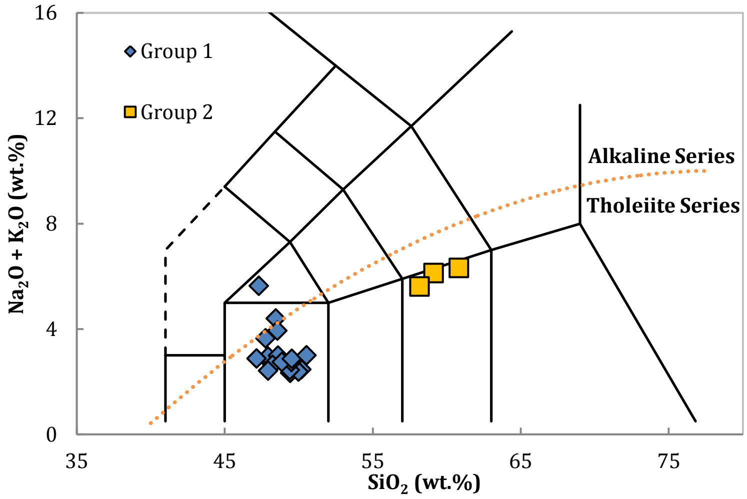

Fig. 4.47. Total alkali vs. SiO_2 (TAS) diagram for the Leopard dyke swarm samples. Field boundaries defined by Le Maitre et al. (1989). Field names are shown in **Fig. 4.2**.

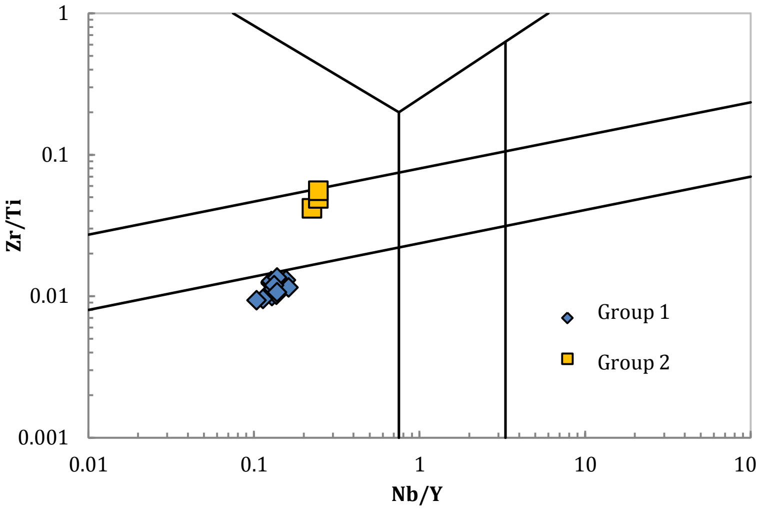

Fig. 4.48. Total alkali vs. SiO_2 (TAS) diagram for the Leopard dyke swarm samples. Field boundaries defined by Le Maitre et al. (1989). Field names are shown in **Fig. 4.2**. Symbols as in **Fig. 4.47**.

4.7.3. Major Element Variation

Group 1 Leopard dykes range in MgO, Fe_2O_3 and TiO_2 from 1.6-7.0 wt.%, 3.6-13.1 wt.% and 0.3-1.3 wt.% respectively. These ranges correspond to a range in Mg# of 31-39. SiO_2 in the Leopard dykes ranges from 47.2-50.5 wt.% while total alkalis range from 2.3-5.6 wt.%. SiO_2, TiO_2, Fe_2O_3, P_2O_5 and MnO show good ($R^2 > 0.75$) positive correlations with MgO while Al_2O_3 records a strong negative linear correlation with MgO. The Leopard dykes exhibit moderate-poor correlations between CaO, Na_2O, and K_2O and MgO which confirm the suspicions raised by **(Fig. 4.46)** that these elements have been remobilised since the intrusion of the Leopard dykes. Group 2 Leopard dykes show little variation in MgO, Fe_2O_3 and TiO_2 from 2.3-2.4 wt.%, 8.3-8.9 wt.% and 1.3-1.4 wt.% respectively. These ranges correspond to a range in Mg# of 23-24.. SiO_2 in Group 2 Leopard dykes ranges from 58.2-60.8 wt.% while total alkalis range from 5.6-6.3 wt.%. SiO_2, TiO_2, Fe_2O_3, Na_2O, and K_2O and MnO show poor ($R^2 < 0.5$) correlations with MgO while P_2O_5 and Al_2O_3 record good positive correlations with MgO, while CaO and MnO have moderately strong negative correlations with MgO.

4.7.4. Trace Element Variation

Group 1 Leopard dykes range in Ni and Cr from 26-348 and 48-327 ppm respectively. Group 1 Leopard dykes exhibit good ($R^2 > 0.75$) positive correlations between MgO and Cr, Sc, V and Co **(Fig. 4.50)**. Ni has a poor correlation with MgO in the Group 1 Leopard dykes, the coefficient of which is affected by three samples which have significantly higher Ni concentrations than the range displayed by the majority of the dykes. Incompatible trace elements including La, Sm, Yb and Nb all have good ($R^2 > 0.84$) negative correlations with MgO. Group 2 Leopard dykes range in Ni and Cr from 25-60 and 52-199 ppm respectively. Group 2 Leopard dykes exhibit a good ($R^2 > 0.75$) negative correlation between MgO and Cr but poor correlations ($R^2 < 0.37$) for Ni, Sc, V and Co **(Fig. 4.50)**. Incompatible trace elements including La, Sm, Yb and Nb all have good ($R^2 > 0.76$) negative correlations with MgO in Group 2 Leopard dykes.

Chondrite-normalised REE diagrams **(Fig. 4.51)** for Group 1 Leopard dykes show sub-parallel trends with elemental concentrations ~4-25× that of chondrite. Group 1 Leopard dykes are very slightly enriched in LREE relative to HREE [$(La/Yb)_N = 1.7$] which in turn, show flat patterns [$(Gd/Yb)_N = 1.0$]. The Leopard dykes have variable Eu/Eu* anomalies which range from 0.9-1.6. The chondrite-normalised REE patterns displayed by the Group 1 Leopard dykes are most similar to that of E-MORB.

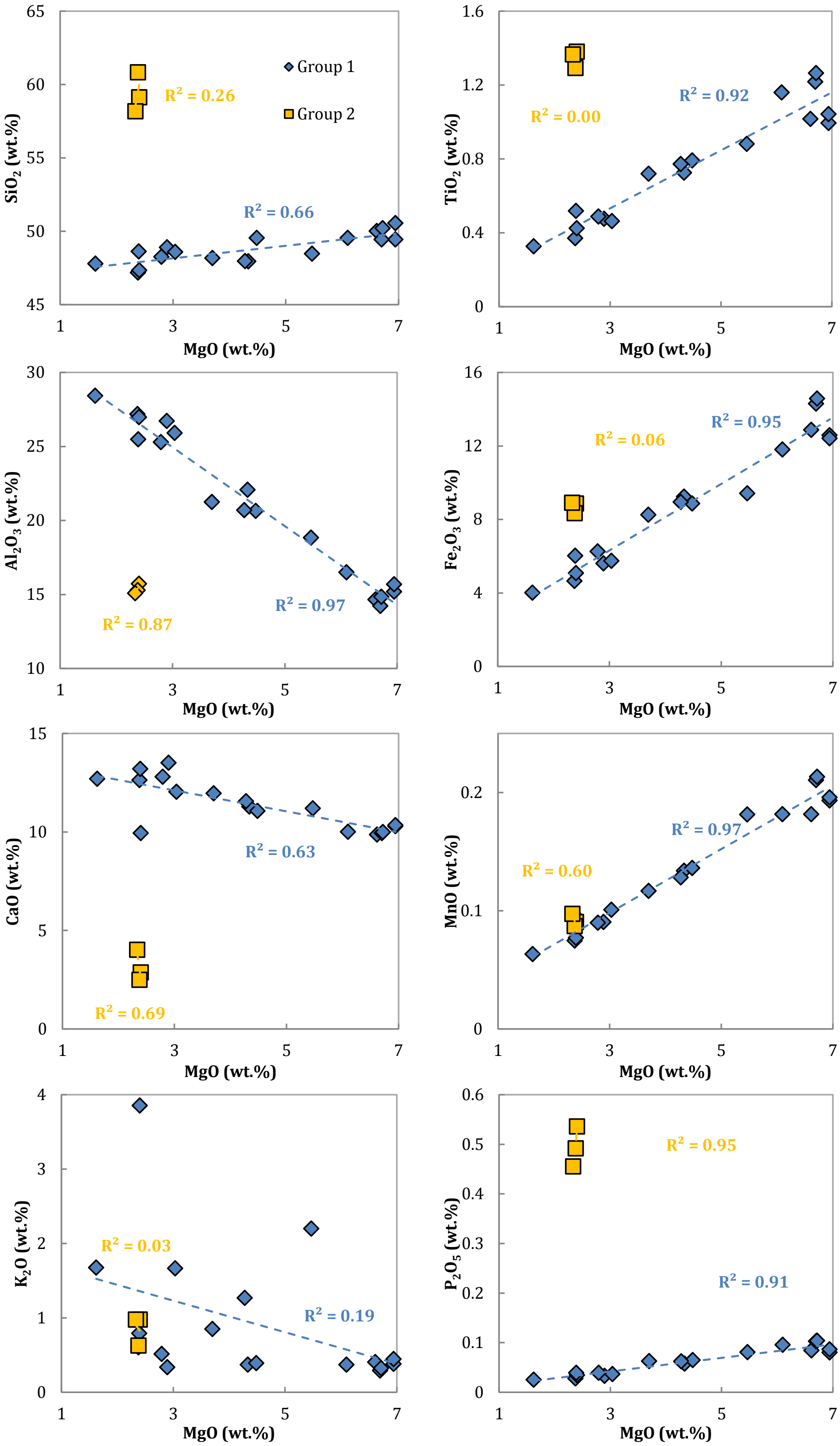

Fig. 4.49. Bivariate diagrams of selected major elements vs. MgO for the Leopard dyke swarm.

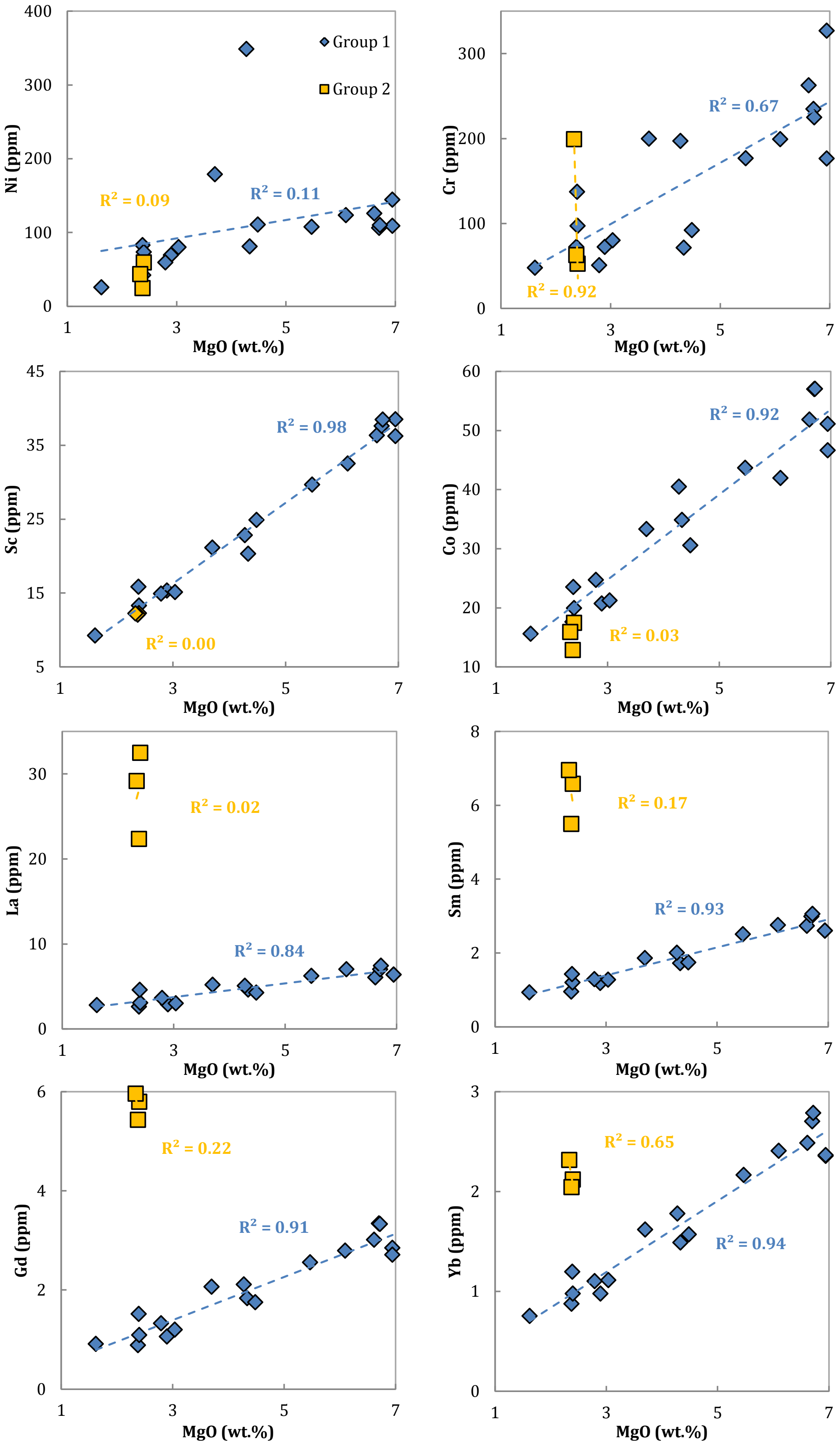

Fig. 4.50. Bivariate diagrams of selected trace elements vs. MgO for the Leopard dyke swarm

Chondrite-normalised REE diagrams for Group 2 Leopard dykes show sub-parallel trends with ΣREE concentrations 237-265 × chondritic values. Group 2 Leopard dykes are enriched in the LREE relative to the HREE (such that the average $(La/Yb)_N$ value of the dykes is 14.1), while the HREE themselves are slightly depleted having $(Gd/Yb)_N$ = 2.4. Group 2 Leopard dykes have sizeable negative Eu anomalies (Eu/Eu* = 0.5). The chondrite-normalised REE patterns displayed by the Group 2 Leopard dykes are similar to that of OIB.

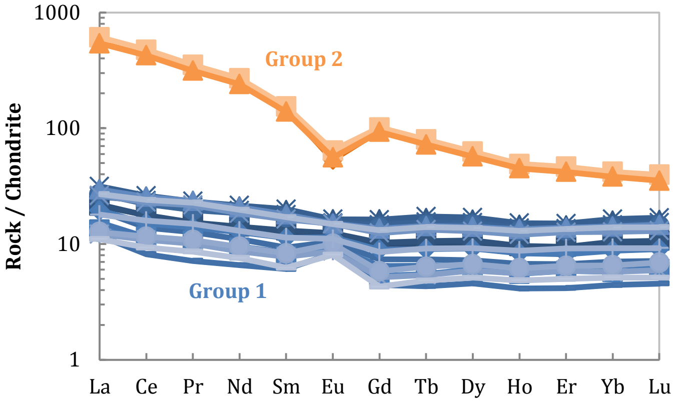

Fig. 4.51. Chondrite-normalised REE diagrams for Leopard dykes. Normalising values from McDonough and Sun (1995).

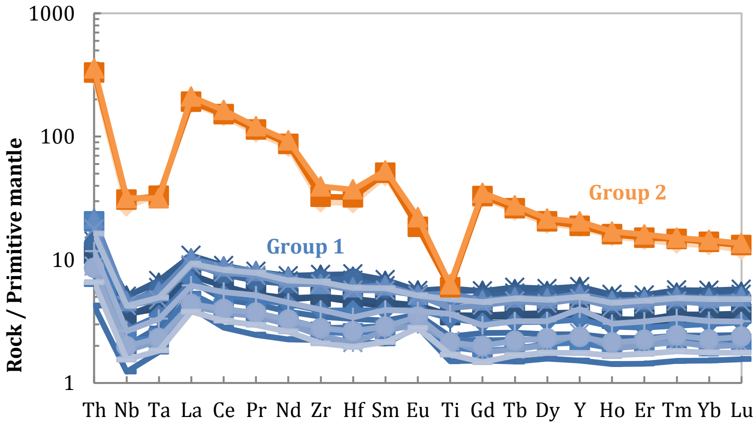

Fig. 4.52. Primitive Mantle-normalised multi-element diagrams for Leopard dykes. Normalising values from McDonough and Sun (1995).

On Primitive Mantle-normalised multi-element plots **(Fig. 4.52)**, Group 1 Leopard dykes show sub-parallel trends with trace element concentrations ~2-21× that of Primitive Mantle. The samples show similar patterns to those observed in **Fig. 4.51**, in being convex upwards with enrichment in the most incompatible elements relative to the less incompatible elements. All samples show distinctive Nb/Nb* anomalies

(0.2-0.4). On the same diagrams, Group 2 Leopard dykes **(Fig. 4.52)** show similar patterns to those observed in **Fig. 4.51** in that they are convex-up with enrichment in the most incompatible elements relative to the least incompatible ones. Group 2 Leopard dykes contain trace element concentrations 35-540 × that of Primitive Mantle. All of the Group 2 Leopard dykes have negative Nb-Ta (Nb/Nb* = 0.1) Zr-Hf (Zr/Zr* = 0.5) and Ti (Ti/Ti* = 0.2) anomalies; all of which are greater in magnitude than those observed in Group 1 Leopard dykes.

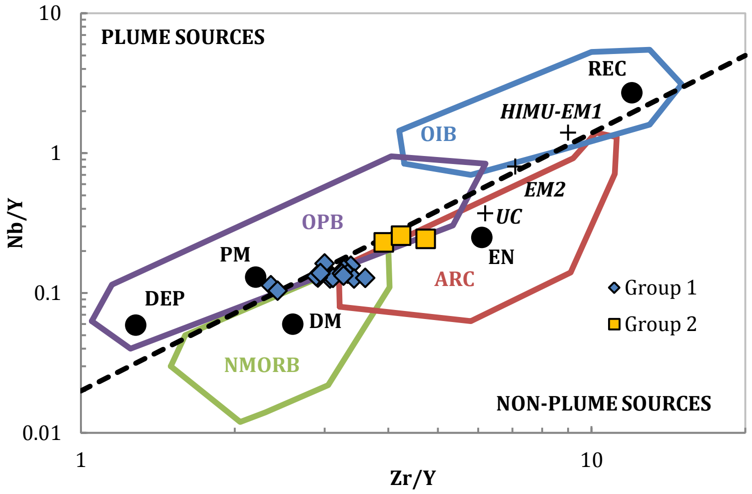

Fig. 4.53. Nb/Y vs. Zr/Y diagram for the Leopard dyke swarm samples. Field boundaries and end-member compositions from Condie (2005).

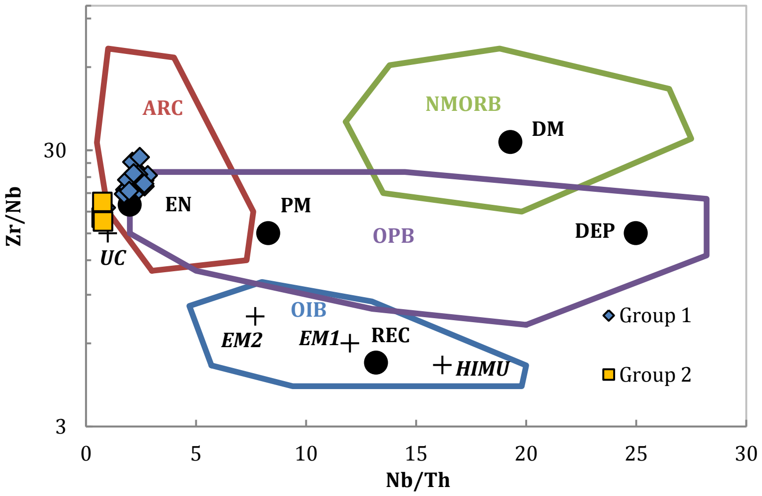

Fig. 4.54. Zr/Nb vs. Nb/Th diagram for the Leopard dyke swarm samples. Field boundaries and end-member compositions from Condie (2005). Abbreviations as in **Fig. 4.8**.

On a Nb/Y vs. Zr/Y diagram **(Fig. 4.53)**, Group 1 Leopard dykes straddle the boundary between plume and non-plume sources and plot in overlapping areas of the oceanic plate basalt, volcanic arc and normal mid-ocean ridge basalt fields. On the same diagram, Group 2 Leopard dykes plot in the non-plume sources area in the overlapping portions of the volcanic arc basalt and oceanic plateau basalt fields. On a Zr/Nb vs. Nb/Th diagram **(Fig. 4.54)**, Group 1 Leopard dykes plot within the volcanic arc basalt field, with approximately half in the overlapping portion of the oceanic basalt field. On the same diagram, Group 2 Leopard dykes plot just to the left of the volcanic arc basalt field, very close to the estimated composition of the upper continental crust of Condie (2005).

4.8. Kaminak Dyke Swarm

4.8.1. Alteration and Element Mobility

The LOI values of the studied Kaminak dykes range from 0.16-2.37 wt.%. These values are quite low, which may suggest that little alteration of the dykes has occurred. However, petrographic study of Kaminak dyke samples by this study (see chapter 3) and by Sandeman and Ryan (2008), shows that the Kaminak dykes range from pristine gabbro to being highly altered, with fine grained sericite and quartz replacing plagioclase and fine-grained amphibole replacing primary clinopyroxene. To assess if this alteration has caused element remobilisation, each element has been plotted against Zr **(Fig. 4.55)**, which is generally regarded to be immobile under greenschist-lower amphibolite metamorphism experienced by the Kaminak dykes.

The elements which show a good correlation with Zr ($R^2 > 0.75$), include the REE, SiO_2, TiO_2, MgO, P_2O_5, and the HFSE; Y, Nb, Hf, Ta and Th. Furthermore, these elements show only one trend suggesting that the Kaminak dykes were formed from a single, common parental melt. The elements which show a moderate correlation with Zr ($0.5 < R^2 > 0.75$) include Al_2O_3, Fe_2O_3, K_2O, CaO, Ga, Pb and U. The elements which show a poor correlation with Zr ($R^2 < 0.5$) include MnO, Na_2O, Cr, Ni, Ba, Rb, Cs, Zn, V, Sc, Co, Cu and Sr. These correlations indicate that significant secondary elemental remobilisation of the Kaminak dykes is largely limited to the LILE and transition elements while the concentrations of the HFSE, REE and remaining major elements are likely to closely represent primary compositions.

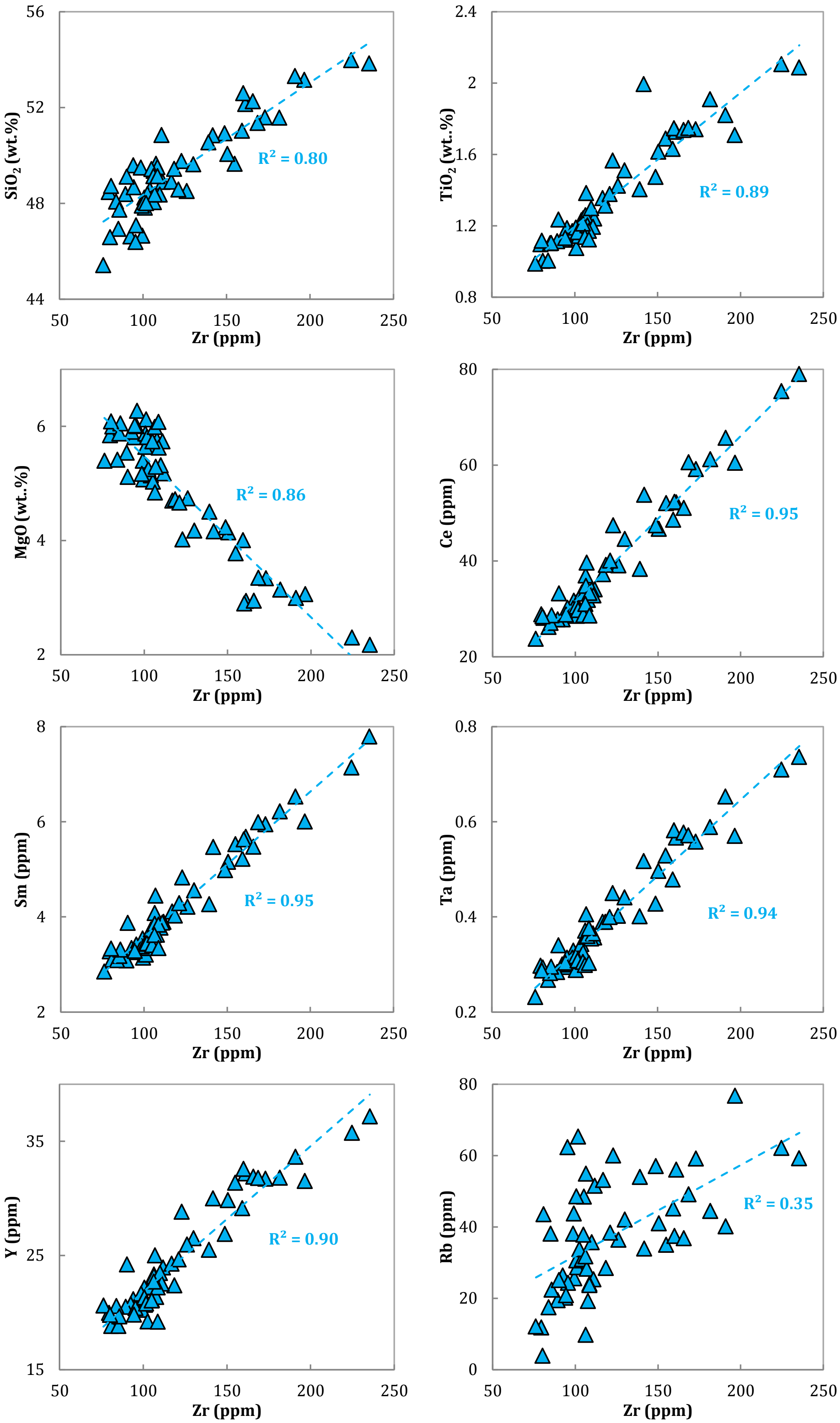

Fig. 4.55. Bivariate diagrams of selected elements vs. Zr for the Kaminak dyke swarm samples.

4.8.2. Classification

On the TAS diagram, the majority of the Kaminak dykes plot as tholeiitic basalts and basaltic andesites. Approximately 30% of the dykes plot as alkaline basalts and three dykes plot in the alkaline trachybasalt field **(Fig 4.56)**.

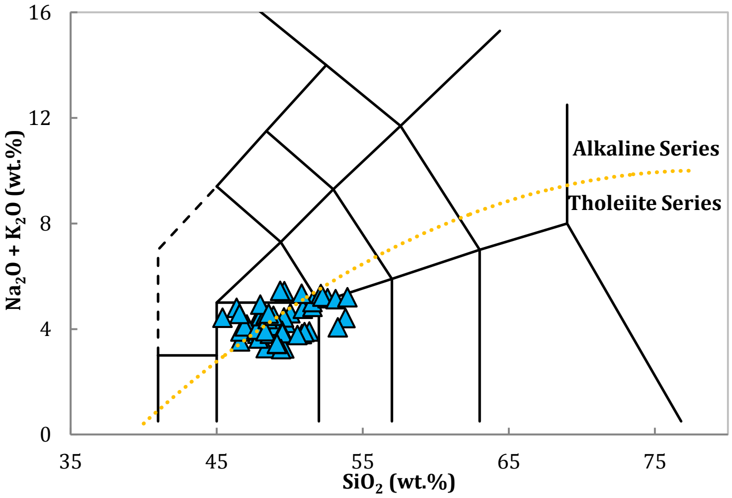

Fig. 4.56. Total alkali vs. SiO_2 (TAS) diagram for the Kaminak dyke swarm samples. Field boundaries defined by Le Maitre et al. (1989). Field names are shown in **Fig. 4.2**.

As the TAS diagram relies on Na and K (two elements which have been shown to have been remobilised in the Kaminak dykes) to classify igneous rocks, its applicability to the Kaminak dykes is questionable. Instead, the Zr/Ti vs. Nb/Yb diagram is more useful as the elements used in the classification have been shown to be immobile during greenschist facies metamorphism. On this diagram, the majority of the Kaminak dykes plot as subalkaline basalts while approximately 30% of the dykes plot as subalkaline basaltic andesites (**Fig. 4.57**).

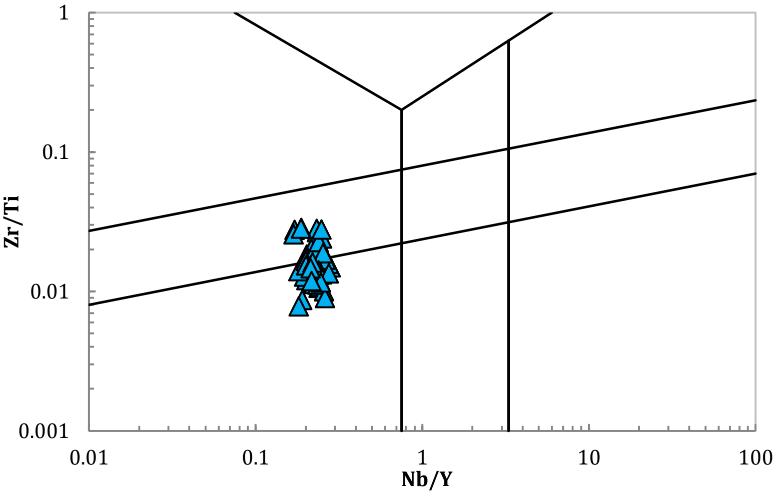

Fig. 4.57. Zr/Ti vs. Nb/Y diagram for the Kaminak dyke swarm samples.

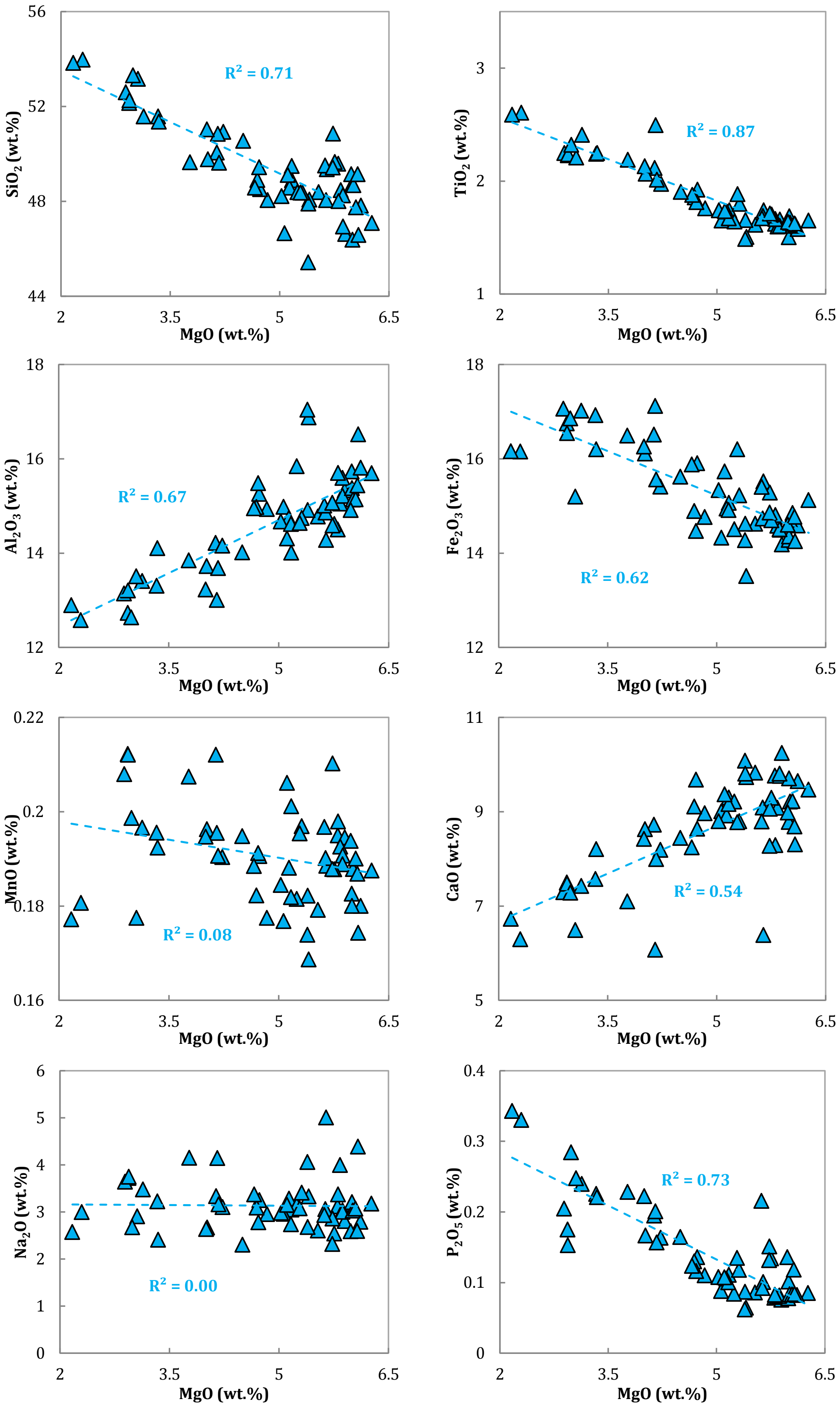

Fig. 4.58. Bivariate diagrams of selected elements vs. MgO for the Kaminak dyke swarm samples.

4.8.3. Major Element Variation

The Kaminak dykes range in MgO, Fe_2O_3 and TiO_2 from 2.1-6.37 wt.%, 13.5-17.1 wt.% and 1.0-2.1 wt.% respectively. These values correspond to a range in Mg# of 13.0-32.2. SiO_2 in the Kaminak dykes ranges from 45.4-54.0 wt.% while total alkalis range from 3.2-5.4 wt.%. SiO_2, P_2O_5 and TiO_2 show good linear negative correlations with MgO (R^2= 0.71, 0.73 and 0.87 respectively) while Fe_2O_3 and K_2O show moderately good linear negative correlations with Mg (R^2 = 0.67 and 0.52 respectively). In contrast, Al_2O_3 and CaO show moderately good linear positive correlations with MgO (R^2 = 0.67 and 0.54 respectively). MnO and Na_2O display no significant correlation with MgO which confirms the suspicions raised by **Fig. 4.55** that these elements have been remobilised since the intrusion of the Kaminak dykes.

4.8.4. Trace Element Variation

Trace elements which are compatible during fractionation of mafic melts either show no correlation with MgO as is the case with Co and Sc, a slightly positive correlation [e.g., V) or a good positive correlation as is the case with Ni and Cr which range in concentration from 11 – 220 ppm and 4 – 89 ppm respectively. For samples with greater than ~5% MgO, Cr appears to form two distinct trends **(Fig. 4.59)**. La, Sm, Yb and Nb all show good negative correlations with MgO (R^2 = 0.88 - 0.85) indicating that they have behaved incompatibly.

Chondrite-normalised REE diagrams for the Kaminak dyke swarm show subparrallel trends with ∑REE concentrations ~26-79 x chondritic values **(Fig. 4.60)**. The Kaminak samples are enriched in LREE, $(La/Sm)_N$ = 2.87 relative to the HREE which have relatively flat patterns; $(Gd/Yb)_N$ = 1.50. The Kaminak dyke swarms have variable Eu anomalies, and range in Eu/Eu* between 0.79-1.10 with an average of 0.97. The chondrite normalised patterns displayed by the Kaminak samples best approximate those shown by estimates of the continental crust and E-MORB (Rudnick and Fountain 1995; Sun and McDonough 1989).

Primitive Mantle-normalised multi-element plots **(Fig. 4.61)** show sub-parallel trends with ∑REE concentrations ~9-27 x that of the Primitive Mantle. The samples in this diagram show a similar shape to the chondrite normalised REE diagrams in that the patterns are convex upwards with the most incompatible elements enriched relative

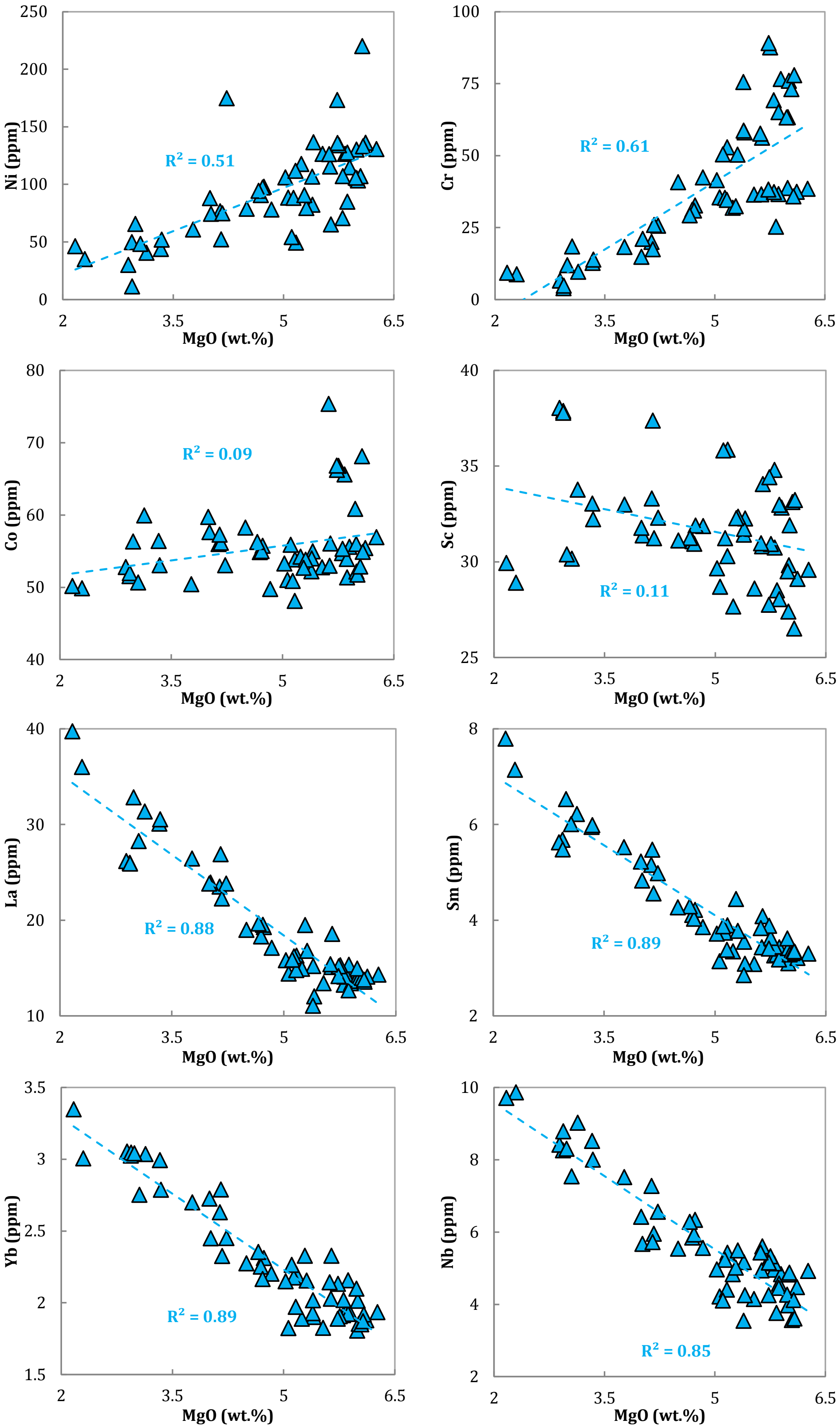

Fig. 4.59. Bivariate diagrams of selected trace elements vs. MgO for the Kaminak dyke swarm.

to the less incompatible elements. The patterns also show distinct negative Nb-Ta (0.65-0.86 range, 0.77 mean) and Ti (0.15-0.28 range, 0.22 mean) anomalies.

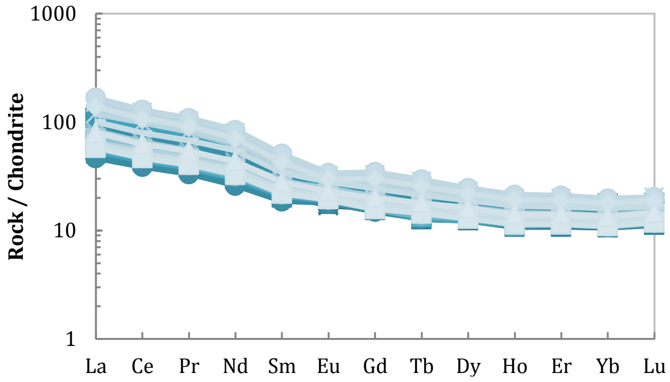

Fig. 4.60. Chondrite-normalised REE diagram for the Kaminak dyke swarm samples. Normalising values from McDonough and Sun (1995).

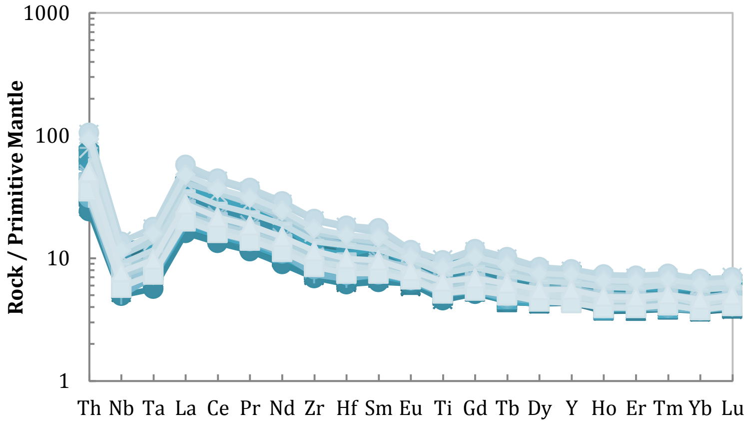

Fig. 4.61. Primitive Mantle-normalised multi-element diagram for the Kaminak dyke swarm samples. Normalising values from McDonough and Sun (1995).

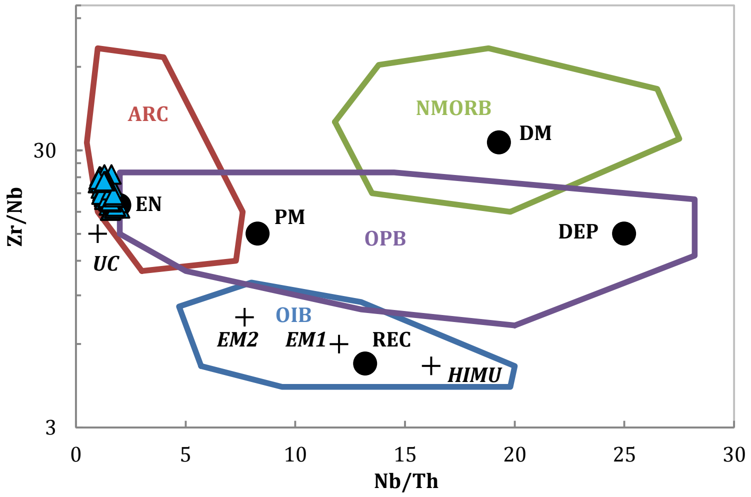

Fig. 4.62. Zr/Nb vs. Nb/Th diagram for the Kaminak dyke swarm samples. Field boundaries and end-member compositions from Condie (2005). Abbreviations as in **Fig. 4.8**.

The anomalies described above have a bearing on the tectonic environment to which rocks are assigned on the Nb/Y vs. Zr/Y and Zr/Nb vs. Nb/Th diagrams. On the Zr/Nb vs. Nb/Th diagram **(Fig. 4.62)**, the Kaminak dykes plot in a tight cluster within the volcanic arc field very close to the enriched end-member of Condie (2005). On the Nb/Y vs. Zr/Y diagram **(Fig. 4.63)**, the Kaminak samples plot on an array of increasing Nb/Y with increasing Zr/Y in the non-plume sources area of the diagram and within the volcanic arc basalt field.

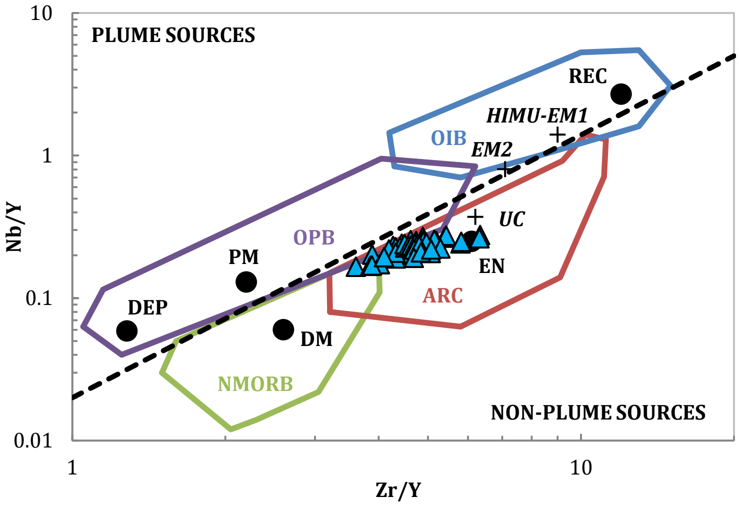

Fig. 4.63. Nb/Y vs. Zr/Y diagram for the Kaminak dyke swarm samples. Field boundaries and end-member compositions from Condie (2005). Abbreviations as in **Fig. 4.8**.

4.9. Viianki Dyke Swarm

4.9.1. Alteration and Element Mobility

Vogel et al. (1998b) do not report the LOI values of the studied Viianki dykes. However, Vuollo and Huhma (2005) suggest that alteration of the dykes has been mild to non-existent. Where observed, alteration of the dykes is characterised by alteration of primary orthopyroxene and clinopyroxene and olivine to amphibole and serpentine respectively. The observations of Vuollo and Huhma (2005) suggest that the Viianki dykes only experienced lower greenschist facies which has affected the Finnish Viianki dykes, but not the Russian Viianki dykes which are relatively pristine. To assess if this alteration caused secondary element remobilisation, each element has been plotted against Zr. Representative graphs are shown in **(Fig. 4.64)**.

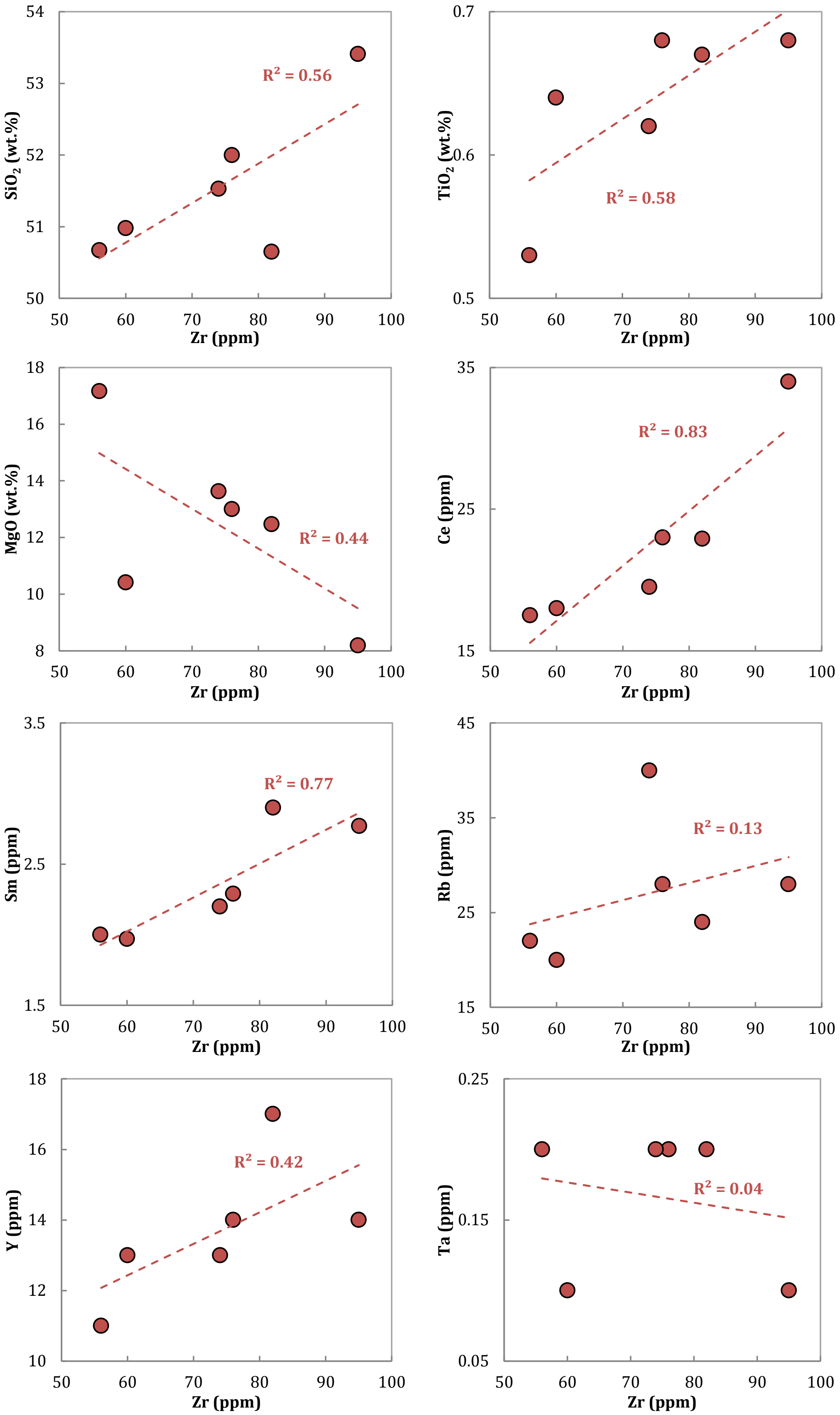

Fig. 4.64. Bivariate diagrams of selected elements vs. Zr for the Viianki dyke swarm samples.

The elements which show good correlations with Zr ($R^2 > 0.75$) in the Viianki dykes include the REE (except Yb) and Ba. The elements which show a moderate correlation with Zr ($0.75 > R^2 > 0.5$) include SiO_2, TiO_2, P_2O_5, Na_2O, K_2O, Sr and Tm. Elements which show poor correlation with Zr include Al_2O_3, MgO Fe_2O_3, MnO, CaO, Cr, V, Sc, Co, Cu, Zn, Y, Ga, Rb, Nb, Yb, Ta, Pb, Th and U. These correlations indicate that significant secondary elemental remobilisation of the Leopard dykes has occurred, affecting the major element, LILE and compatible trace element chemistry. The REE element chemistry of the Viianki dykes appears to be largely unaffected and can be treated as being close to primary. The poor correlation of the HFSE elements (Th, Ta, Nb and Y) is interesting as such elements are thought to be immobile under greenschist facies metamorphism (Pearce 1996). Instead, the poor correlation of these elements with Zr may be a product of contamination of heterogeneous crust with varying Th/Nb ratios.

4.9.2. Classification

On the TAS diagram, the majority of the Viianki dykes plot as tholeiitic basalts while one sample is a tholeiitic basaltic andesite **(Fig. 4.65)**. As Na and K have been shown to have been remobilised in the Viianki dyke swarm, the applicability of the TAS diagram is questionable. Instead, the Zr/Ti vs. Nb/Yb diagram **(Fig. 4.66)** is used. On this diagram, the Viianki dyke swarm plots as a diffuse grouping of sub-alkaline basaltic andesites.

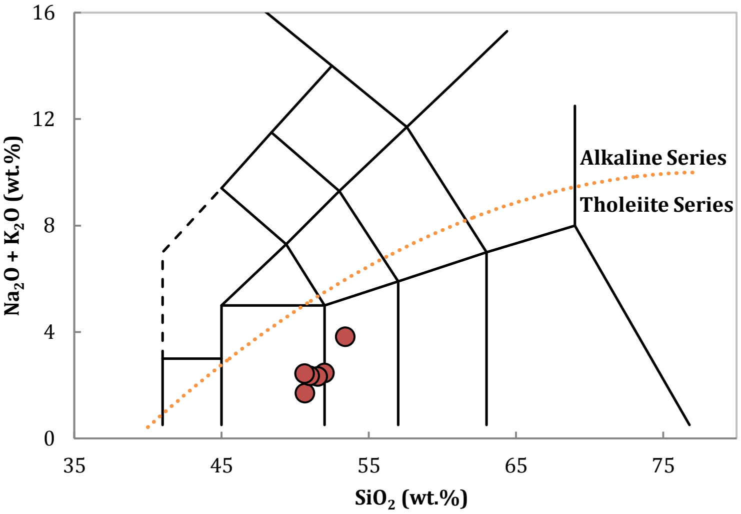

Fig. 4.65. Total alkali vs. SiO_2 (TAS) diagram for the Viianki dyke swarm samples. Field boundaries defined by Le Maitre et al. (1989). Field names are shown in **Fig. 4.2**.

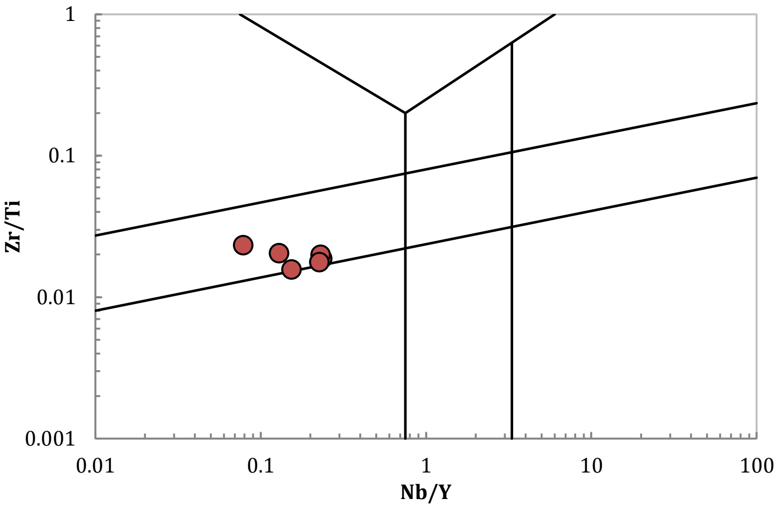

Fig. 4.66. Zr/Ti vs. Nb/Y diagram for the Viianki dyke swarm samples.

4.9.3. Major Element Variation

The Viianki dykes range in MgO, Fe_2O_3 and TiO_2 from 8.2-17.2 wt.%, 9.9-11.5 wt.% and 0.5-0.78 wt.% respectively **(Fig. 4.67)**. These ranges correspond to a range in Mg# of 48-63. SiO_2 in the Viianki dykes ranges from 50.7-53.4 wt.% while total alkalis range from 1.7-3.8 wt.%. SiO_2, CaO and K_2O show poor negative correlations with MgO (R^2 = 0.44, 0.36 and 0.21 respectively). Moderate negative correlations are observed between TiO_2, and P_2O_5 while Al_2O_3 and Na_2O have good negative correlations (R^2 = 0.92 and 0.90 respectively). Fe_2O_3 and MnO show moderate-weak linear positive correlations with MgO (R^2 = 0.54 and 0.45 respectively).

4.9.4. Trace Element Variation

Trace elements which are compatible during fractionation of mafic melts either show no correlation with MgO as is the case with V and Sc, or a good positive linear correlation as is the case with Ni, Co and Cr which range in concentration from 209-510 ppm, 53-68 ppm and 520-1708 ppm respectively **(Fig. 4.68)**.

La, Sm and Yb show poor negative linear correlations with MgO ($R^2 < 0.36$) while Nb shows a poor positive correlation (R^2 = 0.46). The positive correlation of Nb with MgO is surprising as Nb is considered incompatible during normal fractionation of basaltic magma. Instead, it is likely that Nb contents of the Viianki dykes have been affected either by post-emplacement alteration or through contamination of individual dykes by heterogeneous crustal material as is suggested by **Fig. 4.64**.

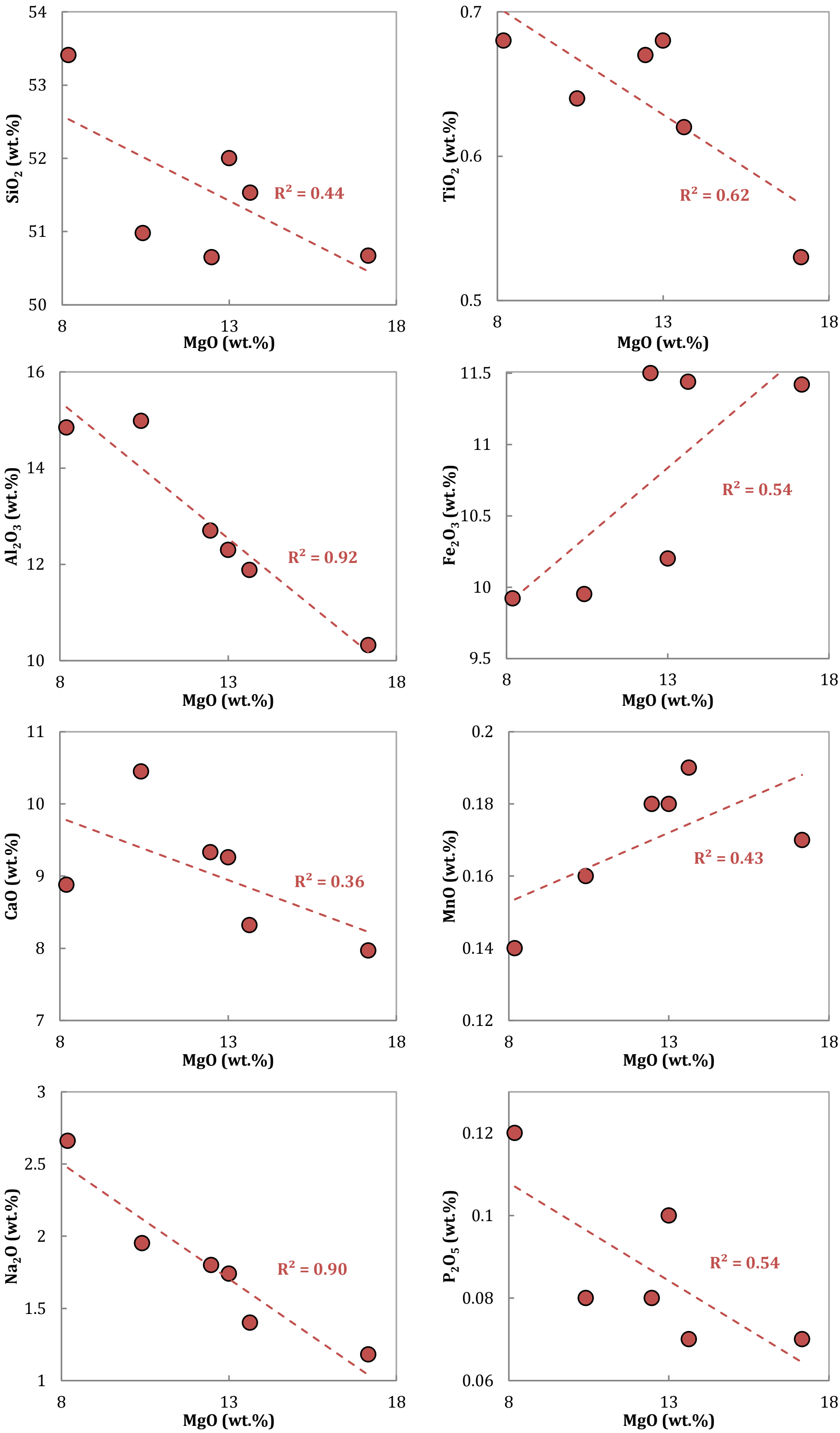

Fig. 4.67. Bivariate diagrams of selected elements vs. MgO for the Viianki dyke swarm samples.

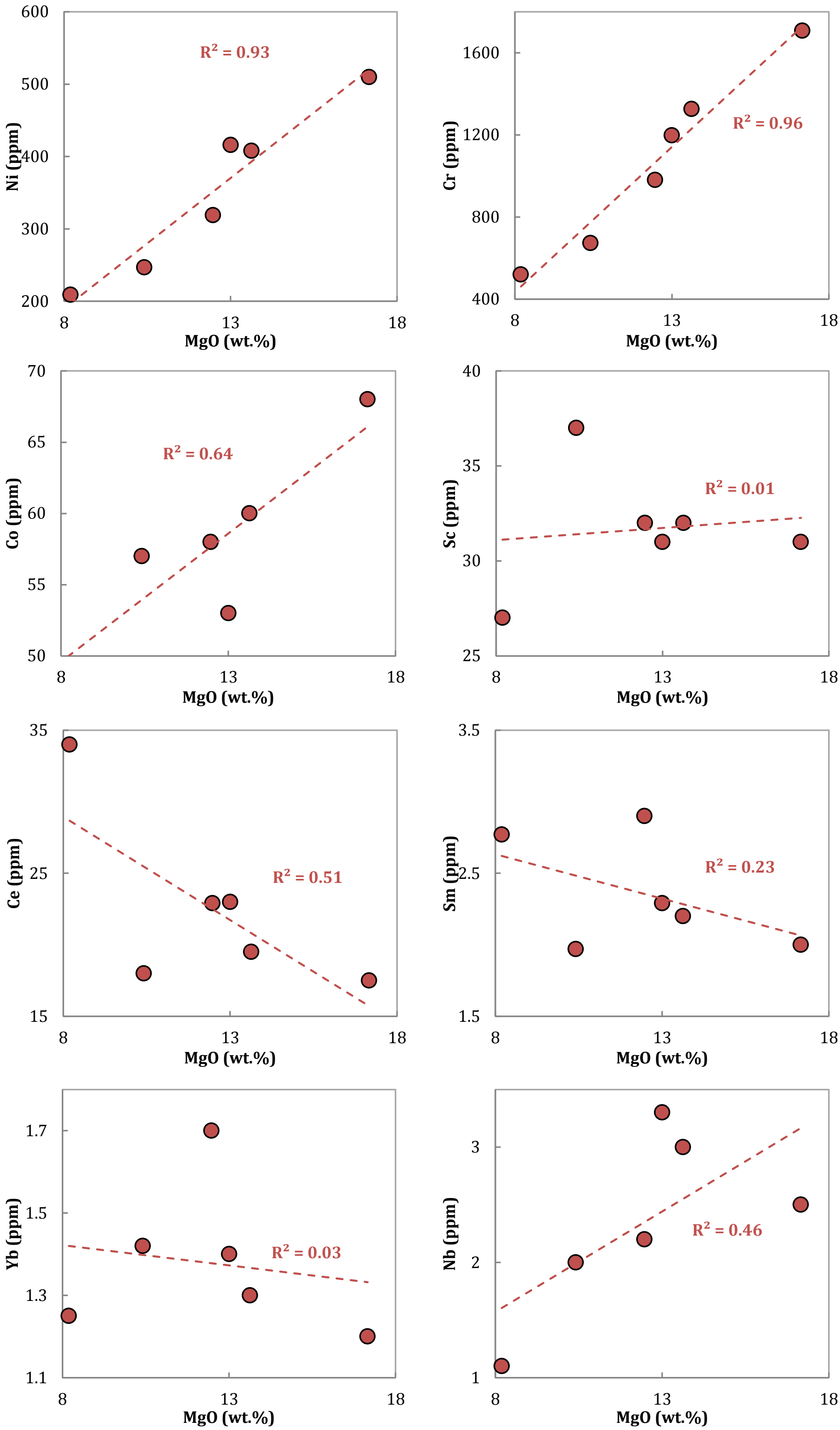

Fig. 4.68. Bivariate diagrams of selected trace elements vs. MgO for the Viianki dyke swarm.

Chondrite-normalised REE diagrams for the Viianki dykes show sub-parallel trends with ∑REE concentrations ~19-42 × chondritic values **(Fig. 4.69)**. The Viianki samples are enriched in LREE, $(La/Sm)_N$ = 3.0 relative to the HREE which have relatively flat patterns; $(Gd/Yb)_N$ = 1.7, with no appreciable Eu anomaly. The chondrite normalised patterns displayed by the Viianki samples are most similar to those of E-MORB.

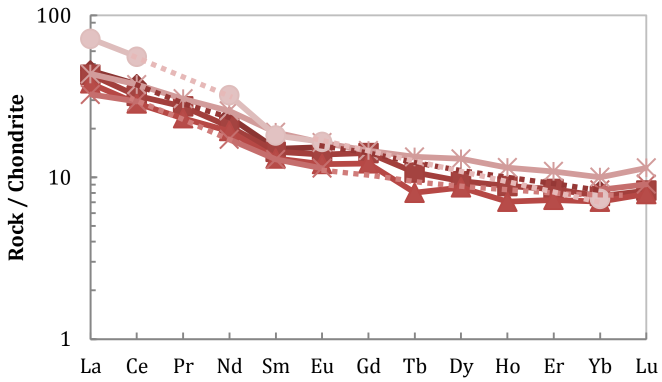

Fig. 4.69. Chondrite-normalised REE diagram for the Viianki dyke swarm samples. Normalising values from McDonough and Sun (1995). Dotted lines are estimations of unanalysed elements.

Primitive Mantle-normalised multi-element plots of the Viianki dyke samples **(Fig. 4.70)** show sub-parallel trends, similar in shape to the chondrite normalised REE diagrams **(Fig. 4.69)** in that the patterns are concave upwards with the most incompatible elements enriched relative to the less incompatible elements. The patterns also show very large, negative Nb-Ta (Nb/Nb* = 0.1-0.2) and Ti (Ti/Ti* = 0.5-0.6) anomalies.

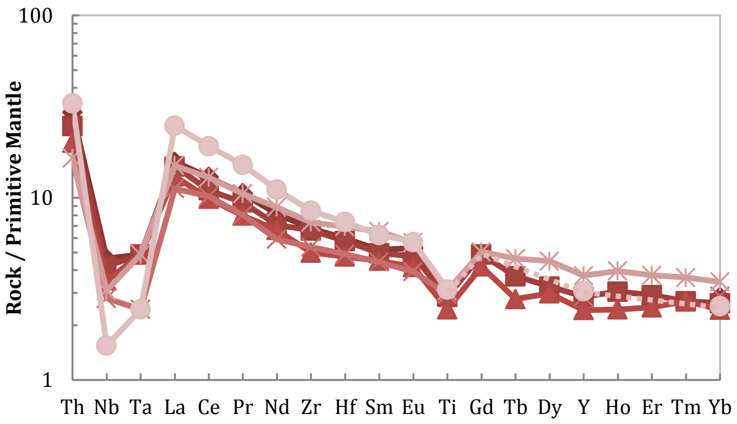

Fig. 4.70. Primitive Mantle-normalised multi-element diagram for the Viianki dyke swarm samples. Normalising values from McDonough and Sun (1995). Dotted lines are estimations of unanalysed elements.

The anomalies described above have a bearing on the tectonic environment to which rocks are assigned on Nb/Y vs. Zr/Y and Zr/Nb vs. Nb/Th diagrams. On a Zr/Nb vs. Nb/Th diagram **(Fig. 4.71)**, the Viianki dykes plot in the volcanic arc field and define an array of variable Zr/Nb over a relatively constant Nb/Th, while on the Nb/Y vs. Zr/Y diagram **(Fig. 4.72)**, the Viianki samples plot in the non-plume sources area of the diagram within the volcanic arc basalt field.

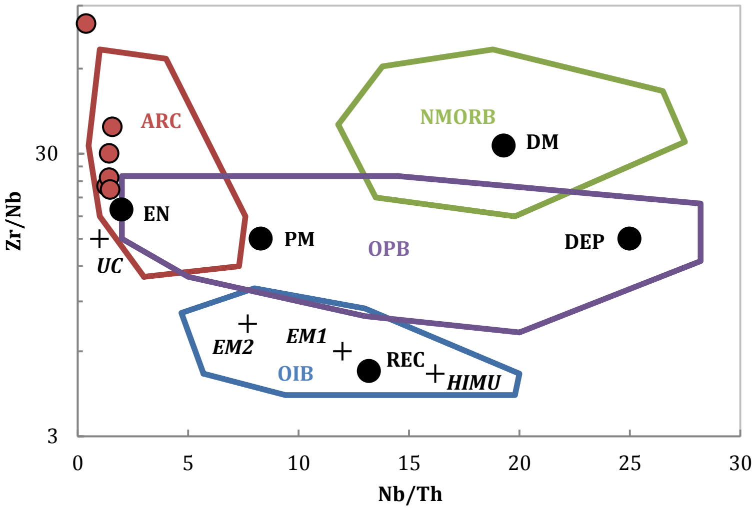

Fig. 4.71. Zr/Nb vs. Nb/Th diagram for the Viianki dyke swarm samples. Field boundaries and end-member compositions from Condie (2005). Abbreviations as in **Fig. 4.8**.

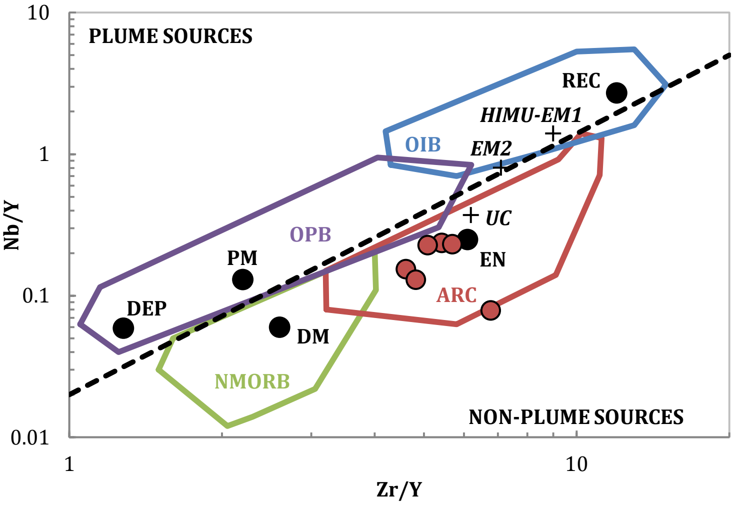

Fig. 4.72. Nb/Y vs. Zr/Y diagram for the Viianki dyke swarm samples. Field boundaries and end-member compositions from Condie (2005). Abbreviations as in **Fig. 4.8**.

4.10. Seidorechka Formation

4.10.1. Alteration and Element Mobility

Due to constraints of time and expense, no material was collected from the Seidorechka Formation by this study. Instead, this study uses the raw data of V.V. Chashchin and M. Mints who respectively collected 41 and 13 samples from the Seidorechka Formation. Some of the data collected by V.V. Chashchin is published (Chashchin et al. 2008) while the rest has not been published, but has been supplied for this study. The data collected by M. Mints is published in Mints et al. (1996).

The LOI values of the Seidorechka Formation samples range from 0.5-3.6 wt.%. These values are quite low, which may suggest that little alteration of the volcanics has occurred. However, Chashchin et al. (2008) note that the Seidorechka Formation rocks have experienced greenschist facies metamorphism, the temperature of which was higher in the south of the Seidorechka basin. To assess if this alteration caused secondary element remobilisation, each element has been plotted against Zr. Representative graphs are shown in **Fig. 4.73**. SiO_2, CaO, P_2O_5 and Nb show good correlations with Zr ($R^2 > 0.75$) while Fe_2O_3, MgO, K_2O, Sc, Co, Cr, Sn and Pb show a moderate correlation with Zr ($0.75 > R^2 > 0.5$). Elements which show a poor correlation with Zr include TiO_2, Al_2O_3, MnO, Na_2O, the REE, Hf, Ta, Rb, Ba, Y, Sr, Zn, Ni, Cu and V. The poor correlation of the REE and other high field strength elements is interesting as such elements are considered to be some of the most immobile under greenschist facies metamorphism (Pearce 1996).

The correlations described above may indicate that significant secondary elemental remobilisation of the Seidorechka Formation has affected abundances of the REE and other elements thought to be immobile under greenschist facies metamorphism. However, examination of the trace element data supplied by Mints et al. (1996) shows that for many of the elements (particularly Zr) the data appears to fit in discrete bins, which in the case of Zr appears to have 20 ppm intervals. This may suggest that the trace element data of Mints et al. (1996) is imprecise and should be treated with caution.

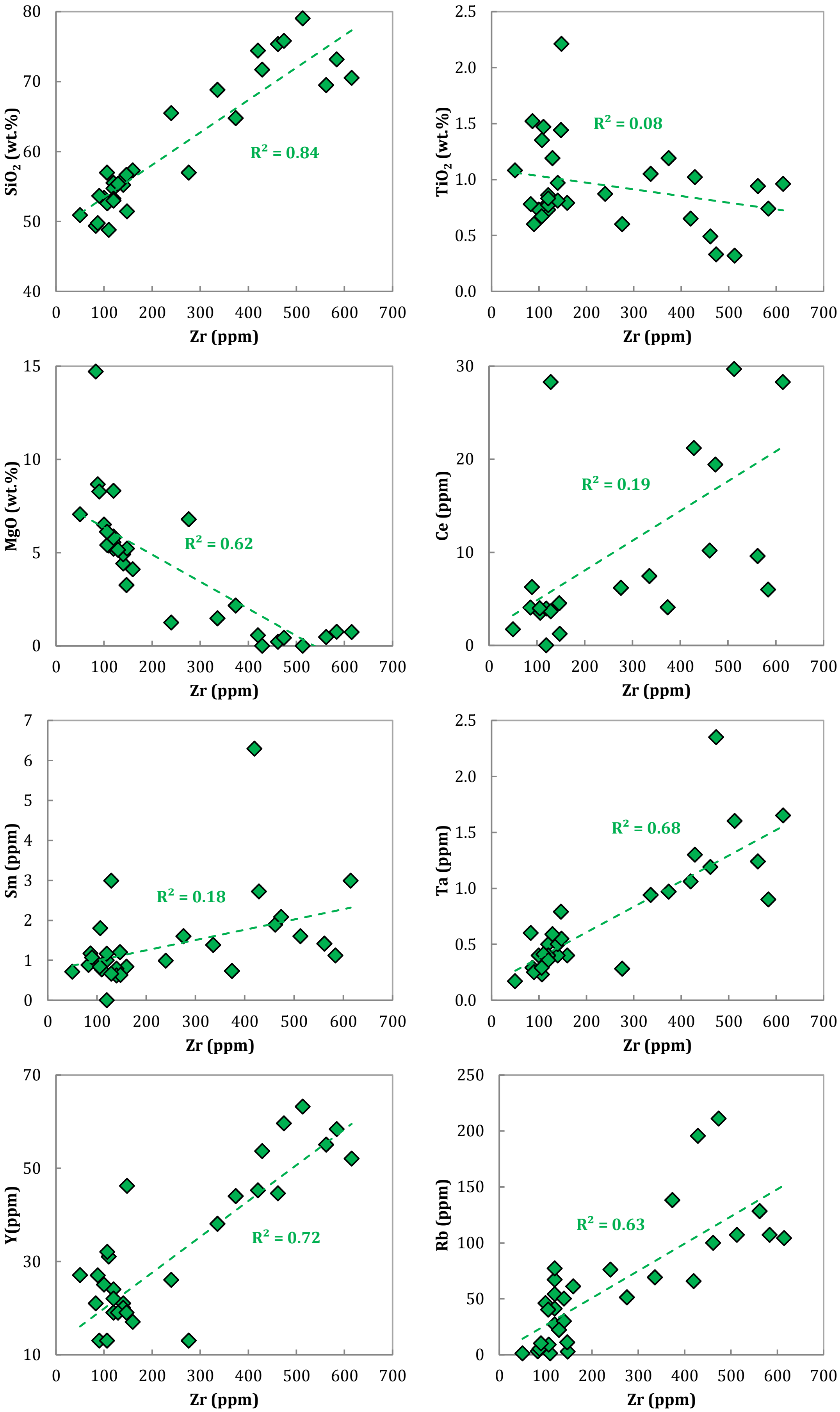

Fig. 4.73. Bivariate diagrams of selected elements vs. Zr for the Seidorechka Formation samples.

4.10.2. Classification

On the TAS diagram, the Seidorechka Formation plot as a continuous array of dominantly tholeiitic basaltic andesites, andesites, dacites and rhyolites, with the majority being basaltic andesites. One sample plots as a tholeiitic trachybasalt and another as an alkaline basaltic trachyandesite **(Fig. 4.74)**.

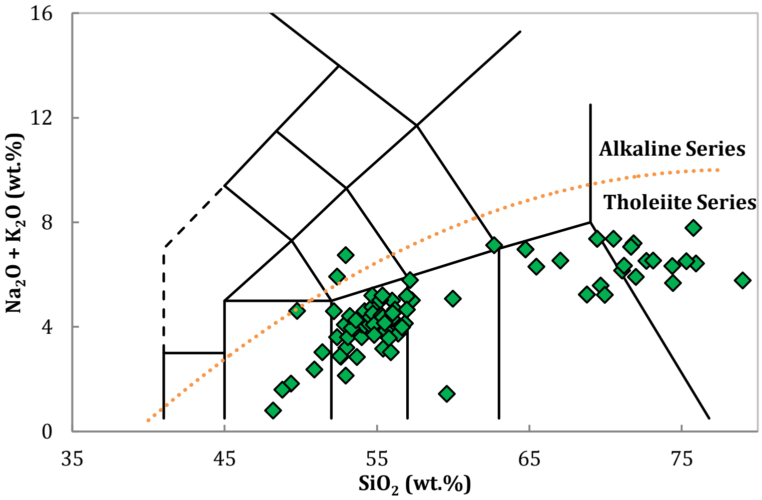

Fig. 4.74. Total alkali vs. SiO_2 (TAS) diagram for the Seidorechka Formation samples. Field boundaries defined by Le Maitre et al. (1989). Field names are shown in **Fig. 4.2**.

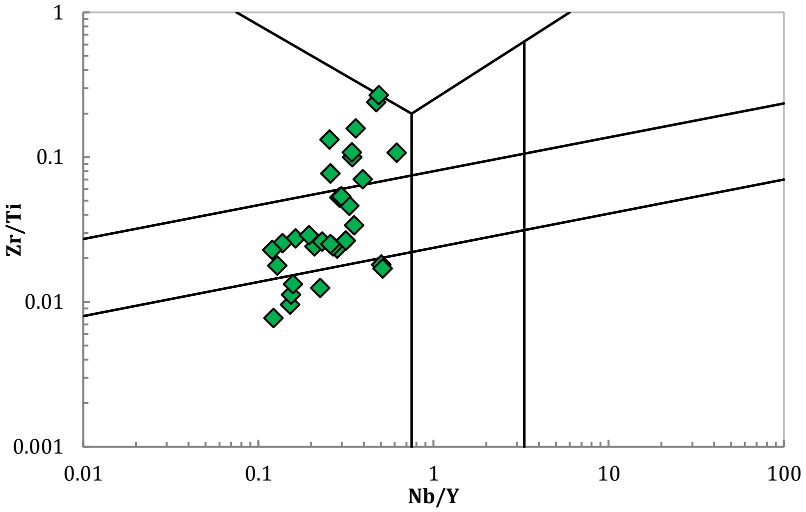

Fig. 4.75. Zr/Ti vs. Nb/Y diagram for the Seidorechka Formation swarm samples.

As Na and K have potentially been remobilised in the Seidorechka rocks, the applicability of the TAS diagram is questionable. On a Zr/Ti vs. Nb/Yb diagram, the Seidorechka Formation rocks plot on a relatively scattered trend of increasing Nb/Y with increasing Zr/Ti which trends from the subalkaline basaltic field to subalkaline rhyolite field.

4.10.3. Major Element Variation

The Seidorechka Formation ranges in MgO, Fe_2O_3 and TiO_2 from 0-20.8 wt.%, 0.3-5.0 wt.% and 0.3-2.2 wt.% respectively. These ranges correspond to a range in Mg# of 8-60. SiO_2 in the Seidorechka Formation varies from 48.2-79.0 wt.% while total alkalis range from 0.8-7.8 wt.%.

Unlike many of the other suites of rocks studied in this project, the Seidorechka Formation does not exhibit obvious, linear trends when major element oxides are plotted against MgO and instead, show more complex curves **(Fig. 4.76)**. SiO_2, in the Seidorechka Formation rocks decreases steadily from ~55 wt.% to ~48 wt.% in samples containing 5-20 wt.% MgO. In samples containing < 5 wt.% MgO, SiO_2 increases sharply to reach ~79 wt.% in the least magnesian Seidorechka Formation rocks (MgO = 0 wt.%). K_2O shows a similar pattern to SiO_2 in that in the most magnesian rocks, K_2O only increases slightly from 0.1-1.2 wt.% but once MgO decreases below ~5 wt.%, K_2O increases sharply to reach ~4.3 wt.% in the least magnesian rocks. Al_2O_3 in the Seidorechka Formation rocks shows a similar trend to K_2O and SiO_2 albeit a different shape in that in the most magnesian Seidorechka rocks, Al_2O_3 increases from 7.7 wt.% in rocks containing 20 wt.% MgO to ~14 wt.% in rocks containing ~5 wt.% MgO. In rocks which contain < 5 wt.% MgO, Al_2O_3 decreases to ~11 wt.% in the least magnesian samples. FeO, CaO and MnO share common trends with MgO in the Seidorechka Formation rocks and plot on positive slopes which concave downwards. The point of inflection for these three oxides seems to occur at ~5 wt.% MgO. Na_2O and P_2O_5 do not show a discernable, systematic variation with MgO.

4.10.4. Trace Element Variation

Trace elements which are compatible during fractionation of mafic melts all show curved positive correlations with MgO. V, Co and Sc show a concave down pattern while Ni, Co and Cr record concave up trends. These latter three elements range in concentration from 0-700 ppm, 0-72 ppm and 0-1400 ppm respectively. The point of inflection of the curves for these elements occurs at approximately 5 wt.% MgO.

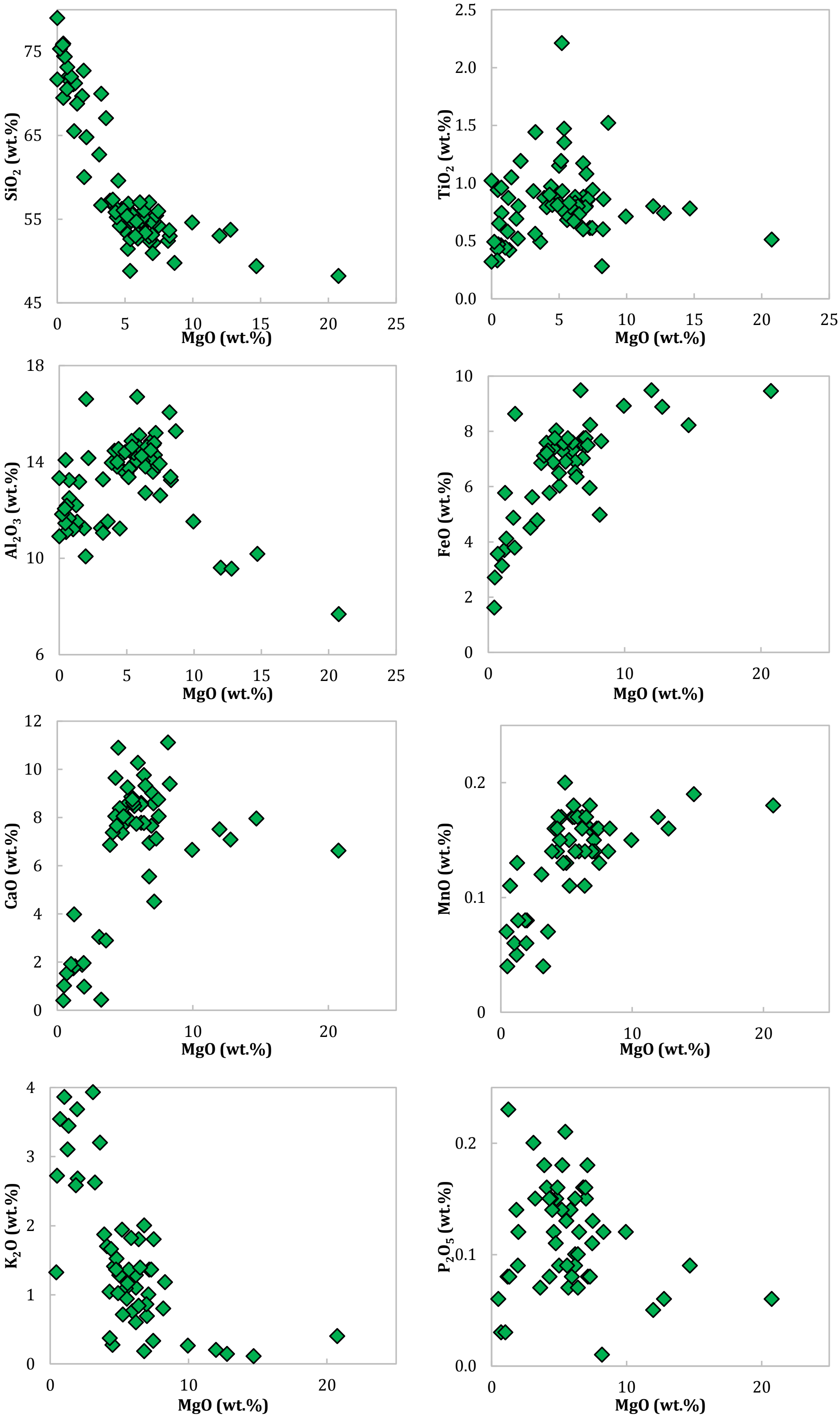

Fig. 4.76. Bivariate diagrams of selected major elements vs. MgO for the Seidorechka Formation.

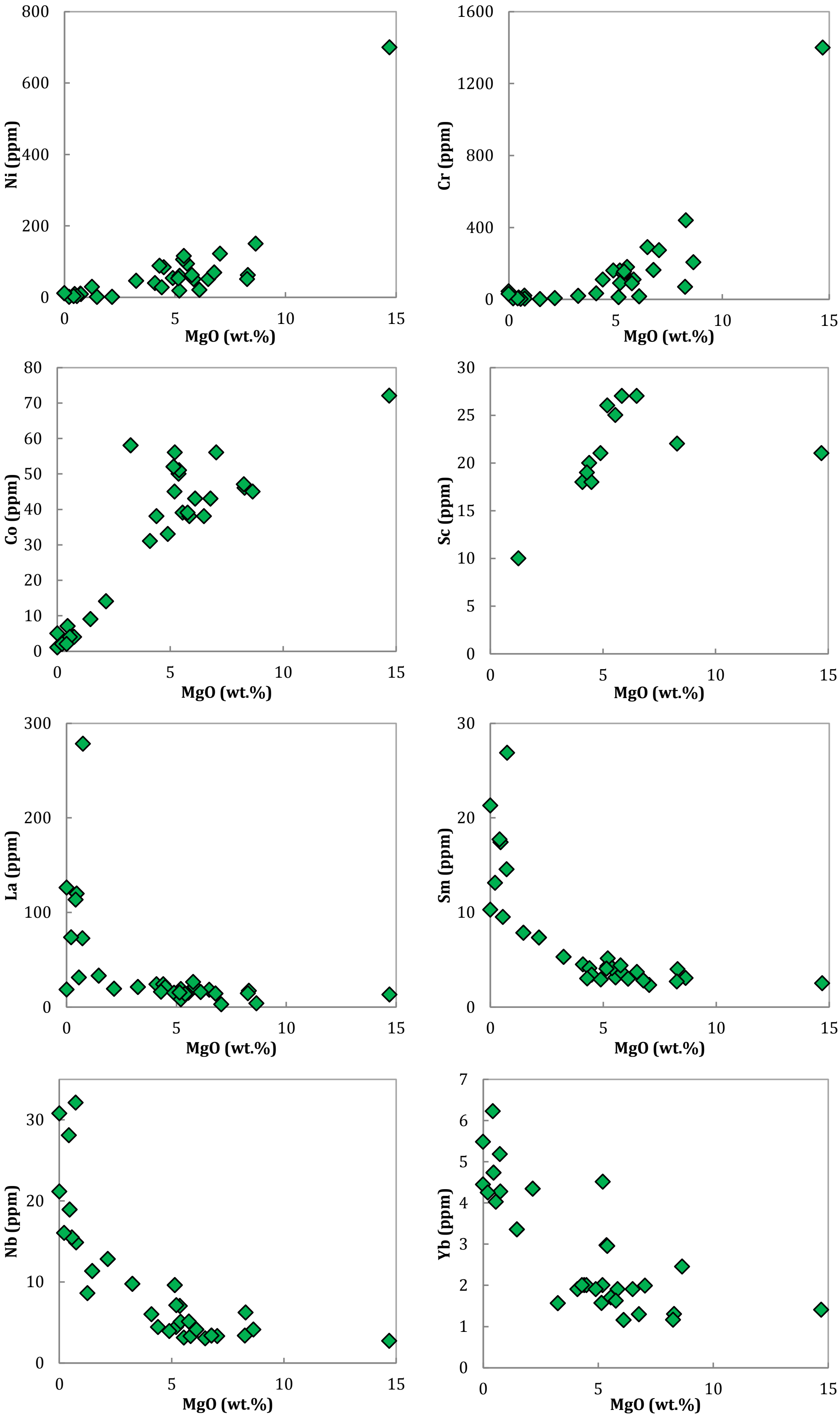

Fig. 4.77. Bivariate diagrams of selected trace elements vs. MgO for the Seidorechka Formation.

La, Nb, Sm and Yb show negative curved correlations with MgO. The negative correlations observed are unsurprising as these four elements are expected to behave incompatibly during basaltic fractionation. The trends of these elements show a slight inflection at ~5 wt.% MgO but also a second, more pronounced one at ~1 wt.% MgO where rocks with < 1 wt.% MgO, contain much greater abundances of incompatible elements than more magnesian rocks.

Chondrite-normalised REE diagrams for the Seidorechka Formation show sub-parallel trends with ∑REE concentrations ~14-475 × chondritic values **(Fig. 4.78)**. The Seidorechka samples are enriched in LREE, $(La/Sm)_N$ = 3.2 relative to the HREE which have relatively flat patterns; $(Gd/Yb)_N$ = 1.8. The Seidorechka Formation generally records negative Eu anomalies (average Eu/Eu* = 0.74) with only one sample showing a positive anomaly. The chondrite normalised patterns displayed by the Seidorechka Formation are intermediate between those of E-MORB and the continental crust.

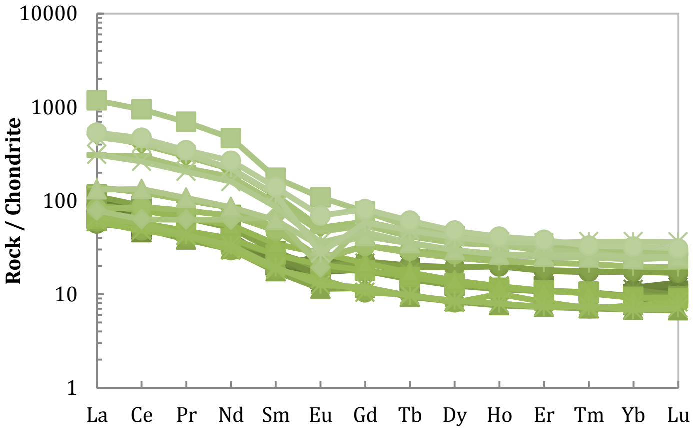

Fig. 4.78. Chondrite-normalised REE diagram for the Seidorechka Formation samples. Normalising values from McDonough and Sun (1995).

Primitive Mantle-normalised multi-element plots of the Seidorechka Formation samples **(Fig. 4.79)** show sub-parallel trends, similar in shape to the chondrite normalised REE diagrams **(Fig. 4.78)** in that the patterns are convex upwards with the most incompatible elements enriched relative to the less incompatible elements. All of the Seidorechka Formation samples record negative Nb-Ta anomalies which average at Nb/Nb* = 0.49. Likewise, all of the samples record negative Ti anomalies which average at Ti/Ti* = 0.75. The samples record variable Zr-Hf anomalies which are positive, negative or not observed and range in Zr/Zr* between 1.2-0.5.

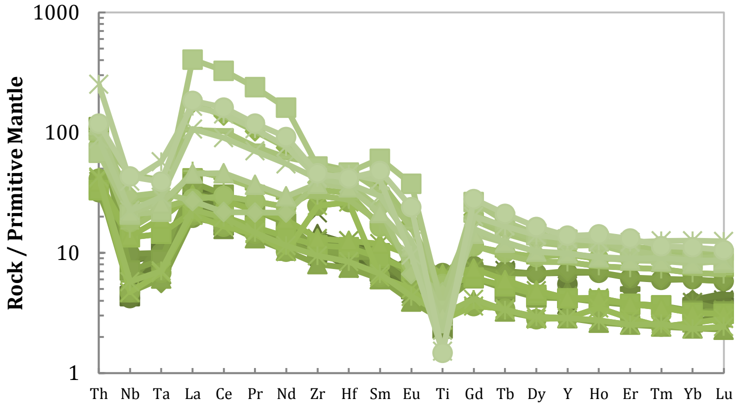

Fig. 4.79. Primitive Mantle-normalised multi-element diagram for the Seidorechka Formation samples. Normalising values from McDonough and Sun (1995).

The anomalies help determine the tectonic environment to which rocks are assigned on Nb/Y vs. Zr/Y and Zr/Nb vs. Nb/Th diagrams. On a Zr/Nb vs. Nb/Th diagram **(Fig. 4.80)**, the Seidorechka Formation samples plot in the volcanic arc field, clustering somewhat around the enriched mantle end-member. On a Zr/Y vs. Nb/Y diagram **(Fig. 4.81)**, the Seidorechka Formation volcanic rocks plot within the volcanic arc field in the non-plume sources area of the diagram. The samples with trace element data define a trend of increasing Nb/Y with increasing Zr/Y.

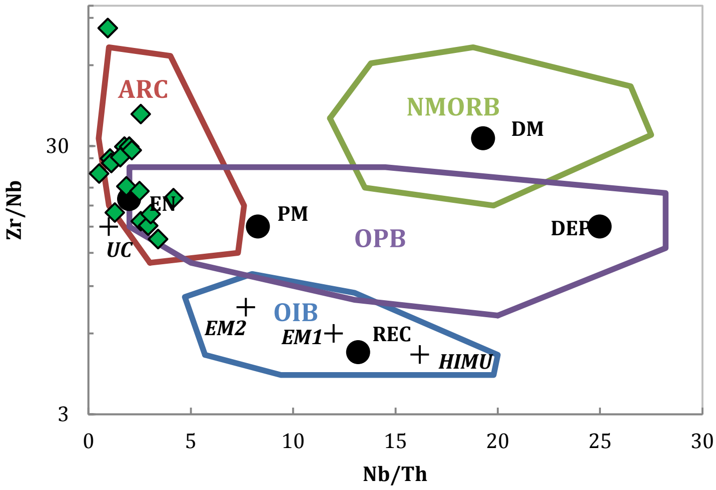

Fig. 4.80. Zr/Nb vs. Nb/Th diagram for the Seidorechka Formation samples. Field boundaries and end-member compositions from Condie (2005). Abbreviations as in **Fig. 4.8**.

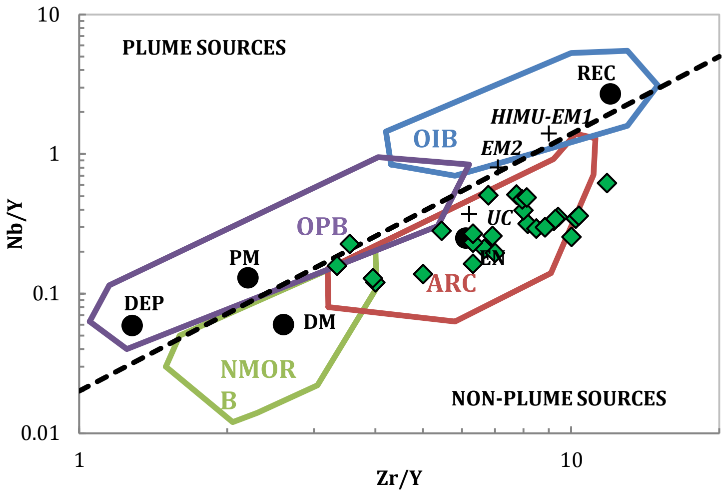

Fig. 4.81. Nb/Y vs. Zr/Y diagram for the Seidorechka Formation samples. Field boundaries and end-member compositions from Condie (2005). Abbreviations as in **Fig. 4.8**.

4.11. Radiogenic Isotope Analyses

Eighteen samples were analysed for Sr-Pb-Nd-Hf isotopes. Six samples were selected from the Blue Draw Metagabbro while four each were selected from the three principal East Bull Lake suite intrusions (East Bull Lake, Agnew and River Valley). The aims of the isotopic study were; firstly, to better understand the mantle sources responsible for the Matachewan LIP magmatism, and secondly, to apply the criteria developed by Zhang et al. (2008) to both the mineralised (East Bull Lake suite) and un-mineralised (Blue Draw Metagabbro) intrusions in an attempt to correlate mineralisation potential with mantle source. Nd, Hf and Sr isotopes were successfully determined for all samples. However, the four River Valley samples failed to yield Pb isotopic ratios. All of the isotopic data collected are presented in **Appendix D** and are briefly described below.

4.11.1. Sr Isotopes

^{87}Sr/^{86}Sr$_{(i)}$ data (which measures the Sr isotopic ratio of a sample at the time of intrusion – see Fig. 2.31 for intrusion ages used in calculation initial $_{(i)}$ isotopic values) for each of the layered intrusions are shown in **Fig. 4.81A**. The Blue Draw Metagabbro samples exhibit the largest range in ^{87}Sr/^{86}Sr$_{(i)}$ of between 0.69448-0.71272. The River Valley samples show the smallest range in ^{87}Sr/^{86}Sr$_{(i)}$ of 0.70202-0.70399 while the East Bull Lake and Agnew intrusions also have relatively small and quite similar ranges of 0.69810-0.70375 and 0.69698-0.70317 respectively.

4.11.2 Nd isotopes

The ^{143}Nd/^{144}Nd$_{(i)}$ data for each of the layered intrusions are shown in **Fig. 4.81A**. The Blue Draw Metagabbro samples exhibit the largest range in Nd between 0.50864-0.50931. The smallest range is exhibited by the River Valley samples (0.50938-0.50940). The East Bull Lake intrusion samples also exhibit a narrow range of 0.50932-0.50942. Three of the four Agnew samples have a narrow range (0.50932-0.50939) while the fourth samples (AG007) records a distinctly lower ^{143}Nd/^{144}Nd$_{(i)}$ value of 0.50890. The epsilon notation (εNd$_{(i)}$) describes the magnitude of deviations in Nd from the chondritic uniform reservoir (CHUR) line at the time of intrusion. The εNd$_{(i)}$ values of the Blue Draw Metagabbro samples range between -15.4 and -2.3 while the East Bull Lake and River Valley samples range from -3.6 to 0.0 and from -0.9 to -0.5 respectively **(Fig. 4.81B)**. The three Agnew samples with similar ^{143}Nd/^{144}Nd$_{(i)}$ values have a narrow range of εNd$_{(i)}$ values between -0.4 and -1.7. The Agnew sample which displays a very low ^{143}Nd/^{144}Nd$_{(i)}$ value has an εNd$_{(i)}$ value of -9.9.

4.11.3 Hf isotopes

The ^{176}Hf/^{177}Hf$_{(i)}$ data for each of the layered intrusions are shown in **Fig. 4.81C**. The Blue Draw Metagabbro samples exhibit the largest range in ^{176}Hf/^{177}Hf$_{(i)}$ between 0.28114-0.28268. The River Valley and Agnew intrusions record almost identical ranges of 0.281278-0.281359 and 0.28128-0.28135 respectively. The East Bull Lake suite samples define a range in ^{176}Hf/^{177}Hf$_{(i)}$ of 0.28099-0.28138. The εHf$_{(i)}$ values of the Blue Draw Metagabbro samples range between -2.3 and +52.7 **(Fig. 4.81D)**. The validity of some of the very positive εHf$_{(i)}$ values of the Blue Draw Metagabbro is questioned in Chapter 5. The East Bull Lake suite intrusions define much smaller ranges such that the East Bull Lake intrusion samples display εHf$_{(i)}$ ranges between -7.6 and +6.3 while the Agnew and River Valley intrusions show even smaller ranges of +3.0 to +5.9 and +2.6 to +5.2 respectively.

4.11.4 Pb Isotopes

The four River Valley samples failed to run on the mass spectrometer. The Blue Draw Metagabbro samples have the largest range of isotopic ratios of ^{206}Pb/^{204}Pb$_{(i)}$ 20^{7}Pb/^{204}Pb$_{(i)}$ and ^{208}Pb/^{204}Pb$_{(i)}$ which range between 12.55-29.14, 14.86-16.43 and 29.87-52.34 respectively. The Agnew intrusion has the narrowest ranges of initial isotope ratios: 14.72-21.23 (^{206}Pb/^{204}Pb$_{(i)}$), 15.04-16.17 (^{207}Pb/^{204}Pb$_{(i)}$), 33.795-40.630 (^{208}Pb/^{204}Pb$_{(i)}$). The East Bull Lake intrusion samples define intermediate ranges in Pb isotopes of 14.74-16.123 (^{206}Pb/^{204}Pb$_{(i)}$), 15.21-15.62 (^{207}Pb/^{204}Pb$_{(i)}$) and 32.84-36.17 (^{208}Pb/^{204}Pb$_{(i)}$).

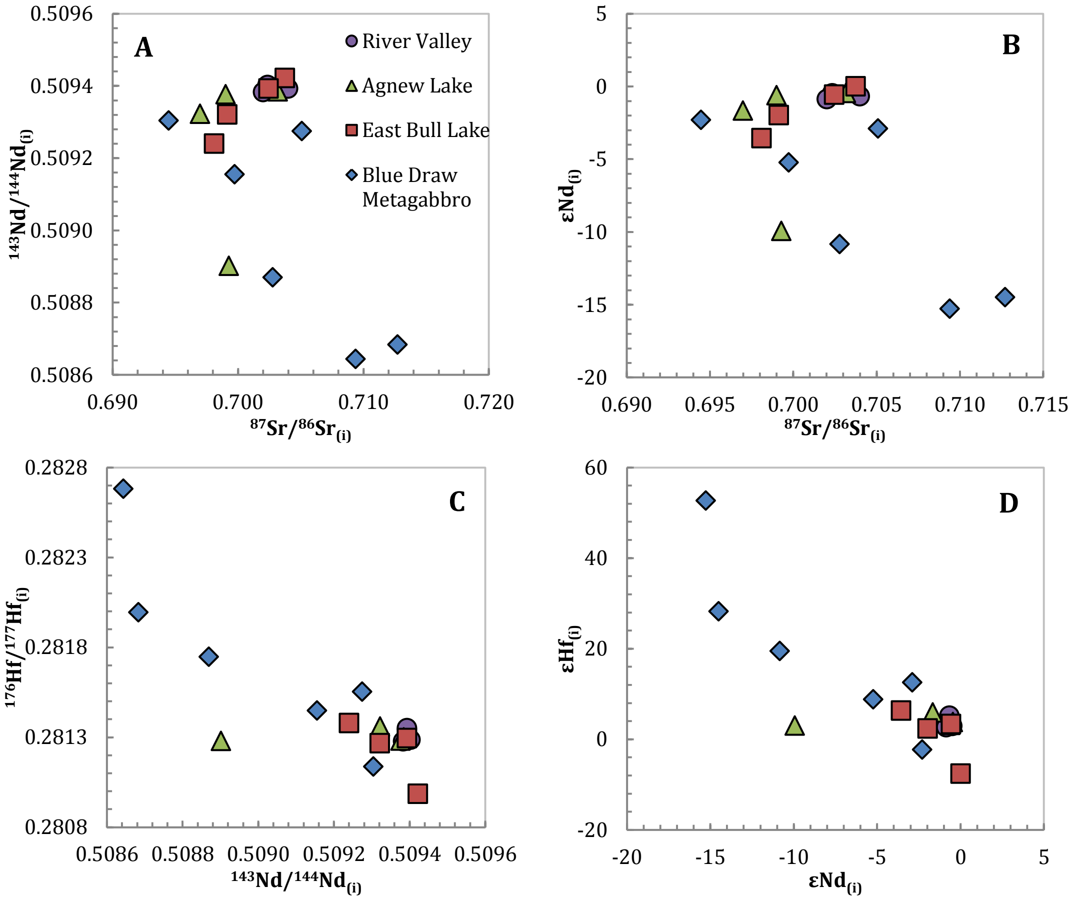

Fig. 4.81. Age-corrected radiogenic isotope diagrams for the East Bull Lake, Agnew, River Valley and Blue Draw Metagabbro layered intrusions of the Matachewan LIP.

On **Fig. 4.82A**, all but two of the samples plot above the northern hemisphere reference line (NHRL) of Hart (1985). The two samples which plot below the NHRL belong to the Blue Draw Metagabbro and East Bull Lake intrusions. On **Fig. 4.82B**, the majority of the samples plot below the NHRL. However, three of the four East Bull Lake intrusions samples plot above the line, as do one each of the Blue Draw Metagabbro and Agnew intrusions.

4.11.5 Isotopic Considerations

Isotopic ratios of suites of mafic rocks can be used to characterise the mantle source region from which the mafic rocks were derived. This is because (owing to the negligible mass difference between the isotopes of an element) isotopic ratios are unaffected by partial melting and fractional crystallisation. Thus, the initial isotopic ratios of the mafic suite ('initial' meaning the isotopic ratio when the parental magmas was extracted from the mantle) will be the same as the isotopic ratio of the source region at the time of extraction. The isotopic ratios measured in a sample are a function of the initial isotopic ratio and the rocks age. **Equation 4.5** shows why this is so, using the Sm-Nd system as an example.

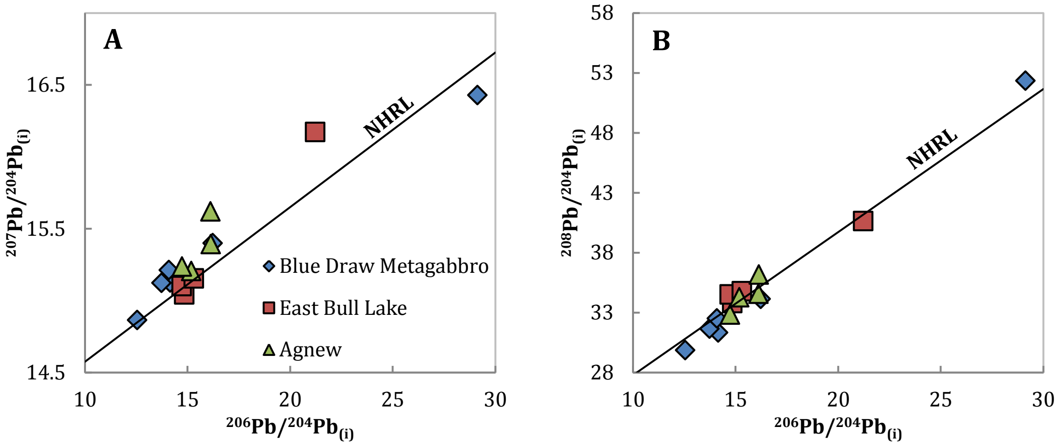

Fig. 4.82. Age-corrected radiogenic Pb isotope diagrams for the East Bull Lake, Agnew, and Blue Draw Metagabbro layered intrusions of the Matachewan LIP. The Northern Hemisphere Reference Line (NHRL) is taken from Hart (1985).

$$\left(\frac{^{143}Nd}{^{144}Nd}\right)(i) = \left(\frac{^{143}Nd}{^{144}Nd}\right)(m) - \left(\frac{^{147}Sm}{^{144}Nd}\right)(m) \times \left(e^{\lambda t} - 1\right)$$

Equation 4.5

Where (i) denotes the initial ratio, (m) denotes the measured ratio, t denotes the age of the rock and λ is the decay constant.

Owing to the very long half life of ^{147}Sm (1.06 × 10^{11} years) and limited range of Sm/Nd in nature, differences in ^{143}Nd/^{144}Nd between suites tend to be small. Thus, DePaolo and Wasserburg (1976) developed the epsilon notation (**Equation 4.6**) which measures the isotopic ratio of a sample at time (t) as variations relative to a reference sample, which in the case of the Sm-Nd system, is the chondritic uniform reservoir (CHUR).

$$\varepsilon_{Nd}^{t} = \left(\frac{{}^{143}Nd/{}^{144}Nd(rock,t)}{{}^{143}Nd/{}^{144}Nd(CHUR,t)} - 1\right) \times 10^{4}$$

Equation 4.6

Equation 4.6 shows that samples which have higher ^{143}Nd/^{144}Nd (i.e. more of the radiogenic ^{143}Nd) than CHUR yield a +ε_{Nd} value while samples which have lower ^{143}Nd/^{144}Nd (i.e. less of the radiogenic ^{143}Nd) than CHUR yield –ε_{Nd} value. This observation in itself is important as +ε_{Nd} values are acquired by material which has a Sm/Nd ratio greater than that of CHUR and thus are characteristic of rocks derived from a depleted mantle source, or those contaminated by continental material. Conversely, –ε_{Nd} values are acquired by material which has a Sm/Nd ratio less than that of CHUR and are thus characteristic of rocks derived from an enriched mantle source (Rollinson 1993).

Intrusion	Sm	Nd	Hf	Lu	Rb	Sr	Th	U	Pb
Blue Draw Metagabbro	0.98	0.99	1.00	0.94	0.98	0.67	1.00	0.99	0.97
East Bull Lake	0.92	0.93	0.99	0.74	0.40	0.06	0.91	0.76	0.03
Agnew	0.83	0.85	0.99	0.77	0.21	0.18	0.85	0.20	0.16
River Valley	0.48	0.64	0.84	0.27	0.08	0.00	0.69	0.60	-

Table 4.1. Correlation coefficients of elements plotted against Zr for each of the intrusions studied.

Gaffney et al. (2011) experimented on samples of lunar basalt to determine the effects of metamorphism on the Rb-Sr, Sm-Nd and U-Pb isotopic systems. By comparing the isochrons of a control sample with those derived from samples which had been subjected to increased temperature and pressure, Gaffney et al. (2011) showed that, of the three systems studied, the Sm-Nd system was the least affected by metamorphism while the U-Pb and (to a lesser extent) Rb-Sr systems are liable to modification. Thus, before the isotopic data obtained in this study can be interpreted, it must be demonstrated that the data has not been affected by post-intrusion metamorphic events which may have disturbed the isotopic systems. This is achieved by plotting the elements in the relevant radioactive decay schemes against an element considered to be immobile [e.g., Zr) under the greenschist facies metamorphism experience by the four intrusions studied (Pearce 1996). Strong linear correlations with Zr would suggest that an element has not been mobilised and thus, the isotopic ratios of that element may be considered unaffected by post-intrusion heating events.

The correlation coefficients of each element are presented in **Table 4.1**. The Blue Draw Metagabbro records the strongest correlation coefficients of all of the intrusions with all of the elements. Sr in the Blue Draw Metagabbro shows a somewhat weaker correlation with Zr (r^2 = 0.67) indicating that Sr may have been remobilised. The East Bull Lake shows similarly strong correlations to the Blue Draw Metagabbro for all elements except Rb, Sr and Pb which record weak or no correlation with Zr. On further examination, the seemingly non-existent correlation of Pb with Zr in the East Bull Lake intrusion is largely caused by sample EB006 which contains an order of magnitude more Pb than the other samples from the intrusion. Exclusion of this data point increases the correlation of Pb with Zr to r^2 = 0.83 which may mean that in the East Bull Lake intrusion, Pb has not been remobilised to a great extent and that the high Pb in sample EB006 may be a singular occurrence. The weakest correlations with Zr are observed in the River Valley intrusion indicating that the majority of elements studied have been remobilised. This observation is somewhat unsurprising as, unlike the other East Bull Lake suite intrusions, the River Valley intrusion occurs within the Mesoproterozoic Grenville Front Tectonic Zone where metamorphic grade exceeds upper amphibolites facies (Ashwal and Wooden 1988), the point at which immobile behaviour exhibited by elements with intermediate ionic potential ceases (Pearce 1996). The Agnew intrusion samples generally record moderate-poor correlations of the considered elements with Zr suggesting that moderate amounts of element remobilisation has occurred. The poor correlations exhibited by the Agnew samples are surprising as previous studies of the intrusion have suggested that metamorphism of the Agnew intrusion peaked at lower amphibolite grade during the ~1.85 Ga Penokean orogeny (Vogel et al. 1998b) and thus, the elements studied may have been expected to have remained immobile (Pearce 1996).

In summary, the River Valley and Agnew intrusions record geochemical evidence which suggests the isotopic systems studied here have been disturbed by post-intrusion metamorphism. Conversely, data from the Blue Draw Metagabbro and East

Bull Lake samples suggest that the Sm-Nd and Lu-Hf isotopic systems of these two intrusions have not been affected. Further discussion will only use these less mobile isotope systems to characterise the mantle sources responsible for the Matachewan LIP magmatism, the degree and nature of any contamination experiences by the Matachewan LIP suites, and also to determine if the mineralisation observed in some of the Matachewan LIP layered intrusions can be correlated with a specific mantle source region.

4.12. Summary

This chapter has presented the geochemistry of the igneous suites which constitute the Matachewan LIP as analysed or collated by this study. The following is a summary of some of the key points which are also displayed in **Table 4.2**.

One of the most striking things about the Matachewan LIP is the lack of high Mg rocks. Only a single komatiitic sample is reported from the Seidorechka Formation which gives the formation a large range in MgO content of 0.5-20.7 wt.%. However, discounting this single komatiite decreases the range of the other 51 samples and defines an upper limit of 14.7 wt.% MgO. This smaller range is comparable to the ranges in MgO recorded by the potential parent magmas of the Fennoscandian and Blue Draw Metagabbro intrusions. However, the majority of the Matachewan LIP rocks contain less than ~8 wt.% MgO and can be classified as picrobasalts (Le Bas 2000) and consistently plot as tholeiitic basalts-andesites on the TAS diagram and as subalkaline basalts-basaltic andesites on the Zr/Ti vs. Nb/Y diagram.

Three of the Matachewan LIP suites are composite formations, made up of subgroups which are readily identifiable by their different trace element geochemistry. Two of these composite suites (the Matachewan and Leopard dyke swarms) are composed of one subgroup of numerous dykes, characterised by slight LREE enrichment and flat HREE patterns on chondrite-normalised REE diagrams and a second, less numerous group of dykes with much greater LREE enrichment and steep HREE patterns. These trace element groups are also found in the third composite suite (the Thessalon Formation) which has a more complex geochemistry made up of four subgroups.

	Matachewan Dykes		**East Bull Lake Suite†**	**Thessalon Formation**				**Blue Draw Metagabbro†**	**Leopard Dykes**		**Kaminak Dykes**	**Viianki Dykes**	**Seidorechka Formation**
	Group 1	**Group 2**		**Group 1**	**Group 2**	**Group 3**	**Group 4**		**Group 1**	**Group 2**			
MgO (wt.%)	2.2-8.8	23.0-5.9	7.5-8.0	4.1-7.1	1.5-8.2	8.4-9.9	3.7-5.2	13.0	1.6-7.0	2.3-2.4	2.2-6.3	8.2-17.2	0.5-20.8
Fe_2O_3 (wt.%)	11.0-18.0	11.2-14.6	10.0-10.5	10.1-17.0	10.2-16.7	12.5-14.6	9.7-13.3	10.2	4.0-14.6	8.3-8.9	13.5-17.1	9.9-11.5	4.2-12.3
Mg#	12.0-45.4	18.5-31.6	44.2-47.2	25.2-41.9	14.0-38.3	41.2-46.4	28.4-31.8	58.5	30.7-39.3	22.6-24.1	13.0-32.2	47.9-62.6	7.5-52.3
SiO_2 (wt.%)	48.4-55.7	48.3-53.5	49.1-50.4	45.2-56.6	47.8-61.7	50.1-52.9	53.1-58.1	52.9	47.2-50.5	58.2-60.8	45.4-54.0	50.7-53.4	48.2-76.0
Alkali (wt.%)	2.3-5.6	4.1-7.1	2.6-3.7	2.2-8.2	3.3-7.4	2.8-3.9	3.1-6.5	3.9	2.3-5.6	5.6-6.3	3.2-5.4	1.7-3.8	2.8-7.2
Ni (ppm)	8-170	8-817	27-709	49-152	1-205	302-357	63-78	20-1357	26-348	25-60	11-220	209-510	0-700
Cr (ppm)	9-476	5-339	10-604	23-179	1-44	997-1080	27-30	20-3131	48-327	52-199	4-89	520-1708	0-1400
$(La/Sm)_N$	2.0	2.8	2.1	2.4	2.9	2.5	3.6	3.2	1.7	3.9	2.9	3.0	3.4
$(Gd/Yb)_N$	1.1	2.2	1.1	1.5	2.9	2.3	1.5	1.5	1.0	2.4	1.5	1.7	1.6
Eu/Eu*	0.9	0.9	1.3	0.9	0.9	0.9	0.7	0.9	1.2	0.5	1.0	1.0	0.8
Nb/Th	3.0	1.5	2.1	1.7	3.6	5.5	0.7	0.8	2.2	0.8	1.5	1.3	-
Zr/Nb	19.8	21.7	27.1	21.1	14.5	10.3	16.7	22.8	60.5	4.5	20.9	37.3	31.2
Zr/Y	3.6	6.6	3.4	4.3	7.7	6.2	5.2	5.3	8.0	1.1	4.7	5.4	6.3
Nb/Y	0.2	0.3	1.3	0.2	0.5	0.6	0.3	0.2	0.2	0.2	0.2	0.2	0.2
Nb/Nb*	0.5	0.2	0.3	0.3	0.6	0.7	0.2	0.1	0.3	0.1	0.2	0.2	0.3
Ti/Ti*	0.8	0.6	0.8	0.6	0.5	0.5	0.4	0.5	0.9	0.3	0.8	0.6	0.6
Zr/Zr*	1.0	0.9	1.0	0.9	0.7	0.8	0.8	1.0	1.0	0.5	0.9	1.0	1.2
Y/Y*	1.1	1.1	1.0	0.9	0.8	0.9	0.9	1.0	1.1	1.1	1.1	0.9	1.0
$^{87}Sr/^{86}Sr_{(i)}$			0.69698-0.70375					0.69448-0.71272					
$^{143}Nd/^{144}Nd_{(i)}$			0.50890-0.50942					0.50864-0.5093					
$\varepsilon Nd_{(i)}$			-9.9					-17.6					
$^{206}Pb/^{204}Pb_{(i)}$			14.72-21.23					12.55-29.14					
$^{207}Pb/^{204}Pb_{(i)}$			15.04-16.17					14.86-16.43					
$^{208}Pb/^{204}Pb_{(i)}$			32.84-40.63					29.869-52.337					
$^{176}Hf/^{177}Hf_{(i)}$			0.28099-0.28138					0.28114-0.28268					
$\varepsilon Hf_{(i)}$			-13.9					-55					

Table 4.2. Summary of the geochemical characteristics of the Matachewan LIP suites. † See Chapter 5 for discussion of parental magmas for the East Bull Lake Suite and Blue Draw Metagabbro layered intrusions.

The trace element geochemistries of the Matachewan LIP suites are consistently enriched in the most incompatible elements relative to the least incompatible elements on Primitive Mantle-normalised multi-element diagrams. All of the suites studied have sizeable negative anomalies in Nb-Ta and Ti, the largest of which are observed in the Group 2 Leopard dykes. Anomalies in Zr and Y are also observed in some of the Matachewan LIP suites, however, these anomalies are not ubiquitous, nor as consistently negative as the Nb-Ta and Ti anomalies. For example, variably negative Zr anomalies are observed in seven of the twelve suites studied, while in the remaining five suites (including all of the layered intrusion parental magmas), no appreciable Zr anomalies are observed. More variable still are the Y anomalies which occur in ten of the Matachewan suites and may be either slightly negative or slightly positive (Y/Y* range = 0.8-1.1).

This consistent trace element geochemistry means that the Matachewan LIP suites plot as overlapping clusters on tectonic discrimination diagrams as predominantly volcanic-arc basalts. The only suite which differs from these general trace element patterns is the Gerow intrusion of the East Bull Lake Suite which itself is characterised by LREE depletion relative to the HREE and small-nonexistent, negative Nb-Ta anomalies. However, the Gerow intrusion is the only East Bull Lake Suite intrusion which lacks any geochronological control and thus, may not be cogenetic with the other East Bull Lake Suite intrusions.

In terms of radiogenic isotope data, the three East Bull Lake Suite intrusions define the narrowest ranges in Nd, Hf, Sr and Pb isotopic space and have similar mean initial ratios. In contrast, samples from the Blue Draw Metagabbro intrusion define very large ranges in isotopic compositions which encompass the smaller ranges recorded by the East Bull Lake Suite intrusions in all systems except Sm-Nd. Initial Nd isotopic ratios for the East Bull Lake Suite have an average of ~0.50939, which is outside the range of the Blue Draw Metagabbro samples (0.50864-0.50930).

5. DISCUSSION

This chapter will discuss the implications of the Matachewan LIP geochemical data presented in Chapter 4. The first point of discussion will be to determine the conditions of melting needed to produce the Matachewan LIP primary magmas. This will be done using the PRIMELT2.XLS petrogenetic modelling software developed by Professor Claude T. Herzberg of Rutgers University. The mantle sources of the Matachewan LIP magmatism will then be investigated by using trace elements to model the crystallisation of magmas produced from melting different mantle reservoirs. Several different models will be constructed in an attempt to establish the most likely mantle sources of the Matachewan LIP magmas. The validity of the mantle plume paradigm for explaining the Matachewan LIP [as is popular in the literature (see Chapter 2)] is explored by comparing the potential temperature of the Matachewan LIP magmatism with estimates of the upper mantle temperature at ~2.45 Ga. This will be done in order to determine if the Matachewan LIP formed from the melting of anomalously hot mantle, as is predicted by the mantle plume model. The major and trace element variations exhibited by the individual Matachewan LIP suites are investigated using a number of different petrogenetic models which attempt to characterise how and under what conditions the Matachewan LIP parental magmas evolved in the crust. These models rely, in part, on the PELE computer program developed by Dr. Alan E. Boudreau of Duke University. The controls on the Ni-Cu-PGE mineralisation observed in the different Matachewan LIP suites are discussed and geochemical criteria thought to be vital to the genesis of such mineralisation are tested against each of the Matachewan LIP suites. The efficacy of the criteria in predicting the known Ni-Cu-PGE mineralisation will be determined first before being used to determine the economic potential of currently unexplored suites. The last point of discussion concerns the environmental impact of the Matachewan LIP magmatism by exploring its potential link to the Great Oxidation Event (the point in Earth's history where free O_2 first appeared). Finally, a summary will be presented which debates whether the geochemical data presented for each of the igneous suites by this study is consistent with the dominant view presented in the literature- that they are cogenetic and related to mantle-plume driven continental break-up.

5.1. Primary Magmas

5.1.1. PRIMELT2.XLS

Herzberg and Asimow (2008) produced the PRIMELT2.XLS software which can calculate primary magma compositions for evolved lavas. PRIMELT2.XLS uses forward and inverse models to compute a melt fraction which is capable of; (a) being produced by partial melting of mantle peridotite [as derived from parameterisation of experimentally determined partial melt compositions of fertile mantle peridotite KR-4003 (Walter 1998)] and (b) producing the major element composition of the evolved lava through fractionation or accumulation of olivine.

PRIMELT2.XLS can model mantle melting as accumulated perfect fractional melting, where-by, melting of mantle peridotite occurs at a given pressure and produces a small fraction of melt which is in equilibrium with the residue. This small amount of fractional melt is removed and the composition of the residual peridotite is modified to reflect the generation and removal of the melt. The residue then moves upwards and with decreasing pressure the residual peridotite melts again in the same manner. This process is repeated until melting ceases at some lower pressure. The compositions of the small fractions of melt produced at each step are aggregated by PRIMELT2.XLS to give a primary magma composition. PRIMELT2.XLS is also able to model batch melting for harzburgite, dunite, spinel lherzolite, lherzolite and garnet peridotite residues.

To determine if this primary magma capable of fractionating or accumulating olivine to give the geochemistry of the evolved lava being studied, PRIMELT2.XLS adds and subtracts olivine in a series of small increments to and from the measured lava composition to ascertain if the primary magma composition can be reproduced. PRIMELT2.XLS presents a potential primary magma for the evolved lava when the composition of primary magma generated during the forward model of mantle melting reaches parity with the inverse model of olivine addition to the measured evolved lava composition in both FeO-MgO and olivine-anorthite-diopside-silica projection space.

PRIMELT2.XLS is only applicable to lava compositions which have experienced olivine fractionation or accumulation and fails to compute primary magma solutions for samples if other mineral phases have fractionated. To screen for clinopyroxene fractionation, PRIMELT2.XLS examines the CaO and MgO contents of the evolved lava. If the CaO and MgO content of the lavas studied fall outside the field defined by olivine fractionation of a peridotite-sourced partial melt **(Fig. 5.1)**, PRIMELT2.XLS warns the user that no solution is possible. The incorrect application of PRIMELT2.XLS to lavas which have experienced clinopyroxene removal may result in primary magma compositions that overestimate the MgO content. PRIMELT2.XLS also uses MgO and CaO contents to filter out lavas likely derived from a pyroxenite rather than peridotite source. Application of PRIMELT2.XLS to lavas sourced from pyroxenitic mantle is a source of error and can produce primary melt compositions that contain 2-3 wt.% more MgO and overestimate the T_P of a primary magma by up to 70°C.

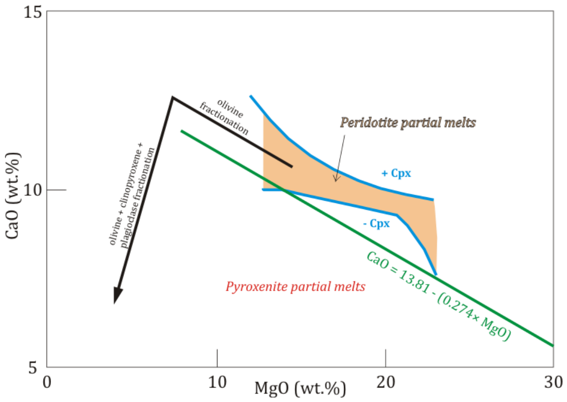

Fig. 5.1. CaO vs. MgO contents of primary magmas of fertile peridotite produced by accumulated fractional melting. Blue lines define upper and lower CaO contents of potential primary magmas. Lavas which plot below the green line are potentially sourced from partial melts of pyroxenite or have experienced clinopyroxene fractionation. Black line with closed arrow is the typical liquid line of descent for basaltic primary magmas. Modified after Herzberg and Asimow (2008).

PRIMELT2.XLS is also capable of screening out lavas derived from primary magmas produced during mantle melting facilitated by CO_2 addition. The screening is achieved by comparing the CaO and SiO_2 contents of the studied lavas to CaO and SiO_2 contents of partial melts of carbonated and anhydrous peridotite. As partial melting of carbonated peridotite produces melts high in CaO and low in SiO_2 relative to melting of dry peridotite (Dasgupta et al. 2007), Herzberg and Asimow (2008) suggest that evolved lavas which contain $CaO > (2.318 \times SiO_2) - 93.626$ are sourced from fractionated melts of carbonated peridotite. It is important to screen for volatile-enhanced melting as melting under such conditions occurs at relatively low temperatures and can produce melts with very high MgO and FeO contents (Dasgupta et al. 2007). Such melts may be incorrectly interpreted to be sourced from melting of anhydrous peridotite and yield a high T_P in error of hundreds of degrees.

The oxidation state of the mantle source can be adjusted as PRIMELT2.XLS allows the user to alter the $Fe^{2+}/\Sigma Fe$ and Fe_2O_3/TiO_2 ratios of the model.

All of the samples from the dyke swarms and flood basalt provinces studied in this project were analysed using PRIMELT2.XLS as were parental magmas for the layered intrusions. Literature data for suites of rocks thought to be equivalent to the Matachewan LIP suites studied was also analysed (Puchtel et al. 1996; Stepanova and Stepanov 2010). The results are discussed below. For all samples studied, $Fe^{2+}/\Sigma Fe$ and Fe_2O_3/TiO_2 ratios in the mantle peridotite were kept at 0.9 and 0.5 respectively. **Table 5.1** contains the major element compositions, degrees of partial melting and potential temperatures (T_P) of all of the primary magmas produced in this study for each of the Matachewan LIP suites.

5.1.1.1. Matachewan LIP Layered Intrusions

As layered intrusions are fractionated bodies of magma, cumulate samples taken from their stratigraphy may not represent the original magma from which the intrusions crystallised. Instead, the compositions of magmas parental to layered intrusions can be estimated from compositions of fine-grained, cogenetic dykes which fed the intrusion [e.g., Vogel et al. 1999), melt inclusions trapped within early forming cumulus phases [e.g., Spandler et al. 2000) or through estimates of average composition of the intrusion as a whole [e.g., Ciborowski et al. in press).

In the case of the Blue Draw Metagabbro, fieldwork in 2010 failed to identify potential feeder dykes to the BDM or definite chilled margin material which would record the composition of the BDM parental magma. Furthermore, scanning electron microscopy (SEM) observations have revealed that the early-formed spinels from within the Peridotite Unit (which might have contained melt inclusions with remnants of the unfractionated parent magma) are altered and show evidence of significant recrystallisation**.**

I therefore estimated the parental melt composition of the BDM by summing the compositions of each stratigraphic unit into a weighted average for the whole intrusion [e.g., James et al. 2002; Polat et al. 2011). To do this, the chemostratigraphic profiles for each element were divided into segments where the data approximates a straight line. By substituting the median stratigraphic height for each segment into the straight line equation for the segment, the average concentration of an element in that segment can be estimated. Multiplying the average concentration of an element in a segment by the thickness of the segment as a proportion of the intrusions as a whole, and summing the result from each of the segments, an estimate of the elemental concentrations of the whole intrusion (and hence parent magma) can be made **(Fig. 5.2)**.

Sample	**BR4C**	**BR4C**	**NBH13A**	**91113**	**234**
Suite	Leopard dykes	Leopard dykes	Leopard dykes	Seidorechka Formation	East Bull Lake Suite
Melting model	B	AF	B	AF	B
SiO_2	46.34	46.36	46.39	49.03	47.06
TiO_2	0.54	0.55	0.52	0.56	0.35
Al_2O_3	19.53	19.62	17.43	10.78	12.82
Cr_2O_3	0.01	0.01	0.02	0.22	0.02
Fe_2O_3	0.68	0.69	0.64	1.14	0.83
FeO	7.63	7.63	8.28	9.13	9.04
MnO	0.14	0.14	0.15	0.18	0.18
MgO	12.36	12.20	14.36	17.04	18.69
CaO	10.49	10.54	9.61	9.76	8.94
Na_2O	1.60	1.60	1.35	1.78	1.47
K_2O	0.38	0.38	0.78	0.24	0.43
NiO	0.26	0.25	0.43	0.07	0.16
P_2O_5	0.04	0.04	0.04	0.08	0.01
T (°C)	1286	1282	1333	1390	1422
T_P (°C)	1384	1379	1442	1508	1545
F	29.8	29.8	29.9	31.1	30.3
Fo	90.7	90.5	91.2	91.5	92.4
% ol	22.4	21.9	31.4	7.3	32.3

Table 5.1. Primary magma compositions for different Matachewan LIP suites as calculated by PRIMELT2.XLS. B – batch melting; AF – accumulated fractional melting; T – eruption temperature; T_P – mantle potential temperature; F – degree of melting; Fo – forsterite content of olivine in equilibrium with the melt; % ol – percentage of olivine added to sample composition needed to obtain primary magma composition.

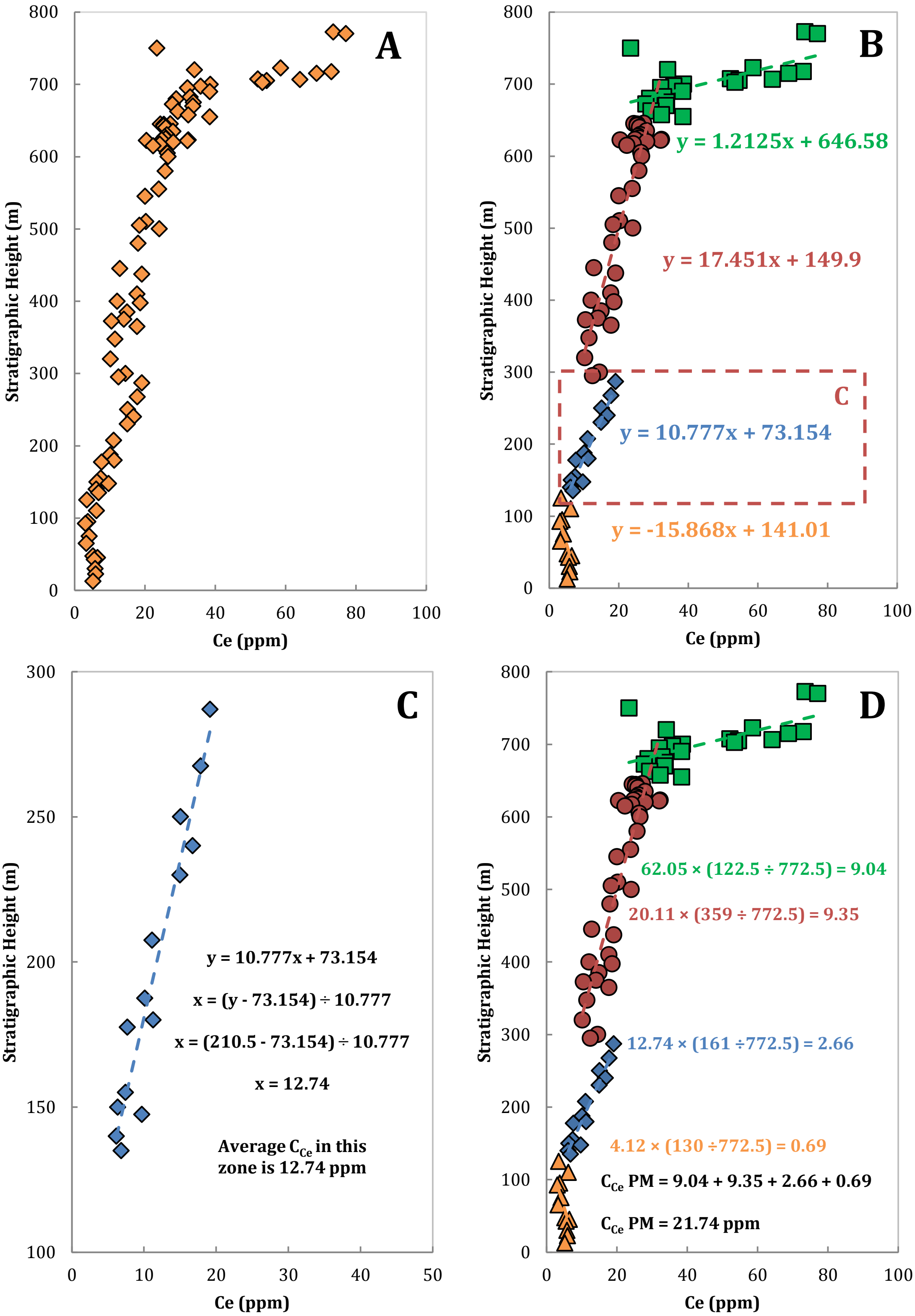

Figure 5.2. Method used to calculate average composition (parental magma) of the Blue Draw Metagabbro. **A)** Chemostratigraphic profile of Cerium. **B)** Chemostratigraphic profile subdivided into straight-line portions. **C)** Illustration of method of finding the Ce concentration (C_{Ce}) of a single portion. **D)** Complete method for all portions and estimate average Ce concentration (C_{Ce}) of the BDM and thus, the parental magma (PM).

When calculated using the weighted-average method, the BDM parent magma (BDM-PM) is estimated to have been a basaltic magma containing ~12.7 wt.% MgO with a Primitive Mantle-normalised trace element pattern which shows LREE and LILE enrichment and significant negative Nb-Ta and Ti anomalies, but no significant Eu anomaly, similar to the bulk of the samples shown in **Fig. 4.40** (See **Appendix I** for full parental melt composition).

While estimating the parental magma of layered intrusions using this method has been shown to be successful with layered intrusions similar to the BDM, [e.g., James et al. 2002; Polat et al. 2011), its applicability to the BDM is questionable. Firstly, while the evolved nature of the intrusion, presence of pegmatites and its lack of extrusive equivalents suggest that the intrusion evolved as a closed system, the possibility of the intrusion having had material extracted during eruptive episodes cannot be ruled out as any such material may have been lost during an period of erosion marked by the angular Estes unconformity which separates the Boxelder Creek Quartzite and overlying <1.89 Ga Montana Mine Formation (Frei et al. 2008).

The second issue to note is that the bimodal distribution of olivine in the peridotite unit **(Fig. 3.10A)** suggests that the BDM parent magma was intruded as a mixture of magma and olivine crystals rather than as a homogenous liquid. If this is the case, the composition of the olivine crystal phases injected with the melt would be erroneously included in the whole-intrusion average calculation. To address this issue, 2.64 volume % of olivine was subtracted from the weighted average to account for the estimated volume % of the peridotite unit made up of megacrystic olivine. Despite these potential issues, given the lack of other suitable material which may be used to estimate the composition of the BDM parent magma described above, it is the opinion of the authors than the weighted-average calculation presented here currently represents the best estimate of the parental magma of the BDM intrusion. The veracity of this estimate is discussed later.

In the case of the East Bull Lake suite of intrusions the estimates of parental magma used in this study are taken from Vogel et al. (1998) and James et al. (2002). James et al. (2002) provides a composition of a probable feeder dyke from the eastern lobe of the East Bull Lake intrusion and a weighted bulk composition for the whole East

Bull Lake intrusion determined by proportionally summing the average compositions of each of the stratigraphic units of the intrusion, similar to the method used in this study to calculate the composition of the BDM. Vogel et al. (1998) provides geochemical data for several samples of the Streich-type dykes which are interpreted to be the most likely feeders to the Agnew Intrusion based on field relationships, permissive fractional crystallisation models and similar Primitive Mantle-normalised trace element chemistries. Vogel et al. (1999) also provide geochemical data for several Viianki dykes which represent the most likely parental magmas to have fed some of the Fennoscandian intrusions.

PRIMELT2.XLS was able to calculate primary magma compositions for only one of the thirteen potential parent magmas studied here [sample 234 of Vogel et al. (1998)]. PRIMELT2.XLS was only able to generate a primary magma for sample 234 using batch melting and produced a primary magma containing 18.69 wt.% MgO, which is in equilibrium with olivine of composition $Fo_{92.4}$. The degree of partial melting required to produce this primary magma from a peridotite of a composition similar to KR-4003 is 30.3%. The remaining layered intrusion parent magmas modelling in this study failed to produce primary magmas as all of these samples may have originated from a pyroxenite source or have fractionated clinopyroxene.

5.1.1.2. Matachewan LIP Dyke Swarms

Every sample from the dyke swarms studied in this project was tested with PRIMELT2.XLS. PRIMELT2.XLS is unsuccessful in obtaining primary magmas for any of the Kaminak or Matachewan dykes sampled. This is somewhat unsurprising as available evidence suggests that many of the dykes from these swarms evolved, in part, through fractional crystallisation of clinopyroxene and plagioclase. This evidence includes the relatively low MgO contents (< 9.00 wt.% in the Matachewan and < 6.41 wt.% in the Kaminak), which are associated with clinopyroxene + olivine + plagioclase fractionation **(Fig. 5.1)** and also the presence of ubiquitous plagioclase phenocrysts within the dykes, which have been interpreted to be products of fractional crystallisation of the dyke magma during its residence in a deeper crustal chamber (Sandeman and Ryan 2008; Phinney and Halls 2001).

Applying PRIMELT2.XLS to the Leopard dykes is more difficult as evidence suggests that, unlike the Matachewan and Kaminak dykes, which evolved through fractional crystallisation, the Leopard dykes evolved, in part, through accumulation of varying amounts of exotic plagioclase (see Section 5.4.2.4). Thus, without accounting for the fraction of each Leopard dyke sample composed of this exotic plagioclase fraction, erroneous compositions would be used with PRIMELT2.XLS. The exotic plagioclase crystals can be up to < 5 cm in length and can constitute up to ~50 % of the sample volume **(Fig. 3.12)**. The size of these phenocrysts suggest that rather than crystallising in situ in the several-metre thick Leopard dykes, they crystallised prior to emplacement and were entrained in the dyke magmas as they left a deeper magma chamber. Thus, these plagioclase phenocrysts probably do not reflect the composition of the evolving liquid. To minimise the effect of the phenocrystic plagioclase on the major element chemistry of the rocks, their composition was estimated and removed from the whole-rock analysis. To do this, the fraction of each sample made up of phenocrystic plagioclase was estimated from hand samples while the plagioclase composition was estimated using the calculated CIPW-normative composition of the sample. The wt.% composition of the plagioclase portion of each sample was subtracted from the whole rock analysis to give an estimated composition for the glassy groundmass (and hence the liquid) of the Leopard dykes. The resulting estimates for the Leopard dykes are shown in **Appendix J**.

PRIMELT2.XLS was successful in calculating primary magma compositions for two of the eighteen Leopard dykes sampled. PRIMELT2.XLS was able to calculate melt fractions using both batch and accumulated fractional melting of fertile peridotite KR-4003 for sample BR4C. The primary magma produced by the batch melting model contains 12.36 wt.% MgO, is in equilibrium with olivine of composition $Fo_{90.7}$ and requires 29.8 % melting of the source. In the case of accumulated fractional melting, the primary magma predicted by PRIMELT2.XLS contains 12.20 wt.% MgO, is in equilibrium with olivine of composition $Fo_{90.5}$ and is produced by 29.8 % melting of the source. PRIMELT2.XLS was also successful in providing a solution for sample NBH13A using the batch melting model. The primary magma predicted by PRIMELT2.XLS contains 14.36 wt.% MgO, is in equilibrium with olivine of composition $Fo_{91.2}$ and requires 29.9 % melting of the source.

5.1.1.3. Matachewan LIP Flood Basalts

Every sample from the flood basalts studied in this project was tested with PRIMELT2.XLS. PRIMELT2.XLS is unsuccessful in obtaining primary magmas for any of the Thessalon Formation volcanic rocks studied by this project from the analyses of Tomlinson (1996). All of the Thessalon Formation volcanics sampled contain < 10 wt.% MgO and plot on positively correlated trends of MgO vs. CaO **(Fig. 4.27)**. Both of these observations are indicative of clinopyroxene fraction (Herzberg and Asimow 2008) and thus render the samples non-applicable to PRIMELT2.XLS. PRIMELT2.XLS is also unsuccessful in obtaining primary magmas for any of the Seidorechka Formation rocks directly studied by this project from the analyses of (Chashchin et al. 2008). This too is somewhat unsurprising as the majority of Seidorechka rocks (especially those with MgO < 10 wt.%) show a positive correlation of MgO vs. CaO **(Fig. 4.76)**.

The Seidorechka Formation volcanic rocks studied by Puchtel et al. (1996) were also tested with PRIMELT2.XLS. Of the eighteen samples analysed by Puchtel et al. (1996), PRIMELT2.XLS was able to calculate a primary magma for only one (sample 91113) using the accumulated fractional melting model. The primary magma predicted by PRIMELT2.XLS contains 17.04 wt.% MgO, is in equilibrium with olivine of composition $Fo_{91.5}$ and requires 31.1% melting of a mantle peridotite similar in composition to KR-4003.

5.1.2. Summary

PRIMELT2.XLS (Herzberg and Asimow 2008) is a piece of computer software that adds olivine to an evolved lava composition in incremental steps. At the same time, the software models partial melting of a peridotite source. Where the two models produce a common chemistry, the program presents the degree of mantle melting and amount of subsequent fractionation (of olivine) required to produce the evolved magma composition. PRIMELT2.XLS is only applicable to evolved lavas which have experienced olivine fractionation alone and screens the input lava compositions for clinopyroxene fractionation by examining CaO and MgO contents.

PRIMELT2.XLS was successful in calculating primary magmas for four of the 442 analyses tested by this study. These primary magmas range in MgO and SiO_2 contents between 12.2-18.7 wt.% and 46.3-49.0 wt.% respectively. The primary magmas require between 29.8-31.1% partial melting of mantle peridotite and also require a subsequent residence period in crustal magma chambers where they fractionated between 7.3-32.3% olivine before reaching the enriched compositions recorded by the lavas today.

The degrees of partial melting and fractional crystallisation predicted by PRIMELT.2XLS can be used to constrain the mantle sources of some of the Matachewan LIP suites. This is discussed in section 5.2.

5.2. Mantle Source

Based on similar ages of intrusive units (Dahl et al. 2006), comparable tectonic relationships (Vogel et al. 1998b), stratigraphic similarities in associated sedimentary sequences (Roscoe and Card 1993) and consistent palaeomagnetic properties of coeval mafic dyke swarms (Harlan 2005), igneous rocks preserved on now separate cratons have been reconstructed into the Matachewan Large Igneous Province (see chapter 2). The Matachewan LIP magmatism has been interpreted to have formed during mantle melting initiated during plume-driven continental break-up of an Archaean supercontinent (Heaman 1997; Phinney and Halls 2001; James et al. 2002; Ernst 2007; Bryan and Ernst 2008).

5.2.1. Trace Element Considerations

Paradoxically, the trace element geochemistry of the different Matachewan LIP units do not record typical “mantle plume-like” OIB signatures and instead display primitive normalised trace element signatures which are characterised by enrichments in the LILE and LREE elements relative to the HREE and negative anomalies in Nb, Ta and Ti **(Table 4.2)**. These trace element signatures are typical of igneous rocks formed in modern volcanic arc settings (Pearce and Peate 1995) where the negative anomalies in Nb and Ta are thought to be the product of either; melting in the mantle wedge occurring in the presence of residual rutile that retains Nb and Ta; dehydration of the subducting slab in the presence of rutile; or, the relative insolubility of Nb and Ta compared to the LREE during dehydration of the subducting slab. Thus, previous studies have interpreted the trace element chemistry recorded by some of the Matachewan LIP rocks to be due to formation in an arc-like environment [e.g., Van Boening 2007; Van Boening and Nabelek 2008].

The problem with such an interpretation is that, the arc-like trace element compositions shown by some of the Matachewan LIP suites which preserve only equivocal field evidence regarding their genesis (such as the Leopard dyke swarm) is shared by other Matachewan LIP rocks which preserve field evidence that precludes them having formed in an arc environment, (such as the Blue Draw Metagabbro, Matachewan radiating dyke swarm, and Huronian Supergroup flood basalts). This observation suggests that using geochemistry alone to determine the tectonic settings of igneous rocks (especially ones as ancient as those which constitute the Matachewan LIP) is inadvisable (see Wang and Glover 1992). Therefore, an alternative mechanism for the generation of trace element signatures characterised by incompatible element enrichment and negative Nb, Ta and Ti anomalies is required in order to explain the geochemistry of at least some of the Matachewan LIP suites. Such alternative explanations which have been proposed to explain similar geochemistry in other Palaeoproterozoic rocks include: the contamination of mantle melts by crustal material in deep-mid level crustal chambers, where the latent heat of crystallisation promoted melting and assimilation of the host rock [e.g., Nelson et al. 1990) or, through mixing of mantle melts with partial melts of sub-continental lithospheric mantle (SCLM) which has previously been modified by subduction-related fluids (Sandeman and Ryan 2008).

The following paragraphs attempt to determine whether the action of one of these two mechanisms (mixing of partial melts vs. crustal contamination) on primary magmas derived from a known mantle reservoir can explain the trace element compositions of the Matachewan LIP suites.

Five mantle reservoirs are modelled **(Table 5.2)**: Depleted MORB mantle (DMM), Enriched Mantle (EM1 and EM2) High-μ Mantle (HIMU) and Primitive Mantle (PM). The composition of DMM is constrained by Workman and Hart (2005) from the trace element depletion trends of abyssal peridotites. The composition of the EM1 and EM2 reservoirs is estimated from inverse modelling of the compositions of

EM1 and EM2 basalts from the Tristan da Cuhna, Gough, Samoan and Society islands (Willbold and Stracke 2006). Willbold and Stracke (2006) found that the EM1 reservoir is best modelled by a mixture of 90% DMM (Workman and Hart 2005), 1% lower continental crust (Rudnick and Gao 2003) and 9% oceanic crust, which itself is composed of 40% NMORB (Sun and McDonough 1989), 50% gabbro (Hart et al. 1999) and 10% altered NMORB (Kelley et al. 2003). The EM2 reservoir is best modelled by a mixture of 90% DMM, 9.8% oceanic crust and 0.2% upper continental crust (Rudnick and Gao 2003). The HIMU reservoir is similarly estimated from inverse modelling using the compositions of basalts from Tubuai, Mangaia and Rurutu (Chauvel et al. 1992) and can be derived from a mixture of 75% DMM and 25% NMORB. The composition of PM is derived from studies of chondritic meteorites and refractory element ratios of mantle peridotites (McDonough and Sun 1995). **Fig. 5.3** shows the Primitive Mantle-normalised trace element patterns for compositions of the five mantle reservoirs studied here. Also plotted are the trace element patterns for low degree partial melt of Archaean SCLM from beneath the Hearne craton (Cousens et al. 2001) and an estimate of the composition of the bulk continental crust (Rudnick and Gao 2003).

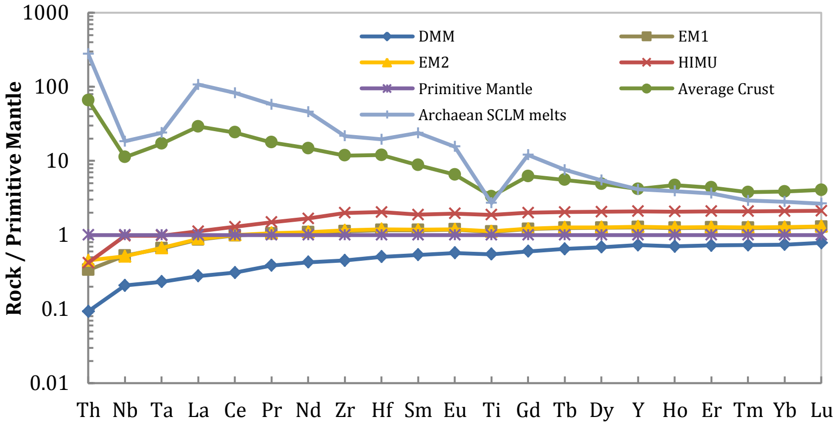

Fig. 5.3. Primitive Mantle-normalised multi element diagrams showing trace element compositions of end members modelled in this study. Data presented in **Table 5.2**.

5.2.1.1. Crustal Contamination

Crustal contamination was modelled for the Matachewan suites using samples for which PRIMELT2.XLS was able to successfully calculate primary magma compositions. The degree of partial melting predicted by PRIMELT2.XLS for the solution-yielding samples was modelled using non-modal batch melting **(Equation**

5.1) after Shaw (1970) for spinel lherzolites from the five different mantle reservoirs. Spinel lherzolite was chosen for the models as all of the Matachewan LIP suites have relatively flat HREE patterns (see chapter 4) which indicates that either, mantle melting occurred in the spinel stability field, or that, if melting occurred deeper, it melted all of the garnet in the source. The mineral modes for spinel lherzolite and derived partial melts are taken from Johnson et al. (1990) and are shown in **Table 5.3**. Contamination of partial melts derived from these reservoirs was modelled using the AFC equation **(Equation 5.2 and 5.3)** of DePaolo (1981), the average continental crust composition of Rudnick (2003) and the degrees of fractionation predicted by PRIMELT2.XLS **(Table 5.1)**.

Element (ppm)	DMM	EM1	EM2	HIMU	PM	Bulk cont. crust	Archaean SCLM melt
Th	0.01	0.03	0.04	0.04	0.09	5.60	23.57
Nb	0.15	0.38	0.37	0.69	0.71	8.00	13.09
Ta	0.01	0.03	0.03	0.04	0.04	0.70	0.98
La	0.19	0.60	0.61	0.77	0.69	20.00	73.63
Ce	0.55	1.75	1.77	2.29	1.78	43.00	147.08
Pr	0.11	0.29	0.29	0.41	0.28	4.90	15.94
Nd	0.58	1.47	1.48	2.26	1.35	20.00	62.28
Zr	5.00	13.00	13.00	22.00	11.00	132.00	243.00
Hf	0.16	0.36	0.37	0.63	0.31	3.70	6.04
Sm	0.24	0.52	0.52	0.84	0.44	3.90	10.57
Eu	0.10	0.20	0.20	0.33	0.17	1.10	2.62
Ti	716	1433	1457	2437	1300	4316	3513
Gd	0.36	0.72	0.73	1.19	0.60	3.70	7.17
Tb	0.07	0.13	0.14	0.22	0.11	0.60	0.82
Dy	0.51	0.92	0.94	1.52	0.74	3.60	4.05
Y	3.33	5.77	5.88	9.50	4.55	19.00	18.79
Ho	0.12	0.20	0.21	0.34	0.16	0.77	0.64
Er	0.35	0.60	0.61	1.00	0.48	2.10	1.75
Tm	0.05	0.09	0.09	0.15	0.07	0.28	0.22
Yb	0.37	0.62	0.63	1.04	0.49	1.90	1.39
Lu	0.06	0.10	0.10	0.16	0.07	0.30	0.20

Table 5.2. Trace element compositions of mantle end members modelled. See text for data sources.

$$C^{i}_{liq} = \frac{C^{i}_{S}}{D + F - FP}$$

Equation 5.1

Where $\mathrm{C}^{i}_{\mathrm{liq}}$ = the concentration of element *i* in the melt, $\mathrm{C}^{i}_{\mathrm{S}}$ = the concentration of element *i* in the source, D = the bulk distribution coefficient in the source when melting begins, F = the fraction of melting experienced by the source, and P = the bulk distribution coefficient of the minerals in the partial melt.

$$\frac{C_{liq}^{i}}{C_{0}^{i}} = f^{-z} + \left(\frac{r}{r-1}\right)\frac{C_{ass}^{i}}{zC_{0}^{i}}\left(1 - f^{-z}\right)$$

Equation 5.2

$$z = \frac{r - 1 + D^{i}}{r - 1}$$

Equation 5.3

Where C_0^i = the concentration of element *i* in the parent liquid; C_{ass}^i = the concentration of element *i* in the assimilant; *f* = the residual parent liquid fraction; D^i = the bulk partition coefficient for element *i*; and *r* = the rate of assimilation/fractional crystallisation.

	Olivine	Orthopyroxene	Clinopyroxene	Spinel
Spinel lherzolite	0.55	0.25	0.18	0.02
Partial melt	0.10	0.20	0.67	0.02

Table 5.3. Mineral modes for spinel lherzolite and partial melts. Taken from Johnson et al. (1990).

PRIMELT2.XLS predicts that; Leopard dyke BR4C formed from a magma derived by 29.8% partial melting of mantle peridotite which subsequently underwent 22.37% olivine fractionation; Leopard dyke NBH13A formed from a magma derived by 29.9% partial melting which underwent 31.38% olivine fractionation; Seidorechka Formation basalt 91113 formed from a magma derived by 31.1% partial melting which underwent 7.31% olivine fractionation; and, East Bull Lake Suite feeder dyke 234 formed from a magma derived from 30.3% partial melting which fractionated 32.32% olivine **(Table 5.1)**.

Figures 5.4-5.7 show the Primitive Mantle-normalised multi-element patterns for the four samples (91113, 234, NBH13A and BR4C) for which PRIMELT2.XLS was able to define partial melting and fractionation parameters. Also plotted are the compositions of magmas formed via AFC of primary magmas derived from melting of spinel lherzolites from the DMM, EM1, EM2, HIMU and PM mantle reservoirs using the parameters of melting and fractionation stated above (see **Table 5.1**). **Figures 5.4-5.7** show that with larger amounts or higher rates of AFC, primary mantle melts from any of the reservoirs studied can form magmas which record the general shape of the Primitive Mantle-normalised trace element geochemistry observed in samples 91113, BR4C, NBH13A and 234 (negative Nb-Ta and Ti anomalies and LILE-LREE enrichment relative to the HREE). However, none of the models presented adequately replicate the trace element chemistry observed in the four samples. For the Seidorechka Formation basalt sample 91113, all of the models predict lower La/Sm ratios and much higher HREE contents than those observed in the sample. For the two Leopard dyke samples, the models which use higher rates of

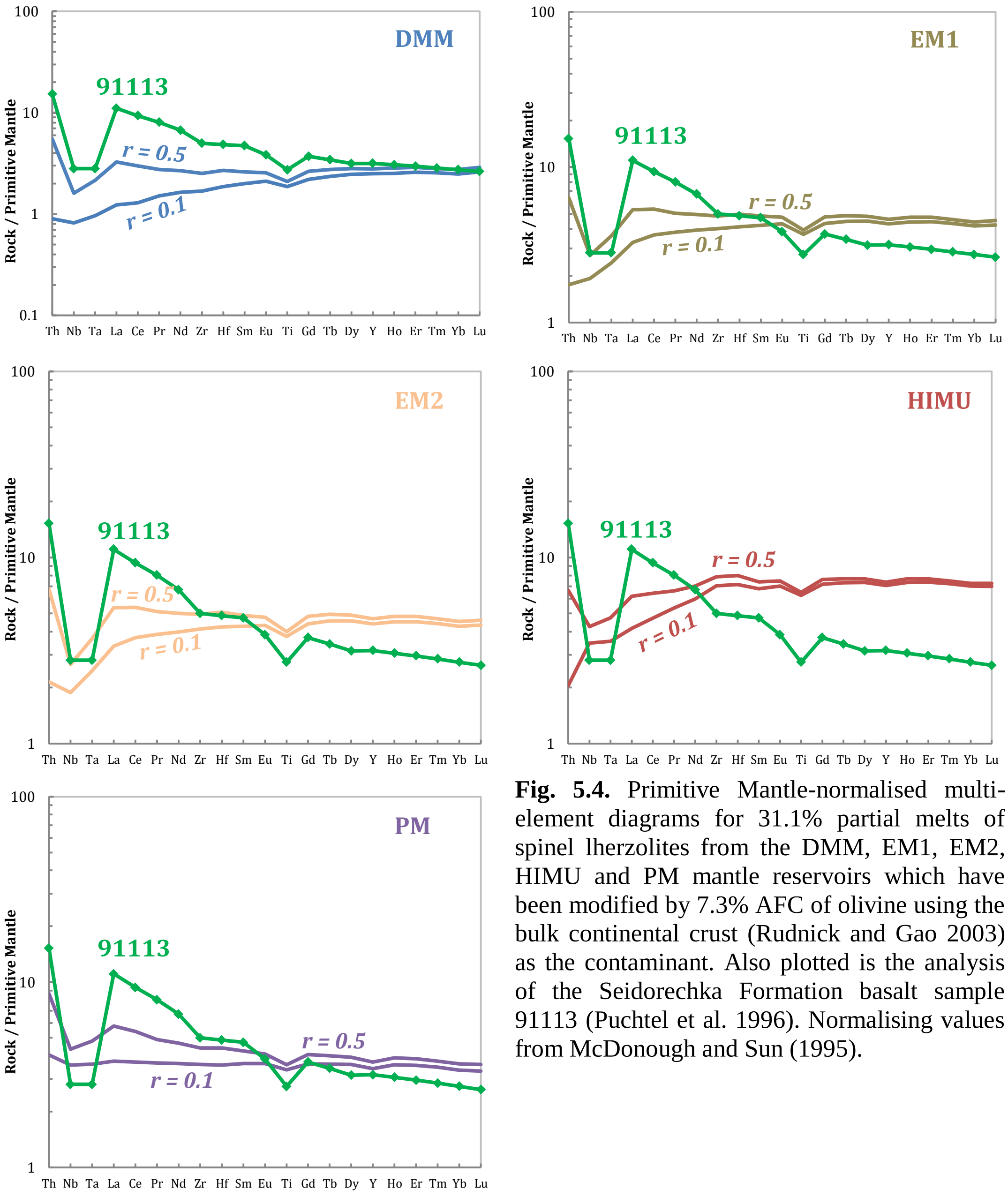

Fig. 5.4. Primitive Mantle-normalised multi-element diagrams for 31.1% partial melts of spinel lherzolites from the DMM, EM1, EM2, HIMU and PM mantle reservoirs which have been modified by 7.3% AFC of olivine using the bulk continental crust (Rudnick and Gao 2003) as the contaminant. Also plotted is the analysis of the Seidorechka Formation basalt sample 91113 (Puchtel et al. 1996). Normalising values from McDonough and Sun (1995).

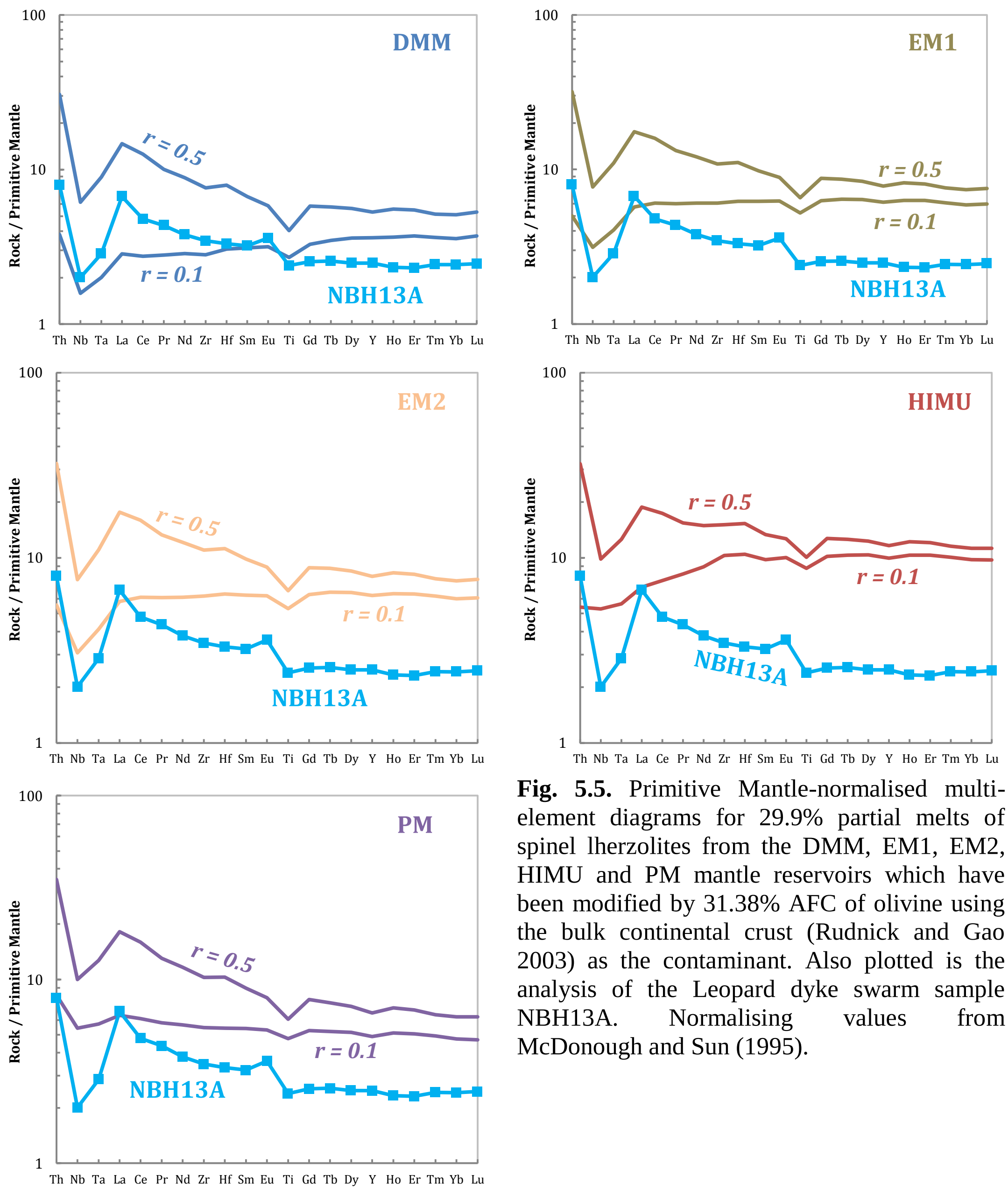

Fig. 5.5. Primitive Mantle-normalised multi-element diagrams for 29.9% partial melts of spinel lherzolites from the DMM, EM1, EM2, HIMU and PM mantle reservoirs which have been modified by 31.38% AFC of olivine using the bulk continental crust (Rudnick and Gao 2003) as the contaminant. Also plotted is the analysis of the Leopard dyke swarm sample NBH13A. Normalising values from McDonough and Sun (1995).

assimilation/fractionation predict Primitive Mantle-normalised patterns most similar in shape to the dykes, with similar La/Sm and Gd/Yb ratios and similarly sized Nb-Ta and Ti anomalies. However, the models predict magmas with trace element abundances at least twice that observed in the dykes. For the East Bull Lake Suite feeder dyke sample 234 all of the models predict much greater abundances of HREE than is recorded by the sample.

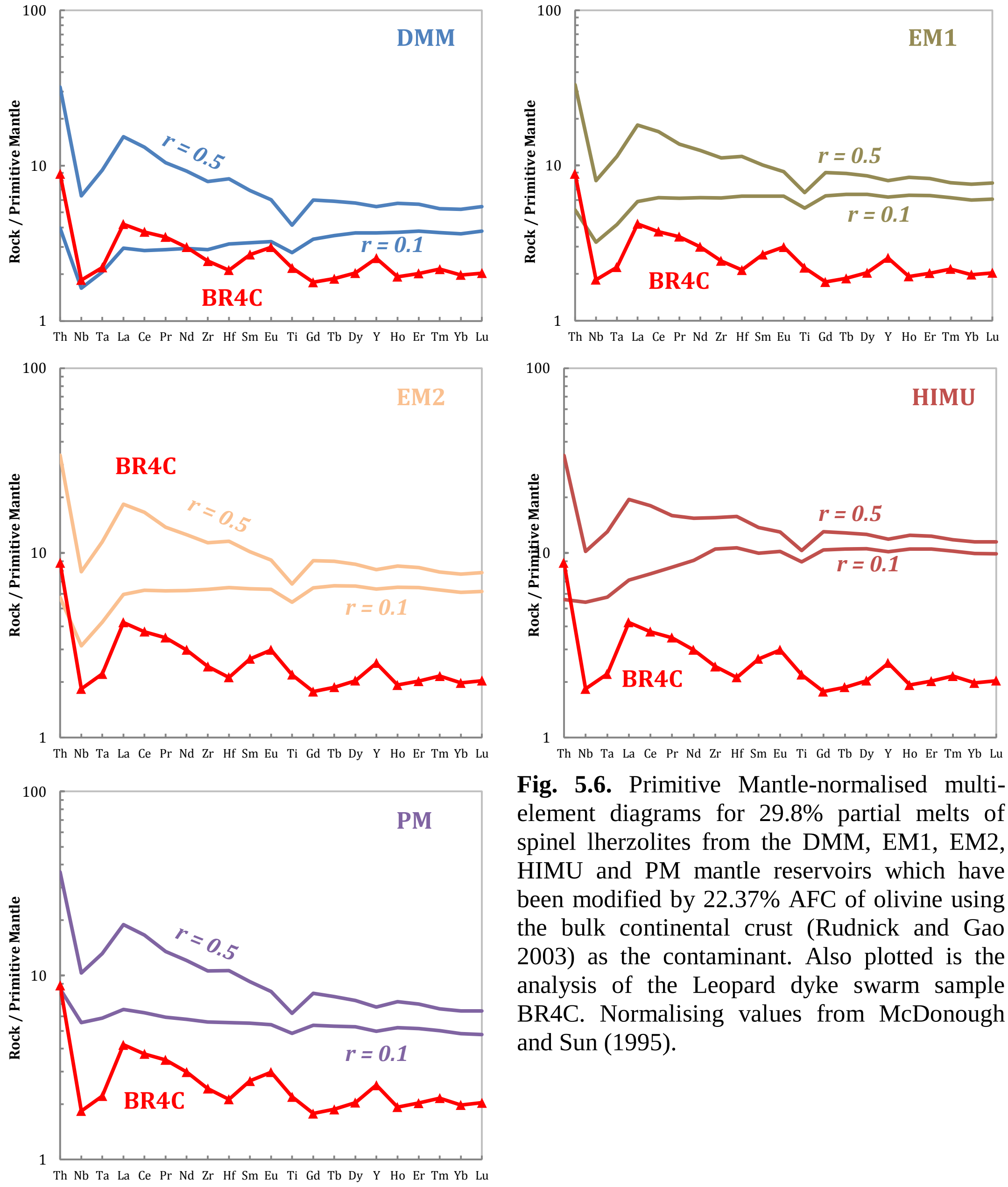

Fig. 5.6. Primitive Mantle-normalised multi-element diagrams for 29.8% partial melts of spinel lherzolites from the DMM, EM1, EM2, HIMU and PM mantle reservoirs which have been modified by 22.37% AFC of olivine using the bulk continental crust (Rudnick and Gao 2003) as the contaminant. Also plotted is the analysis of the Leopard dyke swarm sample BR4C. Normalising values from McDonough and Sun (1995).

5.2.1.2. Magma Mixing

To determine whether mixing of primary mantle melts with low degree partial melts of subduction-modified SCLM is a better mechanism for explaining the trace element composition of the Matachewan LIP suites [as suggested by Sandeman and Ryan (2008)], several models have been constructed. These models mix the primary mantle melts derived from the five different mantle reservoirs shown in **Table 5.2** with varying amounts of low degree partial melts of subduction-modified SCLM using a simple binary mixing equation **(Equation 5.4)**. Fractionation of olivine from the resulting mixtures was then modelled to the degree predicted by PRIMELT2.XLS using the equation for fractional crystallisation **(Equation 5.5)**.

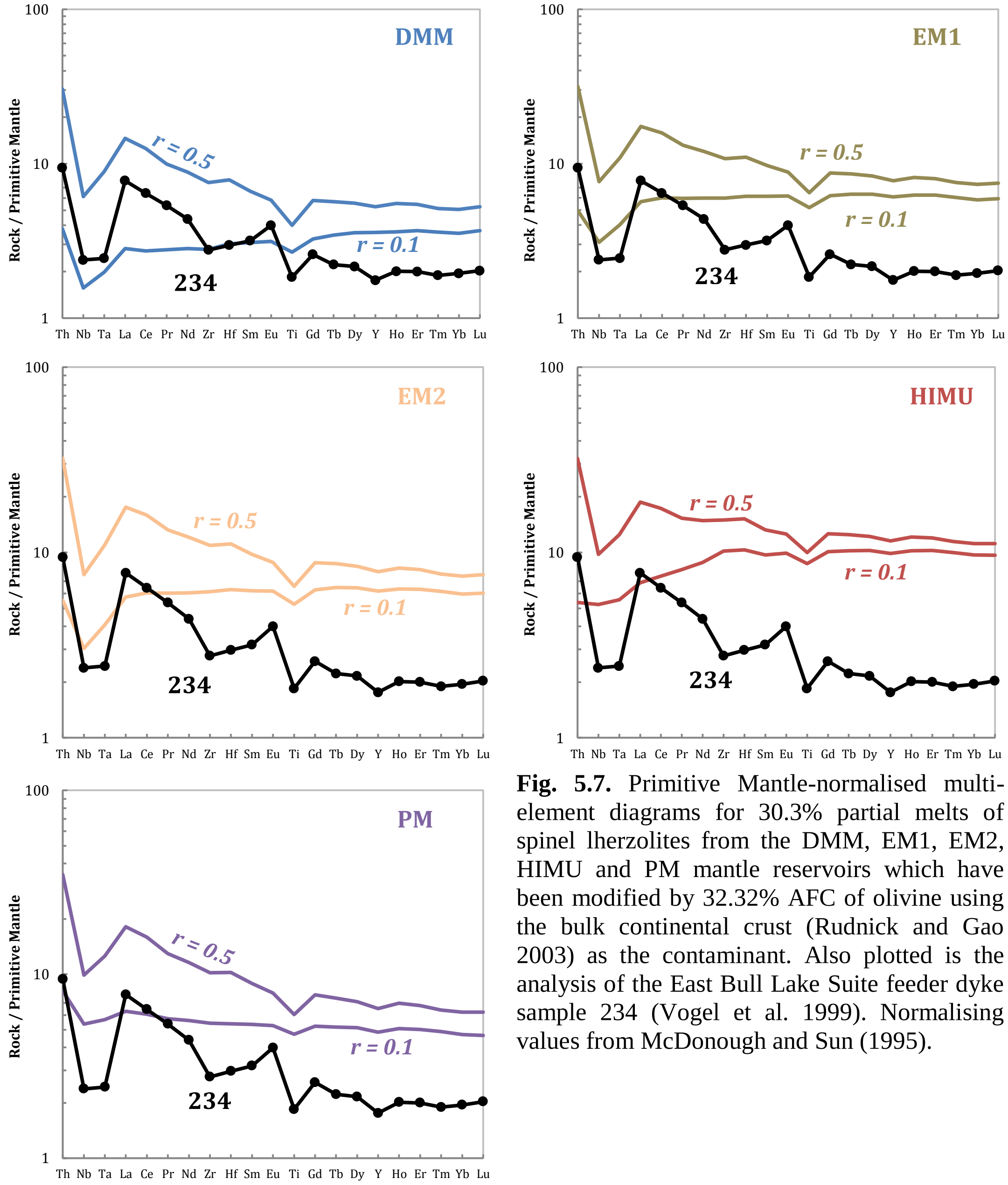

Fig. 5.7. Primitive Mantle-normalised multi-element diagrams for 30.3% partial melts of spinel lherzolites from the DMM, EM1, EM2, HIMU and PM mantle reservoirs which have been modified by 32.32% AFC of olivine using the bulk continental crust (Rudnick and Gao 2003) as the contaminant. Also plotted is the analysis of the East Bull Lake Suite feeder dyke sample 234 (Vogel et al. 1999). Normalising values from McDonough and Sun (1995).

The estimate for partial melts of the subduction-modified SCLM was taken from an average of 113 analyses of ultrapotassic rocks of the Christopher Island Formation (Sandeman et al. 2003, unpublished data). The Christopher Island Formation of the Baker Lake Group are minette-lamproite lavas and dykes which are preserved on the Hearne craton, Nunavut. Despite being significantly younger (~1.88 Ga) than the Matachewan LIP magmatism, Sandeman and Ryan (2008) and Cousens et al. (2001)

argue that the rocks of the Christopher Island Formation represent low degree partial melts of a subcontinental lithospheric mantle source which developed beneath the Hearne and Superior cratons during the Archaean and was thus, an available source for the Palaeoproterozoic Matachewan LIP magmatism. Three different models that mix low degree partial melts of subduction modified SCLM with the primary mantle melts in the proportions 0.1-5 : 99.9-95 before fractionation olivine from the mixture to the degree shown in **Table 5.1** are shown in **Figures 5.8-5.11**.

$$C_L = (C_{M1} \times x) + (C_{M2} \times (1 - x))$$

Equation 5.4

Where C_L = concentration of element in mixture, C_{M1} = concentration of element in melt 1, C_{M2} = concentration of element in melt 2, x = proportion of melt 1 in mixture.

$$\mathrm{C}^i_{liq} = \mathrm{C}^i_0 f^{D^i - 1}$$

Equation 5.5

Where C^i_{liq} = concentration of element i in the evolving liquid, C^i_0 = concentration of element i in the parent magma, f = the residual parent liquid fraction; D^i = the bulk partition coefficient for element *i*.

Figs. 5.8-5.11 show that the mixing of partial melts from the five modelled mantle reservoirs with small amounts (~5%) of low degree partial melt from subduction modified SCLM is a viable mechanism in producing the general trace element signature observed in the Matachewan LIP rocks (LREE enrichment relative to HREE, significant negative Nb-Ta and Ti anomalies). However, like the AFC models **(Figs. 5.8-5.11)** the SCLM mixing models predict HREE concentrations that are at least 2-3× higher than that observed in the samples for the EM1, EM2, HIMU and PM mantle reservoirs. Mixtures of low degree SCLM partials melts with DMM partial melts also predict HREE abundances higher than those observed in the NBH13A, BR4C and 234 samples. In contrast to these three samples, the trace element chemistry of Seidorechka Formation sample 91113 (Puchtel et al. 1996), can be closely approximated by a mixture of ~8% SCLM partial melt and 92% DMM partial melt.

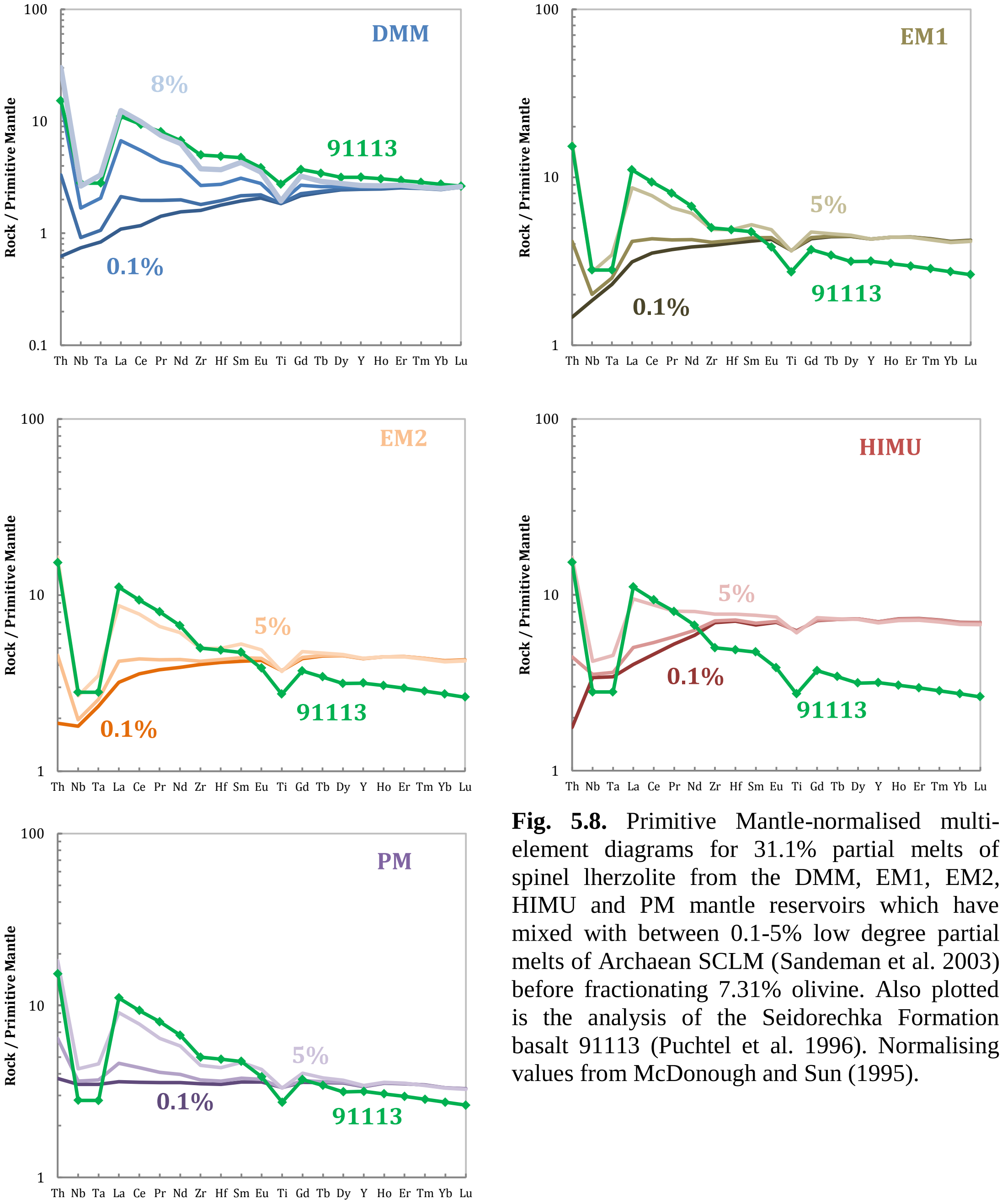

Fig. 5.8. Primitive Mantle-normalised multi-element diagrams for 31.1% partial melts of spinel lherzolite from the DMM, EM1, EM2, HIMU and PM mantle reservoirs which have mixed with between 0.1-5% low degree partial melts of Archaean SCLM (Sandeman et al. 2003) before fractionating 7.31% olivine. Also plotted is the analysis of the Seidorechka Formation basalt 91113 (Puchtel et al. 1996). Normalising values from McDonough and Sun (1995).

5.2.1.3. Two-stage Melting

The models described above attempt to determine whether the trace element signatures observed in the Matachewan LIP suites are better explained by contamination of primary magmas by crustal material during fractionation of the magma in lower crustal bodies; or, through mixing of primary magmas with low-degree partial melts of subduction modified SCLM. The models show that the two mechanisms can produce evolved magmas with chondrite-normalised trace element chemistries characterised by LILE and LREE enrichment relative to the HREE, and

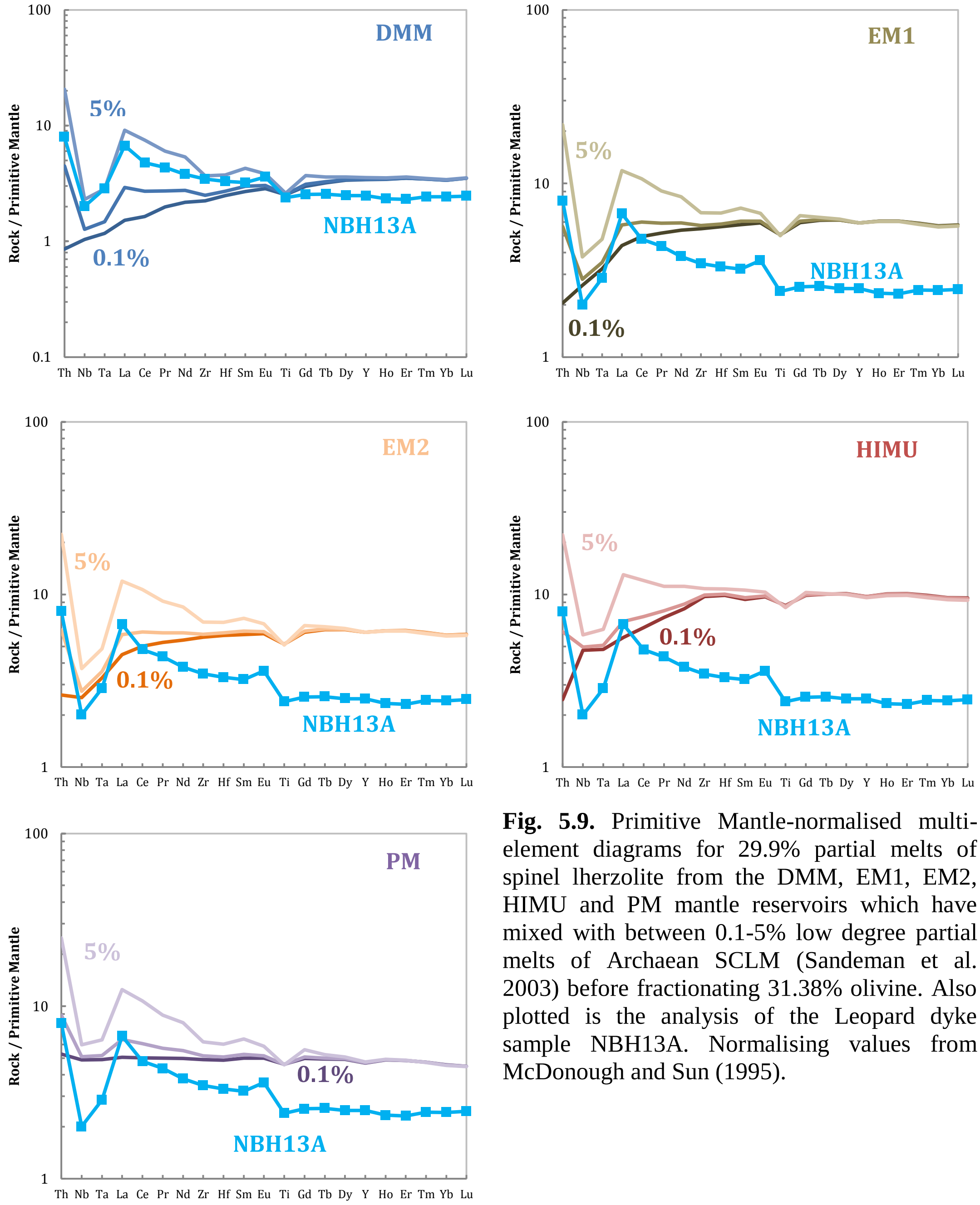

Fig. 5.9. Primitive Mantle-normalised multi-element diagrams for 29.9% partial melts of spinel lherzolite from the DMM, EM1, EM2, HIMU and PM mantle reservoirs which have mixed with between 0.1-5% low degree partial melts of Archaean SCLM (Sandeman et al. 2003) before fractionating 31.38% olivine. Also plotted is the analysis of the Leopard dyke sample NBH13A. Normalising values from McDonough and Sun (1995).

large, negative Nb-Ta anomalies, similar to the Matachewan LIP suites studied. However, for all samples except Seidorechka Formation basalt 91113 (the composition of which can be replicated by a mixture of ~8% SCLM partial melt and 92% DMM partial melt) both sets of models over-estimate the abundance of the HREE in the samples studied by a factor of ≥3. This overestimation stems from the fact that the ~30% partial melting predicted by PRIMELT2.XLS for these three samples produces primary magmas with higher abundances of HREE than the samples studied, irrespective of the mantle source modelled **(Fig. 5.12)**. Modelling suggests that in order to produce primary magmas with the HREE contents observed in the samples (~5.5x chondritic values), partial melting of the DMM spinel lherzolite modelled would need to exceed ~45%. Simply speaking, the problem is that the HREE abundances observed in samples NBH13A, BR4C and 234 cannot be obtained through melting the modelled mantle sources, to the degrees predicted by PRIMELT2.XLS.

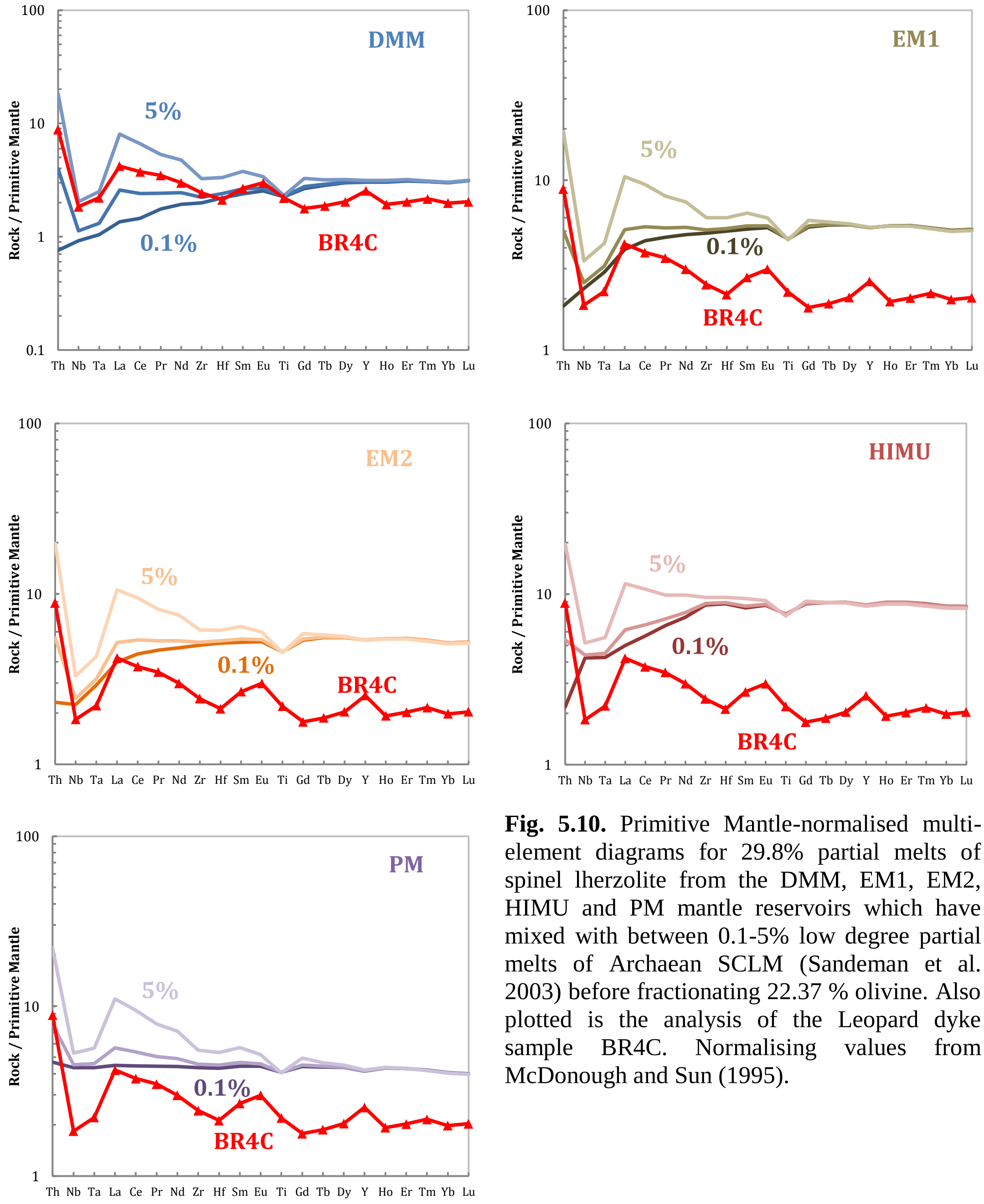

Fig. 5.10. Primitive Mantle-normalised multi-element diagrams for 29.8% partial melts of spinel lherzolite from the DMM, EM1, EM2, HIMU and PM mantle reservoirs which have mixed with between 0.1-5% low degree partial melts of Archaean SCLM (Sandeman et al. 2003) before fractionating 22.37 % olivine. Also plotted is the analysis of the Leopard dyke sample BR4C. Normalising values from McDonough and Sun (1995).

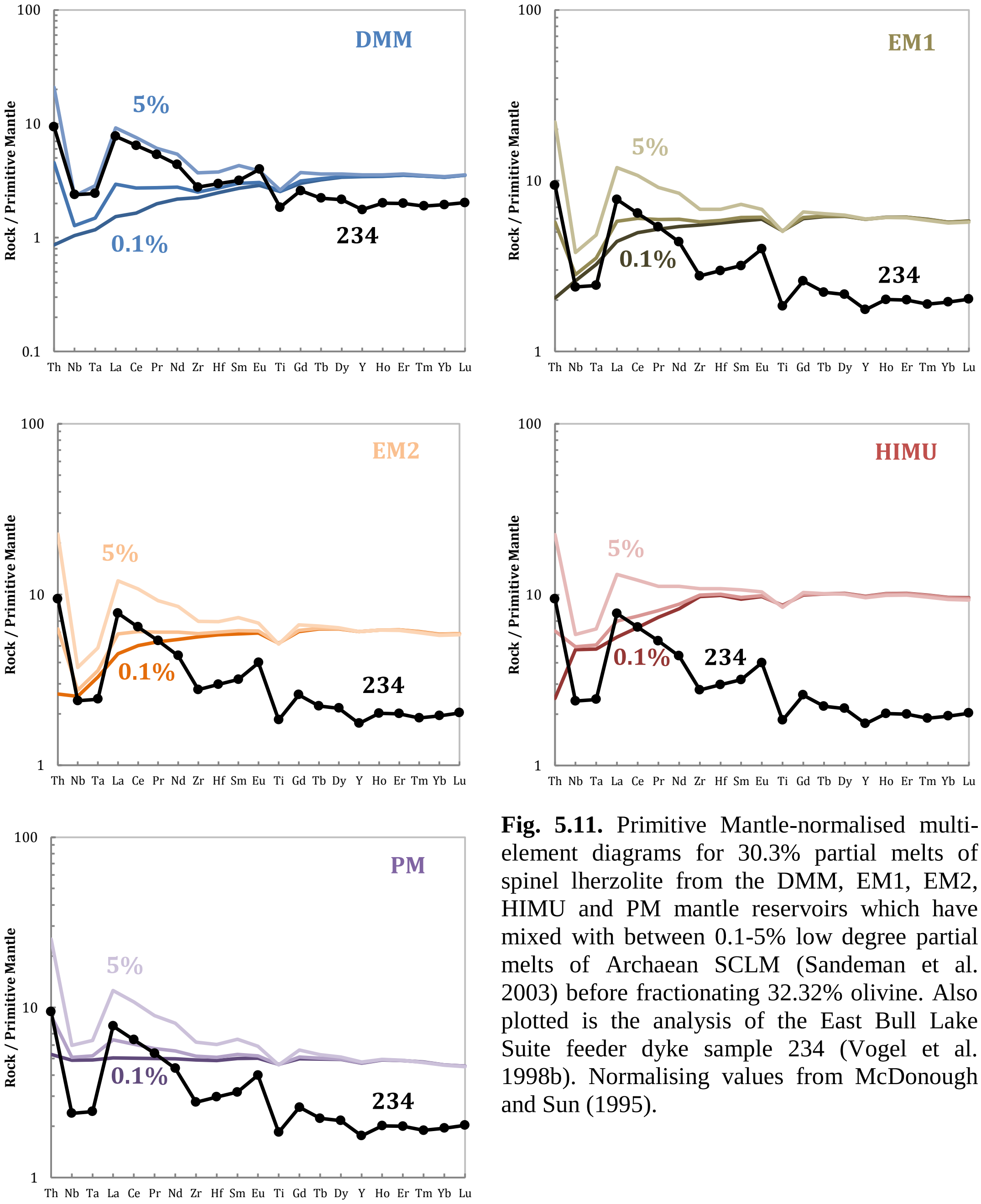

Fig. 5.11. Primitive Mantle-normalised multi-element diagrams for 30.3% partial melts of spinel lherzolite from the DMM, EM1, EM2, HIMU and PM mantle reservoirs which have mixed with between 0.1-5% low degree partial melts of Archaean SCLM (Sandeman et al. 2003) before fractionating 32.32% olivine. Also plotted is the analysis of the East Bull Lake Suite feeder dyke sample 234 (Vogel et al. 1998b). Normalising values from McDonough and Sun (1995).

Thus, if we assume that the mantle reservoirs modelled are applicable to the ~2.48 Ga Matachewan LIP suites, then the degrees of melting predicted by PRIMELT2.XLS are too low. As PRIMELT2.XLS calculates degree of melting by examination of FeO and MgO concentrations, a potential source of error in the calculation may be caused by sub-solidus remobilisation of these elements. However, in the case of the Leopard dykes, FeO and MgO record very strong ($r^2 > 0.9$) linear correlations with Zr **(Fig. 4.46)**, indicating that the concentrations have not been significantly affected by post-magmatic alteration events.

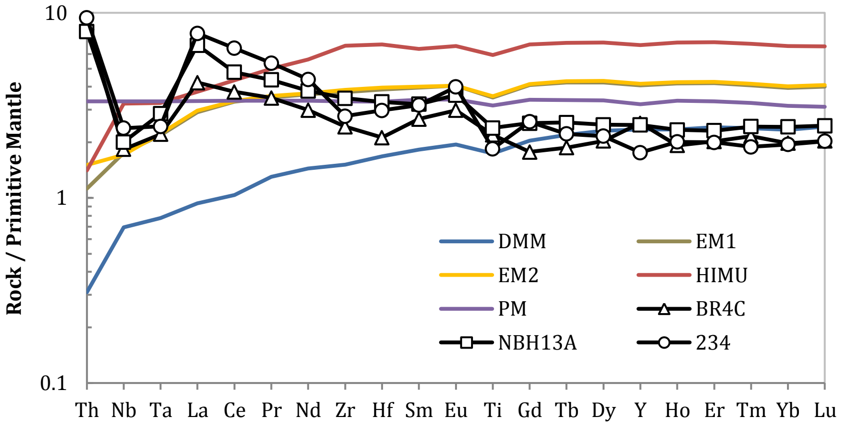

Fig. 5.12. Primitive Mantle-normalised multi element diagrams showing trace element compositions of 30% partial melts of spinel lherzolites from the DM, EM1, EM2, HIMU and PM mantle end members modelled in this study. Normalising values from McDonough and Sun (1995).

The second explanation for the poor fit of the models in terms of HREE abundances is that, if we assume that the degrees of partial melting predicted by PRIMELT2.XLS are correct then the trace element compositions mantle reservoirs modelled are not representative of the sources available to the Matachewan LIP magmatism. The inference being that the Matachewan LIP mantle source was more depleted than any of those modelled.

The presence of a strongly depleted mantle source available for the Matachewan LIP magmatism may be inferred by the presence of the ~2.7 Ga greenstone belts (including the Abitibi and Ennadai-Rankin belts of the Superior and Hearne cratons) which host many of the Matachewan LIP suites. These greenstone belts contain large amounts of komatiitic lavas which have been interpreted by Sproule et al. (2002) to have formed through ~30% partial melting of the mantle. This partial melting event would have depleted the mantle source in incompatible elements such that any further melting events from the source would produce melts with much lower incompatible element contents than those which formed the komatiitic lavas of the greenstone belts. If such a residual mantle source persisted beneath the Superia supercontinent (Bleeker 2003) from its formation at ~2.7 Ga to the period of melting which formed the Matachewan LIP magmas at ~2.48 Ga, it may have been a compositional source for the Matachewan LIP magmatism.

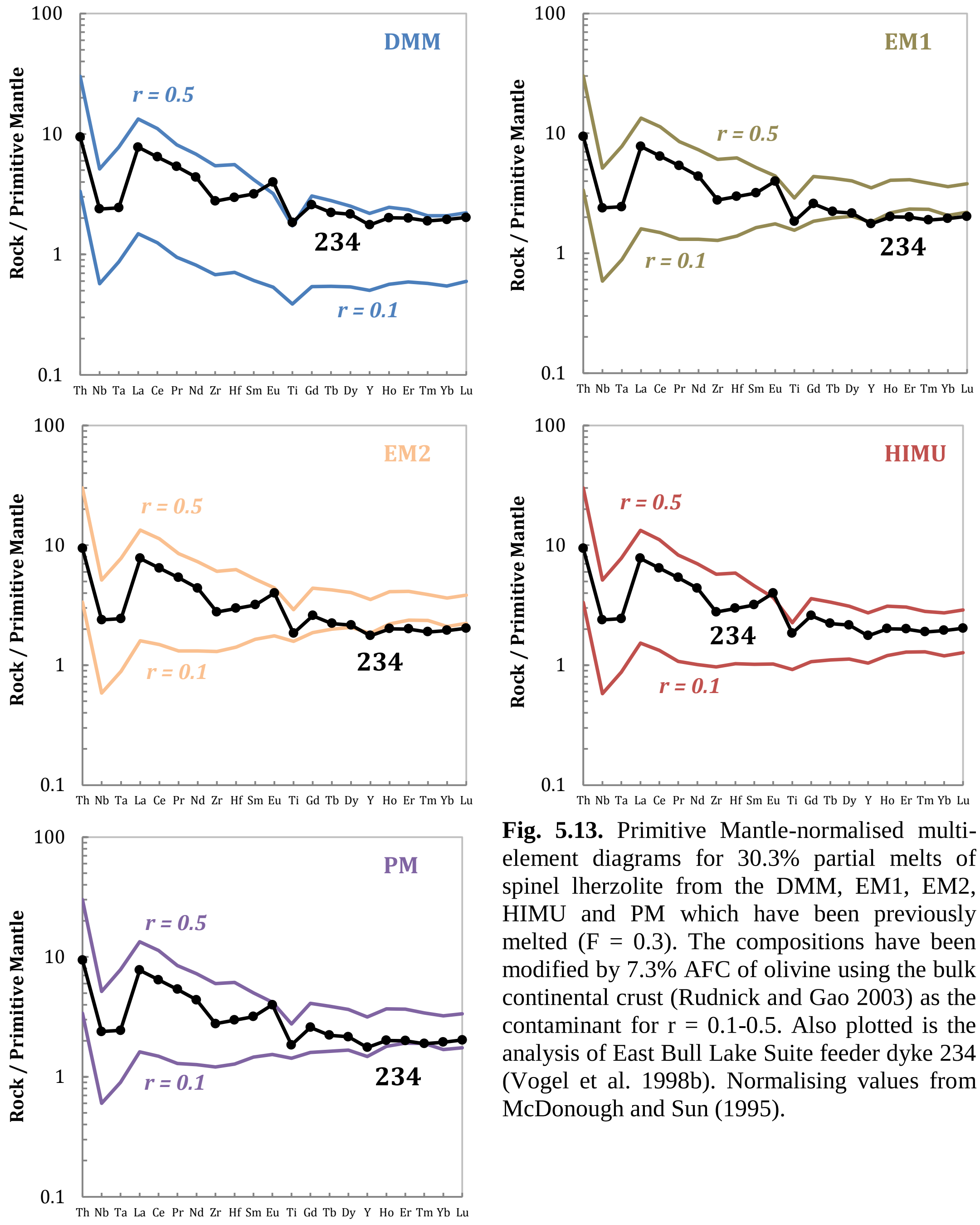

Fig. 5.13. Primitive Mantle-normalised multi-element diagrams for 30.3% partial melts of spinel lherzolite from the DMM, EM1, EM2, HIMU and PM which have been previously melted (F = 0.3). The compositions have been modified by 7.3% AFC of olivine using the bulk continental crust (Rudnick and Gao 2003) as the contaminant for r = 0.1-0.5. Also plotted is the analysis of East Bull Lake Suite feeder dyke 234 (Vogel et al. 1998b). Normalising values from McDonough and Sun (1995).

To test whether melting of such a depleted source is a potential mechanism for producing the trace element compositions observed in the Matachewan LIP suites, models similar to those shown in **Figures 5.4-5.7** were constructed, this time using trace element composition of residues of DMM, EM1, EM2, HIMU and PM spinel lherzolite formed by ~30% batch partial melting as suggested by Sproule et al. (2002) and Maier et al. (2003). The compositions of these residues are determined using **Equation 5.6** and are shown in **Table 5.4**.

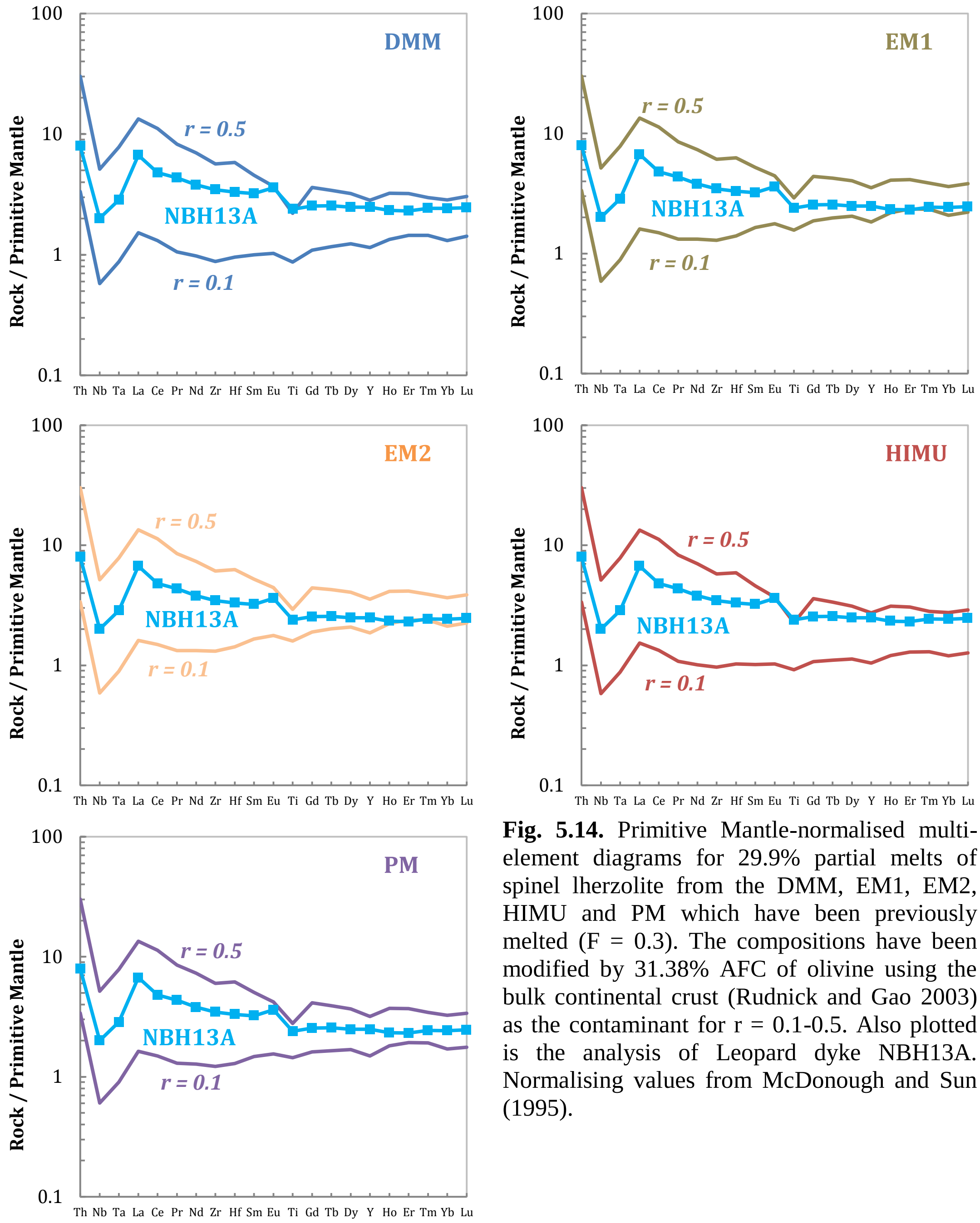

Fig. 5.14. Primitive Mantle-normalised multi-element diagrams for 29.9% partial melts of spinel lherzolite from the DMM, EM1, EM2, HIMU and PM which have been previously melted (F = 0.3). The compositions have been modified by 31.38% AFC of olivine using the bulk continental crust (Rudnick and Gao 2003) as the contaminant for r = 0.1-0.5. Also plotted is the analysis of Leopard dyke NBH13A. Normalising values from McDonough and Sun (1995).

AFC models which use partial melts of these previously-melted reservoirs in the same way as those shown in **Figs. 5.4-5.7** show that such a mechanism is capable of producing the trace element geochemistry of the Matachewan LIP suites modelled using several different starting reservoirs. The models show that East Bull Lake Suite feeder dyke 234 could well have been derived from a previously-melted HIMU or DMM source which was contaminated by continental crust with an assimilation/fractionation ratio of ~0.4-0.5 **(Fig. 5.13)**. Sample 234 is less likely to have been derived from a previously melted EM or PM reservoir as sample 234 records a La/Sm$_N$ ratio higher than those predicted by the model for these reservoirs. The two Leopard dyke samples are similar to sample 234 in that they exhibit La/Sm$_N$ ratios too high to have been derived from a previously-melted EM reservoir, but may have been sourced from previously melted DMM, HIMU or PM spinel lherzolites which were contaminated by continental crust with an assimilation/fractionation ratio of ~0.4 **(Figs. 5.14 and 5.15)**.

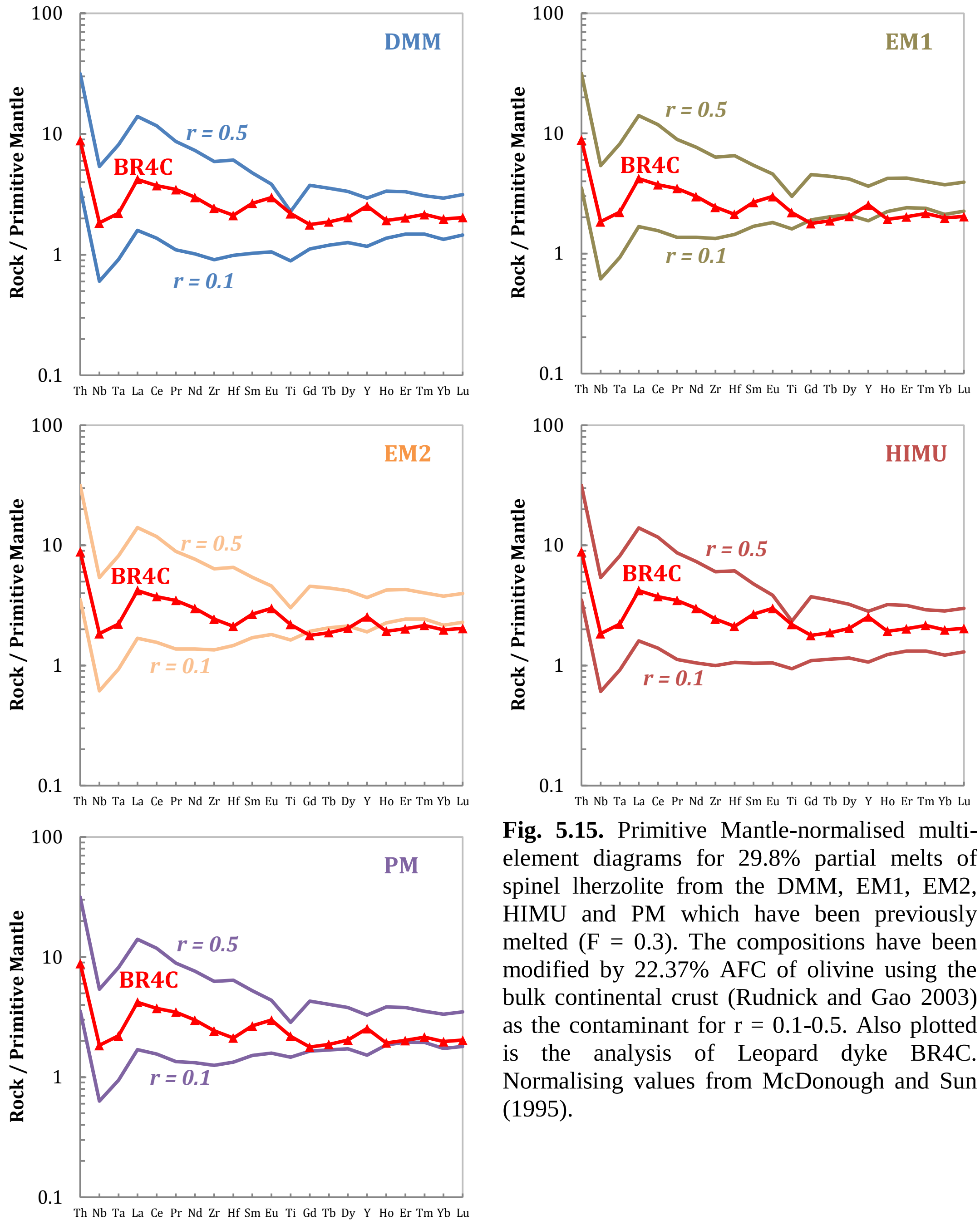

Fig. 5.15. Primitive Mantle-normalised multi-element diagrams for 29.8% partial melts of spinel lherzolite from the DMM, EM1, EM2, HIMU and PM which have been previously melted (F = 0.3). The compositions have been modified by 22.37% AFC of olivine using the bulk continental crust (Rudnick and Gao 2003) as the contaminant for r = 0.1-0.5. Also plotted is the analysis of Leopard dyke BR4C. Normalising values from McDonough and Sun (1995).

$$\frac{C_S^i}{C_0^i} = \frac{D^i}{D^i + F(1 - D^i)}$$

Equation 5.6

Where C_S^i = concentration of element *i* in the residue, C_0^i = concentration of element *i* in the original source, D^i = the bulk partition coefficient for element *i*; and *F* = the degree of melting.

Element (ppm)	**C_S DMM** **F = 0.3**	**C_S EM1** **F = 0.3**	**C_S EM2** **F = 0.3**	**C_S HIMU** **F = 0.3**	**C_S PM** **F = 0.3**
Th	0.00008	0.00027	0.00037	0.00034	0.00081
Nb	0.00100	0.00260	0.00250	0.00470	0.00480
Ta	0.00007	0.00018	0.00019	0.00027	0.00028
La	0.00600	0.01800	0.01800	0.02300	0.02000
Ce	0.02900	0.09400	0.09500	0.12200	0.09500
Pr	0.00900	0.02300	0.02400	0.03300	0.02200
Nd	0.06200	0.15700	0.15900	0.24200	0.14500
Zr	0.64300	1.58900	1.63400	2.82400	1.41800
Hf	0.02200	0.05100	0.05200	0.08900	0.04400
Sm	0.05000	0.10700	0.10800	0.17400	0.09200
Eu	0.02300	0.04900	0.04900	0.08000	0.04100
Ti	198	396	403	674	360
Gd	0.09300	0.18700	0.18900	0.31000	0.15600
Tb	0.01900	0.03700	0.03800	0.06100	0.03000
Dy	0.14800	0.27000	0.27500	0.44500	0.21600
Y	0.91100	1.58000	1.61100	2.60000	1.24600
Ho	0.03700	0.06600	0.06700	0.10900	0.05300
Er	0.12200	0.21200	0.21500	0.35300	0.16900
Tm	0.02000	0.03400	0.03400	0.05600	0.02700
Yb	0.12100	0.20400	0.20800	0.34300	0.16300
Lu	0.02000	0.03300	0.03400	0.05500	0.02600

Table 5.4. Trace element compositions of mantle end members modelled in this study following 30% batch partial melting of spinel lherzolite. See text for sources of data.

Models which mix partial melts of Archaean SCLM with partial melts of these previously-melted reservoirs in the same way as those shown in **Figs. 5.4-5.7** also show that this mechanism is capable of producing the trace element geochemistry of the Matachewan LIP suites modelled using several different starting reservoirs **(Figs. 5.16-5.18)**. The trace element geochemistry recorded by the two Leopard dykes and the East Bull Lake Suite feeder dyke is not compatible with derivation from a previously-melted DMM or HIMU source as mixing of partial melts from these two reservoirs with low degree partial melts of Archaean SCLM do not yield mixtures with the observed HREE contents or La/Yb ratios. Alternatively, East Bull Lake Suite feeder dyke 234 may have been derived from mixing of melts of previously-melted enriched or Primitive Mantle source with low degree partial melts of Archaean SCLM in the ratio of ~19:1.

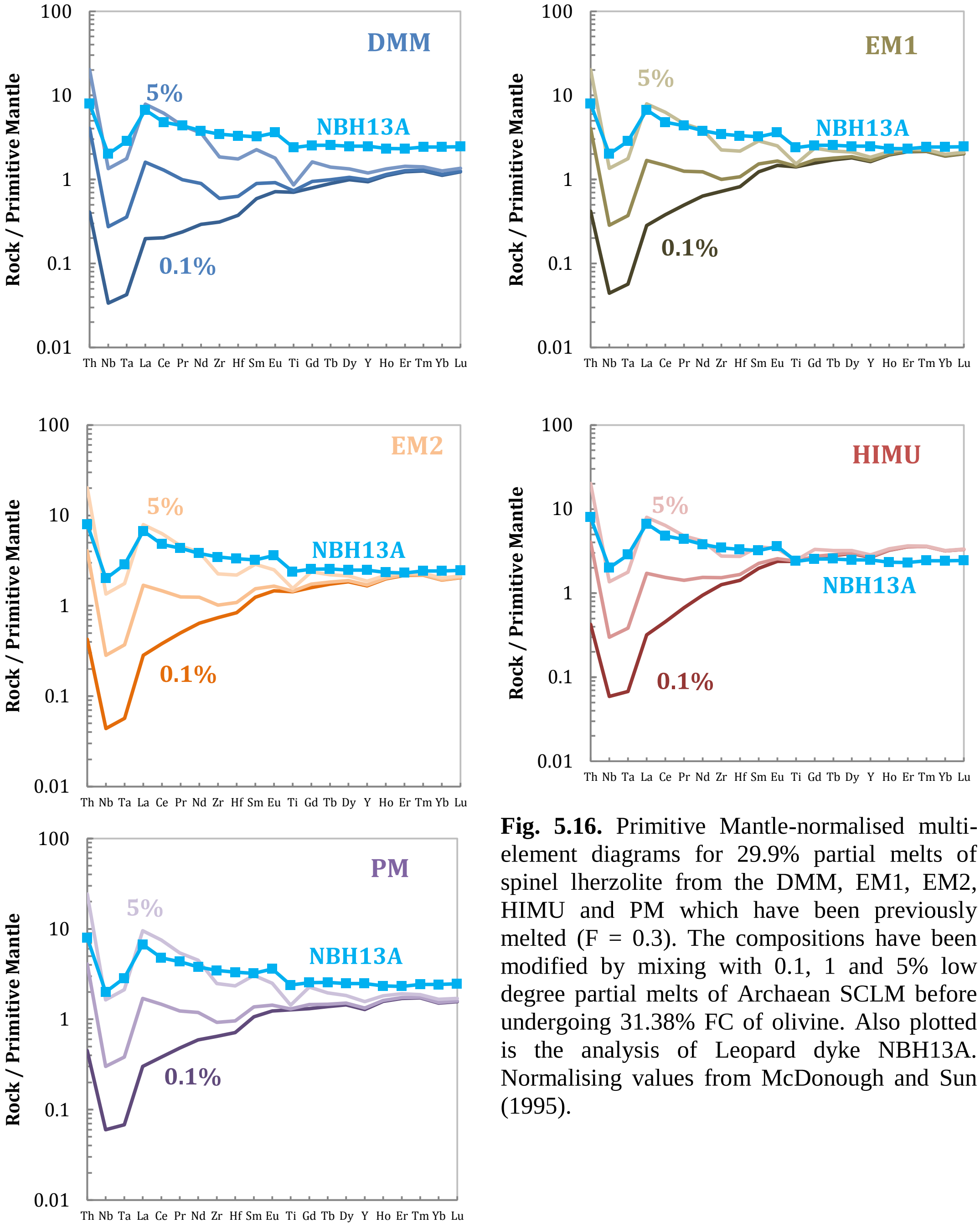

Fig. 5.16. Primitive Mantle-normalised multi-element diagrams for 29.9% partial melts of spinel lherzolite from the DMM, EM1, EM2, HIMU and PM which have been previously melted (F = 0.3). The compositions have been modified by mixing with 0.1, 1 and 5% low degree partial melts of Archaean SCLM before undergoing 31.38% FC of olivine. Also plotted is the analysis of Leopard dyke NBH13A. Normalising values from McDonough and Sun (1995).

5.2.1.4. Summary

Trace element modelling of the Matachewan LIP suites for which PRIMELT2.XLS could calculate the degree of partial melting and subsequent fractionation has been carried out in order to determine the most likely mantle sources for the magmatism. The modelling has shown that both AFC and magma mixing are potential mechanisms for producing the trace element chemistry of the Matachewan LIP suites. This is because both processes produce magmas with trace element chemistries characterised by enrichments in the most incompatible elements relative to the least incompatible elements as well as negative anomalies in Nb-Ta and Ti on normalised diagrams. Thus, trace element modelling is unable to determine which of these processes ‘fit’ the data better. The modelling does, however, suggest that the mantle source for at least the Leopard dyke swarm and East Bull Lake Suite had been significantly melted prior to its involvement in the formation of the two suites,

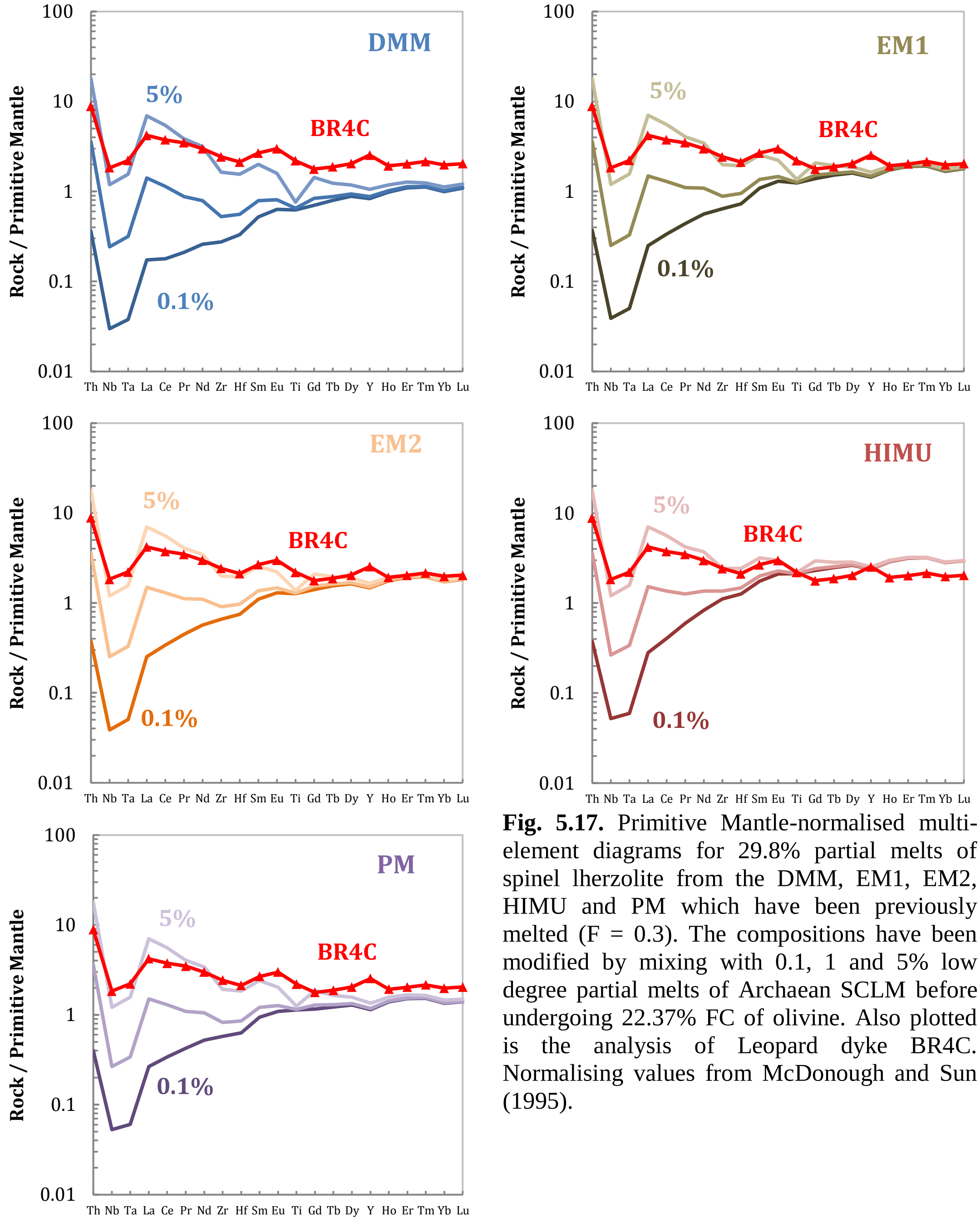

Fig. 5.17. Primitive Mantle-normalised multi-element diagrams for 29.8% partial melts of spinel lherzolite from the DMM, EM1, EM2, HIMU and PM which have been previously melted (F = 0.3). The compositions have been modified by mixing with 0.1, 1 and 5% low degree partial melts of Archaean SCLM before undergoing 22.37% FC of olivine. Also plotted is the analysis of Leopard dyke BR4C. Normalising values from McDonough and Sun (1995).

potentially during the formation of the 2.8-2.6 Ga greenstone belts which host much of the Matachewan LIP. In contrast, the Seidorechka Formation magmatism does not require derivation from such a previously-melted source region.

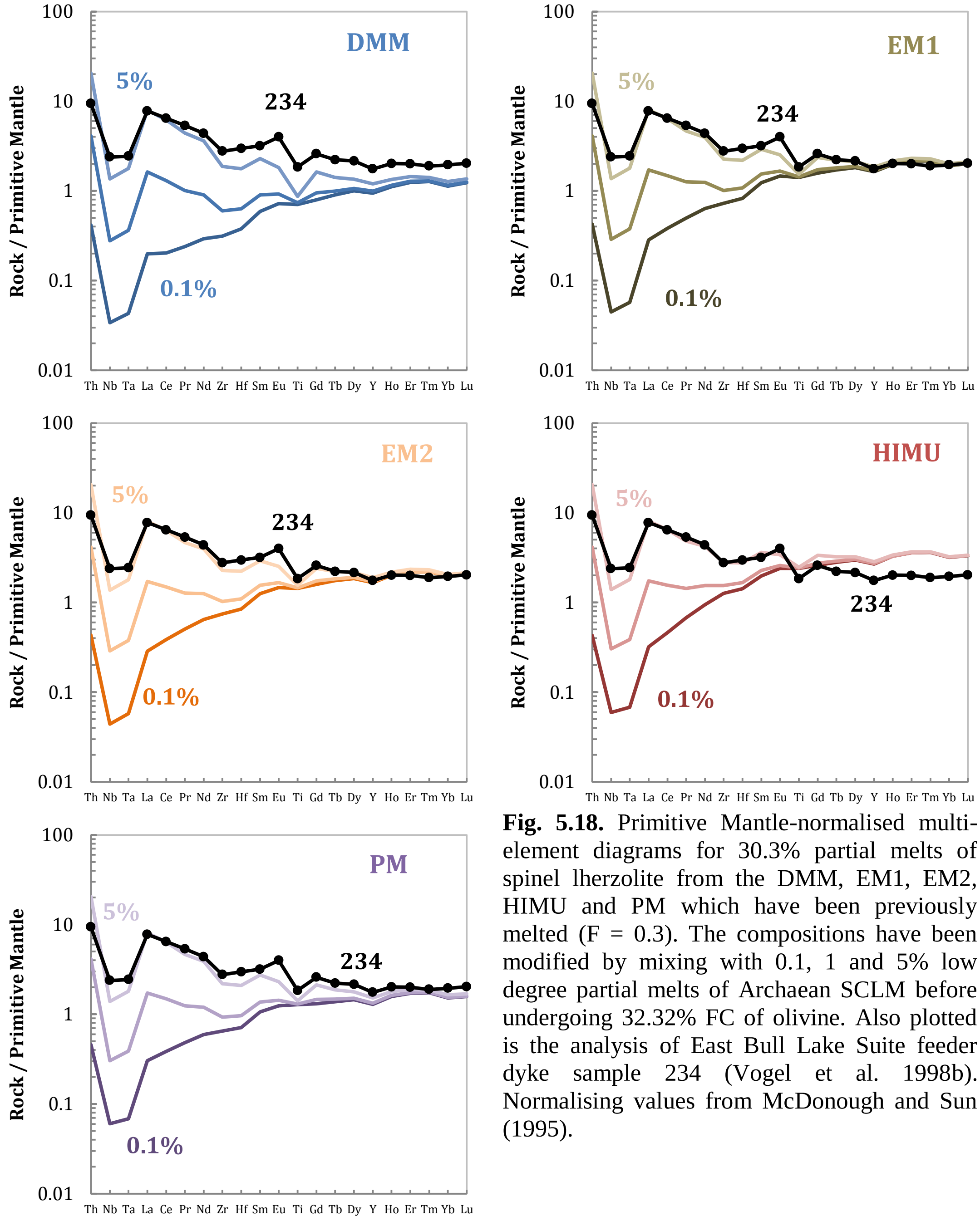

Fig. 5.18. Primitive Mantle-normalised multi-element diagrams for 30.3% partial melts of spinel lherzolite from the DMM, EM1, EM2, HIMU and PM which have been previously melted (F = 0.3). The compositions have been modified by mixing with 0.1, 1 and 5% low degree partial melts of Archaean SCLM before undergoing 32.32% FC of olivine. Also plotted is the analysis of East Bull Lake Suite feeder dyke sample 234 (Vogel et al. 1998b). Normalising values from McDonough and Sun (1995).

As debate regarding the precise timing of the initiation of plate tectonics and subduction continues (Harrison et al. 2005; Stern 2005), the application of reservoirs recognised in the modern mantle which are thought to be related to subduction and recycling [e.g., Willbold and Stracke (2006)] is questionable. Instead, previous workers have suggested that rather than being the product of contamination or mantle mixing, that the trace element chemistry exhibited by the Matachewan LIP which is ubiquitous in Palaeoproterozoic continental magmatic rocks [e.g., (Buchan et al. 2007)] is due to a fundamental difference in the geochemistry of the ancient mantle compared to the modern mantle.

This explanation was postulated by Vogel et al. (1998) who, when studying the Agnew intrusion of the East Bull Lake suite, noted that the arc-like trace element geochemistry of the East Bull Lake suite feeder dykes is shared by all magmatic rocks coeval with the intrusions on the Superior craton. Further, global analysis of greenstone volcanic rocks and mafic dyke swarms (Condie 1994; Ernst and Bleeker 2010) shows that this signature is ubiquitous in such rocks older than ~2 Ga. Vogel et al. (1998) suggest that the ubiquity of this signature in mafic continental intrusions in the Archaean-Palaeoproterozoic is due to a fundamental difference in the composition of the ancient mantle compared to the modern. Vogel et al. (1998) speculate that this arc-like signature may have been caused by the slow, upward migration of LILE- and LREE-enriched fluids through the mantle during early differentiation of the Earth. They argue that such a process would have metasomatised the entire mantle, so that any subsequent partial melts would record a subduction-like geochemical signature. Vogel et al. (1998) argue that continued continental growth, subduction (and recycling) of slabs and partial melting could have obliterated this ephemeral signature by the end of the Palaeoproterozoic.

In conclusion, the trace element geochemical signatures recorded by the Matachewan LIP suites are held in common by the majority of Archaean-Palaeoproterozoic intracontinental magmatic rocks. The debate regarding the magmatic source of such widespread rocks which retain signatures more associated with modern subduction-related rocks is ongoing (Gallagher and Hawkesworth 1992; Xie et al. 1993; Baker et al. 1996; Vogel et al. 1998b; Sandeman and Ryan 2008) and not something this study aims to resolve. However, the geochemical modelling presented here suggests that crustal contamination of primary magmas during prolonged residence in the continental crust, or, mixing of the primary magmas from known mantle reservoirs with low degree partial melts of subduction-modified SCLM are potential mechanisms producing the trace element signatures of the Matachewan LIP suites studied (assuming the mantle reservoir had already been significantly melted). The models do not require the input of an alternate Archaean-Palaeoproterozoic mantle reservoir, one which was defined by higher LILE and LREE concentrations relative to HFSE and HREE, but nor do the models rule out the input (or existence) of such a reservoir. Isotopic data can also be used in the investigation of the mantle source of igneous rocks and these data collected for the Matachewan LIP are discussed in section 5.4.

5.3. A Matachewan Thermal Plume?

5.3.1. Mantle Plume Theory

The mantle plume theory is favoured when explaining the formation of the Matachewan and, indeed, the majority of LIPs preserved in the geological record (Campbell and Griffiths 1990; Coffin and Eldholm 1994; Ernst and Bleeker 2010). The theory was first postulated by Wilson (1965) who challenged the then popular ‘rigid Earth’ model by proposing that ocean island chains are related to convection of the mantle, rather than trans-crustal faulting as had been previously accepted. Wilson (1965) proposed that island chains are formed by the interaction of a laterally moving plate with an underlying, anomalously hot and upwelling source. This theory was expanded on by Morgan (1971) who suggested that these mantle hot-spots are fixed, that the source of the convective upwelling comes from deep in the mantle, (perhaps even as deep as the core-mantle boundary) and that it is this convection which helps drive plate motion. Morgan (1971) also proposed that adiabatic rising of this deep mantle material to shallower levels is a viable process for melt production and that this process of sampling deep (undepleted) mantle reservoirs neatly explains the geochemical differences seen between these ocean island lavas and the shallow-sourced mid-ocean ridge lavas (Davies 1990). Finally, and of particular interest to this current study, Morgan (1971) suggested that this hotspot volcanism could be responsible for intracontinental magmatism and continental breakup and that the paucity of data for such events is due to the more complex nature of continental crust with respect to oceanic crust.

Griffiths and Campbell (1990) built on the plume theory by conducting laboratory experiments to determine the dynamics of thermally driven plumes **(Fig 5.19)**. They modelled a compositionally homogenous mantle (considered an oversimplification by Griffiths (1986)) and studied the effect of heating such a mantle from a basal point source. Griffiths and Campbell (1990) found that thermally driven plumes begin as growing spheres directly above the heat source. At some point, an embryonic plume head becomes large enough to rise through the ambient mantle at a rate which is faster than the radial increase in size of the plume head. The spherical plume head rises through the mantle but remains connected to the point source by a narrow conduit of heated material. As the plume head continues to rise, conduction of heat from the plume head into the ambient mantle produces a buoyant boundary layer in the mantle which is entrained in, and rises with, the plume head (Davies 1990). Once the plume reaches the base of the lithosphere, additional input of material from the conduit is accommodated by thinning and lateral spreading of the plume head into a more disk-shaped feature (Hill et al. 1992).

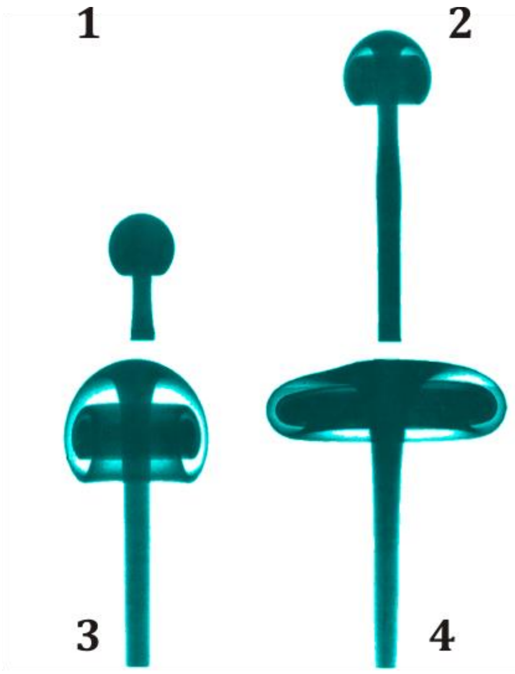

Fig. 5.19. Photographs of a starting plume in glucose syrup at several stages during its ascent. After Griffiths and Campbell (1990).

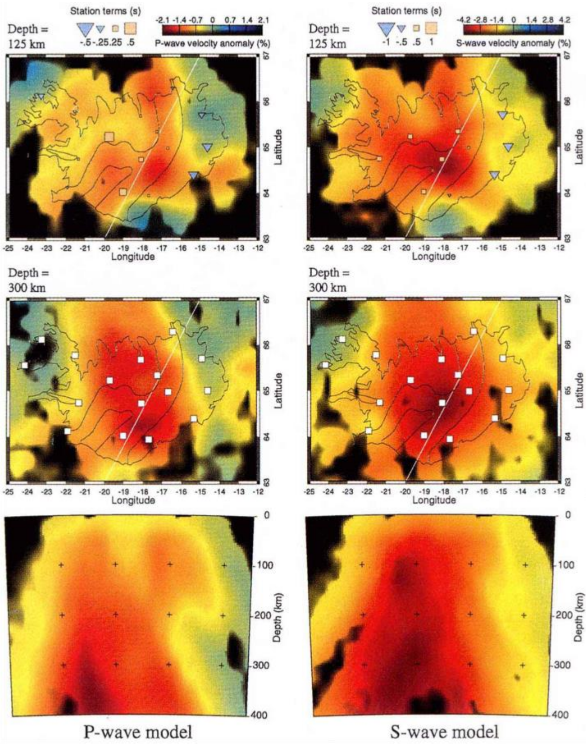

Fig. 5.20. Seismic models of the mantle beneath Iceland showing a cylindircal low-velocity anomaly interpreted to be a mantle plume. After Wolfe et al. (1997).

Extrapolating this work to the true mantle, Griffiths and Campbell (1991) showed that a plume starting at the core-mantle boundary would form a disk at the base of the lithosphere 2000-2500 km wide and 100-200 km thick. This model is thought to explain the form of many continental flood basalt provinces including; their characteristic surface uplift (Campbell and Griffiths 1990) due to the buoyant plume head; the immense quantities of magmatism (Griffiths and Campbell 1991) due to the proposed size (~2000 km) of a plume head sourced from the core-mantle boundary and; the variation of lavas seen in CFBs being related to the entrainment and mixing of a plume head with the ambient mantle (Hart et al. 1992).

5.3.2. Mantle Plumes and Temperature

Since, the formulation of the mantle plume theory, numerous geophysical and geochemical studies have been focussed on better understanding their structure and source regions (Nataf and Van Decar 1993; Hannan 1996; Wolfe et al. 1997; Helmberger et al. 1998; Shen et al. 1998; Bijwaard and Spakman 1999; Schersten et al. 2004). Most of the geophysical studies which focus on imaging plumes concentrate on the two better known examples of Hawaii and Iceland. In studies of the latter, Wolfe et al. (1997) and Bijwaard and Spakman (1999) used seismic tomography to investigate the physical properties of the mantle beneath Iceland. Both studies found evidence of a cylindrical low-velocity anomaly 150-500 km in diameter **(Fig 5.20)** which extends to the core-mantle boundary (Bijwaard and Spakman 1999). Assuming that this velocity anomaly is controlled by temperature, Bijwaard and Spakman (1999) and Wolfe et al. (1997) calculate the temperature of the mantle in the low-velocity anomaly to be 200-300°C higher than the surrounding upper mantle. These findings are similar to those of Li et al. (2000) who interpreted the cylindrical, low-velocity anomaly observed in the upper mantle beneath Hawaii to be caused by the presence of material ~300°C hotter than the surrounding mantle.

Thus, mantle plumes active in the modern era are characterised by anomalously hot upper mantle hundreds of degrees hotter than the ambient mantle. For ancient magmatic systems, seismic imaging of mantle plumes is not feasible. Instead, the existence of anomalously high temperature magmatism, indicative of a mantle plume can be investigated by examining the geochemistry of primary magmas and calculating mantle potential temperature (T_P). The T_P of the mantle is the temperature the mantle would reach if it was brought to the surface adiabatically without melting (McKenzie and Bickle 1988). The T_P of the mantle source of a primary magma may be recorded in its petrology and major element geochemical composition and can be inferred by calibration and parameterisation of laboratory data to the magma in question. However, this method is complicated by the fact that, firstly, magma generation in the mantle may occur via fractional melting which cannot be easily simulated in the laboratory (Asimow and Longhi 2004) and secondly, following melting, fractional crystallisation of the primary magma can alter its geochemical composition. The question is, then, how can we infer T_P from the geochemistry of evolved lavas?

A relatively recent method for calculating T_P, and the one used by this study is the one used by the PRIMELT2.XLS software developed by Herzberg and Asimow (2008) which is discussed in section 5.4. Once PRIMELT2.XLS obtains a primary magma composition, the MgO concentration is used to calculate T_P via **Equation 5.7.**

$$T_P(°C) = 1463 + (12.74 \times \mathrm{MgO}) - \frac{2924}{\mathrm{MgO}}$$

Equation 5.7

PRIMELT2.XLS was able to calculate primary magmas (and hence potential temperatures) for just two of the Matachewan LIP suites studied; the East Bull Lake Suite and Leopard dyke swarm **(Table 5.1)**. Data from previous studies of the Thessalon Formation (Jolly 1987a; 1987b; Jolly et al. 1992), Viianki dyke swarm (Stepanova and Stepanov 2010) and Seidorechka Formation (Puchtel et al. 1996) were also tested with PRIMELT2.XLS. PRIMELT2.XLS was able to calculate a primary magma for just one of these samples – a Seidorechka Formation basalt from the Vetreny Poyas Belt [sample 91113 of Puchtel et al. (1996)].

The primary magma of the East Bull Lake suite records a T_P of 1545°C while the two Leopard dyke samples which provide a potential primary magma for the swarm record a T_P of 1379-1442°C. The primary magma of the Seidorechka Formation (as calculated from the analysis of Puchtel et al. (1996) records a T_P of 1496°C. The total uncertainty in T_P calculated by PRIMELT2.XLS due to potential errors in determining the MgO content of primary magmas is ± 60°C (2σ) (Herzberg and Asimow 2008; Herzberg et al. 2010).

5.3.3. Anomalously Hot Matachewan Magmatism?

The mantle plume theory (Campbell 2007) predicts, and observations of the mantle beneath Hawaii and Iceland (Bijwaard and Spakman 1999; Li et al. 2000) have confirmed, that mantle plumes are characterised by thermal anomalies in the upper mantle in the order of hundreds of degrees. Thus, by comparing the potential temperatures of the primary magmas studied here, with temperature estimates of the ambient upper mantle in the Palaeoproterozoic, we can determine whether the magmatism which formed the Matachewan LIP suites was sourced from an anomalously hot upper mantle (i.e. plume).

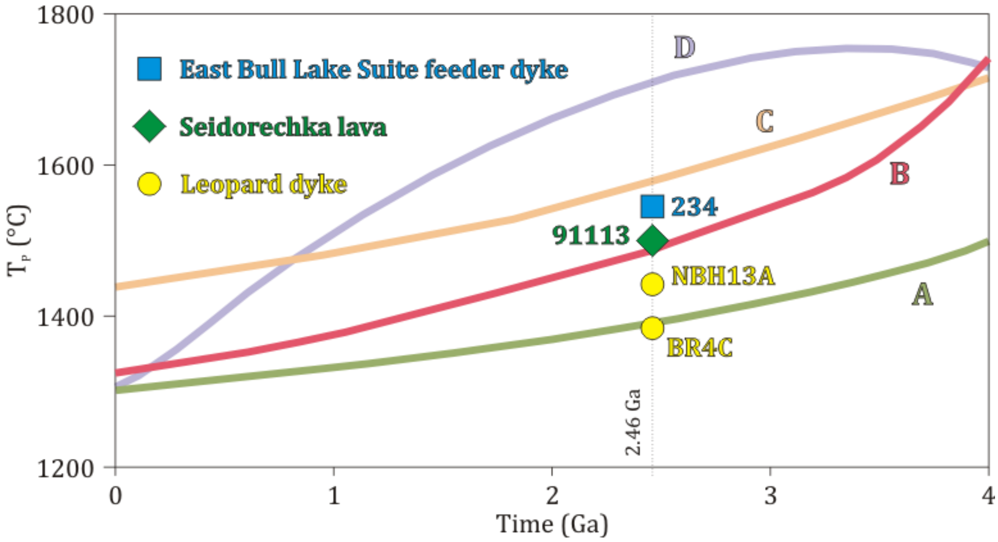

Fig 5.21. Temperature evolution of the upper mantle through time using different models; A – Davies (2009); B – Richter (1988); C – Abbot et al. (1994); D – Korenaga (2008).

General consensus opinion states that the mantle was significantly hotter during the Palaeoproterozoic than it is today. Exactly how much hotter is a contentious point as different models predict different cooling histories for the Earth **(Fig 5.21)**. Richter (1988) presents models whereby the starting temperature of the upper mantle at 4.5 Ga was either 2000°C or 2500°C which cooled at a continuously decreasing rate to reach a present day value of 1350°C. Regardless of the two starting temperatures used by Richter (1988), his model predicts that at ~2.5 Ga the temperature of the upper mantle was ~1500°C. Abbot et al. (1994) produced a thermal history of the upper mantle using 15-3750 Ma samples thought to record NMORB compositions. From their data, Abbot et al. (1994) calculated the most primitive liquidus temperature for each suite studied. The model produced by Abbot et al. (1994)

indicates the upper mantle has cooled from ~1700°C at 4 Ga to ~1450°C today. Korenaga (2008) presents a model which is characterised by an initial increase in mantle T_P from ~1650°C at 4.5 Ga to ~1700°C at 3.6 Ga. This initial temperature increase is followed by an increasingly rapid drop in T_P to a present day values of 1350°C. Davies (2009) suggests that the low urey ratio (heat produced by radioactive decay/heat loss) used by Korenaga (2008) is extreme and instead favours a model of constantly decreasing temperature from an initial upper mantle temperature of 1800°C at 4.5 Ga to reach a modern day temperature of 1300°C.

Fig. 5.21 shows the four secular cooling models described above. The T_P of the four samples which yield primary magma estimates with PRIMELT2.XLS are also plotted. Leopard dyke sample BR4C records the lowest T_P of the samples studied and plots directly on the cooling curve of Davies (2009). Thus, sample BR4C does not record an anomalously higher T_P with respect to any of the models studied. The other Leopard dyke studied (NBH13A) records a T_P of 1442°C. This T_P is 58°C higher than that of the upper mantle according to the model of Davies (2009) but lower than that predicted by the other models studied. Seidorechka Formation sample 91113 of Puchtel et al. (1996) records a T_P of 1496°C, which is very close to the temperature of the upper mantle at 2.46 Ga as predicted by Richter (1988), but ~120°C hotter than the prediction of Davies (2009). The highest T_P sample is the East Bull Lake Suite feeder dyke [sample 234 of Vogel et al. (1998)] which records a T_P of 1545°C. This T_P is 161-57°C higher than the temperature of the upper mantle as modelled by Davies (2009) and Richter (1988) respectively, but lower than that modelled by Korenaga (2008) and Abbot et al. (1994).

Determining the veracity of the disparate models presented in **Fig. 5.21** is beyond the scope of this project. However, the suitability of the model produced by Abbot et al. (1994) may be questioned as their model suggests a range in upper mantle temperature through time of up to 300°C. In **Fig 5.21**, the model of Abbot et al. (1994) is displayed as a line which defines the median of their range (Line C). The enormous range of upper mantle temperatures reported by Abbot et al. (1994) makes it difficult to use this model to determine if the Matachewan LIP suites studied are formed from anomalously hot upper mantle. Study of the relevant literature also indicates that the model of Korenaga (2008) (Line D in **Fig. 5.21**) is heavily criticised by Davies (2009) and Karato (2010). Davies (2009) takes issue with the assumption of Korenaga (2008) that plate thickness is determined by dehydration during melting at mid-ocean ridges and instead suggests that plate thickness is determined by conductive cooling. Davies (2009) also states that the model of Korenaga (2008) is overly sensitive to the radius of curvature of bending plates at subduction zones. Karato (2010) demonstrates that plate curvature at subduction zones depends on the flexural rigidity which in turn, depends on plate thickness. This finding by Karato (2010) thus invalidates the model of Korenaga (2008) who assumes that the radius of curvature of bending plates remains constant. Thus, this study prefers the models of Richter (1988) and Davies (2009) in estimating the temperature of the upper mantle during the eruption of the Matachewan LIP at ~2.46 Ga.

Other studies have estimated the temperature of the upper mantle at various points during the Archaean (Ohta et al. 1996; Galer and Mezger 1998; Komiya et al. 2004). Galer and Mezger (1998) examined the regional metamorphic grade of ten undisturbed Archaean granite-greenstone segments and showed that metamorphic facies exposed at the surface today are indicative of burial pressures of ~1.5 kbar. From these burial pressures, Galer and Mezger (1998) infer that, since 3 Ga, the undisturbed portions of cratons have been uplifted ~5 km, implying a mean continental thickness of ~46 km when the cratons were stabilised at ca. 2.5 Ga (Bleeker 2003). Galer and Mezger (1998) argue that during the Archaean, in order to maintain isostatic equilibrium with the cratons, the oceanic crust would have had to have been ~14 km thick (assuming a relatively fixed cratonic mass through time). Under these conditions, Galer and Mezger (1998) infer an upper mantle temperature of ~90 °C hotter than the present day at 3 Ga. Using a linear cooling rate of 30 °C Gy^{-1} (which is comparable to estimates of the present day cool rate of the Earth), the temperature of the upper mantle at 2.46 Ga can be estimated as 1424 °C.

Ohta et al. (1996) used the geochemistry of Archaean MORB rocks preserved in a 3.1-3.3 Ga accretionary complex in Pilbara, western Australia to constrain the ambient temperature of the upper mantle at 3.1-3.3 Ga to be 1400 °C. Using this temperature of 1400 °C as an estimate for T_P at 3.2 Ga and a simplistic, linear cooling modelling between 1400 °C at 3.2 Ga and 1350 °C today, the temperature of the mantle at 2.46 Ga can be estimated at 1388 °C. In a similar study, Komiya et al. (2004) use the geochemistry of Archaean MORB rocks preserved in the 3.8 Ga Isua Supracrustal Belt, southwest Greenland to constrain upper mantle temperatures at that time to be ~1480 °C. Again, using a simplistic, linear cooling model between 1480 °C at 3.8 Ga and 1350 °C today, the temperature of the upper mantle at 2.46 Ga can be estimated at 1434 °C.

These three estimates of upper mantle temperature at ~2.46 Ga using the work of Ohta et al. (1996), Galer and Mezger (1998) and Komiya et al. (2004) are either very similar to or higher than the T_P recorded by the Leopard dykes. This reinforces the evidence presented by **Fig. 5.21** that the Leopard dyke swarm did not originate from anomalously hot upper mantle. The Seidorechka Formation and East Bull Lake Suite feeder dyke samples record respective T_Ps of; 72 °C and 121 °C hotter than the temperature of the ~2.46 Ga mantle as derived from the work of Galer and Mezger (1998), 108 °C and 157 °C hotter than that derived from the work of Ohta et al. (1996), and 62 °C and 111 °C hotter than that derived from the work of Komiya et al. (2004).

5.3.4. Summary

In summary, the Leopard dyke swarm appears to have originated from mantle which was little or no hotter than any of the estimates presented above and thus, does not require a thermal anomaly (i.e. mantle plume) for the genesis of the swarm. The East Bull Lake Suite feeder dyke and Seidorechka Formation basalt samples originate from anomalously hot mantle according to the models of Davies (2009) and Richter (1988) as well as other estimates derived from studies of Archaean mantle rocks (Ohta et al. 1996; Galer and Mezger 1998; Komiya et al. 2004). Thus, these two latter suites may be the product of mantle plume-driven magmatism as proposed by James et al. (2002), Easton et al. (2010) and Ernst and Bleeker (2010). However, alternate models of the cooling of the mantle [e.g., Korenaga (2008) and Abbot et al. (1994)] indicate that the East Bull Lake Suite and Seidorechka Formation are not the product of an anomalously hot mantle plume. Continued research into the thermal evolution of the mantle and derivation of robust models which estimate the temperature of the upper mantle at ~2.46 Ga will help better determine the nature of the petrogenetic mechanism of the Matachewan LIP suites.

5.4. Fractional Crystallisation

In this section, fractional crystallisation, the processes whereby a cooling magma differentiates into crystals and an evolving liquid, will be evaluated as a potential mechanism for generating the geochemical trends observed in the different Matachewan LIP suites. Fractional crystallisation has been modelled using the PELE computer software program (Boudreau 1999). These models help assess under what conditions, and to what extent fractional crystallisation occurred in order to produce the geochemistry of the different Matachewan LIP suites.

Fractional crystallisation for the dyke swarms and flood basalt suites is modelled using the most primitive sample from each suite (i.e., highest MgO and lowest incompatible element concentration). The most primitive sample is unlikely to be a primary magma given the evolved nature of many of the Matachewan LIP suites (see section 5.1). However, the most primitive sample is assumed to be the closest estimate of the primary magma for the suite. Fractional crystallisation of the layered intrusions is modelled using the compositions of parental magmas published in the literature or determined by this study.

Model	Pressure	H_2O content	Oxygen buffer
Model 1	1 kbar	0%	QFM
Model 2	1 kbar	1%	QFM
Model 3	3 kbar	0%	QFM
Model 4	7 kbar	0%	QFM
Model 5	10 kbar	0%	QFM

Table 5.5. Parameters used to model fractional crystallisation of the Matachewan LIP dyke swarms and flood basalt suites

The major element geochemical trends for each of the dyke swarms and flood basalt provinces has been modelled using five different scenarios **(Table 5.5)**: *Model 1*: fractional crystallisation at 1 kbar (anhydrous); *Model 2*: fractional crystallisation at 1 kbar (1% H_2O); *Model 3*: fractional crystallisation at 3 kbar (anhydrous); *Model 4*: fractional crystallisation at 7 kbar (anhydrous) and *Model 5*: fractional crystallisation at 10 kbar (anhydrous). All models use a quartz-fayalite- magnetite (QFM) oxygen buffer and calculate the composition of the liquid at 10% crystallisation intervals. The model which best predicts the major element geochemical trends observed in each of the dyke swarms and flood basalt suites are further tested using incompatible trace elements. To do this, the evolution of the trace element chemistry of the parent melt has been modelled using the equation for fractional crystallisation **(Equation 5.5)**, the mineral assemblages predicted to form by PELE during crystallisation and the empirically derived mineral/melt partition coefficients shown in **Table 5.6**.

Element	Olivine	Ortho-pyroxene	Clino-pyroxene	Spinel	Plagioclase	Magnetite
Th	0.0000001	0.0004	0.014	0.013	0.3435	0.1
Nb	0.0001	0.002825	0.00605	0.01	0.09725	0.7
Ta	0.0001	0.002825	0.00605	0.01	0.0795	0.23
La	0.000007	0.0000535	0.05025	0.0006	0.0631	0.015
Ce	0.00001	0.0026	0.089	0.0006	0.0457	0.016
Pr	0.00004	0.0065	0.1335	0.0006	0.1375	0.02
Nd	0.00007	0.010267	0.178	0.0006	0.0478	0.026
Zr	0.0005	0.01775	0.1975	0.07	0.0094	0.71
Hf	0.0038	0.027225	0.2115	0.003	0.082	0.16
Sm	0.0007	0.018	0.3775	0.0006	0.06575	0.024
Eu	0.00095	0.0215	0.458	0.0006	0.3254	0.025
Ti	0.015	0.082	0.3955	0.15	0.0473	16.5
Gd	0.002	0.028	0.487	0.0009	0.07175	0.018
Tb	0.003	0.035	0.516	0.0012	0.084	0.019
Dy	0.004	0.041	0.5455	0.0015	0.057167	0.018
Y	0.007365	0.0935	0.412	0.002	0.00989	0.0039
Ho	0.0065	0.05	0.603	0.0023	0.0592	0.017
Er	0.009	0.063917	0.66	0.003	0.07633	0.017
Tm	0.015	0.078	0.66	0.0038	0.072	0.017
Yb	0.023	0.093917	0.5165	0.0045	0.0903	0.018
Lu	0.03	0.1	0.536	0.0053	0.1175	0.023

Table 5.6. Mineral/melt partition coefficients for basaltic and basaltic andesite liquids. Compiled from the dataset listed by Bèdard (2001). See reference for data sources.

Where fractional crystallisation fails to accurately model the incompatible element geochemical trends observed in the different Matachewan LIP suites, modelling assimilation-fraction crystallisation (AFC) has been attempted. These models predict the geochemical evolution of a magma which assimilates, and is contaminated by its host rocks during crystallisation. These models are constructed using the equation for AFC **(Equation 5. 2 and 5.3)**, the mineral assemblages predicted by PELE to form during crystallisation and the empirically derived mineral/melt partition coefficients shown in **Table 5.6**, the composition of felsic crust (Rudnick and Fountain 1995), and the ratio of assimilation/crystallisation which is taken to be 0.3. For suites which are better modelled by AFC, more robust models are constructed using contaminants of Archaean crustal rocks which are spatially associated with the individual Matachewan LIP suites.

5.4.1. PELE

The MELTS software (Ghiorso & Sack 1995) allows the user to evaluate crystallisation of silicate magma at varying physical conditions. The MELTS software is currently usable as a JAVA® enabled web applet from http://melts.ofm-research.org/applet.html. Boudreau (1999) used published descriptions of the database and numerical models used by MELTS to produce a modified version of the program for use with Windows® systems (PELE). A brief summary is given below of the workings of MELTS, of which PELE is a modification. Ghiorso & Sack (1995); Asimow and Ghiorso (1998); and Boudreau (1999) present more detailed descriptions of the MELTS and PELE software.

PELE can model fractional crystallisation in both hydrous and anhydrous magmatic systems which range in composition from alkaline mafic magmas to rhyolite magmas between temperatures of ~500-2000 °C and pressures of <2 GPa. The PELE and MELTS software calculates chemical mass transfers in such magmatic systems and both are able to model crystallisation paths of known silicate magmas under constrained pressure, oxygen fugacity, total enthalpy, total entropy and total volume parameters. MELTS and PELE are able to model fractional crystallisation of silicate magmas by utilising thousands of experimentally-determined compositions of silicate liquids co-existing at known temperature, pressure and oxygen fugacity with apatite ± feldspar ± leucite ± olivine ± pyroxene ± quartz ± rhombohedral oxides ± spinel ± whitlockite ± water.

5.4.2. Matachewan LIP Dyke Swarms

5.4.2.1. Matachewan Dyke Swarm

Sample FA65-037-02 is used as an estimate for the parent magma of the Group 1 Matachewan dyke swarm as this sample has the highest MgO content (8.84 wt.%) and lowest Zr content (76 ppm) of the dykes sampled.

It is not entirely obvious which model best predicts the major element composition of the Matachewan Group 1 dykes. The SiO_2 and Cr_2O_3 trends exhibited by the Group 1 Matachewan dykes are better predicted by fractional crystallisation at 10 kbar, while the majority of the major elements (including CaO, TiO_2, Al_2O_3, Fe_2O_3, Na_2O and P_2O_5) are better predicted by fractional crystallisation at 7 kbar **(Fig. 5.22)**.

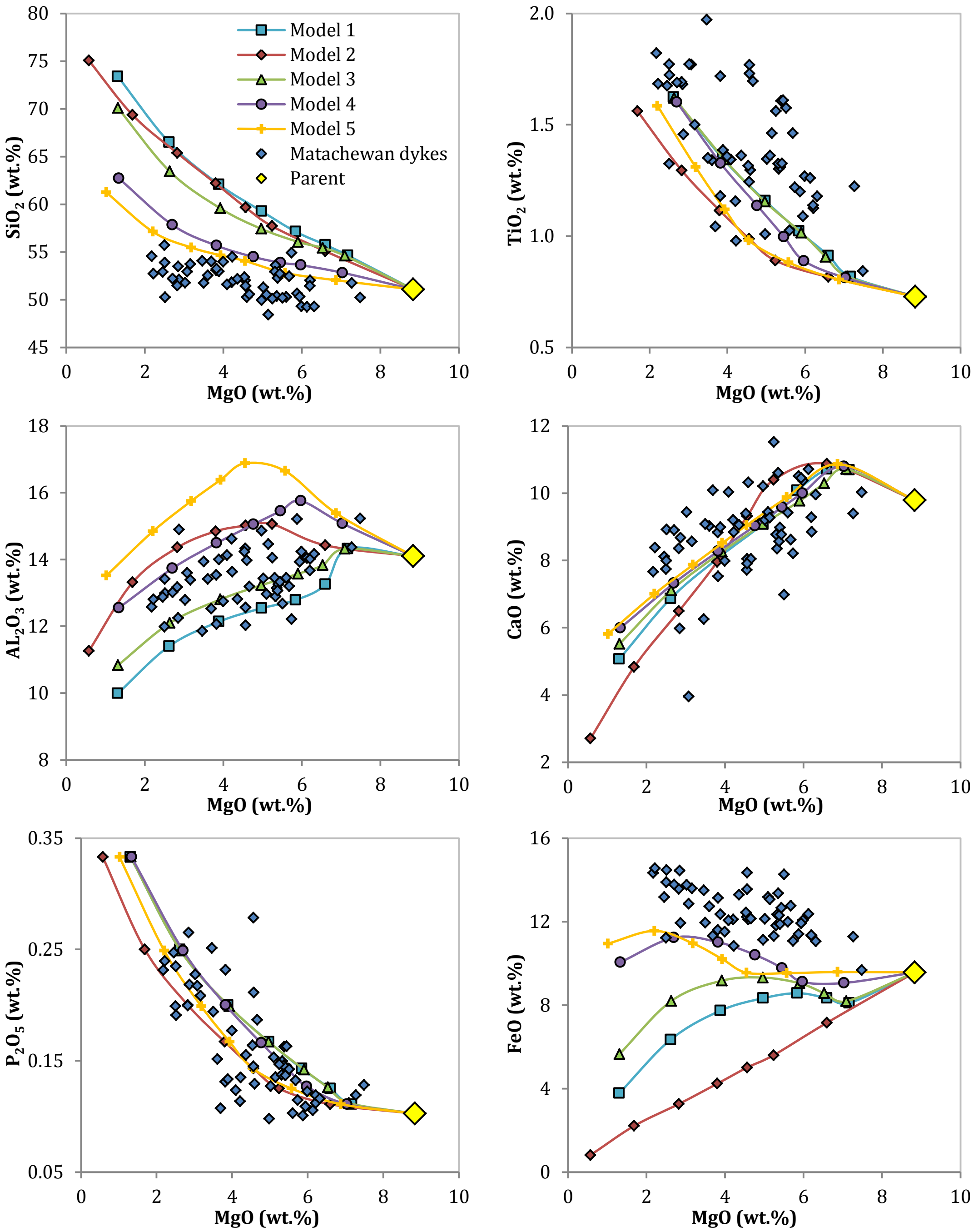

Fig. 5.22. Bivariate diagrams of selected major elements vs. MgO trends for the Group 1 Matachewan dykes and those predicted by fractional crystallisation of a parent magma with a composition equal to that of sample FA65-037-02. Markers on the model lines are placed at intervals of 10% crystallisation.

The 7 kbar model predicts that crystallisation begins at ~1375 °C with spinel being the first mineral to crystallise. Orthopyroxene joins spinel at ~1295 °C after ~3.3% of the magma has crystallised. Orthopyroxene is followed by clinopyroxene which joins the assemblage at ~1242 °C after ~11% of the magma has crystallised. The model predicts that plagioclase joins the crystallising assemblage soon after at ~1228 °C after ~18% of the magma has crystallised. This assemblage continues to crystallise until the end of the model at ~70% crystallisation at which point, the evolved liquid contains <2 wt.% MgO which is lower than that observed in the Matachewan dykes **(Fig. 5.23)**.

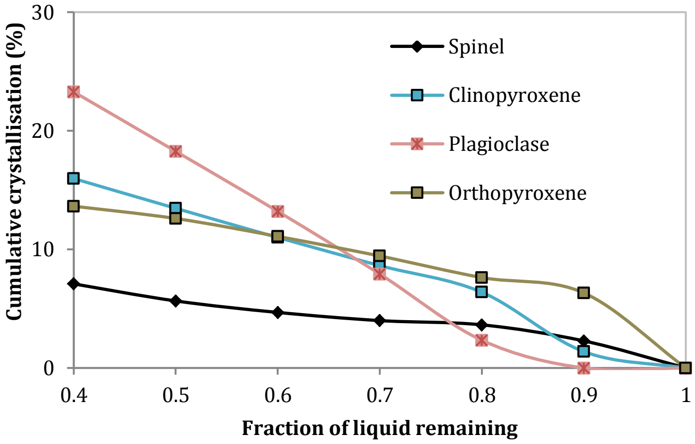

Fig. 5.23. Diagram showing the cumulative proportions of crystals formed by fractional crystallisation of the Matachewan parent at 10% intervals of crystallisation.

Models which use trace elements to model FC and AFC (where r = 0.3) using the parameters and assemblages predicted to form during fractionation at 7 kbar are shown in **Fig. 5.24**. Both FC and AFC models of sample FA65-037-02 predict the general trends observed in the Matachewan Group 1 dykes. For example, both models predict incompatible element increases, slight increases in La/Sm ratios, increases in the size of the negative and Eu anomalies and no appreciable trend in Gd/Yb or Nb anomalies, the latter being hugely variable in the Matachewan dykes.

While the trends predicted by the FC and AFC models are very similar, the differences in trace element abundances predicted by the models are marked with the AFC model predicting much greater trace element concentrations than the FC model at the same degree of fractionation. For example, at 65% crystallisation (the point at which the evolving liquid contains major element abundances similar to those observed in the most evolved dykes) the AFC model predicts that the evolved liquid contains ~25% more Zr than the FC model and also ~25% more Zr than the most evolved Matachewan dyke (sample 89M40). The inability of the AFC model to adequately model the changes in trace element abundances observed in the dykes,

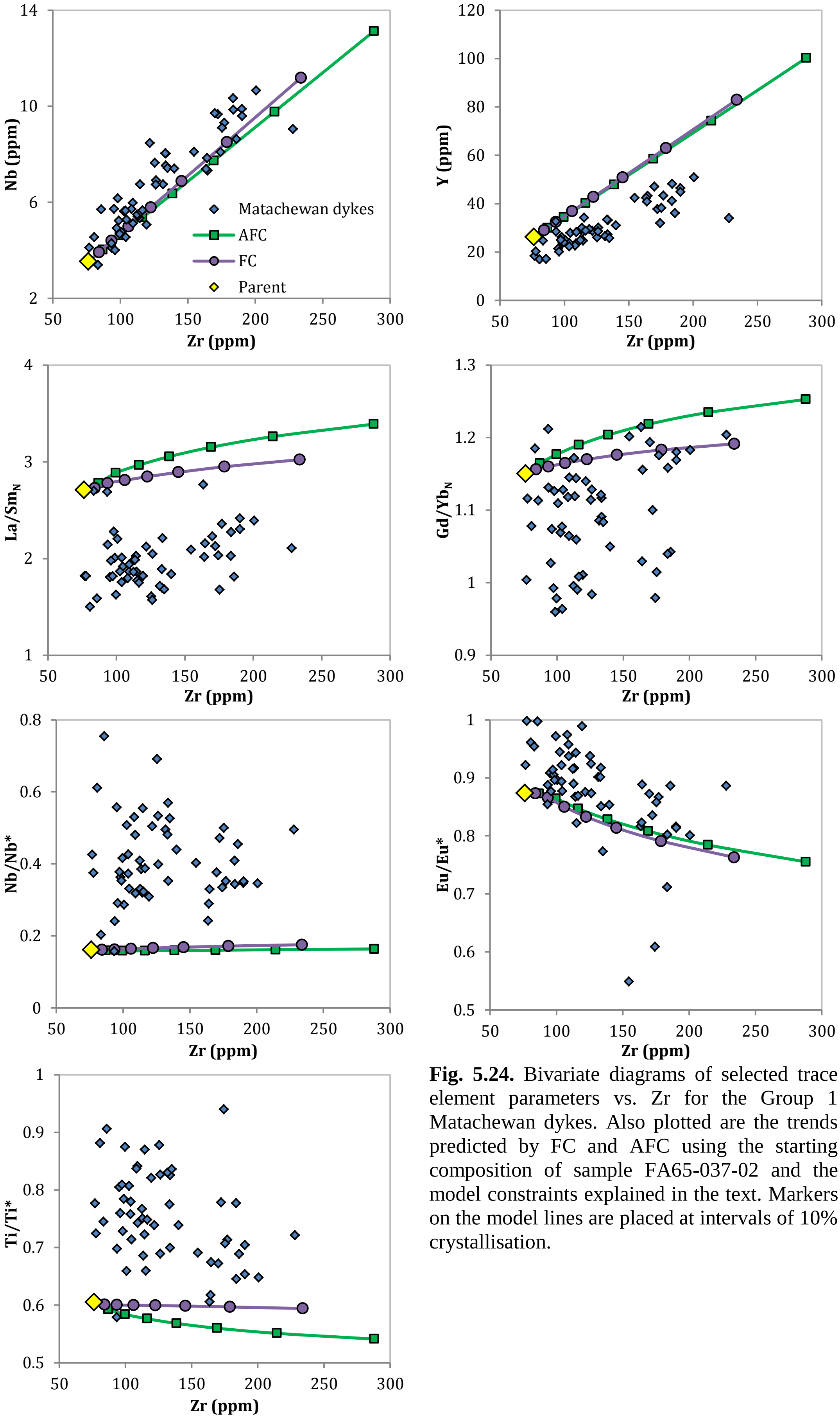

Fig. 5.24. Bivariate diagrams of selected trace element parameters vs. Zr for the Group 1 Matachewan dykes. Also plotted are the trends predicted by FC and AFC using the starting composition of sample FA65-037-02 and the model constraints explained in the text. Markers on the model lines are placed at intervals of 10% crystallisation.

despite accurately modelling the general trace element trends suggests that FC is a more viable mechanism for producing the geochemical trends observed in the Group 1 Matachewan dykes. However, the massive variations in the Gd/Yb_N ratio and sizes of the negative Ti and Nb anomalies in the Group 1 Matachewan dykes are not predicted by the FC model. Instead, these variations may be the product of in situ contamination of individual dykes by a heterogeneous contaminant. This mechanism is made more plausible by the areal distribution of the entire swarm which crops out across three separate terranes over 100s of kilometres meaning that individual dykes from the swarm intrude a plethora of different rock types with a potentially enormous range of trace element compositions.

In summary, the major element chemistry observed in the Matachewan Group 1 dykes is best explained whereby a body of basaltic magma containing ~8.84 wt.% MgO ponded at ~21 km (~7 kbar) and fractionated spinel, plagioclase, clinopyroxene and orthopyroxene. Trace element modelling is not definitive in determining if the Matachewan parent magma was contaminated by felsic country rock during fractionation. However, AFC modelling using the average composition of felsic crust (Rudnick 1995) even at a low assimilation/fractionation ratio of 0.1, predicts magmas with trace element abundances ~25% higher than the most evolved Matachewan dykes. Conversely, simple FC models predict incompatible trace element abundances much closer to those observed in the Matachewan dykes. Thus, it is the author’s opinion that AFC did not operate to any great extent during the evolution of the Matachewan parent magma during its residence in the crust and instead, the Matachewan parent magma evolved via simple fractional crystallisation with little to no input from its crustal host rock. This chamber was tapped periodically and liquids removed to form Matachewan dykes which record the geochemical evolution of the parental magma. It is also the author’s opinion that some of these evolved melts became contaminated in-situ by the various crustal components which the swarm intrudes to produce some of the variation observed in **Fig. 5.24**.

5.4.2.2. Kaminak Dyke Swarm

Fractionation of the Kaminak dykes was modelled using the composition of sample FA71-068-04 as the proposed parent magma, as this sample has the highest MgO content (6.27 wt.%) and one of the lowest REE contents of the Kaminak dykes sampled.

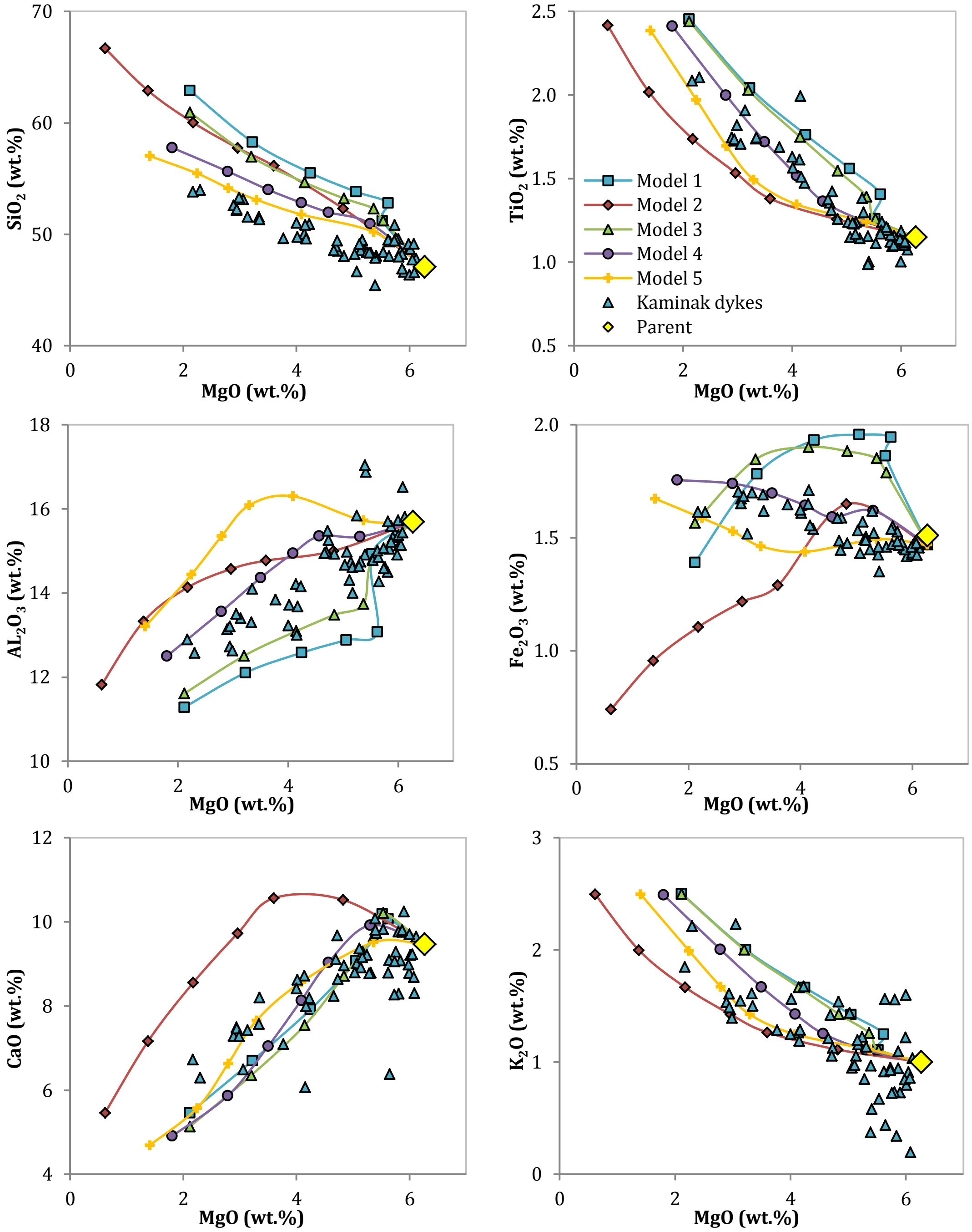

Fig. 5.25. Bivariate diagrams of selected major elements vs. MgO trends for the Kaminak dykes and those predicted fractional crystallisation of a parent magma with a composition equal to that of sample FA71-068-04. Markers on the model lines are placed at intervals of 10% crystallisation.

It is not totally clear which model best approximates the major element geochemical trends exhibited by the Kaminak dyke swarm as there is not a single model which consistently fits the data **(Fig. 5.25)**. For example, the observed trends in SiO_2 vs.

MgO are best approximated by *Model 5* (10 kbar, anhydrous), while *Model 1* (1 kbar, anhydrous) best predicts the relationship between P_2O_5 and MgO. Overall, of the models used in this study *Model 4* (7 kbar, anhydrous) best predicts the observed major element geochemical trends observed in the Kaminak dyke swarm and produces very good fits with the data on MgO vs. TiO_2, Fe_2O_3, Al_2O_3, CaO, FeO and to a lesser extent, SiO_2.

Model 4 predicts that the FA71-068-04 magma begins to crystallise at 1283 °C with spinel being the first mineral to join the crystallising assemblage. Clinopyroxene joins the crystallising assemblage at ~1207 °C after ~8% of the magma has crystallised. Plagioclase joins the crystallising assemblage at ~1151 °C after ~30% of the magma has crystallised. This assemblage of spinel + clinopyroxene + plagioclase continues to crystallise in rough proportions of 1:1:5 until the end of the model at 60% crystallisation (1034 °C) at which point, the evolved liquid contains ~1.8 wt.% MgO **(Fig. 5.26)**.

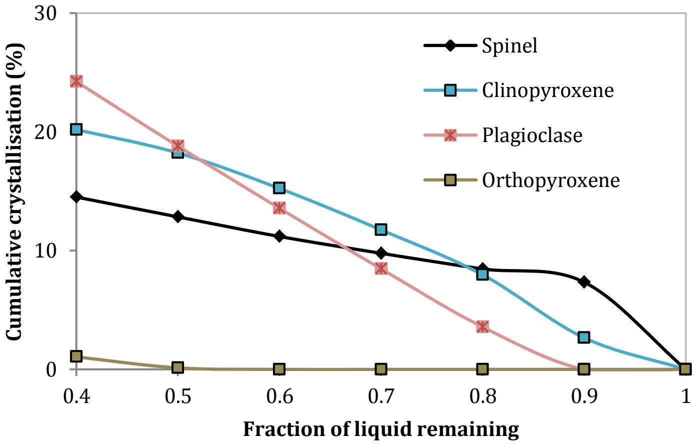

Fig. 5.26. Diagram showing the cumulative proportions of crystals formed during fractional crystallisation of the Kaminak parent at 10% intervals of crystallisation.

Despite *Model 4* predicting much of the major element geochemical variation exhibited by the Kaminak dykes, not one of the models presented is entirely conclusive. Modelling using incompatible trace elements and the starting composition, model parameters and mineral assemblages predicted to form in *Model 4*, predicts the general incompatible element trends exhibited by the Kaminak dykes i.e. an increase in incompatible element concentrations as crystallisation progresses

(Fig. 5.27). However, in the case of Y, the model overestimates enrichment as crystallisation progresses while, in the case of Th, the model underestimates the enrichment. *Model 4* also predicts the change in variation in the LREE as shown by the similar non-linear increase in La/Sm in the dykes and the model. However, *Model 4* does not predict the variation in the HREE as, in the Kaminak dykes, Gd/Yb increases non-linearly during fractionation, while *Model 4* predicts that the Gd/Yb ratio remains constant at ~1.8. The Kaminak dykes record increasingly large Nb, Eu and Ti as fractionation progresses. *Model 4* does not predict this observed trend for the Nb and Ti anomalies and instead predicts the Ti anomaly to stay relatively constant at ~0.8 and the size of the Nb anomaly to decrease during fractionation. *Model 4* does predict the size of the Eu anomaly to increase during fractionation but underestimates the magnitude of the increase observed in the Kaminak dykes. The AFC model which uses the composition of felsic crust (Rudnick and Fountain 1995) and an assimilation/fractionation ratio of 0.1 better predicts not only the rate of trace element enrichment in the evolving dykes, but also the variations in La/Sm_N, Gd/Yb_N and the increase in the size of the negative Nb and Ti anomalies than the FC model.

As AFC better predicts the trace element variation exhibited by the Kaminak dyke swarm than simple FC, more AFC models were constructed in an attempt to better define the contaminant utilised during fractionation of the Kaminak dyke parent magma. Four different granitoid contaminants were modelled using the using the starting composition, model parameters and mineral assemblages predicted to form in *Model 4*. The four other potential contaminants are taken from analyses of Archaean granitoid plutons which intrude the Kaminak segment of the Central Hearne Supracrustal Belt, which itself, hosts the Kaminak dykes (Sandeman et al. 2004). The composition of these four granitoids **(Fig. 5.28)**: H525B, H450, H375 and H25A are found in **Appendix I**.

Modelling using these four granitoid contaminants does not produce a unique solution of the evolution of the Kaminak dykes **(Fig. 5.29)**. Contamination of relative small amounts (r = 0.1) of each of the granitoids is capable of reproducing some of the trace element variation in the Kaminak dyke swarm. However, a single granitoid contaminant cannot satisfy all of the parameters modelled. For example,

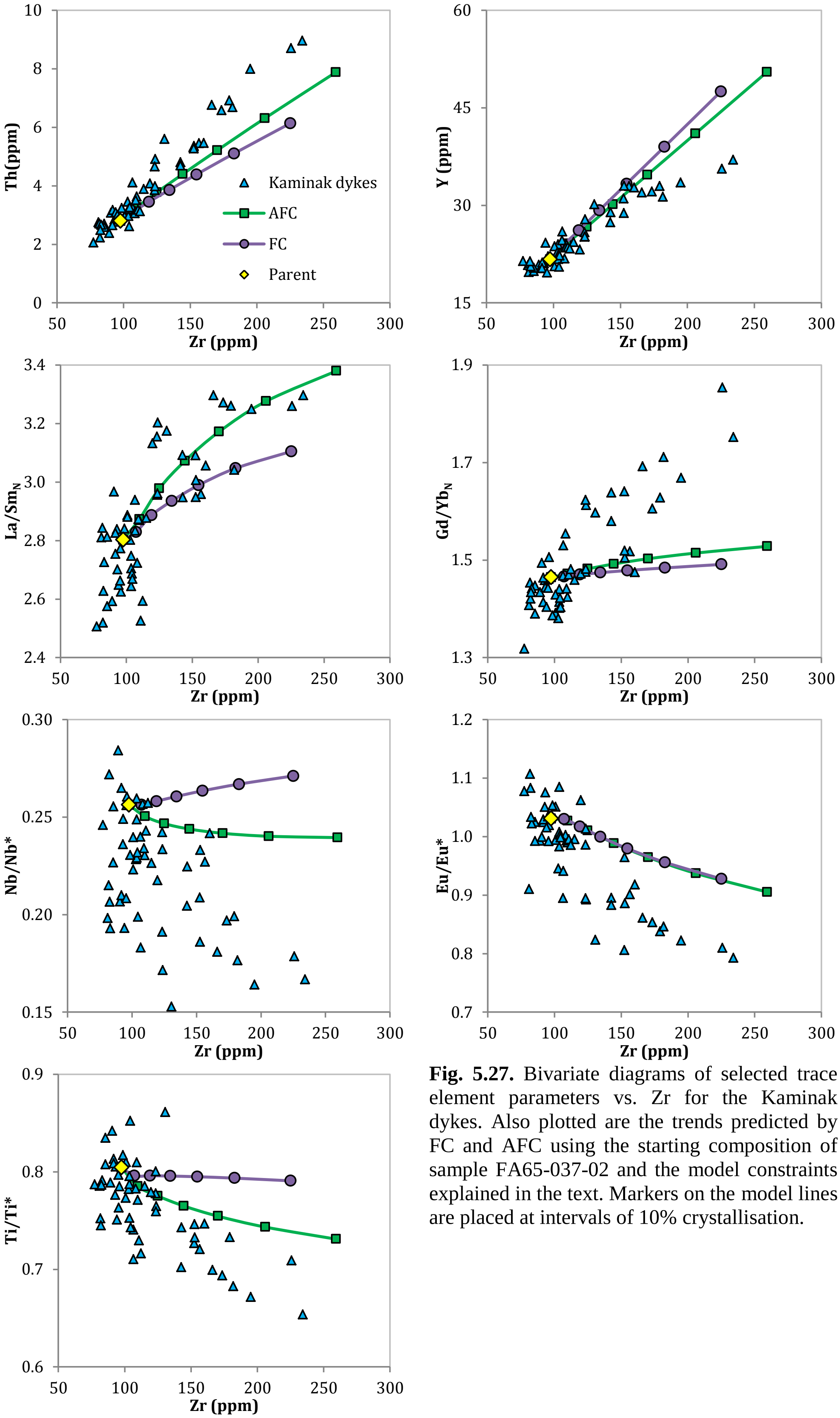

Fig. 5.27. Bivariate diagrams of selected trace element parameters vs. Zr for the Kaminak dykes. Also plotted are the trends predicted by FC and AFC using the starting composition of sample FA65-037-02 and the model constraints explained in the text. Markers on the model lines are placed at intervals of 10% crystallisation.

contamination by a granitoid with a composition similar to H525B is a very satisfactory mechanism for explaining the increase in Th in the suite, while contamination of the Kaminak parent magma by granite similar in composition to H375 is better at explaining the variation in La/Sm$_N$. None of the contaminants modelled can accurately predict the variation observed in the dykes in terms of Gd/Yb$_N$ or the negative Nb and Eu anomalies, although they do get closer to the trend of the data than the FC model **(Fig. 5.28)**.

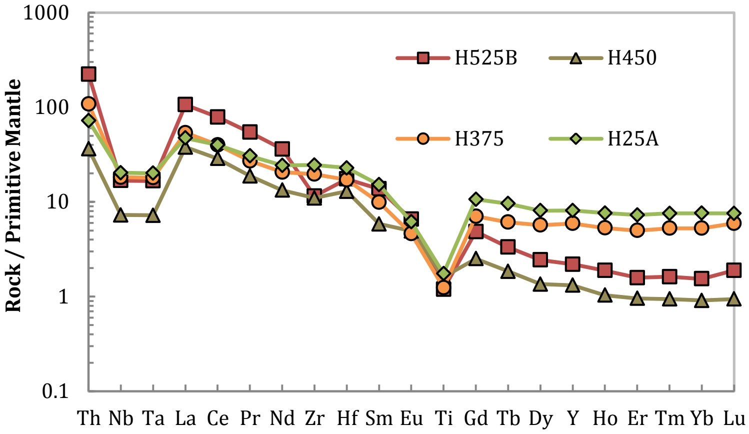

Fig. 5.28. Primitive Mantle-normalised multi-element diagrams for four Archaean granitoid contaminants used in AFC models of the Kaminak dyke swarm (Sandeman et al. 2003). Normalising values from McDonough and Sun (1995).

The modelling presented here suggests that the contaminant which was utilised during the evolution of the Kaminak dyke parental magma is characterised by more negative Eu, Ti and Nb anomalies and steeper HREE slopes than any of the granitoids modelled. One such rock type might have been derived by low-degree partial melting of subduction-modified Archaean SCLM. Such a rock type may exist at depth on the Hearne craton and have been available as a contaminant during the evolution of the Kaminak dyke swarm parental magma.

In summary, the trends in major element chemistry of the Kaminak dykes are best explained by a model whereby a body of basaltic magma containing (~6.3 wt.% MgO) ponded at ~21 km depth (~7 kbar assuming an average crust density of 3×10^3 kgm^{-3}) and began to fractionate assemblages of spinel, plagioclase, clinopyroxene and orthopyroxene. Trace element modelling suggests that during fractionation, this magma assimilated relatively small amounts of granitic country rock which likely

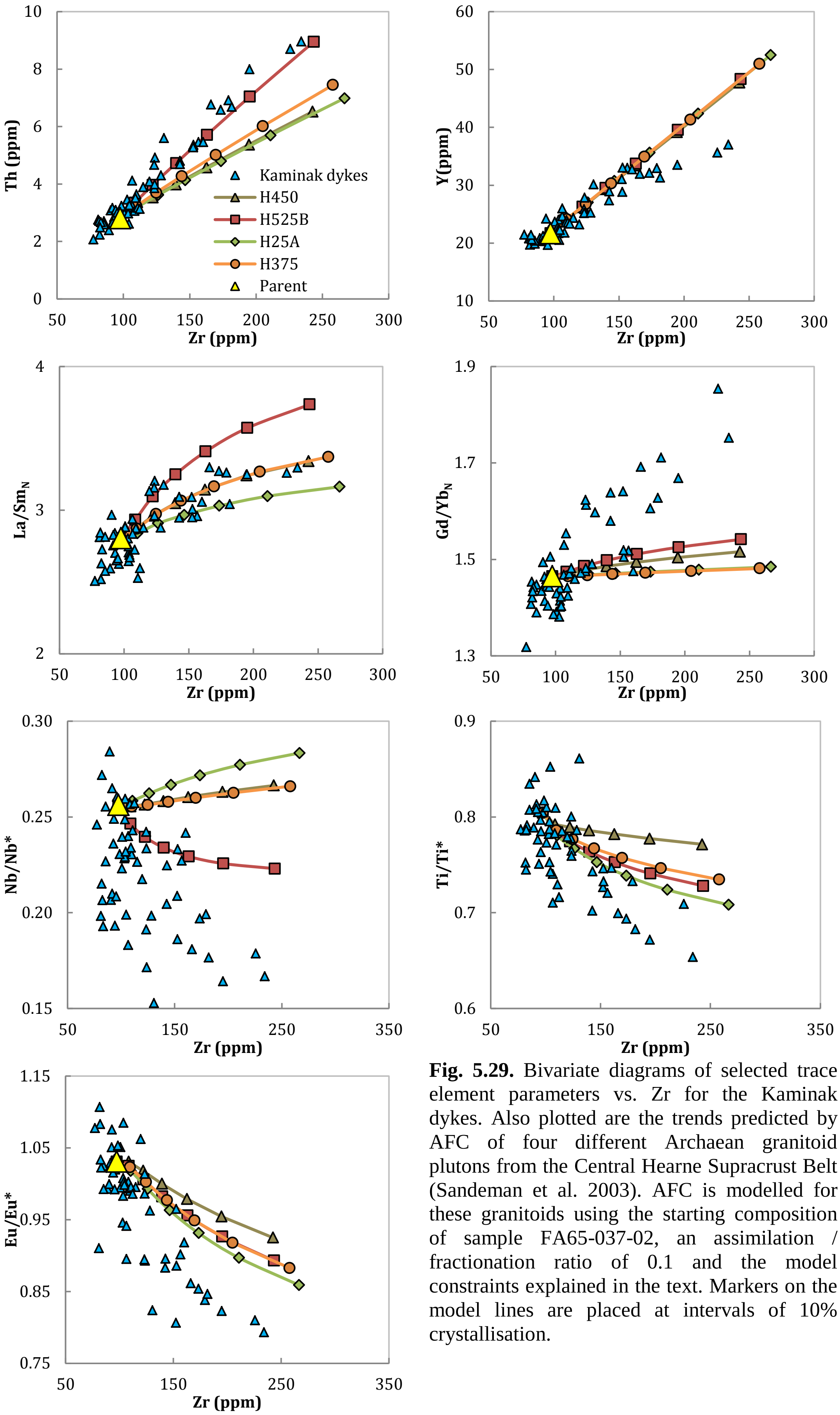

Fig. 5.29. Bivariate diagrams of selected trace element parameters vs. Zr for the Kaminak dykes. Also plotted are the trends predicted by AFC of four different Archaean granitoid plutons from the Central Hearne Supracrust Belt (Sandeman et al. 2003). AFC is modelled for these granitoids using the starting composition of sample FA65-037-02, an assimilation / fractionation ratio of 0.1 and the model constraints explained in the text. Markers on the model lines are placed at intervals of 10% crystallisation.

had a similar composition to low-degree partial melts of subduction-modified Archaean SCLM. The Kaminak dykes likely represent periodic melt extractions from this fractionating magma chamber which, on leaving the chamber, migrated upwards through the crust to be emplaced as a sub-linear dyke swarm or extruded as flood basalts where the magma reached the surface, as in the case of the Spi Group (Sandeman and Ryan 2008).

5.4.2.3. Viianki Dyke Swarm

Sample SUO-134 of Vogel et al. (1998) is used as an estimate for the parent magma of the Viianki dykes as this sample has the highest MgO content (17.16 wt.%) and lowest Zr content (56 ppm) of the Viianki dykes sampled.

The major element trends exhibited by the Viianki dykes are better predicted by models which use lower pressures (≤ 3 kbar) as shown by the inability of the higher pressure models in replicating the trends observed in SiO_2 and FeO vs. MgO. Of the three lower pressure models, it is not entirely obvious which of them best predicts the major element composition of the Viianki dykes. This is because all three models suggest that crystallisation over the interval modelled involves slightly varying proportions of spinel and olivine and thus, the major element trends predicted by the models are quite similar. Overall, the model which best predicts the major element trends exhibited by the Viianki dykes is Model 2 which models fractional crystallisation at 1 kbar pressure with 1 wt.% H_2O in the system **(Fig. 5.30)**. The scatter on plots of K_2O and P_2O_5 vs. MgO inhibit the use of these elements in petrogenetic models.

The 1 kbar (1 wt.% H_2O) model predicts that crystallisation begins at ~1475 °C with spinel being the first mineral to crystallise. Olivine joins spinel at 1395 °C after just ~1% of the parent magma has crystallised. Clinopyroxene replaces olivine in the crystallising assemblage at 1127 °C after ~29% of the magma has crystallised. The model ends soon after the appearance of clinopyroxene at 30% crystallisation, at which point MgO reaches ~6 wt.% which is lower than that observed in the Viianki dykes dykes **(Fig. 5.31)**. This model predicts magmas with MgO contents equal to the most evolved Viianki dyke (~8 wt.%) form when ~24% of the original magma has crystallised.

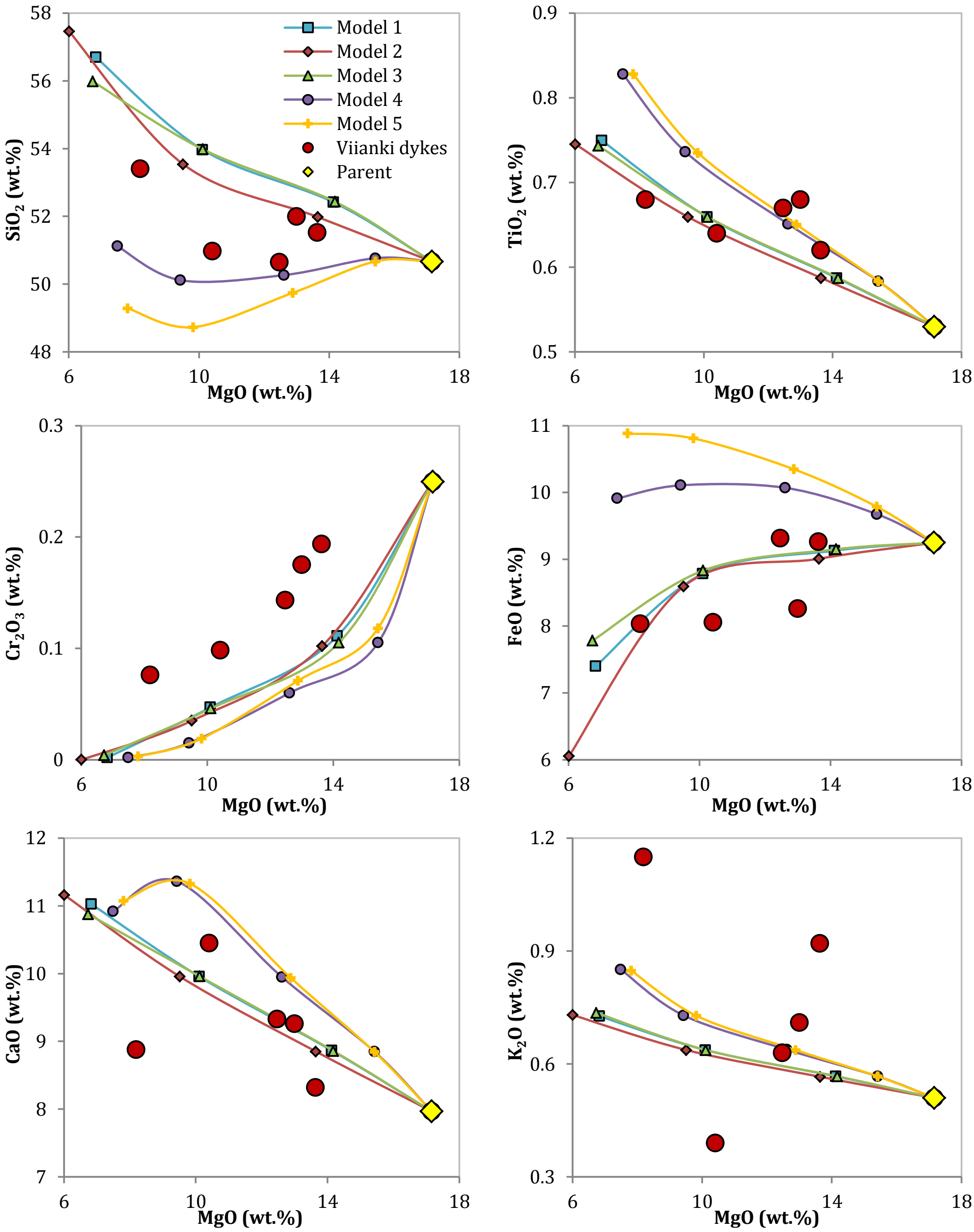

Fig. 5.30. Bivariate diagrams of selected major elements vs. MgO trends for the Viianki dykes and those predicted by fractional crystallisation of a parent magma with a composition equal to that of sample SUO-134. Markers on the model lines are placed at intervals of 10% crystallisation.

Models which use trace elements to model FC and AFC (where r = 0.25) using the parameters and assemblages predicted to form during fractionation at 1 kbar (1 wt.% H_2O) for the Viianki dykes are not robust. One of the reasons for the lack of robustness is that, only six Viianki dykes have been analysed for trace elements, half of which have not been analysed for the full suite of elements. The second reason is that, the trace element data for the Viianki dykes as published by Vogel et al. (1998) may be quite imprecise as shown by the discretely binned nature of the data (see Ta and Y analysis in **Fig. 4.64**). Thus, using trace element trends in parameters such as Gd/Yb_N ratios or the Eu and Ti anomalies recorded by the dykes is not possible with the current data set. However, the relative efficacy of FC or AFC in explaining the trace element geochemistry of the Viianki dykes can be qualified by examining the trends in incompatible element abundances.

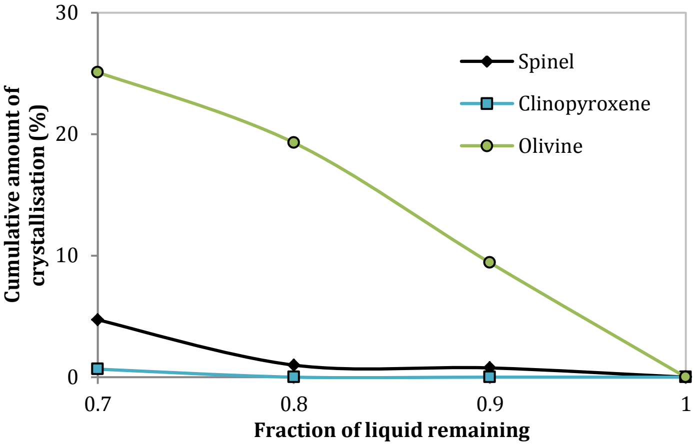

Fig. 5.31. Diagram showing the cumulative proportions of crystals formed by fractional crystallisation of the Viianki parent at 10% intervals of crystallisation.

For example, the 1 kbar (1 wt.% H_2O) major element model predicts that the most evolved Viianki dyke lavas formed after the primitive parent magma had undergone ~24% crystallisation. Trace element fractional crystallisation models consistently predict that after ~24% crystallisation the most evolved Viianki dykes should contain significantly lower abundances of incompatible trace elements than in reality. Assimilation-fractional crystallisation models which model assimilation of felsic continental crust (Rudnick 1995) when r = 0.25 are better at predicting the increases in trace element abundances observed in the Viianki dykes **(Fig. 5.32)**. The AFC model also predicts an increase in the La/Yb_N and La/Sm_N ratios in the evolved Viianki dykes, something that the FC model fails to do.

In summary, the major element chemistry observed in the Viianki dykes is best explained whereby a body of basaltic magma containing ~17.16 wt.% MgO and 1 wt.% H_2O ponded at ~3 km depth (~1 kbar) and fractionated spinel and olivine.

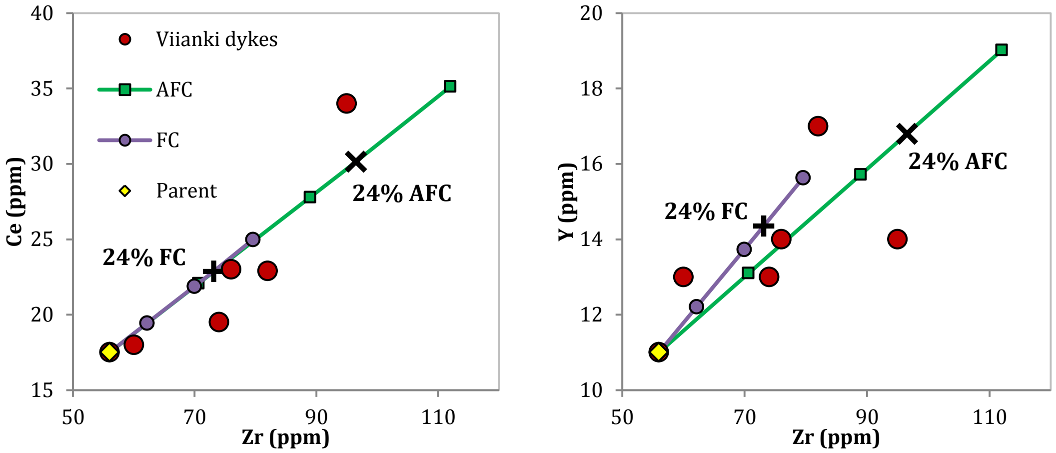

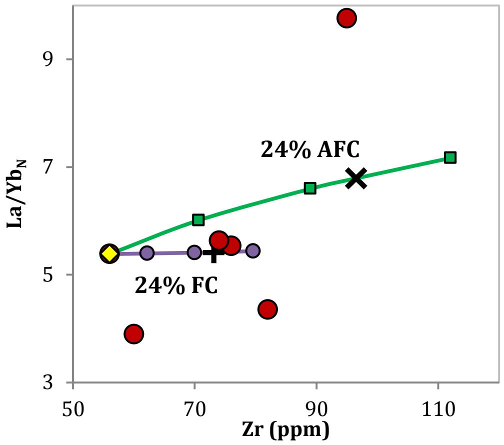

Fig. 5.32. Bivariate diagrams of selected trace element parameters vs. Zr for the Viianki dykes. Also plotted are the trends predicted by FC and AFC using the starting composition of sample SUO-134 and the model constraints explained in the text. Markers on the model lines are placed at intervals of 10% crystallisation.

During crystallisation, the magma chamber was periodically tapped and liquids removed which went on to form Viianki dykes. The applicability of trace element modelling to the Viianki dykes is limited due to a small and potentially imprecise data set. However, the data available shows that FC models cannot replicate the changes in trace element abundances or the trends in Primitive Mantle normalised REE ratios. AFC models which use the average composition of felsic crust (Rudnick 1995) and a moderate assimilation/fractionation ratio of 0.25 are more successful than the FC model at predicting the aforementioned trends. Thus, it is the author's opinion that AFC is more likely to have operated than simple FC during the evolution of the Viianki parent magma during its residence in the crust. However, determining precisely what the contaminant was, and to what extent it was utilised during fractionation of the Viianki parent magma, remains an open question which would be better answered using a larger and more precise Viianki dyke swarm dataset.

5.4.2.4. Leopard Dyke Swarm

The Group 1 Leopard dykes exhibit interesting whole-rock geochemistry in that they display a strong positive linear correlation between MgO and incompatible elements **(Fig. 4.50)** such that that the highest MgO samples contain the highest concentrations of incompatible elements. The positive correlation observed between MgO and the incompatible elements is also observed between the incompatible elements and remaining immobile major element oxides except CaO and Al_2O_3, which themselves show moderate-strong negative correlations with incompatible elements.

Thus, if we are to interpret the geochemistry of the Leopard dykes as showing a series of liquids derived from fractionation of a common magma, we have two potential scenarios to consider. The first scenario is that our potential parental magma is the one with the lowest incompatible element contents, but also lowest MgO contents (NBH13FA). In order to produce the major element trends observed in the Leopard dykes using NBH13FA as our starting composition, this potential parental magma would likely have to crystallise anorthite-rich plagioclase in order to decrease the Ca and Al content of the resulting magmas while, at the same time, increasing the incompatible element contents. The second scenario is that our potential parental magma is the one with the highest MgO content, but also highest incompatible element contents (NBH7HB). In order to produce the element trends observed in the Leopard dykes, this potential parent magma would likely have to crystallise and remove mafic silicates (to decrease the Mg, Fe and Si content of the resulting liquids) and also crystallise and remove a phase in which the REE are compatible in order to produce the decreasing REE content with MgO content observed in the dykes **(Fig. 4.50)**.

Fractional crystallisation models **(Fig. 5.33)** of both of these potential parental magmas utterly fail to produce fractionating melts capable of producing the geochemical trends observed in the Leopard dykes. Another mechanism, which may be suggested by the presence of the ubiquitous, large plagioclase phenocrysts is crystal entrainment [e.g., Mitchell et al. 1998) whereby, the whole-rock geochemistry of magma is modified by adding varying proportions of an exotic mineral phase.

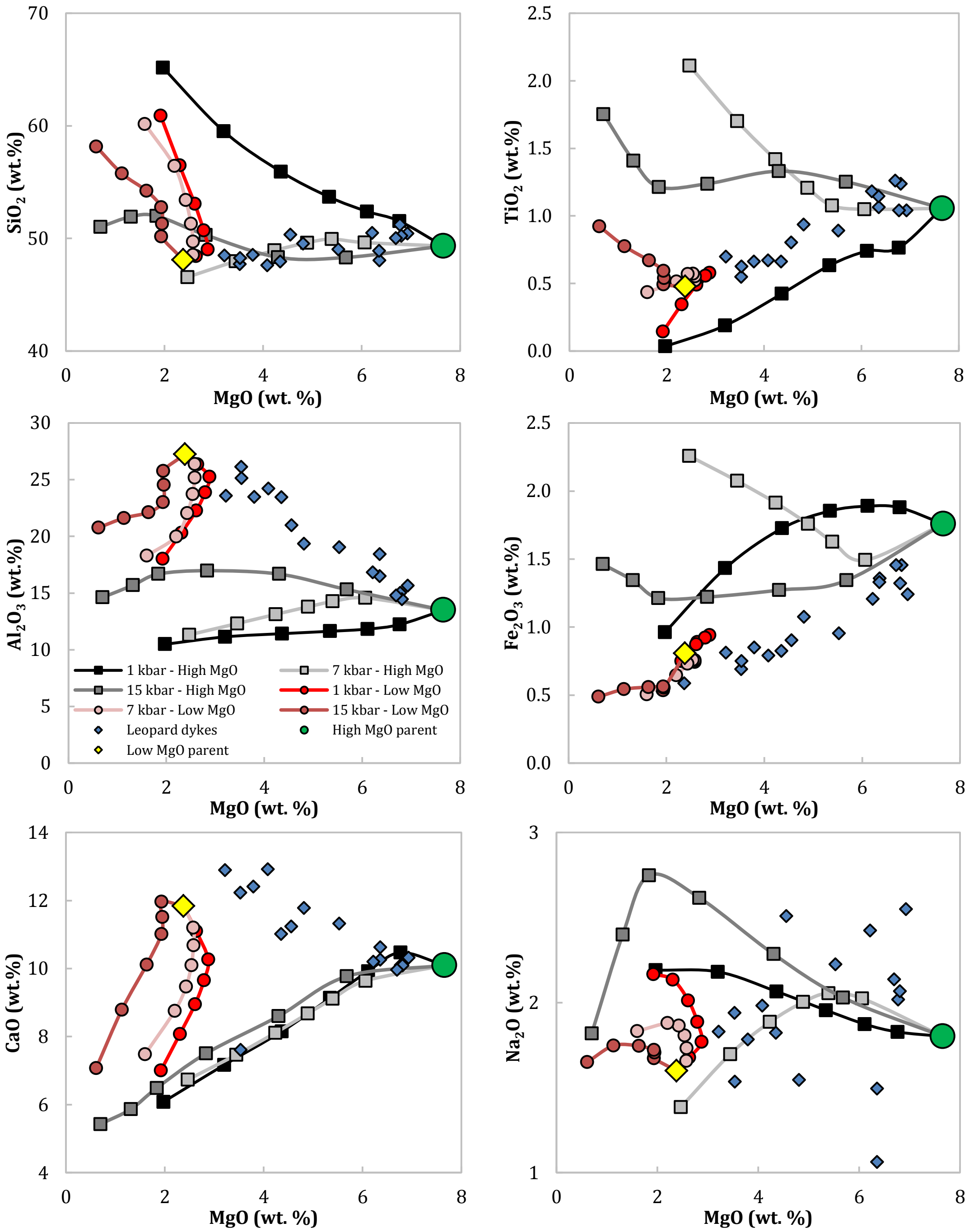

Fig. 5.33. Bivariate diagrams of selected major elements vs. MgO trends for the Group 1 Leopard dykes and those predicted by fractional crystallisation of a high and low MgO parent magma with compositions equal to that of samples NBH7HB and NBH13FA respectively. Markers on the model lines are placed at intervals of 10% crystallisation.

To model whether this process is feasible in producing the geochemistry of the Leopard dykes, 10% increments of plagioclase of varying anorthite-albite compositions was added to the most magnesium-rich Leopard dyke sample (NBH7HB). Addition of varying amounts of exotic plagioclase (of composition ~An 80) predicts the major element chemistry of the dykes very well. The fit of the model to the data becomes less good as the entrained plagioclase becomes more albite rich, as shown by the divergence of the model from the data in terms of SiO_2, CaO, Al_2O_3 and Na_2O **(Fig. 5.34)**.

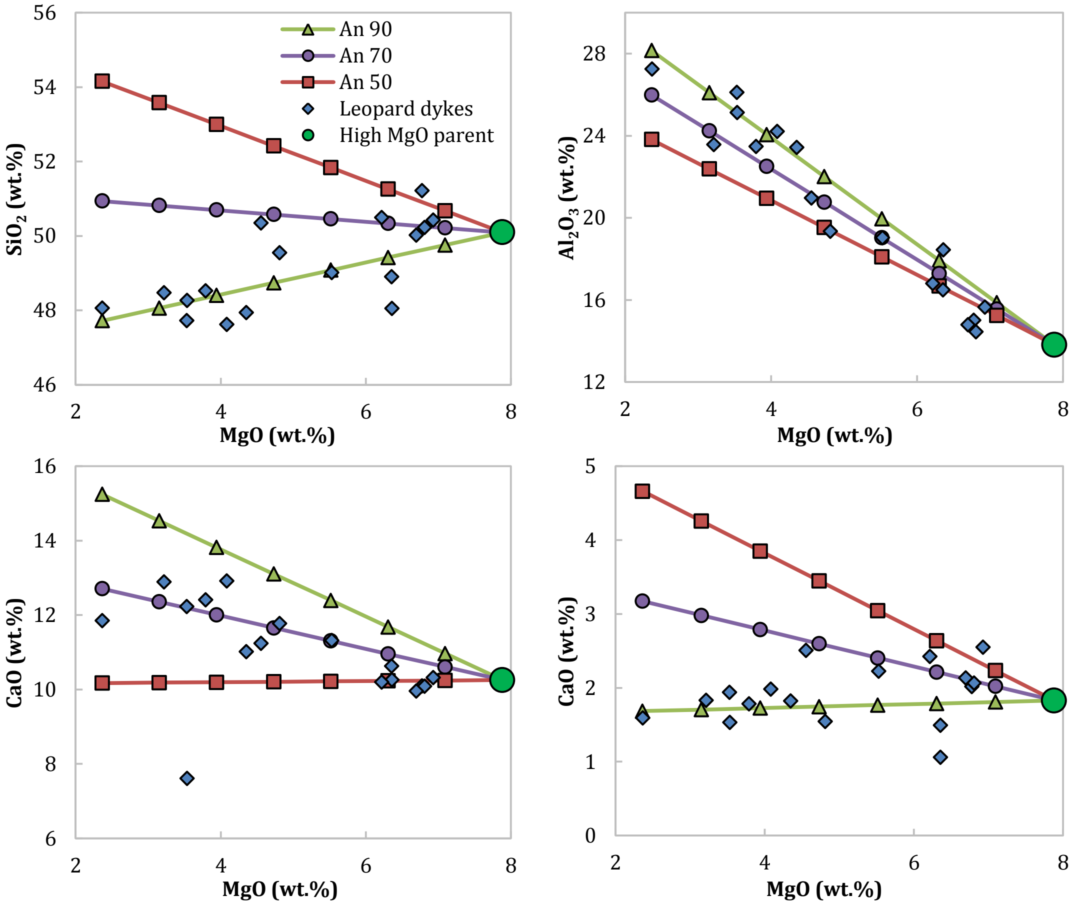

Fig. 5.34. Bivariate diagrams of selected major elements vs. MgO trends for the Group 1 Leopard dykes and those predicted by the addition of plagioclase of composition An 90, 70 and 50 to the high MgO parent magma NBH7HB. Markers on the model lines are placed at intervals of 10% addition.

The data presented suggest that the geochemical trends observed in the Leopard dykes are the product of the entrainment of varying amounts of exotic anorthite-rich plagioclase by a basaltic parent magma containing ~7.9 wt.% MgO. This interpretation requires the Leopard dyke parent magma to have intruded a pre-existing, evolved magma chamber which had already fractionated to produce plagioclase cumulates which were fissile enough to be entrained in the Leopard dyke magma. Other than the requirement of such a chamber by the models presented **Figs. 5.33** and **5.34** the only other data which can be presented which (indirectly) suggests the presence of such a chamber is the geochemistry of another aphanitic, mafic dyke collected from the Big Horn Mountains by Prof. Harlan.

Samples of this dyke (NBH14) are characterised by very steep chondrite-normalised REE slopes (La/Yb_N = 14.14) and large, negative Eu anomalies (Eu/Eu* = 0.47) which may indicate that these dykes evolved from a magma which had undergone extensive plagioclase fractionation **(Fig. 4.51)**. As this dyke crops out in the same area as the Leopard dykes, there is potential for this dyke to have been derived from the same crustal magma chamber which was later inhabited by the Leopard dyke parental magma. However, at this stage, and with this amount of data, linking these Group 2 Leopard dykes with the plagioclase megacrysts preserved in the Group 1 Leopard dykes is largely speculative.

Petrographic evidence also suggests that the plagioclase megacrysts in the Leopard dykes are exotic. Examination of the plagioclase megacrysts show that the crystals have extremely uneven margins, characterised by sizeable embayments and irregularities **(Fig. 5.35A)** which are indicative of resorption of the plagioclase megacrysts (Maaløe 1976). Resorption of minerals occurs when the crystals are out of equilibrium with the liquid, with disequilibrium commonly caused by magma mixing (Nelson and Montana 1992). Thus, the disequilibrium between the fine grained groundmass (liquid) and the plagioclase megacrysts defined by the resorption textures in the latter, suggest that the two phases (liquid and megacrysts) were not derived from a common parent magma. The second piece of petrographic evidence which suggests the plagioclase megacrysts are exotic is that, close to the margin of the phenocrysts, the groundmass plagioclase crystals are much finer grained and aligned parallel to the megacryst margins than they are further away from the plagioclase megacrysts. This textural relationship indicates that the plagioclase megacrysts were potentially much cooler than the magma which formed the finer grained groundmass (thus inhibiting larger crystal growth of groundmass plagioclase near to the megacrysts) while at the same time, acting to channel the flow of the liquid around their margins to produce the alignment of the groundmass plagioclase as observed in **Fig. 5.35B**. If this interpretation is correct, then the plagioclase phenocrysts formed prior to their incorporation into the Group 1 Leopard dyke magma.

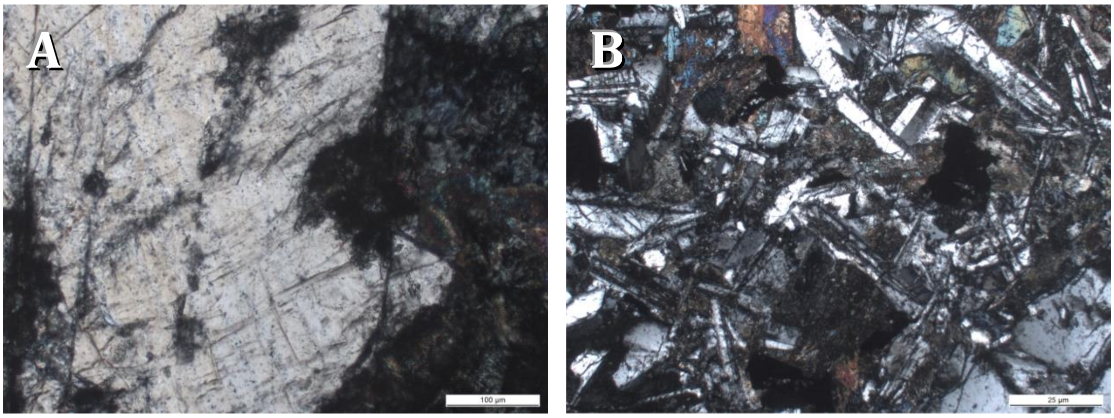

Fig. 5.35. XPL micrographs of Leopard dykes. **A)** View of embayments along margin of plagioclase megacryst indicative of resorption; **B)** Crystal size change in groundmass from finer grained closer to the margin of plagioclase megacryst (bottom right) to coarser toward the top left of the image.

The proof required to test this hypothesis may be recorded by the chemistry of the plagioclase megacrysts. Analysis of the composition of the megacrysts would allow the models shown in **Fig. 5.34** to be tested. Secondly, such an analysis would allow comparison between the composition of the megacrysts and the groundmass plagioclase in order to determine if the two populations are geochemically different, and hence, derived from different parent magmas. Unfortunately, sufficient quantities of purely-megacryst or purely-groundmass required for such an analysis were not collected and constraints of time have meant that laser ablation of the two types of plagioclase was not completed. Future studies of the Leopard dykes should analyse the groundmass and megacrystic plagioclase in order to test the hypotheses presented here.

In summary, the geochemistry of the Group 1 Leopard dykes is inexplicable using conventional models of fractional crystallisation. The major element geochemical trends exhibited by the dykes can instead be modelled by adding increasing proportions of anorthite-rich plagioclase to a parental magma which contains ~7.9 wt.% MgO. The origin of this exotic plagioclase has not been determined, but may be related to the Group 2 Leopard dykes which crop out in the same area. Future work should aim to test these hypotheses by analysing and comparing the chemical compositions of the groundmass and megacrystic plagioclase, potentially using laser ablation ICP-MS (Davidson et al. 2001).

5.4.3. Matachewan LIP Flood Basalts

5.4.3.1. Seidorechka Formation

Fractional crystallisation of the Seidorechka Formation was modelled using a starting composition equal to that of sample 13081 (Chashchin et al. 2008). This sample is assumed to be the most primitive partly because it has the highest MgO content and also because the Seidorechka Formation rocks record decreasing incompatible element contents with increase MgO contents.

It is unclear which model best approximates the major element geochemical trends exhibited by the Seidorechka Formation samples as there is not a single model which consistently fits the data **(Fig. 5.36)**. For example, fractional crystallisation of a magma of composition similar to sample 13081 at 1 kbar with 1 wt.% H_2O best explains the trends in SiO_2, while the FeO and K_2O vs. MgO trends are better explained by fractional crystallisation using the anhydrous 1 kbar model. All of the models predict the general trends in Al_2O_3 and CaO observed in the Seidorechka Formation, i.e., an initial increase followed by sharp decreases which begins at ~5 wt.% MgO. Overall, I judge that fractional crystallisation of a magma with a composition similar to sample 13081 at 1 kbar (anhydrous) best predicts the major element trends observed in the Seidorechka Formation rocks.

The anhydrous 1 kbar model predicts that crystallisation of a magma with a composition similar to sample 13081 begins at 1479 °C with olivine the first mineral to crystallise. Olivine remains the only mineral to crystallise until ~38% of the magma has crystallised, at which point orthopyroxene begins to crystallise. Olivine stops crystallising and spinel starts once the magma reaches 1163 °C and 40% of the original liquid has crystallised. Clinopyroxene and plagioclase join the crystallising assemblage soon after at ~1145 °C when ~43% of the magma has crystallised. Quartz is the last mineral to crystallise, joining the assemblage when the magma reaches 1025 °C, after 72% of the magma has crystallised. This assemblage of quartz, orthopyroxene, plagioclase, spinel and clinopyroxene continues to fractionate until the end of the model at 90% crystallisation at which point, the magma contains <0.5 wt.% MgO **(Fig. 5.37)**.

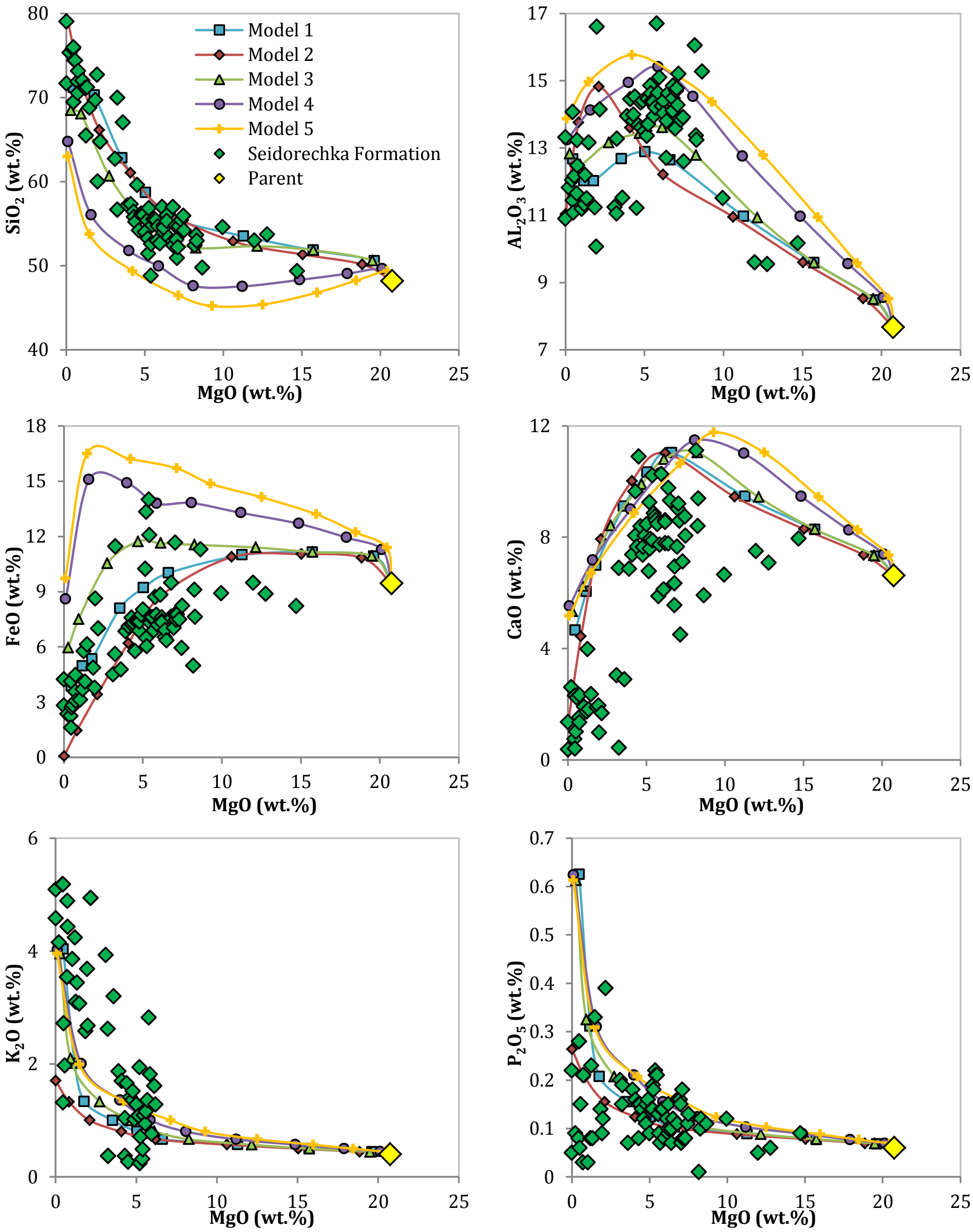

Fig. 5.36. Bivariate diagrams of selected major elements vs. MgO trends for the Seidorechka Formation volcanics and those predicted by fractional crystallisation of a parent magma with a composition equal to that of sample 13081. Markers on the model lines are placed at intervals of 10% crystallisation.

Trace element modelling using the starting parameters of the anhydrous 1kbar model is not possible as sample 13081 was not analysed for trace elements. Instead, the trace element composition for the most primitive sample BT-12/04, for which such data exists is used. This sample contains 8.65 wt.% MgO, and intersects the major element trends predicted by the anhydrous 1 kbar model at ~35% crystallisation. The evolution of the trace element composition of sample BT-12/04 is modelled using the model parameters and mineral assemblages predicted to form by the anhydrous 1 kbar model from this point in the model, forwards.

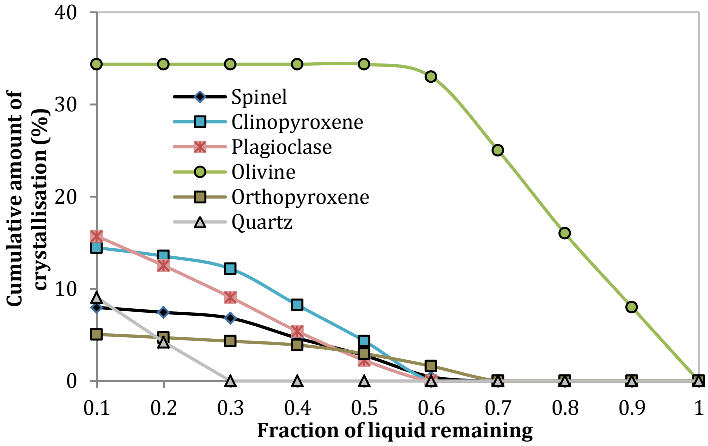

Fig. 5.37. Diagram showing the cumulative proportions of crystals formed by fractional crystallisation of the Seidorechka Formation parent at 10% intervals of crystallisation.

Fractional crystallisation models using these parameters predict the general increase in incompatible element concentrations as crystallisation progresses **(Fig. 5.38)** observed in the Seidorechka Formation. However, in the case of Y, the model wildly overestimates the enrichment for the most evolved magmas while, in the case of Th, the model underestimates the enrichment.

The Seidorechka Formation samples do not show any obvious trends between La/Sm$_N$ or Gd/Yb$_N$ and MgO and instead exhibit a large, scattered range. The Seidorechka Formation rocks do, however, show a trend of increasingly negative Nb-Ta anomalies with fractionation. This is not predicted by simple fractional crystallisation models. The AFC model which uses the composition of felsic crust (Rudnick and Fountain 1995) and an assimilation/fractionation ratio of 0.1 produces similar trends to the FC model in terms of the variation of Y, La/Sm$_N$, Gd/Yb$_N$, Ti/Ti* and Eu/Eu* but better predicts both the trends in Th and Nb/Nb*. This observation suggests that AFC is a more likely mechanism for producing the trace element geochemistry exhibited by the Seidorechka Formation volcanic rocks.

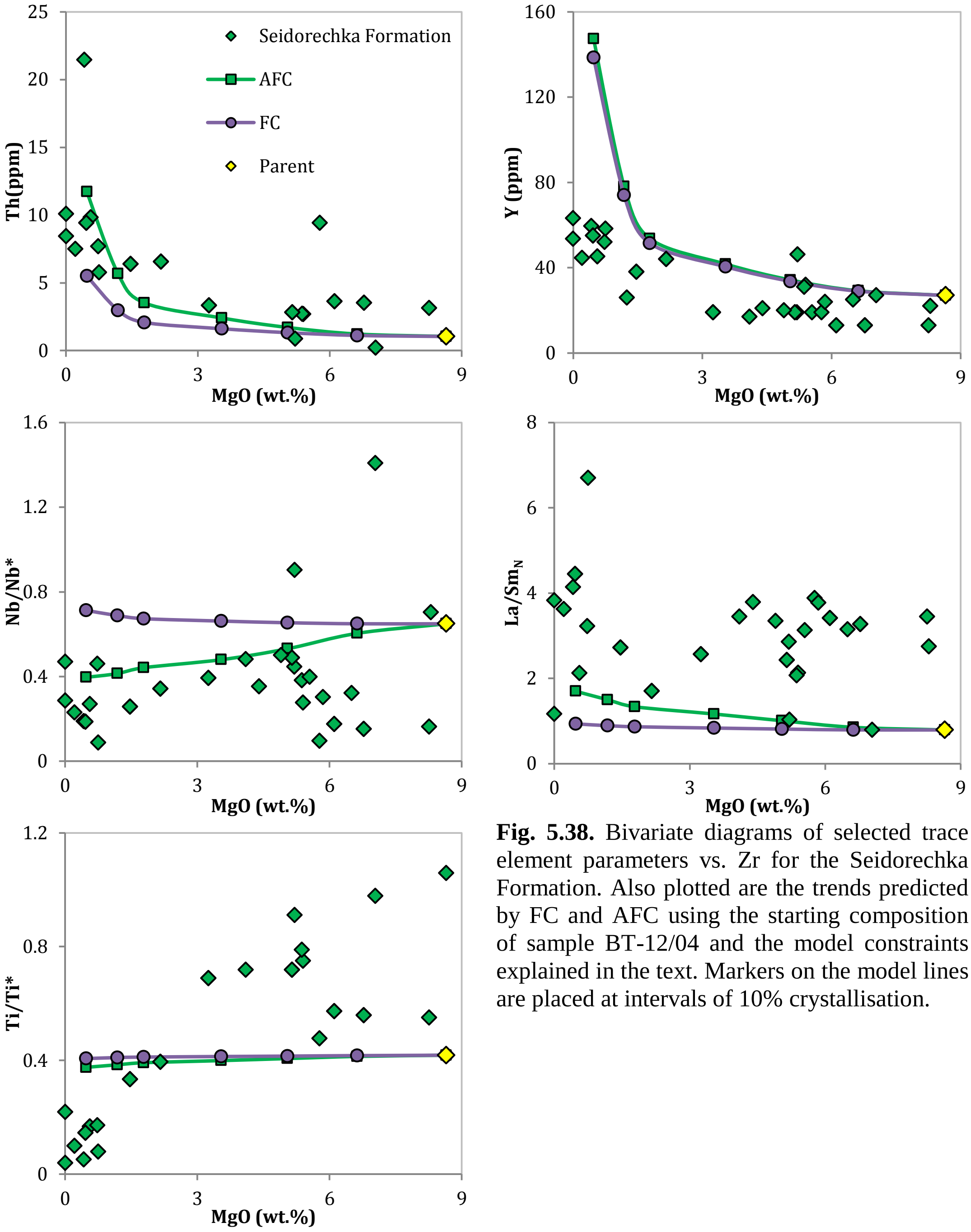

Fig. 5.38. Bivariate diagrams of selected trace element parameters vs. Zr for the Seidorechka Formation. Also plotted are the trends predicted by FC and AFC using the starting composition of sample BT-12/04 and the model constraints explained in the text. Markers on the model lines are placed at intervals of 10% crystallisation.

5.4.3.2. Thessalon Formation

Group 1

Sample KYT483 (Tomlinson 1996) is used as an estimate for the parent magma of the Group 1 Thessalon Formation lavas as this sample has very nearly the highest MgO content (6.70 wt.%) and lowest REE content (18× chondrite) of the Group 1 Thessalon Formation samples studied.

Only a few of the major elements are helpful in determining the most likely conditions of fractionation of the Group 1 Thessalon parent magma. This is because the wide scatter of the Group 1 data on many of the major element vs. MgO plots **(Fig. 4.27)** does not allow robust discrimination of the models. However, trends of increasing SiO_2 and decreasing Fe_2O_3 and Al_2O_3 with decreasing MgO are better approximated by Model 2 which models fractionation at 1 kbar in the presence of 1 wt.% H_2O **(Fig. 5.39)**.

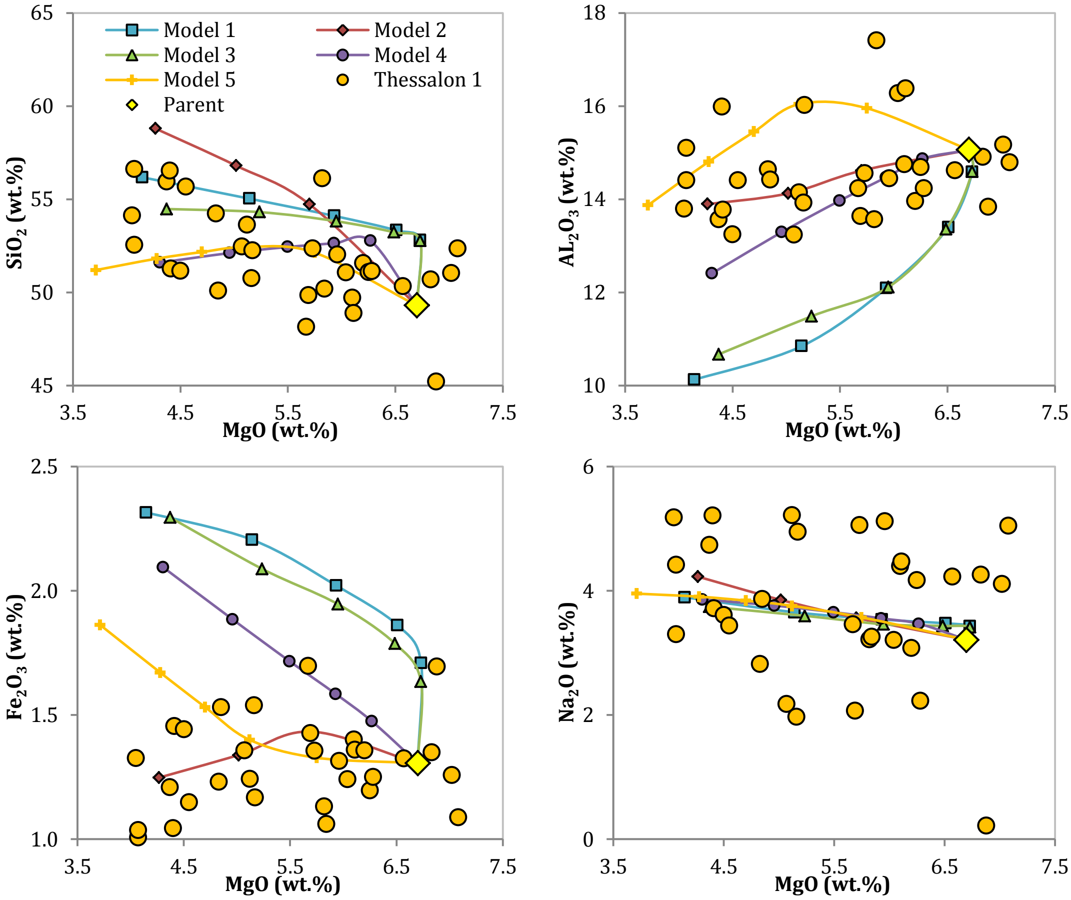

Fig. 5.39. Bivariate diagrams of selected major elements vs. MgO trends for the Group 1 Thessalon Formation volcanics and the trends predicted by fractional crystallisation of a parent magma with a composition equal to that of sample KYT483. Markers on the model lines are placed at intervals of 10% crystallisation.

The 1 kbar (1 wt.% H_2O) model predicts that crystallisation of the Group 1 parent magma begins at ~1245 °C with spinel being the first mineral to crystallise. Plagioclase and olivine join spinel at 1130 °C after ~11% of the parent magma has crystallised. Clinopyroxene follows and joins the assemblage once the magma has cooled to 1126 °C and after ~14% crystallisation. This assemblage of spinel, olivine, clinopyroxene and plagioclase continues to crystallise until the end of the model at

30% crystallisation, at which point the evolved lava contains ~4 wt.% MgO which is similar to that observed in the most evolved Group 1 sample **(Fig. 5.40)**.

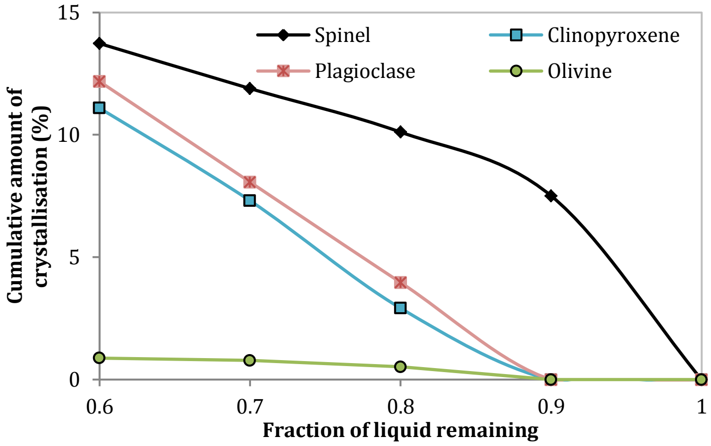

Fig. 5.40. Diagram showing the cumulative proportions of crystals formed by fractional crystallisation of the Thessalon Formation Group 1 parent at 10% intervals of crystallisation.

Trace element models of the Group 1 Thessalon formation rocks unequivocally support an AFC mechanism for their evolution. This is signified by the FC model predicting incompatible element increases less than half the magnitude observed in the lavas and also its apparent failure in predicting the Group 1 rocks changing REE ratios and Ti anomalies. The failures of the FC model are mirrored by successes by the AFC model using the same criteria **(Fig. 5.41)**. The trace element trends in the Group 1 rocks are best explained by AFC models which use the average Archaean felsic crust (Rudnick 1995) and an assimilation/fractionation ratio of 0.2.

Group 2

Sample KYT477 (Tomlinson 1996) is used as an estimate for the parent magma of the Group 2 Thessalon Formation lavas as this sample has the highest MgO content (6.79 wt.%) and lowest REE content (53× chondrite) of the Group 2 Thessalon Formation samples studied.

The scattered nature of many of the major element vs. MgO plots of the Group 2 volcanics mean that for the majority of major elements, the modelled trends overlap the spread of the sample data with no single model producing a better fit than the others. However, trends of SiO_2, Al_2O_3 and FeO vs. MgO are better modelled by fractional crystallisation at higher pressures. The model which is most successful in replicating the major element trends exhibited by the Group 2 volcanics is Model 5 which models fractionation at 10 kbar **(Fig. 5.42)**.

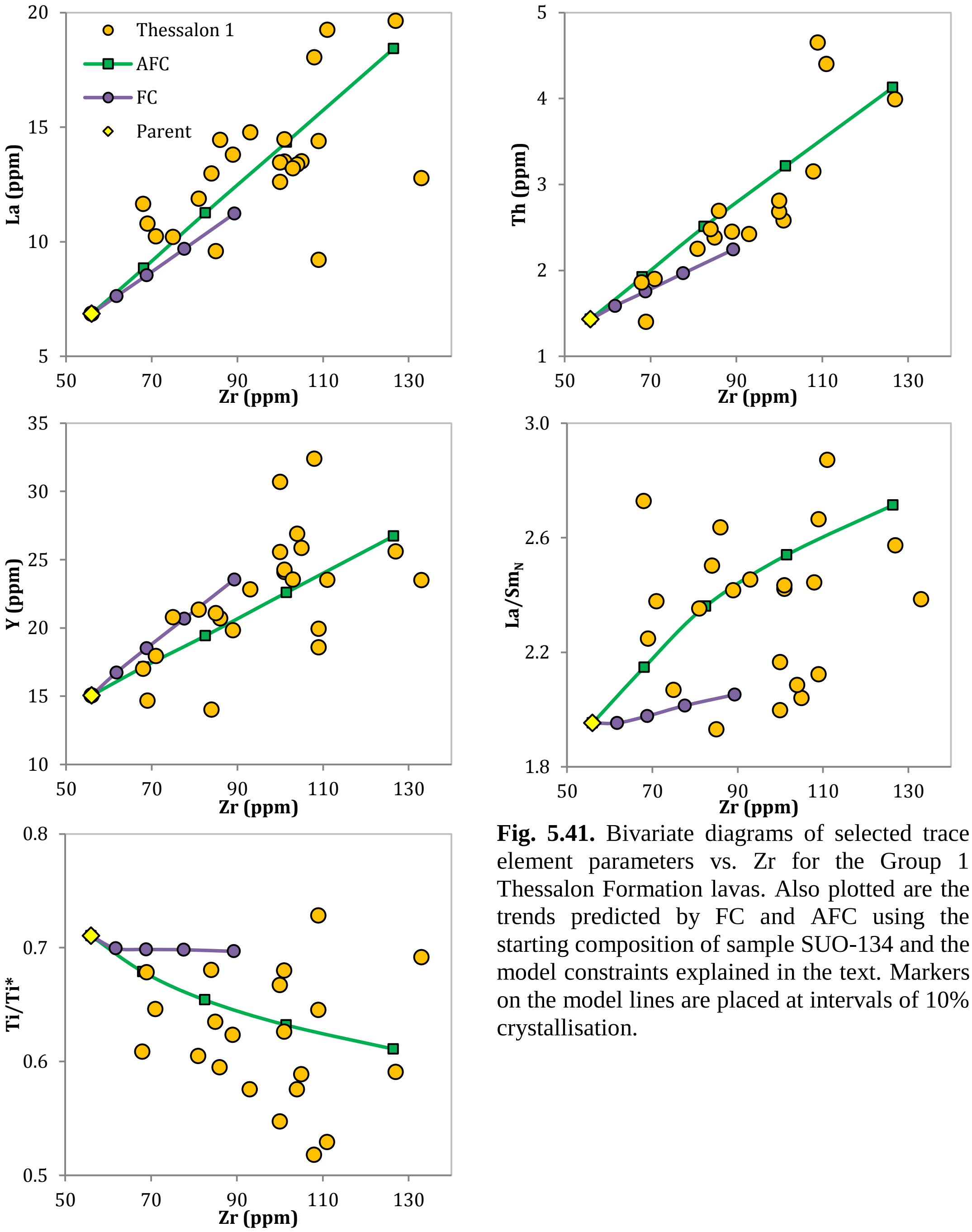

Fig. 5.41. Bivariate diagrams of selected trace element parameters vs. Zr for the Group 1 Thessalon Formation lavas. Also plotted are the trends predicted by FC and AFC using the starting composition of sample SUO-134 and the model constraints explained in the text. Markers on the model lines are placed at intervals of 10% crystallisation.

The 10 kbar model predicts that crystallisation begins at ~1378 °C with spinel being the first mineral to crystallise. Orthopyroxene joins spinel at 1328 °C after ~4% of the parent magma has crystallised. Clinopyroxene follows and joins orthopyroxene and spinel in the crystallising assemblage at 1229 °C after ~16% of the original parent magma has crystallised. Plagioclase begins crystallising soon after, once the magma has cooled to 1224 °C and ~17% of it has crystallised. This assemblage of spinel, orthopyroxene, clinopyroxene and plagioclase continues to crystallise until the end of the model at 60%, at which point the evolved lava contains <1.5 wt.% MgO which is lower than that observed in the most evolved Group 2 sample **(Fig. 5.43)**.

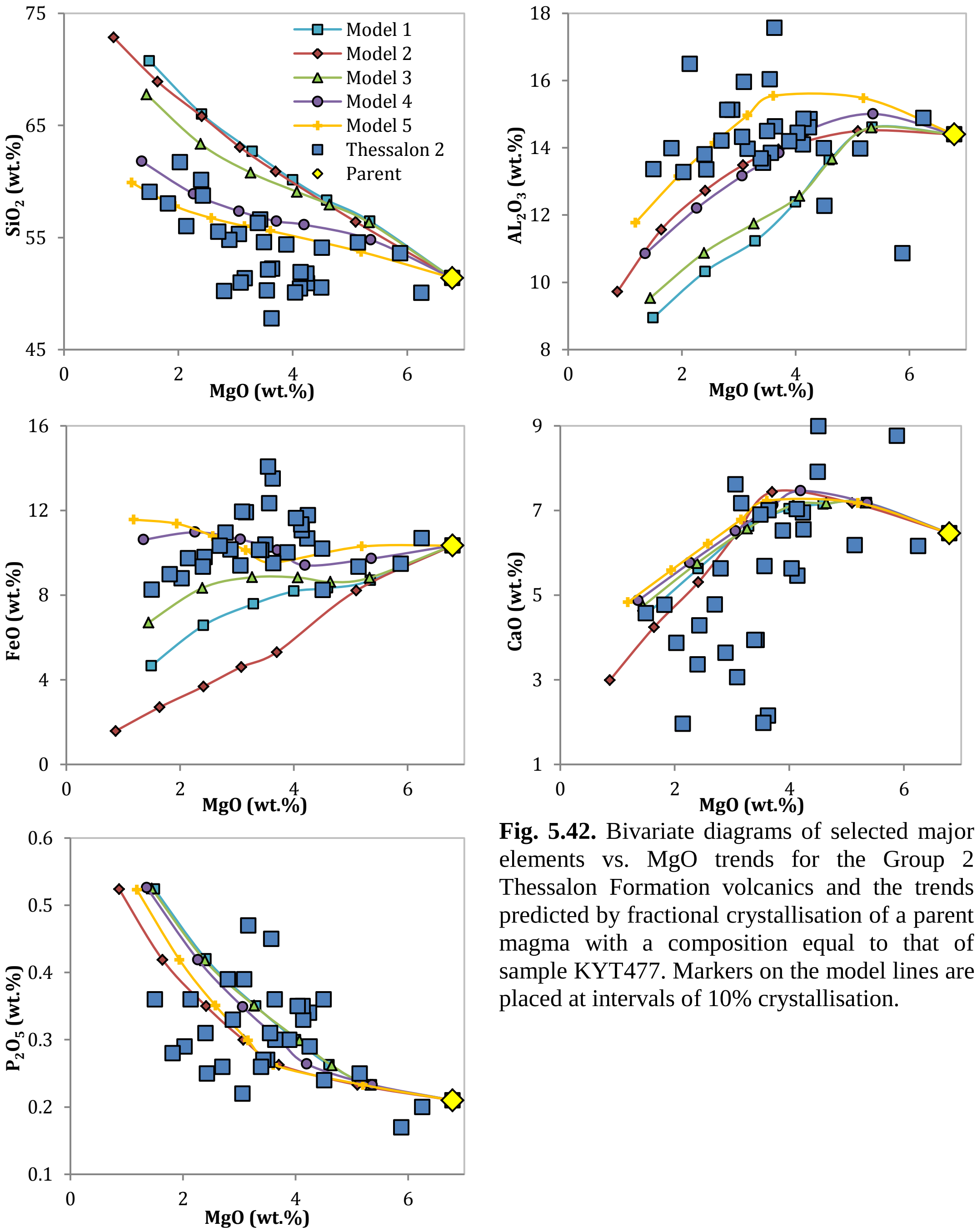

Fig. 5.42. Bivariate diagrams of selected major elements vs. MgO trends for the Group 2 Thessalon Formation volcanics and the trends predicted by fractional crystallisation of a parent magma with a composition equal to that of sample KYT477. Markers on the model lines are placed at intervals of 10% crystallisation.

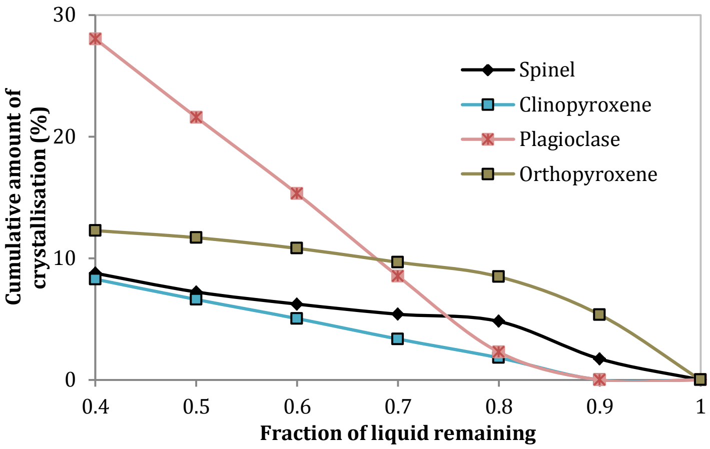

Fig. 5.43. Diagram showing the cumulative proportions of crystals formed by fractional crystallisation of the Thessalon Formation Group 2 parent at 10% intervals of crystallisation.

The trace element data for the Group 2 volcanics appear to give conflicting evidence for whether FC or AFC operated during the evolution of the Group 2 parent magma. The conflict is manifested by the superior ability of the FC model to predict the magnitude of the incompatible element increase observed in the volcanics, and the same models failure at predicting the increase in La/Yb$_N$ ratios or size of the negative Ti anomalies. The trends in La/Yb$_N$ and Ti/Ti* are predicted by the AFC model, but the AFC model overestimates the incompatible element increase observed in the lavas to a slightly greater extent than the FC model **(Fig. 5.44)**.

These observations suggest that as FC is unable to replicate the increasing La/Yb$_N$ ratio and increasingly negative Ti anomalies observed in the Group 2 lavas, AFC operated during the evolution of the Group 2 parent magma. Further to this, the contaminant must have had a more pronounced negative Ti anomaly than either the average continental crust, or the low degree partial melts of subduction-modified SCLM as modelled in section 5.2. The contaminant must also have had a steeper normalised REE slope than these two potential contaminants for the same reason. Unfortunately, a literature search was unsuccessful in identifying a potential contaminant with these attributes in the southern Superior Province. However, as major element modelling suggests that fractionation of the Group 2 parent magma occurred at great depth (10 kbar ≈ 30 km) and given the region's fairly limited amount of tectonic uplift since 2.5 Ga, it is likely that the crustal material which contaminated the group 2 parent magma during its evolution is currently unexposed.

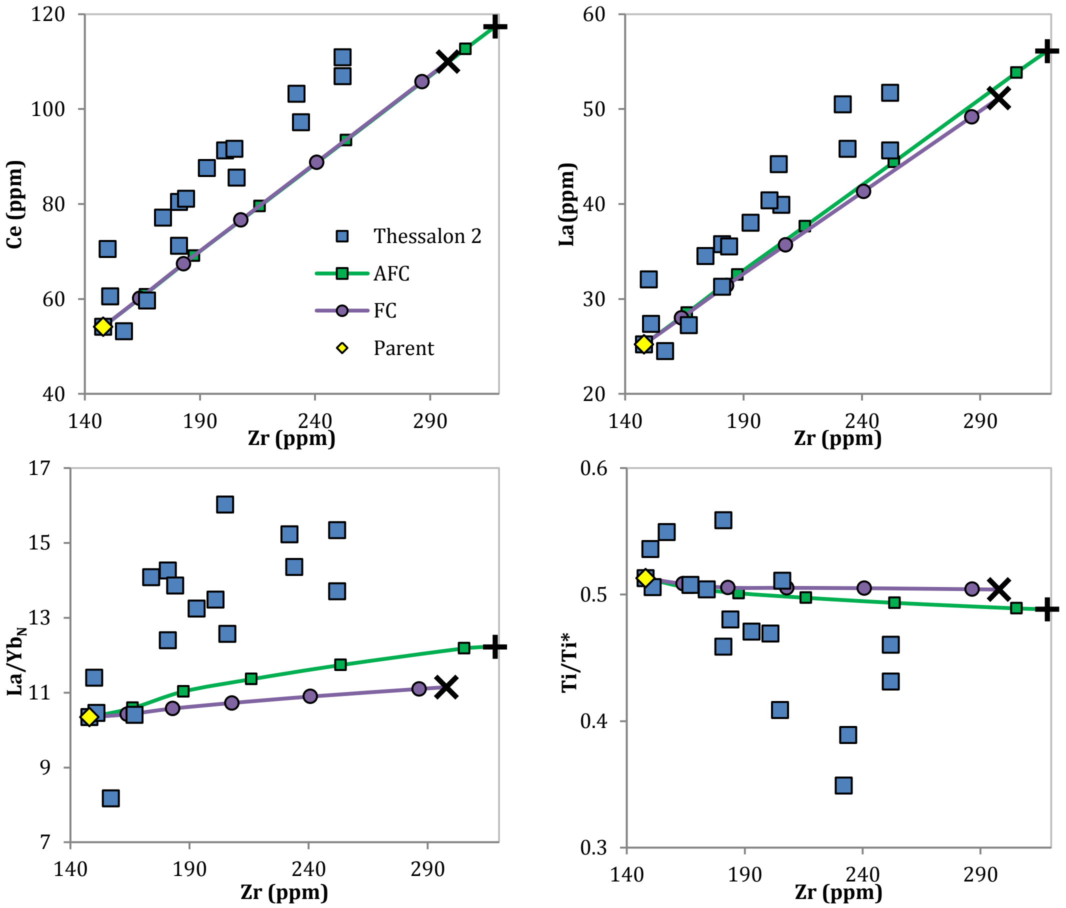

Fig. 5.44. Bivariate diagrams of selected trace element parameters vs. Zr for the Group 2 Thessalon Formation volcanics. Also plotted are the trends predicted by FC and AFC using the starting composition of sample KYT477 and the model constraints explained in the text. Markers on the model lines are placed at intervals of 10% crystallisation. The end of the trace element models is shown by the black crosses which marks when the original parent magma has reached 52% crystallisation. 52% is chosen as this is when the evolved liquid approaches 1.8 wt.% MgO, which corresponds to the magnesium content of the most evolved sample for which trace element data is available.

Summary

Trace element modelling of the Thessalon Formation basalts has shown that the formation is a composite, consisting of evolved melts sourced from at least two separate magma chambers. One of the magma chambers was situated in the shallow crust where the hydrous magma it contained assimilated moderate amounts of felsic continental crust as it fractionated. The second magma chamber was situated much deeper in the crust at approximately 30 km depth. This second chamber also assimilated its host rocks, the trace element chemistry of which is more similar to low degree partial melts of subduction-modified SCLM than it is to felsic Archaean crust. However, no such satisfactory potential contaminant could be found in the literature and thus, the contaminant remains poorly defined. These two separate chambers were periodically tapped with the increasingly evolved melts extracted and extruded on the surface to form the Thessalon Formation.

5.4.4. Matachewan LIP Layered Intrusions

5.4.4.1. Blue Draw Metagabbro

As no potential feeder dykes, or early-formed melt inclusions were found in the Blue Draw Metagabbro rocks, fractional crystallisation of the intrusion was modelled using the parental magma composition discussed in section 5.1. Fractional crystallisation of this melt was modelled using PELE to determine if this magma is capable of producing a bulk mineralogy similar to that observed in the BDM.

The crystallisation model calculated by PELE for fractionation of the BDM parent magma using a quartz-fayalite-magnetite (QFM) oxygen buffer at 3 kbar predicts initial crystallisation of olivine and spinel until ~15% crystallisation, at which point clinopyroxene joins the assemblage followed by plagioclase at ~22% crystallisation. The model predicts that olivine stops crystallising at ~53% which coincides with the onset of orthopyroxene crystallisation which continues to crystallise until ~74% crystallisation. Quartz and alkali feldspar are last to crystallise, appearing after approximately 80% of the original magma has crystallised **(Fig. 5.45)**. The crystallisation sequence and modal abundances predicted to form from fractionation of the proposed parental melt is in good agreement with that observed in thin section of samples from the stratigraphy of the BDM (see section 3.4).

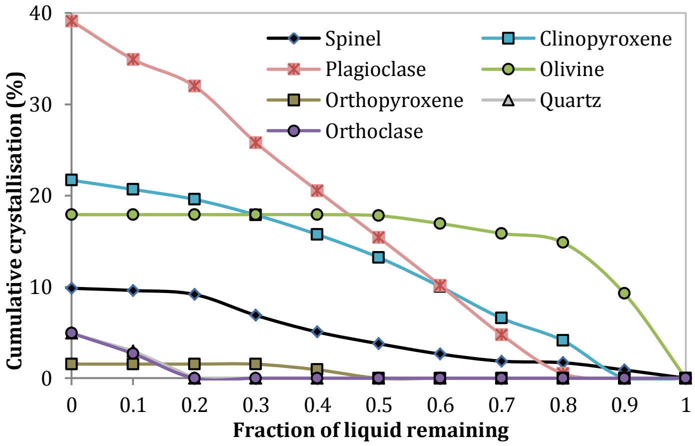

Fig. 5.45. Diagram showing the cumulative proportions of crystals formed during fractional crystallisation of the Blue Draw Metagabbro parent at 10% intervals of crystallisation.

To semi-quantitatively determine whether the proposed parental magma is capable of producing the modal mineralogy of the Blue Draw Metagabbro, the mineralogy predicted to form by PELE (as estimated from **Fig. 5.45** when the degree of liquid remaining = 0) is compared to that estimated by stratigraphic profiles of the CIPW normative mineralogy of the intrusion **(Fig. 5.46)**. By estimating the modal mineralogy for each portion of the stratigraphy for the Blue Draw Metagabbro and then summing them into a weighted average (much like the method shown in **Fig. 5.2**), an average mineralogy for the intrusion can be constructed. **Fig. 5.47** compares this estimated modal mineralogy with that predicted to form from the parental magma modelled by PELE and shows that both estimates are in good agreement in terms of abundances of plagioclase, olivine, quartz and orthoclase, but differ slightly in their estimates of spinel and pyroxene in the intrusion.

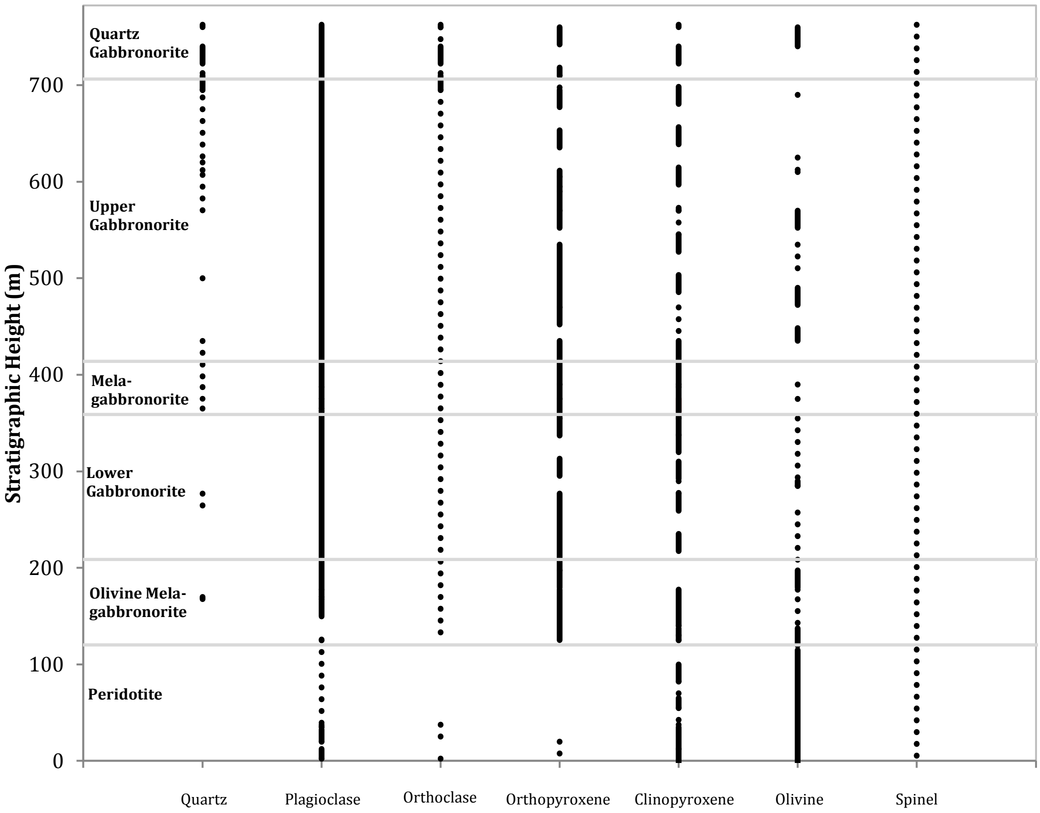

Fig. 5.46. CIPW normative composition of the Blue Draw Metagabbro against stratigraphic height. Solid lines show where minerals are present in quantities >25%, dashed lines show where minerals are present in quantities between 10 and 25% and dotted lines show where minerals are present in quantities between 0 and 10%.

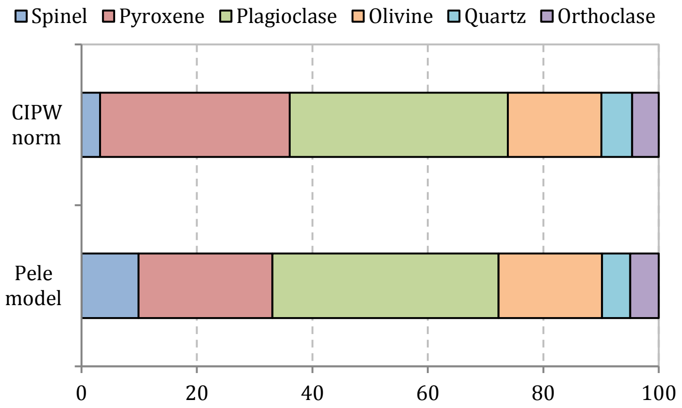

Fig. 5.47. Comparison of modal mineral abundances formed via fractional crystallisation of the Blue Draw Metagabbro parent magma, as predicted by PELE and that estimated from the CIPW normative composition of the intrusion.

To further test the validity of the estimated parent melt, the chemistry of the cumulates predicted to form during fractional crystallisation of the melt was modelled at 5% intervals using the mineral assemblages predicted by PELE and then compared to the composition of the cumulates in the intrusion. The model predicts the first cumulates to form in the intrusion are olivine-dominated and are MgO rich (40-50 wt.%), Al_2O_3 poor (0-4 wt.%) and contain ~40 wt.% SiO_2. Crystallisation of these olivine-dominated cumulates is followed by crystallisation of clinopyroxene + plagioclase-rich rocks which are much lower in MgO (~10 wt.%), higher in Al_2O_3 (~16 wt.%) and contain ~50 wt.% SiO_2. Comparison of these modelled cumulates with the stratigraphic geochemical profiles for cumulate rocks near the base of the BDM show that the two are in good agreement **(Fig. 5.48)** in terms of cumulate composition. Moreover, the model predicts that the significant compositional change between the olivine and clinopyroxene + plagioclase-rich rocks occurs over a relatively short (5-10%) crystallisation interval. In this, the model is again in good agreement with the stratigraphic geochemical profiles of the intrusion which show the same stark change in cumulate chemistry occurring over ~10 m at ~125 m. The fit of the model with the data can be greatly improved by including a 10% trapped melt fraction of the coexisting liquid at the given point in the crystallisation history. While these models predict much of the compositional trends in the lower portion of the BDM, the models do not perfectly predict the compositional variability of the cumulates close to the basal margin of the intrusion (between 0-40 m). However, these samples are also variable in their trace element compositions and show petrographic evidence of contamination by the country rock hosting the intrusion.

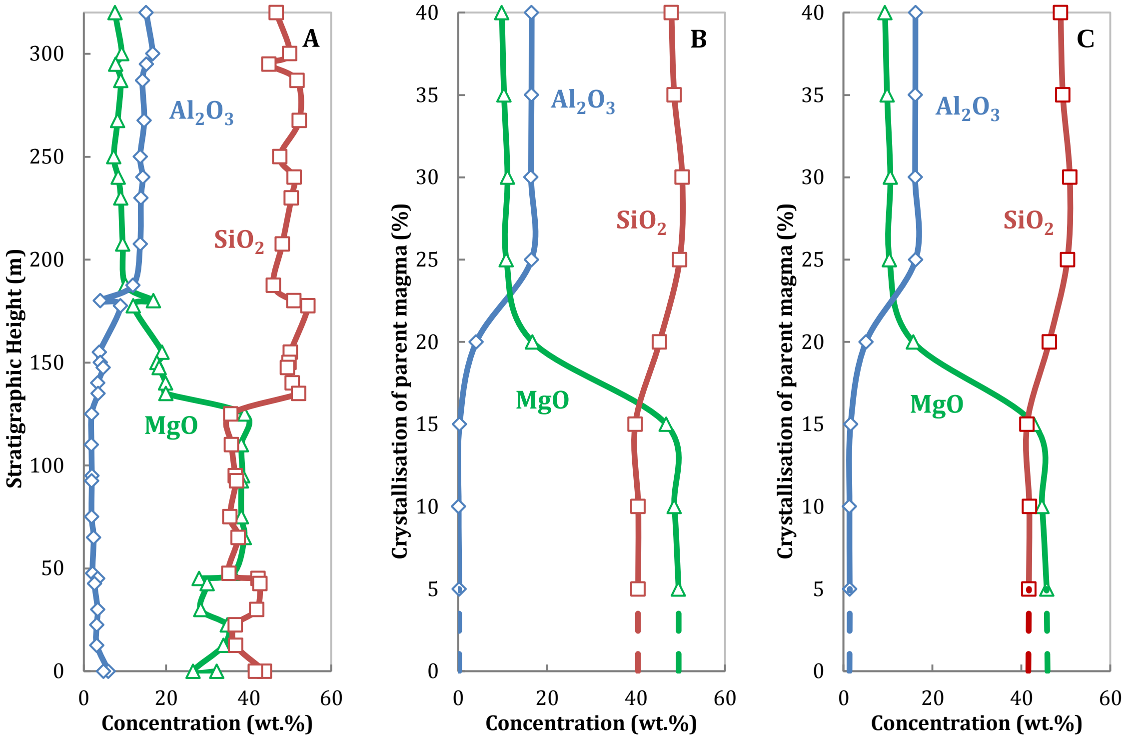

Fig. 5.48. (A) Measured major element geochemistry of cumulate rocks from the lower half of the BDM; **(B)** modelled chemistry of cumulates predicted to form at 5% intervals of crystallisation from estimated parental melt and; **(C)** modelled chemistry of cumulates predicted to form at 5% intervals of crystallisation from estimated parental melt including a 10% melt fraction of the coexisting liquid. Dashed line between 0-5% in (B) and (C) denotes extrapolation from first data point at 5%.

Assimilation of country rock by a magma undergoing fractional crystallisation (AFC) is a common process in the petrogenesis of layered intrusions [e.g., Palacz 1985; Amelin et al. 1996; Maier et al. 2000). Crustal assimilation is also important from an economic perspective as it is thought to be a key prerequisite in the formation of Ni-Cu-PGE deposits (Maier 2005; Naldrett 2011).

The importance of assimilation of country rock during fractionation of the BDM can be investigated using the trace element and radiogenic isotope chemistry of the intrusion. As the BDM intrudes (and is entirely hosted by) the Boxelder Creek Quartzite **(Fig. 3.9)**, the Boxelder Creek Quartzite represents the most obvious crustal contaminant of the BDM. To test whether AFC operated during crystallisation of the BDM, trace element ratios which are insensitive to fractional crystallisation are plotted for both the BDM and Boxelder Creek Quartzite against stratigraphic height **(Fig. 5.49)**. In these diagrams, the Boxelder Creek Quartzite

(BCQ) is plotted as a field defined by the range of values of the Boxelder Creek Quartzite (n = 6) in an attempt to display the variable trace element composition of the unit.

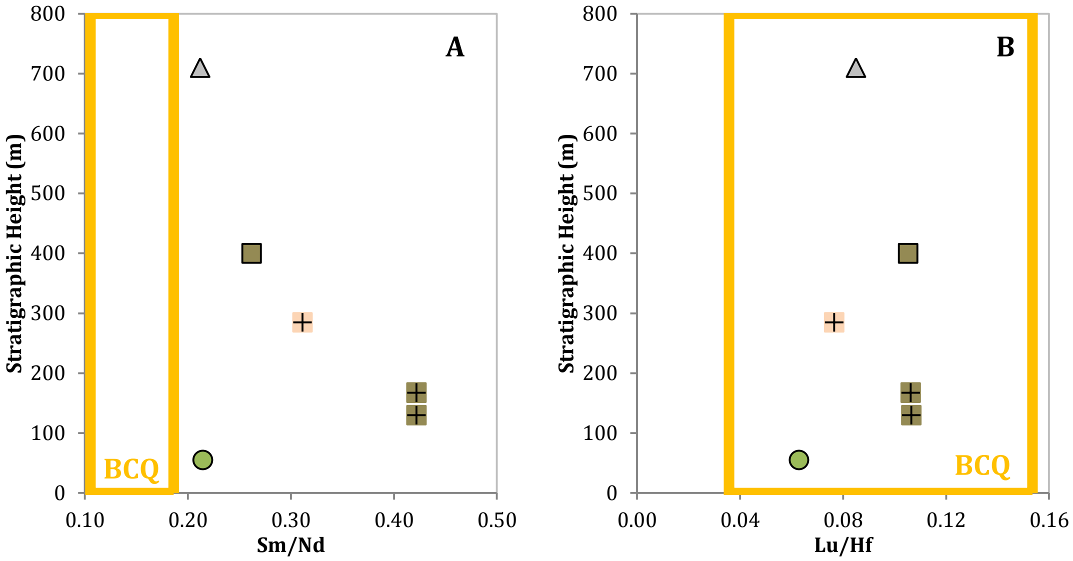

Fig. 5.49. Ratios of element pairs Sm/Nd (A) and Lu/Hf (B) with similar bulk partition coefficients plotted against stratigraphic height in the BDM. Field of the Boxelder Creek Quartzite (BCQ) defined by compositional range of the six samples studied. Lithological symbols as in **Fig. 4.34**.

As the BDM shows general trends of fractionation with increasing stratigraphic height **(Fig. 4.43)**, it should be expected that the rocks near the top of the intrusion would be the most contaminated by the Boxelder Creek Quartzite host rock if AFC had occurred. **Fig. 5.49A** shows that in general, the Sm/Nd in the BDM decreases linearly from 0.422 in the olivine melagabbronorite unit to reach 0.212 at the top of the intrusion. Crucially, the Sm/Nd ratios trend towards the relatively tight range of the Boxelder Creek Quartzite, which supports the notion that the changes in the Sm/Nd ratio observed in the BDM are a product of AFC. The trend is somewhat complicated by the peridotite unit sample which records a low Sm/Nd ratio of 0.214, however, this sample is from near the basal margin of the intrusion and may have been contaminated on contact with the BCQ which is an interpretation consistent with other trace element data **(Fig. 4.34)** and previous field observations (Maranate 1979). Equivalent data using the Lu/Hf ratio **(Fig. 5.49B)** show that there is no systematic variation in the Lu/Hf ratio with stratigraphic height which may be more suggestive of an FC mechanism. However, the BCQ samples analysed define a wide range of Lu/Hf ratios and thus cannot distinguish FC from AFC using this method.

The relative suitability of the FC and AFC mechanisms in explaining the chemistry of the BDM can be further investigated using Sm-Nd and Lu-Hf radiogenic isotope systems. The utility of these isotopic systems comes from the fact that during normal basaltic fraction, the element pairs Sm-Nd and Lu-Hf are not easily fractionated and thus, the initial isotopic ratios of ^{143}Nd/^{144}Nd and ^{176}Hf/^{177}Hf of a suite of rocks derived from a single parent magma should remain constant providing no contamination of the evolving magma has occurred. **Fig. 5.50A** shows a similar trend to that observed in **Fig. 5.49A** in that following the initially high ^{143}Nd/^{144}Nd$_{(i)}$ ratio in the peridotite unit, the isotope ratio increases linearly from 0.50864 in the olivine melagabbronorite unit to 0.50930 at the top of the intrusion, showing that the BDM became more radiogenic as fractionation continued. The complimentary trend is observed using equivalent data for the Lu-Hf system **(Fig. 5.50B)**. In this figure, following the initially low ^{176}Hf/^{177}Hf$_{(i)}$ ratio in the peridotite unit, the isotope ratio increases curvilinearly from 0.28268 in the olivine melagabbronorite unit to 0.28114 at the top of the intrusion.

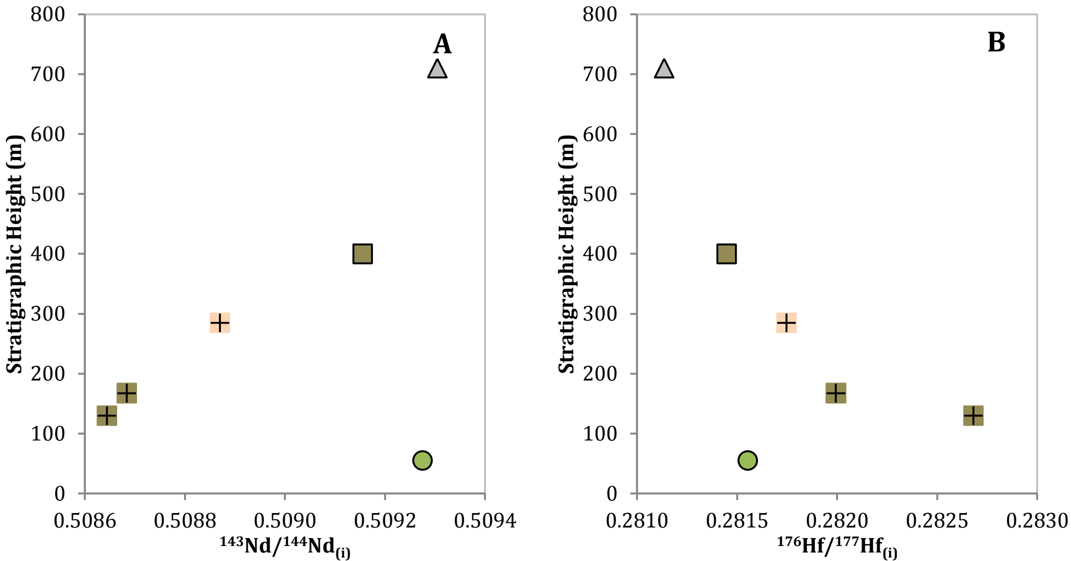

Fig. 5.50. Initial isotopic ratios of ^{143}Nd/^{144}Nd (A) and ^{176}Hf/^{177}Hf (B) plotted against stratigraphic height in the BDM. Lithological symbols as in Fig. 4.34.

These trends suggest that when the Blue Draw Metagabbro parent magma was intruded into the crust it was contaminated by material which was characterised by higher Sm/Nd and ^{143}Nd/^{144}Nd ratios but also lower ^{176}Hf/^{177}Hf ratios than itself. Some of this contamination occurred locally and quickly, along the rapidly cooling margin of the intrusion while contamination of the remaining uncontaminated BDM parent magma occurred gradually during fractionation.

Unfortunately, no samples of the Boxelder Creek Quartzite were selected for radiogenic isotope analysis and thus it cannot be categorically determined if this was the contaminant responsible for the trace element and geochemical trends observed in the intrusion. In fact, relatively little whole rock Lu-Hf isotopic data with equivalent Sm-Nd information exists for potential crustal contaminants in the literature, though some may be extracted from work by Vervoort et al. (1999) and Blichert-Toft et al. (1999) who studied the Sm-Nd and Lu-Hf systematic of Archaean supracrustal rocks from the Isua supracrustal belt, West Greenland and elsewhere.

The Isua supracrustal belt (West Greenland) is made of various lithologies, interpreted to be the products of deformed and metamorphosed sedimentary, metamorphic and igneous protoliths. Rock types exposed in the belt include banded iron formations, basaltic volcanics, peridotites, marbles, felsic gneisses and micaschists (Blicher-Toft and Frei 2001). **Fig. 5.51** shows $\varepsilon Nd_{(t)}$ vs. $\varepsilon Hf_{(t)}$ (where t = 2480 Ma) respectively which show the isotopic compositions of several mantle reservoirs, the Blue Draw Metagabbro samples and samples of supracrustal rocks from the Isua belt (Blichert-Toft et al. 1999) and Archaean shales from various basins across the globe (Vervoort et al. 1999). The diagram shows that the BDM samples define a curved trace from values which have a nearly chondritic Nd-Hf isotopic signature towards strongly $-\varepsilon Nd_{(t)}$ and strongly $+\varepsilon Hf_{(t)}$ values. Further to this, the plot shows that the BDM samples which appear the most contaminated using trace elements **(Fig. 5.49)** are the ones which are closest to having chondritic $\varepsilon Nd_{(t)}$ and $\varepsilon Hf_{(t)}$ values. The data of Vervoort et al. (1999) show that Archaean shales also share this chondritic Nd-Hf isotopic signature, and may suggest that the contaminant utilised during AFC of the BDM parent magma had a similar isotopic composition to these shales. However, this interpretation remains speculative and will until isotopic analysis of the Boxelder Creek Quartzite is carried out.

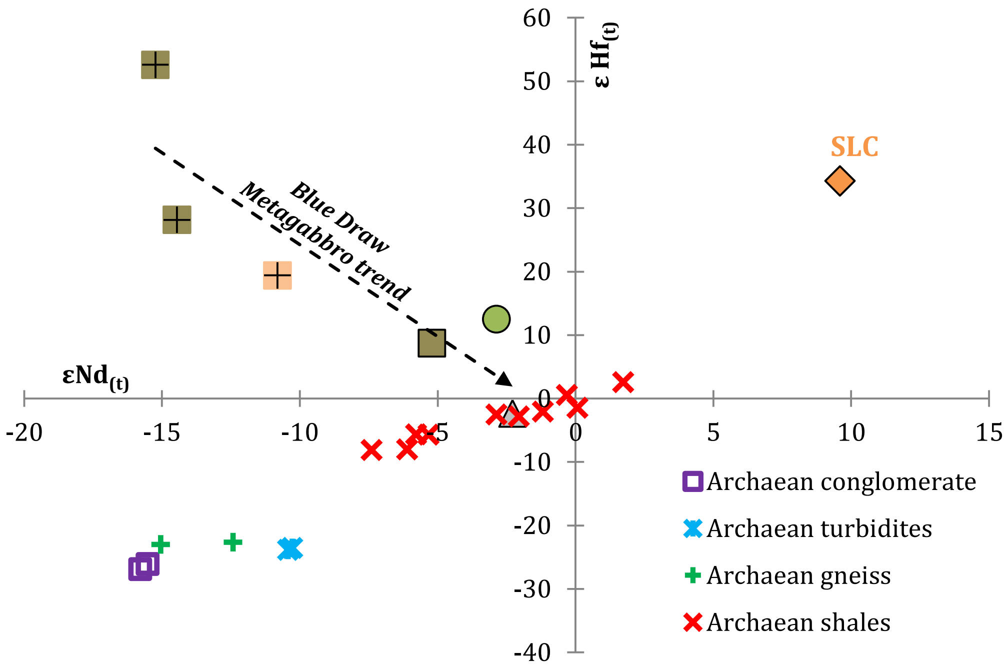

Fig. 5.51. Isotopic ratios of $\varepsilon Nd_{(t)}$ vs. $\varepsilon Hf_{(t)}$ for the Blue Draw Metagabbro samples (lithological symbols as in **Fig. 4.34**) where t = 2.48 Ga.. Isotopic signatures for conglomerates, turbidites and gneiss from the Archaean Isua supracrust belt (Blichert-Toft et al. 1999) and other Archaean shales (Vervoort et al. 1999) are shown, as is the average composition of the peridotite mantle xenoliths from Salt Lake Crater (SLC), O'ahu (Bizimis et al. 2007).

Should this future analysis show that the Boxelder Creek Quartzite is isotopically similar to the Archaean shales of Vervoort et al. (1999), then the following question should be, 'what is the nature of the mantle reservoir from which the BDM was derived?'. The trend of the BDM samples indicates that the parent magma, and hence mantle source region was characterised by low $^{143}Nd/^{144}Nd_{(t)}$ ($-\varepsilon Nd_{(t)}$) and high $^{177}Hf/^{176}Hf_{(t)}$ ($+\varepsilon Hf_{(t)}$) ratios. **Fig. 5.51** shows that such a reservoir is distinctly different to any of those recognised today.

Extreme +εHf values have been recorded in peridotite mantle xenoliths from the island of O'ahu, Hawai'i and have been interpreted by (Bizimis et al. 2007) to be sourced from ancient (>2 Ga) depleted mantle lithosphere caught up in the upwelling Hawaiian plume. However, the O'ahu xenoliths also have +εNd values (in contrast to those observed in the BDM samples), thus ruling out a similar source for the BDM samples which have –εNd. In an attempt to come up with a feasible mantle reservoir from which the BDM parent magma was extracted, isotopic mixing models involving the periodites of Bizimis et al. (2007), and Isua supracrustal belt conglomerates (which have a –Nd value similar to the most primitive BDM samples) were constructed **(Fig. 5.52)**. These models use the isotopic data presented by Bizimis et al. (2007) and Blichert-Toft et al. (1999) and the Hf and Nd whole-rock element concentration of the O'ahu xenoliths (Frey 1980) and Archaean greywackes (Condie 1993) to constrain the model. The Hf and Nd concentrations of Archaean greywacke were used as they are thought by the author to be the closest facsimile of the Isua supracrustal belt conglomerates studied by Blichert-Toft et al. (1999).

The model shows that using the constraints provided above, mixing between these sources is not a feasible mechanism in forming a mantle reservoir (and hence, a parent magma) capable of producing the trends recorded by the BDM samples in isotopic space **(Fig. 5.52)**. Manipulation of the Hf and Nd concentrations of the mantle source indicate that in order to produce a Hf-Nd isotopic composition similar to the most primitive BDM samples would require the mantle source to have a Nd/Hf ≈ 0.2 which requires the inverse of the Nd/Hf recorded by the O'ahu xenoliths (Nd/Hf ≈ 5) and is not supported by any published analyses. Clearly more work is required before the mantle source of the BDM can be classified.

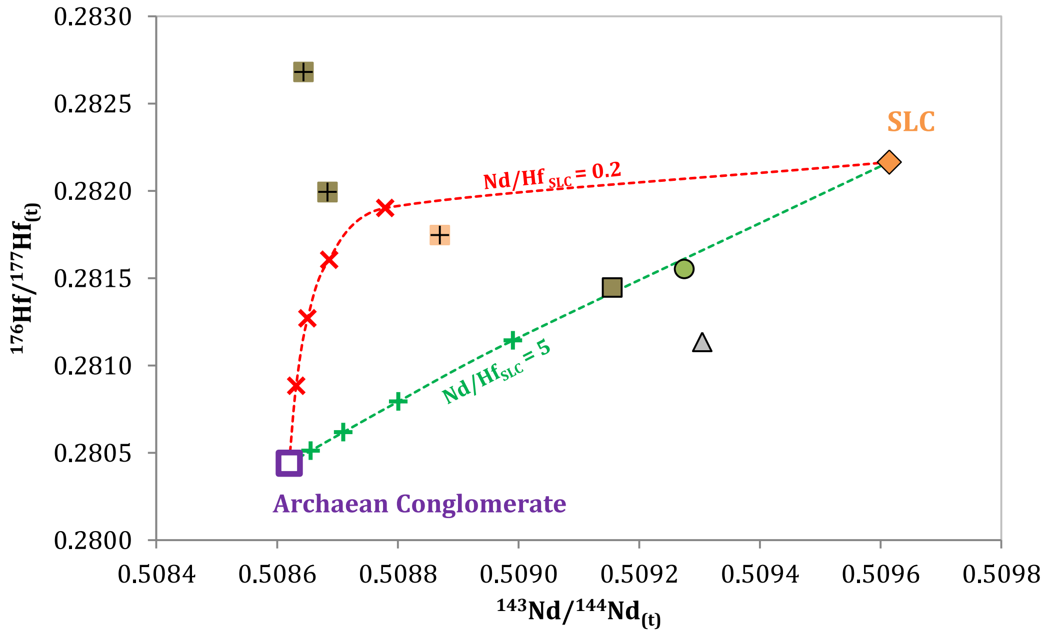

Fig. 5.52. Isotopic ratios of ^{143}Nd/^{144}Nd$_{(t)}$ vs. ^{176}Hf/^{177}Hf$_{(t)}$ for the Blue Draw Metagabbro samples (lithological symbols as in **Fig. 4.34**) where t = 2.48 Ga. Isotopic signatures for the Isua supracrustal belt conglomerates and peridotite mantle xenoliths from Salt Lake Crater, O'ahu (SLC) are also shown. Two models where the Nd/Hf ratio in the SLC is 5 and 0.5 are presented. Marks on the mixing lines between the two end-members denote increments of 20% mixing.

In summary, the major element chemistry and modal mineral abundances observed in the Blue Draw Metagabbro are best explained whereby a body of basaltic magma containing ~13 wt.% MgO ponded at ~9 km (~3 kbar) depth, where it fractionated olivine, spinel, plagioclase and clinopyroxene, orthopyroxene, alkali feldspar and quartz. Evolving assemblages of these minerals settled sequentially at the base of the intrusion to build the stratigraphy observed today. Chemostratigraphic profiles for the BDM show a significant and ubiquitous change in composition at ~300-350 m from the base of the intrusion to less evolved compositions, most obviously signified by spikes in the concentration of compatible elements **(Fig. 4.43)**. These geochemical trends coincide with a return of abundant olivine in the melagabbronorite unit, suggesting that after ~300 m of cumulates had formed, the system was recharged by a less fractionated magma which mixed with the residual melt fraction retained in the chamber before the resulting hybrid melt fractionated again. The trace element and radiogenic isotope trends recorded in the Blue Draw Metagabbro require assimilation of material similar in composition to the Archaean shales of the Isua supracrustal belt by the parent magma which itself was sourced from a presently unconstrained reservoir. This reservoir was characterised by high ^{176}Hf/^{177}Hf and low ^{143}Nd/^{144}Nd ratios relative to the bulk earth at 2.45 Ga.

5.4.4.2. East Bull Lake Suite

Based on detailed petrography, igneous textural relationships and CIPW-normative compositions, previous workers have interpreted the crystallisation order in the East Bull Lake Suite to be plagioclase, olivine, orthopyroxene, clinopyroxene, spinel followed by quartz and orthoclase (Vogel 1996; Vogel et al. 1999; James et al. 2002). Vogel et al. (1999) investigated five different potential feeder dykes (including members of the Matachewan swarm) which crop out in the area of the East Bull Lake Suite in an attempt to find a likely parent magma composition for the intrusions and suggested that the most likely feeders to the suite are the Streich dykes. This conclusion is based on similar trace element chemistries (LREE enrichment and depletions in the HFSE) between the Streich dykes and the East Bull Lake Suite, the modelled ability of a basaltic magma with the major element chemistry of the Streich dykes to fractionate and produce the plagioclase-rich, olivine-normative stratigraphy of the Marginal and Lower Series in the intrusions, and field relationships which show that at the point at which the Streich dyke intersects with the Agnew intrusion the stratigraphy is disrupted in a way which is suggestive of the influx of a new magma. In a separate study of the East Bull Lake intrusion, James et al. (2002) used a weighted average of the entire stratigraphy of the intrusion to produce an estimated composition of the parent magma. Both of these estimates yield similar results and indicate that the parent magma to the East Bull Lake Suite was a high-Al, low-Ti tholeiitic basalt which contained ~6.6-7.7 wt.% MgO.

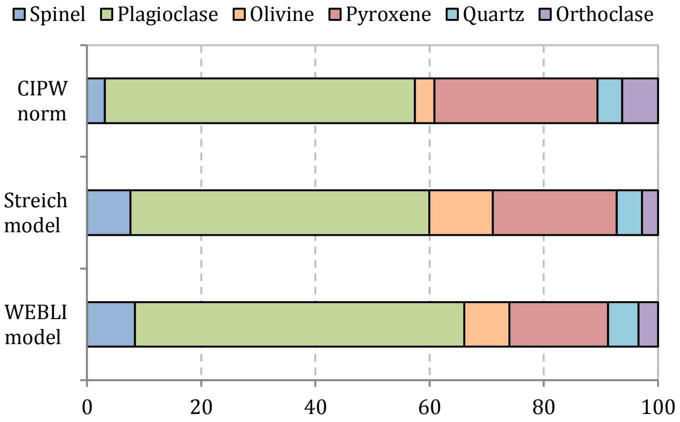

Fig. 5.53. Diagram showing the cumulative proportions of crystals formed by fractional crystallisation of the WEBLI (James et al. 2002) and Streich (Vogel et al. 1999) parent magmas and the CIPW norm composition of the Agnew intrusion (Vogel 1996).

To test the validity of these potential parent magmas, they were modelled using PELE at 3 kbar pressure and the mineral assemblages predicted to form compared to that observed in the Agnew intrusion [the best preserved of the East Bull Lake Suite (Vogel 1996)]. This pressure was used because previous studies have shown that the East Bull Lake suite were intruded at the interface between the Archaean basement of the Superior craton and the overlying Huronian Supergroup (Vogel et al. 1998a), which itself is thought to have a maximum thickness of ~1.2 km (Tomlinson 1996). The model which uses the parent magma estimate of James et al. (2002) predicts that the magma begins to crystallise at 1267 °C while the average Streich dyke composition of Vogel et al. begins crystallising at 1251 °C. Both models predict the same crystallisation order of spinel, plagioclase, olivine, clinopyroxene, orthopyroxene, quartz and orthoclase. The proportions of the mineral species predicted to form from crystallisation of these magmas is presented in **Fig. 5.53**, along with the volume % of mineral species which make up the Agnew intrusion, as estimated by Vogel (1996) from CIPW norms of samples taken from throughout the intrusion stratigraphy. **Fig. 5.53** shows that the proportions of minerals predicted to form via fractionation of these two potential parents are similar and that they closely follow the proportions predicted by CIPW norms from the Agnew intrusion. This similarity suggests that the magmas presented by Vogel et al. (1999) and James et al. (2002) are likely to be good approximations of the parent magmas of the East Bull Lake Suite.

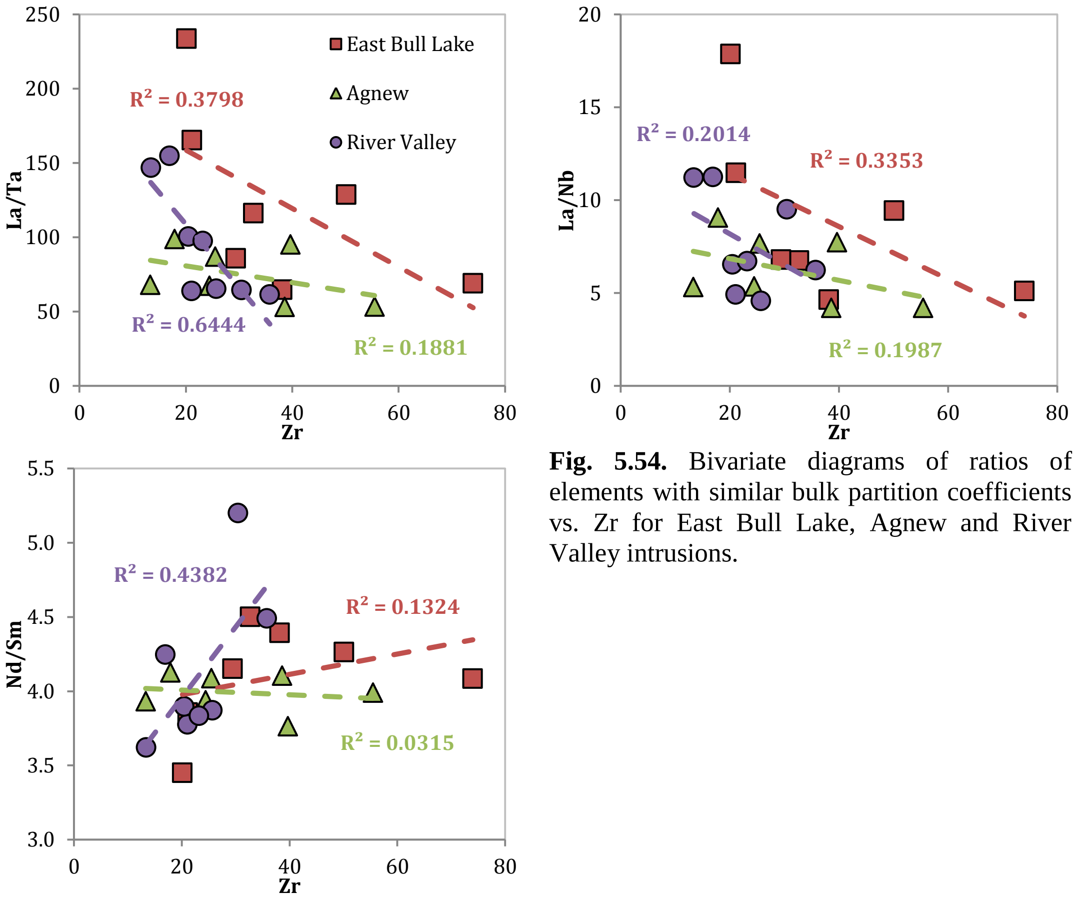

Fig. 5.54. Bivariate diagrams of ratios of elements with similar bulk partition coefficients vs. Zr for East Bull Lake, Agnew and River Valley intrusions.

The question of whether the East Bull Lake Suite intrusions evolved through fractional crystallisation or some other process like assimilation-fractional crystallisation can be investigated using certain incompatible element ratios. The element pairs La-Nb, La-Ta and Sm-Nd are interpreted to have very similar bulk partition coefficients, meaning that during partial melting and fractional crystallisation, the ratio of these element pairs does not change in either the evolving liquid or crystallising cumulates (Weaver 1991; Rollinson 1993). This has been confirmed using the average trace element composition of the Streich dykes (Vogel et al. 1999) and the crystallising assemblages predicted to form in the model described above and in **Fig. 5.53**. **Fig. 5.54** shows plots of these three incompatible element ratios against Zr (which is used as a qualitative measure of the evolution of the parent magma). The East Bull Lake and River Valley samples record decreasing La/Ta, La/Nb and Sm/Nd with increasing Zr while the Agnew samples record decreasing La/Ta and La/Nb with increasing Zr but fairly constant Sm/Nd. These data may suggest that as the East Bull Lake Suite parent magma fractionated, it mixed with, or was contaminated by material with a lower La/Nb and La/Ta but variable Sm/Nd ratio relative to itself.

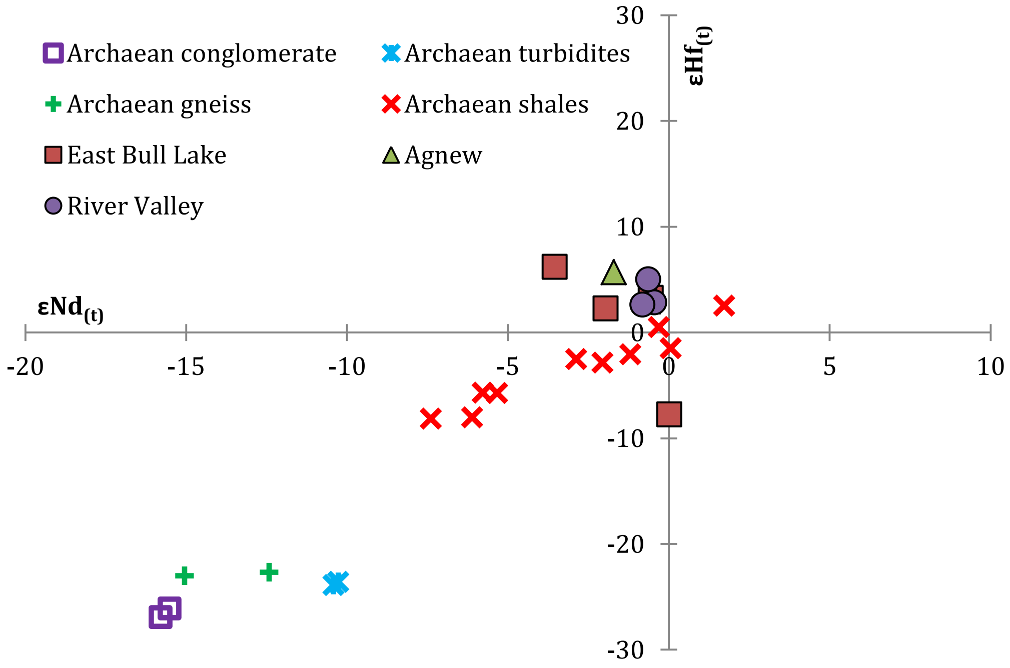

Fig. 5.55. Isotopic ratios of $\varepsilon Nd_{(t)}$ vs. $\varepsilon Hf_{(t)}$ for the East Bull Lake Suite samples where t = 2.48 Ga. Isotopic signatures for conglomerates, turbidites and gneiss from the Archaean Isua supracrust belt (Blichert-Toft et al. 1999) and other Archaean shales (Vervoort et al. 1999) are shown.

The potential for contamination can be investigated further using isotope chemistry. On the $\varepsilon Nd_{(t)}$ vs. $\varepsilon Hf_{(t)}$ diagram **(Fig. 5.55)**, all of the East Bull Lake Suite samples cluster near to chondritic values within the array defined by the mantle reservoir end members. This may suggest that the mantle reservoir of the East Bull Lake Suite intrusions was similar in composition to the primitive mantle.

5.4.10. Summary

The paragraphs above have investigated the geochemical trends exhibited by individual Matachewan LIP suites in order to determine how each of the suite's parent magmas evolved in the crust. For each suite, several major element models were constructed to assess under what physical conditions the magma evolved. In many cases, the parent magma used in the modelling is unlikely to be primary in the sense of being unmodified since its removal from the mantle. However, in all cases, the parent magma used in the modelling is assumed to be the closest approximation of the primary magma and this assumption is based on the negative correlation between MgO and strongly incompatible trace elements exhibited by many of the suites (see Chapter 4).

The crystallising assemblages and degrees of fractionation predicted by the most effective major element model have been used to determine whether the trace element geochemical trends exhibited by individual Matachewan LIP suites are better explained by AFC or FC. The models have consistently shown that geochemical trends indicative of AFC using felsic crust as the contaminant include increasingly negative Ti and Nb anomalies. FC models do not predict that the magnitude of these anomalies changes since during normal basaltic fractionation, the bulk partition coefficients of the trace elements used to define these anomalies remain largely the same. Increasing normalised LREE/HREE ratios are predicted by both the FC and AFC models, though the rate of increase is greater for the AFC mechanism. Isotopic data gathered for the East Bull Lake Suite and Blue Draw Metagabbro intrusions record trends indicative of contamination of the parent magma during fractionation, although post magmatic alteration of the East Bull Lake Suite may have affected some of the isotopic systems, especially in the case of the River Valley intrusion.

Four of the Matachewan LIP suites studied (Groups 3 and 4 of the Thessalon Formation and the Group 2 Matachewan and Leopard dykes) could not be modelled in this way as not enough data (see **Appendix C**) were collected so as to allow definitive modelling. Future work should resample these suites in the hope of collecting more data which will allow the opportunity of modelling their petrogenetic evolution. **Table 5.7** summarises the results of the petrogenetic modelling carried out by this study.

Suite	MgO cont. parent	Pressure (kbar)	1 wt.% H_2O	Liquidus temp. (°C)	Crystallisation sequence	% FC recorded	Preferred mechanism
Matachewan Dykes (Grp. 1)	8.8	7	×	1375	sp, ol, cpx, plg	60	FC
East Bull Lake Suite	6.6-7.7	3	×	1267-1251	sp, plg, ol, cpx, opx, qz, or	100	AFC
Thessalon Formation (Grp. 1)	6.7	1	✓	1245	sp, ol, plg, cpx	30	AFC
Thessalon Formation (Grp. 2)	6.8	10	×	1378	sp, opx, cpx, plg	60	AFC
Blue Draw Metagabbro	13.0	3	×	1446	ol, sp, plg, cpx, opx, or, qz	100	AFC
Leopard Dykes (Grp. 1)	7.9	-	-	-	-	-	ACC
Kaminak Dykes	6.3	7	×	1283	sp, cpx, plg	60	AFC
Viianki Dykes	8.0	1	✓	1475	sp, ol, cpx	30	AFC
Seidorechka Formation	20.8	1	×	1479	ol, opx, sp, cpx, plg, qz	90	AFC

Table 5.7. Summary of the modelling presented in this chapter showing the MgO content of the parent magma, most successful model parameters, predicted crystallisation sequence, the degree of fractionation required to account for the geochemical variation observed and the preferred mechanism for each of the Matachewan LIP suites studied. Abbreviations: sp – spinel, ol – olivine, cpx – clinopyroxene, plg – plagioclase, opx – orthopyroxene, or – orthoclase, qz – quartz, FC – fractional crystallisation, AFC – assimilation-fractional crystallisation, ACC – accumulation.

5.5. Magmatic Ni-Cu-PGE Deposits

The genesis of magmatic Ni-Cu-PGE deposits has been studied by numerous authors for several decades [e.g., Campbell et al. 1983; Naldrett 1999; Maier 2005; Naldrett 2011] and our current understanding is summarised below. Essentially, magmatic Ni-Cu-PGE sulphide deposits form via the accumulation of a chalcophile element-bearing immiscible sulphide liquid which precipitates from an evolving mafic-ultramafic magma (Naldrett 2011). Not all mafic-ultramafic bodies host Ni-Cu-PGE mineralisation as, in order to form an economic deposit, four essential criteria must be met by the evolving magmatic system.

The first criterion to be met occurs during mantle melting. As Ni, Cu and the PGE are chalcophile and have very large sulphide/silicate partition coefficients [e.g., D_{Ni} = >500, $D_{Cu} = 1.4 \times 10^3$, $D_{Ir} = 3.5 \times 10^4$ and $D_{Pd} = 3.4 \times 10^4$ (Peach et al. 1990; 1994)], they strongly partition into sulphide phases during fractional crystallisation. Thus, in order to liberate Ni, Cu and the PGE from the mantle, the degree of partial melting must be sufficient to melt all of the sulphide present in the source as any un-melted sulphide will retain these very refractory chalcophile elements (Prichard et al. 1996). The degree of melting required to completely melt mantle sulphides and liberate the chalcophile elements has been estimated to be ~15% (Barnes et al. 1985; Naldrett 2010), though may be as high as 25-40% (Mungall 2002; Jowitt and Ernst 2012).

The second criterion which must be met is that following sufficient mantle melting and ascent through the crust, the magma must crystallise its chalcophile content as Ni-Cu-PGE bearing sulphides. This is achieved when the magma becomes saturated in sulphur, at which point, an insoluble sulphide liquid exsolves from the magma, taking with it the chalcophile Ni, Cu and PGE (Naldrett 2011). The solubility of sulphur in magma is dependent on several factors including temperature, pressure, magma composition and oxygen fugacity. Mavrogenes and O'Neill (1999) demonstrated that decreasing pressure increases the amount of sulphur which can be dissolved in a magma while decreasing temperature has the opposite effect **(Fig. 5.57A)**. Naldrett (1989) showed that composition of the magma is also important to sulphur solubility and demonstrated that magmas containing ~20 wt.% FeO + TiO_2 are capable of dissolving ~7× the amount of sulphur than a magma containing ~5 wt.% FeO + TiO_2. Naldrett (1989) also showed that the solubility of sulphur is affected by oxygen fugacity and demonstrated that magmas with less negative Log *f* O_2 values are capable of dissolving more sulphur than magmas with less negative Log *f* O_2 values **(Fig. 5.57B)**.

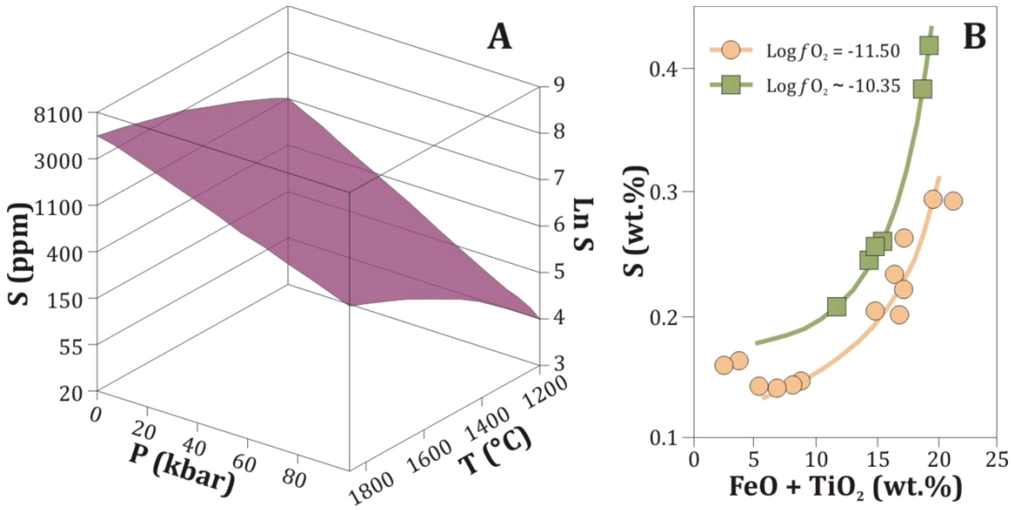

Fig. 5.57. Effects of temperature and pressure (A) and FeO + TiO_2 content and oxygen fugacity (B) on the maximum amount of sulphur which can be dissolved in hypothetical basaltic magmas. Modified after Mavrogenes and O'Neill (1999) and (Naldrett 2011).

Thus, we can expect magma derived from partial melting of the mantle to initially become less saturated in sulphur as it rises through the crust, only to begin to approach sulphur saturation during cooling and accompanying crystallisation of Fe-bearing silicates. Attaining sulphur saturation in this passive manner is not particularly conducive to forming high grade Ni-Cu-PGE mineralisation as fractionation of mafic-ultramafic magma tends to crystallise significant volumes of olivine and chrome spinel prior to reaching sulphur saturation. This is important because Ni and the IPGE are very compatible during fractionation of olivine and chrome spinel (Capobianco and Drake 1990; Tredoux et al. 1995; Brenan et al. 2003; Finnigan et al. 2008) and thus these metals are scavenged from the magma during the early stages of fractional crystallisation. Hence, when the remaining magma reaches sulphur saturation, there is little Ni and IPGE remaining in the melt which can be incorporated into the immiscible sulphide liquid. Instead, high grade Ni-Cu-PGE deposits are favoured by magmas which attain sulphur saturation early in their crystallisation history (prior to significant silicate fractionation) via a more active mechanism. Possible mechanisms include; (1) the mixing of two different magmas (Scoates and Mitchell 2000), (2) contamination of the magma by partial melts of crustal material (Naldrett 2011), (3) assimilation of sulphur-bearing country rocks (Ripley and Li 2003), and (4) pressure changes caused by the influx of new magma from depth (Cawthorn 2005).

The third criterion that must be satisfied in order to create an economic Ni-Cu-PGE deposit is an enrichment of the immiscible sulphide liquid in chalcophile elements. This enrichment is partially controlled by the R factor (Campbell et al. 1983) which is the ratio of silicate magma to immiscible sulphide liquid with which the silicate magma interacts following sulphur saturation. High grade Ni-Cu-PGE mineralisation is favoured by magmatic systems with high R factors as, in such systems, the immiscible sulphide liquid is able to interact with (and scavenge chalcophile elements from) a large volume of silicate magma, thus greatly increasing the Ni-Cu-PGE tenor of the immiscible sulphide liquid. A high R factor can be attained either through interaction of the immiscible sulphide liquid with magma already in the chamber [e.g., Andersen et al. 1998) or through interaction with recharging pulses of sulphur-undersaturated magma [e.g., Peck et al. 2001; Kerr and Leitch 2005) which enter the magma chamber following sulphur saturation of the initial magma.

Finally after enrichment, the immiscible sulphide liquid must accumulate and be deposited, either as a stratiform Ni-Cu-PGE sulphide rich reef in layered intrusions, or at the base of komatiitic lava flows **(Fig. 5.58)**, often concentrated in structural embayments or troughs [e.g., Beresford et al. (2002)].

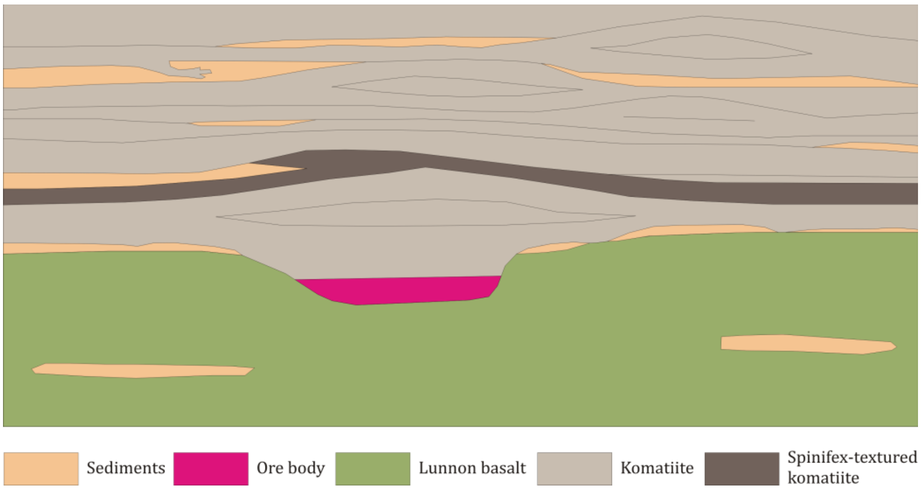

Fig. 5.58. Schematic model of the facies architecture in the komatiite-hosted Ni-sulphide Victor orebody, Kambalda. Modified after (Beresford et al. 2002).

5.5.1. Matachewan LIP Ni-Cu-PGE Mineralisation

The Ni-Cu-PGE mineralisation preserved in the different igneous suites of the Matachewan LIP has been discussed in Chapter 2 and is only summarised here. The Matachewan LIP lacks a world-class Ni-Cu-PGE deposit on the scale of Sudbury, the Bushveld or Noril'sk-Talnakh. That said, numerous deposits have been identified in Matachewan LIP intrusions, some of which have been mined with many others being actively explored (Saltikoff et al. 2006). Ni-Cu-PGE mineralisation within the Matachewan LIP is concentrated in the Fennoscandian and East Bull Lake Suite intrusions (Peck et al. 2001; Iljina 2007), while other Matachewan LIP intrusions including the Blue Draw Metagabbro have been shown to contain no appreciable mineralisation (Ciborowski et al. in press). This observation poses the question; why are some of the Matachewan magmatic suites fertile (Ni-Cu-PGE deposit-bearing) while others are barren?

5.5.2. Fertile and Barren LIPs – Source Characteristics

Zhang et al. (2008) studied the geochemistry of lavas from ten separate mineralised and unmineralised LIPs in an attempt to understand the relationship between mantle source region and Ni-Cu-PGE mineralisation potential of a LIP. In doing so, Zhang et al. (2008) developed geochemical criteria which are able to discern Ni-Cu-PGE fertile LIPs from barren ones. The criteria developed by Zhang et al. (2008) are described below and are applied to the Matachewan LIP, first to determine their effectiveness in predicting the mineralisation observed in the Matachewan LIP layered intrusions and secondly, to use them to characterise the mineralisation potential of other, currently unexplored, Matachewan LIP suites.

Fertile Large Igneous Provinces	**Barren Large Igneous Provinces**
High proportion of high MgO rocks	Low proportion of high MgO rocks
Depleted in Al_2O_3 and Na_2O: (Al_2O_3 > 3.5-6 wt.%, Na_2O > 0.3 wt.%*)	High Al_2O_3 and Na_2O (Al_2O_3 > 10 wt.%, Na_2O > 1.2 wt.%*)
High CaO/Al_2O_3 (> 0.9)	Low CaO/Al_2O_3 (< 0.9)
Enriched in incompatible elements: (Up to 4.5 wt.% K_2O, 0.5 wt.% P_2O_5, 1500 ppm Ba and Sr, 16 ppm Pb, 11 ppm Th, 35 ppm Nb, 80 ppm La, 100 ppm Nd.)	No enrichment in incompatible elements
LREE enrichment. Smooth lines on normalised diagrams. (La/Yb up to 63)	LREE enrichment. Curved lines on normalised diagrams. (La/Yb to ~17)
Enriched in Ba, Pb and Sr relative to other LILE	No significant enrichment in Ba, Pb and Sr relative to other LILE
Generally lower K_2O/Ba (≤ 25), lower Rb/Ba (<1.4) and higher Ba/La (≥ 20)	Generally higher K_2O/Ba (≥ 25), higher Rb/Ba (>1.4) and lower Ba/La (≤ 20)
Low Re/Os (< 10)	High Re/Os (> 10)
High Os content (0.02-11 ppb)	Low Os content (0.02-0.0004 ppb)
Generally lower Pd/Ir (< 82)	Generally higher Pd/Ir (>67)
Lower $^{87}Sr/^{86}Sr_i$	Higher $^{87}Sr/^{86}Sr_i$
FOZO-EM1 isotopic trends	FOZO-EM2 isotopic trends

Table 5.8. Geochemical differences between fertile and barren LIPs. Summarised from Zhang et al. (2008).

Zhang et al. (2008) adopted the mantle plume paradigm for the origin of LIPs and suggest that some mantle plumes are more predisposed to generating Ni-Cu-PGE mineralisation than others. They further suggest that this predisposition is recorded by the geochemistry of LIP magmas and based their discrimination criteria on analysis of samples from ten fertile and barren LIPs. These criteria are summarised in **Table 5.8**. Zhang et al. (2008) contend that the geochemical differences listed in the table reflect the interaction between geochemically heterogeneous plume magmas and other mantle reservoirs. Lesher et al. (2001) also argue that Th-U-LREE enrichment and negative Nb-Ta-Ti anomalies are characteristic of prospective LIP lavas as such characteristics are indicative of crustal contamination - a key mechanism in triggering sulphur saturation of a magma (Ripley and Li 2003; Naldrett 2011). Lesher et al. (2001) used ratios of Nb/Th, Th/Yb and La/Sm plotted against MgO, Ni and PGE to distinguish crustally contaminated (and hence potentially fertile) magmas from uncontaminated (likely barren) ones.

In terms of major elements, Zhang et al. (2008) demonstrated that fertile LIPs contain a high proportion of high MgO lavas which are depleted in Al_2O_3 and Na_2O and have CaO/Al_2O_3 ratios commonly > 0.9. In contrast, barren LIP lavas usually contain < 9 wt.% MgO and have CaO/Al_2O_3 ratios < 0.9 **(Fig. 5.59)**.

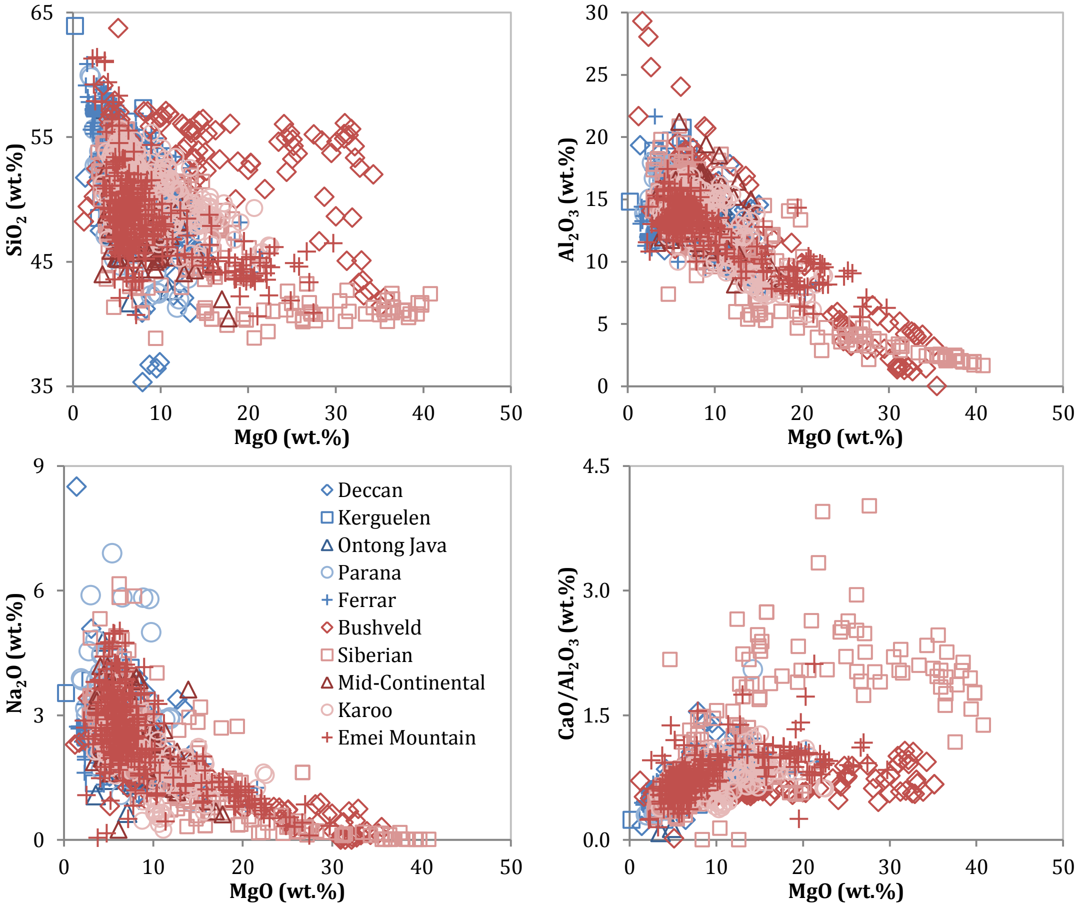

Fig. 5.59. Major element diagrams from Zhang et al. (2008) used to distinguish Ni-Cu-PGE fertile LIPs from barren ones. Fertile LIP samples are shades of red, while barren LIPs are shaded blue.

In terms of incompatible elements, Zhang et al. (2008) show that the primitive lavas of fertile LIPs are more enriched in the incompatible elements than those of barren LIPs **(Fig. 5.60)**. Zhang et al. (2008) also suggest that fertile LIPs are also generally characterised by steeply sloping chondrite-normalised REE patterns, defined by (La/Yb_N) < 63 while barren LIPs have more curved REE patterns. This observation is in contrast to that of Jowitt and Ernst (2012) who suggest that barren LIPs are characterised by steeper REE patterns than fertile LIPs. Plotting the data of Zhang et al. (2008) on chondrite-normalised REE diagrams **(Fig. 5.61)** shows that there does not appear to be an obvious difference between the majority of fertile and barren LIP lavas. This is also confirmed on bivariate diagrams **(Fig. 5.62)** which show that in chondrite-normalised trace element space, the barren and fertile LIP lavas largely overlap.

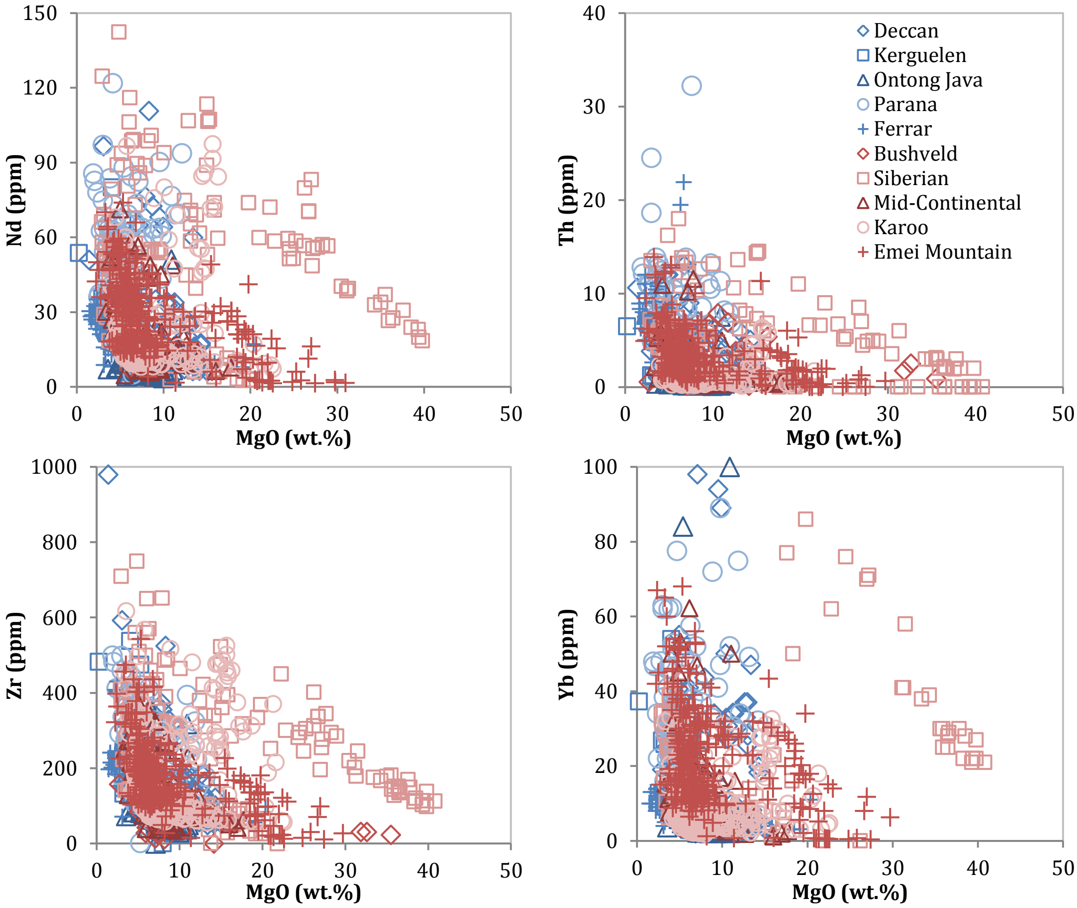

Fig. 5.60. Trace element diagrams from Zhang et al. (2008) used to distinguish Ni-Cu-PGE fertile LIPs from barren ones. Fertile LIP samples are shades of red, while barren LIPs are shaded blue.

On Primitive Mantle-normalised multi element diagrams, both barren and fertile LIPs record negative Nb-Ta and Ti anomalies **(Fig. 5.63)** indicating that LIP parent magmas are either contaminated by continental crust during fractionation, or that they are partly derived from subduction-modified mantle. As both types of LIP share these geochemical characteristics, their identification cannot be used to constrain the prospectivity of a LIP.

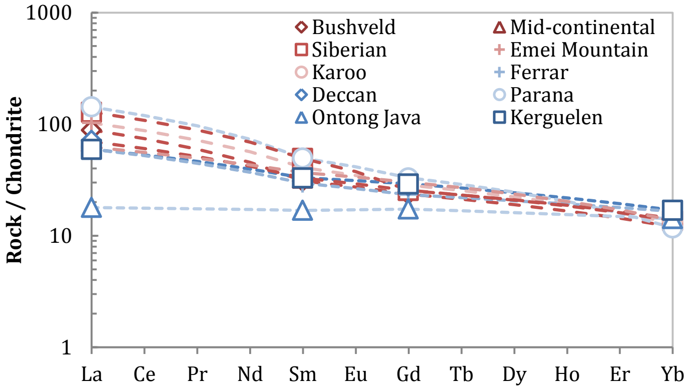

Fig. 5.61. Chondrite-normalised REE diagrams for the fertile (red) and barren (blue) LIPs of Zhang et al. (2008). Normalising values from McDonough and Sun (1995).

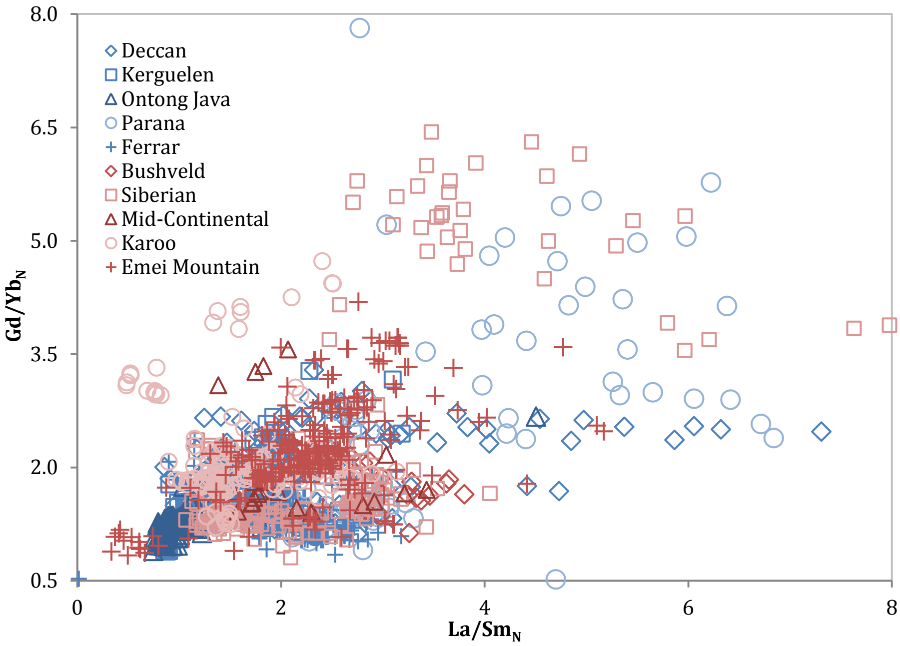

Fig. 5.62. La/Sm$_N$ vs. Gd/Yb$_N$ diagram for the fertile and barren LIPs of Zhang et al. (2008). Normalising values from McDonough and Sun (1995).

The Sr-Nd-Pb data presented by Zhang et al. (2008) is also of interest to this study as it demonstrates a correlation between mineralisation potential and source reservoir. **Fig. 5.64** shows that fertile LIPs define trends between depleted mantle signatures and the EM1 reservoir while barren LIPs share the same depleted mantle signature, but instead trend towards EM2 compositions.

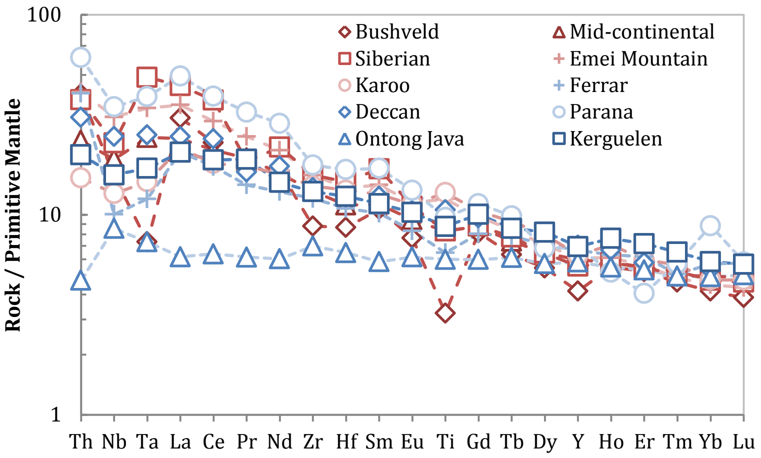

Fig. 5.63. Primitive Mantle-normalised multi-element diagrams for the fertile (red) and barren (blue) LIPs of Zhang et al. (2008). Normalising values from McDonough and Sun (1995).

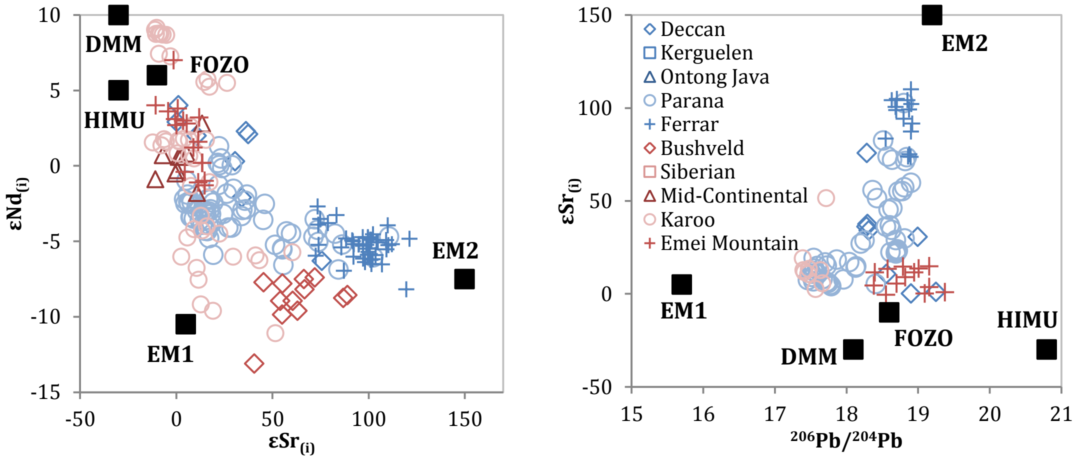

Fig. 5.64. Isotope variation diagrams from Zhang et al. (2008) used to distinguish Ni-Cu-PGE fertile LIPs from barren ones. Fertile LIP samples are shades of red, while barren LIPs are shaded blue. Note the trends between EM1 and depleted mantle end-members recorded by fertile LIPs and trends between EM2 and depleted mantle end-members recorded by barren LIPs.

The preceding paragraphs have described the geochemical criteria defined by Zhang et al. (2008) as useful in determining how prospective for Ni-Cu-PGE mineralisation a LIP might be. Despite the conclusions of Zhang et al. (2008), it is my opinion that examination of the **Figs 5.59-5.63** suggests that barren and fertile LIPs cannot be distinguished based on major and trace element geochemistry as, other than the apparent greater abundance of high MgO rocks preserved in fertile LIPs, the two types have largely indistinguishable geochemistry. That said, isotope geochemistry does appear to be more useful in distinguishing fertile suites from barren ones as the two types define differing trends on isotope variation diagrams **(Fig. 5.64)**. However, the isotope data presented by Zhang et al. (2008) shows that the trends are only truly apparent when the LIPs are treated as types (barren or fertile) since some LIPs [e.g., Emei Mountain and Mid-continental) do not exhibit a definite trend when looked at in isolation.

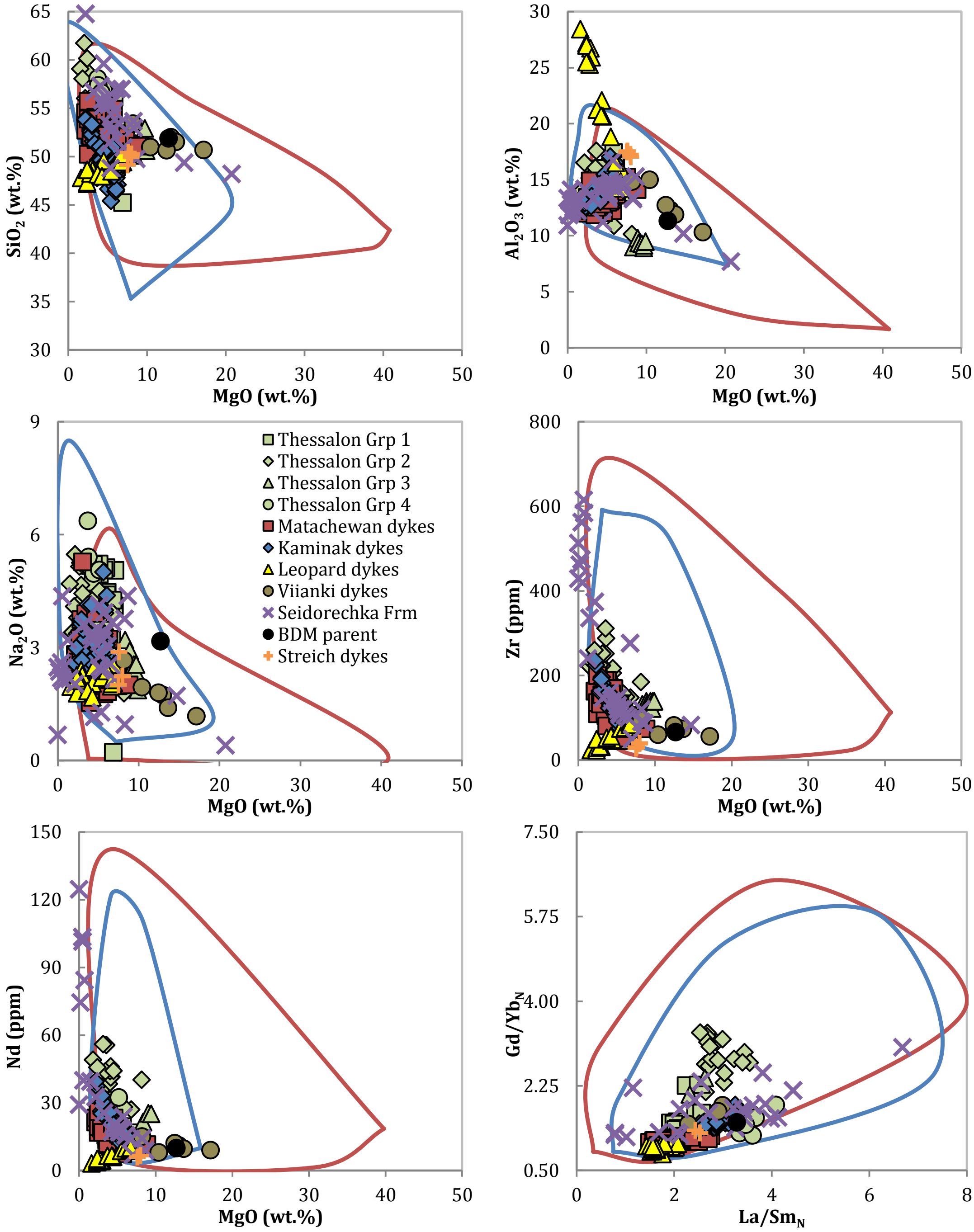

Fig. 5.65. Bivariate diagrams of selected major and trace elements the Matachewan LIP suites. Also shown are the fields defined by the fertile (red) and barren (blue) LIPs of Zhang et al. (2008).

As expected, the major and trace element diagrams of Zhang et al. (2008) are not effective in distinguishing potentially mineralised Matachewan LIP suites from those likely to be barren as the vast majority studied lavas plot in the overlapping portions of the fertile and barren fields **(Fig. 5.65)**. What does become apparent though, is the distinct lack of high MgO lavas in any of the suites studied, something argued by Zhang et al. (2008) to be characteristic of poorly mineralised LIPs.

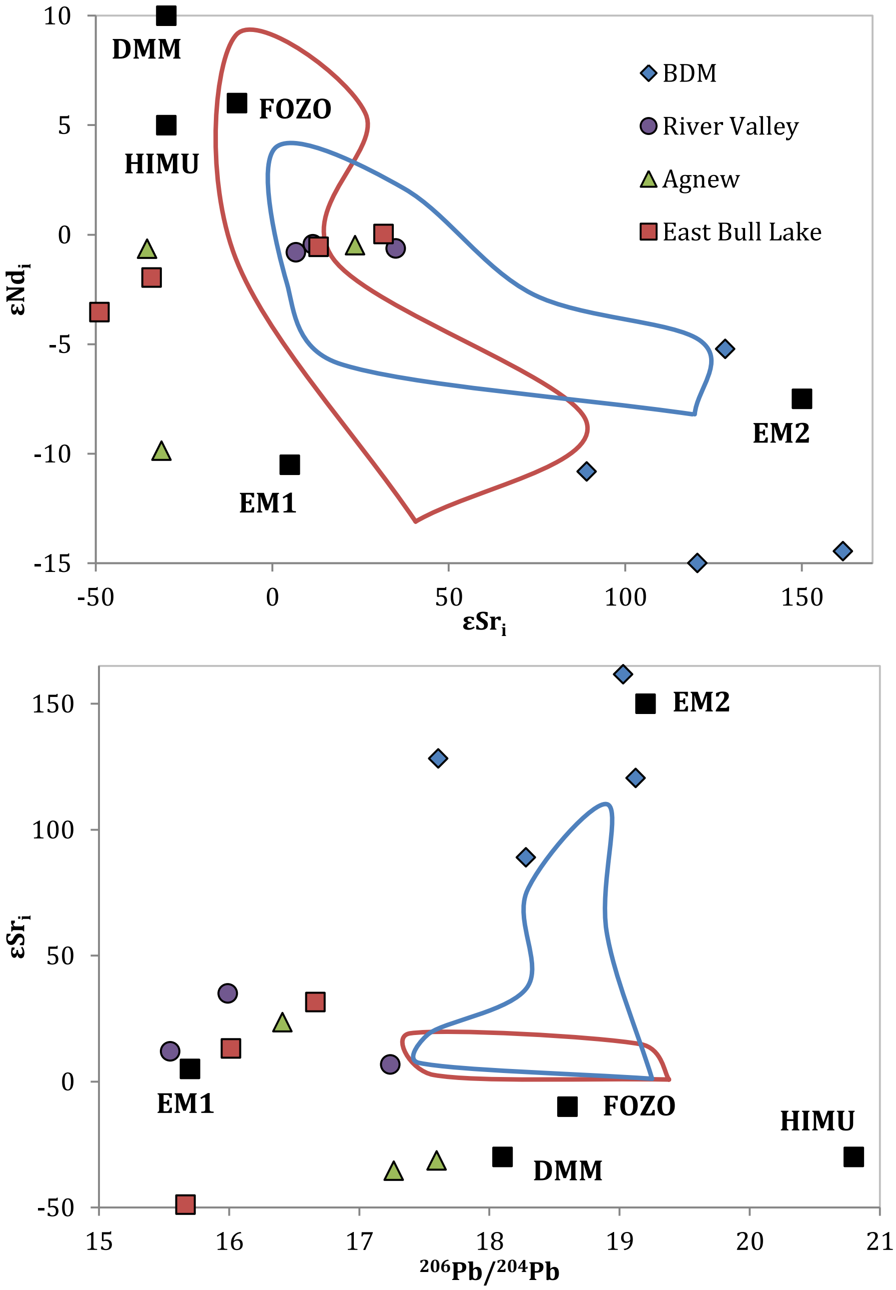

Fig. 5.66. Isotope variation diagrams for the Matachewan LIP layered intrusions. Also shown are the fields defined by the fertile (red) and barren (blue) LIPs of Zhang et al. (2008). Note how the East Bull Lake suite intrusions which are known to be mineralised plot on an array between depleted mantle end members and the EM1 reservoir while the unmineralised BDM plots close to the EM2 composition.

Despite the failure of the major and trace element diagrams in predicting the mineralisation observed in the Matachewan LIP, the isotopic diagrams of Zhang et al. (2008) are more successful. **Fig. 5.66** shows that the samples from intrusions known to host significant Ni-Cu-PGE mineralisation (the East Bull Lake suite) define arrays between depleted mantle signatures and the EM1 end member, while the barren Blue Draw Metagabbro (Ciborowski et al. in press) samples plot between the depleted mantle end members and the EM2 reservoir.

5.5.3. Fertile and Barren LIPs – Magma Processing

In a different study to that of Zhang et al. (2008) who studied the Ni-Cu-PGE prospectivity of LIPs by investigating mantle source characteristics, Jowitt and Ernst (2012) investigated how magma processing in the crust influences the Ni-Cu-PGE mineralisation potential. To that end, Jowitt and Ernst (2012) compared the geochemistry of four barren LIPs with four fertile LIPs in an attempt to discern what geochemical signatures and thus, which processes favour Ni-Cu-PGE mineralisation.

Jowitt and Ernst (2012) showed that fertile LIPs can be distinguished from barren LIPs using Ti/V ratios of LIP lavas. Their study of eight Proterozoic mineralised and unmineralized Canadian LIPs show that those with known mineralisation are characterised by MORB- or CFB-like Ti/V ratios between 20 and 50, whereas unmineralised LIPs are characterised by alkaline- or OIB-like Ti/V ratios >50 **(Fig. 5.67A)**. The REEs are less diagnostic in determining Ni-Cu-PGE prospectivity, as both fertile and barren LIPs record large variation both within and between different LIPs. However, Jowitt and Ernst (2012) note that the barren LIPs record relatively high Gd/Yb_N ratios which are characteristic of low degree partial melts of garnet-bearing peridotite while more fertile LIPs, particularly the Chukotat and Matachewan LIPs, have Gd/Yb ratios close to that of the Primitive Mantle **(Fig. 5.67B)**.

All of the LIPs investigated by Jowitt and Ernst (2012) plot on mixing trends between mantle end members and the continental crust, indicating that all of the LIP lavas were contaminated during their residence in, and transport through, the crust **(Fig. 5.67C)**. Jowitt and Ernst (2012) argue that the LIPs which define tighter mixing trends were hotter and more turbulent (allowing more efficient assimilation and mixing) than those which define more scattered trends. Crucially, Jowitt and Ernst (2012) show that the more fertile LIPs generally define tighter trends than the barren LIPs.

Jowitt and Ernst (2012) also use Cu/Zr, Pd/Yb ratios and chalcophile element abundances as a measure of sulphide budget of a magma **(Fig. 5.67D)**. As these four elements are incompatible to highly incompatible during basaltic fractionation, the ratios of Cu/Zr and Pd/Yb should remain constant (Keays 1995). Jowitt and Ernst (2012) interpret changes in these ratios as signifying episodes of sulphide segregation or accumulation caused by the magma reaching sulphur saturation. They interpret suites of rocks with uniformly low Cu/Zr, Pd/Yb ratios as having resulted from partial melting insufficiently high to melt all of the sulphide in the source, while also interpreting unmineralised suites with uniformly high Cu/Zr, Pd/Yb ratios and chalcophile abundances as having resulted from a magma which formed via partial melting of a high enough degree to melt all of the mantle sulphides, yet never attained sulphur saturation during fractionation in the crust. Jowitt and Ernst (2012) demonstrate that lavas from fertile LIPs have variable Cu/Zr, Pd/Yb ratios and chalcophile element abundances and interpret their findings to show that suites of rocks with such variable ratios evolved from a magma which was both metal-fertile and reached sulphur saturation.

In summary, the work of Jowitt and Ernst (2012) indicates that LIPs which are prospective for Ni-Cu-PGE are characterised by lavas which; record MORB- or CFB-like Ti/V ratios <50; plot on mixing lines between mantle end-members and the upper continental crust and; contains both chalcophile-depleted and chalcophile-enriched members.

Plotting the Matachewan LIP data collected by this study on the diagrams presented by Jowitt and Ernst (2012) yields interesting interpretations. Firstly, on the Ti/100 vs. V diagram **(Fig. 5.68)** virtually all of the Matachewan LIP suites fall in the ‘prospective’ MORB- or CFB-like fields defined by Ti/V ratios of between 20-50. Only the Seidorechka Formation samples which themselves record a very large range of Ti and V contents and several of the Thessalon Group 2 volcanics plot within the ‘barren’ Alkaline- or OIB-like field of Ti/V > 50 while the estimated parent magma of the BDM intrusion and the Streich dykes which fed the East Bull Lake Suite plot above the Ti / V = 20 line.

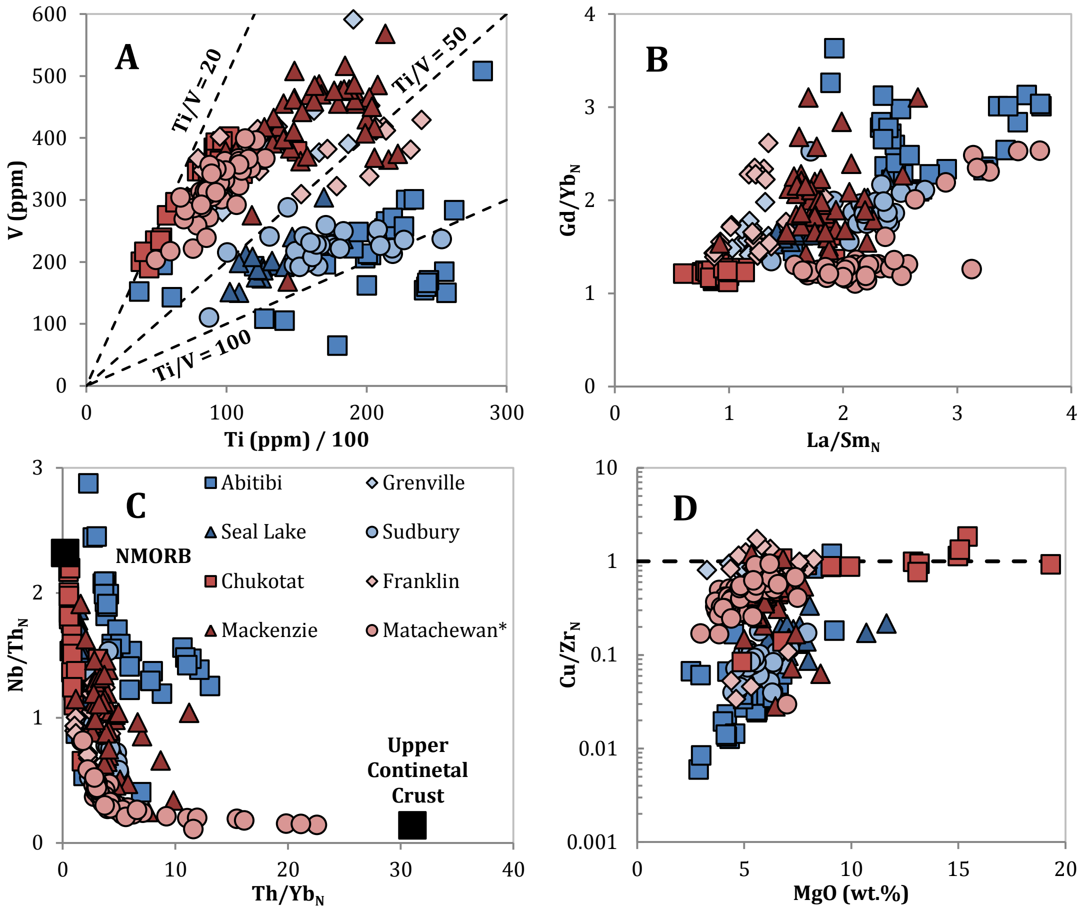

Fig. 5.67. A selection of diagrams from Jowitt and Ernst (2012) used to distinguish Ni-Cu-PGE fertile LIPs from barren ones. Fertile LIP samples are shades of red, while barren LIPs are shaded blue. Particularly note the separation of fertile and barren samples on the Ti/100 vs. V diagram, the similar trends on La/Sm$_N$ vs. Gd/Yb$_N$ and Th/Yb$_N$ vs. Nb/Th$_N$ diagrams and the much greater ranges in chalcophile element abundances at a given MgO exhibited by the fertile LIP samples relative to the barren samples.

The La/Sm$_N$ vs. Gd/Yb$_N$ diagram for the Matachewan LIP suites **(Fig. 5.69)** is again similar to that of Jowitt and Ernst (2012) in that many of the suites overlap, but that the suites which plot in the 'barren' alkaline- or OIB-like field in **Fig. 5.68** also record the highest Gd/Yb$_N$ ratios.

The Matachewan LIP suites all show evidence of mixing between mantle end-members and the upper continental crust **(Fig. 5.70)**. The majority of the suites define tight mixing trends and thus may be interpreted as extremely hot and turbulent magmas which were very efficient at assimilating continental crust and mixing within crustal chambers. This type of trend is thought to be indicative of Ni-Cu-PGE fertility by Jowitt and Ernst (2012). The most scattered trend is recorded by the Seidorechka Formation rocks. This is somewhat surprising as the Seidorechka Formation rocks record the most complete record of mixing between the mantle and

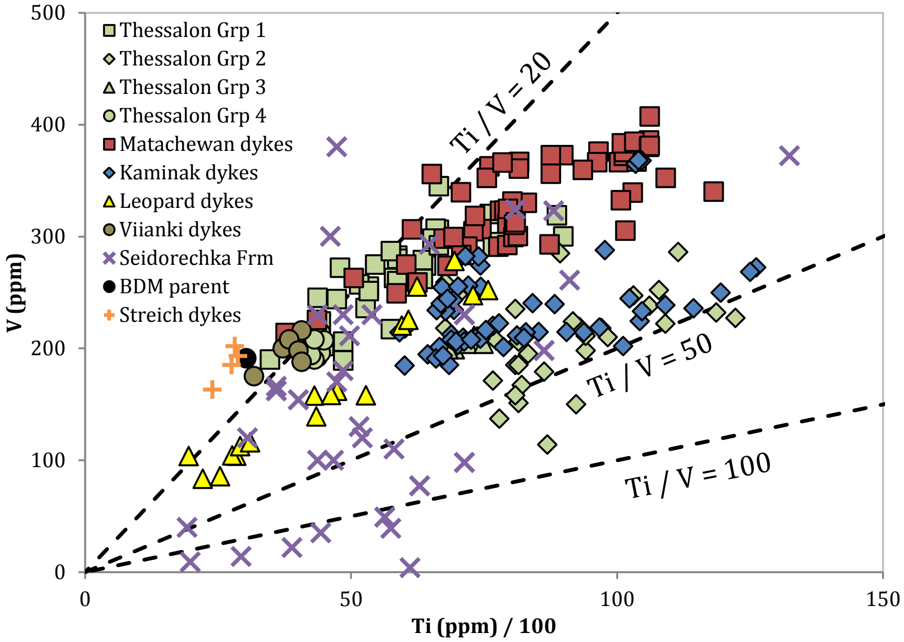

Fig. 5.68. Ti / 100 vs. V diagram for the Matachewan LIP suites after Jowitt and Ernst (2012).

continental crust. This suggests that the Seidorechka Formation parent magma was hot enough to assimilate significant amounts of continental crust, yet was not able to remain well mixed. Instead, the trends recorded by the Seidorechka Formation on this diagram may indicate that several parent magmas, each contaminated by different types of crust, evolved separately in crustal chambers before being erupted.

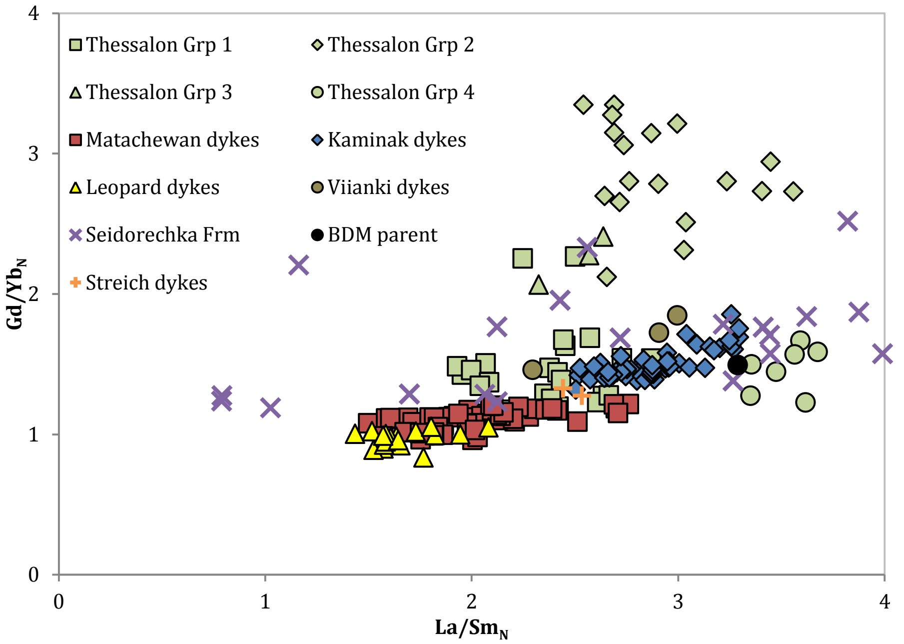

Fig. 5.69. La/Sm$_N$ vs. Gd/Yb$_N$ diagram for the Matachewan LIP suites where $_N$ denotes normalisation to the Primitive Mantle of (Sun and McDonough 1989).

On the Cu/Zr$_N$ vs. MgO diagram, the 'barren' LIPs of Jowitt and Ernst (2012) record either fairly constant Cu/Zr$_N$ ratios over the entire range of MgO contents or uniformly chalcophile depleted signatures **(Fig. 5.67D)**. Conversely, the 'fertile' LIPs show huge ranges in Cu/Zr$_N$ from chalcophile depleted to chalcophile enriched which is thought to signify that the parent magma to the LIP reached sulphur saturation during fractional crystallisation. The equivalent diagram for the Matachewan LIP suites **(Fig. 5.71)** shows that the Viianki, Kaminak, Matachewan, Leopard and Streich dykes and the Group 1 Thessalon volcanics contain both chalcophile-depleted and chalcophile-enriched rocks indicating that the parent magmas for each of these suites reached sulphur saturation during its fractionation in the crust. Conversely, samples from the Seidorechka and Thessalon groups 2, 3 and 4 volcanics are all chalcophile-depleted which may suggest that the parent magmas which formed these suites were produced by partial melting of an insufficient degree to melt all of the sulphides in the mantle source.

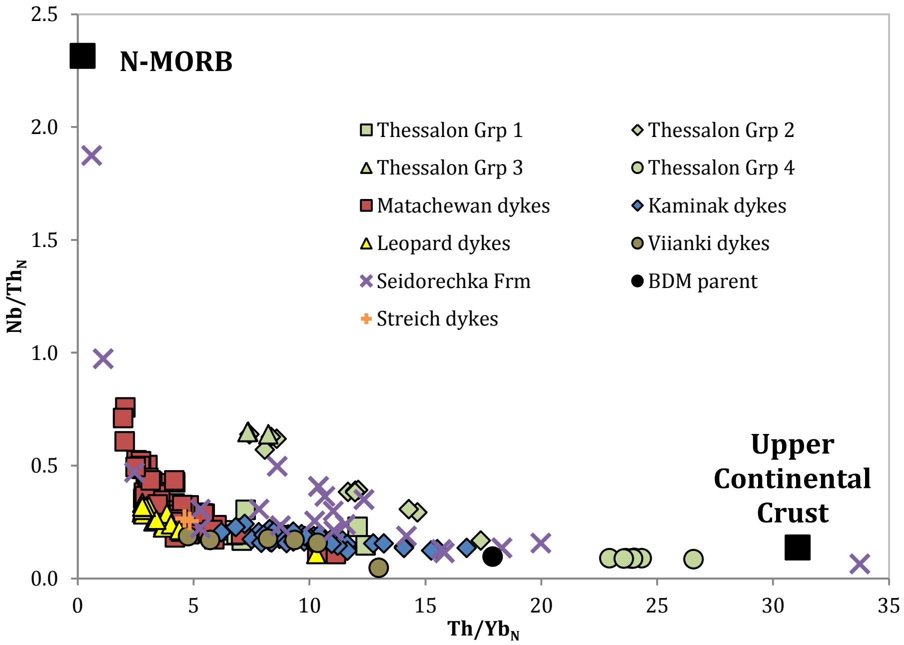

Fig. 5.70. Th/Yb$_N$ vs. Nb/Th$_N$ diagram for the Matachewan LIP suites showing mixing trends between N-MORB (Sun and McDonough 1989) and the upper continental crust (Rudnick and Gao 2003). $_N$ denotes normalisation to the Primitive Mantle of (Sun and McDonough 1989).

5.5.4. Summary

Analysis of the data presented by Zhang et al. (2008) shows that Ni-Cu-PGE fertile and barren LIPs share a similar major and trace element chemistry, albeit fertile LIPs have a higher proportion of high MgO lavas. This suggests that the major and trace element chemistry of an igneous suite cannot be used in isolation to determine its Ni-Cu-PGE prospectivity with any great degree of confidence. That said, the isotope data presented by Zhang et al. (2008) suggests that barren and fertile LIPs can be distinguished by using the Sr-Nd-Pb isotope systems, as the former record trends between the depleted mantle and EM2 reservoirs while the latter record the involvement of the EM1 reservoir.

The equivalent data of the Matachewan LIP appears to be consistent with the findings of Zhang et al. (2008). Firstly, in major and trace element space, the Matachewan LIP suites known to be associated with mineralisation (the Streich and Viianki feeder dykes) cannot be distinguished from those for which no related mineralisation has been observed. Secondly, isotopic data for the East Bull Lake suite of layered intrusions (which host significant Ni-Cu-PGE mineralisation) record trends similar to those of other fertile LIPs while the unmineralised Blue Draw Metagabbro records isotopic ratios similar to those of barren terranes. The consistency of the isotopic data presented by this study with that presented by Zhang et al. (2008) suggests that the involvement of the EM1 reservoir in mantle plume magmas may be key in forming economic Ni-Cu-PGE mineralisation and Sr-Nd-Pb isotope analysis may have some ‘broad-brush’ potential use in future exploration for such deposits. This isotopic variation between the East Bull Lake suite and Blue Draw Metagabbro attests to the compositional heterogeneity of mantle plumes as observed in other large igneous provinces [e.g., Kerr et al. 2002; Millet et al. 2008).

The work of Jowitt and Ernst (2012) suggests that Ni-Cu-PGE fertile LIPs contain lavas which; record MORB- or CFB-like Ti/V ratios <50; record low Gd/Yb_N ratios; plot on mixing lines between mantle end-members and the upper continental crust and; contain both chalcophile-depleted and chalcophile-enriched members. Conversely, the lavas of Ni-Cu-PGE barren LIPs are characterised by OIB-like Ti/V ratios >50; record high Gd/Yb_N ratios; plot on poorly defined trace element trends between the upper continental crust and mantle end members and; record either chalcophile-enriched or chalcophile-depleted signatures, but not both.

These criteria are examined in **Figs. 5.68-5.71** which show that the majority of the Matachewan LIP suites meet the criteria for Ni-Cu-PGE fertility as presented by

Jowitt and Ernst (2012). Only the Seidorechka Formation and Thessalon Group 2 volcanics consistently fail to meet these criteria. This indicates that any layered intrusions which may be directly associated with these two suites would not be prospective for Ni-Cu-PGE mineralisation. The Thessalon Group 2 and 3 also record uniformly chalcophile-depleted signatures which likely indicate that the parent magma was similarly chalcophile-depleted and thus wouldn't have had the Ni-Cu-PGE budget with which to form significant mineralisation.

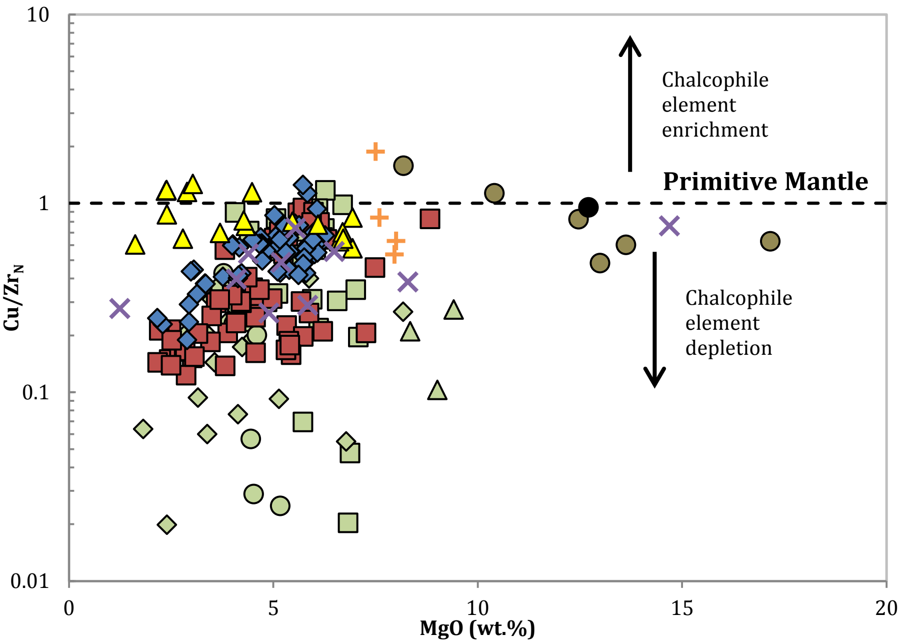

Fig. 5.71. Cu/Zr$_N$ vs. MgO diagram for the Matachewan LIP suites showing chalcophile element variations and potential for sulphide saturation in each suite. $_N$ denotes normalisation to Primitive Mantle (Sun and McDonough 1989). Vectors from Jowitt and Ernst (2012). Symbols as in **Fig. 5.70**.

5.5.5. The Blue Draw Metagabbro – Prospective?

Intrusions genetically linked to the BDM, including the EBLS, host significant contact-type Ni-Cu-PGE sulphide mineralisation (Peck et al. 1995; Vogel et al. 1999; James et al. 2002; Iljina 2007), the economic potential of which is being explored. If the proposed genetic link between the BDM and EBLS exists (Dahl et al. 2008; Ernst and Buchan 2010), then the BDM represents a Ni-Cu-PGE target which was, prior to this work, understudied. The following paragraphs discuss the Ni-Cu-PGE potential of the BDM and will be published in Ciborowski et al. (in press) - see **Appendix G**.

Primary sulphides were not observed in BDM outcrops in the study area, however, abundant malachite staining is present in outcrops near the upper contact of the intrusion **(Fig. 5.72A)** and very fine grained disseminated Cu- and Ni-bearing sulphides are present in the most evolved BDM rocks **(Fig. 5.72B)**. In order to better constrain where any potential Ni-Cu-PGE mineralisation may be present in the BDM, chemostratigraphic profiles of Ni, Cu, the PGE and other associated elements can be used to identify prospective horizons of stratiform Ni-Cu-PGE mineralisation **(Fig. 5.73)**. This approach is made possible by using the sampling strategy shown in **Fig. 3.9** and projecting these samples onto line A-B. The chemostratigraphic profile of Ni shows three conspicuous peaks in concentration at ~50, ~370 and ~650 m, of which the two lowest peaks correspond to the highest concentrations in MgO which indicates that the Ni concentration peaks at ~50 and ~370 m are caused by the presence of olivine-rich cumulates in which Ni is compatible.

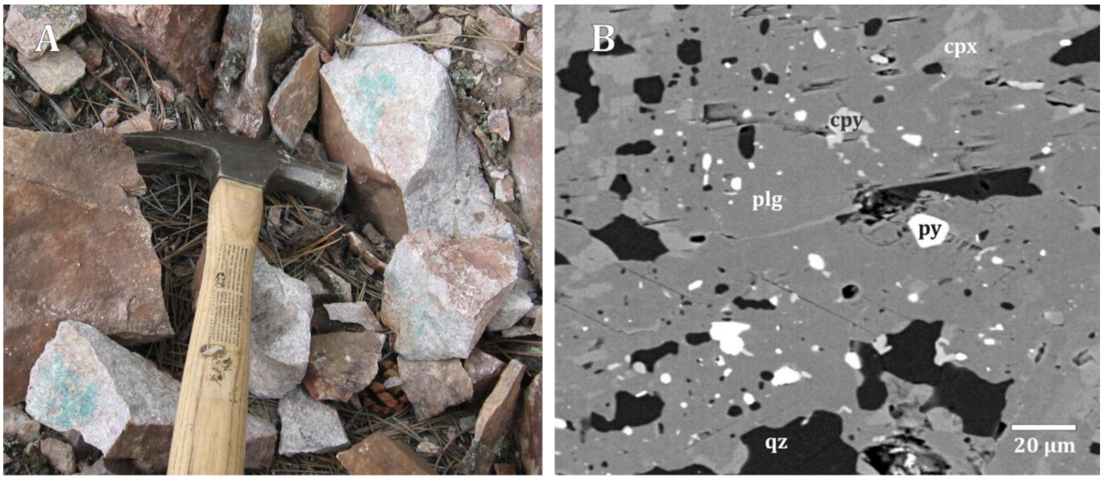

Fig. 5.72. Photograph (A) and SEM micrograph (B) of Cu and Ni-bearing mineralisation in the quartz gabbronorite unit of the BDM.

The lowermost of these peaks also corresponds to the highest IPGE concentrations but the lowest PPGE concentrations which suggests that during accumulation of the olivine-rich peridotite unit, the IPGE have behaved compatibly while the PPGE have behaved incompatibly. This decoupling of the PGE in fractionated systems is commonly observed and has been explained either by the IPGE being compatible during olivine and/or chrome spinel fractionation (Capobianco and Drake 1990; Brenan et al. 2003) or by the precipitation of IPGE (but not PPGE) alloys directly from the magma (Tredoux et al. 1995) or in local reduction fronts at chromite grain boundaries (Finnigan et al. 2008). The uppermost peak in Ni at ~650 m coincides with a conspicuous spike in Cu and highest Pd(+Pt) and Au concentrations in the intrusion. These associations suggest that these chalcophile elements are present to-

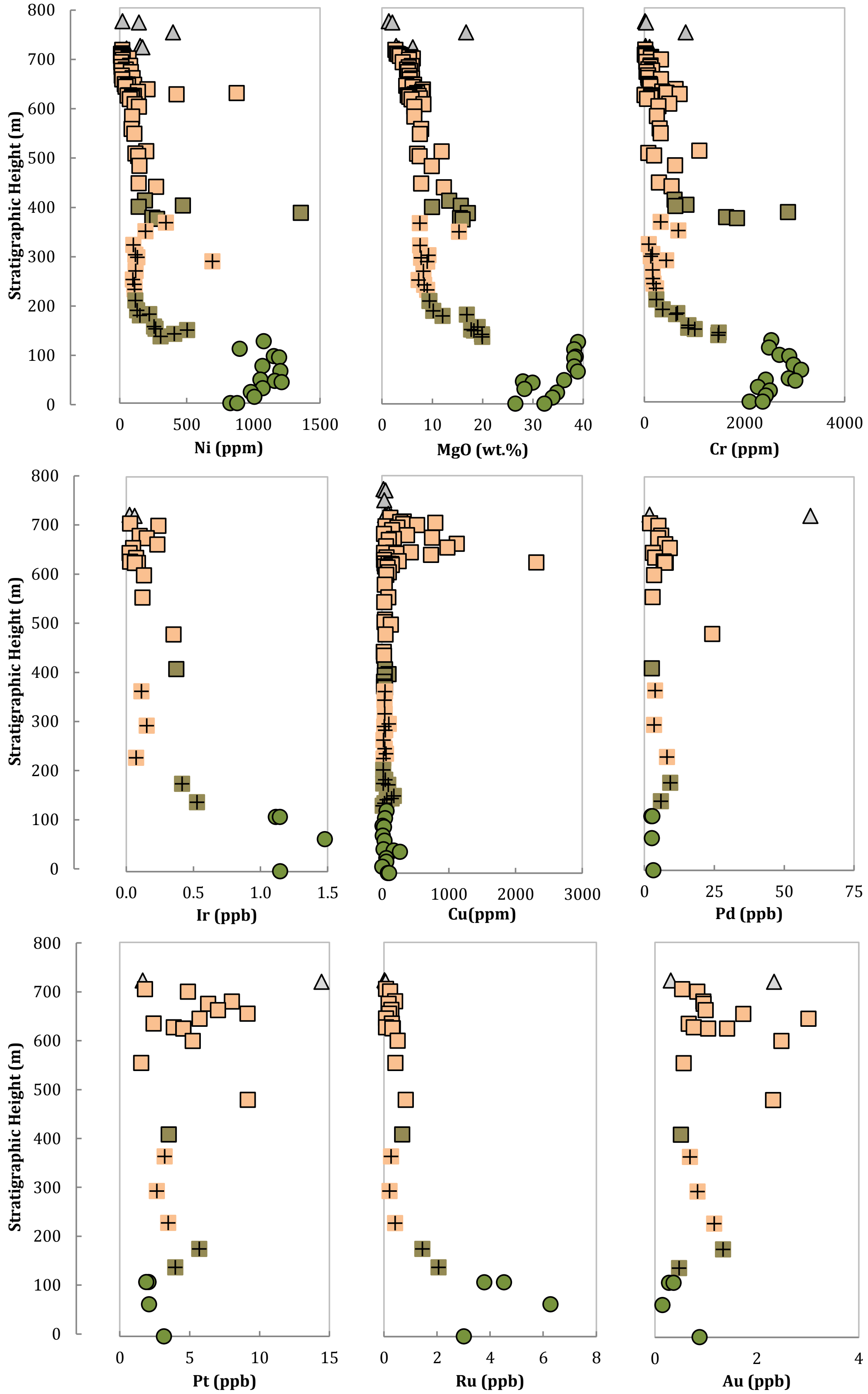

Fig. 5.73. Chemostratigraphic profiles through the Blue Draw Metagabbro for selected major and trace elements. Lithological symbols the same as in **Fig. 4.34**.

gether in sulphide phases. SEM imaging of rocks from this stratigraphic height has confirmed the presence of very fine grained (≤ 12 μm) disseminated sulphides, dominated by pyrite and chalcopyrite. The presence of these minerals indicates that through fractional crystallisation, the BDM magma attained sulphur saturation and precipitated Ni-Cu-PGE-bearing sulphides – a key prerequisite in Ni-Cu-PGE deposit formation (Naldrett 1999). Despite this, the BDM contains decidedly uneconomic concentrations of PGE (Pt+Pd+Au < 80 ppb). These concentrations of precious metals are in contrast to those recorded by other mineralised, tholeiitic intrusions [e.g., Skaergaard and Sonju Lake) which preserve well defined, stratiform zones of significant PGE-bearing sulphide mineralisation, which (in the case of Skaergaard) can contain up to 5.5 ppm Pt+Pd (Andersen et al. 1998; Miller 1999).

As has been described above, in order for a mafic-ultramafic magma to form an economic Ni-Cu-PGE deposit, the magma must first precipitate an immiscible sulphide liquid through crystallisation and/or interaction with crustal rocks [e.g., Arndt et al. (2005); Maier (2005); Naldrett (2011)]. This sulphide liquid must then raise its PGE tenor by scavenging chalcophile elements from chalcophile element-bearing silicate magma, either through interaction with magma already in the chamber [e.g., Andersen et al. 1998) or through interaction with recharging pulses of sulphur-undersaturated magma [e.g., Peck et al. (2001); Kerr and Leitch (2005)]. However, data from the BDM intrusion suggest that it lacks some of these steps.

Firstly, while trace element and isotopic data indicate that in-situ contamination of the BDM occurred during fractionation of the magma, the likely contaminant, the Boxelder Creek Quartzite shows no evidence of containing sulphide-bearing horizons (Lee 1996; Hill 2006). With no additional sulphur assimilated from the potential sedimentary contaminant with which to trigger sulphur saturation of the magma, the BDM was limited to reaching sulphur saturation through fractional crystallisation of Fe-bearing silicate minerals. Secondly, while there is good evidence of the BDM having undergone magma recharge during crystallisation (section 5.4), geochemical evidence suggests that recharge of the system occurred prior to sulphide saturation, meaning that there was no immiscible sulphide liquid present to scavenge chalcophile elements from the recharging magma. Thirdly, incompatible element trends through the intrusion **(Fig. 4.34)** suggest that the BDM formed through fractional crystallisation and gravity settling to build an igneous stratigraphy upwards from the base of the intrusion. If this interpretation is correct, then sulphur saturation of the magma occurred after most (~75%) of the intrusion had crystallised. The immiscible sulphide liquid would thus have been restricted to concentrate the Ni-Cu-PGE budget of a relatively small amount of magma which had already seen extensive removal of Ni + IPGE by silicate fractionation.

These data suggest that the BDM parent magma was metal-bearing and sulphur-undersaturated when it was injected into the Boxelder Creek Quartzite. The melt reached sulphur saturation through fractional crystallisation of silicates to produce a low-grade (Pt+Pd+Au < 80 ppb) disseminated sulphide zone near the top of the upper gabbronorite unit. This interpretation is strengthened when the data from the BDM is plotted on the Cu vs. Pd sulphur-saturation discrimination diagram **(Fig. 5.74)** of Vogel and Keays (1997). On this diagram, the peridotite, olivine melagabbronorite, lower gabbronorite and melagabbronorite units plot inside the sulphur-undersaturated field indicating that they formed from a sulphur-undersaturated magma, while samples from the quartz gabbronorite and upper gabbronorite units mainly plot in the sulphur-saturated field, which indicates that during fractional crystallisation to form the upper gabbronorite unit, the BDM magma reached sulphur saturation.

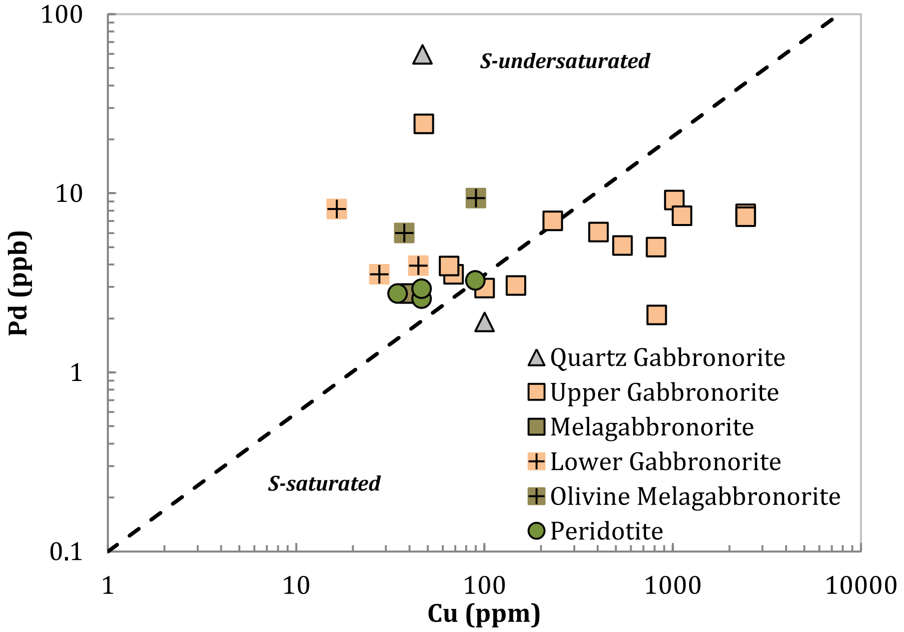

Fig. 5.74. Cu vs. Pd diagram (Vogel and Keays 1997) for discriminating between sulphur saturated and sulphur undersaturated BDM rocks.

5.6. The Great Oxidation Event

The U-Pb isotope data presented in Chapter 2 define an average age of intrusion for the Matachewan LIP of approximately 2.46 Ga. This age coincides with the point at which Earth's atmosphere changed irrevocably with the first appearance of free oxygen (Holland 2006, Kerr 2005, Frei et al. 2009, Sessions et al. 2009). This catastrophic period in Earth's history is referred to as the Great Oxidation Event (GOE).

5.6.1. Recognising the Great Oxidation Event

The existence of the GOE is supported by two main lines of evidence. The first is the preservation of redox-sensitive detrital minerals in Archaean terrestrial sandstones, which support the change from an anoxic to an oxic atmosphere. As pyrite and siderite are unstable in the presence of oxygen (Garrels et al. 1973), their preservation as detrital grains in a terrestrial sediment indicates that either the sediment was deposited and buried quickly (before oxidation could occur), or that deposition occurred in an anoxic environment. In a multi-disciplinary study, Rasmussen and Buick (1999) investigated the composition of detrital mineral grains in terrestrial sandstones from separate Archaean sedimentary sequences in the Pilbara. They found abundant pyrite and siderite grains, the textures of which strongly support a detrital origin rather than a hydrothermal or diagenetic one.

Crucially, the detrital siderite and pyrite grains studied by Rasmussen and Buick (1999) are preserved within compositionally and texturally mature trough-cross-bedded sandstones, the inference being that rather than having been buried quickly (before the pyrite and siderite could oxidise to goethite and haematite) the sediment travelled in, and was deposited by, turbulent streams which were likely to have been well aerated. Given this inferred mode of deposition, Rasmussen and Buick (1999) argue that the atmosphere in the Archaean was largely devoid of oxygen otherwise the redox-sensitive minerals would not have been preserved in such mature sediments.

Similar detrital assemblages are found in the ~2.87 Ga Witwatersrand placer gold fields (Frimmel 2005) where radiometric dating of uraninite (another mineral which is unstable in the presence of oxygen) and pyrite has proved their detrital nature by showing that the grains are older than the oldest possible deposition age for the placer deposits in which they are hosted. Frimmel (2005) interprets the inclusion of these redox-sensitive detrital minerals within fluvially deposited placers to evidence the anoxic nature of the atmosphere at ~2.87 Ga. Sverjensky and Lee (2010) suggest that the presence of reduced mineral species such as siderite, pyrite and uraninite in surficial deposits older than ~2.45 Ga attest to the anoxic nature of the Archaean atmosphere at this time and that the near-disappearance of such mineral species in facies-equivalent rocks younger than ~2.45 Ga is most favourably explained by a sustained increase in the oxygen content of the late Archaean/early Proterozoic atmosphere.

The second line of evidence which supports a wholescale change of the atmosphere at ~2.45 Ga can be deduced from studies of sulphur isotopes [e.g., Bekker et al. (2004)]. Sulphur has four stable isotopes, the distribution of which among sulphur bearing compounds at thermodynamic equilibrium depends on the relative mass differences of the isotopes. This mass-dependent fractionation means that terrestrial samples plot on δS variation diagrams along linear trends **(Fig. 5.75)**, which in the case of the $\delta^{34}S$ vs. $\delta^{33}S$ diagram has a gradient of 0.515 (Buhn et al. 2012). This mass-dependent fractionation characterises samples throughout Earth's history from the present to ~2.45 Ga, while samples older than this display significant mass-independent signatures **(Fig. 5.76)**.

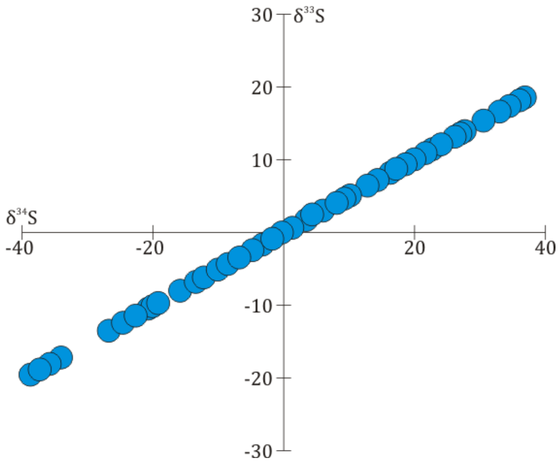

Fig. 5.75. Plot of $\delta^{33}S$ vs. $\delta^{34}S$ for terrestrial sulphide and sulphate younger than 2000 Ma (Johnston 2011).

These mass independent signatures were investigated by Farquhar and Wing (2003) who found that similarly large mass-independent fractionations are produced by ultraviolet (UV) radiation-driven photolysis of SO_2 to SO. Farquhar and Wing (2003) argue that the presence of a sulphur isotope signature indicative of deep atmosphere UV penetration in >2.45 Ga samples precludes the existence of ozone (which filters these wavelengths) during the Archaean. As ozone (O_3) is predominantly produced via the interaction of solar radiation with O_2 in the upper atmosphere, the lack of any appreciable ozone suggests that atmospheric O_2 was also absent. Farquhar and Wing (2003) propose that the lack of mass independent fractions of sulphur in samples younger than ~2.45 Ga suggests that ozone, and hence O_2, appeared and was sustained from the early Proterozoic.

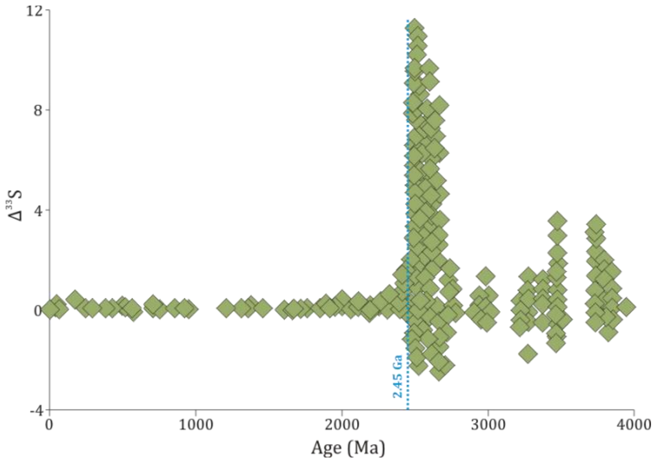

Fig. 5.76. Plot of $\Delta^{33}S$ vs. age after Johnston (2011). This record shows the change in $\Delta^{33}S$ from variable sign and magnitude in rocks older than ~2.45 Ga to much less variable values in younger rocks. The change in $\Delta^{33}S$ behaviour at ~2.45 Ga is attributed to the oxygenation of Earth's atmosphere at this time.

Other evidence used to constrain the existence and timing of the GOE include the marked decrease in abundance of banded iron formation (rich in reduced Fe) in sequences younger than 2.45 Ga (Cloud 1973), changes in chromium and manganese contents of marine sedimentary rocks- thought to reflect oxidative weathering of the continents (Kirschvink et al. 2000; Frei et al. 2009; Konhauser et al. 2011) and more general changes in the rock record to lithologies typical of oxic environments (Kump et al. 2013).

5.6.2. Causes of the Great Oxidation Event

Photosynthetic cyanobacteria are widely credited with producing the oxygen which drove the oxygenation of the atmosphere following ~2.45 Ga (Canfield 2005). However, the evolution of cyanobacteria in itself is not thought to have caused the

GOE as evidence of cyanobacterial photosynthesis is preserved in the geologic record as far back as 2.7 Ga (Brocks et al. 1999; Bosak et al. 2009). The reason for this ≥250 million year lag between the onset of photosynthesis and the permanent oxygenation of the atmosphere is unresolved but may be caused by buffering of newly produced oxygen by pre-existing sinks until such time as the sinks became saturated (Claire et al. 2006; Anbar et al. 2007).

Evidence from BIFs indicates that the influx of Ni to the oceans fell prior to the GOE and that the lag between photosymbiosis and oxygenation is not the product of buffering, but instead secular cooling of the upper mantle causing a decrease in the frequency of high-Ni mafic-ultramafic lava erupted on the surface (Konhauser et al. 2009). Konhauser et al. (2009) assert that with a restricted magmatic nickel input, the productivity of marine methanogens would be limited, causing a concomitant decrease in the amount of methane available to act as an oxygen sink.

A change in volcanic style from submarine to subareal following the emergence of the continents during the late Archaean may have driven oxygenation of the atmosphere (Kump and Barley 2007; Gaillard et al. 2011). As submarine volcanism produces gases that are more reducing (H_2, CO, CH_4 and H_2S) than those produced by subaerial volcanism (H_2O, CO_2, SO_2), the change in volcanic style to a more subaerial style may have resulted in a decreased volcanic sink for O_2 and allowed photogenic O_2 to build up in the atmosphere **(Fig. 5.78)**.

Tectonic cycles have also been invoked as a potential mechanism for driving the oxygenation of the atmosphere during the GOE. In two different studies Knoll et al. (1986) and Lindsay and Brasier (2002) linked periods of increased organic burial (as denoted by significant excursions $\delta^{13}C$ in sedimentary rocks) with periods of continental rifting and dispersal. Lenton et al. (2004) suggest that increased rates of organic burial during rifting are caused by an increase in the size of the continental shelf during continental breakup while Bekker et al. (2004) suggest that the submarine volcanism associated with rifting promotes widespread anoxia which suppresses the oxidation of organic carbon from the sediment. However, Campbell and Allen (2008) and Campbell and Squire (2010) suggest that rather than rifting being the driver of the GOE, it is actually continental collision which allowed photosynthetic oxygen to build up in the atmosphere. These two studies argue that the mountain ranges produced by continental collision are quickly eroded and increase the sediment and nutrient supply to the ocean. Campbell and Allen (2008) argue that the increase in nutrient supply would enhance photosynthesis and that the overall increase in sediment input would enable larger amounts of organic carbon to be preserved and buried.

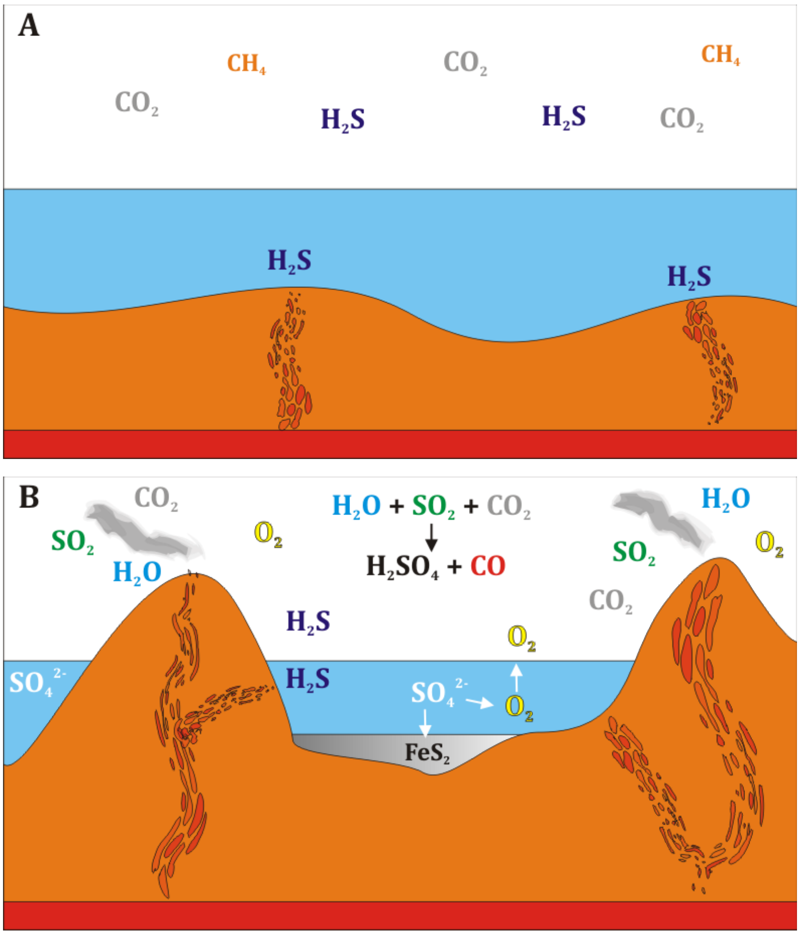

Fig. 5.78. Schematic diagram showing the changing volcanic styles from the middle Archaean (A) to the late Archaean – early Proterozoic (B) and the effect on atmospheric chemistry. The emergence of volcanoes from the ocean during the late Archaean – early Proterozoic increased the production of SO_2. SO_2 is soluble in water and produces sulphate (SO_4^{2-}) upon dissolution. The reduction of sulphate in the ocean releases oxygen which cycles back into the atmosphere and drives the GOE. Modified after Gaillard et al. (2011).

As the Matachewan LIP represents a period of massive volcanic activity and continental breakup (Aspler et al. 2001; Dahl et al. 2006; Ernst and Bleeker 2010), it engenders some of the processes described above, postulated as enabling the oxygenation of the atmosphere. Thus, given the timing of the igneous activity, the Matachewan LIP represents an intriguing candidate for driving the GOE. The following paragraphs attempt to understand how the breakup of the Superia supercontinent (Bleeker 2003) may have changed the size and distribution of the continental shelf and how the subareal volcanism preserved in the Matachewan LIP may have affected the oxygen cycle.

5.6.3. Continental Shelf Increase

As continental break up is suggested as a driving mechanism in the production of oxygen (Knoll et al. 1986; Lindsay and Brasier 2002; Lenton et al. 2004), there is potential for the rifting of the Superia supercontinent which initiated sometime between ~2.50-2.45 Ga to be greatly significant to the GOE. To quantify the potential influence the rifting of Superia had on the GOE, the amount of continental shelf produced during the rifting event is investigated using the ~2.5 Ga configuration of Superia (Ernst and Bleeker 2010) as a starting point **(Fig. 5.79)**. Rifting of Superia along the craton margins shown in **Fig. 5.79A** is problematic as the spreading does not occur in typical linear or 120° triple junction geometries typically observed at spreading centres today. Instead, the most parsimonious rifting configuration based on the Superia reconstruction of Ernst and Bleeker (2010) is that initial rifting began as a triple junction between the Superior, Karelia and Wyoming-Hearne cratons (Dahl et al. 2006) with the Wyoming and Hearne cratons rifting at some later time.

Magmatism on Superia began at ~2.5 Ga and was related to the Mistassini plume centred near to the eastern margin of the continent (Ernst and Buchan 2001; Bleeker and Ernst 2006). Shortly after, magmatism and rifting initiated around the Matachewan centre to form the dyke swarms and layered intrusions preserved on the Superior, Karelia, Wyoming and Hearne cratons **(Fig. 5.79B)** studied by this project. The rifting initiated by the Matachewan plume continued and the related subsidence facilitated the formation of the volcano-sedimentary basins which host the flood basalt provinces of the Huronian, Snowy Pass, Hurwitz and Karelian Supergroups **(Fig. 5.79C)**. Continued rifting of Superia led to passive margin development and seafloor spreading **(Fig. 5.79D-5.79E)**.

Archaean continental reconstructions are poorly constrained and attempts at refining them are in progress (Oliveira et al. in press; Gumsley et al. in press). Thus, the pos-

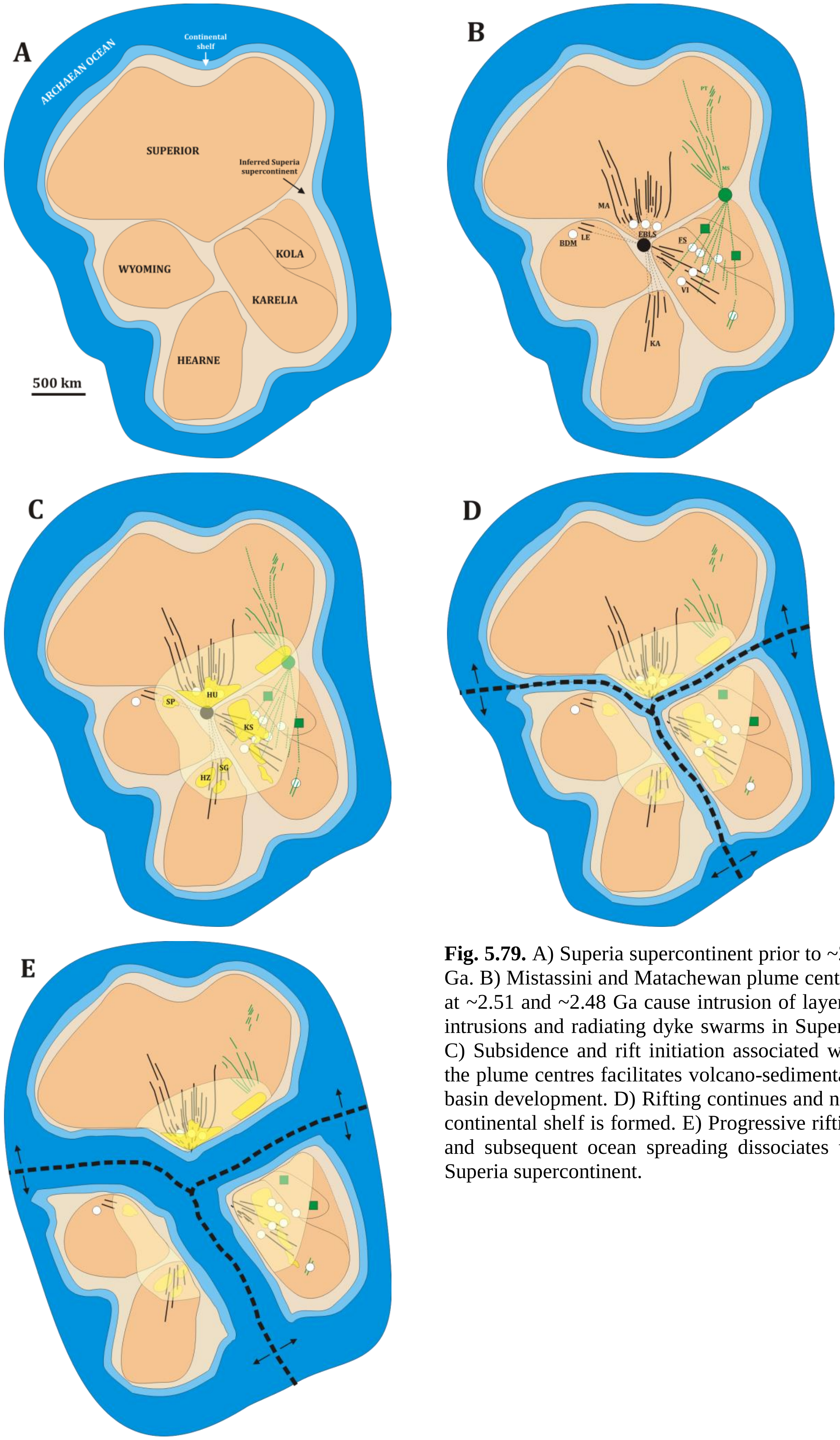

Fig. 5.79. A) Superia supercontinent prior to ~2.5 Ga. B) Mistassini and Matachewan plume centres at ~2.51 and ~2.48 Ga cause intrusion of layered intrusions and radiating dyke swarms in Superia. C) Subsidence and rift initiation associated with the plume centres facilitates volcano-sedimentary basin development. D) Rifting continues and new continental shelf is formed. E) Progressive rifting and subsequent ocean spreading dissociates the Superia supercontinent.

ition of Superia relative to other Archaean continental landmasses is unknown. However, Bleeker (2003) notes that current data indicates that prior to 2.5 Ga the other Archaean cratons not part of the Superia reconstruction record a distinctly different geological history to those that are. Bleeker (2003) uses this observation to suggest that at ~2.5 Ga, Superia was a self contained continental landmass, separated from other Archaean continents by sizeable ocean basins.

The increase in the amount of continental shelf caused by the rifting of Superia can be investigated despite the reconstruction presented by Ernst and Bleeker (2010) being somewhat schematic. By assuming the existence of a ~80 km wide (Pinet 2003) continental shelf ringing Superia, the pre-rifting area of ocean underlain by continental shelf can be estimated as 1.2×10^4 km^2 **(Fig. 5.79A)**. By assuming that the rifting produced continental shelf of a similar width around the Superior, Karelia and Hearne-Wyoming cratons post-rifting, then the area of continental shelf increases by 2.5×10^4 km^2, or ~200% **(Fig. 5.79E)**.

Further to this, the amount of time needed to create an 80 km wide continental shelf during continental rifting can be estimated using plate velocities. Plate velocities in the Archaean are not well defined, though Bickle (1986) suggest they may have been 2-3x greater than today. Prawirodirdjo and Bock (2004) use time-integrated position data from 160 globally distributed GPS stations to estimate absolute plate motions. Averaging the data presented by Prawirodirdjo and Bock (2004) suggests that the average absolute velocity of tectonic plates today is ~28mma^{-1}. Using the estimation of Bickle (1986), this equates to an absolute plate velocity of ~70mma^{-1} during the Archaean. Assuming that the plate motions during the rifting of Superia were constant, the time required to move 80 km from a stationary spreading centre is ~114,000 kyr.

These calculations rely on assumptions and may require caution when interpreting their impact on the GOE. For example, continued plate interactions have likely modified the Superia supercontinents constituent cratons such that the morphology of Superia as presented by Ernst and Bleeker (2010) may be highly speculative. Secondly, the palaeogeographic distributions of the continents in the Archaean is poorly constrained and it cannot be said with confidence that Superia was not part of a larger supercontinent (Bleeker 2003; Söderlund et al. 2010) which would have affected the area of pre-existing continental shelf. Thirdly, applying modern-day continental shelf parameters to the Archaean Earth may not be reasonable as may also be the case in applying the estimate plate velocities described above.

However, this speculation is useful in highlighting the potential importance of the break-up of Superia in driving the oxygenation of the atmosphere during the GOE as it demonstrates that the rifting of Superia was capable of greatly increasing the area of continental shelf on which organic carbon could be deposited in a geologically short time period (Knoll et al. 1986; Lindsay and Brasier 2002).

5.6.4. Volcanic Forcing

Volcanic input of SO_2 into the atmosphere has also been suggested as a mechanism for driving the oxygenation of the atmosphere via increased sulphate reduction in the oceans (Gaillard et al. 2011). Sizeable flood basalt provinces which are interpreted to have erupted subareally (Tomlinson 1996; Puchtel et al. 1996; Sandeman and Ryan 2008) constitute a large part of the overall magmatic volume of the Matachewan LIP. Thus, it is likely that the eruption of these flood basalts produced significant quantities of SO_2 which may have affected the atmosphere.

To investigate this question, this study modifies the method of Thordarson et al. (1996) who attempted determining the quantity of volatiles emitted by the 1783-1784 AD Laki eruption. Thordarson et al. (1996) collected samples of the Laki lavas and analysed the volatile contents of melt inclusions trapped in olivine and plagioclase phenocrysts which grew while the magma was still in some sub-surface chamber. The volatile contents of the melt inclusions are thought to record the volatile budget of the magma prior to eruption and are compared to the volatile content of the glassy groundmass of the lava. Thordarson et al. (1996) argue that the discrepancy between the two is accounted for by the amount of volatiles released by the lava during eruption **(Fig. 5.80)**.

Due to the presence of several polyatomic species with atomic mass 32, sulphur is a troublesome element to measure by ICP-MS. Consequently, there is not much sulphur data for the Matachewan LIP suites published in the literature. However, ICP-MS sulphur data does exist for 11 dykes from the Kaminak swarm (Ernst and Buchan 2010) and for 3 samples of Spi Group basalt which have been shown to be the extrusive equivalents of the Kaminak dykes (Sandeman and Ryan 2008). The 11 Kaminak dykes define an average sulphur content of 1036 ppm while the Spi Group basalts contain, on average 710 ppm. This is interpreted as showing that the Kaminak dyke parent magma contained ~1036 ppm sulphur, which was trapped within the magma as it crystallised in the dykes while on route to the surface. The magma which did reach the surface to be erupted as the Spi Group basalts released some of its dissolved sulphur to the atmosphere, leaving the lavas to crystallise with ~710 ppm sulphur. The 326 ppm deficit in sulphur between the dykes and the lavas is likely to have been lost to the atmosphere as predominantly SO_2 gas.

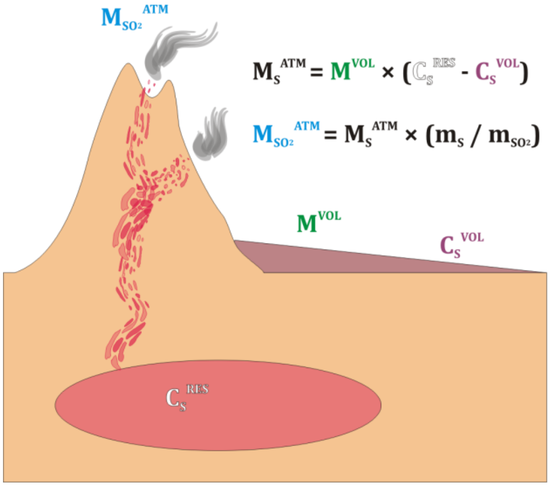

Fig. 5.80. Schematic illustration showing the volatile budget of a lava erupted from a deeper chamber. The mass of SO_2 lost to the atmosphere $\mathbf{M_{SO_2}^{ATM}}$ can be calculated by taking the product of the mass of the volcanic province $\mathbf{(M^{VOL})}$ multiplied by the deficit in concentration (wt. %) of S between non-degassed magma preserved in dykes $\mathbf{(C_S^{RES})}$ and the S concentration of the degassed lavas $\mathbf{(C_S^{VOL})}$ and multiplying it by the ratio of the atomic mass of S $\mathbf{(m_S)}$ divided by the atomic mass of SO_2 $\mathbf{(m_{SO_2})}$. Modified after Thordarson et al. (1996).

The total mass of SO_2 released to the atmosphere during the eruption of the Spi Group basalts can be quantified using the approach of Thordarson et al. (1996): The Spi Group basalts record a stratigraphic thickness of 75-100 m and occupy an elongate basin which is approximately 8 km^2 (Sandeman and Ryan 2008) which equates to an igneous volume of ~0.7 km^3. PELE calculates that the density of the Spi basalts during eruption was ~2.64 gcm^{-3} which yields an estimate of the total mass of magma erupted to form the Spi Group basalts of 1.85×10^{13} kg. The difference between the sulphur content of the Kaminak dykes and the Spi Group basalts is 326 ppm, which when applied to the magmatic volume recorded by the Spi Group basalts equates to a release of 1.2×10^{9} kg or 1.2 Mt of SO_2 into the atmosphere. The Spi Group basalts and other correlative packages (Carpenter 2003; Sandeman and Ryan 2008) are preserved in synformal structures and are likely to be the last surviving remnants of a much larger flood basalt province which has since been eroded. Thus, the amount of SO_2 released by the eruption of the Spi Group basalts calculated above likely represents a gross underestimation of the actual amount released.

The Matachewan LIP reconstruction presented by Ernst and Bleeker (2010) suggests that eroded flood basalt provinces now preserved in the Spi Group, Huronian Supergroup and Karelian Supergroup are the erosional remnants of what was once a continuous flood basalt province which covered an area of ≥ 1,200,000 km^2 **(Fig. 5.81)**. For comparison, two of the better known Phanerozoic flood basalt provinces, the Deccan and Siberian Traps, cover areas of 500,000 km^2 and 1,500,000 km^2 respectively (Lightfoot et al. 1990; Dessert et al. 2001). As has been stated above, the Spi Group basalts record an average thickness of 75-100 m. Estimates of the thickness of the Thessalon Formation of the Huronian Supergroup range between 500-1500 m (Jolly 1991; Tomlinson 1996) while the thickness of the volcanic Seidorechka Formation of the Karelia Supergroup is estimated to be ~3000 m thick (Melezhik and Sturt 1994; Puchtel et al. 1997). Taking the average of the median thicknesses of these three flood basalt provinces (1.36 km) and applying it to the areal extent of the original Matachewan flood basalt province **(Fig. 5.81)** the original igneous volume of the Matachewan flood basalts can be estimated to be as large as 1,600,000 km^3, comparable to volume estimated for the Siberian Traps (Renne and Basu 1991).

By applying this igneous volume to the calculations of Thordarson et al. (1996) using the constraints of density and sulphur deficit defined above for the Spi Group basalts, the amount of SO_2 release to the atmosphere during the eruption of the Matachewan flood basalts may have been as much as 2.75×10^{15} kg or 2750 Gt. Gaillard et al. (2011) suggests that the SO_2 released by volcanic eruptions produces oxygen by, firstly, forming sulphuric acid in the atmosphere which dissolves in the ocean. The soluble sulphate ions (SO_4^{2-}) reduces Fe^{2+} ions dissolved in the ocean water to produce pyrite and liberate O_2 **(Equation 5.8)**.

Balancing this equation shows that for every 2 moles of SO_2 erupted by a volcano, 4 moles of O_2 can be liberated. 2750 Gt of SO_2 = 4.3×10^{16} moles of SO_2, which accor-

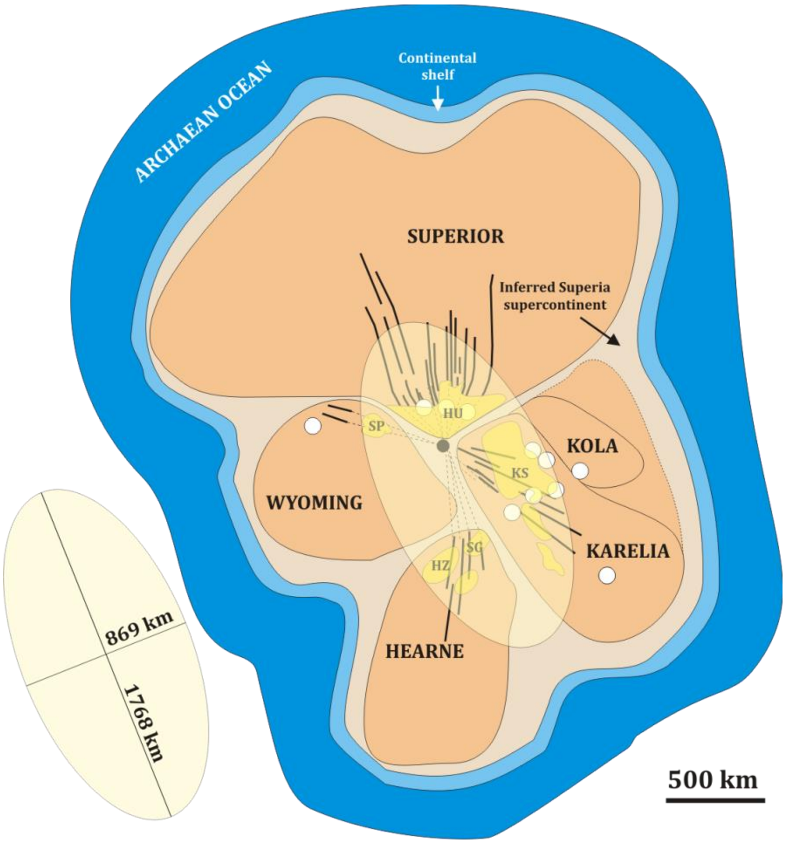

Fig. 5.81. The supercontinent Superia (Ernst and Bleeker 2010) showing the area of the continent potentially covered by flood basalt provinces (Easton et al. 2010).

ding to equation 5.8 can go on to produce 8.6×10^{16} moles (2750 Gt) of O_2. For comparison, the modern atmosphere has a mass of 5×10^{18} kg, 21% of which (1×10^{18} kg or 1×10^{6} Gt) is O_2. The oxygen level of the Archaean atmosphere, prior to the GOE has been estimated by various proxies to have been $\leq1\times10^{-5}$ times lower than present atmospheric levels (Anbar et al. 2007; Catling 2012). Assuming that the mass of the atmosphere has remained fairly constant since ~2.45 Ga, just prior to the GOE, then the oxygen budget of the atmosphere in the Archaean may be roughly estimated as 10.5 Gt. Thus, if the 2750 Gt of O_2 liberated by the eruption of the Matachewan flood basalts is an accurate estimate, it represents an absolutely enormous addition to the Palaeoproterozoic atmosphere, the potential importance of which cannot be overstated.

5.6.5. Summary

The calculations described above are somewhat abstract and rely on assumptions which may not be realistic. For example when assessing the changes in continental shelf area during break up of Superia, it is important to note that continued plate interactions since the Palaeoproterozoic have likely modified the Superia constituent cratons. Thus, the morphology of Superia as presented by Ernst and Bleeker (2010) is speculative. Secondly, the palaeogeographic distribution of the continents in the Archaean is poorly constrained and it cannot be said with confidence that Superia was not part of a larger supercontinent (Bleeker 2003; Söderlund et al. 2010) which would affect the estimate of the area of pre-existing continental shelf. Thirdly, applying modern-day continental shelf parameters to the Palaeoproterozoic Earth may not be reasonable as may also be the case when applying the estimated plate velocities described above. Finally, without better constraints the magnitude of the organic carbon flux to the continental shelf during the Palaeoproterozoic, it isn't currently possible to definitively model how an increase in continental shelf area would affect the atmospheric oxygen budget.

1 $$2SO_2 + 2H_2O + 2CO_2 \rightarrow 2H_2SO_4 + 2CO$$

2 $$2H_2SO_4 \leftrightarrow 4H^+ + 2SO_4^{2-}$$

3 $$2SO_4^{2-} + Fe^{2+} \rightarrow FeS_2 + 4O_2$$

Equation 5.8

Where: 1) shows the reaction of the sulphur dioxide released by subareal eruptions with water and carbon dioxide in the atmosphere to produce sulphuric acid and carbon monoxide gas. 2) The sulphuric acid produced in (1) dissolves in seawater to produce hydrogen and sulphate ions. 3) The sulphate ions produced in (2) reduce soluble Fe^{2+} in the seawater to produce pyrite and oxygen.

Despite these somewhat contentious assumptions, this speculation is useful in highlighting the potential importance of the break-up of Superia in driving the oxygenation of the atmosphere during the GOE as it shows that the rifting of Superia is capable of greatly increasing the area of continental shelf on which organic carbon can be deposited in a geologically short time period (Knoll et al. 1986; Lindsay and Brasier 2002). An increased rate of organic carbon burial decreases the amount of carbon available to be oxidised by oxygen which consequently remains free in the atmosphere to potentially build up and drive the GOE.

The equations regarding the release of SO_2 by the Matachewan LIP flood basalt volcanism are also somewhat speculative. The first issue is that the sulphur deficits recorded by the Spi Group basalts and Kaminak feeder dykes have been applied to the whole province which may not be accurate as variation between the various basalt packages may exist. Secondly, the igneous volumes modelled may not be realistic as erosion of the province has removed an unknown amount of the original flood basalts. A third issue is that the estimate of the mass of oxygen released by sulphate reduction in the ocean assumes that all of the sulphate reacts to form oxygen and all of that oxygen is released to the atmosphere. In actual fact, it is likely that a sizeable proportion of the oxygen is used up in the oxidation of organic carbon in the ocean and weathering of terrestrial rocks before the oxygen can build up in the atmosphere (Rasmussen and Buick 1999). Finally, there is little control on eruptive rates for the Matachewan LIP flood basalts which makes understanding the rate at which the SO_2 was released to the atmosphere a point of speculation. However, Bryan and Ernst (2008) note that LIP magmatism is typically characterised by short bursts of igneous activity (~1-5 million years) during which time, a large proportion (>75%) of the total igneous volume is emplaced. Thus, it is likely that the SO_2 released by the Matachewan LIP flood basalts represents a significant environmental perturbation which initiated relatively quickly.

Aside from SO_2 aerosols, volcanic eruptions release vast amounts of CO_2 and fine grained ash particles which persist in the atmosphere and severely affect climatic systems. For example, the sulphuric veil produced by the 1783-1784 Laki eruption is estimated to have caused a 1.3 °C decrease in the average surface temperature in the northern hemisphere which persisted for 2-3 years (Thordarson and Self 2003). Compared to the proposed Matachewan flood basalt eruption, the 1783-1784 Laki eruption was miniscule (1,600,000 km^3 vs. 15.1 km^3), the inference being that if just a fraction of the aerosol produced during the Matachewan flood basalt eruption persisted in the atmosphere at any one time, the affect on the global climate would have been enormous. Indeed, aerosol loading of the atmosphere has been suggested as the dominant mechanism in initiating ‘snow ball’ episodes during Earth’s history (Stern et al. 2008).

In conclusion, this section of discussion has demonstrated the sheer scale of the Matachewan LIP magmatism and speculated how that magmatism may have affected the Earth’s climate. The release of vast quantities of SO_2 into the atmosphere and an increase in the size of continental shelf on which to deposit organic carbon may have aided in the production and preservation of free oxygen in the atmosphere, which in turn, allowed more complex forms of life to evolve (Raymond and Segrè 2006). Conversely, the input of enormous quantities of sulphuric aerosols and fine-grained particulate matter from the volcanic eruption may have increased the Earth's albedo, causing a decrease in the amount of radiation received by the surface and driving the planet into a global glaciation or Snowball Earth event (Kirschvink et al. 2000) of the magnitude associated with the greatest mass extinction events in the geologic record (Jin et al. 2000). Such an event may be evidenced by the occurrence of widespread glacial diamictites in early Proterozoic sediments (Melezhik 2006).

5.7. Future Work

This project represents the most complete available synthesis of the geochemistry of the Matachewan LIP. Constraints of time and expense precluded the collection of original sample material from many of the suites, thus previously studied collections were a primary source of some of the analyses presented. Unfortunately the archived samples of the Thessalon Group volcanic rocks collected by Wayne Jolly and Kirsty Tomlinson have since been lost while the Viianki dyke samples collected by Derek Vogel are not currently available for study. For these suites and others not reanalysed by this project, previously published data has been presented alongside the data produced in Cardiff. As some of this previously published data may be considered imprecise or otherwise unreliable [e.g., (Mints et al. 1996)], the relevant suites should be reanalysed, ideally at Cardiff to produce a truly coherent geochemical database of the Matachewan LIP.

An aim of future work should also be to collect a number of high-precision U-Pb ages for individual Matachewan LIP suites – work which is ongoing in collaboration with Ulf Söderlund at Lund University. The most obvious target for dating are the Leopard dykes of the Wyoming craton which are effectively undated, making their inclusion in the Matachewan LIP reconstruction somewhat tenuous. Dating of the suites made up of compositionally distinct subgroups such as the Matachewan dyke swarm and Thessalon Formation should also be carried out to assess how the magmatism in the Matachewan LIP changed with time. For example, the Matachewan dyke swarm may be a composite swarm made up of a widespread group of dykes characterised by flat HREE patterns and a second, less voluminous subgroup of dykes characterised by more inclined HREE patterns ($Gd/Yb_N = 2.2$). These changes in rare earth element contents of the dykes may indicate that the depth of melting or degree of partial melting changed during the intrusion of the swarm. Understanding how the Matachewan swarm and similarly variable suites evolved with time will better aid our understanding of LIPs and mantle plumes in general.

The data presented in section 5.5 suggests that Sr-Nd-Pb isotopes are useful indicators of Ni-Cu-PGE prospectivity (Zhang et al. 2008) and thus, are valuable tools during exploration for such deposits. A subset of the samples collected by this study should be reanalysed for these isotopes in order to determine which Matachewan LIP suites have potential for this type of mineralisation. This said, and despite the evidence presented in this project that suggests the BDM is unmineralised, it should be noted that only one transect through the intrusion was sampled. To truly establish whether the BDM is prospective for Ni-Cu-PGE mineralisation, several more sample transects should be completed, particularly through the high Cu zone in order to determine if the mineralisation potential of the intrusion varies along strike.

The formation of the Matachewan LIP resulted in the eruption of an enormous flood basalt province which almost certainly had the potential to cause severe and long-term changes in Earth’s climate. Such a change is perhaps manifested by the Great Oxidation Event, the timing of which is coincident with the average age of the Matachewan LIP magmatism. By understanding the eruption rates of the Matachewan LIP flood basalt provinces, elucidated by future high-precision U-Pb work and the amount of volatiles released, as estimated by subsequent analysis of undegassed melt inclusions [e.g., (Thordarson et al. 1996)] or cogenetic lavas and feeder dykes, the amount of volatiles added to the Palaeoproterozoic atmosphere by the Matachewan LIP can be estimated. These estimates may be used in atmospheric models to better understand if and how, the Matachewan LIP forced the climate onto a path of irreversible oxygenation.

The ~2.46 Ga age of the Matachewan LIP places it between the slightly younger ~2.41 Ga Du Chef and slightly older ~2.51 Ga Mistassini dyke swarms preserved on the Superior craton (Krogh 1994; Buchan et al. 1998). These latter dyke swarms are also interpreted to be the products of mantle plume-induced magmatism (Bleeker et al. 2008; Söderlund et al. 2010) and thus, along with the Matachewan LIP give the opportunity to understand the secular evolution of the Archaean-Proterozoic mantle beneath the Superior craton over ~100 million years. Samples of these dyke swarms were collected by this study, the analyses of which are presented in **Appendix E** as is a geological overview **(Appendix F)**.

6. CONCLUSIONS

The Matachewan LIP is composed of dyke swarms, layered intrusions and flood basalt provinces preserved on the Superior, Karelia, Wyoming and Hearne cratons.

The Matachewan, Kaminak, Viianki and Leopard dyke swarms are tholeiitic basalt-basaltic andesites which, when reconstructed as part of the Superia supercraton, radiate out from a point source near to Sudbury, Ontario. This point is interpreted to be the site of impact of an early Proterozoic mantle plume which led to the breakup of this ancient supercontinent. Aside from the dyke swarms, the mantle plume caused the eruption of a large volcanic province, the remnants of which are now preserved in the Spi basin and Huronian and Karelian Supergroups. The volcanic rocks in these groups are compositionally similar to the dyke swarms in that they are predominantly tholeiitic basalts-basaltic andesites. The layered intrusions of the Matachewan LIP which were emplaced throughout the duration of the province predominate along the margins of these volcano-sedimentary groups. These intrusions comprise igneous rocks derived from fractionation of low-Ti tholeiitic basaltic parental magmas.

The age of the Matachewan LIP magmatism is bracketed by the emplacement of members of the Kaminak dykes at 2498 Ma and the eruption of the Seidorechka Formation volcanics at 2437 Ma with the entire LIP having an average age of 2461 Ma. The oldest magmatism (> 2480 Ma) occurs on the Superior, Wyoming and Hearne cratons while the magmatism on the Karelia craton is distinctly younger with an average age of 2442 Ma.

Since their formation, the igneous rocks which make up the Matachewan LIP have been variably altered and metamorphosed such that the original igneous mineralogy is rarely preserved. The metamorphic facies recorded by the alteration mineral assemblages suggests that the metamorphism rarely exceeded greenschist facies for the majority of the suites studied, though did reach lower amphibolite facies in some of the Kaminak dykes and the Blue Draw Metagabbro and River Valley intrusions. This metamorphism has altered the geochemistry of the suites by remobilising some of the more mobile elements. Thus, only the more immobile major and trace elements and isotopic systems are suitable for studying the petrogenesis of the Matachewan LIP.

Aside from their tholeiitic composition, the Matachewan LIP suites all have a similar trace element geochemistry, characterised by enrichment in the most incompatible large ion lithophile and light rare earth elements and depletion in the heavy rare earth and other high field strength elements. This similar geochemistry in the Matachewan LIP suites is consistent with the suites being derived from a common mantle source. However, this shared geochemistry cannot be used as proof of a cogenetic origin for the LIP suites as this trace element signature is shared by the vast majority of early Proterozoic intracontinental igneous rocks. This ubiquitous trace element signature may suggest the existence of a once widespread mantle reservoir not recognised in the modern mantle. Alternatively, this trace element signature can be explained by the mixing of partial melts of already-melted known mantle reservoirs with partial melts of subduction modified sub-continental lithospheric mantle, or via contamination of primary magmas in crustal magma chambers.

Comparison of the potential temperatures of the suites of known Matachewan LIP age with the best estimates of the early Proterozoic upper mantle suggest that the province is the product of anomalously hot magmatism as would be expected given its proposed plume origin. Trace element and isotopic data from coeval intrusions suggest that the mantle plume head was compositionally heterogeneous and sampled material from both the depleted and enriched mantle.

The majority of the Matachewan LIP suites record incompatible trace element trends which suggest that during fractionation, the LIP parent magmas were contaminated by crustal material. This contamination occurred in crustal magma chambers at varying depths and involved felsic material of varying composition. The progressive contamination of the Matachewan LIP parent magmas is recorded by the dykes and lavas which were periodically extracted from these evolving crustal chambers.

The Canadian Matachewan LIP layered intrusions are known to contain significant Ni-Cu-PGE mineralisation. The supposedly cogenetic Blue Draw Metagabbro in South Dakota is barren, despite having reached sulphur saturation during fractional crystallisation. Sr-Nd-Pb isotope systematics from these intrusions are consistent with previous work which suggests that intrusions which are more prospective for

Ni-Cu-PGE mineralisation are derived, in part, from melting of the EM2 mantle reservoir. The data presented by this study suggests that Sr-Nd-Pb isotopic analyses are useful indicators of Ni-Cu-PGE potential and could be used in future exploration of the Matachewan LIP and others like it.

The flood basalt volcanism and continental breakup associated with the emplacement of the Matachewan LIP would have caused an enormous perturbation in the Earth's atmosphere. The increase in continental shelf on which to bury organic carbon, coupled with the potential sulfur-reducing bacterial bloom initiated by loading the atmosphere with volcanogenic SO_2 could have forced the atmosphere onto a path of irreversible oxygenation. At the same time, the persistence of fine grained ejecta and sulphuric aerosols in the upper atmosphere may have raised Earth's albedo and triggered a Snowball Earth event. Precisely how such an event would have affected the early Proterozoic biota and subsequent evolution of the biosphere is still open to debate.

This project had the aim of improving our understanding of the petrogenesis of the Matachewan LIP. To that end, the project has been a success; for the first time, data from all of the Matachewan LIP suites has been synthesised into a single, coherent format and has been used to investigate how this enormous magmatic system evolved in both space and time. This work, and future studies which build on it, will continue to illuminate the processes which operate in, and the global perturbations caused by, these immense Large Igneous Provinces.

REFERENCES

Adam, J. and Green, T., 2006. Trace element partitioning between mica- and amphibole-bearing garnet lherzolite and hydrous basanitic melt: 1. Experimental results and the investigation of controls on partitioning behaviour. *Contributions to Mineralogy and Petrology,* 152**,** 1-17.

Alapieti, T. T., 2005. Chapter 1 - Early Palaeoproterozoic (2.5-2.4 Ga) Tornio - Näränkävaara layered intrusion belt and related chrome and platinum-group element mineralization, Northern Finland. In *Guide 51a,* eds. T. T. Alapieti and A. J. Kärki. Geological Survey of Finland.

Alapieti, T. T., 2005. Classification of the Fennoscandian early Palaeoproterozoic (2.5-2.4 Ga) layered intrusions and related PGE deposits. In *10th International Platinum Symposium*. Oulu.

Amelin, Y. V., Heaman, L. M. and Semenov, V. S., 1995. U---Pb geochronology of layered mafic intrusions in the eastern Baltic Shield: implications for the timing and duration of Paleoproterozoic continental rifting. *Precambrian Research,* 75**,** 31-46.

Amelin, Y. V., Neymark, L. A., Ritsk, E. Y. and Nemchin, A. A., 1996. Enriched Nd-Sr-Pb isotopic signatures in the Dovyren layered intrusion (eastern Siberia, Russia): evidence for source contamination by ancient upper-crustal material. *Chemical Geology,* 129**,** 39-69.

Anbar, A. D., Duan, Y., Lyons, T. W., Arnold, G. L., Kendall, B., Creaser, R. A., Kaufman, A. J., Gordon, G. W., Scott, C., Garvin, J. and Buick, R., 2007. A Whiff of Oxygen Before the Great Oxidation Event? *Science,* 317**,** 1903-1906.

Anderson, D. L., 1982. Hotspots, polar wander, Mesozoic convection and the geoid. *Nature,* 297**,** 391-393.

Anderson, D. L., 2000. The Thermal State of the Upper Mantle; No Role for Mantle Plumes. *Geophysical Research Letters,* 27**,** 3623-3626.

Anderson, D. L., 2005. Large Igneous Provinces, Delamination, and Fertile Mantle. *ELEMENTS,* 1**,** 271-275.

Arndt, N. T., Lesher, C. M. and Czamanske, G. K., 2005. Mantle-derived magmas and magmatic Ni-Cu-(PGE) deposits. In *100th Anniversary Volume*, 5-23. Society of Economic Geologists.

Ashwal, L. D. and Wooden, J. L., 1989. River Valley pluton, Ontario: A late-Archean/early-Proterozoic anorthositic intrusion in the Grenville Province. *Geochimica et Cosmochimica Acta,* 53**,** 633-641.

Aspler, L. B., Wisotzek, I. E., Chiarenzelli, J. R., Losonczy, M. F., Cousens, B. L., McNicoll, V. J. and Davis, W. J., 2001. Paleoproterozoic intracratonic basin processes, from breakup of Kenorland to assembly of Laurentia: Hurwitz Basin, Nunavut, Canada. *Sedimentary Geology,* 141-142**,** 287-318.

Aspler, L. B., Armitage, A. E., Ryan, J. J., Hauseux, M., Surmacz, S. and Harvey, B. J. A., 2000. Precambrian geology, Victory and Mackenzie lakes, Nunavut, and significance of 'Mackenzie Lake metasediments', Paleoproterozoic Hurwitz Group. In *Current Research*, 10.

Aspler, L. B. and Chiarenzelli, J. R., 1998. Two Neoarchean supercontinents? Evidence from the Paleoproterozoic. *Sedimentary Geology,* 120**,** 75-104.

Aspler, L. B., Cousens, B. L. and Chiarenzelli, J. R., 2002. Griffin gabbro sills (2.11 Ga), Hurwitz Basin, Nunavut, Canada: long-distance lateral transport of magmas in western Churchill Province crust. *Precambrian Research,* 117**,** 269-294.

Baker, J. A., Thirlwall, M. F. and Menzies, M. A., 1996. Sr□Nd□Pb isotopic and trace element evidence for crustal contamination of plume-derived flood basalts: Oligocene flood volcanism in western Yemen. *Geochimica et Cosmochimica Acta,* 60**,** 2559-2581.

Barnes, S.-J. and Gomwe, T. S., 2011. The Pd deposits of the Lac des Iles Complex, Northwestern Ontario. In *Magmatic Ni-Cu and PGE deposits: Geology, Geochemistry, and Genesis,* eds. C. Li and E. M. Ripley, 351-370. Denver, Colorado: Society of Economic Geologists.

Barnes, S.-J., Naldrett, A. J. and Gorton, M. P., 1985. The origin of platinum-group elements in terrestrial magmas. *Chemical Geology,* 53**,** 303-323.

Bates, M. P. and Halls, H. C., 1990. Regional variation in paleomagnetic polarity of the Matachewan dyke swarm related to the Kapuskasing Structural Zone, Ontario. *Canadian Journal of Earth Sciences,* 27**,** 200-211.

Bayanova, T., Ludden, J. and Mitrofanov, F., 2009. Timing and duration of Palaeoproterozoic events producing ore-bearing layered intrusions of the Baltic Shield: metallogenic, petrological and geodynamic implications. *Geological Society, London, Special Publications,* 323**,** 165-198.

Bédard, J., 2001. Parental magmas of the Nain Plutonic Suite anorthosites and mafic cumulates: a trace element modelling approach. *Contributions to Mineralogy and Petrology,* 141**,** 747-771.

Bédard, J. H., 2005. Partitioning coefficients between olivine and silicate melts. *Lithos,* 83**,** 394-419.

Bédard, J. H., 2007. Trace element partitioning coefficients between silicate melts and orthopyroxene: Parameterizations of D variations. *Chemical Geology,* 244**,** 263-303.

Bekker, A., Holland, H. D., Wang, P. L., Rumble, D., Stein, H. J., Hannah, J. L., Coetzee, L. L. and Beukes, N. J., 2004. Dating the rise of atmospheric oxygen. *Nature,* 427**,** 117-120.

Bekker, A., Kaufman, A. J., Karhu, J. A. and Eriksson, K. A., 2005. Evidence for Paleoproterozoic cap carbonates in North America. *Precambrian Research,* 137**,** 167-206.

Bennett, G., Dressler, B. O. and Robertson, J. A., 1991. The Huronian Supergroup and associated intrusive rocks. *In: Thurston, P.C., Williams, H.R., Sutcliffe, R.H. and Stott, G.M., Editors,,* Geology of OntarioOntario Geological Survey, Special Volume**,** 549-591.

Beresford, S., Cas, R., Lahaye, Y. and Jane, M., 2002. Facies architecture of an Archean komatiite-hosted Ni-sulphide ore deposit, Victor, Kambalda, Western Australia: implications for komatiite lava emplacement. *Journal of Volcanology and Geothermal Research,* 118**,** 57-75.

Bickle, M. J., 1986. Implications of melting for stabilisation of the lithosphere and heat loss in the Archaean. *Earth and Planetary Science Letters,* 80**,** 314-324.

Bijwaard, H. and Spakman, W., 1999. Tomographic evidence for a narrow whole mantle plume below Iceland. *Earth and Planetary Science Letters,* 166**,** 121-126.

Bizimis, M., Griselin, M., Lassiter, J. C., Salters, V. J. M. and Sen, G., 2007. Ancient recycled mantle lithosphere in the Hawaiian plume: Osmium–Hafnium isotopic evidence from peridotite mantle xenoliths. *Earth and Planetary Science Letters,* 257**,** 259-273.

Blackwelder, E., 1926. Precambrian geology of the Medicine Bow Mountains. *Geological Society of America Bulletin,* 37**,** 617-658.

Bleeker, W., 2003. The late Archean record: a puzzle in ca. 35 pieces. *Lithos,* 71**,** 99-134.

Bleeker, W., 2004. Taking the pulse of planet Earth: a proposal for a new multi-disciplinary flagship project in Canadian solid Earth sciences. *Geoscience Canada,* 31**,** 179-190.

Bleeker, W. and Ernst, R., 2006. Short-lived mantle generated magmatic events and their dyke swarms: The key unlocking Earth's paleogeographic record back to 2.6 Ga. . *In Dyke Swarms - Time Markers of Crustal Evolution. Edited by E. Hanski, S. Mertanen, T. Rämö, and J. Vuollo. Taylor***,** 3-26.

Bleeker, W., Hamilton, M. A., Ernst, R. E. and Kulikov, V. S., 2008. The search for Archean-Paleoproterozoic supercratons: New constraints on Superior-Karelia-Kola correlations within supercraton Superia, including the first ca. 2504 Ma (Mistassini) ages from Karelia. In *International Geological Congress*. Oslo.

Blichert-Toft, J., Albarède, F., Rosing, M., Frei, R. and Bridgwater, D., 1999. The Nd and Hf isotopic evolution of the mantle through the Archean. results from the Isua supracrustals, West Greenland, and from the Birimian terranes of West Africa. *Geochimica et Cosmochimica Acta,* 63**,** 3901-3914.

Blichert-Toft, J. and Frei, R., 2001. Complex Sm-Nd and Lu-Hf isotope systematics in metamorphic garnets from the Isua supracrustal belt, West Greenland. *Geochimica et Cosmochimica Acta,* 65**,** 3177-3189.

Bosak, T., Liang, B., Sim, M. S. and Petroff, A. P., 2009. Morphological record of oxygenic photosynthesis in conical stromatolites. *Proceedings of the National Academy of Sciences,* 106**,** 10939-10943.

Boudreau, A. E., 1999. PELE-a version of the MELTS software program for the PC platform. *Comput. Geosci.,* 25**,** 201-203.

Brenan, J. M., McDonough, W. F. and Dalpé, C., 2003. Experimental constraints on the partitioning of rhenium and some platinum-group elements between olivine and silicate melt. *Earth and Planetary Science Letters,* 212**,** 135-150.

Brocks, J. J., Logan, G. A., Buick, R. and Summons, R. E., 1999. Archean Molecular Fossils and the Early Rise of Eukaryotes. *Science,* 285**,** 1033-1036.

Bryan, S. E. and Ernst, R. E., 2008. Revised definition of Large Igneous Provinces (LIPs). *Earth-Science Reviews,* 86**,** 175-202.

Buchan, K. L. and Ernst, R. E., 2004. Diabase dyke swarms and related units in Canada and adjacent regions, Canada and Northern USA. Geological Survey of Canada.

Buchan, K. L., Goutier, J., Hamilton, M. A., Ernst, R. E. and Matthews, W. A., 2007. Paleomagnetism, UPb geochronology, and geochemistry of Lac Esprit and other dyke swarms, James Bay area, Quebec, and implications for Paleoproterozoic deformation of the Superior Province. *Canadian Journal of Earth Sciences,* 44**,** 643-664.

Buchan, K. L., Mortensen, J. K., Card, K. D. and Percival, J. A., 1998. Paleomagnetism and U-Pb geochronology of diabase dyke swarms of Minto block, Superior Province, Quebec, Canada. *Canadian Journal of Earth Sciences,* 35**,** 1054-1069.

Bühn, B., Santos, R. V., Dardenne, M. A. and de Oliveira, C. G., 2012. Mass-dependent and mass-independent sulfur isotope fractionation (δ34S and δ33S) from Brazilian Archean and Proterozoic sulfide deposits by laser ablation multi-collector ICP-MS. *Chemical Geology,* 312–313**,** 163-176.

Campbell, I. H., 2007. Testing the plume theory. *Chemical Geology,* 241**,** 153-176.

Campbell, I. H. and Allen, C. M., 2008. Formation of supercontinents linked to increases in atmospheric oxygen. *Nature Geosci,* 1**,** 554-558.

Campbell, I. H. and Griffiths, R. W., 1990. Implications of mantle plume structure for the evolution of flood basalts. *Earth and Planetary Science Letters,* 99**,** 79-93.

Campbell, I. H., Naldrett, A. J. and Barnes, S. J., 1983. A Model for the Origin of the Platinum-Rich Sulfide Horizons in the Bushveld and Stillwater Complexes. *Journal of Petrology,* 24**,** 133-165.

Campbell, I. H. and Squire, R. J., 2010. The mountains that triggered the Late Neoproterozoic increase in oxygen: The Second Great Oxidation Event. *Geochimica et Cosmochimica Acta,* 74**,** 4187-4206.

Canfield, D. E., 2005. THE EARLY HISTORY OF ATMOSPHERIC OXYGEN: Homage to Robert M. Garrels. *Annual review of Earth and planetary sciences,* 33**,** 1-36.

Cann, J. R., 1970. Rb, Sr, Y, Zr and Nb in some ocean floor basaltic rocks. *Earth and Planetary Science Letters,* 10**,** 7-11.

Capobianco, C. J. and Drake, M. J., 1990. Partitioning of ruthenium, rhodium, and palladium between spinel and silicate melt and implications for platinum group element fractionation trends. *Geochimica et Cosmochimica Acta,* 54**,** 869-874.

Card, K. D., 1990. A review of the Superior Province of the Canadian Shield, a product of Archean accretion. *Precambrian Research,* 48**,** 99-156.

Carpenter, R. L., 2003. Relative and absolute timing of supracrustal deposition, tectonothermal activity and gold mineralization, welst Meliadine regio, Rankin Inlet greenstone belt, Nunaut, Canada. London, Ontario: The Universit of Western Ontario.

Catling, D. C., 2012. The Great Oxidation Event transition. In *The Atmosphere - History,* eds. D. Canfield, J. Farquhar and J. F. Kasting. Elsevier.

Cawthorn, R., 2005. Pressure fluctuations and the formation of the PGE-rich Merensky and chromitite reefs, Bushveld Complex. *Mineralium Deposita,* 40**,** 231-235.

Chashchin, V., Bayanova, T. and Levkovich, N., 2008. Volcanoplutonic association of the early-stage evolution of the Imandra-Varzuga rift zone, Kola Peninsula, Russia: Geological, petrogeochemical, and isotope-geochronological data. *Petrology,* 16**,** 279-298.

Chauvel, C., Hofmann, A. W. and Vidal, P., 1992. HIMU-EM: The French Polynesian connection. *Earth and Planetary Science Letters,* 110**,** 99-119.

Christie, K. W., Davidson, A. and Fahrig, W. F., 1975. The Paleomagnetism of Kaminak Dikes - No Evidence of Significant Hudsonian Plate Motion. *Canadian Journal of Earth Sciences,* 45**,** 745-767.

Chubb, P. T., 1994. Petrogenesis of the eastern portion of the Early Proterozoic East Bull Lake gabbro-anorthosite intrusion, District of Sudbury/Algoma, Ontario. 230. Sudbury, Ontario: Laurentian.

Ciborowski, T. J. R., Kerr, A. C., McDonald, I., Ernst, R. E. and Minife, M. J., The geochemistry and petrogenesis of the Blue Draw Metagabbro. *Lithos*.

Claire, M. W., Catling, D. C. and Zahnle, K. J., 2006. Biogeochemical modelling of the rise in atmospheric oxygen. *Geobiology,* 4**,** 239-269.

Cloud, P., 1973. Paleoecological Significance of the Banded Iron-Formation. *Economic Geology,* 68**,** 1135-1143.

Coffin, M. F. and Eldholm, O., 1991. Large Igneous Provinces. *JOI/USSAC Workshop Report. Austin TX, USA, University of Texas at Austin Institute for Geophysics***,** 79pp.

Coffin, M. F. and Eldholm, O., 1994. Large Igneous Provinces: Crustal Structure, Dimensions, and External Consequences. *Rev. Geophys.,* 32.

Coffin, M. F. and Eldholm, O., 2005. Large igneous provinces. In: Selley RC, Cocks R, Plimer IR (Eds). *Encyclopedia of Geology***,** 315-323.

Coltice, N., Bertrand, H., Rey, P., Jourdan, F., Phillips, B. R. and Ricard, Y., 2009. Global warming of the mantle beneath continents back to the Archaean. *Gondwana Research*, 15**,** 254-266.

Coltice, N., Phillips, B. R., Bertrand, H., Ricard, Y. and Rey, P., 2007. Global warming of the mantle at the origin of flood basalts over supercontinents. *Geology,* 35**,** 391-394.

Condie, K. C., 1993. Chemical composition and evolution of the upper continental crust: contrasting results from surface samples and shales. . *Chemical Geology* 104**,** 1-37.

Condie, K. C., 1997. Plate Tectonics and Crustal Evolution. 282. Oxford: Butterworth-Heinemann.

Condie, K. C., 1994. Chapter 3 Greenstones Through Time. In *Developments in Precambrian Geology,* ed. K. C. Condie, 85-120. Elsevier.

Condie, K. C., 2005. High field strength element ratios in Archean basalts: a window to evolving sources of mantle plumes? *Lithos,* 79**,** 491-504.

Cousens, B. L., Aspler, L. B., Chiarenzelli, J. R., Donaldson, J. A., Sandeman, H., Peterson, T. D. and LeCheminant, A. N., 2001. Enriched Archean lithospheric mantle beneath western Churchill Province tapped during Paleoproterozoic orogenesis. *Geology,* 29**,** 827-830.

Dahl, P. S., Hamilton, M. A., Wooden, J. L., Foland, K. A., Frei, R., McCombs, J. A. and Holm, D. K., 2006. 2480 Ma mafic magmatism in the northern Black Hills, South Dakota: a new link connecting the Wyoming and Superior cratons. *Canadian Journal of Earth Sciences***,** 1579-1600.

Dasgupta, R., Hirschmann, M. M. and Smith, N. D., 2007. Partial Melting Experiments of Peridotite + CO2 at 3 GPa and Genesis of Alkalic Ocean Island Basalts. *Journal of Petrology,* 48**,** 2093-2124.

Davidson, J., Tepley Iii, F., Palacz, Z. and Meffan-Main, S., 2001. Magma recharge, contamination and residence times revealed by in situ laser ablation isotopic analysis of feldspar in volcanic rocks. *Earth and Planetary Science Letters,* 184**,** 427-442.

Davies, G. F., 1990. Mantle plumes, mantle stirring and hotspot chemistry. *Earth and Planetary Science Letters,* 99**,** 94-109.

Davies, G. F., 2009. Effect of plate bending on the Urey ratio and the thermal evolution of the mantle. *Earth and Planetary Science Letters,* 287**,** 513-518.

de Hoog, J. C. M. and van Bergen, M. J., 2000. Volatile-induced transport of HFSE, REE, Th and U in arc magmas: evidence from zirconolite-bearing vesicles in potassic lavas of Lewotolo volcano (Indonesia). *Contributions to Mineralogy and Petrology,* 139**,** 485-502.

DePaolo, D. J., 1981. Trace element and isotopic effects of combined wallrock assimilation and fractional crystallization. *Earth and Planetary Science Letters,* 53**,** 189-202.

DePaolo, D. J., 1985. Isotopic studies of processes in mafic magma champers: I. The Kiglapait intrusion, Labrador. *Journal of Petrology,* 26**,** 925-951.

DePaolo, D. J. and Wasserburg, G. J., 1976. Nd isotopic variations and petrogenetic models. *Geophysical Research Letters,* 3**,** 249-252.

Dessert, C., Dupré, B., François, L. M., Schott, J., Gaillardet, J., Chakrapani, G. and Bajpai, S., 2001. Erosion of Deccan Traps determined by river geochemistry: impact on the global climate and the 87Sr/86Sr ratio of seawater. *Earth and Planetary Science Letters,* 188**,** 459-474.

Dietz, R. S. and Holden, J. C., 1966. Miogeosynclines in space and time. *Journal of Geology,* 74**,** 566-583.

Doblas, M., Lopez-Ruiz, J., Cebria, J.-M., Youbi, N. and Degroote, E., 2002. Mantle insulation beneath the West African craton during the Precambrian-Cambrian transition. *Geology,* 30**,** 839-842.

Easton, R. M., 2003. Geology and mineral potential of the Paleoproterozoic River Valley intrusion and related rocks, Grenville Province. In *Open File Report*, 171. Ontario Geological Survey.

Easton, R. M., 2007. Precambrian geology, Crerar-River Valley area (41 I/9 and 41 I/10E); P.3453. In *Preliminary Map*. Ontario Geological Survey.

Easton, R. M., Davidson, A. and Murphy, E. I., 1999. Tansects across the Southern-Grenville Province boundary near Sudbury, Ontario. In *Guidebook*, 52. Sudbury: Geological Association of Canada.

Easton, R. M. and Hrominchuk, J. L., 1999. Geology and copper-platinum group element mineral potential of Dana and Crerar townships, River Valley area, Grenville Province. In *Open File*. Ontario Geological Survey.

Easton, R. M., James, R. S. and Jobin-Bevans, L. S., 2010. Geological Guidebook to the Paleoproterozoic East Bull Lake Intrusive Suite Plutons at East Bull Lake, Agnew Lake and River Valley: a field trip for the 11th International Platinum Symposium. In *Open File Report*, 108. Ontario Geological Survey.

Elkins-Tanton, L. T., 2005. Continental magmatism caused by lithospheric delamination, . *in Foulger, G.R., Natland, J.H., Presnall, D.C., and Anderson, D.L., eds., Plates, plumes, and paradigms:,* Geological Society of America Special Paper 388**,** 449-461.

Ernst, R. and Buchan, K. L., 2003. Recognising mantle plumes in the geological record. *Annual review of Earth and planetary sciences,* 31.

Ernst, R. and Buchan, K. L., 2010. Geochemical database of Proterozoic intraplate mafic magmatism in Canada. In *Open File 6016*. Geological Survey of Canada.

Ernst, R. E., 2007. Large igneous provinces in Canada through time and their metallogenic potential. *in Goodfellow, W.D., ed., Mineral Deposits of Canada: A Synthesis of Major Deposit-Types, District Metallogeny, the Evolution of Geological Provinces, and Exploration Methods,* Geological Association of Canada, Mineral Deposits Division, Special Publication No. 5**,** 929-937.

Ernst, R. E. and Bleeker, W., 2010. Large igneous provinces (LIPs), giant dyke swarms, and mantle plumes: significance for breakup events within Canada and adjacent regions from 2.5 Ga to the Present. *Canadian Journal of Earth Sciences,* 47**,** 695-739.

Ernst, R. E., Bleeker, W., Hamilton, M. A. and Söderlund, U., 2008. Continental Reconstructions Back To 2.6 Ga Using The Large Igneous Province (LIP) Record, With Implications For Mineral Deposit Targeting And Hydrocarbon Resource Exploration [extended Abstract]. In *Palaeogeography: The Spatial Context for Understanding the Earth System,* ed. R. L. P. Markwick, M. Huber (conveners). Cambridge U.K.

Ernst, R. E. and Buchan, K. L., 2001. The use of mafic dike swarms in identifying and locating mantle plumes. *Geological Society of America Special Papers,* 352**,** 247-265.

Ernst, R. E. and Buchan, K. L., 2002. Maximum size and distribution in time and space of mantle plumes: evidence from large igneous provinces. *Journal of Geodynamics,* 34 309-342.

Ernst, R. E. and Buchan, K. L., 2004. Large Igneous Provinces (LIPs) in Canada and adjacent regions: 3 Ga to Present. *Geoscience Canada,* 31**,** 103-126.

Ernst, R. E., Head, J. W., Parfitt, E., Grosfils, E. and Wilson, L., 1995. Giant radiating dyke swarms on Earth and Venus. *Earth-Science Reviews,* 39**,** 1-58.

Fadda, S., Fiori, M., Grillo, S. M. and Prochaska, W., 2012. REE Mobilization in Complex Hydrothermal–Metasomatic Systems: Fluid Chemistry Evidence of Albitite And Chlorite-Talc Mineralisations in Central Sardinia, Italy. Proceedings of the 10th International Congress for Applied Mineralogy (ICAM). ed. M. A. T. M. Broekmans, 171-178. Springer Berlin Heidelberg.

Farquhar, J. and Wing, B. A., 2003. Multiple sulfur isotopes and the evolution of the atmosphere. *Earth and Planetary Science Letters,* 213**,** 1-13.

Finnigan, C. S., Brenan, J. M., Mungall, J. E. and McDonough, W. F., 2008. Experiments and Models Bearing on the Role of Chromite as a Collector of Platinum Group Minerals by Local Reduction. *Journal of Petrology,* 49**,** 1647-1665.

Frei, R., Dahl, P. S., Duke, E. F., Frei, K. M., Hansen, T. R., Frandsson, M. M. and Jensen, L. A., 2008. Trace element and isotopic characterization of Neoarchean and Paleoproterozoic iron formations in the Black Hills (South Dakota, USA): Assessment of chemical change during 2.9–1.9 Ga deposition bracketing the 2.4–2.2 Ga first rise of atmospheric oxygen. *Precambrian Research,* 162**,** 441-474.

Frei, R., Gaucher, C., Poulton, S. W. and Canfield, D. E., 2009. Fluctuations in Precambrian atmospheric oxygenation recorded by chromium isotopes. *Nature,* 461**,** 250-253.

Frey, F. A., 1980. The origin of pyroxenites and garnet pyroxenites from Salt Lake Crater, Oahu, Hawaii: trace element evidence. *American Journal of Science,* 280**,** 427-449.

Frimmel, H. E., 2005. Archaean atmospheric evolution: evidence from the Witwatersrand gold fields, South Africa. *Earth-Science Reviews,* 70**,** 1-46.

Gaffney, A. M., Borg, L. E., Asmerom, Y., Shearer, C. K. and Burger, P. V., 2011. Disturbance of isotope systematics during experimental shock and thermal metamorphism of a lunar basalt with implications for Martian meteorite chronology. *Meteoritics & Planetary Science,* 46**,** 35-52.

Gaillard, F., Scaillet, B. and Arndt, N. T., 2011. Atmospheric oxygenation caused by a change in volcanic degassing pressure. *Nature,* 478**,** 229-232.

Galer, S. J. G. and Mezger, K., 1998. Metamorphism, denudation and sea level in the Archean and cooling of the Earth. *Precambrian Research,* 92**,** 389-412.

Gallagher, K. and Hawkesworth, C., 1992. Dehydration melting and the generation of continental flood basalts. *Nature,* 358**,** 57-59.

Garrels, R. M., Perry, E. A. and Mackenzie, F. T., 1973. Genesis of Precambrian Iron-Formations and the Development of Atmospheric Oxygen. *Economic Geology,* 68**,** 1173-1179.

Ghiorso, M. S. and Sack, R. O., 1995. Chemical mass transfer in magmatic processes IV. A revised and internally consistent thermodynamic model for the interpolation and extrapolation of liquid-solid equilibria in magmatic systems at elevated temperatures and pressures. *Contributions to Mineralogy and Petrology,* 119**,** 197-212.

Gieré, R., 1993. Transport and deposition of REE in H2S-rich fluids: evidence from accessory mineral assemblages. *Chemical Geology,* 110**,** 251-268.

Gill, R. 2011. *Igneous Rocks and Processes: A Practical Guide.* Wiley.

Gorbunov, G. I., Zagorodny, V. G. and Robonen, W. I., 1985. Main features of the geological history of the Baltic Shield and the epochs of ore formation. *Geological Survey of Finland Bulletin,* 333**,** 2-41.

Graham, I. J., Coombs, D. S. and Cook, N. D. J., 1993. Effects of low-temperature alteration on the Rb□Sr age of andesitic igneous rocks: Park Volcanics Group, Southland, New Zealand. *Chemical Geology,* 104**,** 281-292.

Gray, C. M., Cliff, R. A. and Goode, A. D. T., 1981. Neodymium-strontium isotopic evidence for extreme contamination in a layered basic intrusion. *Earth and Planetary Science Letters,* 56**,** 189-198.

Griffiths, R. W., 1986. Dynamics of mantle thermals with constant buoyancy or anomalous internal heating. *Earth and Planetary Science Letters,* 78**,** 435-446.

Griffiths, R. W. and Campbell, I. H., 1990. Stirring and structure in mantle starting plumes. *Earth and Planetary Science Letters,* 99**,** 66-78.

Griffiths, R. W. and Campbell, I. H., 1991. Interaction of Mantle Plume Heads With the Earth's Surface and Onset of Small-Scale Convection. *J. Geophys. Res.*, 96.

Gumsley, A. P., de Kock, M. O., Rajesh, H. M., Knoper, M. W., Söderlund, U. and Ernst, R. E., The Hlagothi Complex: The identification of fragments from a Mesoarchaean large igneous province on the Kaapvaal Craton. *Lithos*.

Halls, H. C., 1991. The Matachewan dyke swarm, Canada: an early Proterozoic magnetic field reversal. *Earth and Planetary Science Letters,* 105**,** 279-292.

Halls, H. C., 2009. A 100 km-long paleomagnetic traverse radial to the Sudbury Structure, Canada and its bearing on Proterozoic deformation and metamorphism of the surrounding basement. *Tectonophysics,* 474**,** 493-506.

Halls, H. C. and Davis, D. W., 2004. Paleomagnetism and U-Pb geochronology of the 2.17 Ga Biscotasing dyke swarm, Ontario, Canada: evidence for vertical-axis crustal rotation across the Kapuskasing Zone. *Canadian Journal of Earth Sciences,* 41**,** 255-269.

Halls, H. C., Kumar, A., Srinivasan, R. and Hamilton, M. A., 2007. Paleomagnetism and U–Pb geochronology of easterly trending dykes in the Dharwar craton, India: feldspar clouding, radiating dyke swarms and the position of India at 2.37 Ga. *Precambrian Research,* 155**,** 47-68.

Halls, H. C., Stott, G. M. and Davis, D. W., 2005. Paleomagnetism, geochronology and geochemistry of several Proterozoic mafic dike swarms in northwestern Ontario. *Ontario Geological Survey,* Open File Report 6171**,** 59.

Hanan, B. B. and Graham, D. W., 1996. Lead and helium isotope evidence from oceanic basalts for a common deep source of mantle plumes. *Science* 272**,** 991-995.

Hanski, E., Huhma, H. and Vaasjoki, M., 2001. Geochronology of Northern Finland: A Summary and Discussion. In *Radiometric age determinations from Finnish Lapland and their bearing on the timing of Precambrian volcano-sedimentary sequences, Special Paper,* ed. M. Vaasjoki, 255-279. Geological Survey of Finland.

Harlan, S. S., 2005. The Paleoproterozoic Leopard Dikes of Montana and Wyoming: A Dismembered fragment of the 2.45Ga Hearst-Matachewan giant radiating dike swarm of the Superior Craton? *Geological Society of America Abstracts with Programs,* 37**,** p. 50.

Harlan, S. S., Geissman, J. W. and Premo, W. R., 2003. Paleomagnetism and geochronology of an Early Proterozoic quartz diorite in the southern Rind River Range, Wyoming, USA. *Tectonophysics,* 362**,** 105-122.

Harrison, T. M., Blichert-Toft, J., Müller, W., Albarede, F., Holden, P. and Mojzsis, S. J., 2005. Heterogeneous Hadean Hafnium: Evidence of Continental Crust at 4.4 to 4.5 Ga. *Science,* 310**,** 1947-1950.

Hart, W. K., 1985. Chemical and isotopic evidence for mixing between depleted and enriched mantle, northwestern U.S.A. *Geochimica et Cosmochimica Acta,* 49**,** 131-144.

Hart, S. R., Blusztajn, J., Dick, H. J. B., Meyer, P. S. and Muehlenbachs, K., 1999. The fingerprint of seawater circulation in a 500-meter section of ocean crust gabbros. *Geochimica et Cosmochimica Acta,* 63**,** 4059-4080.

Hart, S. R., Hauri, E. H., Oschmann, L. A. and Whitehead, J. A., 1992. Mantle plumes and entrainment: Isotopic evidence. *Science,* 256**,** 517-520.

Hastie, A. R., Kerr, A. C., Pearce, J. A. and Mitchell, S. F., 2007. Classification of Altered Volcanic Island Arc Rocks using Immobile Trace Elements: Development of the Th–Co Discrimination Diagram. *Journal of Petrology,* 48**,** 2341-2357.

Heaman, L. M., 1994. 2.45 Ga global mafic magmatism: Earth's oldest superplume? *Eighth International Conference on Geochronology, Cosmochronology, and Isotope Geology; Program with Abstracts,* U.S. Geological Survey Circular 1107**,** 132.

Heaman, L. M., 1997. Global mafic magmatism at 2.45 Ga: Remnants of an ancient large igneous province? *Geology,* 25**,** 299-302.

Heaman, L. M., 2004. 2.5-2.4 Ga global magmatism: Remnants or supercontinents or products of superplumes. . *Geological Society of America, Abstracts with Programs,* 36**,** 255.

Heimlich, R. A. and Manzer , G. H., 1972. Flow differentiation within Leopard rock dikes, Bighorn Mountains, Wyoming. *Earth and Planetary Science Letters,* 17**,** 350-356.

Helmberger, D. V., Wen, L. and Ding, X., 1998. Seismic evidence that the source of the Iceland hotspot lies at the core-mantle boundary. *Nature,* 396**,** 251-255.

Herzberg, C., 1995. Generation of plume magmas through time: An experimental perspective. *Chemical Geology,* 126**,** 1-16.

Herzberg, C. and Asimow, P. D., 2008. Petrology of some oceanic island basalts: PRIMELT2.XLS software for primary magma calculation. *Geochem. Geophys. Geosyst.,* 9**,** Q09001.

Herzberg, C., Condie, K. and Korenaga, J., 2010. Thermal history of the Earth and its petrological expression. *Earth and Planetary Science Letters,* 292**,** 79-88.

Hill, J. C., 2006. Structural geology and tectonics of the paleoproterozoic rocks of the Mount Rushmore quadrangle, Black Hills, South Dakota. 160. University of Missouri-Columbia.

Hill, R. I., Campbell, I. H., Davies, G. F. and Griffiths, R. W., 1992. Mantle Plumes and Continental Tectonics. *Science,* 256**,** 186-193.

Holland, H. D., 2006. The oxygenation of the atmosphere and oceans. *Philosophical Transactions of the Royal Society B: Biological Sciences,* 361**,** 903-915.

Hrominchuk, J. L., 1999. Geology, stratigraphy and copper-platinum group element mineralization of the River Valley Intrusion, Dana Township. In *Open File*. Ontario Geological Survey.

Hrominchuk, J. L., 2000. Geology, stratigraphy and copper-platinum group element mineralization of the River Valley Intrusion, Dana Township. In *Open File*. Ontario Geological Survey.

Iljina, M., 2007. The Suhanko-PGE prospect and the Portimo Layered Intrusion. In *Guide*. Geological Survey of Finland.

Iljina, M. and Hanski, E., 2005. Chapter 3 Layered mafic intrusions of the Tornio—Näränkävaara belt. In *Developments in Precambrian Geology,* eds. P. A. N. M. Lehtinen and O. T. Rämö, 101-137. Elsevier.

Ingle, S. and Coffin, M. F., 2004. Impact origin for the greater Ontong Java Plateau? *Earth and Planetary Science Letters,* 218**,** 123-134.

Jackson, S. L., 2001. On the structural geology of the Southern Province between Sault Ste. Marie and Espanola, Ontario. *Ontario Geological Survey,* Open File Report 55.

James, R. S., Easton, R. M., Peck, D. C. and Hrominchuk, J. L., 2002. The East Bull Lake Intrusive Suite: Remnants of a ~2.48 Ga Large Igneous and Metallogenic Province in the Sudbury Area of the Canadian Shield. *Economic Geology,* 97**,** 1577-1606.

Jin, Y. G., Wang, Y., Wang, W., Shang, Q. H., Cao, C. Q. and Erwin, D. H., 2000. Pattern of Marine Mass Extinction Near the Permian-Triassic Boundary in South China. *Science,* 289**,** 432-436.

Johnson, K. T. M., Dick, H. J. B. and Shimizu, N., 1990. Melting in the oceanic upper mantle: an ion microprobe study of diopsides in abyssal peridotites. *Journal of Geophysical Research,* 95**,** 2661-2678.

Johnston, D. T., 2011. Multiple sulfur isotopes and the evolution of Earth's surface sulfur cycle. *Earth-Science Reviews,* 106**,** 161-183.

Jolly, W. T., 1987a. Geology and geochemistry of Huronian rhyolites and low-Ti continental tholeiites from the Thessalon region, central Ontario. *Canadian Journal of Earth Sciences,* 24**,** 1360-1385.

Jolly, W. T., 1987b. Lithophile elements in Huronian low-Ti continental tholeiites from Canada, and evolution of the Precambrian Mantle. *Earth and Planetary Science Letters,* 85**,** 401-415.

Jolly, W. T., Dickin, A. P. and Wu, T.-W., 1992. Geochemical stratigraphy of the Huronian continental volcanics at Thessalon, Ontario: contributions of two-stage crustal fusion. *Contributions to Mineralogy and Petrology,* 110**,** 411-428.

Jones, A. P., 2005. Meteorite Impacts as Triggers to Large Igneous Provinces. *ELEMENTS,* 1**,** 277-281.

Jones, A. P., Price, G. D., Price, N. J., DeCarli, P. S. and Clegg, R. A., 2002. Impact induced melting and the development of large igneous provinces. *Earth and Planetary Science Letters,* 202**,** 551-561.

Jowitt, S. M. and Ernst, R. E., Geochemical assessment of the metallogenic potential of Proterozoic LIPs of Canada. *Lithos*.

Karato, S.-i., 2010. Rheology of the deep upper mantle and its implications for the preservation of the continental roots: A review. *Tectonophysics,* 481**,** 82-98.

Keays, R. R., 1995. The role of komatiitic and picritic magmatism and S-saturation in the formation of ore deposits. *Lithos,* 34**,** 1-18.

Kelley, K. A., Plank, T., Ludden, J. and Staudigel, H., 2003. Composition of altered oceanic crust at ODP Sites 801 and 1149. *Geochem. Geophys. Geosyst.,* 4**,** 8910.

Kerr, A. and Leitch, A. M., 2005. Self-Destructive Sulfide Segregation Systems and the Formation of High-Grade Magmatic Ore Deposits. *Economic Geology,* 100**,** 311-332.

Kerr, A. C. and Mahoney, J. J., 2007. Oceanic plateaus: Problematic plumes, potential paradigms. *Chemical Geology,* 241**,** 332-353.

Kerr, A. C., Tarney, J., Kempton, P. D., Spadea, P., Nivia, A., Marriner, G. F. and Duncan, R. A., 2002. Pervasive mantle plume head heterogeneity: Evidence from the late Cretaceous Caribbean-Colombian oceanic plateau. *Journal of Geophysical Research: Solid Earth,* 107**,** ECV 2-1-ECV 2-13.

Kerr, R. A., 2005. The Story of O2. *Science,* 308**,** 1730-1732.

King, S. D. and Anderson, D. L., 1995. An alternative mechanism of flood basalt formation. *Earth and Planetary Science Letters,* 136**,** 269-279.

King, S. D., 2007. Hotspots and edge-driven convection. *Geology,* 35**,** 223-226.

King, S. D. and Ritsema, J., 2000. African Hot Spot Volcanism: Small-Scale Convection in the Upper Mantle Beneath Cratons. *Science,* 290**,** 1137-1140.

Kirschvink, J. L., Gaidos, E. J., Bertani, L. E., Beukes, N. J., Gutzmer, J., Maepa, L. N. and Steinberger, R. E., 2000. Paleoproterozoic snowball earth: extreme climatic and geochemical global change and its biological consequences. *Proceedings of the National Academy of Sciences of the United States of America,* 97**,** 1400-1405.

Knoll, A. H., Hayes, J. M., Kaufman, A. J., Swett, K. and Lambert, I. B., 1986. Secular variation in carbon isotope ratios from Upper Proterozoic successions of Svalbard and East Greenland. *Nature,* 321**,** 832-838.

Komiya, T., Maruyama, S., Hirata, T., Yurimoto, H. and Nohda, S., 2004. Geochemistry of the oldest MORB and OIB in the Isua Supracrustal Belt, southern West Greenland: Implications for the composition and temperature of early Archean upper mantle. *Island Arc,* 13**,** 47-72.

Konhauser, K. O., Pecoits, E., Lalonde, S. V., Papineau, D., Nisbet, E. G., Barley, M. E., Arndt, N. T., Zahnle, K. and Kamber, B. S., 2009. Oceanic nickel depletion and a methanogen famine before the Great Oxidation Event. *Nature,* 458**,** 750-753.

Krogh, T. E., 1994. Precise U-Pb ages for Grenvillian and pre-Grenvillian thrusting of Proterozoic and Archean metamorphic assemblages in the Grenville Front tectonic zone, Canada. *Tectonics,* 13**,** 963-982.

Krogh, T. E., Davis, D. W. and Corfu, F., 1984. Precise U-Pb zircon and baddelyite ages for the Sudbury area. In *The geology and ore deposits of the Sudbury structure.,* eds. E. G. Pye, A. J. Naldrett and P. E. Giblin, 431-446.

Krogh, T. E., Kamo, S. L. and Bohor, B. F., 1996. Shock metamorphosed zircons with correlated U-Pb discordance and melt rocks with concordant protolith ages indicate an impact origin for the Sudbury Structure. In *Earth Processes: Reading the Isotopic Code*, 343-352. American Geophysical Union.

Kulikov, V. S., Bychkova, Y. V., Kulikova, V. V. and Ernst, R., 2010. The Vetreny Poyas (Windy Belt) subprovince of southeastern Fennoscandia: An essential component of the ca. 2.5–2.4 Ga Sumian large igneous provinces. *Precambrian Research*, 183**,** 589-601.

Kump, L., Fallick, A., Melezhik, V., Strauss, H. and Lepland, A., 2013. 8.1 The Great Oxidation Event. In *Reading the Archive of Earth's Oxygenation,* eds. V. A. Melezhik, A. R. Prave, E. J. Hanski, A. E. Fallick, A. Lepland, L. R. Kump and H. Strauss, 1517-1533. Springer Berlin Heidelberg.

Kump, L. R. and Barley, M. E., 2007. Increased subaerial volcanism and the rise of atmospheric oxygen 2.5[thinsp]billion years ago. *Nature*, 448**,** 1033-1036.

Larson, E. E., Reynolds, R. and Hoblitt, R., 1973. New Virtual and Paleomagnetic Pole Positions from Isotopically Dated Precambrian Rocks in Wyoming, Montana, and Arizona: Their Significance in Establishing a North American Apparent Polar Wandering Path. *Geological Society of America Bulletin*, 84**,** 3231-3248.

Lauri, L. S., Mikkola, P. and Karinen, T., 2012. Early Paleoproterozoic felsic and mafic magmatism in the Karelian province of the Fennoscandian shield. *Lithos*.

Le Maitre, R. W., 2002. Igneous Rocks: A Classification and Glossary of Terms, Recommendations of the International Union of Geological Sciences Subcommission on the Systematics of Igneous Rocks. 236. Cambridge: Cambridge University Press.

Le Maitre, R. W., Bateman, P., Dudek, A., Keller, J., Lameyre, J., Le Bas, M., Sabine, P. A., Schmid, R., Sorensen, H., Streckeisen, A., Woolley, A. R. and Zanettin, R. 1989. *A Classification of Igneous Rocks and Glossary of Terms: Recommendations of the International Union of Geological Sciences Subcommission on the Systematics of Igneous Rocks.* Oxford: Blackwell Scientific.

LeBas, M. J., LeMaitre, R. W., Streckeisen, A. and Zanettin, B., 1986. A Chemical Classification of Volcanic Rocks Based on the Total Alkali-Silica Diagram. *J. Petrology*, 27**,** 745-750.

Lee, K. H., 1996. Structure and geochemistry of the Nemo area Black Hills, South Dakota, United States of America. Lincoln: University of Nebraska.

Lenton, T. M., Schellnhuber, H. J. and Szathmary, E., 2004. Climbing the co-evolution ladder. *Nature,* 431**,** 913-913.

Lesher, C. M., Burnham, O. M., Keays, R. R., Barnes, S. J. and Hulbert, L., 2001. TRACE-ELEMENT GEOCHEMISTRY AND PETROGENESIS OF BARREN AND ORE-ASSOCIATED KOMATIITES. *The Canadian Mineralogist,* 39**,** 673-696.

Li, X., Kind, R., Priestley, K., Sobolev, S. V., Tilmann, F., Yuan, X. and Weber, M., 2000. Mapping the Hawaiian plume conduit with converted seismic waves. *Nature,* 405**,** 938-941.

Lightfoot, P. C., Naldrett, A. J., Gorbachev, N. S., Doherty, W. and Fedorenko, V. A., 1990. Geochemistry of the Siberian Trap of the Noril'sk area, USSR, with implications for the relative contributions of crust and mantle to flood basalt magmatism. *Contributions to Mineralogy and Petrology,* 104**,** 631-644.

Lindsay, J. F. and Brasier, M. D., 2002. Did global tectonics drive early biosphere evolution? Carbon isotope record from 2.6 to 1.9 Ga carbonates of Western Australian basins. *Precambrian Research*, 114**,** 1-34.

Maaløe, S., 1976. The Zoned Plagioclase of the Skaergaard Intrusion, East Greenland. *Journal of Petrology,* 17**,** 398-419.

Maier, W. D., 2005. Platinum-group element (PGE) deposits and occurrences: Mineralization styles, genetic concepts, and exploration criteria. *Journal of African Earth Sciences,* 41**,** 165-191.

Maier, W. D., Arndt, N. T. and Curl, E. A., 2000. Progressive crustal contamination of the Bushveld Complex: evidence from Nd isotopic analyses of the cumulate rocks. *Contributions to Mineralogy and Petrology,* 140**,** 316-327.

Maier, W. D., Roelofse, F. and Barnes, S.-J., 2003. The Concentration of the Platinum-Group Elements in South African Komatiites: Implications for Mantle Sources, Melting Regime and PGE Fractionation during Crystallization. *Journal of Petrology,* 44**,** 1787-1804.

Maranate, S., 1979. Petrogenesis of a layered amphibolite sill in the Nemo district, Black Hills, South Dakota. 60. Rapid City: South Dakota School of Mines and Technology.

Martignole, J. and Martelat, J.-E., 2005. Proterozoic mafic dykes as monitors of HP granulite facies metamorphism in the Grenville Front Tectonic Zone (western Quebec). *Precambrian Research,* 138**,** 183-207.

Mavrogenes, J. A. and O'Neill, H. S. C., 1999. The relative effects of pressure, temperature and oxygen fugacity on the solubility of sulfide in mafic magmas. *Geochimica et Cosmochimica Acta,* 63**,** 1173-1180.

McCrank, G. F. D., Kamineni, D. C., Ejeckam, R. B. and Sikorsky, R., 1989. Geology of the East Bull Lake gabbro–anorthosite pluton, Algoma District, Ontario. *Canadian Journal of Earth Sciences,* 26**,** 357-375.

McDonough, W. F. and Sun, S. S., 1995. The composition of the Earth. *Chemical Geology,* 120**,** 223-253.

McHone, J. G., 2000. Non-plume magmatism and rifting during the opening of the central Atlantic Ocean. *Tectonophysics,* 316**,** 287-296.

McHone, J. G., Anderson, D. L., Beutel, E. K. and Fialko, Y. A., 2005. Giant dikes, rifts, flood basalts, and plate tectonics: A contention of mantle models. In *Plates, plumes, and paradigms,* eds. G. R. Foulger, J. H. Natland, D. C. Presnall and D. L. Anderson, 401-420. Geological Society of America.

McKenzie, D. and Bickle, M. J., 1988. The Volume and Composition of Melt Generated by Extension of the Lithosphere. *Journal of Petrology,* 29**,** 625-679.

Melezhik, V. A., 2006. Multiple causes of Earth's earliest global glaciation. *Terra Nova,* 18**,** 130-137.

Melezhik, V. A. and Sturt, B. A., 1994. General geology and evolutionary history of the early proterozoic Polmak-Pasvik-Pechenga-Imandra/Varzuga-Ust'Ponoy greenstone belt in the northeastern Baltic Shield. *Earth-Science Reviews,* 36**,** 205-241.

Mertanen, S., Halls, H. C., Vuollo, J. I., Pesonen, L. J. and Stepanov, V. S., 1999. Paleomagnetism of 2.44 Ga mafic dykes in Russian Karelia, eastern Fennoscandian Shield — implications for continental reconstructions. *Precambrian Research,* 98**,** 197-221.

Miller, J. D., 1999. Geochemical Evaluation of Platinum Group Element (PGE) Mineralization in the Sonju Lake Intrusion, Finland, Minnesota. In *Minnesota Geological Survey Information Circular,* p. 31.

Millet, M.-A., Doucelance, R., Schiano, P., David, K. and Bosq, C., 2008. Mantle plume heterogeneity versus shallow-level interactions: A case study, the São Nicolau Island, Cape Verde archipelago. *Journal of Volcanology and Geothermal Research,* 176**,** 265-276.

Mints, M. V., Glaznev, V. N., Konilov, A. N., Kunina, N. M., Nikitichev, A. P., Raevsky, A. B., Sedikh, Y. N., Stupak, V. M. and Fonarev, V. I. 1996. *The Early Precambrian of the Northeastern Baltic Shield: Palaeogeodynamics, Crustal Structure and Evolution.* Moscow: Nauchny Mir Pub.

Mitchell, A. A., Eales, H. V. and Kruger, J. F., 1998. Magma replenishment, and the significance of poikilitic textures, in the Lower Main Zone of the western Bushveld Complex, South Africa. *Mineralogical Magazine,* 62**,** 435-350.

Morgan, W. J., 1971. Convection Plumes in the Lower Mantle. *Nature,* 230**,** 42-43.

Mossman, D. J. and Harron, G. A., 1983. Origin and distribution of gold in the Huronian Supergroup, Canada — the case for Witwatersrand-type paleoplacers. *Precambrian Research,* 20**,** 543-583.

Mungall, J. E., 2002. Roasting the mantle: Slab melting and the genesis of major Au and Au-rich Cu deposits. *Geology,* 30**,** 915-918.

Naldrett, A. J., 1989. Sulfide melts–crystallization temperatures, solubilities in silicate melts, and Fe, Ni, and Cu partitioning between basaltic magmas and olivine. *Reviews in Economic Geology,* 4**,** 5-20.

Naldrett, A. J., 1999. World-class Ni-Cu-PGE deposits: key factors in their genesis. *Mineralium Deposita,* 34**,** 227-240.

Naldrett, A. J., 2010. Secular Variation of Magmatic Sulfide Deposits and Their Source Magmas. *Economic Geology,* 105**,** 669-688.

Naldrett, A. J., 2011. Fundamentals of Magmatic Sulfide Deposits. In *Magmatic Ni-Cu and PGE deposits: Geology, Geochemistry, and Genesis,* eds. C. Li and E. M. Ripley. Society of Economic Geologists.

Nataf, H.-C. and VanDecar, J., 1993. Seismological detection of a mantle plume? *Nature,* 364**,** 115-120.

Neal, C. R., Coffin, M. F., Arndt, N. T., Duncan, R. A., Eldholm, O., Erba, E., Farnetani, C., Fitton, J. G., Ingle, S. P., Ohkouchi, N., Rampino, M. R., Reichow, M. K., Self, S. and Tatsumi, Y., 2008.

Investigating Large Igneous Province Formation and Associated Paleoenvironmental Events: A White Paper for Scientific Drilling. *Scientific Drilling*.

Nelson, D. O., Morrison, D. A. and Phinney, W. C., 1990. Open-system evolution versus source control in basaltic magmas: Matachewan-Hearst dike swarm, Superior Province, Canada. *Canadian Journal of Earth Sciences,* 27**,** 767-783.

Nelson, S. T. and Montana, A., 1992. Sieve-textured plagioclase in volcanic rocks produced by rapid decompression. *American Mineralogist,* 77**,** 1242-1249.

Ohta, H., Maruyama, S., Takahashi, E., Watanabe, Y. and Kato, Y., 1996. Field occurrence, geochemistry and petrogenesis of the Archean Mid-Oceanic Ridge Basalts (AMORBs) of the Cleaverville area, Pilbara Craton, Western Australia. *Lithos,* 37**,** 199-221.

Ojakangas, R. W., Marmo, J. S. and Heiskanen, K. I., 2001. Basin evolution of the Paleoproterozoic Karelian Supergroup of the Fennoscandian (Baltic) Shield. *Sedimentary Geology,* 141-142**,** 255-285.

Oliveira, E. P., Silveira, E. M., Söderlund, U. and Ernst, R. E., U–Pb ages and geochemistry of mafic dyke swarms from the Uauá Block, São Francisco Craton, Brazil: LIPs remnants relevant for Late Archaean break-up of a supercraton. *Lithos*.

Palacz, Z. A., 1985. SrNdPb isotopic evidence for crustal contamination in the Rhum intrusion. *Earth and Planetary Science Letters,* 74**,** 35-44.

Park, J. K., Buchan, K. L. and Harlan, S. S., 1995. A proposed giant radiating dyke swarm fragmented by the separation of Laurentia and Australia based on paleomagnetism of ca. 780 Ma mafic intrusions in western North America. *Earth and Planetary Science Letters,* 132**,** 129-139.

Patterson, J. G. and Heaman, L. M., 1991. New geochronologic limits on the depositional age of the Hurwitz Group, Trans-Hudson hinterland, Canada. *Geology,* 19**,** 1137-1140.

Peach, C. L., Mathez, E. A. and Keays, R. R., 1990. Sulfide melt-silicate melt distribution coefficients for noble metals and other chalcophile elements as deduced from MORB: Implications for partial melting. *Geochimica et Cosmochimica Acta,* 54**,** 3379-3389.

Pearce, J. A., 1996. A user's guide to basalt discrimination diagrams. In *Trace element geochemistry of volcanic rocks: appliction for massive sulphide exploration,* ed. D. Wyman, 79-113. Winnipeg: Geological Association of Canada, Mineral Deposits Division.

Pearce, J. A. and Cann, J. R., 1973. Tectonic setting of basic volcanic rocks determined using trace element analyses. *Earth and Planetary Science Letters,* 19**,** 290-300.

Pearce, J. A. and Peate, D. W., 1995. Tectonic implications of the composition of volcanic arc magmas *Annual review of Earth and planetary sciences,* 23**,** 251-285.

Peck, D. C., Chubb, P. T. and James, R. S., 1991. Magmatic platinum-group elements and copper + nickel mineralization along the base of the East Bull Lake gabbro-anorthosite intrusion. In *Summary of Field Work and Other Activities*, 62-66. Ontario Geological Survey.

Peck, D. C. and James, R. S., 1992. Preliminary report on the geology and platinum-group element-sulphide mineralization of the East Bull Lake gabbro-anorthosite intrusion. *Ontario Geological Survey, Open File Report,* 58**,** 13.

Peck, D. C., James, R. S., Chubb, P. T. and Keays, R. R., 1995. Geology, metallogeny and petrogenesis of the East Bull Lake intrusion, Ontario. *Ontario Geological Survey, Open File Report,* 59237**,** 117.

Peck, D. C., Keays, R. R., James, R. S., Chubb, P. T. and Reeves, S. J., 2001. Controls on the Formation of Contact-Type Platinum-Group Element Mineralization in the East Bull Lake Intrusion. *Economic Geology,* 96**,** 559-581.

Phinney, W. C. and Halls, H. C., 2001. Petrogenesis of the Early Proterozoic Matachewan dyke swarm, Canada, and implications for magma emplacement and subsequent deformation. *Canadian Journal of Earth Sciences,* 38**,** 1541-1563.

Pinet, P. R. 2003. *Invitation to Oceanography.* Jones and Bartlett Publishers.

Plank, T., 2005. Constraints from Thorium/Lanthanum on Sediment Recycling at Subduction Zones and the Evolution of the Continents. *Journal of Petrology,* 46**,** 921-944.

Polat, A., Fryer, B. J., Appel, P. W. U., Kalvig, P., Kerrich, R., Dilek, Y. and Yang, Z., 2011. Geochemistry of anorthositic differentiated sills in the Archean (~2970 Ma) Fiskenæsset Complex, SW Greenland: Implications for parental magma compositions, geodynamic setting, and secular heat flow in arcs. *Lithos,* 123**,** 50-72.

Prawirodirdjo, L. and Bock, Y., 2004. Instantaneous global plate motion model from 12 years of continuous GPS observations. *Journal of Geophysical Research: Solid Earth,* 109**,** n/a-n/a.

Prichard, H. M., Lord, R. A. and Neary, C. R., 1996. A model to explain the occurrence of platinum- and palladium-rich ophiolite complexes. *Journal of the Geological Society,* 153**,** 323-328.

Puchtel, I. S., Haase, K. M., Hofmann, A. W., Chauvel, C., Kulikov, V. S., Garbe-Schönberg, C. D. and Nemchin, A. A., 1997. Petrology and geochemistry of crustally contaminated komatiitic basalts from the Vetreny Belt, southeastern Baltic Shield: Evidence for an early Proterozoic mantle plume beneath rifted Archean continental lithosphere. *Geochimica et Cosmochimica Acta,* 61**,** 1205-1222.

Puchtel, I. S., Hofmann, A. W., Mezger, K., Shchipansky, A. A., Kulikov, V. S. and Kulikova, V. V., 1996. Petrology of a 2.41 Ga remarkably fresh komatiitic basalt lava lake in Lion Hills, central Vetreny Belt, Baltic Shield. *Contributions to Mineralogy and Petrology,* 124**,** 273-290.

Rasmussen, B. and Buick, R., 1999. Redox state of the Archean atmosphere: Evidence from detrital heavy minerals in ca. 3250–2750 Ma sandstones from the Pilbara Craton, Australia. *Geology,* 27**,** 115-118.

Raymond, J. and Segrè, D., 2006. The Effect of Oxygen on Biochemical Networks and the Evolution of Complex Life. *Science,* 311**,** 1764-1767.

Redden, J. A., Peterman, Z. E., Zartman, R. E. and DeWitt, E. R., 1990. U-Th-Pb geochronology and preliminary interpretation of Precambrian events in the Black Hills, South Dakota. *In The Trans-Hudson orogen. Edited by J.F. Lewry and M.R. Stauffer,* Geological Association of Canada Special Paper 37**,** 229-251.

Renne, P. R. and Basu, A. R., 1991. Rapid Eruption of the Siberian Traps Flood Basalts at the Permo-Triassic Boundary. *Science,* 253**,** 176-179.

Richter, F. M., 1988. A Major Change in the Thermal State of the Earth at the Archean-Proterozoic Boundary: Consequences for the Nature and Preservation of Continental Lithosphere. *Journal of Petrology,* Special_Volume**,** 39-52.

Ripley, E. M. and Li, C., 2003. Sulfur isotopic exchange and metal enrichment in the formation of magmatic Cu-Ni-(PGE) deposits. *Economic Geology,* 98**,** 635-641.

Rollinson, H. 1993. *Using geochemical data: evaluation, presentation, interpretation.* Harlow: Pearson Education Limited.

Roscoe, S. M. and Card, K. D., 1993. The reappearance of the Huronian in Wyoming: rifting and drifting of ancient continents. *Canadian Journal of Earth Sciences,* 30**,** 2475-2480.

Rudnick, R. L. and Gao, S., 2003. 3.01 - Composition of the Continental Crust. In *Treatise on Geochemistry,* eds. D. H. Editors-in-Chief: Heinrich and K. T. Karl, 1-64. Oxford: Pergamon.

Rudnick, R. L. and Fountain, D. M., 1995. Nature and composition of the continental crust: a lower crustal perspective. *Reviews of Geophysics,* 33**,** 267-309.

Russell, S. A., Lay, T. and Garnero, E. J., 1998. Seismic evidence for small-scale dynamics in the lowermost mantle at the root of the Hawaiian hotspot. *Nature,* 396**,** 255-258.

Saltikoff, B., Puustinen, K. and Tontti, M., 2006. Metallogenic zones and metallic mineral deposits in Finland - Explanation to the Metallogenic Map of Finland. In *Special Paper*. Espoo: Geological Survey of Finland.

Sandeman, H. A., Cousens, B. L. and Hemmingway, C. J., 2003. Continental tholeiitic mafic rocks of the Paleoproterozoic Hurwitz Group, Central Hearne sub-domain, Nunavut: insight into the evolution of the Hearne sub-continental lithosphere. *Canadian Journal of Earth Sciences,* 40**,** 1219-1237.

Sandeman, H. A., Hanmer, S., Davis, W. J., Ryan, J. J. and Peterson, T. D., 2004. Neoarchaean volcanic rocks, Central Hearne supracrustal belt, Western Churchill Province, Canada: geochemical and isotopic evidence supporting intra-oceanic, supra-subduction zone extension. *Precambrian Research,* 134**,** 113-141.

Sandeman, H. A. and Ryan, J. J., 2008. The Spi Lake Formation of the central Hearne domain, western Churchill Province, Canada: an axial intracratonic continental tholeiite trough above the cogenetic Kaminak dyke swarm. *Canadian Journal of Earth Sciences,* 45**,** 745-767.

Schersten, A., Elliott, T., Hawkesworth, C. and Norman, M., 2004. Tungsten isotope evidence that mantle plumes contain no contribution from the Earth's core. *Nature,* 427**,** 234-237.

Scoates, J. S. and Mitchell, J. N., 2000. The Evolution of Troctolitic and High Al Basaltic Magmas in Proterozoic Anorthosite Plutonic Suites and Implications for the Voisey's Bay Massive Ni-Cu Sulfide Deposit. *Economic Geology,* 95**,** 677-701.

Scoates, R. F. J. and Eckstrand, O. R., 1986. Platinum-group elements in the upper central layered zone of the Fox River Sill, northeastern Manitoba. *Economic Geology,* 81**,** 1137-1146.

Sessions, A. L., Doughty, D. M., Welander, P. V., Summons, R. E. and Newman, D. K., 2009. The Continuing Puzzle of the Great Oxidation Event. *Current Biology,* 19**,** R567-R574.

Shaw, D. M., 1970. Trace element fractionation during anatexis. *Geochimica et Cosmochimica Acta,* 34**,** 237-243.

Shen, Y., Solomon, S. C., Bjarnason, I. T. and Wolfe, C. J., 1998. Seismic evidence for a lower-mantle origin of the Iceland plume. *Nature,* 395**,** 62-65.

Smith, P. E., Farquhar, R. M. and Halls, H. C., 1992. U-Th-Pb isotope study of mafic dykes in the Superior Province, Ontario, Canada : uniformity of initial Pb isotope ratios of the Hearst dykes. *Chemical Geology,* 94**,** 261-280.

Söderlund, U., Hofmann, A., Klausen, M. B., Olsson, J. R., Ernst, R. E. and Persson, P.-O., 2010. Towards a complete magmatic barcode for the Zimbabwe craton: Baddeleyite U–Pb dating of regional dolerite dyke swarms and sill complexes. *Precambrian Research,* 183**,** 388-398.

Spandler, C. J., Eggins, S. M., Arculus, R. J. and Mavrogenes, J. A., 2000. Using melt inclusions to determine parent-magma compositions of layered intrusions: Application to the Greenhills Complex (New Zealand), a platinum group minerals–bearing, island-arc intrusion. *Geology,* 28**,** 991-994.

Sproule, R. A., Lesher, C. M., Ayer, J. A. and Thurston, P. C., 2003. Geochemistry and metallogenesis of komatiitic rocks in the Abitibi greenstone belt, Ontario. ed. O. G. Survey, 119.

Stepanova, A. and Stepanov, V., 2010. Paleoproterozoic mafic dyke swarms of the Belomorian Province, eastern Fennoscandian Shield. *Precambrian Research,* 183**,** 602-616.

Stern, R., Avigad, D., Miller, N. and Beyth, M., 2008. From Volcanic Winter to Snowball Earth: An Alternative Explanation for Neoproterozoic Biosphere Stress. In *Links Between Geological Processes, Microbial Activities&Evolution of Life,* eds. Y. Dilek, H. Furnes and K. Muehlenbachs, 313-337. Springer Netherlands.

Stupavsky, M. and Symons, D. T. A., 1983. Penokean remagnetization of the basal Huronian Dollyberry Lake basalts near Elliot Lake, Ontario. *Canadian Journal of Earth Sciences,* 20**,** 49-56.

Sun, S. s. and McDonough, W. F., 1989. Chemical and isotopic systematics of oceanic basalts: implications for mantle composition and processes. *Geological Society, London, Special Publications,* 42**,** 313-345.

Sverjensky, D. A. and Lee, N., 2010. The Great Oxidation Event and Mineral Diversification. *ELEMENTS,* 6**,** 31-36.

Thordarson, T., Self, S., Oskarsson, N. and Hulsebosh, T., 1996. Sulphur, chlorine, and flourine degassing and atmospheric loading by the 1783-1784 AD Laki (Skaftar Fires) eruption in Iceland. *Bulletin of Volcanology***,** 205-225.

Thordarson, T. and Self, S., 2003. Atmospheric and environmental effects of the 1783–1784 Laki eruption: a review and reassessment. *J. Geophys. Res,* 108**,** 4011.

Timm, C., Hoernle, K., Werner, R., Hauff, F., den Bogaard, P. v., Michael, P., Coffin, M. F. and Koppers, A., 2011. Age and geochemistry of the oceanic Manihiki Plateau, SW Pacific: New evidence for a plume origin. *Earth and Planetary Science Letters,* 304**,** 135-146.

Tomlinson, K. Y., 1996. The geochemistry and tectonic setting of early Precambrian greenstone belts, Northwestern Ontario, Canada., 287. University of Portsmouth.

Tredoux, M., Lindsay, N. M., Davies, G. and McDonald, I., 1995. The fractionation of platinum-group elements in magmatic systems, with the suggestion of a novel causal mechanism. *South African Journal of Geology,* 98**,** 157-167.

Van Boening, A. M., 2007. Petrogenesis and Tectonic Implications of Mafic Rocks in the Precambrian Core of the Black Hills, South Dakota. In *Department of Geological Sciences,* 75. Missouri: University of Missouri.

Van Boening, A. M. and Nabelek, P. I., 2008. Petrogenesis and tectonic implications of paleoproterozoic mafic rocks in the Black Hills, South Dakota. *Precambrian Research,* 167**,** 363-376.

Vervoort, J. D., Patchett, P. J., Blichert-Toft, J. and Albarède, F., 1999. Relationships between Lu–Hf and Sm–Nd isotopic systems in the global sedimentary system. *Earth and Planetary Science Letters,* 168**,** 79-99.

Vogel, D. C., 1996. The geology and geochemistry of the Agnew intrusion: implications for the petrogenesis of early Huronian mafic igneous rocks in central Ontario, Canada. 455. Victoria: University of Melbourne.

Vogel, D. C. and Keays, R. R., 1997. The petrogenesis and platinum-group element geochemistry of the Newer Volcanic Province, Victoria, Australia. *Chemical Geology,* 136**,** 181-204.

Vogel, D. C., James, R. S. and Keays, R. R., 1998a. The early tectono-magmatic evolution of the Southern Province: implications from the Agnew Intrusion, central Ontario, Canada. *Canadian Journal of Earth Sciences,* 35**,** 854-870.

Vogel, D. C., Vuollo, J. I., Alapieti, T. T. and James, R. S., 1998b. Tectonic, stratigraphic, and geochemical comparisons between ca. 2500-2440 Ma mafic igneous events in the Canadian and Fennoscandian Shields. *Precambrian Research,* 92**,** 89-116.

Vogel, D. C., Keays, R. R., James, R. S. and Reeves, S. J., 1999. The Geochemistry and Petrogenesis of the Agnew Intrusion, Canada: A Product of S-Undersaturated, High-Al and Low-Ti Tholeiitic Magmas. *Journal of Petrology,* 40**,** 423-450.

Vuollo, J. and Huhma, H., 2005. Chapter 5 Paleoproterozoic mafic dikes in NE finland. In *Developments in Precambrian Geology,* eds. P. A. N. M. Lehtinen and O. T. Rämö, 195-236. Elsevier.

Walter, M. J., 1998. Melting of garnet peridotite and the origin of komatiite and depleted lithosphere. *Journal of Petrology,* 39**,** 29-60.

Wang, P. and Glover Iii, L., 1992. A tectonics test of the most commonly used geochemical discriminant diagrams and patterns. *Earth-Science Reviews,* 33**,** 111-131.

Weaver, B. L., 1991. The origin of ocean island basalt end-member compositions: trace element and isotopic constraints. *Earth and Planetary Science Letters,* 104**,** 381-397.

Weihed, P., Arndt, N. T., Billström, K., Duchesne, J.-C., Eilu, P., Martinsson, O., Papunen, H. and Lahtinen, R., 2005. 8: Precambrian geodynamics and ore formation: The Fennoscandian Shield. *Ore Geology Reviews,* 27**,** 273-322.

West, G. F. and Ernst, R. E., 1991. Evidence from aeromagnetics on the configuration of Matachewan dykes and the tectonic evolution of the Kapuskasing Structural Zone, Ontario, Canada. *Canadian Journal of Earth Sciences,* 28**,** 1797-1811.

Willbold, M. and Stracke, A., 2006. Trace element composition of mantle end-members: Implications for recycling of oceanic and upper and lower continental crust. *Geochem. Geophys. Geosyst.,* 7**,** Q04004.

Williams, H., 1991. Anatomy of North America: thematic geologic portrayals of the continent. *Tectonophysics,* 187**,** 117-134.

Wilson, J. T., 1965. Evidence from Ocean Islands Suggesting Movement in the Earth. *Philosophical Transactions of the Royal Society of London. Series A, Mathematical and Physical Sciences,* 258**,** 145-167.

Wolfe, C. J., Bjarnason, I. T., VanDecar, J. C. and Solomon, S. C., 1997. Seismic structure of the Iceland mantle plume. *Nature,* 385**,** 245-247.

Woo, C. C., 1952. The Pre-Cambrian geology and amphibolites of the Nemo district, Black Hills, South Dakota. 148. Chicago: University of Chicago.

Workman, R. K. and Hart, S. R., 2005. Major and trace element composition of the depleted MORB mantle (DMM). *Earth and Planetary Science Letters,* 231**,** 53-72.

Xie, Q., Kerrich, R. and Fan, J., 1993. HFSE/REE fractionations recorded in three komatiite-basalt sequences, Archean Abitibi greenstone belt: Implications for multiple plume sources and depths. *Geochimica et Cosmochimica Acta,* 57**,** 4111-4118.

Young, G. M., 1988. Proterozoic plate tectonics, glaciation and iron-formations. *Sedimentary Geology,* 58**,** 127-144.

Zhang, B., 1999. A Study of Crustal Uplift along the Kapuskasing Zone Using 2.45 Ga Matachewan Dykes. In *Department of Geology*. Toronto: University of Toronto.

Zhang, M., O'Reilly, S. Y., Wang, K.-L., Hronsky, J. and Griffin, W. L., 2008. Flood basalts and metallogeny: The lithospheric mantle connection. *Earth-Science Reviews,* 86**,** 145-174.

NOTES ON APPENDICES

Appendix A.	Excel spreadsheet which presents the geographic locations of each of the samples collected and studied by this work. For each suite, the coordinate system used is stated in columns B and C.
Appendix B.	Word document which describes the laboratory methods used to collect the major, trace and platinum group element and isotopic data presented by this study
Appendix C.	Excel spreadsheet which presents the major, trace and platinum group element data collected by this study. Also presented is information on the geochemical standards used to determine the accuracy and precision of the data.
Appendix D.	Excel spreadsheet which presents the isotopic data collected by this study. Also presented is information on the geochemical standards used to determine the accuracy and precision of the data.
Appendix E.	Excel spreadsheet which presents the major and trace element data collected by this study for the Mistassini and Du Chef dyke swarms not discussed in the text.
Appendix F.	Word document which presents a geological overview of the Mistassini and Du Chef dyke swarms not discussed in the text.
Appendix G.	Adobe .pdf presenting the work of Ciborowski et al. (in press) regarding the petrogenesis of the Blue Draw Metagabbro.
Appendix H.	Excel spreadsheet which presents the method used to calculate the composition of the Blue Draw Metagabbro parent magma.
Appendix I.	Excel spreadsheet which presents the contaminants and mantle end members used to constrain the petrogenetic modelling presented in Chapter 5.
Appendix J.	Excel spreadsheet which presents the method used to calculate the composition of the fine grained groundmass of the Leopard dykes.

Appendix A

Agnew Intrusion

Sample Number	Easting UTM 17T	Northing UTM 17T	Description	Sample Type	Sample Source
AG001	426718	5137364	Nodular Anorthosite	Rock	Jake Ciborowski
AG002	-	-	Layered Gabbonorite	Rock	Jake Ciborowski
AG003	426718	5137364	Nodular anorthosite	Rock	Jake Ciborowski
AG004	426662	5137146	Inclusion bearing unit	Rock	Jake Ciborowski
AG005	-	-	Layered Gabbonorite	Rock	Jake Ciborowski
AG006a	425850	5137339	Layered Gabbonorite	Rock	Jake Ciborowski
AG006b	425850	5137339	Layered Gabbonorite	Rock	Jake Ciborowski
AG007	426691	5137144	Inclusion bearing unit	Rock	Jake Ciborowski

Blue Draw Metagabbro

Sample Number	Easting UTM 14T	Northing UTM 14T	Description	Sample Type	Sample Source	Strat. Height (m)
BD001	618079	494606	Upper Gabbronorite unit	Rock	Jake Ciborowski	615
BD002	618082	494598	Upper Gabbronorite unit	Rock	Jake Ciborowski	630
BD003	618085	494589	Upper Gabbronorite unit	Rock	Jake Ciborowski	635.5
BD004	618088	494581	Upper Gabbronorite unit	Rock	Jake Ciborowski	645
BD005	618091	494572	Upper Gabbronorite unit	Rock	Jake Ciborowski	652.5
BD006	618094	494564	Upper Gabbronorite unit	Rock	Jake Ciborowski	662.5
BD007	618097	494556	Upper Gabbronorite unit	Rock	Jake Ciborowski	665
BD008	618100	494547	Upper Gabbronorite unit	Rock	Jake Ciborowski	670
BD009	618103	494539	Upper Gabbronorite unit	Rock	Jake Ciborowski	680
BD010	618106	494530	Upper Gabbronorite unit	Rock	Jake Ciborowski	685
BD011	618109	494522	Upper Gabbronorite unit	Rock	Jake Ciborowski	690
BD012	618112	494514	Upper Gabbronorite unit	Rock	Jake Ciborowski	692.5
BD013	618115	494505	Upper Gabbronorite unit	Rock	Jake Ciborowski	695
BD014	618118	494497	Upper Gabbronorite unit	Rock	Jake Ciborowski	696.5
BD015	618121	494488	Upper Gabbronorite unit	Rock	Jake Ciborowski	697.5
BD016	618124	494480	Upper Gabbronorite unit	Rock	Jake Ciborowski	705
BD017	618104	494632	Upper Gabbronorite unit	Rock	Jake Ciborowski	632.5
BD018	618106	494632	Upper Gabbronorite unit	Rock	Jake Ciborowski	634.5
BD019	618114	494643	Upper Gabbronorite unit	Rock	Jake Ciborowski	635
BD020	618109	494657	Upper Gabbronorite unit	Rock	Jake Ciborowski	625

BD021	618099	494668	Upper Gabbronorite unit	Rock	Jake Ciborowski	610
BD022	618096	494663	Upper Gabbronorite unit	Rock	Jake Ciborowski	612
BD023	618107	494688	Upper Gabbronorite unit	Rock	Jake Ciborowski	612.5
BD024	618116	494702	Upper Gabbronorite unit	Rock	Jake Ciborowski	613
BD025	618125	494719	Upper Gabbronorite unit	Rock	Jake Ciborowski	617.5
BD026	618116	494723	Upper Gabbronorite unit	Rock	Jake Ciborowski	605
BD027	618112	494738	Upper Gabbronorite unit	Rock	Jake Ciborowski	595
BD028	617514	494912	Peridotite unit	Rock	Jake Ciborowski	-25
BD029	617531	494902	Peridotite unit	Rock	Jake Ciborowski	-10
BD030	617524	494881	Peridotite unit	Rock	Jake Ciborowski	-10
BD031	617531	494874	Peridotite unit	Rock	Jake Ciborowski	2.5
BD032	617543	494874	Peridotite unit	Rock	Jake Ciborowski	12.5
BD033	617548	494865	Peridotite unit	Rock	Jake Ciborowski	20
BD034	617559	494851	Peridotite unit	Rock	Jake Ciborowski	35
BD035	617554	494830	Peridotite unit	Rock	Jake Ciborowski	32.5
BD036	617555	494847	Peridotite unit	Rock	Jake Ciborowski	37.5
BD037	617571	494830	Peridotite unit	Rock	Jake Ciborowski	55
BD038	617578	494822	Peridotite unit	Rock	Jake Ciborowski	65
BD039	617595	494808	Peridotite unit	Rock	Jake Ciborowski	82.5
BD040	617595	494800	Peridotite unit	Rock	Jake Ciborowski	85
BD041	617600	494784	Peridotite unit	Rock	Jake Ciborowski	100
BD042	617616	494777	Peridotite unit	Rock	Jake Ciborowski	115
BD043	617635	494784	Olivine Melagabbronorite unit	Rock	Jake Ciborowski	125
BD044	617625	494780	Olivine Melagabbronorite unit	Rock	Jake Ciborowski	130
BD045	617645	494773	Olivine Melagabbronorite unit	Rock	Jake Ciborowski	140
BD046	617646	494769	Olivine Melagabbronorite unit	Rock	Jake Ciborowski	145
BD047	617567	494586	Olivine Melagabbronorite unit	Rock	Jake Ciborowski	137.5
BD048	617857	494709	Melagabbronorite unit	Rock	Jake Ciborowski	387.5
BD049	617888	494457	Upper Gabbronorite unit	Rock	Jake Ciborowski	470
BD050	617911	494460	Upper Gabbronorite unit	Rock	Jake Ciborowski	500
BD051	617905	494439		Rock	Jake Ciborowski	-
BD052	617908	494426		Rock	Jake Ciborowski	-
BD053	617806	494389	Lower Gabbronorite unit	Rock	Jake Ciborowski	355
BD054	617894	494364		Rock	Jake Ciborowski	-
BD055	617912	494365	Upper Gabbronorite unit	Rock	Jake Ciborowski	535
BD056	617924	494364	Upper Gabbronorite unit	Rock	Jake Ciborowski	545

BD057	617946	494355	Upper Gabbronorite unit	Rock	Jake Ciborowski	570
BD058	617961	494348	Upper Gabbronorite unit	Rock	Jake Ciborowski	590
BD059	617982	494350	Upper Gabbronorite unit	Rock	Jake Ciborowski	620
BD060	618008	494367		Rock	Jake Ciborowski	-
BD061	618014	494357	Upper Gabbronorite unit	Rock	Jake Ciborowski	647.5
BD062	618028	494347	Upper Gabbronorite unit	Rock	Jake Ciborowski	660
BD063	618039	494343	Upper Gabbronorite unit	Rock	Jake Ciborowski	672.5
BD064	618055	494336	Upper Gabbronorite unit	Rock	Jake Ciborowski	687.5
BD065	618077	494331	Quartz Gabbronorite unit	Rock	Jake Ciborowski	710
BD066	618096	494316	Quartz Gabbronorite unit	Rock	Jake Ciborowski	707.5
BD067	618190	494278	Boxelder Creek Quartzite	Rock	Jake Ciborowski	822.5
BD068	618216	494279	Boxelder Creek Quartzite	Rock	Jake Ciborowski	850
BD069	618216	494279	Boxelder Creek Quartzite	Rock	Jake Ciborowski	850
BD070	618182	494271	Boxelder Creek Quartzite	Rock	Jake Ciborowski	815
BD071	618163	494268	Boxelder Creek Quartzite	Rock	Jake Ciborowski	797.5
BD072	618151	494261	Boxelder Creek Quartzite	Rock	Jake Ciborowski	785
BD073	618135	494279	Quartz Gabbronorite unit	Rock	Jake Ciborowski	762.5
BD074	618134	494289	Quartz Gabbronorite unit	Rock	Jake Ciborowski	760
BD075	618120	494306	Quartz Gabbronorite unit	Rock	Jake Ciborowski	740
BD076	618099	494302	Quartz Gabbronorite unit	Rock	Jake Ciborowski	712.5
BD077	617579	494540	Olivine Melagabbronorite unit	Rock	Jake Ciborowski	170
BD078	617585	494556	Olivine Melagabbronorite unit	Rock	Jake Ciborowski	167.5
BD079	617592	494551	Olivine Melagabbronorite unit	Rock	Jake Ciborowski	177.5
BD080	617613	494534	Olivine Melagabbronorite unit	Rock	Jake Ciborowski	197.5
BD081	617635	494520	Lower Gabbronorite unit	Rock	Jake Ciborowski	220
BD082	617644	494516	Lower Gabbronorite unit	Rock	Jake Ciborowski	230
BD083	617659	494515	Lower Gabbronorite unit	Rock	Jake Ciborowski	240
BD084	617674	494514	Lower Gabbronorite unit	Rock	Jake Ciborowski	257.5
BD085	617709	494514	Lower Gabbronorite unit	Rock	Jake Ciborowski	277
BD086	617751	494508		Rock	Jake Ciborowski	-
BD087	617767	494486	Lower Gabbronorite unit	Rock	Jake Ciborowski	337.5
BD088	617817	494440	Melagabbronorite unit	Rock	Jake Ciborowski	370
BD089	617826	494488	Post intrusion dyke	Rock	Jake Ciborowski	382.5
BD090	617833	494483	Melagabbronorite unit	Rock	Jake Ciborowski	390
BD091	617844	494481	Melagabbronorite unit	Rock	Jake Ciborowski	400
BD092	617871	494496	Upper Gabbronorite unit	Rock	Jake Ciborowski	427.5

BD093	617880	494507	Upper Gabbronorite unit	Rock	Jake Ciborowski	435
BD094	617920	494515	Upper Gabbronorite unit	Rock	Jake Ciborowski	490
BD095	617928	494524	Upper Gabbronorite unit	Rock	Jake Ciborowski	495
BD096	617743	494656	Lower Gabbronorite unit	Rock	Jake Ciborowski	285
BD097	617749	494650	Lower Gabbronorite unit	Rock	Jake Ciborowski	290
BD098	617773	494673	Lower Gabbronorite unit	Rock	Jake Ciborowski	310
BD099	617802	494677		Rock	Jake Ciborowski	-
BD100	617836	494669	Melagabbronorite unit	Rock	Jake Ciborowski	375
BD101	617834	494711	Melagabbronorite unit	Rock	Jake Ciborowski	362.5
BD102	617839	494711	Melagabbronorite unit	Rock	Jake Ciborowski	365

East Bull Lake Intrusion

Sample Number	Easting UTM 17T	Northing UTM 17T	Description	Sample Type	Sample Source
EB001	406755	5142610	Dendritic Unit	Rock	Jake Ciborowski
EB002	-	-	Anorthosite Subzone	Rock	Jake Ciborowski
EB003	406900	5142790	Rythmically Layered Gabbronorite Zone	Rock	Jake Ciborowski
EB004	409022	5142098	Rythmically Layered Gabbronorite Zone	Rock	Jake Ciborowski
EB005	406755	5142610	Varitextured Gabbronorite Zone	Rock	Jake Ciborowski
EB006	407550	5142670	Rythmically Layered Gabbronorite Zone	Rock	Jake Ciborowski
EB007	409022	5142098	Rythmically Layered Gabbronorite Zone	Rock	Jake Ciborowski

Gerow Intrusion

Sample Number	Easting UTM 17T	Northing UTM 17T	Description	Sample Type	Sample Source
GE001	399675	5137880	Massive Gabbro. Contact with Whiskey Lake host rocks	Rock	Jake Ciborowski
GE002	399744	5137926	Massive Gabbro	Rock	Jake Ciborowski
GE003	399813	5137972	Layered Gabbro	Rock	Jake Ciborowski
GE004	399898	5137950	Massive Gabbro	Rock	Jake Ciborowski
GE005	399813	5137972	Massive Gabbro. Sulphide burn	Rock	Jake Ciborowski
GE006	399983	5137929	Massive Gabbro. Minor disseminated sulphides	Rock	Jake Ciborowski

Kaminak Dyke Swarm

Sample Number	Longitude (degrees E)	Latitude (degrees N)	Description	Sample Type	Sample Source
FA71-063-04	-94.917	62.083		Powder	Ontario Geological Survey
FA71-063-07	-94.917	62.083		Powder	Ontario Geological Survey
FA71-064-07	-94.917	62.083		Powder	Ontario Geological Survey

FA71-065-01	-94.917	62.083	Powder	Ontario Geological Survey
FA71-065-04	-94.917	62.083	Powder	Ontario Geological Survey
FA71-066-07	-94.917	62.083	Powder	Ontario Geological Survey
FA71-066-04	-94.917	62.083	Powder	Ontario Geological Survey
FA71-067-01	-94.967	62.167	Powder	Ontario Geological Survey
FA71-067-04	-94.967	62.167	Powder	Ontario Geological Survey
FA71-068-04	-94.670	62.167	Powder	Ontario Geological Survey
FA71-069-04	-94.967	62.167	Powder	Ontario Geological Survey
FA71-069-07	-94.967	62.167	Powder	Ontario Geological Survey
FA71-070-07	-95.5	62.1	Powder	Ontario Geological Survey
FA71-072-04	-95.5	62.133	Powder	Ontario Geological Survey
FA71-072-07	-95.5	62.133	Powder	Ontario Geological Survey
FA71-073-01	-95.483	62.133	Powder	Ontario Geological Survey
FA71-073-04	-95.483	62.133	Powder	Ontario Geological Survey
FA71-074-01	-95.5	62.033	Powder	Ontario Geological Survey
FA71-074-04	-95.5	62.033	Powder	Ontario Geological Survey
FA71-075-01	-94.333	62.133	Powder	Ontario Geological Survey
FA71-075-02	-94.333	62.133	Powder	Ontario Geological Survey
FA71-075-06	-94.333	62.133	Powder	Ontario Geological Survey
FA71-076-01	-94.617	62.3	Powder	Ontario Geological Survey
FA71-076-04	-94.617	62.3	Powder	Ontario Geological Survey
FA71-077-07	-94.617	62.3	Powder	Ontario Geological Survey
FA71-078-04	-94.633	62.3	Powder	Ontario Geological Survey
FA71-079-02	-94.417	62.283	Powder	Ontario Geological Survey
FA71-079-05	-94.417	62.283	Powder	Ontario Geological Survey
FA71-080-01	-94.4	62.283	Powder	Ontario Geological Survey
FA71-080-04	-94.4	62.283	Powder	Ontario Geological Survey
FA71-081-01	-94.4	62.283	Powder	Ontario Geological Survey
FA71-081-04	-94.4	62.283	Powder	Ontario Geological Survey
FA71-083-04	-94.85	62.167	Powder	Ontario Geological Survey
FA71-083-06	-94.85	62.167	Powder	Ontario Geological Survey
FA71-083-07	-94.85	62.167	Powder	Ontario Geological Survey
FA71-084-01	-94.85	62.167	Powder	Ontario Geological Survey
FA71-085-01	-95.967	62.117	Powder	Ontario Geological Survey
FA71-085-04	-95.967	62.117	Powder	Ontario Geological Survey
FA71-086-04	-95.967	62.117	Powder	Ontario Geological Survey

FA71-087-01	-95.967	62.117		Powder	Ontario Geological Survey
FA71-087-05	-95.967	62.117		Powder	Ontario Geological Survey
FA71-088-02	-94.983	62.117		Powder	Ontario Geological Survey
FA71-088-02	-94.983	62.117		Rock	Ontario Geological Survey
FA71-090-04	-95.517	62.133		Powder	Ontario Geological Survey
FA71-086-02	-94.983	62.117		Powder	Ontario Geological Survey
LAA-91-T64	-94.848	62.163		Powder	Ontario Geological Survey
LAA-91-T65	-94.851	62.163		Rock	Ontario Geological Survey
PHA97-N87	-94.537	62.261		Powder	Ontario Geological Survey
PHA97-H10	-94.879	62.383		Powder	Ontario Geological Survey
PHA97-H49	-95.414	62.155		Powder	Ontario Geological Survey
PHA97-H50	-95.405	62.165		Powder	Ontario Geological Survey
PHA97-H50	-94.971	62.160		Powder	Ontario Geological Survey
PHA97-H50	-94.680	62.279		Rock	Ontario Geological Survey
PHA97-H51	-95.494	62.136		Powder	Ontario Geological Survey
PHA97-H51	-95.474	62.063		Powder	Ontario Geological Survey
PHA97-H52	-95.094	62.116		Powder	Ontario Geological Survey
PHA97-H52	-94.897	62.152		Powder	Ontario Geological Survey

Leopard Dyke Swarm

Sample Number	**Longitude (degrees E)**	**Latitude (degrees N)**	**Description**	**Sample type**	**Sample source**
BR1K	-107.167	44.571		Rock	Prof. Steve Harlan
BR3	-	-		Rock	Prof. Steve Harlan
BR3A	-	-		Rock	Prof. Steve Harlan
BR4C	-107.413	44.601		Rock	Prof. Steve Harlan
BR4I	-107.413	44.601		Rock	Prof. Steve Harlan
BR5	-	-		Rock	Prof. Steve Harlan
BR5K	-	-		Rock	Prof. Steve Harlan
BR6A	-107.42	44.621		Rock	Prof. Steve Harlan
NBH13A	-107.396	44.567		Rock	Prof. Steve Harlan
NBH13FA	-107.396	44.567		Rock	Prof. Steve Harlan
NBH13KA	-107.396	44.567		Rock	Prof. Steve Harlan
NBH13UNO	-107.396	44.567		Rock	Prof. Steve Harlan
NBH14	-107.374	44.587		Rock	Prof. Steve Harlan

NBH14B	-107.374	44.587		Rock	Prof. Steve Harlan
NBH14CB	-107.374	44.587		Rock	Prof. Steve Harlan
NBH1CB	-107.195	44.549		Rock	Prof. Steve Harlan
NBH2KA	-107.195	44.791		Rock	Prof. Steve Harlan
NBH3D	-107.471	44.785		Rock	Prof. Steve Harlan
NBH3UNOR	-107.471	44.785		Rock	Prof. Steve Harlan
NBH6A	-107.422	44.792		Rock	Prof. Steve Harlan
NBH7HB	-107.415	44.78		Rock	Prof. Steve Harlan

Matachewan Dyke Swarm

Sample Number	**Longitude (degrees E)**	**Latitude (degrees N)**	**Description**	**Sample type**	**Sample source**
37-A53	-83.690	47.030		Powder	Ontario Geological Survey
39-A33	-83.610	47.030		Powder	Ontario Geological Survey
44-A1	-83.550	47.030		Powder	Ontario Geological Survey
89M16B	-83.440	47.775		Powder	Ontario Geological Survey
89M16B-1A	-83.440	47.775		Powder	Ontario Geological Survey
89M18A	-83.491	47.775		Powder	Ontario Geological Survey
89M18A-1A	-83.491	47.775		Powder	Ontario Geological Survey
89M18C	-83.491	47.775		Powder	Ontario Geological Survey
89M21-A	-83.523	47.788		Powder	Ontario Geological Survey
89M21A-1A	-83.523	47.788		Powder	Ontario Geological Survey
89M22A	-83.529	47.789		Powder	Ontario Geological Survey
89M27A	-83.558	47.805		Powder	Ontario Geological Survey
89M27A-1A	-83.558	47.805		Powder	Ontario Geological Survey
89M31A	-83.702	47.827		Powder	Ontario Geological Survey
89M31A-W	-83.702	47.827		Powder	Ontario Geological Survey
89M33A-1A	-83.799	47.855		Powder	Ontario Geological Survey
89M34A	-83.865	47.861		Powder	Ontario Geological Survey
89M34A2	-83.865	47.861		Powder	Ontario Geological Survey
89M37I	-83.945	47.873		Powder	Ontario Geological Survey
89M39A	-83.997	47.888		Powder	Ontario Geological Survey
89M40A2	-84.096	47.892		Powder	Ontario Geological Survey
89M40D	-84.096	47.892		Powder	Ontario Geological Survey
89M40D-10	-84.096	47.892		Powder	Ontario Geological Survey
89M46B	-84.141	47.943		Powder	Ontario Geological Survey
89M47A	-84.148	47.943		Powder	Ontario Geological Survey

89M48B	-85.196	48.604		Powder	Ontario Geological Survey
89M52C	-84.967	48.641		Powder	Ontario Geological Survey
89M54A	-84.872	48.777		Powder	Ontario Geological Survey
89M55B	-84.776	49.266		Powder	Ontario Geological Survey
89M62A	-84.849	48.802		Powder	Ontario Geological Survey
89M63A	-84.848	48.791		Powder	Ontario Geological Survey
89M67A	-84.193	48.167		Powder	Ontario Geological Survey
89M73E	-84.090	48.180		Powder	Ontario Geological Survey
89M74-A	-84.119	48.159		Powder	Ontario Geological Survey
89M74A-10	-84.119	48.159		Powder	Ontario Geological Survey
89M77B	-84.039	48.155		Powder	Ontario Geological Survey
89M8B	-83.301	47.869		Powder	Ontario Geological Survey
FA62-009-02	-80.700	47.667		Powder	Ontario Geological Survey
FA62-013-02	-80.700	47.983		Powder	Ontario Geological Survey
FA62-026-04	-78.997	48.235		Powder	Ontario Geological Survey
FA62-032-03	-80.383	48.550		Powder	Ontario Geological Survey
FA62-038-01	-80.433	48.467		Powder	Ontario Geological Survey
FA62-041-02	-81.550	48.517		Powder	Ontario Geological Survey
FA62-042-02	-81.533	48.517		Powder	Ontario Geological Survey
FA62-077-01	-82.583	46.367		Powder	Ontario Geological Survey
FA63-045-01	-88.216	51.293		Powder	Ontario Geological Survey
FA65-035-01	-79.35	48.95		Powder	Ontario Geological Survey
FA65-036-01	-79.359	48.883		Powder	Ontario Geological Survey
FA65-037-01	-79.40	48.93		Powder	Ontario Geological Survey
FA65-037-02	-79.400	48.930		Powder	Ontario Geological Survey
HP15-8	-84.967	48.641		Powder	Ontario Geological Survey
HP19-1	-83.820	48.270		Powder	Ontario Geological Survey
HP3-6	-84.776	49.266		Powder	Ontario Geological Survey
HP7-3	-84.757	49.074		Powder	Ontario Geological Survey
HT27-A	-85.430	49.770		Powder	Ontario Geological Survey
KS23-1B	-83.500	48.434		Powder	Ontario Geological Survey
KS3-9	-83.536	48.422		Powder	Ontario Geological Survey
KS9-8C	-83.704	48.354		Powder	Ontario Geological Survey
MA001	-82.197	46.400	Fine grained dolerite	Rock	Jake Ciborowski
MA002	-82.197	46.405	Fine grained dolerite	Rock	Jake Ciborowski
MA003	-82.197	46.405	Fine grained dolerite	Rock	Jake Ciborowski

MA004	-81.954	46.384	Fine grained dolerite	Rock	Jake Ciborowski
MA005	-81.954	46.384	Fine grained dolerite	Rock	Jake Ciborowski
MA006	-81.953	46.386	Fine grained dolerite	Rock	Jake Ciborowski
MA16-6	-85.820	48.713		Powder	Ontario Geological Survey
MK14-10	-84.329	48.197		Powder	Ontario Geological Survey
MK46-5	-84.167	48.270		Powder	Ontario Geological Survey
MK4-8	-84.392	48.160		Powder	Ontario Geological Survey
MP12-5	-87.163	50.823		Powder	Ontario Geological Survey
OL1-2-4A	-87.169	50.866		Powder	Ontario Geological Survey
RL11-02-2	-83.060	46.902		Powder	Ontario Geological Survey
RL12-3-1	-83.045	46.902		Powder	Ontario Geological Survey
RL23-1-3	-83.326	46.847		Powder	Ontario Geological Survey
SL15-1	-84.900	48.283		Powder	Ontario Geological Survey
SL16-1	-84.933	48.300		Powder	Ontario Geological Survey
WA7-1	-84.728	48.063		Powder	Ontario Geological Survey

River Valley Intrusion

Sample Number	**Easting UTM 17T**	**Northing UTM 17T**	**Description** ***RV denotes sample collected from the River Valley intrusion**	**Sample type**	**Sample source**
RV001	527397	5152100	Shear-Zone Hosted Orthopyroxene Hornblendite Body	Rock	Jake Ciborowski
RV002	556066	5153940	Crerar Gneiss	Rock	Jake Ciborowski
RV003	556066	5153940	Crerar Gneiss	Rock	Jake Ciborowski
RV004	556050	5153980	Crerar Gneiss	Rock	Jake Ciborowski
RV005	554777	5168511	Nipissing Gabbro	Rock	Jake Ciborowski
RV006	554057	5170254	RV - Mylonitised Anorthosite	Rock	Jake Ciborowski
RV007	554057	5170254	RV - Mylonitised Anorthosite	Rock	Jake Ciborowski
RV008	559309	5167322	RV - Inclusion bearing unit	Rock	Jake Ciborowski
RV009	559309	5167322	RV - Inclusion bearing unit	Rock	Jake Ciborowski
RV010	562910	5158631	Red Cedar Lake Gneiss	Rock	Jake Ciborowski
RV011	554043	5170264	RV - Mylonitised Anorthosite	Rock	Jake Ciborowski
RV012	559785	5167228	Alkali Feldspar Granite	Rock	Jake Ciborowski
RV013	558650	5165205	RV - Coarse Grained Gabbronorite. Mineralised	Rock	Jake Ciborowski
RV014	559150	5167678	RV - Medium Grained matrix. Inclusion Bearing unit. Mineralised.	Rock	Jake Ciborowski
RV015	559145	5167685	RV - Medium Grained matrix. Inclusion Bearing unit. Mineralised.	Rock	Jake Ciborowski
RV016	558655	5165215	RV - Coarse Grained Gabbronorite. Mineralised	Rock	Jake Ciborowski
RV017	559149	5167677	RV - Fine Grained matrix. Inclusion Bearing unit. Mineralised.	Rock	Jake Ciborowski
RV018	559150	5167678	RV - Gabbronoritic inclusion. Inclusion Bearing unit. Mineralised.	Rock	Jake Ciborowski

RV019	558643	5165245	RV - Medium Grained matrix. Inclusion Bearing unit.	Rock	Jake Ciborowski
RV020	558644	5165393	RV - Medium Grained matrix. Inclusion Bearing unit.	Rock	Jake Ciborowski
RV021	559160	5167652	RV - Medium Grained matrix. Inclusion Bearing unit. Mineralised.	Rock	Jake Ciborowski
RV022	559913	5174428	Matachewan Dyke	Rock	Jake Ciborowski
RV023	559913	5174428	Matachewan Dyke	Rock	Jake Ciborowski
RV024	560005	5173855	Footwall Metasediments	Rock	Jake Ciborowski

APPENDIX B – LABORATORY METHODS USED IN THIS STUDY

B.1. Major and Trace element analysis

B.1.1. Preparation of rock samples into powder

Rock samples were prepared into powder using the rock preparation laboratories at Cardiff University. Weathered surfaces, veins and altered areas were removed from the sample using a diamond-bladed mechanical rock saw. Samples were then crushed to a coarse grit using a steel jaw crusher. Approximately 80 ml of this coarse crush fraction was milled to a fine powder in an agate planetary ball mill. Approximately 2 g of this fine powder was ignited for two hours in a furnace at 900°C to remove any volatile substances and determine loss on ignition (LOI) values for each sample (Equation B.1).

$$LOI(wt.\%) = \frac{Mass\,of\ wet\ powder - Mass\,of\ ignited\ \ powder}{Mass\,of\ wet\ powder} \times 100$$

Equation B.1

B.1.2. Preparation of solutions for ICP-OES and ICP-MS analysis

Samples in this study were prepared for ICP analysis using the lithium metaborate fusion method. 0.1 ± 0.001 g of each ignited sample was mixed with 0.6 ± 0.004 g of lithium metaborate flux in a platinum crucible. 3-4 drops of lithium iodide wetting agent were added to each mixture which was then fused using the Claisse Fluxy automated fusion system. Each mixture was then dissolved in a 50 ml solution of 20 ml of 10% HNO_3 and 30 ml of 18.2 Ω deionised water obtained using a Milli-Q purification system. After the mixture had fully dissolved, 1 ml of 100 ppm Rh spike was added to the solution which was then made up to 100 ml with 18.2 Ω deionised water. Approximately 20 ml of each solution was run on the ICP-OES to obtain major element and some trace element abundances. An aliquot of 1 ml of each solution was added to 1 ml of In and Tl and 8 ml of 2% HNO_3 and run on the ICP-MS to obtain trace element abundances. The instruments at Cardiff University used to analyse elemental abundances are a Jobin Yvon Horiba Ultima 2 inductively-coupled plasma optical emission spectrometer and a Thermo Elemental X7 series inductively-coupled plasma mass spectrometer. The samples were run on the mass spectrometers by Dr. Iain McDonald and Dr. Ley Woolley.

B.1.3. Evaluation of the accuracy and precision of the geochemical data

B.1.3.1. Standards

In order to assess the accuracy and precision of the whole-rock elemental data obtained by ICP-OES and ICP-MS external were analysed. The external standards used were JB-1a and NIM-G. JB-1a and NIM-G are a basalt and a granite respectively. The former is issued by the Geological Survey of Japan while NIM-G is issued by the South African Bureau of Standards. The certified element concentrations in JB-1a and NIM-G are given in Appendix C. These two standards were run in every batch of samples analysed mainly to assess the accuracy of the results but also to help determine the precision of the results.

B.1.3.2. Accuracy

All of the results from the different runs of standards JB-1a and NIM-G are given in Appendix C along with the percentage errors of the measured values compared with the certified values. The percentage error for each element was calculated using Equation B.2.

$$\%\,error = \frac{Difference\ between\ measured\ and\ certified\ concentrations\ of\ element}{Certified\ concentration\ of\ element} \times 100$$

Equation B.2

The vast majority of elements have percentage errors less than 5% for both analytical methods. This suggests that the sample analyses for all the batches can be considered accurate and can be relied upon during interpretation. The ICP-OES and ICP-MS methods gave very similar results for nearly all the elements which were measured on both machines.

B.1.3.3. Precision

The precision of the elemental data can be determined by examining the multiple analyses of the standards. The precision of a standard sample with respect to each element is represented by the relative standard deviation (RSD). The RSD is a percentage value and is calculated for each element using Equations B.3-B.5.

.

$$RSD\,(\%) = \frac{100s}{\bar{x}}$$

Equation B.3

Where x = the mean of each element; s = the standard deviation of each element.

The RSD for all the elements in the external and internal standards are given in Appendix C. The data for the standards in Appendix C show that the sample analyses for JB-1a are precise as the vast majority of elements have RSD less than 5%. Cu and Pb are the only analyses which may be considered imprecise as they have RSD > 10%. The equivalent data for standard NIM-G are not as consistently precise as the data for JB-1a. However, the majority of the elements analysed for in standard NIMG-G record RSD values < 10%. The exceptions to this are ICP-OES measured analyses of TiO_2, MnO and MgO. Both ICP-OES and ICP-MS analyses of NIM-G record imprecise (RSD > 10%) values for Sc, V, Cr, Co, Ni, Cu, Zn and Sr.

In summary, the repeated analyses of the external and internal standards generally have low RSD values and so the geochemical data obtained for this study can be considered precise. The standard analyses also show that there is little difference in the precision levels between the ICP-OES and ICP-MS methods.

B.2. Sr-Nd-Pb-Hf isotopic analysis

B.2.1. Sample selection and initial preparation

Care was taken in sample selection to choose the least altered samples that were representative of each of the principal studied layered intrusions of the Matachewan LIP. This was achieved by examining polished thin sections the major and trace element chemistry of all the rocks samples. Samples were initially cut using a diamond-bladed mechanical rock saw to remove any weathered surfaces. The samples were then crushed to a coarse grit using a steel jaw crusher and ground into a fine powder using an agate planetary ball mill. The initial preparation steps were conducted at Cardiff University.

B.2.2. Preparation for Sr-Nd-Pb isotopic analyses

B.2.2.1. Leaching

Samples were prepared for Sr-Nd-Pb isotopic analysis at the NERC Isotope Geosciences Laboratory (NIGL) in Keyworth under the supervision of Dr. Ian Millar. The methods for preparing samples for Sr-Nd-Pb isotopic analysis are described in detail in Royse et al. (1998) and Kempton & McGill (2002) and are only summarised here. Approximately 0.2 g of each sample was weighed out and then leached. Leaching the sample acts to remove secondary phases from slightly altered rocks and was achieved by adding ~5 ml of 6M HCl to each sample and heating at ~100°C for three hours. Each sample was then centrifuged at 4000 rpm for 5 minutes. After centrifugation, the acid leachate was removed and discarded and ~5 ml of deionised water added to the remaining sample material. After half an hour the water was removed and the samples were transferred to clean Savillex beakers ready for the sample dissolution step.

B.2.2.2. Sample dissolution

To dissolve silicate material strong acids need to be used. To each sample beaker, ~1 ml of Teflon-distilled (TD) 16M HNO_3 was added prior to the addition of ~4 ml of TD 29M HF. The beakers were sealed and placed on the hotplate at ~60°C overnight. After being taken off the hotplate and allowed to cool, the lids were removed and the beakers returned to the hotplate until the solutions had evaporated to leave behind a sample residue. Once dry, ~2 ml of TD 16M HNO_3 was added to each beaker on the hotplate and allowed to evaporate again. When dry, ~2 ml of TD 6M HCl was added to the beakers which were then sealed and kept on the hotplate for thirty minutes. The lids were then removed and the solutions allowed to evaporate a third time. 1 ml of 1M HBr was added to each beaker and then the beakers were sealed.

B.2.2.3. Chemical separation of Pb

To separate the Pb fraction from the rest of the sample anion exchange columns are used. The columns are pre-cleaned polypropylene tubes fitted with a porous polyethylene frit in the tip. After setting up the columns with waste beakers beneath, one column volume of quartz-distilled (QD) 6M HCl was added to each column and allowed to drain through. Then about five drops of pre-cleaned Dowex AG1-X8 resin were added to each column. The resin was then washed by adding one column volume of TD 6M HCl to each column and allowed to drain through. This was followed by adding one column volume of deionised water to each column and allowed to drain through. The acid wash and water wash were then repeated. Afterwards, half a column volume of 1M HBr was added to each column. Clean Savillex beakers were then placed under the columns.

Each sample (currently in 1 ml of 1M HBr- see previous step) was transferred to the columns using a clean pipette. Once the sample solution had eluted, half a column volume of 1M HBr was added to each column. When this had drained through, three-quarters of a column volume of 1M HBr was added to each column and allowed to drain through. The clean collector beakers were then removed and sealed and used for Sr and Nd chemical separation (see section B.3.4.). Clean Savillex beakers were placed under the columns to collect the Pb fraction. This was done by adding one column volume of TD 6M HCl and allowing to drain. 1 ml of TD 16M HNO_3 was pipetted into the Pb fraction beakers which were then transferred to the hotplate and the solutions allowed to evaporate to dryness.

B.2.2.4. Chemical separation of Sr and Nd

To separate Sr and Nd fractions from the rest of the sample quartz columns are used. The separation of Sr uses Dowex AG 50W-X8 resin and the separation of Nd uses S-X8 biobeads coated in bis diethylhexyl hydrogen phosphate (HDEHP).

Firstly the excess Br needs to be removed from the Sr-Nd fractions collected during the Pb chemical separation procedure. This was achieved by adding 2 ml of TD 16M HNO_3 to each sample beaker and then evaporated to dryness before adding 2 ml of 2.5M HCl to leave cold overnight.

The sample solutions were then transferred to a centrifuge tube and centrifuged for five minutes at 3000 rpm. Then 1.5 ml of the solution from the centrifuge tubes were added to the quartz columns with Dowex AG 50W-X8 resin. Afterwards, 1 ml of 2.5M HCl was added to each column to wash in the sample. This step was then repeated. An additional 45 ml of 2.5M HCl was added to each column and allowed to drain through. Clean Savillex beakers were then placed under each column and 9 ml of 2.5M HCl added to collect the Sr fraction. This solution was then evaporated to dryness on a hotplate. To collect the REE fraction, 10 ml of 6M HCl was eluted through the columns and collected in clean Savillex beakers before evaporation to dryness on a hotplate. 1 ml of 0.25M HCl was then added to each of these beakers. 0.5 ml of each solution was taken up by a clean pipette and loaded onto each quartz column with HDEHP-coated S-X8 biobeads and allowed to drain through the resin. Two steps of adding 0.5 ml of 0.25M HCl and allowing to drain through were then performed. After this, an additional 6.4 ml of 0.25M HCl was added and drained through. To collect the Nd fraction, 3.5 ml of 0.3M HCl was added to each column and collected in clean Savillex beakers. 2 μl of chlorophosphonazo III was then added to each solution before evaporation to dryness on a hotplate.

B.2.2.5. Loading

The Pb separates were dissolved in ~1 ml of 2% HNO_3 and doped with Tl solution in polystyrene cups that fit into the mass spectrometers. The Sr and Nd fractions were loaded onto outgassed Ta single and double filaments respectively. The filaments were outgassed at 3.5 A for ten minutes. When loading the Sr fraction, initially 1 μl of 1M H_3PO_4 was loaded onto the Ta filament at a current just below 1 A and dried to a small spot. 3 μl of deionised water was added to the Sr fraction and then 1 μl of this solution loaded onto the spot of H_3PO_4. When dried, the filament was turned to a current of ~2 A and held there for a few seconds until phosphoric fumes were liberated. For Nd, 2 μl of 0.6M HCl was added to the Nd fraction and then pipetted onto the filament which was turned up to a current just below 1 A. After the solution had dried, the current was turned down.

B.2.2.6. Mass spectrometric analysis

Analyses of Sr and Nd isotopes were carried out using the Thermo-Electron Triton 1 thermal ionisation mass spectrometer at NIGL. Analysis of Pb isotopes was carried out using the Nu Plasma multi-collector ICP-MS at NIGL. All samples were run on the mass spectrometers by Dr. Ian Millar.

B.2.3. Preparation for Hf isotopic analyses

B.2.3.1. Leaching

Samples were prepared for Hf isotopic analysis at NIGL under the supervision of Dr. Ian Millar. The method for preparing samples for Hf isotopic analysis is outlined in detail in Kempton et al. (2001) and is summarised here. Samples were weighed and leached using the same method described in section D.2.1.

B.2.3.2. Sample dissolution

2 ml of 16M HNO_3 was added to each sample beaker prior to the addition of 10 ml of 29M HF. The beakers were left on the hotplate overnight at ~120°C. After being allowed to cool the solutions were evaporated to dryness. 4 ml of 4N HF was added to each beaker and these were then sealed and agitated. The slurry was then transferred to centrifuge tubes and centrifuged at 4000 rpm for ninety minutes. The sample was then decanted into the centrifuge tubes and centrifuged again. A final 2 ml of 4N HF was added directly to the residues in the centrifuge tubes before a final centrifuging stage.

B.2.3.4. Chemical separation of Hf

The extraction of Hf from the rest of the sample was achieved using large anion exchange columns with BioRad anion exchange resin AG1-X8. Sample solutions were loaded on to the columns and the undesired elements were eluted by first adding 6 ml of 4N HF, then 200 ml of 4N HF, and then 30 ml of 4N HF. Solutions were then collected in clean Savillex beakers by adding 60 ml of 1N HF-1N HCl to each column. 30 µl of 36.6N H_2SO_4 was then added to each beaker and the solutions were dried down on the hotplate. Afterwards 1 ml of 0.52N H_2SO_4-5% H_2O_2 was added to each sample and the solutions pipetted into a second set of columns. The sample beakers were washed with 1 ml of 0.52N H_2SO_4-5% H_2O_2 and added to the appropriate columns. An additional 1 ml of 0.52N H_2SO_4-5%H_2O_2 was eluted through the columns, followed by 12 ml of the same solution. The Hf fraction was collected in the clean Savillex beakers by adding 13 ml of 1N HF-2N HCl to each column. The Hf solutions were then dried down on a hotplate.

B.2.3.5. Loading

The dry Hf fractions were transferred into 1 ml microcentrifuge tubes in a dilute solution of 2% HNO_3 and 0.1M HF and placed into the mass spectrometer.

B.2.4.6. Mass spectrometric analysis

Analysis of Hf isotopes was carried out using the VG Plasma P54 multi-collector ICP-MS at NIGL. The samples were run on the mass spectrometer by Dr. Ian Millar.

B.2.4. Age-correcting

Given the age of the Matachewan LIP suites it is necessary to age-correct the measured isotopic ratios. The necessary calculates required for isotopic age correction presented here were initially compiled by Matthew Minifie during his study of the Circum-Superior LIP (Minifie 2010).

B.2.4.1. Sr isotopes

To age-correct the Sr isotopic data the sum of all the Sr isotope ratios (with ^{86}Sr as the denominator) and the percentage of each isotope (^{84}Sr, ^{86}Sr, ^{87}Sr and ^{88}Sr) have to be calculated (Equations B.4 to B.8).

	Value	Reference
Sr isotopes		
$(^{88}\mathrm{Sr}/^{86}\mathrm{Sr})^{P}_{UR}$	8.375209	Steiger & Jager (1977)
$(^{84}\mathrm{Sr}/^{86}\mathrm{Sr})^{P}_{UR}$	0.056492	Thirlwall (1991)
^{88}Sr (amu)	87.9056167	de Laeter et al. (2003)
^{87}Sr (amu)	86.9088816	de Laeter et al. (2003)
^{86}Sr (amu)	85.9092647	de Laeter et al. (2003)
^{84}Sr (amu)	83.913426	de Laeter et al. (2003)
Rb (amu)	85.4678	Wieser (2006)
^{87}Rb (% abundance)	27.83	Rosman & Taylor (1998)
λ ^{87}Rb (y^{-1})	1.42×10^{-11}	Steiger & Jager (1977)
Nd isotopes		
$(^{142}\mathrm{Nd}/^{144}\mathrm{Nd})^{P}_{CHUR}$	1.141827	Wasserburg et al. (1981)
$(^{143}\mathrm{Nd}/^{144}\mathrm{Nd})^{P}_{CHUR}$	0.512638	DePaolo & Wasserburg (1976)
$(^{145}\mathrm{Nd}/^{144}\mathrm{Nd})^{P}_{CHUR}$	0.348417	Wasserburg et al. (1981)
$(^{146}\mathrm{Nd}/^{144}\mathrm{Nd})^{P}_{CHUR}$	0.7219	Wasserburg et al. (1981)
$(^{148}\mathrm{Nd}/^{144}\mathrm{Nd})^{P}_{CHUR}$	0.241578	Wasserburg et al. (1981)
$(^{150}\mathrm{Nd}/^{144}\mathrm{Nd})^{P}_{CHUR}$	0.236418	Wasserburg et al. (1981)
$(^{147}\mathrm{Sm}/^{144}\mathrm{Nd})^{P}_{CHUR}$	0.1967	DePaolo & Wasserburg (1976)
^{142}Nd (amu)	141.907719	de Laeter et al. (2003)
^{143}Nd (amu)	142.909810	de Laeter et al. (2003)
^{144}Nd (amu)	143.910083	de Laeter et al. (2003)
^{145}Nd (amu)	144.912569	de Laeter et al. (2003)
^{146}Nd (amu)	145.913113	de Laeter et al. (2003)
^{148}Nd (amu)	147.916889	de Laeter et al. (2003)

^{150}Nd (amu)	149.920887	de Laeter et al. (2003)
Sm (amu)	150.36	Wieser (2006)
^{147}Sm (% abundance)	14.99	Rosman & Taylor (1998)
λ ^{147}Sm (y^{-1})	6.54×10^{-12}	Lugmair & Marti (1978)
Pb isotopes		
^{204}Pb (amu)	203.973028	de Laeter et al. (2003)
^{206}Pb (amu)	205.974449	de Laeter et al. (2003)
^{207}Pb (amu)	206.975880	de Laeter et al. (2003)
^{208}Pb (amu)	207.976636	de Laeter et al. (2003)
U (amu)	238.02891	Wieser (2006)
Th (amu)	232.03806	Wieser (2006)
^{238}U (% abundance)	99.2745	Rosman & Taylor (1998)
^{235}U (% abundance)	0.72	Rosman & Taylor (1998)
^{232}Th (% abundance)	100	Rosman & Taylor (1998)
λ ^{238}U (y^{-1})	1.55125×10^{-10}	Steiger & Jager (1977)
λ ^{235}U (y^{-1})	9.8485×10^{-10}	Steiger & Jager (1977)
λ ^{232}Th (y^{-1})	4.9475×10^{-11}	Steiger & Jager (1977)
Hf isotopes		
$(^{174}Hf/^{177}Hf)^{P}_{CHUR}$	0.008659	Thirlwall & Anczkiewicz (2004)
$(^{176}Hf/^{177}Hf)^{P}_{CHUR}$	0.282772	Blichert-Toft & Albarede (1997)
$(^{178}Hf/^{177}Hf)^{P}_{CHUR}$	1.46734	Thirlwall & Anczkiewicz (2004)
$(^{179}Hf/^{177}Hf)^{P}_{CHUR}$	0.7325	Thirlwall & Anczkiewicz (2004)
$(^{180}Hf/^{177}Hf)^{P}_{CHUR}$	1.88676	Thirlwall & Anczkiewicz (2004)
$(^{176}Lu/^{177}Hf)^{P}_{CHUR}$	0.0332	Blichert-Toft & Albarede (1997)
^{174}Hf (amu)	173.940042	de Laeter et al. (2003)
^{176}Hf (amu)	175.941403	de Laeter et al. (2003)
^{177}Hf (amu)	176.9432204	de Laeter et al. (2003)
^{178}Hf (amu)	177.9436981	de Laeter et al. (2003)
^{179}Hf (amu)	178.9458154	de Laeter et al. (2003)
^{180}Hf (amu)	179.9465488	de Laeter et al. (2003)
Lu (amu)	174.9668	Wieser (2006)
^{176}Lu (% abundance)	2.59	Rosman & Taylor (1998)
λ ^{176}Lu (y^{-1})	1.865×10^{-11}	Scherer et al. (2001)

Table B.1. Values used in age-correcting the isotope data

$$\sum Sr = \left(\frac{^{84}Sr}{^{86}Sr}\right)^{P}_{UR} + \frac{^{86}Sr}{^{86}Sr} + \left(\frac{^{87}Sr}{^{86}Sr}\right)_{m} + \left(\frac{^{88}Sr}{^{86}Sr}\right)^{P}_{UR}$$

Equation B.4

Where; Σ Sr is the sum of Sr isotope ratios, the subscript m denotes the measured isotopic ratio and the subscript UR denotes the isotopic ratio of a uniform reservoir of chondritic composition at the present day (superscript P). The chondritic Sr isotopic ratios are given in **Table B.1.** The ^{86}Sr/^{86}Sr isotopic ratio is equal to 1.

$$\%^{84}Sr = \frac{100}{\sum Sr} \times \left(\frac{^{84}Sr}{^{86}Sr} \right)_{UR}^{P}$$

Equation B.5

$$\%^{86}Sr = \frac{100}{\sum Sr} \times \frac{^{86}Sr}{^{86}Sr}$$

Equation B.6

$$\%^{87}Sr = \frac{100}{\sum Sr} \times \left(\frac{^{87}Sr}{^{86}Sr} \right)_{m}$$

Equation B.7

$$\%^{88}Sr = \frac{100}{\sum Sr} \times \left(\frac{^{88}Sr}{^{86}Sr} \right)_{UR}^{P}$$

Equation B.8

The previous five equations are then used to calculate the atomic mass of Sr in each sample (Equation B.9).

$$Sr\ (amu) = \left(\frac{\%^{84}Sr}{100} \times {}^{84}Sr\,(amu) \right) + \left(\frac{\%^{86}Sr}{100} \times {}^{86}Sr\,(amu) \right) + \left(\frac{\%^{87}Sr}{100} \times {}^{87}Sr\,(amu) \right) + \left(\frac{\%^{88}Sr}{100} \times {}^{88}Sr\,(amu) \right)$$

Equation B.9

Where; the atomic mass of Sr is measured in atomic mass units (amu). The mass of each Sr isotope is given in Table B.1.

The next step is to calculate the ^{87}Rb/^{86}Sr ratio as follows (Equation B.10).

$$\frac{{}^{87}Rb}{{}^{86}Sr} = \frac{Rb}{Sr} \times \frac{Sr\ (amu)}{85.4678} \times \frac{27.83}{\%^{86}Sr}$$

Equation B.10

Where; Rb and Sr are the measured concentrations (ppm) of these elements in the leached sample and the numbers 85.4678 and 27.83 are the atomic mass of Rb (in amu) and the percentage abundance of ^{87}Rb respectively.

The final equation to calculate the initial Sr isotopic ratio is given below.

$$\left(\frac{{}^{87}Sr}{{}^{86}Sr}\right)_i = \left(\frac{{}^{87}Sr}{{}^{86}Sr}\right)_m - \frac{{}^{87}Rb}{{}^{86}Sr}\left(e^{\lambda t} - 1\right)$$

Equation B.11

Where; the subscripts i denotes the initial isotopic ratio, t is the age of the rock in years, and λ is the decay constant of ^{87}Rb (1.42×10^{-11} y^{-1}).

B.2.4.2. Nd isotopes

The equations below are used to age-correct the Nd isotopic data. Initially the sum of all the Nd isotope ratios (with ^{144}Nd as the denominator) and the percentage of each Nd isotope (^{142}Nd, ^{143}Nd, ^{144}Nd, ^{145}Nd, ^{146}Nd, ^{148}Nd and ^{150}Nd) needs to be known and are calculated using **Equations B.12-B.19**.

$$\sum Nd = \left(\frac{{}^{142}Nd}{{}^{144}Nd}\right)_{CHUR}^{P} + \left(\frac{{}^{143}Nd}{{}^{144}Nd}\right)_m + \frac{{}^{144}Nd}{{}^{144}Nd} + \left(\frac{{}^{145}Nd}{{}^{144}Nd}\right)_{CHUR}^{P} + \left(\frac{{}^{146}Nd}{{}^{144}Nd}\right)_{CHUR}^{P} + \left(\frac{{}^{148}Nd}{{}^{144}Nd}\right)_{CHUR}^{P} + \left(\frac{{}^{150}Nd}{{}^{144}Nd}\right)_{CHUR}^{P}$$

Equation B.12

where Σ Nd is the sum of Nd isotope ratios, the subscript m denotes the measured isotopic ratio and the subscript CHUR denotes the isotopic ratio of the chondritic uniform reservoir (CHUR) at the present day (superscript P). The Nd isotopic ratios of CHUR are given in Table D.1. The ^{144}Nd/^{144}Nd isotopic ratio is equal to 1.

$$\%^{142}Nd = \frac{100}{\sum Nd} \times \left(\frac{^{142}Nd}{^{144}Nd} \right)_{CHUR}^{P}$$

Equation B.13

$$\%^{143}Nd = \frac{100}{\sum Nd} \times \left(\frac{^{143}Nd}{^{144}Nd} \right)_{m}$$

Equation B.14

$$\%^{144}Nd = \frac{100}{\sum Nd} \times \frac{^{144}Nd}{^{144}Nd}$$

Equation B.15

$$\%^{145}Nd = \frac{100}{\sum Nd} \times \left(\frac{^{145}Nd}{^{144}Nd} \right)_{CHUR}^{P}$$

Equation B.16

$$\%^{146}Nd = \frac{100}{\sum Nd} \times \left(\frac{^{146}Nd}{^{144}Nd} \right)_{CHUR}^{P}$$

Equation B.17

$$\%^{148}Nd = \frac{100}{\sum Nd} \times \left(\frac{^{148}Nd}{^{144}Nd} \right)_{CHUR}^{P}$$

Equation B.18

$$\%^{150}Nd = \frac{100}{\sum Nd} \times \left(\frac{^{150}Nd}{^{144}Nd} \right)_{CHUR}^{P}$$

Equation B.19

The next step in the age-correction of Nd isotopes is to calculate the atomic mass of Nd in each sample **(Equation B.20)**.

$$Nd\ (amu) = \left(\frac{\%^{142}Nd}{100}\times{}^{142}Nd\,(amu)\right)+\left(\frac{\%^{143}Nd}{100}\times{}^{143}Nd\,(amu)\right)+$$
$$\left(\frac{\%^{144}Nd}{100}\times{}^{144}Nd\,(amu)\right)+\left(\frac{\%^{145}Nd}{100}\times{}^{145}Nd\,(amu)\right)+\left(\frac{\%^{146}Nd}{100}\times{}^{146}Nd\,(amu)\right)+$$
$$\left(\frac{\%^{148}Nd}{100}\times{}^{148}Nd\,(amu)\right)+\left(\frac{\%^{150}Nd}{100}\times{}^{150}Nd\,(amu)\right)$$

Equation B.20

Where; the atomic mass of Nd is measured in atomic mass units (amu). The mass of each Nd isotope is given in Table D.1.

The next equation calculates the ^{147}Sm/^{144}Nd ratio.

$$\frac{^{147}Sm}{^{144}Nd}=\frac{Sm}{Nd}\times\frac{Nd(amu)}{150.36}\times\frac{14.99}{\%^{144}Nd}$$

Equation B.21

Where; Sm and Nd are the measured concentrations (ppm) of these elements in the leached sample and the numbers 150.36 and 14.99 are the atomic mass of Sm (in amu) and the percentage abundance of ^{147}Sm respectively.

The final equation to calculate the initial Nd isotopic ratio is as follows.

$$\left(\frac{^{143}Nd}{^{144}Nd}\right)_i=\left(\frac{^{143}Nd}{^{144}Nd}\right)_m-\frac{^{147}Sm}{^{144}Nd}\left(e^{\lambda t}-1\right)$$

Equation B.22

Where; the subscript i denotes the initial Nd isotopic ratio, t is the age of the rock in years, and λ is the decay constant for ^{147}Sm (6.54×10^{-12} y^{-1}).

The initial epsilon Nd value is calculated using **Equation B.23**.

$$\varepsilon Nd_i = \left(\frac{\left(\frac{^{143}Nd}{^{144}Nd} \right)_i}{\left(\frac{^{143}Nd}{^{144}Nd} \right)_{CHUR}^{t}} - 1 \right) \times 10000$$

Equation B.23

Where; the subscript i denotes the initial isotopic ratio of the sample and $(^{143}Nd/^{144}Nd)_{CHUR}^{t}$ is the ^{143}Nd/^{144}Nd isotopic ratio of the chondritic uniform reservoir (CHUR) at the time (t) in years to which the rock sample has been age-corrected. The ^{143}Nd/^{144}Nd isotopic ratio of CHUR at time t can be calculated using **Equation B.22** by using the using the present day ^{143}Nd/^{144}Nd ratio of CHUR of 0.512638 and the ^{147}Sm/^{144}Nd ratio of CHUR of 0.1967 (DePaolo & Wasserburg, 1976).

B.2.4.3. Pb isotopes

To age-correct Pb isotope ratios the sum of the Pb isotope ratios (with ^{204}Pb as the denominator) needs to be known, as does the percentage of each Pb isotope (^{204}Pb, ^{206}Pb, ^{207}Pb and ^{208}Pb). These values are worked out using the following equations (Equations B.24 to B.28).

$$\sum Pb = \frac{^{204}Pb}{^{204}Pb} + \left(\frac{^{206}Pb}{^{204}Pb} \right)_m + \left(\frac{^{207}Pb}{^{204}Pb} \right)_m + \left(\frac{^{208}Pb}{^{204}Pb} \right)_m$$

Equation B.24

Where; Σ Pb is the sum of Pb isotope ratios, the subscript m denotes the measured isotopic ratio and the ^{204}Pb/^{204}Pb ratio is 1.

$$\%^{204}Pb = \frac{100}{\sum Pb} \times \frac{^{204}Pb}{^{204}Pb}$$

Equation B.25

$$\%^{206}Pb = \frac{100}{\sum Pb} \times \left(\frac{^{206}Pb}{^{204}Pb} \right)_m$$

Equation B.26

$$\%^{207}Pb = \frac{100}{\sum Pb} \times \left(\frac{^{207}Pb}{^{204}Pb} \right)_m$$

Equation B.27

$$\%^{208}Pb = \frac{100}{\sum Pb} \times \left(\frac{^{208}Pb}{^{204}Pb} \right)_m$$

Equation B.28

The next stage in the age-correction process for Pb isotope ratios is to calculate the atomic mass of Pb in each sample and this is achieved using the following equation.

$$Pb\ (amu) = \left(\frac{\%^{204}Pb}{100} \times {}^{204}Pb(amu) \right) + \left(\frac{\%^{206}Pb}{100} \times {}^{206}Pb(amu) \right) + \left(\frac{\%^{207}Pb}{100} \times {}^{207}Pb(amu) \right) + \left(\frac{\%^{208}Pb}{100} \times {}^{208}Pb(amu) \right)$$

Equation B.29

Where; the atomic mass of Pb is measured in atomic mass units (amu). The mass of each Pb isotope is given in **Table B.1**.

The following three equations calculate the $^{238}U/^{204}Pb$, $^{235}U/^{204}Pb$ and $^{232}Th/^{204}Pb$ ratios.

$$\frac{^{238}U}{^{204}Pb} = \frac{U}{Pb} \times \frac{Pb\ (amu)}{238.02891} \times \frac{99.2745}{\%^{204}Pb}$$

Equation B.30

Where; U and Pb are the measured concentrations of these elements (ppm) in the leached sample and the numbers 238.02891 and 99.2745 are the atomic mass of U (in amu) and the percentage abundance of ^{238}U respectively.

$$\frac{^{235}U}{^{204}Pb} = \frac{U}{Pb} \times \frac{Pb\ (amu)}{238.02891} \times \frac{0.72}{\%^{204}Pb}$$

Equation B.31

Where; the numbers 238.02891 and 0.72 are the atomic mass of U (in amu) and the percentage abundance of ^{235}U respectively.

$$\frac{^{232}Th}{^{204}Pb} = \frac{Th}{Pb} \times \frac{Pb\ (amu)}{232.03806} \times \frac{100}{\%^{204}Pb}$$

Equation B.32

Where; the numbers 232.03806 and 100 are the atomic mass of Th (in amu) and the percentage abundance of ^{232}Th respectively.

The final set of equations to calculate the initial Pb isotope ratios are as follows.

$$\left(\frac{^{206}Pb}{^{204}Pb}\right)_i = \left(\frac{^{206}Pb}{^{204}Pb}\right)_m - \frac{^{238}U}{^{204}Pb}\left(e^{\lambda t} - 1\right)$$

Equation B.33

Where; the subscript i denotes the initial Pb isotopic ratio and λ is the decay constant for ^{238}U and is 1.55125×10^{-10} y^{-1}.

$$\left(\frac{^{207}Pb}{^{204}Pb}\right)_i = \left(\frac{^{207}Pb}{^{204}Pb}\right)_m - \frac{^{235}U}{^{204}Pb}\left(e^{\lambda t} - 1\right)$$

Equation B.34

Where; λ is the decay constant for ^{235}U and is 9.8485×10^{-10} y^{-1}.

$$\left(\frac{^{208}Pb}{^{204}Pb}\right)_i = \left(\frac{^{208}Pb}{^{204}Pb}\right)_m - \frac{^{232}Th}{^{204}Pb}\left(e^{\lambda t} - 1\right)$$

Equation B.35

Where; λ is the decay constant for ^{232}Th and is 4.9475 × 10^{-11} y^{-1}.

B.2.4.4. Hf isotopes

Initially the sum of the Hf isotope ratios (with ^{177}Hf as the denominator) and the percentage of each isotope are calculated using the equations below.

$$\sum Hf = \left(\frac{^{174}Hf}{^{177}Hf}\right)^P_{CHUR} + \left(\frac{^{176}Hf}{^{177}Hf}\right)_m + \frac{^{177}Hf}{^{177}Hf} + \left(\frac{^{178}Hf}{^{177}Hf}\right)^P_{CHUR} + \left(\frac{^{179}Hf}{^{177}Hf}\right)^P_{CHUR} + \left(\frac{^{180}Hf}{^{177}Hf}\right)^P_{CHUR}$$

Equation B.36

Where; Σ Hf is the sum of Hf isotope ratios, the subscript m denotes the measured isotopic ratio and the subscript CHUR denotes the isotopic ratio of the chondritic uniform reservoir (CHUR) at the present day (superscript P). The Hf isotopic ratios of CHUR are given in Table B.1. The ^{177}Hf/^{177}Hf isotopic ratio is equal to 1.

$$\%^{174}Hf = \frac{100}{\sum Hf} \times \left(\frac{^{174}Hf}{^{177}Hf}\right)^P_{CHUR}$$

Equation B.37

$$\%^{176}Hf = \frac{100}{\sum Hf} \times \left(\frac{^{176}Hf}{^{177}Hf}\right)_m$$

Equation B.38

$$\%^{177}Hf = \frac{100}{\sum Hf} \times \frac{^{177}Hf}{^{177}Hf}$$

Equation B.39

$$\%^{178}Hf = \frac{100}{\sum Hf} \times \left(\frac{^{178}Hf}{^{177}Hf} \right)^{P}_{CHUR}$$

Equation B.40

$$\%^{179}Hf = \frac{100}{\sum Hf} \times \left(\frac{^{179}Hf}{^{177}Hf} \right)^{P}_{CHUR}$$

Equation B.41

$$\%^{180}Hf = \frac{100}{\sum Hf} \times \left(\frac{^{180}Hf}{^{177}Hf} \right)^{P}_{CHUR}$$

Equation B.42

The next stage is to determine the atomic mass of Hf in each sample and this is achieved using the following equation.

$$Hf\ (amu) = \left(\frac{\%^{174}Hf}{100} \times {}^{174}Hf(amu) \right) + \left(\frac{\%^{176}Hf}{100} \times {}^{176}Hf(amu) \right) + \left(\frac{\%^{177}Hf}{100} \times {}^{177}Hf(amu) \right) + \left(\frac{\%^{178}Hf}{100} \times {}^{178}Hf(amu) \right) + \left(\frac{\%^{179}Hf}{100} \times {}^{179}Hf(amu) \right) + \left(\frac{\%^{180}Hf}{100} \times {}^{180}Hf(amu) \right)$$

Equation B.43

Where; the atomic mass of Hf is measured in atomic mass units (amu). The mass of each Hf isotope is given in Table D.1.

The next equation is used to calculate the ^{176}Lu/^{177}Hf ratio.

$$\frac{^{176}Lu}{^{177}Hf} = \frac{Lu}{Hf} \times \frac{Hf(amu)}{174.9668} \times \frac{2.59}{\%^{176}Hf}$$

Equation B.44

Where; Lu and Hf are the measured concentrations of these elements (ppm) in the leached sample and the numbers 174.9668 and 2.59 are the atomic mass of Lu (in amu) and the percentage abundance of ^{176}Lu respectively.

The final equation to calculate the initial Hf isotopic ratio is given below.

$$\left(\frac{^{176}Hf}{^{177}Hf}\right)_i = \left(\frac{^{176}Hf}{^{177}Hf}\right)_m - \frac{^{176}Lu}{^{177}Hf}\left(e^{\lambda t} - 1\right)$$

Equation B.45

Where; the subscript i denotes the initial Hf isotopic ratio and λ is the decay constant for ^{176}Lu (1.865×10^{-11} y^{-1}).

The epsilon Hf value is calculated using the following equation.

$$\varepsilon Hf_i = \left(\frac{\left(\frac{^{176}Hf}{^{177}Hf}\right)_i}{\left(\frac{^{176}Hf}{^{177}Hf}\right)^t_{CHUR}} - 1\right) \times 10000$$

Equation B.46

Where; the subscript i denotes the initial isotopic ratio of the sample and $(^{176}\mathrm{Hf}/^{177}\mathrm{Hf})^t_{CHUR}$ is the ^{176}Hf/^{177}Hf isotopic ratio of the chondritic uniform reservoir (CHUR) at the time (t) in years to which the rock sample has been age-corrected. The ^{176}Hf/^{177}Hf isotopic ratio of CHUR at time t can be calculated using Equation B.42 by using the using the present day ^{176}Hf/^{177}Hf ratio of CHUR of 0.282772 and the ^{176}Lu/^{177}Hf ratio of CHUR of 0.0332 (Blichert-Toft & Albarede, 1997).

B.3. PGE analysis

Concentrations of the PGE and Au were determined by Ni sulphide fire assay with Te coprecipitation followed by analysis by ICP-MS following the methods describe by Huber et al. (2001). Mixtures made up of 6g of Na_2CO_3, 12g of borax, 0.9g of sulphur, 1.08g of carbonyl-purified Ni, and 2.5g of silica were required for fusion of 7.5g of crushed and milled sample material. These listed reagents were thoroughly mixed and transferred into a fire-clay crucible before being heated for 90 minutes at 1050°C. After cooling, the sulphide buttons were extracted from the crucibles and left to dissolve in concentrated HCl. The dissolved PGE and Au were coprecipitated with Te using $SnCl_2$ as a reductant. The resulting mixture was filtered under vacuum using the Satrorius filtration system before the solid filtrates were transferred to 27ml screw-top Teflon vials. To each sample was added 0.1ml of 2500ppb Tl spike to act as an internal standard to monitor for instrumental drift. 4ml primar grade HCl and 2ml of concentrated HNO_3 was added to each of the vials to form PGE chloro-complex solutions which were then run on the ICP-MS.

B.3.1. Evaluation of the accuracy and precision of the PGE data

B.3.1.1. Standards

In order to assess the accuracy and precision of the whole-rock PGE data obtained by ICP-MS external standards were analysed. The external standards used were TDB1 and WMG1. TDB1 and WMG1 are a basalt and a gabbro respectively. The certified element concentrations in TDB1 and WMG1 are given in Appendix C. These two standards were run in the two PGE sample batches analysed mainly to assess the accuracy of the results but also to help determine the precision of the results.

B.3.1.2. Accuracy

All of the results from the different runs of standards TDB1 and WMG1 are given in Appendix C along with the percentage errors of the measured values compared with the certified values. All of the elements measured of elements have percentage errors less than 5% for both analytical methods.

B.3.1.3. Precision

The RSD for all the elements in the external and internal standards are given in Appendix C. The data for the standards in Appendix C show that the sample analyses for WMG1 are quite precise as all of the elements have RSD less than or close to 10%. The equivalent data for standard TDB1 are similarly precise for Ir, Rh, Pd, Pt and Au but not for Ru which records and RSD value of ~44%. In summary, the repeated analyses of the external and internal standards generally have low RSD values and so the geochemical data obtained for this study can be considered precise.

B.4. References

Blichert-Toft, J. and Albarède, F., 1997. The Lu-Hf isotope geochemistry of chondrites and the evolution of the mantle-crust system. *Earth and Planetary Science Letters,* 148**,** 243-258.

De Laeter, J. R., Böhlke, J. K., De Bievre, P., Hidaka, H., Peiser, H. S., Rosman, K. J. R. and Taylor, P. D. P., 2003. Atomic weights of the elements: Review 2000. *Pure Appl. Chem,* 75**,** 683-800.

DePaolo, D. J. and Wasserburg, G. J., 1976. Nd isotopic variations and petrogenetic models. *Geophysical Research Letters,* 3**,** 249-252.

Huber, H., Koeberl, C., McDonald, I. and Reimold, W. U., 2001. Geochemistry and petrology of Witwatersrand and Dwyka diamictites from South Africa: Search for an extraterrestrial component:. *Geochimica et Cosmochimica Acta,* 65**,** 2007-2016.

Lugmair, G. W. and Marti, K., 1978. Lunar initial143Nd/144Nd: Differential evolution of the lunar crust and mantle. *Earth and Planetary Science Letters,* 39**,** 349-357.

Minifie, M. J., 2010. The Nature and Origin of the ~1880 Ma Circum-Superior Large Igneous Province. 545. Cardiff University.

Rosmana, K. J. R. and Taylor, P. D. P., 1998. Isotopie compositions of the elements 1997. *Pure and Appi. Chem,* 70**,** 217.

Scherer, E., Münker, C. and Mezger, K., 2001. Calibration of the lutetium-hafnium clock. *Science,* 293**,** 683-687.

Steiger, R. H. and Jäger, E., 1977. Subcommission on geochronology: convention on the use of decay constants in geochronology and cosmochronology. *Earth and Planetary Science Letters,* 36**,** 359-362.

Thirlwall, M. F., 1991. Long-term reproducibility of multicollector Sr and Nd isotope ratio analysis. *Chemical Geology: Isotope Geoscience section,* 94**,** 85-104.

Thirlwall, M. F. and Anczkiewicz, R., 2004. Multidynamic isotope ratio analysis using MC–ICP–MS and the causes of secular drift in Hf, Nd and Pb isotope ratios. *International Journal of Mass Spectrometry,* 235**,** 59-81.

Wasserburg, G. J., Jacousen, S. B., DePaolo, D. J., McCulloch, M. T. and Wen, T., 1981. Precise determination of SmNd ratios, Sm and Nd isotopic abundances in standard solutions. *Geochimica et Cosmochimica Acta,* 45**,** 2311-2323.

Wieser, M. E., 2006. Atomic weights of the elements 2005. *Pure Appl. Chem,* 78**,** 2051-2066.

Appendix C - Geochemical data used in this study

Suite	Sample	**SiO2**	**TiO2**	**Al2O3**	**Fe2O3**	**FeO**	**MnO**	**MgO**	**CaO**	**Na2O**	**K2O**	**P2O5**	LOI	Total	**Sc**	**V**	**Cr**	**Co**
		wt. %	wt. %	wt. %	wt. %	wt. %	wt. %	wt. %	wt. %	wt. %	wt. %	wt. %	wt. %	wt. %	ppm	ppm	ppm	ppm
Agnew Intrusion	**AG001**	50.52	0.24	26.98	4.30		0.06	1.51	12.72	2.88	0.67	0.03	1.37	101.27	8.4	47.1	15.1	15.4
Agnew Intrusion	**AG002**	46.46	0.34	16.06	11.61		0.17	10.73	9.49	1.38	0.40	0.04	2.37	99.05	18.8	92.6	167.4	60.7
Agnew Intrusion	**AG003**	50.28	0.47	24.58	6.29		0.09	2.89	12.96	2.36	0.31	0.04	0.80	101.08	17.7	121.5	103.6	22.8
Agnew Intrusion	**AG004**	49.18	0.33	24.21	6.35		0.08	3.10	11.27	2.79	1.03	0.02	1.33	99.70	11.7	88.8	82.6	26.7
Agnew Intrusion	**AG005**	52.77	0.72	15.32	11.08		0.16	6.20	10.54	2.47	0.53	0.06	0.77	100.62	37.3	209.6	198.4	42.7
Agnew Intrusion	**AG006**	50.19	0.38	13.26	13.65		0.18	7.40	12.25	1.67	0.31	0.04	0.75	100.09	43.9	189.8	164.1	49.7
Agnew Intrusion	**AG007**	50.24	0.20	15.82	8.90		0.15	8.50	10.18	2.35	0.40	0.01	1.71	98.47	24.8	325.6	187.1	47.3
Blue Draw Metagabbro	**BD001**	52.91	0.50	14.39	9.77		0.16	6.47	10.37	2.48	1.12	0.03	0.51	98.70	29.44	188.7	854.4	42.6
Blue Draw Metagabbro	**BD002**	53.60	0.52	14.62	9.97		0.16	6.10	10.40	2.60	1.10	0.06	0.59	99.74	30.07	205.3	126.9	39.1
Blue Draw Metagabbro	**BD003**	53.34	0.52	14.69	10.04		0.16	5.95	10.43	2.60	1.05	0.06	0.65	99.48	29.66	195.5	102.7	40.3
Blue Draw Metagabbro	**BD004**	55.58	0.75	13.47	11.09		0.17	5.52	9.12	2.41	1.25	0.10	0.53	99.98	30.83	221.5	356.5	40.5
Blue Draw Metagabbro	**BD005**	54.48	0.58	14.01	10.16		0.16	5.50	9.52	2.76	1.02	0.07	0.61	98.84	28.63	197.9	77.9	38.2
Blue Draw Metagabbro	**BD006**	54.41	0.57	14.16	9.95		0.15	5.58	8.93	3.11	1.32	0.08	0.63	98.88	28.55	196.9	163.6	33.6
Blue Draw Metagabbro	**BD007**	54.66	0.66	14.70	10.86		0.16	4.99	8.51	2.97	1.40	0.08	0.64	99.64	29.53	204.0	83.0	37.7
Blue Draw Metagabbro	**BD008**	53.64	0.63	13.73	12.61		0.17	5.31	9.20	2.64	1.07	0.08	0.61	99.68	31.99	205.9	128.8	40.8
Blue Draw Metagabbro	**BD009**	55.18	0.95	13.66	13.01		0.18	4.10	8.26	2.47	1.22	0.10	0.62	99.75	30.90	291.0	41.6	41.4
Blue Draw Metagabbro	**BD010**	54.05	0.56	13.84	11.99		0.17	5.39	7.86	3.37	1.48	0.08	0.61	99.41	29.90	192.6	363.1	38.2
Blue Draw Metagabbro	**BD011**	54.32	0.67	14.07	11.00		0.17	5.41	8.26	3.72	1.23	0.07	0.87	99.78	28.68	191.0	141.4	38.4
Blue Draw Metagabbro	**BD012**	56.49	1.43	13.49	13.35		0.18	3.56	6.81	3.00	1.60	0.13	0.60	100.64	29.91	296.4	33.5	41.0
Blue Draw Metagabbro	**BD013**	60.64	1.31	12.13	12.32		0.17	3.56	4.52	3.50	1.87	0.17	0.69	100.89	27.54	253.5	8.5	37.3
Blue Draw Metagabbro	**BD014**	61.00	1.16	13.26	10.57		0.13	3.20	3.64	3.88	2.26	0.18	0.71	99.98	24.59	196.9	19.2	29.4
Blue Draw Metagabbro	**BD015**	58.61	0.92	13.03	11.83		0.15	2.91	4.83	3.52	1.77	0.15	0.85	98.56	25.40	218.0	16.1	33.0
Blue Draw Metagabbro	**BD016**	60.09	1.47	12.66	12.52		0.15	2.67	4.45	3.15	2.17	0.18	0.63	100.13	23.12	264.82	18.99	37.71
Blue Draw Metagabbro	**BD017**	54.55	0.64	15.37	11.19		0.16	4.85	9.69	2.69	0.97	0.07	0.68	100.85	30.89	227.27	113.42	42.49
Blue Draw Metagabbro	**BD018**	53.40	0.53	14.78	9.97		0.16	6.36	10.07	2.75	1.04	0.07	0.66	99.79	29.60	179.71	126.32	40.75
Blue Draw Metagabbro	**BD019**	53.46	0.62	14.44	12.90		0.18	5.17	8.84	2.31	1.17	0.06	0.62	99.79	33.48	240.33	94.47	58.39
Blue Draw Metagabbro	**BD020**	55.43	0.56	12.67	9.84		0.17	8.14	10.19	2.67	0.80	0.06	0.69	101.21	32.69	222.43	599.55	46.84
Blue Draw Metagabbro	**BD021**	54.74	0.54	14.50	11.06		0.17	5.42	9.58	2.38	1.20	0.07	0.96	100.61	30.25	223.26	125.74	47.93
Blue Draw Metagabbro	**BD022**	55.28	0.71	15.37	7.87		0.12	7.27	6.44	4.69	0.40	0.08	3.04	101.26	30.42	199.71	146.01	31.16
Blue Draw Metagabbro	**BD023**	52.76	0.52	14.62	11.55		0.18	5.37	9.73	2.52	0.77	0.06	0.77	98.83	35.49	232.51	6.52	49.32
Blue Draw Metagabbro	**BD024A**	53.02	0.44	15.05	10.65		0.17	5.44	10.34	2.87	0.68	0.05	1.00	99.72	33.38	191.58	19.10	43.41
Blue Draw Metagabbro	**BD024B**	56.06	0.67	14.42	9.95		0.15	5.14	9.12	2.88	0.70	0.10	0.57	99.75	29.83	191.36	23.55	41.65
Blue Draw Metagabbro	**BD025**	54.12	0.61	13.25	10.63		0.16	6.99	10.22	2.74	0.74	0.06	0.51	100.02	32.87	229.41	431.81	45.29
Blue Draw Metagabbro	**BD026**	53.01	0.48	14.84	10.77		0.17	5.87	10.56	2.62	0.81	0.06	0.74	99.91	31.86	196.30	56.44	45.89
Blue Draw Metagabbro	**BD027**	52.90	0.57	12.57	10.44		0.16	8.24	10.71	2.07	0.73	0.06	0.97	99.41	33.21	205.67	512.70	42.65
Blue Draw Metagabbro	**BD028**	86.99	0.30	6.68	0.82		0.01	0.73	0.03	0.70	1.85	0.03	1.24	99.37	3.20	9.17	96.39	5.09
Blue Draw Metagabbro	**BD029**	43.82	0.46	6.00	11.06		0.20	26.50	6.54	0.13	0.03	0.06	5.23	100.02	21.96	93.77	2276.09	92.63
Blue Draw Metagabbro	**BD030**	41.61	0.28	4.83	12.13		0.18	32.30	0.30	0.01	0.01	0.03	8.37	100.03	15.85	51.85	2723.96	89.83
Blue Draw Metagabbro	**BD031**	36.81	0.18	3.20	10.98		0.14	33.93	1.85	0.02	0.00	0.02	12.22	99.35	10.98	47.78	2745.33	100.12
Blue Draw Metagabbro	**BD032**	36.74	0.17	3.16	10.90		0.14	34.80	2.06	0.00	0.00	0.02	12.45	100.44	10.84	47.67	2839.66	103.01
Blue Draw Metagabbro	**BD033**	41.95	0.19	3.39	12.20		0.16	28.35	2.22	0.02	0.03	0.02	12.27	100.80	11.69	72.35	3122.34	122.34
Blue Draw Metagabbro	**BD034**	42.24	0.19	3.42	12.20		0.16	28.03	2.20	0.03	0.04	0.03	11.10	99.65	12.02	87.97	3182.36	125.70

Blue Draw Metagabbro	**BD035**	42.77	0.15	2.64	12.26	0.15	29.94	0.93	0.01	0.01	0.01	11.58	100.43	10.21	72.78	3298.27	129.89
Blue Draw Metagabbro	**BD036**	35.20	0.12	2.17	11.06	0.15	36.24	1.11	0.00	0.00	0.01	11.93	97.98	8.40	43.08	2993.80	135.84
Blue Draw Metagabbro	**BD037**	37.45	0.12	2.43	10.84	0.13	38.94	0.10	0.01	0.00	0.01	11.18	101.20	8.86	43.44	3390.87	127.26
Blue Draw Metagabbro	**BD038**	35.46	0.11	1.91	11.30	0.14	38.22	0.55	0.00	0.00	0.01	11.40	99.11	7.84	31.79	3020.93	135.73
Blue Draw Metagabbro	**BD039**	37.04	0.11	1.97	11.24	0.16	38.24	0.64	0.00	0.00	0.02	11.60	101.01	8.14	35.05	3190.33	125.32
Blue Draw Metagabbro	**BD040**	36.76	0.11	1.99	11.60	0.14	38.52	0.19	0.00	0.00	0.01	11.04	100.35	8.10	36.42	3072.41	125.01
Blue Draw Metagabbro	**BD041**	35.86	0.12	1.89	10.41	0.13	38.22	2.18	0.01	0.00	0.01	12.14	100.97	8.52	27.42	2658.42	127.90
Blue Draw Metagabbro	**BD042**	35.70	0.11	1.92	11.31	0.11	38.99	0.31	0.07	0.00	0.02	12.42	100.97	7.75	26.86	2978.01	124.92
Blue Draw Metagabbro	**BD043**	52.13	0.25	3.49	8.50	0.20	19.95	12.75	1.11	0.04	0.02	3.02	101.46	44.25	222.40	1747.91	49.19
Blue Draw Metagabbro	**BD044**	50.58	0.28	3.44	8.24	0.18	19.88	13.07	0.99	0.03	0.02	3.58	100.29	45.15	225.93	1567.11	45.98
Blue Draw Metagabbro	**BD045**	49.80	0.32	4.05	9.28	0.19	17.75	13.19	0.80	0.04	0.01	3.72	99.14	51.59	253.82	926.70	52.85
Blue Draw Metagabbro	**BD046**	50.08	0.29	3.81	9.92	0.20	19.03	12.27	0.69	0.03	0.02	3.15	99.48	54.58	266.15	962.03	63.65
Blue Draw Metagabbro	**BD047**	49.38	0.31	4.76	8.97	0.19	18.27	13.63	1.36	0.05	0.02	3.48	100.42	47.61	236.18	1122.17	47.34
Blue Draw Metagabbro	**BD048**	52.01	0.43	13.38	9.43	0.15	9.97	8.62	3.58	0.14	0.05	1.59	99.33	35.14	245.28	609.36	43.01
Blue Draw Metagabbro	**BD049**	52.01	0.45	13.58	9.53	0.16	9.91	8.84	3.75	0.16	0.06	1.60	100.04	35.90	247.22	609.77	45.97
Blue Draw Metagabbro	**BD050**	51.40	0.47	10.89	10.86	0.17	11.85	10.30	2.56	0.12	0.06	1.40	100.08	39.91	256.02	1073.87	53.23
Blue Draw Metagabbro	**BD051**	51.88	0.28	6.11	12.40	0.19	17.16	6.99	0.11	0.03	0.02	3.39	98.57		94.90	970.90	50.80
Blue Draw Metagabbro	**BD052**	52.91	0.53	13.24	10.58	0.17	7.48	10.44	2.33	0.95	0.07	0.82	99.52		207.45	344.17	46.06
Blue Draw Metagabbro	**BD053**	51.59	0.48	14.41	9.97	0.17	7.54	11.25	2.43	0.72	0.04	0.80	99.41	31.31	200.32	325.60	47.48
Blue Draw Metagabbro	**BD054**	48.48	0.45	6.41	15.25	0.23	17.62	8.20	0.12	0.29	0.03	3.04	100.12		187.19	1036.52	64.78
Blue Draw Metagabbro	**BD055**	50.93	0.50	13.62	10.63	0.13	7.55	10.38	2.92	0.62	0.04	1.63	98.97	31.88	196.72	333.99	51.96
Blue Draw Metagabbro	**BD056**	51.07	0.53	13.49	10.52	0.15	7.79	9.39	3.52	0.75	0.06	2.31	99.59	32.35	195.17	298.04	46.10
Blue Draw Metagabbro	**BD057**	50.05	0.53	11.93	9.54	0.15	6.44	9.27	2.70	1.28	0.08	9.03	101.00	27.94	172.45	270.75	34.95
Blue Draw Metagabbro	**BD058**	52.28	0.59	12.07	10.08	0.16	6.44	8.08	3.04	1.26	0.04	7.13	101.18	30.56	212.59	287.08	41.00
Blue Draw Metagabbro	**BD059**	53.20	0.56	13.33	10.50	0.16	7.97	9.71	3.29	0.84	0.06	0.75	100.36	32.12	231.72	358.25	40.58
Blue Draw Metagabbro	**BD060**	89.41	0.17	5.18	1.39	0.03	0.82	0.42	2.12	0.04	0.02	0.65	100.25		24.33	69.20	4.67
Blue Draw Metagabbro	**BD061**	53.09	0.61	12.93	9.75	0.14	5.97	7.62	3.37	1.48	0.08	5.56	100.59	27.33	184.84	79.61	35.85
Blue Draw Metagabbro	**BD062**	54.25	0.71	13.39	13.43	0.17	5.15	7.23	4.11	0.77	0.09	0.81	100.11	33.20	236.61	42.67	49.99
Blue Draw Metagabbro	**BD063**	54.23	0.68	13.19	11.88	0.16	5.92	8.56	3.89	0.42	0.09	1.38	100.41	29.10	229.67	124.94	42.31
Blue Draw Metagabbro	**BD064**	56.27	0.77	14.32	10.18	0.11	6.13	4.39	5.20	1.15	0.12	1.46	100.11	31.71	244.72	131.79	28.78
Blue Draw Metagabbro	**BD065**	55.06	0.62	13.89	10.71	0.17	6.15	9.42	2.82	1.31	0.08	0.63	100.86	28.72	203.34	110.27	39.06
Blue Draw Metagabbro	**BD066**	61.08	1.25	12.23	11.69	0.15	3.38	4.49	2.60	2.52	0.17	1.12	100.68	21.10	192.71	24.15	31.55
Blue Draw Metagabbro	**BD067**	91.76	0.14	4.26	0.55	0.00	0.45	0.03	0.70	1.09	0.01	0.68	99.65	1.08	8.77	76.96	6.06
Blue Draw Metagabbro	**BD068**	93.34	0.06	3.71	0.25	0.00	0.16	0.04	0.29	1.33	0.04	0.89	100.12	0.52	8.83	49.37	5.33
Blue Draw Metagabbro	**BD069**	92.42	0.06	3.59	0.30	0.00	0.17	0.05	0.19	1.01	0.01	1.01	98.82	0.61	5.85	76.00	13.41
Blue Draw Metagabbro	**BD070**	93.14	0.08	4.24	1.02	0.00	0.27	0.03	0.05	1.13	0.02	1.11	101.08	1.23	12.96	91.03	3.87
Blue Draw Metagabbro	**BD071**	93.32	0.06	3.61	1.19	0.00	0.21	0.06	0.00	0.80	0.01	1.11	100.37	0.18	8.46	45.23	2.68
Blue Draw Metagabbro	**BD072**	89.51	0.06	4.92	0.90	0.00	0.26	0.10	0.71	1.85	0.42	1.21	99.94	0.98	20.15	27.24	2.34
Blue Draw Metagabbro	**BD073**	69.84	1.05	11.29	7.59	0.20	1.37	1.26	2.23	3.42	0.18	1.27	99.70	12.72	96.61	11.70	16.13
Blue Draw Metagabbro	**BD074**	64.24	1.24	12.47	10.86	0.13	2.05	3.74	2.70	2.66	0.19	0.78	101.07	18.66	186.26	35.31	26.50
Blue Draw Metagabbro	**BD075**	46.17	0.59	10.94	12.59	0.20	16.74	8.14	1.73	1.60	0.07	2.42	101.20	28.37	207.66	837.01	59.36
Blue Draw Metagabbro	**BD076**	59.13	1.03	12.96	12.57	0.16	2.80	6.44	3.11	1.82	0.12	0.77	100.92	24.88	229.53	10.61	37.79
Blue Draw Metagabbro	**BD077**	50.94	0.38	4.05	10.75	0.20	16.90	13.51	0.87	0.06	0.03	2.42	100.10	56.55	279.92	668.63	44.07
Blue Draw Metagabbro	**BD078**	54.40	0.25	8.94	7.89	0.15	12.06	10.06	0.73	0.22	0.01	4.41	99.11	37.87	208.20	641.90	32.21
Blue Draw Metagabbro	**BD079**	46.00	0.22	11.97	6.68	0.13	10.19	10.92	3.11	0.02	0.01	9.94	99.19	29.41	200.37	352.49	38.34

Blue Draw Metagabbro	**BD080**	48.14	0.31	13.69	7.92		0.12	9.46	8.28	3.32	0.12	0.02	8.56	99.93	33.54	192.42	254.40	39.13
Blue Draw Metagabbro	**BD081**	50.35	0.32	13.88	9.03		0.16	8.99	13.27	1.97	0.57	0.03	0.76	99.34	32.41	200.16	245.78	42.49
Blue Draw Metagabbro	**BD082**	51.06	0.35	14.33	8.59		0.16	8.39	13.08	2.25	0.39	0.03	1.58	100.21	31.00	173.34	203.03	40.49
Blue Draw Metagabbro	**BD083**	47.51	0.33	13.69	7.52		0.14	7.31	11.46	2.19	0.55	0.04	9.67	100.39	23.45	162.59	171.12	39.49
Blue Draw Metagabbro	**BD084**	52.27	0.34	14.68	8.19		0.15	8.22	12.76	2.12	0.56	0.05	1.08	100.42	28.07	178.67	174.47	41.18
Blue Draw Metagabbro	**BD085**	51.74	0.44	14.24	8.92		0.16	9.00	11.84	2.00	0.69	0.04	1.06	100.13	30.09	186.44	455.49	37.32
Blue Draw Metagabbro	**BD087**	50.89	0.45	9.12	11.33		0.18	15.34	7.63	1.99	0.05	0.05	2.78	99.80	32.86	215.88	675.83	53.77
Blue Draw Metagabbro	**BD088**	79.64	0.39	10.69	0.98		0.03	2.44	0.69	5.09	0.08	0.01	1.10	101.13	3.02	27.39	28.13	4.85
Blue Draw Metagabbro	**BD089**	92.63	0.15	3.51	0.99		0.01	0.78	0.14	1.40	0.05	0.01	0.57	100.24	1.14	12.39	74.34	6.75
Blue Draw Metagabbro	**BD090**	53.31	0.49	8.53	10.83		0.18	15.67	7.76	1.63	0.07	0.04	2.68	101.20	25.52	178.89	861.51	57.19
Blue Draw Metagabbro	**BD091**	52.75	0.37	8.40	10.74		0.18	13.38	10.22	1.64	0.45	0.03	1.98	100.14	34.06	245.81	628.74	57.81
Blue Draw Metagabbro	**BD092**	51.09	0.45	8.46	10.38		0.17	12.31	9.30	2.00	0.05	0.05	4.95	99.21	35.89	243.09	528.92	46.47
Blue Draw Metagabbro	**BD093**	47.49	0.29	13.37	7.73		0.14	7.77	10.09	3.39	0.05	0.03	10.30	100.64	24.89	159.78	275.00	30.01
Blue Draw Metagabbro	**BD094**	53.49	0.51	13.61	10.49		0.17	7.48	11.09	2.47	0.82	0.08	0.79	101.00	31.70	211.46	192.43	46.91
Blue Draw Metagabbro	**BD095**	52.39	0.42	14.45	9.95		0.17	6.96	11.72	2.54	0.67	0.05	0.70	100.04	30.65	209.13	79.09	46.34
Blue Draw Metagabbro	**BD096**	44.91	0.30	15.19	7.13		0.13	7.79	10.71	2.47	0.28	0.05	10.73	99.69	23.51	149.22	130.28	31.03
Blue Draw Metagabbro	**BD097**	49.93	0.33	16.72	9.09		0.16	9.25	11.17	2.56	0.42	0.06	1.45	101.12	29.47	167.38	159.97	41.73
Blue Draw Metagabbro	**BD098**	46.72	0.27	15.16	7.60		0.13	7.59	10.29	2.28	0.30	0.05	10.47	100.85	24.00	150.54	99.60	28.35
Blue Draw Metagabbro	**BD099**	49.27	0.38	11.00	9.86		0.15	15.38	6.98	3.03	0.08	0.05	3.04	99.22		193.03	1674.92	27.40
Blue Draw Metagabbro	**BD100**	52.09	0.39	5.77	11.49		0.21	17.09	9.65	0.79	0.21	0.05	2.18	99.92	36.80	232.51	2831.81	67.38
Blue Draw Metagabbro	**BD101**	51.99	0.42	6.70	11.04		0.21	16.04	8.80	1.43	0.28	0.06	2.02	98.98	36.23	219.74	1881.07	62.32
Blue Draw Metagabbro	**BD102**	52.15	0.41	7.21	11.12		0.20	15.53	9.46	1.45	0.38	0.05	2.39	100.33	39.80	241.31	1652.26	62.76
Blue Draw Metagabbro	**BD103**	84.91	0.28	8.21	0.60		0.00	0.81	0.08	4.10	0.09	0.05	0.86	100.01		16.10	87.38	4.55
Blue Draw Metagabbro	**BD104**	52.56	0.49	16.43	9.58		0.16	7.52	10.14	2.74	0.99	0.08	0.70	101.38	29.05	199.75	129.09	43.25
Blue Draw Metagabbro	**BD105**	45.64	0.13	2.77	10.81		0.14	28.70	1.58	0.03	0.01	0.03	11.23	101.07		80.19	5219.24	98.56
East Bull Lake Intrusion	**EB001**	51.37	0.83	13.48	12.96		0.20	6.84	9.99	1.90	1.18	0.10	1.38	100.23	42.2	269.6	193.5	47.4
East Bull Lake Intrusion	**EB002**	49.24	0.38	22.77	5.93		0.09	0.65	18.26	1.37	0.19	0.06	1.08	100.01	6.9	151.7	10.4	6.1
East Bull Lake Intrusion	**EB003**	48.54	0.33	11.89	14.41		0.21	11.03	9.63	1.35	0.46	0.02	1.86	99.74	37.2	165.7	257.3	77.4
East Bull Lake Intrusion	**EB004**	46.12	0.19	18.20	10.08		0.15	9.46	9.23	1.82	0.53	0.03	3.14	98.94	14.7	94.0	104.7	54.2
East Bull Lake Intrusion	**EB005**	48.50	0.18	24.44	4.86		0.09	4.18	12.77	2.38	0.64	0.02	1.71	99.77	16.9	87.4	412.1	22.8
East Bull Lake Intrusion	**EB006**	45.32	0.25	14.81	13.37		0.21	11.62	8.23	1.18	0.31	0.03	3.61	98.95	15.0	106.2	64.5	79.8
East Bull Lake Intrusion	**EB007**	49.82	0.41	23.45	4.45		0.07	4.01	11.85	3.24	0.60	0.05	1.37	99.34	11.29	88.6	26.2	21.8
Gerow Intrusion	**GE001**	48.58	0.80	15.01	11.76		0.19	7.39	11.20	2.36	0.29	0.04	1.67	99.30	43.6	263.4	426.9	35.5
Gerow Intrusion	**GE002**	48.61	1.06	14.20	13.62		0.21	7.12	9.54	2.06	0.79	0.07	1.59	98.88	42.6	268.3	259.7	50.7
Gerow Intrusion	**GE003**	52.22	0.70	15.03	10.71		0.17	6.90	9.03	2.30	0.62	0.03	2.02	99.75	38.0	185.9	365.2	39.5
Gerow Intrusion	**GE004**	52.28	0.55	13.09	10.50		0.16	8.23	10.83	1.42	0.43	0.02	1.66	99.17	42.3	177.5	372.1	39.0
Gerow Intrusion	**GE005**	52.43	0.69	14.07	10.76		0.16	8.03	6.53	3.88	0.22	0.08	2.27	99.11	46.7	188.2	271.5	29.4
Gerow Intrusion	**GE006**	49.96	1.07	17.57	12.88		0.15	4.41	7.87	3.47	0.86	0.09	1.97	100.30	34.0	330.5	7.8	36.6
Kaminak Dyke Swarm	**FA71-063-04**	49.58	1.12	14.50	14.76		0.19	5.80	9.77	3.11	0.73	0.08	0.26	99.91	34.8	254.3	69.2	54.7
Kaminak Dyke Swarm	**FA71-063-07**	48.89	1.24	14.01	15.07		0.20	5.17	9.30	3.05	1.16	0.11	1.10	99.28	35.8	274.1	52.8	53.8
Kaminak Dyke Swarm	**FA71-064-07**	46.62	1.12	15.33	14.18		0.19	5.90	10.25	2.80	0.73	0.08	1.91	99.11	32.8	238.5	76.6	55.5
Kaminak Dyke Swarm	**FA71-065-01**	48.46	1.10	15.05	14.58		0.19	5.84	9.09	3.99	0.34	0.08	2.11	100.82	28.5	194.7	25.2	65.6
Kaminak Dyke Swarm	**FA71-065-04**	48.72	1.00	15.73	14.28		0.18	6.00	8.78	3.17	1.22	0.08	1.30	100.45	27.4	184.4	38.7	56.0
Kaminak Dyke Swarm	**FA71-066-04**	50.05	1.61	14.21	16.51		0.21	4.14	8.72	3.33	1.26	0.19	0.84	101.10	33.3	218.7	20.0	55.9
Kaminak Dyke Swarm	**FA71-066-07**	49.64	1.69	13.85	16.49		0.21	3.77	7.09	4.15	1.28	0.23	1.47	99.87	33.0	202.1	18.2	50.4

Kaminak Dyke Swarm	**FA71-067-01**	50.92	1.47	14.16	15.41		0.19	4.23	8.19	3.10	1.67	0.16	0.94	100.44	32.3	239.3	25.6	53.0
Kaminak Dyke Swarm	**FA71-067-04**	46.64	1.15	14.98	14.32		0.18	5.07	9.01	2.96	0.95	0.09	1.31	96.66	28.7	212.1	35.4	51.0
Kaminak Dyke Swarm	**FA71-068-04**	47.08	1.15	15.69	15.12		0.19	6.27	9.47	3.17	1.00	0.08	1.19	100.42	29.6	207.6	38.4	56.9
Kaminak Dyke Swarm	**FA71-069-04**	47.81	1.08	15.81	14.58		0.18	6.12	9.65	2.78	1.03	0.08	1.66	100.79	29.1	194.6	37.4	55.4
Kaminak Dyke Swarm	**FA71-069-07**	48.38	1.11	14.78	14.62		0.18	5.53	9.83	2.60	0.67	0.09	1.68	99.47	28.6	201.1	36.4	52.7
Kaminak Dyke Swarm	**FA71-070-07**	48.06	1.00	16.88	13.51		0.17	5.41	9.73	3.33	0.58	0.06	1.54	100.28	32.3	217.8	58.0	54.9
Kaminak Dyke Swarm	**FA71-072-04**	48.24	1.16	15.21	14.50		0.19	5.87	9.76	3.03	0.94	0.08	1.23	100.21	33.0	234.3	65.0	51.3
Kaminak Dyke Swarm	**FA71-072-07**	45.42	0.99	17.04	14.27		0.17	5.39	10.08	4.06	0.37	0.06	1.83	99.69	31.4	214.3	75.5	52.2
Kaminak Dyke Swarm	**FA71-073-01**	49.76	1.56	13.72	16.11		0.20	4.02	8.63	2.67	1.56	0.17	0.77	99.17	31.4	214.2	21.0	57.6
Kaminak Dyke Swarm	**FA71-073-04**	49.62	1.51	13.68	15.56		0.19	4.17	8.00	3.16	1.29	0.16	1.00	98.33	31.2	214.6	25.8	56.1
Kaminak Dyke Swarm	**FA71-074-01**	51.58	1.74	13.30	16.92		0.20	3.33	7.57	3.22	1.61	0.23	0.16	99.87	33.0	224.3	12.7	56.4
Kaminak Dyke Swarm	**FA71-074-04**	51.57	1.91	13.40	17.02		0.20	3.14	7.43	3.48	1.55	0.24	0.46	100.38	33.8	235.6	9.6	59.9
Kaminak Dyke Swarm	**FA71-075-01**	52.14	1.73	12.73	16.75		0.21	2.94	7.50	3.72	1.61	0.17	0.30	99.79	37.9	364.9	3.9	51.5
Kaminak Dyke Swarm	**FA71-075-02**	52.60	1.75	13.14	17.06		0.21	2.89	7.29	3.64	1.53	0.20	0.44	100.75	38.0	367.8	6.5	52.8
Kaminak Dyke Swarm	**FA71-075-06**	52.26	1.74	13.20	16.54		0.21	2.94	7.47	3.74	1.49	0.15	0.36	100.11	37.8	368.0	4.8	51.9
Kaminak Dyke Swarm	**FA71-076-01**	49.35	1.24	14.27	15.52		0.19	5.65	6.38	5.00	0.44	0.10	2.08	100.23	34.0	255.0	56.2	56.0
Kaminak Dyke Swarm	**FA71-076-04**	47.90	1.15	14.91	14.62		0.18	5.40	9.81	2.67	0.97	0.09	1.53	99.23	31.7	243.2	58.7	54.0
Kaminak Dyke Swarm	**FA71-077-07**	46.38	1.19	15.38	14.35		0.18	6.00	9.70	3.20	1.60	0.10	2.15	100.23	29.8	209.4	63.2	52.2
Kaminak Dyke Swarm	**FA71-078-04**	50.84	1.99	13.00	17.12		0.20	4.15	6.07	4.14	1.19	0.20	2.10	101.00	37.4	249.6	17.4	57.3
Kaminak Dyke Swarm	**FA71-079-02**	46.93	1.10	15.59	14.50		0.19	5.87	9.80	3.00	1.10	0.08	1.25	99.42	28.0	190.9	36.5	53.9
Kaminak Dyke Swarm	**FA71-079-05**	48.57	1.23	14.74	14.94		0.19	5.14	8.92	3.28	1.06	0.11	1.10	99.26	31.2	210.4	35.2	50.8
Kaminak Dyke Swarm	**FA71-080-01**	48.22	1.24	14.67	15.33		0.18	5.03	8.80	2.97	1.44	0.11	0.92	98.91	29.6	208.7	41.4	53.3
Kaminak Dyke Swarm	**FA71-080-04**	48.38	1.14	15.84	14.50		0.18	5.25	9.22	3.14	1.23	0.08	0.95	99.91	27.6	185.2	31.8	54.2
Kaminak Dyke Swarm	**FA71-081-01**	49.49	1.17	14.61	14.91		0.18	5.17	9.16	2.73	1.20	0.10	1.18	99.89	30.3	202.9	34.5	48.1
Kaminak Dyke Swarm	**FA71-081-04**	48.05	1.19	14.85	14.73		0.19	5.64	9.09	3.05	1.56	0.09	1.03	99.48	30.8	206.1	36.5	53.0
Kaminak Dyke Swarm	**FA71-083-04**	48.67	1.13	15.13	14.70		0.19	6.01	9.21	3.03	0.80	0.08	0.64	99.59	31.9	233.2	75.9	51.7
Kaminak Dyke Swarm	**FA71-083-06**	47.74	1.10	15.14	14.85		0.19	6.05	9.23	3.07	0.91	0.08	0.74	99.09	33.1	234.0	73.0	52.8
Kaminak Dyke Swarm	**FA71-083-07**	46.58	1.12	16.52	14.25		0.17	6.08	8.30	4.38	0.20	0.08	2.37	100.05	33.2	239.9	77.9	54.9
Kaminak Dyke Swarm	**FA71-084-01**	49.11	1.23	14.31	15.73		0.21	5.11	9.37	3.15	0.97	0.11	0.29	99.57	35.8	282.0	50.4	55.8
Kaminak Dyke Swarm	**FA71-085-01**	48.05	1.26	14.93	14.76		0.18	4.84	8.97	2.95	1.54	0.11	1.70	99.29	31.8	216.2	42.4	49.7
Kaminak Dyke Swarm	**FA71-085-04**	48.36	1.30	14.74	15.22		0.20	5.31	8.80	3.41	1.14	0.12	1.72	100.32	32.3	222.1	50.3	53.8
Kaminak Dyke Swarm	**FA71-086-02-04**	48.57	1.38	14.94	15.88		0.19	4.66	8.24	3.37	1.21	0.12	1.73	100.29	31.2	209.4	29.2	56.2
Kaminak Dyke Swarm	**FA71-086-04**	48.50	1.42	15.25	15.91		0.19	4.73	8.64	3.25	1.13	0.14	1.73	100.90	31.9	214.5	32.6	55.7
Kaminak Dyke Swarm	**FA71-087-01**	48.36	1.38	14.64	16.20		0.20	5.29	8.78	3.07	0.85	0.13	1.43	100.32	32.3	214.3	32.4	52.7
Kaminak Dyke Swarm	**FA71-087-05**	48.90	1.35	14.97	14.89		0.18	4.69	9.11	3.09	1.42	0.13	0.97	99.71	31.1	211.3	31.1	54.8
Kaminak Dyke Swarm	**FA71-088-02**	48.00	1.16	15.70	14.80		0.20	5.81	8.29	3.37	1.56	0.08	2.02	100.99	30.7	205.8	37.3	55.3
Kaminak Dyke Swarm	**FA71-088-02B**	51.35	1.75	14.10	16.20		0.19	3.35	8.21	2.40	1.50	0.22	1.25	100.52	32.2	233.2	13.8	53.0
Kaminak Dyke Swarm	**FA71-090-04**	49.43	1.31	15.48	14.47		0.19	4.72	9.68	2.78	1.06	0.12	1.23	100.47	30.9	201.2	30.9	55.0
Kaminak Dyke Swarm	**LAA-91-T64-14**	49.65	1.20	14.61	14.69		0.19	5.76	9.29	2.54	0.72	0.13	0.71	99.50	30.9	256.0	87.5	66.7
Kaminak Dyke Swarm	**LAA-91-T65-3A**	50.85	1.19	14.58	15.28		0.21	5.74	9.06	2.85	0.95	0.15	0.55	101.42	34.4	282.3	89.0	66.2
Kaminak Dyke Swarm	**PHA97-H108**	53.16	1.71	13.51	15.20		0.18	3.06	6.49	2.90	2.23	0.25	1.29	99.96	30.2	244.4	18.3	50.6
Kaminak Dyke Swarm	**PHA97-H492A**	53.97	2.10	12.58	16.15		0.18	2.30	6.30	2.99	2.21	0.33	0.77	99.88	28.9	272.4	8.7	49.8
Kaminak Dyke Swarm	**PHA97-H502B**	53.83	2.09	12.89	16.16		0.18	2.17	6.73	2.57	1.85	0.34	0.80	99.60	29.9	268.3	9.3	50.1
Kaminak Dyke Swarm	**PHA97-H505B**	49.42	1.21	15.06	14.86		0.19	5.73	8.27	2.31	0.93	0.13	1.87	99.99	27.7	207.8	38.1	66.8
Kaminak Dyke Swarm	**PHA97-H506B**	51.03	1.63	13.22	16.26		0.19	4.00	8.42	2.63	1.25	0.22	1.36	100.22	31.8	287.7	14.8	59.7

Kaminak Dyke Swarm	**PHA97-H512A**	49.13	1.14	14.91	14.60		0.19	5.98	8.98	2.58	0.85	0.14	1.04	99.55	29.5	244.4	63.2	60.8
Kaminak Dyke Swarm	**PHA97-H513A**	53.30	1.82	12.63	16.85		0.20	2.99	7.28	2.67	1.40	0.28	0.54	99.97	30.4	238.5	11.9	56.3
Kaminak Dyke Swarm	**PHA97-H520**	49.14	1.12	15.43	14.77		0.19	6.07	8.69	2.59	0.86	0.12	1.02	100.00	26.5	193.3	35.8	68.1
Kaminak Dyke Swarm	**PHA97-H522B**	50.54	1.40	14.01	15.62		0.19	4.50	8.45	2.30	1.46	0.16	1.07	99.72	31.1	240.4	40.7	58.2
Kaminak Dyke Swarm	**PHA97-N87**	49.51	1.17	15.00	15.40		0.20	5.62	8.79	2.93	0.92	0.22	0.98	100.74	31.0	255.2	57.6	75.3
Leopard Dyke Swarm G1	**BR1K**	47.32	0.42	26.97	5.07		0.08	2.40	9.94	1.78	3.85	0.03	3.10	100.98	13.3	85.7	97.1	19.9
Leopard Dyke Swarm G1	**BR3**	49.53	1.16	16.48	11.80		0.18	6.10	10.01	2.38	0.37	0.10	0.94	99.04	32.5	277.9	199.0	41.9
Leopard Dyke Swarm G1	**BR3A**	48.46	0.88	18.82	9.41		0.18	5.47	11.19	2.20	2.20	0.08	2.34	101.23	29.6	157.9	176.6	43.7
Leopard Dyke Swarm G1	**BR4C**	48.89	0.48	26.71	5.59		0.09	2.90	13.51	2.40	0.33	0.03	0.41	101.33	15.3	104.1	72.4	20.7
Leopard Dyke Swarm G1	**BR4I**	48.58	0.46	25.90	5.73		0.10	3.04	12.03	2.27	1.66	0.04	1.38	101.19	15.1	104.1	80.1	21.2
Leopard Dyke Swarm G1	**BR5**	49.54	0.79	20.63	8.85		0.14	4.48	11.06	2.47	0.39	0.06	0.03	98.44	24.9	161.8	91.9	30.5
Leopard Dyke Swarm G1	**BR5K**	50.54	1.04	15.68	12.40		0.20	6.95	10.34	2.56	0.44	0.09	0.40	100.62	38.5	255.2	176.4	46.6
Leopard Dyke Swarm G1	**BR6A**	47.16	0.37	27.16	4.63		0.07	2.38	12.63	2.27	0.60	0.03	2.20	99.51	12.0	83.2	72.4	17.6
Leopard Dyke Swarm G1	**NBH13A**	48.61	0.52	25.46	6.01		0.10	2.39	13.20	2.19	0.79	0.04	1.81	101.11	15.8	116.1	137.1	23.5
Leopard Dyke Swarm G1	**NBH13FA**	47.78	0.33	28.40	4.00		0.06	1.62	12.69	1.96	1.67	0.02	2.14	100.68	9.2	103.5	47.9	15.6
Leopard Dyke Swarm G1	**NBH13KA**	48.26	0.49	25.27	6.24		0.09	2.79	12.80	2.12	0.51	0.04	1.35	99.97	14.9	112.4	50.7	24.7
Leopard Dyke Swarm G1	**NBH13UNOR**	47.94	0.73	22.06	9.22		0.13	4.34	11.28	2.05	0.37	0.06	2.13	100.32	20.3	139.2	71.5	34.8
Leopard Dyke Swarm G1	**NBH1CB**	48.17	0.72	21.23	8.24		0.12	3.70	11.95	1.85	0.85	0.06	2.43	99.32	21.1	157.7	199.9	33.3
Leopard Dyke Swarm G1	**NBH2KA**	47.96	0.77	20.68	8.93		0.13	4.28	11.55	1.68	1.26	0.06	2.58	99.89	22.8	158.3	197.0	40.5
Leopard Dyke Swarm G1	**NBH3D**	50.19	1.26	14.83	14.56		0.21	6.72	9.99	2.14	0.32	0.10	0.84	101.18	38.5	252.1	224.7	57.0
Leopard Dyke Swarm G1	**NBH3UNOR**	49.43	1.22	14.22	14.29		0.21	6.70	9.93	2.03	0.29	0.10	0.89	99.31	37.6	247.3	234.7	57.0
Leopard Dyke Swarm G1	**NBH6A**	50.01	1.02	14.65	12.86		0.18	6.62	9.86	1.97	0.40	0.08	1.50	99.15	36.3	225.5	262.4	51.8
Leopard Dyke Swarm G1	**NBH7HB**	49.42	0.99	15.18	12.57		0.19	6.95	10.28	2.06	0.38	0.08	0.97	99.07	36.2	220.2	327.0	51.1
Leopard Dyke Swarm G2	**NBH14**	60.83	1.29	15.28	8.32		0.09	2.38	2.49	5.69	0.63	0.49	1.95	99.44	12.1	110.0	62.8	12.8
Leopard Dyke Swarm G2	**NBH14B**	58.17	1.37	15.08	8.90		0.10	2.34	4.02	4.63	0.98	0.46	3.39	99.41	12.2	136.4	199.1	15.9
Leopard Dyke Swarm G2	**NBH14CB**	59.12	1.38	15.70	8.85		0.09	2.40	2.86	5.14	0.98	0.54	2.42	99.49	12.2	124.0	52.5	17.4
Matachewan Dyke Swarm G1	**44-A1**	52.02	1.24	14.32	15.09		0.23	4.56	7.71	2.46	0.70	0.14	1.44	99.92	38.5	306.6	94.7	57.1
Matachewan Dyke Swarm G1	**89M168-1A**	53.22	1.72	12.06	16.21		0.22	3.83	7.52	2.63	1.19	0.23	0.29	99.13	36.4	339.2	30.6	56.5
Matachewan Dyke Swarm G1	**89M16B**	52.89	1.68	12.87	16.26		0.22	2.45	8.11	2.64	1.11	0.25	0.29	98.76	37.7	366.4	25.0	56.3
Matachewan Dyke Swarm G1	**89M18A**	52.98	1.39	14.00	15.26		0.21	3.89	8.98	2.54	0.72	0.13	0.37	100.46	39.3	330.1	88.3	56.2
Matachewan Dyke Swarm G1	**89M18A-1A**	53.59	1.30	12.89	15.23		0.21	5.33	8.34	2.52	0.71	0.15	0.17	100.44	36.5	322.8	89.8	57.4
Matachewan Dyke Swarm G1	**89M21-A**	50.25	1.30	13.97	14.93		0.21	4.59	10.32	2.22	0.41	0.13	-0.06	98.27	40.5	291.0	147.1	48.7
Matachewan Dyke Swarm G1	**89M21A-1A**	54.90	1.22	12.21	13.67		0.20	5.74	8.21	2.13	0.38	0.11	0.08	98.84	36.3	304.5	138.3	53.9
Matachewan Dyke Swarm G1	**89M22A**	52.36	1.32	14.23	15.35		0.22	4.54	9.39	2.42	0.91	0.16	0.07	100.97	43.5	323.1	94.5	57.8
Matachewan Dyke Swarm G1	**89M27A**	52.72	1.61	13.32	15.63		0.22	5.44	8.77	2.53	0.52	0.16	0.02	100.95	40.8	375.7	108.6	88.0
Matachewan Dyke Swarm G1	**89M27A-1A**	52.25	1.61	13.06	15.18		0.22	5.38	8.56	2.47	0.52	0.16	0.22	99.63	40.5	366.2	106.5	59.3
Matachewan Dyke Swarm G1	**89M31A**	50.66	1.20	15.21	14.07		0.20	5.88	10.50	2.16	0.32	0.10	0.52	100.81	36.9	290.9	242.3	54.1
Matachewan Dyke Swarm G1	**89M31A-WC**	51.74	1.22	14.36	13.92		0.20	7.27	9.39	2.21	0.33	0.12	0.48	101.24	36.2	318.4	224.8	85.8
Matachewan Dyke Swarm G1	**89M33A-1A**	51.41	1.77	12.03	17.70		0.25	4.57	8.04	2.74	0.37	0.28	0.25	99.40	41.3	385.7	10.7	65.7
Matachewan Dyke Swarm G1	**89M34A**	54.54	1.82	12.58	17.70		0.28	2.17	7.66	2.82	0.72	0.23	0.53	101.06	41.0	352.3	7.8	50.7
Matachewan Dyke Swarm G1	**89M37I**	52.46	1.46	13.20	15.74		0.23	5.68	8.61	2.50	0.45	0.13	0.22	100.68	43.3	355.9	60.6	59.1
Matachewan Dyke Swarm G1	**89M39A**	52.01	1.12	14.01	13.96		0.20	6.21	8.84	2.54	0.61	0.11	0.27	99.90	35.7	297.9	117.3	102.9
Matachewan Dyke Swarm G1	**89M40D**	51.78	1.77	12.79	16.99		0.21	3.02	9.43	2.69	0.94	0.23	0.47	100.32	39.5	407.1	19.4	54.3
Matachewan Dyke Swarm G1	**89M40D-10A**	51.43	1.73	12.56	16.74		0.22	4.57	7.90	2.86	0.98	0.21	0.35	99.55	37.3	366.8	20.2	59.6
Matachewan Dyke Swarm G1	**89M46B**	52.22	1.69	13.01	17.00		0.22	2.71	8.89	3.24	0.91		0.44	100.32	38.3	372.0	30.8	51.9

Matachewan Dyke Swarm G1	**89M48B**	52.52	1.34	13.41	15.71		0.22	3.61	9.02	2.59	0.66	0.15	1.32	100.56	44.6	331.2	64.2	51.6
Matachewan Dyke Swarm G1	**89M52C**	51.46	1.69	13.17	16.75		0.22	2.83	8.35	2.53	0.86	0.20	1.36	99.41	37.2	375.4	38.2	51.0
Matachewan Dyke Swarm G1	**89M62A**	54.49	0.98	13.63	13.37		0.19	4.23	8.84	2.39	0.54	0.13	0.02	98.81	33.9	249.2	116.2	52.7
Matachewan Dyke Swarm G1	**89M67A**	55.69	1.32	11.98	13.86		0.26	2.50	7.74	2.64	0.68	0.20	2.04	98.92	37.0	292.4	12.8	41.7
Matachewan Dyke Swarm G1	**89M73E**	53.09	1.18	13.53	14.32		0.20	3.82	8.83	2.37	0.75	0.13	0.83	99.05	35.4	283.3	103.2	64.1
Matachewan Dyke Swarm G1	**89M74-A**	52.94	1.32	13.45	14.58		0.21	5.31	8.77	2.41	0.61	0.14	-0.58	99.16	39.5	311.4	84.3	117.2
Matachewan Dyke Swarm G1	**89M74A-10A**	52.51	1.33	13.25	14.67		0.21	5.41	8.97	2.41	0.65	0.14	-0.43	99.12	40.4	324.5	83.1	56.7
Matachewan Dyke Swarm G1	**89M8B**	49.94	1.01	14.85	13.73		0.20	4.98	10.21	2.34	0.53	0.10	0.65	98.54	38.5	274.9	181.1	52.1
Matachewan Dyke Swarm G1	**FA62-009-02**	49.26	1.18	14.16	13.66		0.27	6.32	9.95	3.23	2.00	0.12	1.10	101.23	45.2	339.4	139.6	50.8
Matachewan Dyke Swarm G1	**FA62-013-02**	49.30	1.27	14.23	14.89		0.25	5.99	10.37	2.48	0.74	0.12	1.39	101.04	42.9	362.6	98.6	49.6
Matachewan Dyke Swarm G1	**FA62-032-03**	50.56	1.70	13.18	14.99		0.26	4.66	8.04	3.91	1.36	0.19	1.27	100.12	44.3	305.1	64.3	44.2
Matachewan Dyke Swarm G1	**FA62-038-01**	48.42	1.46	14.46	16.13		0.25	5.15	9.27	2.87	1.77	0.14	1.15	101.04	42.3	372.7	74.5	51.5
Matachewan Dyke Swarm G1	**FA62-041-02**	50.51	1.36	12.96	16.27		0.23	5.10	9.43	2.33	0.70	0.15	0.68	99.74	42.9	366.5	66.8	56.5
Matachewan Dyke Swarm G1	**FA62-042-02**	52.17	1.36	12.81	16.41		0.22	4.36	9.06	2.40	0.74	0.16	0.56	100.25	41.6	360.5	60.6	49.7
Matachewan Dyke Swarm G1	**FA63-045-01**	50.09	1.56	14.04	13.96		0.20	5.25	11.51	2.90	0.24	0.15	1.11	101.00	43.5	359.5	116.1	46.1
Matachewan Dyke Swarm G1	**FA65-035-01**	49.24	1.26	14.04	15.26		0.24	6.13	10.70	2.15	1.03	0.11	0.87	101.03	45.3	352.3	144.5	52.6
Matachewan Dyke Swarm G1	**FA65-036-01**	50.31	1.09	13.92	14.71		0.20	5.94	10.44	2.39	0.24	0.11	1.65	101.02	45.0	355.7	93.2	52.8
Matachewan Dyke Swarm G1	**FA65-037-01**	50.21	0.84	15.22	11.95		0.17	7.49	10.02	1.99	0.41	0.13	1.50	99.92	36.1	262.8	350.9	45.7
Matachewan Dyke Swarm G1	**FA65-037-02**	51.08	0.73	14.10	11.82		0.19	8.84	9.79	2.01	0.65	0.10	0.98	100.28	35.1	225.5	475.9	47.9
Matachewan Dyke Swarm G1	**HP3-6**	52.70	1.68	12.80	17.97		0.24	2.22	8.37	2.75	1.01	0.24	0.49	100.47	38.7	383.2	16.2	49.1
Matachewan Dyke Swarm G1	**HT27-A**	51.59	1.34	14.12	14.88		0.20	4.09	10.03	2.19	0.61	0.12	0.68	99.86	39.3	299.5	107.2	49.2
Matachewan Dyke Swarm G1	**KS23-1B**	53.47	1.68	12.24	17.83		0.23	2.85	5.97	3.74	0.40	0.27	2.36	101.04	42.3	332.2	18.1	58.2
Matachewan Dyke Swarm G1	**KS3-9**	50.39	1.31	13.14	16.48		0.24	5.36	10.60	2.17	0.41	0.15	0.55	100.78	43.4	366.2	88.0	52.0
Matachewan Dyke Swarm G1	**KS9-8C**	51.80	1.16	14.62	14.93		0.22	4.21	9.20	2.49	0.71	0.11	0.40	99.84	41.4	299.4	75.8	57.2
Matachewan Dyke Swarm G1	**MA001**	50.28	1.03	13.45	14.80		0.22	5.60	9.42	1.85	0.98	0.10	1.32	99.04	41.0	306.2	77.6	56.5
Matachewan Dyke Swarm G1	**MA002**	51.17	0.63	15.20	10.97		0.18	5.73	12.46	1.77	0.67	0.06	1.39	100.23	35.1	213.8	111.6	40.6
Matachewan Dyke Swarm G1	**MA003**	54.05	1.97	11.85	16.65		0.25	3.47	6.25	3.90	0.42	0.25	0.76	99.82	39.3	339.9	5.0	36.8
Matachewan Dyke Swarm G1	**MA004**	53.98	1.36	12.74	14.22		0.18	3.99	7.98	1.54	1.70	0.18	0.90	98.77	33.5	300.3	102.7	41.6
Matachewan Dyke Swarm G1	**MA005**	51.29	1.35	13.43	14.98		0.19	5.02	9.20	2.03	0.59	0.13	0.57	98.78	44.3	310.4	112.3	45.9
Matachewan Dyke Swarm G1	**MA006**	51.45	1.14	13.67	14.02		0.20	6.21	9.27	1.84	0.47	0.12	1.33	99.71	39.2	273.7	79.7	45.9
Matachewan Dyke Swarm G1	**MA16-6**	50.24	1.72	12.98	17.86		0.24	2.51	8.91	2.62	0.71	0.19	0.95	98.94	41.2	384.6	20.0	49.9
Matachewan Dyke Swarm G1	**MK14-10**	51.74	1.35	13.93	14.75		0.19	3.50	9.08	2.68	0.75	0.19	1.88	100.05	37.4	312.5	50.2	49.2
Matachewan Dyke Swarm G1	**MK46-5**	53.99	1.04	12.52	13.97		0.20	3.69	10.08	2.14	0.48	0.11	0.58	98.81	40.4	258.9	137.6	47.9
Matachewan Dyke Swarm G1	**MK4-8**	53.71	1.50	13.39	16.79		0.24	3.16	8.56	2.69	0.60	0.21	0.16	101.00	44.4	372.6	34.4	57.9
Matachewan Dyke Swarm G1	**OL1-2-4A**	52.12	1.46	14.89	14.74		0.20	2.87	8.67	2.63	0.89	0.22	2.55	101.25	34.6	292.9	63.7	85.9
Matachewan Dyke Swarm G1	**RL23-1-3**	52.95	1.77	13.59	15.87		0.16	3.08	3.95	5.28	0.31	0.22	2.80	99.96	40.6	379.9	20.2	48.4
Matachewan Dyke Swarm G1	**WA7-1**	53.87	1.77	13.41	17.14		0.22	2.51	7.99	2.07	1.07	0.23	0.41	100.70	37.7	380.8	19.7	55.1
Matachewan Dyke Swarm G2	**37-A53**	53.49	1.39	13.87	14.61		0.15	5.37	3.08	4.13	0.69	0.25	2.74	99.78	24.1	288.3	1.3	46.0
Matachewan Dyke Swarm G2	**89M63A**	50.19	1.57	12.67	17.61		0.24	5.51	6.98	3.33	1.03	0.14	0.39	99.67	44.5	376.1	140.2	55.3
Matachewan Dyke Swarm G2	**FA62-026-04**	48.28	1.74	14.15	14.25		0.21	5.92	10.04	2.63	1.49	0.19	2.48	101.38	32.0	407.9	338.8	58.7
Matachewan Dyke Swarm G2	**FA62-077-01**	50.22	1.59	14.72	11.15		0.25	2.28	8.26	5.00	2.13	0.24	5.37	101.21	26.2	380.7	4.5	38.5
River Valley Intrusion	**RV001**	48.68	0.29	5.28	12.25		0.19	25.19	5.04	0.21	0.07	0.06	1.61	98.86	18.83	96.8	4203.3	54.1
River Valley Intrusion	**RV002**	51.51	0.20	19.62	6.16		0.13	5.02	13.06	2.55	0.35	0.02	0.40	99.03	29.79	102.2	144.6	28.5
River Valley Intrusion	**RV003**	51.44	0.26	24.78	5.01		0.09	1.87	11.97	3.57	0.49	0.03	0.52	100.05	13.11	83.3	1.5	24.5
River Valley Intrusion	**RV004**	51.27	0.19	21.68	5.15		0.10	4.08	13.09	2.78	0.46	0.02	0.84	99.67	27.80	93.8	297.3	24.4

River Valley Intrusion	**RV005**	52.47	0.28	13.47	7.52		0.17	10.93	12.58	1.36	0.28	0.02	0.46	99.54	42.73	186.0	500.3	36.4
River Valley Intrusion	**RV006**	50.63	0.34	22.44	4.79		0.10	3.48	12.77	3.30	0.48	0.04	1.38	99.74	22.43	110.4	153.1	23.2
River Valley Intrusion	**RV007**	49.05	0.18	21.97	6.97		0.13	4.35	11.55	3.33	0.68	0.02	1.88	100.11	14.23	72.3	81.4	33.3
River Valley Intrusion	**RV008**	49.84	0.68	13.98	12.25		0.22	7.54	10.45	2.13	0.78	0.01	0.70	98.58	41.54	268.3	84.8	38.9
River Valley Intrusion	**RV009**	48.64	0.60	9.35	13.89		0.17	13.67	9.89	1.73	0.71	0.15	2.04	100.84	40.04	226.2	604.2	66.4
River Valley Intrusion	**RV010**	66.73	0.53	10.85	6.08		0.07	4.02	2.51	3.12	3.69	0.54	0.98	99.11	16.78	101.6	194.7	20.3
River Valley Intrusion	**RV011**	49.18	1.05	9.71	9.06		0.13	12.28	11.08	2.43	1.60	1.55	2.29	100.36	31.95	167.4	51.4	34.0
River Valley Intrusion	**RV012**	59.97	0.68	12.40	5.93		0.09	3.92	3.97	4.23	4.67	2.43	1.97	100.25	10.00	81.4	151.1	12.9
River Valley Intrusion	**RV013**	51.87	0.14	21.22	5.92		0.11	4.64	10.98	3.63	0.57	0.01	1.17	100.27	18.94	59.6	87.4	29.0
River Valley Intrusion	**RV014**	53.01	0.19	17.10	9.43		0.14	6.33	8.15	3.40	0.86	0.01	1.72	100.35	17.33	59.1	139.8	47.4
River Valley Intrusion	**RV015**	52.48	0.35	10.34	13.91		0.22	9.56	7.18	1.26	1.42	0.05	2.13	98.90	28.38	110.7	138.7	68.2
River Valley Intrusion	**RV016**	51.26	0.22	15.58	9.10		0.18	7.42	10.47	2.75	0.38	0.01	0.89	98.26	41.45	139.0	149.2	46.5
River Valley Intrusion	**RV017**	54.74	0.24	13.61	9.42		0.19	9.83	7.90	2.63	0.61	0.07	2.05	101.29	31.67	114.8	460.0	47.3
River Valley Intrusion	**RV018**	54.32	0.58	7.21	13.97		0.28	11.40	8.51	0.44	1.37	0.04	1.70	99.82	48.35	241.9	211.1	68.6
River Valley Intrusion	**RV019**	55.74	0.28	16.88	6.75		0.12	4.47	7.91	4.86	0.66	0.05	0.89	98.62	23.23	118.3	92.9	28.2
River Valley Intrusion	**RV020**	50.64	0.23	13.69	12.91		0.25	9.20	8.33	1.93	0.51	0.02	1.92	99.63	36.51	135.1	346.9	60.7
River Valley Intrusion	**RV021**	52.60	0.20	17.18	7.94		0.15	6.13	10.33	2.93	0.73	0.02	1.10	99.31	30.42	121.0	238.5	35.6
River Valley Intrusion	**RV022**	54.61	1.29	12.39	14.34		0.21	4.00	8.63	2.15	1.10	0.18	0.65	99.54	39.20	323.5	7.3	42.6
River Valley Intrusion	**RV023**	50.89	0.99	13.65	13.70		0.21	6.30	10.99	0.91	1.47	0.10	0.87	100.10	45.29	306.4	122.1	48.0
River Valley Intrusion	**RV024**	54.99	0.48	18.09	7.31		0.09	4.45	4.84	4.82	1.85	0.12	1.61	98.67	11.68	48.1	284.6	34.7
Seidorechka Formation	**13071**	59.6	0.81	11.22	4	5.76	0.15	4.5	10.89	1.16	0.27	0.14	1.22	99.86	18	180		
Seidorechka Formation	**13073**	55.8	0.9	13.99	2.92	7.2	0.16	4.3	9.64	3.2	0.37	0.15	1.07	100	19	230		
Seidorechka Formation	**13081**	48.2	0.51	7.67	2.31	9.45	0.18	20.75	6.62	0.4	0.4	0.06	3.27	100.15	19	120		
Seidorechka Formation	**A-41/3**	65.48	0.87	12.19	2.85	5.76	0.13	1.25	3.97	3.2	3.1	0.23	0.48	99.65	10	120		
Seidorechka Formation	**BT-10/04**	53.64	0.6	13.37	1.12	9.10	0.16	8.26	8.39	3.76	0.49	0.10		99.00		166	70	47
Seidorechka Formation	**BT-12/04**	49.76	1.52	15.27	1.39	11.30	0.22	8.65	5.91	4.37	0.24	0.11		98.74		261	207	45
Seidorechka Formation	**BT-4/04**	56.97	0.67	14.24	1.09	8.82	0.22	6.11	6.12	3.05	1.61	0.12		99.02		154	16	43
Seidorechka Formation	**BT-4/04**	56.97	0.67	14.24	1.09	8.82	0.22	6.11	6.12	3.05	1.61	0.12		99.02		154	16	43
Seidorechka Formation	**BT-5/04**	73.14	0.74	12.48	0.38	3.07	0.03	0.75	2.32	2.10	4.43	0.21		99.65		35	4	4
Seidorechka Formation	**BT-8/04**	64.76	1.19	14.15	0.86	7.00	0.06	2.16	1.67	2.03	4.94	0.39		99.21		98	7	14
Seidorechka Formation	**BT-8/04**	64.76	1.19	14.15	0.86	7.00	0.06	2.16	1.67	2.03	4.94	0.39		99.21		98	7	14
Seidorechka Formation	**BT-9/04**	68.78	1.05	13.16	0.76	6.12	0.08	1.47	2.35	2.17	3.07	0.33		99.34		77	1	9
Seidorechka Formation	**BT-9/04**	68.78	1.05	13.16	0.76	6.12	0.08	1.47	2.35	2.17	3.07	0.33		99.34		77	1	9
Seidorechka Formation	**Bop-28/04**	51.43	2.21	13.71	1.64	13.32	0.19	5.21	7.58	2.79	0.24	0.19		98.51		372	90	56
Seidorechka Formation	**C-75**	53.24	0.77	14.46	4.02	6.48	0.15	5.2	9.25	2.48	1.94	0.14	1.46	99.67	26	300	160	45
Seidorechka Formation	**G-215**	52.96	0.86	13.24	2.86	7.63	0.16	8.3	9.39	0.96	1.18	0.12	1.83	99.67	22	130	440	46
Seidorechka Formation	**G-215/1**	49.36	0.78	10.17	2.86	8.21	0.19	14.7	7.95	1.72	0.11	0.09	3.29	99.62	21	100	1400	72
Seidorechka Formation	**K-41**	56.04	0.81	14.4	2.54	7.74	0.2	4.9	8.05	3.5	1.02	0.16	0.59	100.09	21	230	160	33
Seidorechka Formation	**K-41/1**	55.52	0.73	14.36	2.11	7.56	0.18	5.55	8.74	3.2	0.94	0.13	0.46	99.54	25	230	180	39
Seidorechka Formation	**K41/2**	57.3	0.79	14.45	2.61	7.11	0.16	4.1	7.37	3.32	1.7	0.16	0.53	99.7	18	170	33	31
Seidorechka Formation	**Ож-22-1/04**	52.96	0.83	16.7	1.07	8.70	0.25	5.77	5.88	3.93	2.82	0.14		99.05		211	89	39
Seidorechka Formation	**P-47**	54.7	0.79	14.64	1.91	7.74	0.17	5.85	7.73	3.38	1.82	0.14	0.66	99.62	27	380	110	38
Seidorechka Formation	**S-17/1**	48.8	1.47	14.86	1.73	13.99	0.19	5.37	10.21	1.28	0.32	0.22		98.44		323	143	50
Seidorechka Formation	**S-17/5**	52.59	1.35	14.62	1.49	12.07	0.18	5.40	7.87	2.39	0.49	0.21		98.65		324	155	51
Seidorechka Formation	**S-760**	79.02	0.32	10.9	0.35	2.80	0.12	0.00	0.37	0.68	5.09	0.05		99.70		40	31	5

Seidorechka Formation	**S-771**	71.68	1.02	13.32	0.52	4.23	0.13	0.00	1.35	2.48	4.58	0.22		99.53		4	44	1
Seidorechka Formation	**S-771/2**	70.53	0.96	13.23	0.55	4.46	0.13	0.73	1.34	2.48	4.89	0.21		99.51		39	21	4
Seidorechka Formation	**samp. 10**	71.1	0.58	11.33	2.04	3.69	0.05	1.2	1.73	1.92	4.24	0.08	1.49	99.45				
Seidorechka Formation	**samp. 10241**	54.82	0.75	14.4	2.41	7.29	0.17	5.47	8.86	2.6	1.09	0.21	1.23	99.3				
Seidorechka Formation	**samp. 10242**	69.97	0.56	11.05	1.12	5.61	0.04	3.24	0.43	2.6	2.62	0.15	1.47	98.86				
Seidorechka Formation	**samp. 10242A**	71.23	0.42	11.5	1.09	4.11	0.08	1.33	1.81	2.9	3.44	0.08	0.77	98.76				
Seidorechka Formation	**samp. 10891**	72.01	0.44	11.19	1.99	3.13	0.06	1.03	1.91	2.05	3.86	0.03	1.69	99.39				
Seidorechka Formation	**samp. 1102**	55.4	0.69	14.2	1.58	6.89	0.14	5.69	8.47	3	1.36	0.07	2.32	99.81				
Seidorechka Formation	**samp. 1106B**	52.65	0.77	15.1	1.7	7.18	0.14	5.95	10.27	2.1	0.76	0.08	2.86	99.56				
Seidorechka Formation	**samp. 1601**	54.7	0.86	15.2	1.82	7.75	0.14	7.15	4.5	3.4	1.36	0.08	2	98.96				
Seidorechka Formation	**samp. 1606**	52.4	0.28	16.05	1.19	4.97	0.14	8.18	11.11	2.8	0.8	0.01	2.22	100.15				
Seidorechka Formation	**samp. 1606A**	56.4	0.85	13.8	1.76	7.58	0.14	4.29	8.05	2.7	1.04	0.08	2.18	98.87				
Seidorechka Formation	**samp. 175**	55.41	0.61	13.83	1.32	7.49	0.16	7.3	7.12	1.81	1.36	0.08	2.4	98.89				
Seidorechka Formation	**samp. 1807**	52.18	0.85	14.28	3.05	7.47	0.15	7.1	8.58	3.6	1	0.18	1.44	99.88				
Seidorechka Formation	**samp. 1811**	54.52	0.83	14.03	2.59	7.32	0.17	6.2	8.54	3	1.1	0.15	1.25	99.7				
Seidorechka Formation	**samp. 1815**	54.58	0.71	11.51	1.35	8.91	0.15	9.95	6.65	4.1	0.26	0.12	1.55	99.84				
Seidorechka Formation	**samp. 1817A**	54.74	0.79	13.58	3.02	7.02	0.14	6.95	7.65	3.65	0.86	0.16	1.33	99.89				
Seidorechka Formation	**samp. 1823A**	53.1	0.8	14.7	2.01	7.74	0.14	7	9.01	2.92	0.69	0.15	1.49	99.75				
Seidorechka Formation	**samp. 1825A**	56.84	0.93	13.71	3.28	6.03	0.11	5.25	7.94	3.42	0.71	0.18	1.2	99.6				
Seidorechka Formation	**samp. 195**	52.4	0.88	14.85	2.84	7.56	0.16	6.8	6.94	3.92	2	0.16	1.27	99.78				
Seidorechka Formation	**samp. 197**	57.18	0.87	13.95	2.69	6.84	0.14	3.9	6.86	3.92	1.87	0.18	1	99.4				
Seidorechka Formation	**samp. 2398**	54.2	0.86	13.68	3.44	7.35	0.17	4.62	8.38	2.64	1.41	0.12	2.58	99.45				
Seidorechka Formation	**samp. 2833A**	52.9	1.17	14.1	1.6	9.48	0.18	6.79	5.55	3.9	0.18	0.16	3.52	99.53				
Seidorechka Formation	**samp. 2833D**	55.3	0.8	13.8	2.2	6.9	0.14	6.4	7.77	3.6	0.84	0.1	2.1	99.95				
Seidorechka Formation	**samp. 2837**	56.2	0.91	14.35	2.6	6.87	0.13	4.76	7.36	3.3	1.36	0.11	1.7	99.65				
Seidorechka Formation	**samp. 2841**	54.2	0.94	12.6	1.76	8.22	0.13	7.49	8.05	2.8	1.8	0.13	1.96	100.08				
Seidorechka Formation	**samp. 2845**	54	0.88	14.4	2.28	7.39	0.16	6.2	8.6	3	0.6	0.1	2.14	99.75				
Seidorechka Formation	**samp. 2847**	54.8	0.79	14.4	1.9	7.59	0.16	6.19	7.78	2.8	1.28	0.09	2.44	100.22				
Seidorechka Formation	**samp. 2849E**	53.7	0.74	9.55	0.91	8.88	0.16	12.78	7.08	2.7	0.14	0.06	3.33	100.03				
Seidorechka Formation	**samp. 2849F**	53	0.8	9.6	0.89	9.48	0.17	11.98	7.5	3	0.2	0.05	2.98	99.65				
Seidorechka Formation	**samp. 3021A**	60	0.8	16.6	1.81	8.62	0.08	1.99	0.97	2.4	2.68	0.12	3.56	99.63				
Seidorechka Formation	**samp. 3023A**	54	1.15	13.5	3.35	8.02	0.13	5	8.46	2.8	1.28	0.09	1.96	99.74				
Seidorechka Formation	**samp. 3036B**	56	0.85	13.6	3.68	7.36	0.13	4.79	7.64	2.8	1.52	0.15	2.05	100.57				
Seidorechka Formation	**samp. 3061/2**	75.96	0.43	11.44	2.41	1.61	0.07	0.45	0.4	5.1	1.32		0.8	99.99				
Seidorechka Formation	**samp. 3345**	56	0.65	12.7	1.92	6.52	0.11	6.39	9.76	3.2	1.8	0.07	1.18	100.3				
Seidorechka Formation	**samp. 510A**	55.6	0.68	13.95	1.6	7.61	0.17	5.6	8.6	2.7	1.16	0.09	1.94	99.7				
Seidorechka Formation	**samp. 515A**	71.86	0.46	11.65	1.75	3.56	0.11	0.71	1.52	3.66	3.54	0.03	0.67	99.52				
Seidorechka Formation	**samp. 523**	72.7	0.52	10.07	1.06	3.78	0.06	1.95	1.95	2.84	3.68	0.09	1.32	100.02				
Seidorechka Formation	**samp. 530**	62.7	0.93	11.24	4.97	4.5	0.12	3.1	3.03	3.2	3.93	0.2	1.46	99.38				
Seidorechka Formation	**samp. 532A**	55.92	0.61	13.91	2.65	5.94	0.16	7.45	8.74	2.7	0.33	0.11	1.44	99.96				
Seidorechka Formation	**samp. 551**	74.44	0.47	11.08	2.55	2.7	0.04	0.5	1.01	2.96	2.72	0.06	1.12	99.65				
Seidorechka Formation	**samp. 552**	67.04	0.49	11.52	1.95	4.77	0.07	3.6	2.89	3.34	3.2	0.07	1.09	100.03				
Seidorechka Formation	**samp. 554**	69.7	0.69	11.23	1.9	4.86	0.08	1.85	1.88	3	2.58	0.14	1.71	99.62				
Seidorechka Formation	**X-5**	53.36	0.73	14.62	3.05	6.34	0.17	6.5	9.32	2.56	1.39	0.12	1.39	99.66	27	100	290	38
Seidorechka Formation	**X-5/1**	55.22	0.97	14.53	2.93	7.3	0.17	4.4	7.65	3.36	1.66	0.15	1.15	99.63	20	110	110	38

Seidorechka Formation	**Вор-24/04**	74.4	0.65	12.17	0.35	2.82	0.04	0.56	2.23	4.36	1.97	0.15		99.70		22	3	4
Seidorechka Formation	**Вор-25/04**	75.32	0.49	11.82	0.29	2.35	0.05	0.21	2.61	2.36	4.15	0.09		99.74		14	5	2
Seidorechka Formation	**Вор-31-2**	56.66	1.44	13.27	1.41	11.45	0.18	3.25	6.89	3.62	0.37	0.19		98.73		198	20	58
Seidorechka Formation	**Вор-31-2**	56.66	1.44	13.27	1.41	11.45	0.18	3.25	6.89	3.62	0.37	0.19		98.73		198	20	58
Seidorechka Formation	**Вор-31-5**	55.37	1.19	13.36	1.26	10.23	0.17	5.15	6.78	4.12	1.08	0.14		98.85		230	12	52
Seidorechka Formation	**Вор-31-5**	55.37	1.19	13.36	1.26	10.23	0.17	5.15	6.78	4.12	1.08	0.14		98.85		230	12	52
Seidorechka Formation	**Л-1/03**	50.91	1.08	14.77	1.44	11.65	0.19	7.04	9.20	2.16	0.21	0.07		98.72		293	274	56
Seidorechka Formation	**Л-25-2/03**	75.79	0.33	12.05	0.28	2.24	0.04	0.42	0.74	2.60	5.18	0.08		99.74		9	5	2
Seidorechka Formation	**Л-29/03**	56.97	0.6	14.48	0.94	7.62	0.14	6.78	6.34	3.67	1.50	0.11		99.15		162	163	43
Seidorechka Formation	**Л-29/03**	56.97	0.6	14.48	0.94	7.62	0.14	6.78	6.34	3.67	1.50	0.11		99.15		162	163	43
Seidorechka Formation	**ОЖ-20/04**	69.47	0.94	14.07	0.51	4.11	0.04	0.46	2.30	2.19	5.18	0.28		99.55		49	10	7
Seidorechka Formation	**ОЖ-20/04**	69.47	0.94	14.07	0.51	4.11	0.04	0.46	2.30	2.19	5.18	0.28		99.55		49	10	7
Streich Dyke	**116**	50.25	0.46	17.02	9.97		0.16	8.01	11.4	2.25	0.41			99.93	29	185	229	42
Streich Dyke	**234**	49.11	0.47	17.47	10.53		0.18	7.51	12.11	2.01	0.59			99.98	30	202	172	49
Streich Dyke	**448**	50.43	0.4	17.54	10.28		0.17	7.6	9.87	2.89	0.77			99.95	30	163	278	52
Streich Dyke	**14-B7**	49.92	0.48	17.22	10.06		0.16	7.97	11.49	2.23	0.42			99.95	34	193	230	53
Thessalon Formation G1	**KYT446**	54.24	0.81	14.64	12.33		0.29	4.83	4.49	2.82	4.07	0.12	1.57	100.2	30	206	31	
Thessalon Formation G1	**KYT447**	55.68	0.75	14.41	11.51		0.23	4.55	5.25	3.44	1.96	0.11	2.48	100.38	31	202	30	
Thessalon Formation G1	**KYT469**	56.62	0.81	15.1	10.39		0.29	4.07	3.58	3.3	4.85	0.11	1.73	100.86	27	189	28	
Thessalon Formation G1	**KYT471**	51.58	0.8	13.96	13.6		0.21	6.2	8.37	3.08	1.38	0.1	1.44	100.71	36	272	94	
Thessalon Formation G1	**KYT476**	49.85	1.5	13.64	14.29		0.19	5.69	9.69	2.07	1.07	0.17	2.03	100.18	37	300	108	
Thessalon Formation G1	**KYT482**	45.23	1.48	13.84	16.97		0.19	6.88	8.66	0.22	1.94	0.2	4.54	100.14	41	319	138	
Thessalon Formation G1	**KYT483**	49.3	0.73	15.06	13.08		0.2	6.7	8.86	3.21	0.25	0.08	3.3	100.79	36	245	175	
Thessalon Formation G1	**KYT484**	52.36	0.97	14.56	13.58		0.23	5.73	5.5	5.06	0.15	0.15	2.38	100.67	32	263	127	
Thessalon Formation G1	**KYT485**	50.34	1.07	14.62	13.27		0.18	6.57	6.93	4.23	0.26	0.14	2.53	100.15	36	274	144	
Thessalon Formation G1	**KYT486**	50.7	0.96	14.91	13.52		0.3	6.83	5.38	4.26	0.7	0.15	2.76	100.46	34	287	146	
Thessalon Formation G1	**KYT487**	56.53	1.06	15.99	10.46		0.21	4.4	1.47	5.21	1.9	0.17	2.69	100.08	31	262	132	
Thessalon Formation G1	**KYT488**	50.76	1.06	13.93	15.41		0.2	5.16	8.9	1.97	0.46	0.14	2.78	100.79	34	279	65	
Thessalon Formation G1	**KYT489**	50.1	1.11	14.42	15.34		0.23	4.85	7.44	3.87	0.79	0.15	1.94	100.24	36	292	66	
Thessalon Formation G1	**KYT490**	52.27	0.88	16.02	11.7		0.13	5.17	6.36	4.95	0.2	0.13	3.01	100.81	35	236	179	
Thessalon Formation G1	**KYT491**	51.07	0.98	16.28	12.43		0.13	6.04	5.73	3.21	0.23	0.12	4.55	100.77	34	283	169	
Thessalon Formation G1	**KYT492**	48.9	0.91	16.38	13.62		0.18	6.11	6.42	4.47	0.12	0.13	3.22	100.47	37	275	171	
Thessalon Formation G1	**KYT493**	51.14	0.74	14.24	12.53		0.16	6.28	10.22	2.23	0.1	0.09	2.96	100.69	31	224	139	
Thessalon Formation G1	**KYT494**	56.13	0.79	13.57	11.34		0.13	5.82	7.34	3.22	0.26	0.09	2.21	100.9	32	244	141	
Thessalon Formation G1	**KYT495**	52.47	0.98	13.24	13.6		0.2	5.07	9.52	2.18	1.63	0.13	2.44	101.46	35	280	66	
Thessalon Formation G1	**KYT496**	51.16	1.27	13.25	14.45		0.2	4.5	6.41	3.61	0.58	0.2	4.87	100.49	35	320	25	
Thessalon Formation G1	**KYT501**	50.2	0.58	17.41	10.63		0.19	5.84	7.82	3.26	2.19	0.06	2.61	100.8	29	190	75	
Thessalon Formation G1	**KYT502**	55.96	1.28	13.57	12.11		0.14	4.37	4.66	4.74	1.43	0.19	2.22	100.66	25	291	10	
Thessalon Formation G1	**KYT503**	54.14	1.29	13.8	13.29		0.18	4.05	5.58	5.18	0.65	0.19	2.14	100.49	24	295	8	
Thessalon Formation G1	**KYT504**	49.72	1.11	14.75	14.03		0.24	6.1	4.96	4.4	0.92	0.15	4.19	100.57	41	306	98	
Thessalon Formation G1	**KYT505**	48.16	1.11	14.24	17		0.26	5.67	6.65	3.46	0.32	0.15	3.39	100.41	35	345	58	
Thessalon Formation G1	**KYT506**	53.64	0.98	14.15	12.45		0.23	5.12	6.48	5.22	0.16	0.14	2.23	100.8	30	260	105	
Thessalon Formation G1	**KYT508**	52.55	1.09	14.41	10.09		0.12	4.07	7.28	4.42	0.32	0.13	6.29	100.77	36	298	95	
Thessalon Formation G1	**KYT509**	52.03	0.89	14.45	13.17		0.24	5.96	4.56	5.12	0.41	0.14	3.65	100.62	30	251	133	
Thessalon Formation G1	**KYT510**	51.05	0.86	15.17	12.6		0.19	7.02	6.19	4.11	0.8	0.11	2.72	100.83	29	257	132	

Thessalon Formation G1	**KYT511**	51.28	1.1	13.78	14.57	0.18	4.41	9.13	3.72	0.06	0.15	2.27	100.65	32	307	40
Thessalon Formation G1	**KYT512**	51.1	0.89	14.69	11.98	0.19	6.25	8.06	4.17	0.5	0.1	2.48	100.41	29	255	85
Thessalon Formation G1	**KYT513**	52.37	0.96	14.79	10.9	0.18	7.08	6.08	5.05	0.5	0.12	3.22	101.25	24	217	55
Thessalon Formation G2	**KYT426**	53.6	1.35	10.87	11.7	0.15	5.88	8.76	3.92	0.33	0.17	2.91	99.63	22	185	217
Thessalon Formation G2	**KYT434**	50.09	1.72	14.45	14.36	0.14	4.04	5.63	4.05	2.7	0.35	2.32	99.85	13	247	27
Thessalon Formation G2	**KYT435**	54.79	1.62	15.13	12.54	0.14	2.89	3.64	4.66	0.9	0.33	3.74	100.38	16	218	29
Thessalon Formation G2	**KYT436**	51.92	1.64	14.86	13.65	0.12	4.14	5.46	3.71	2.51	0.33	1.69	100.02	18	210	29
Thessalon Formation G2	**KYT437**	50.47	1.77	14.1	13.99	0.15	4.13	7.03	3.5	1.38	0.35	3.08	99.93	16	238	23
Thessalon Formation G2	**KYT438**	51.79	1.57	14.61	13.18	0.13	4.24	6.95	3.36	1.41	0.34	2.46	100.03	17	211	29
Thessalon Formation G2	**KYT439**	54.37	1.57	14.2	12.37	0.13	3.89	6.52	3	2.08	0.3	1.94	100.35	17	198	32
Thessalon Formation G2	**KYT440**	52.14	1.98	13.85	15.23	0.17	3.57	5.68	3.24	1.16	0.45	2.36	99.84	17	232	18
Thessalon Formation G2	**KYT441**	51.38	2.04	13.97	14.7	0.14	3.16	7.17	3.04	1.93	0.47	1.93	99.93	15	227	19
Thessalon Formation G2	**KYT451**	54.1	1.54	12.28	10.18	0.12	4.51	8.99	3.88	1.09	0.24	2.87	99.8	14	150	98
Thessalon Formation G2	**KYT453**	52.22	1.53	14.64	11.74	0.12	3.64	7	3.66	1.54	0.3	3.33	99.73	17	224	27
Thessalon Formation G2	**KYT455**	50.22	1.8	15.13	13.51	0.12	2.8	5.63	5.25	1.86	0.39	3.8	100.5	16	252	17
Thessalon Formation G2	**KYT456**	50.27	1.45	16.04	17.37	0.24	3.55	1.98	3.55	2.15	0.31	2.97	99.88	13	114	2
Thessalon Formation G2	**KYT457**	50.98	1.36	15.96	14.73	0.29	3.09	3.06	4.44	2.34	0.39	3.29	99.93	14	151	5
Thessalon Formation G2	**KYT459**	56.02	1.35	16.5	12.02	0.15	2.14	1.96	5.48	1.88	0.36	2.22	100.06	14	158	1
Thessalon Formation G2	**KYT460**	59.07	1.3	13.37	10.2	0.15	1.5	4.57	4.69	1.96	0.36	3.29	100.45	16	137	1
Thessalon Formation G2	**KYT461**	58.75	1.29	13.36	12.1	0.13	2.43	4.28	3.79	2.54	0.25	1.23	100.14	19	207	2
Thessalon Formation G2	**KYT463**	47.79	1.86	17.57	16.67	0.19	3.63	2.15	5.14	1.19	0.36	3.31	99.86	23	286	3
Thessalon Formation G2	**KYT464**	55.52	1.28	14.21	12.75	0.17	2.7	4.78	5.15	1.02	0.26	2.36	100.31	21	220	4
Thessalon Formation G2	**KYT465**	55.31	1.13	14.33	11.6	0.15	3.06	7.61	4.28	0.32	0.22	2.31	100.32	19	218	17
Thessalon Formation G2	**KYT466**	50.08	1.17	14.89	13.2	0.15	6.25	6.16	2.72	2.58	0.2	3	100.42	26	248	299
Thessalon Formation G2	**KYT470**	61.71	1.37	13.28	10.86	0.15	2.03	3.87	4.09	0.87	0.29	1.91	100.44	14	167	3
Thessalon Formation G2	**KYT472**	51.58	1.44	10.13	14.62	0.17	8.18	9.18	1.79	1.54	0.18	2.04	100.86	22	179	444
Thessalon Formation G2	**KYT473**	54.55	1.39	13.98	11.54	0.13	5.14	6.18	4.51	1.13	0.25	3.76	102.56	21	195	69
Thessalon Formation G2	**KYT474**	56.31	1.36	13.69	12.52	0.09	3.39	3.94	3.22	3.4	0.26	102	100.21	20	206	147
Thessalon Formation G2	**KYT475**	56.6	1.35	13.56	12.5	0.1	3.43	3.94	3.15	3.38	0.27	1.99	100.26	15	235	9
Thessalon Formation G2	**KYT477**	51.39	1.13	14.4	12.77	0.17	6.79	6.46	3.92	0.91	0.21	2.67	100.71	24	259	251
Thessalon Formation G2	**KYT478**	60.13	1.36	13.81	11.54	0.13	2.4	3.36	3.37	2.91	0.31	1.77	101.1	15	185	2
Thessalon Formation G2	**KYT479**	58.05	1.28	13.99	11.09	0.12	1.82	4.77	3.41	2.94	0.28	2.36	100.1	13	171	4
Thessalon Formation G2	**KYT497**	54.6	1.49	14.5	12.83	0.16	3.5	6.9	4.18	0.43	0.27	2.57	101.41	21	285	20
Thessalon Formation G2	**KYT499**	50.54	1.82	13.99	12.59	0.13	4.5	7.91	3.49	2.26	0.36	3.29	100.78	17	222	77
Thessalon Formation G2	**KYT4S4**	50.94	1.55	14.85	14.54	0.13	4.25	6.55	2.81	2.01	0.29	2.22	100.15	17	219	23
Thessalon Formation G3	**KYT425**	52.31	1.18	9.27	13.44	0.18	9.42	9.47	2.55	0.95	0.15	1.65	100.58	26	205	1055
Thessalon Formation G3	**KYT427**	50.1	1.12	8.97	13.02	0.18	8.35	10.98	3.2	0.46	0.15	4.49	101.02	26	197	1020
Thessalon Formation G3	**KYT433**	51.54	1.16	9.33	14.31	0.18	9.02	8.95	2.44	0.95	0.15	2.13	100.16	28	199	997
Thessalon Formation G3	**KYT448**	52.88	1.2	9.13	12.45	0.17	9.7	9.59	2.55	0.72	0.15	1.67	100.2	28	204	1033
Thessalon Formation G3	**KYT449**	51.48	1.14	8.89	14.49	0.2	9.66	9.42	2.35	0.45	0.14	2.08	100.29	27	199	1026
Thessalon Formation G3	**KYT450**	51.51	1.22	9.77	13.65	0.19	8.9	8.67	2.92	0.98	0.16	2.24	100.21	25	211	1079
Thessalon Formation G3	**KYT452**	50.58	1.25	9.46	14.59	0.19	9.91	9.29	1.87	1.31	0.15	2.18	100.78	25	204	1080
Thessalon Formation G4	**KYT428**	58.07	0.72	14.75	10.45	0.22	3.72	5.01	6.37	0.17	0.11	1.25	100.85	31	201	27
Thessalon Formation G4	**KYT429**	53.06	0.72	14.75	13.34	0.25	5.17	5.98	5.06	0.43	0.11	2.02	100.91	32	208	29
Thessalon Formation G4	**KYT430**	55.74	0.75	14.27	11.71	0.2	4.52	4.74	3.78	2.52	0.12	1.46	99.81	29	207	29

Thessalon Formation G4	**KYT431**		56.95	0.74	14.2	11.47		0.18	4.45	5.08	4.97	1.02	0.11	1.45	100.61	31	196	29	
Thessalon Formation G4	**KYT432**		57.35	0.72	14.39	10.26		0.17	3.79	7.08	5.41	0.29	0.11	1.13	100.71	31	190	29	
Thessalon Formation G4	**KYT444**		55.42	0.73	14	10.95		0.16	4.6	7.21	2.52	0.61	0.11	4.3	100.62	30	192	29	
Thessalon Formation G4	**KYT445**		56.62	0.71	14.3	10.91		0.16	4.19	8.23	3.07	0.36	0.11	1.92	100.59	31	194	29	
Thessalon Formation G4	**KYT500**		55.38	0.74	13.85	9.72		0.12	4.04	4.87	3.34	1.8	0.11	6.73	100.71	36	214	30	
Victoria Lava Lake		**91100**	51.6	0.646	12.5	11.5		0.194	10.3	10	2.9	0.17	0.08	0.7	100.59		243	909	45
Victoria Lava Lake		**91101**	52.4	0.672	13.2	11.1		0.191	8.85	10.7	2.21	0.47	0.09	0.19	100.073		253	688	47
Victoria Lava Lake		**91102**	51.7	0.67	13.3	11		0.193	8.85	10.6	3.07	0.48	0.09	0.17	100.123		258	628	39
Victoria Lava Lake		**91103**	48.2	0.485	9	11.9		0.17	20.4	7.62	1.89	0.26	0.08	1.22	101.225		176	2417	87
Victoria Lava Lake		**91104**	47.9	0.464	8.8	11.7		0.182	21.6	7.26	1.68	0.32	0.07	0.69	100.666		167	2255	91
Victoria Lava Lake		**91105**	46	0.379	7.3	12.3		0.185	26.1	5.88	1.62	0.22	0.06	2.04	102.084		137	3507	107
Victoria Lava Lake		**91106**	47.8	0.451	8.5	11.7		0.177	22.6	7	1.28	0.39	0.07	0.89	100.858		161	2131	96
Victoria Lava Lake		**91107**	52.9	0.662	13.8	10.6		0.183	7.54	11.1	2.79	0.29	0.11	0.22	100.195		266	502	35
Victoria Lava Lake		**91108**	52.6	0.662	14	10.6		0.194	7.55	11.2	2.73	0.35	0.11	0.25	100.246		262	525	39
Victoria Lava Lake		**91109**	52.1	0.681	14	11.2		0.204	7.29	11.7	2.67	0.2	0.11	0.16	100.315		265	447	34
Victoria Lava Lake		**91110**	50.3	0.575	11.1	12.1		0.185	14.6	8.96	1.63	0.43	0.08	2.5	102.46		207	1619	67
Victoria Lava Lake		**91112**	50.5	0.589	11.5	11.6		0.173	13.7	9.59	2.03	0.35	0.09	1.5	101.622		214	1570	56
Victoria Lava Lake		**91113**	49.3	0.593	11.5	11.3		0.184	14.5	10.4	1.9	0.26	0.09	2.42	102.447		219	1552	58
Victoria Lava Lake		**91117**	51.3	0.662	12.9	11.7		0.201	10.1	10.4	2.52	0.13	0.09	0.18	100.183		246	898	53
Victoria Lava Lake		**91119**	51.2	0.651	12.8	11.5		0.204	9.94	10	3.41	0.19	0.09	0.32	100.305		247	837	55
Victoria Lava Lake		**91121**	51.4	0.684	13.2	11.6		0.194	8.81	11.1	2.36	0.52	0.12	0.4	100.388		250	653	52
Victoria Lava Lake		**91122**	51.5	0.673	13.2	11.4		0.205	9.16	10.6	2.81	0.45	0.1	0.39	100.488		242	721	53
Victoria Lava Lake		**91124**	52.5	0.688	13.6	11		0.203	7.3	11	3.14	0.53	0.09	0.21	100.261		259	417	42
Viianky Dyke Swarm	**14**		52	0.68	12.3	10.2		0.18	13	9.26	1.74	0.71	0.1		100.17	31	216	1198	53
Viianky Dyke Swarm	**89-VEN**		50.65	0.67	12.7	11.5		0.18	12.47	9.33	1.8	0.63	0.08		100.01	32	198	981	58
Viianky Dyke Swarm	**AD5-1**		51.53	0.62	11.88	11.44		0.19	13.63	8.32	1.4	0.92	0.07		100	32	200	1326	60
Viianky Dyke Swarm	**CD5-V**		53.41	0.68	14.84	9.92		0.14	8.19	8.88	2.66	1.15	0.12		99.99	27	188	520	
Viianky Dyke Swarm	**RD1-V**		50.98	0.64	14.98	9.95		0.16	10.41	10.45	1.95	0.39	0.08		99.99	37	208	673	57
Viianky Dyke Swarm	**SUO-134**		50.67	0.53	10.32	11.42		0.17	17.16	7.97	1.18	0.51	0.07		100	31	175	1708	68

Ni	**Cu**	**Zn**	**Sr**	**Y**	**Zr**	**Ba**	49Ti	51V	52Cr	55Mn	59Co	60Ni	65Cu	66Zn	71Ga	85Rb	88Sr	89Y	90Zr	93Nb	133Cs	137Ba	139La
ppm	ppm	ppm	ppm	ppm	ppm	ppm	wt.%	ppm	ppm	ppm	ppm	ppm	ppm	ppm	ppm	ppm	ppm	ppm	ppm	ppm	ppm	ppm	ppm
39.0	75.0	24.7	383.7	7.1	13.2	159.5	0.22	48.6	13.7	0.05	13.5	32.0	82.0	11.2	17.2	14.3	342.9	5.5	17.9	0.54	0.96	148.5	4.90
399.7	60.6	81.3	164.5	8.5	24.0	116.3	0.35	102.5	179.7	0.14	64.4	376.8	61.9	71.5	12.8	12.4	157.8	7.8	24.5	0.88	0.73	111.5	4.70
68.1	47.5	39.6	305.8	9.2	38.5	70.3	0.46	113.8	113.2	0.08	22.0	46.7	47.8	30.5	16.6	4.8	279.0	8.3	38.6	1.23	0.34	62.7	5.19
175.6	143.2	74.6	420.2	7.9	24.7	212.0	0.34	80.9	88.9	0.09	29.3	157.2	135.2	75.0	17.7	35.8	397.2	7.2	25.5	0.85	2.65	190.6	6.50
109.4	80.2	119.8	214.6	18.6	53.4	132.3	0.73	219.2	200.2	0.16	42.4	96.7	75.0	108.0	15.8	12.8	198.1	17.5	55.5	2.05	0.60	118.6	8.62
107.9	88.6	87.1	214.5	16.0	38.8	130.7	0.39	180.2	170.8	0.18	53.2	100.5	86.9	75.2	15.7	13.8	200.8	15.1	39.7	0.96	0.96	111.7	7.44
253.9	57.8	104.8	275.9	5.8	12.9	232.0	0.19	90.4	199.4	0.15	51.0	247.5	57.4	89.8	14.8	27.0	259.8	4.7	13.3	0.79	0.80	202.4	4.21
459.4	2452.2	125.6	218.2	12.4	63.2	284.2	0.51	187.6	707.2	0.16	48.2	425.3	2310.9	120.2	15.5	36.7	220.3	13.0	65.9	3.25	0.40	271.4	10.59
46.8	711.1	101.5	232.3	13.6	67.5	298.9	0.53	190.5	121.4	0.16	43.6	44.0	736.2	97.7	15.5	37.9	230.1	13.6	66.8	3.91	0.42	284.2	13.64
39.6	433.5	64.4	227.3	13.3	69.6	274.8	0.54	190.1	101.6	0.16	43.2	38.3	430.2	66.5	16.0	34.5	234.0	14.0	67.2	3.56	0.40	263.9	13.13
18.2	1021.1	74.8	195.3	17.6	93.8	380.6	0.78	220.5	331.5	0.17	42.9	19.8	981.3	76.2	16.3	44.4	206.2	18.3	97.2	5.37	0.52	367.0	21.67
13.2	1124.9	76.8	214.2	14.6	79.3	280.2	0.60	187.9	75.9	0.15	39.7	15.6	1118.8	79.4	15.7	34.8	215.8	15.3	81.1	3.86	0.44	268.6	19.64
13.7	191.8	72.7	156.0	14.7	76.9	341.6	0.56	179.8	158.6	0.14	33.8	15.3	177.1	74.6	14.4	41.8	152.5	14.7	71.1	3.39	0.41	324.9	13.63
47.6	819.2	98.9	217.8	15.9	99.7	419.6	0.65	192.8	79.6	0.15	40.3	44.7	750.6	92.2	16.2	44.6	215.5	16.7	94.5	4.23	0.55	394.2	25.68
10.2	404.5	92.1	216.7	15.4	78.3	347.4	0.64	197.5	123.7	0.17	44.4	13.0	374.9	93.2	15.9	33.9	221.3	16.8	79.5	3.32	0.40	346.3	17.35
8.1	193.7	99.7	204.2	18.7	119.1	380.3	0.97	288.9	42.6	0.17	46.2	11.0	150.2	96.4	17.5	41.3	210.9	20.0	118.0	4.31	0.63	371.9	31.41
23.9	263.7	94.0	149.0	16.8	57.1	467.9	0.59	185.3	332.3	0.16	42.2	23.4	232.8	92.8	17.1	47.5	152.1	18.0	59.7	3.12	0.56	435.7	28.66
12.9	543.1	113.5	270.1	17.7	90.6	376.7	0.74	193.3	138.1	0.17	43.2	15.7	524.7	114.4	17.7	41.3	292.1	19.5	95.9	4.81	0.49	372.8	16.52
6.3	348.0	159.6	176.4	28.4	99.1	453.6	1.52	293.6	36.1	0.18	40.0	9.2	319.6	158.3	18.8	50.0	178.1	29.4	100.2	9.03	0.70	442.6	32.92
15.6	825.4	101.2	92.4	27.6	166.6	463.7	1.35	241.3	10.3	0.16	33.5	16.7	797.8	98.8	17.6	59.0	91.4	27.5	161.5	7.20	0.77	437.3	27.79
6.3	289.0	80.8	132.1	28.1	188.3	618.2	1.21	190.0	25.4	0.12	27.9	9.1	273.2	83.5	19.6	75.4	134.7	29.2	191.8	7.95	0.87	596.4	32.45
13.0	339.5	82.7	163.7	24.0	206.2	439.6	0.91	209.1	22.9	0.14	32.0	14.4	326.1	79.2	16.9	52.6	157.5	24.0	200.9	5.64	0.59	410.4	24.29
21.98	118.09	94.02	125.51	28.38	262.05	581.42	1.36	270.51	20.53	0.15	34.01	19.67	125.49	97.90	18.90	59.76	113.49	27.63	244.32	9.25	0.87	564.63	34.15
54.26	193.55	38.35	226.86	14.49	76.32	238.67	0.61	223.55	112.87	0.15	43.80	62.33	217.36	61.27	17.93	26.88	226.90	13.89	69.44	3.19	0.44	228.78	12.74
103.59	36.50	44.40	211.91	13.97	81.74	3098.75	0.52	188.22	118.29	0.14	42.69	107.91	29.09	56.63	15.17	29.32	213.30	13.57	76.07	3.44	0.40	3085.87	15.38
58.99	147.37	98.44	239.67	13.57	57.75	318.60	0.62	266.77	102.02	0.18	61.37	59.70	166.17	100.42	18.98	36.97	233.65	14.88	61.41	2.60	1.04	308.46	13.34
201.94	65.08	89.12	208.83	15.52	76.49	262.47	0.59	231.48	628.18	0.17	48.27	208.08	66.47	93.33	14.93	23.96	209.79	16.72	81.08	3.60	0.37	261.28	13.30
96.03	141.56	88.60	216.38	15.13	87.24	341.04	0.55	218.58	135.74	0.17	50.14	92.15	149.04	86.40	16.93	38.93	212.11	16.07	91.25	3.46	1.31	329.96	13.52
102.84	118.30	67.78	197.62	17.03	57.63	82.53	0.73	203.37	157.34	0.12	30.18	106.97	140.01	75.23	16.54	8.41	202.96	19.41	62.73	4.63	0.24	89.65	16.72
66.89	101.42	67.86	235.13	13.08	61.78	223.55	0.49	226.86	3.89	0.17	50.29	58.38	98.30	68.25	16.73	20.30	234.51	13.67	59.67	2.84	0.60	221.83	9.74
81.46	48.56	62.40	275.53	14.83	59.02	198.46	0.42	202.76	15.46	0.17	46.67	72.65	42.12	66.84	16.97	16.65	269.60	15.04	59.87	2.31	0.44	197.24	11.70
73.37	45.04	77.07	277.27	14.39	98.46	251.73	0.64	195.10	20.12	0.14	42.85	63.64	38.18	75.26	17.49	19.60	286.23	14.54	99.36	4.81	0.51	246.88	18.53
859.35	231.09	97.42	199.97	15.59	66.11	235.66	0.61	213.72	442.84	0.15	48.03	876.54	250.60	90.07	14.93	20.05	202.87	16.06	70.56	3.67	0.35	237.05	12.94
80.26	85.89	103.02	237.18	13.37	57.78	240.88	0.46	192.66	56.24	0.16	47.82	75.08	84.59	96.09	16.04	21.91	239.13	13.50	58.03	2.62	0.68	245.70	11.17
112.18	105.16	89.68	182.11	15.06	70.09	253.42	0.55	196.55	500.42	0.15	44.23	111.10	102.46	75.24	13.86	21.79	178.01	14.79	69.09	3.68	0.48	253.42	13.27
33.29	10.06	18.66	16.12	15.18	126.03	257.90	0.32	8.24	107.31	0.01	2.72	23.44	10.27	37.50	7.22	42.29	13.28	14.55	125.04	11.24	0.56	240.07	42.82
834.48	89.87	86.35	56.79	10.05	61.06	28.24	0.48	89.18	2106.27	0.19	100.84	828.17	87.66	83.17	8.39	0.81	54.80	10.22	63.67	2.75	0.08	36.27	10.50
902.00	103.37	124.39	6.07	7.23	37.10	38.80	0.29	68.68	2364.45	0.17	97.04	879.19	105.74	122.53	6.92	1.11	5.39	6.67	31.49	1.55	0.10	46.09	6.41
989.73	4.79	79.04	23.82	4.03	23.40	22.06	0.19	50.10	2427.18	0.13	106.86	1009.45	3.32	71.73	4.72	0.63	24.82	3.74	17.60	0.84	0.18	29.05	2.62
978.69	63.62	81.87	22.81	4.04	30.53	18.24	0.18	49.58	2506.85	0.14	112.66	982.92	66.24	73.90	4.66	0.55	22.53	3.77	26.32	1.05	0.16	26.93	3.07
1099.44	52.88	69.89	19.65	5.33	20.34	7.55	0.16	73.99	2270.03	0.12	107.21	1070.55	65.16	70.45	4.03	0.86	15.83	3.54	17.60	0.76	0.20	12.96	2.89
1129.25	161.80	96.44	19.53	5.48	32.10	8.05	0.18	86.89	2425.95	0.13	116.39	1161.89	173.89	92.46	4.26	0.86	17.12	3.70	31.20	0.87	0.21	13.98	3.39

1166.29	240.64	66.16	3.23	3.61	17.65	23.05	0.16	78.72	3015.98	0.15	134.86	1213.71	268.92	74.63	3.73	0.38	3.17	2.42	15.23	0.57	0.04	32.82	3.00
1073.67	24.98	95.12	3.58	2.91	12.11	28.34	0.14	44.16	2885.09	0.15	136.34	1054.40	21.39	91.41	3.49	0.27	3.08	2.63	13.76	0.53	0.07	36.39	3.04
1236.74	34.75	66.92	1.08	3.15	14.62	46.43	0.13	44.12	3131.45	0.13	133.68	1203.88	38.06	66.35	3.67	0.30	1.33	2.48	14.44	0.59	0.05	53.74	2.08
1063.24	20.72	82.48	3.10	2.66	35.00	59.65	0.14	33.67	2980.85	0.15	139.28	1069.06	11.40	79.53	3.29	0.40	2.65	2.48	36.04	1.08	0.04	73.59	2.58
1092.31	34.92	84.82	2.92	2.80	10.34	42.67	0.12	40.85	2894.73	0.15	136.85	1194.30	31.43	78.07	3.32	0.26	2.18	2.16	10.75	0.24	0.04	49.89	1.70
1065.37	10.93	96.14	0.99	2.53	10.97	39.26	0.11	39.64	2701.86	0.13	134.72	1154.83	8.35	84.26	3.05	0.19	1.33	1.99	9.90	0.33	0.02	47.06	3.13
877.13	46.54	69.64	6.50	2.79	17.51	4.66	0.14	39.80	2492.16	0.13	124.02	899.43	44.94	64.88	2.93	0.22	5.99	2.71	15.61	0.43	0.07	9.38	3.41
1022.11	71.18	87.57	2.39	2.92	11.92	5.52	0.11	35.27	2540.35	0.08	126.32	1078.34	69.49	75.55	2.94	0.13	1.41	2.40	11.77	0.39	0.04	11.95	2.33
314.22	12.83	57.07	35.40	7.57	20.95	80.08	0.26	201.26	1480.50	0.18	48.14	306.22	11.24	63.09	4.74	0.51	33.72	7.60	19.24	0.72	0.03	89.96	3.77
364.98	37.68	60.34	27.27	7.03	20.45	10.28	0.28	229.92	1488.47	0.18	50.35	408.46	38.05	66.40	5.30	0.17	26.48	7.54	18.23	0.58	0.01	17.91	3.27
247.65	138.34	52.97	36.12	8.52	24.99	6.50	0.34	254.67	877.62	0.20	57.37	268.76	144.84	60.80	6.22	0.11	36.35	8.58	24.13	0.97	0.02	14.40	2.89
241.75	168.28	63.05	20.45	7.16	21.48	5.14	0.31	263.59	883.66	0.20	70.00	258.01	179.30	65.06	6.13	0.12	20.11	7.33	20.92	0.66	0.03	11.90	3.74
485.13	71.08	68.22	49.90	8.09	26.68	18.34	0.33	233.48	1010.76	0.19	52.55	504.83	73.60	67.60	6.54	0.40	50.12	8.65	24.40	1.11	0.02	25.42	4.54
144.07	35.11	49.52	187.74	11.31	55.82	49.49	0.44	235.54	619.59	0.15	46.39	142.51	41.12	69.54	13.00	2.41	186.52	12.90	55.68	2.57	0.14	50.57	9.98
138.71	47.80	50.15	196.02	11.66	63.27	50.02	0.45	231.66	614.73	0.15	44.98	147.50	53.01	76.05	13.24	2.39	192.56	12.92	53.98	2.62	0.13	51.23	9.68
183.24	40.53	83.63	151.31	12.65	65.43	48.65	0.46	252.88	1102.43	0.16	51.67	199.24	46.29	99.00	11.95	1.37	143.79	13.58	59.37	2.64	0.09	48.54	10.21
260.73	39.55	95.64	11.17	6.54	25.07	276.87	0.28	97.51	818.46	0.18	51.58	268.58	34.82	90.30	8.85	0.94	10.13	6.07	24.62	0.95	0.06	277.57	3.94
97.87	88.19	75.78	178.02	14.32	87.38	279.48	0.57	199.95	371.46	0.17	49.83	89.13	98.65	74.24	16.10	33.89	176.49	14.48	90.90	3.64	0.44	271.15	13.23
337.25	44.71	71.68	220.23	11.85	58.53	212.76	0.47	197.17	330.07	0.17	51.38	346.01	44.46	72.99	16.32	24.55	214.15	11.77	60.58	2.67	0.37	214.93	9.14
293.12	96.76	122.77	16.95	10.17	36.55	252.96	0.45	194.03	1016.11	0.24	76.05	300.91	92.66	120.75	10.78	10.93	16.15	10.40	41.15	1.52	0.28	257.84	1.94
100.76	33.52	80.84	260.84	12.37	59.37	192.42	0.52	207.63	325.97	0.12	56.02	109.94	33.72	84.29	17.04	19.33	277.75	13.04	62.03	3.01	0.25	208.05	10.51
82.11	100.58	73.61	290.30	14.26	69.60	214.71	0.54	194.82	306.37	0.15	43.97	88.66	95.92	67.87	15.50	21.09	277.18	14.10	75.89	3.64	0.33	218.21	12.27
96.70	46.39	92.81	99.11	13.02	75.65	290.09	0.50	183.16	253.19	0.15	38.20	92.31	40.52	88.65	13.38	41.71	95.35	14.21	81.35	3.73	0.82	301.32	13.39
125.96	68.85	69.32	97.27	15.04	76.51	285.40	0.60	219.37	282.63	0.16	44.94	143.37	66.14	66.44	14.21	38.35	102.36	16.10	79.26	4.02	0.76	287.39	13.71
127.44	23.80	76.35	130.47	14.23	69.12	247.41	0.56	219.38	358.29	0.16	44.04	135.82	29.57	72.23	14.92	25.63	130.81	15.11	66.17	3.78	0.38	271.55	13.31
30.49	11.80	43.21	61.32	7.38	86.43	7.52	0.17	21.30	68.94	0.03	4.38	41.43	45.50	27.95	4.53	0.61	58.58	7.02	77.63	3.15	0.01	6.71	23.66
90.39	48.54	76.64	227.37	14.92	85.38	440.81	0.61	194.73	81.39	0.14	38.44	96.35	59.11	70.03	14.64	45.72	229.82	15.65	85.06	4.63	0.92	459.82	16.22
82.95	104.92	83.21	178.05	18.52	90.18	253.27	0.68	229.30	46.03	0.16	51.41	84.23	102.84	78.69	17.96	20.55	177.86	18.98	92.02	4.24	0.50	269.94	16.49
80.82	30.54	82.86	232.34	17.13	87.74	146.71	0.67	217.43	127.81	0.16	44.55	78.14	30.80	79.77	16.10	10.06	242.97	18.89	88.10	4.48	0.44	152.71	16.17
55.76	44.97	74.01	115.37	18.57	125.21	499.05	0.76	236.38	129.11	0.11	31.18	65.87	52.41	72.75	16.50	37.71	117.75	19.56	134.10	4.83	0.86	497.29	17.32
168.48	47.03	83.05	217.37	15.69	97.66	329.60	0.63	208.23	106.40	0.17	46.25	171.29	45.40	81.18	16.61	46.94	217.13	17.22	91.97	4.45	0.60	345.21	16.46
49.52	135.96	108.32	123.45	29.48	173.89	617.07	1.22	189.50	26.36	0.14	29.79	52.07	141.07	111.70	18.83	77.71	122.78	30.54	170.98	9.67	1.83	638.13	35.12
33.35	32.64	64.51	7.94	5.28	64.38	82.15	0.14	12.14	74.53	0.00	7.10	40.62	69.06	61.87	4.87	22.75	9.64	5.30	64.87	5.41	0.46	80.03	22.24
31.88	18.81	45.47	3.94	6.57	68.39	120.49	0.06	7.62	47.09	0.00	3.31	35.13	19.48	32.78	3.62	17.93	5.64	6.27	47.28	1.64	0.32	110.86	23.82
90.38	239.17	334.43	4.27	10.67	50.25	134.32	0.07	7.38	72.18	0.00	14.46	96.73	264.67	325.29	3.83	17.61	6.29	10.72	46.22	1.77	0.39	129.90	22.95
20.37	10.44	54.57	13.97	7.11	105.78	211.11	0.09	13.05	80.02	0.00	1.77	24.11	5.56	48.56	5.14	30.39	15.05	6.90	92.99	2.30	0.41	200.30	19.34
28.57	8.87	41.50	28.45	4.70	80.05	102.73	0.07	8.96	44.57	0.00	2.48	33.27	6.23	29.50	4.08	18.12	29.59	4.94	74.44	2.21	0.28	106.66	23.38
25.86	46.47	43.80	7.91	4.34	48.78	254.21	0.07	13.82	30.10	0.00	1.88	27.49	42.92	31.83	4.76	27.35	9.73	4.34	56.34	3.51	0.73	269.80	7.79
18.81	22.58	81.17	140.13	28.54	100.86	788.76	1.04	97.37	14.26	0.23	15.57	19.99	22.61	75.07	16.27	99.37	135.18	28.56	90.97	9.02	2.27	818.23	37.43
145.65	58.56	119.45	149.16	33.41	395.48	689.50	1.22	183.28	34.64	0.13	25.53	143.84	52.71	111.44	18.92	84.81	151.43	34.33	385.74	9.82	1.95	698.99	34.82
427.60	41.22	95.93	67.50	14.86	87.62	316.48	0.56	191.02	826.52	0.20	61.68	399.36	34.72	84.10	13.33	44.62	67.16	15.43	90.44	3.85	1.02	314.47	9.72
166.76	100.59	97.06	184.60	26.68	182.78	616.87	1.00	225.12	24.48	0.16	38.64	153.41	93.94	89.62	18.55	59.93	178.77	27.27	179.80	6.90	1.46	652.24	28.50
227.77	27.87	70.14	35.69	9.86	36.76	11.01	0.37	293.89	660.28	0.20	41.75	222.31	20.05	60.87	5.68	0.71	36.92	10.52	38.48	1.48	0.07	6.53	4.95
160.62	90.52	49.67	145.09	7.03	21.37	15.08	0.24	191.36	637.87	0.15	30.69	151.76	96.49	55.62	10.94	0.24	134.28	6.88	22.39	1.19	0.04	10.35	3.61
150.47	50.49	59.53	100.26	5.73	23.58	28.44	0.30	193.35	368.66	0.12	36.41	130.68	48.94	54.46	11.56	3.24	91.46	8.04	25.15	1.16	0.09	32.94	4.76

114.33	19.47	62.15	221.41	7.58	33.40	133.69	0.28	179.94	241.83	0.14	42.69	117.46	18.63	46.20	12.31	15.80	220.68	8.32	31.96	1.23	0.41	145.58	5.38
114.85	16.46	60.33	231.98	8.33	33.58	114.76	0.35	193.11	237.19	0.15	42.38	111.31	21.52	57.74	13.80	10.58	221.44	9.68	35.32	1.67	0.21	117.16	6.95
117.92	54.75	66.49	217.18	8.81	39.61	143.68	0.35	161.27	187.75	0.15	41.91	109.08	61.69	50.71	13.62	17.26	188.10	9.72	42.26	2.23	0.28	146.95	7.94
108.79	45.00	56.69	163.92	7.98	42.25	147.55	0.31	154.61	171.28	0.13	38.11	98.96	41.22	53.43	12.55	14.19	187.14	8.17	43.22	1.71	0.23	145.80	7.15
108.82	31.75	65.37	211.09	8.80	43.65	194.37	0.38	182.81	169.09	0.16	45.59	118.78	24.01	57.90	13.90	21.62	210.94	10.43	45.12	2.36	0.32	205.37	8.82
117.91	36.88	60.97	209.34	10.07	54.97	149.62	0.42	183.11	438.65	0.12	36.69	694.82	49.75	61.15	16.26	12.96	216.67	10.74	48.31	2.53	0.23	140.75	8.91
196.56	38.83	79.05	81.44	11.46	50.86	21.15	0.43	205.54	682.24	0.17	55.43	193.24	38.92	73.86	11.03	0.42	79.84	11.46	44.99	2.17	0.03	17.27	4.79
22.84	17.83	41.90	65.76	13.36	194.02	33.90	0.37	24.62	27.77	0.04	2.34	25.71	21.89	24.87	10.28	1.29	63.14	13.05	181.99	5.52	0.04	29.33	3.47
29.31	9.57	46.71	14.64	2.28	40.65	13.72	0.14	11.91	72.48	0.02	4.07	26.10	38.25	27.38	3.08	1.23	15.03	2.10	32.29	2.29	0.06	13.51	5.09
483.90	88.40	122.95	57.97	11.45	54.11	28.91	0.48	174.72	842.91	0.18	60.70	473.55	100.25	117.57	10.95	1.85	60.39	12.71	53.34	2.65	0.08	28.32	4.96
199.53	39.81	79.77	128.58	10.13	47.65	205.87	0.37	226.88	605.02	0.19	59.56	188.58	44.50	71.63	10.34	13.88	132.77	11.47	53.10	1.98	0.35	218.16	8.16
259.03	31.23	91.09	74.67	11.18	57.85	27.57	0.45	232.11	547.17	0.17	47.73	272.16	31.43	102.60	10.17	0.94	75.89	12.07	58.28	2.69	0.10	25.37	9.47
141.60	22.53	112.76	158.71	7.34	32.55	17.70	0.30	166.03	291.78	0.14	30.46	142.62	25.44	103.61	11.68	0.69	161.02	8.37	33.71	1.55	0.04	15.60	6.27
131.10	126.77	123.02	192.66	12.86	63.62	209.71	0.51	213.26	198.36	0.17	49.52	138.76	130.91	119.91	14.91	27.56	193.57	14.11	64.76	3.17	0.90	212.27	11.53
111.71	32.96	71.53	229.79	10.61	50.13	199.20	0.43	211.58	83.06	0.18	48.81	118.19	37.07	64.90	15.40	22.43	232.79	12.01	47.27	2.31	0.77	203.84	9.00
130.77	27.80	120.39	142.50	7.21	37.59	85.63	0.31	154.26	129.85	0.13	34.68	131.79	33.39	121.76	12.58	6.90	142.11	8.33	37.26	1.84	0.09	94.38	6.45
125.81	109.16	73.27	192.43	7.98	37.11	122.98	0.31	169.18	160.43	0.14	42.57	116.91	102.90	79.64	13.80	11.78	183.60	8.86	34.87	1.73	0.27	133.68	7.30
99.47	38.36	85.70	165.09	6.71	33.37	88.27	0.25	140.72	91.87	0.12	28.61	101.39	42.94	86.33	11.63	6.75	154.61	7.42	29.48	1.44	0.12	95.20	5.12
200.92	55.98	167.21	65.95	20.41	72.03	4873.17	0.36	186.95	1708.01	0.14	29.10	209.63	57.80	157.01	13.72	0.93	64.89	21.68	66.94	2.68	0.37	4618.84	4.50
1376.17	37.45	90.02	42.57	10.13	61.12	117.21	0.39	241.74	2873.51	0.20	68.47	1356.70	31.96	94.55	7.84	5.87	40.98	10.86	52.35	2.17	0.26	117.75	8.61
260.72	46.06	102.72	70.28	9.71	46.88	324.80	0.42	238.40	1853.34	0.19	62.31	280.05	46.61	107.64	8.17	8.76	68.43	10.53	44.19	2.24	0.45	321.87	5.07
235.42	36.23	61.53	63.45	10.29	51.07	127.48	0.41	257.09	1633.89	0.18	61.09	244.93	31.35	77.86	8.73	11.37	60.37	11.16	48.46	2.48	0.41	136.23	6.92
26.11	10.19	12.93	32.08	1.70	87.75	14.43	0.28	16.15	81.57	0.00	3.73	20.00	9.88	40.42	6.14	1.08	26.40	1.52	79.92	3.55	0.07	8.48	1.45
88.62	41.32	71.89	224.33	12.57	73.14	272.00	0.48	202.93	130.77	0.15	43.04	91.17	47.14	83.41	16.17	32.44	212.82	13.86	68.49	3.18	0.34	275.22	12.54
1203.59	23.96	64.77	13.26	2.18	15.73	7.12	0.12	76.62	4856.44	0.14	104.33	1231.62	17.14	70.60	3.41	0.17	12.60	2.27	17.12	0.65	0.01	1.47	2.13
88.8	105.4	96.3	221.4	20.7	72.4	251.9	0.84	251.6	219.4	0.19	50.6	88.5	114.1	100.5	15.7	37.0	219.6	21.2	74.0	2.73	0.68	247.5	13.92
26.6	27.5	10.8	649.3	16.0	51.0	39.9	0.40	154.3	8.9	0.08	4.5	26.6	26.1	5.7	26.0	5.9	655.8	16.1	50.1	1.55	0.25	37.3	14.65
275.7	82.1	107.0	130.5	9.2	22.2	167.4	0.34	166.2	267.3	0.20	79.7	273.4	73.2	104.7	11.9	12.2	131.9	8.9	20.1	0.31	0.21	165.6	5.59
342.2	45.7	62.8	220.6	5.8	36.4	115.9	0.18	70.6	111.3	0.13	58.0	323.6	36.9	54.2	12.8	12.9	208.2	5.1	32.7	0.74	0.87	108.4	5.02
119.7	45.8	35.2	363.4	5.0	22.0	107.8	0.19	78.1	415.7	0.08	24.9	116.4	51.3	37.2	15.4	16.2	363.0	4.3	21.1	0.49	1.57	107.0	5.62
450.3	62.5	146.0	146.4	6.9	28.9	116.2	0.25	75.0	70.3	0.19	78.1	435.2	64.6	155.3	11.9	14.1	143.2	6.5	29.4	0.81	1.06	113.7	5.53
150.9	60.4	45.8	368.9	9.8	36.1	190.7	0.42	94.6	27.0	0.08	25.5	149.6	62.4	43.2	16.2	12.1	366.5	8.8	38.1	1.56	0.83	191.5	7.25
90.7	54.2	109.9	154.9	12.6	24.0	107.3	0.77	242.9	428.6	0.17	36.6	83.6	57.1	114.7	14.8	9.2	154.2	13.1	26.5	0.78	0.61	103.6	1.72
240.4	89.2	103.9	114.7	24.1	60.4	158.0	1.00	242.0	259.7	0.19	48.9	232.7	88.1	102.8	15.8	36.1	112.9	23.9	57.8	2.22	2.01	150.0	2.73
73.4	72.7	100.4	137.1	14.2	34.2	167.4	0.66	173.9	365.2	0.15	35.7	68.6	75.1	102.5	14.8	28.7	132.3	13.8	31.4	1.13	1.17	164.2	13.34
88.4	88.8	72.4	103.4	16.1	40.1	51.6	0.58	174.7	378.0	0.16	39.2	87.5	89.1	67.4	13.2	17.7	104.3	16.6	39.1	1.07	0.60	46.3	5.13
49.9	53.1	87.0	63.6	20.1	35.2	54.4	0.67	185.1	271.5	0.15	24.6	46.0	24.3	91.9	11.1	6.8	60.5	19.5	43.4	1.64	0.22	50.8	4.72
35.4	70.0	99.8	212.9	26.9	73.4	135.8	1.07	308.6	7.1	0.14	37.0	32.5	54.5	104.5	18.6	34.5	212.9	27.8	70.5	2.55	2.49	134.2	7.63
70.6	94.8	101.2	225.3	21.1	94.1	263.1	1.12	268.2	75.3	0.20	53.6	66.8	89.0		19.0	20.1	231.2	22.2	96.0	4.95	0.69	260.1	13.23
49.2	109.7	108.9	213.8	23.9	111.8	328.8	1.10	265.7	49.5	0.19	54.8	54.2	97.8		18.1	51.4	207.7	24.0	103.6	5.42	2.85	321.2	16.28
114.8	113.1	105.0	268.2	20.7	92.5	167.4	1.26	228.4	72.8	0.18	58.7	115.4	104.9		18.4	26.3	261.1	20.8	89.2	4.82	1.34	173.2	13.41
126.3	169.7	105.0	203.9	19.9	79.5	76.7	1.08	186.6	25.6	0.19	76.1	130.8	178.5		18.5	11.7	210.2	20.8	81.0	3.76	0.12	80.9	14.24
130.0	126.8	94.5	208.8	18.8	80.8	348.8	1.01	181.4	32.1	0.18	60.9	135.2	117.2		17.9	43.5	210.7	19.7	81.7	3.97	2.15	369.2	13.63
76.6	151.9	117.9	222.8	29.8	150.5	405.1	1.61	218.1	18.2	0.19	52.9	74.8	122.6		19.1	40.9	210.6	28.9	142.7	7.27	2.13	409.1	23.50
60.7	140.9	104.5	177.6	31.3	154.9	389.4	1.52	191.1	17.3	0.20	50.4	60.9	128.6		18.8	34.9	150.4	31.0	152.4	7.51	2.12	410.3	26.42

174.6	128.1	109.4	237.4	26.9	148.8	357.7	1.50	237.2	24.4	0.18	52.1	168.8	117.1		19.1	57.0	229.8	27.4	142.6	6.55	3.20	373.9	23.82
88.4	118.9	94.5	188.5	20.7	99.5	270.0	1.21	212.8	31.1	0.16	52.8	91.9	118.1		17.6	25.5	182.2	20.3	90.5	4.21	1.48	262.1	14.41
130.6	129.8	100.5	187.3	20.4	95.7	264.8	1.10	207.5	40.2	0.19	60.1	142.9	139.5		19.1	24.3	195.3	21.7	97.5	4.92	1.70	290.7	14.30
136.0	110.7	91.5	221.0	20.7	101.1	287.7	1.07	189.0	38.7	0.17	56.6	140.7	113.0		18.7	28.7	224.0	21.1	92.9	4.47	1.99	297.2	14.08
126.4	132.6	99.3	217.6	20.5	89.5	187.4	1.10	183.3	34.6	0.16	54.8	120.9	135.9		17.5	19.4	209.6	19.9	85.4	4.14	1.32	187.4	13.41
136.4	94.9	111.2	269.7	20.6	83.9	157.5	1.03	208.6	56.0	0.16	56.0	136.4	99.0		19.6	17.4	273.5	21.1	82.1	4.24	1.46	163.7	12.03
84.8	101.7	91.3	219.2	22.2	100.7	306.0	1.13	227.9	65.3	0.19	56.9	89.5	110.1		18.5	30.6	227.5	23.7	100.8	4.57	5.04	324.3	15.32
106.6	98.8	100.7	273.2	20.6	76.2	134.2	1.05	206.3	73.2	0.17	56.6	109.8	97.4		20.3	12.0	274.1	21.4	77.4	3.54	1.55	138.6	11.05
74.3	145.6	115.9	246.7	28.8	123.0	481.7	1.54	205.6	20.8	0.18	56.7	74.7	143.7		19.4	60.0	231.9	27.9	123.7	5.66	4.60	481.7	23.91
74.7	143.2	116.2	210.7	26.5	130.0	386.6	1.57	217.1	23.0	0.18	53.2	74.8	145.9		18.6	42.0	199.8	25.8	123.3	5.94	3.38	386.6	22.24
43.8	142.3	129.9	143.2	31.7	173.1	478.1	1.78	222.9	12.0	0.19	55.0	48.8	134.5		20.9	59.1	138.7	32.1	173.5	8.51	3.55	506.9	30.08
40.5	138.0	134.0	154.1	31.8	181.6	429.3	1.87	233.4	11.6	0.19	55.3	43.7	124.9		20.9	44.4	154.9	32.9	179.3	9.01	4.82	470.7	31.34
49.7	104.9	125.5	171.3	32.2	161.2	432.8	1.71	359.2	3.4	0.21	51.1	55.4	81.7		20.7	56.0	169.8	33.0	156.5	8.26	2.05	461.8	25.99
30.0	95.3	125.1	176.8	32.6	160.0	410.0	1.72	359.7	7.9	0.20	50.0	32.6	66.8		20.9	37.4	172.3	33.0	152.8	8.41	1.79	442.8	26.16
11.3	119.4	122.8	178.6	31.9	165.8	399.5	1.75	368.2	4.8	0.21	50.0	15.2	107.3		20.8	36.8	181.2	32.7	160.2	8.78	1.61	442.2	25.89
65.1	111.0	105.8	156.6	23.3	106.4	166.7	1.15	281.3	55.6	0.18	57.2	68.1	106.7		18.3	9.7	157.4	24.6	106.5	5.60	0.25	170.9	18.54
82.2	104.6	94.8	203.4	20.2	99.2	296.1	1.15	237.5	58.3	0.17	55.3	79.7	96.3		18.4	43.7	206.7	21.5	95.5	5.16	1.87	304.5	15.21
105.0	116.8	118.6	349.0	20.4	95.4	595.7	1.17	195.2	61.1	0.17	56.5	117.2	125.5		17.8	62.3	341.4	21.1	93.1	4.82	1.30	595.2	14.28
52.1	115.7	127.5	79.9	30.0	141.7	270.8	1.90	228.1	17.0	0.18	55.7	51.1	99.5		17.5	33.9	50.1	30.1	130.6	5.72	2.37	264.1	26.87
127.6	111.8	104.0	152.2	18.8	85.2	257.7	1.10	187.1	37.9	0.18	60.2	128.7	114.2		18.0	38.1	135.8	20.4	85.5	4.45	2.88	263.8	12.67
88.0	125.1	103.9	162.8	22.2	104.1	308.0	1.22	204.2	35.9	0.18	51.6	92.3	131.2		18.1	30.9	140.1	22.8	102.9	5.22	2.63	311.0	16.19
106.0	166.5	124.9	135.2	21.1	105.2	324.2	1.22	201.3	39.8	0.17	57.6	104.6	179.9		18.3	48.4	89.6	22.3	103.6	4.96	5.72	319.5	15.80
117.6	133.2	96.6	175.1	19.2	102.6	301.2	1.15	188.7	34.1	0.18	57.9	121.1	136.2		18.4	33.8	178.9	20.6	100.8	4.83	3.70	318.6	14.90
111.5	132.3	96.7	178.8	21.6	98.7	349.2	1.10	186.7	34.7	0.17	49.1	106.1	118.5		17.2	38.1	148.2	21.2	91.7	4.40	5.34	343.5	14.77
115.3	156.9	102.7	170.7	21.3	100.7	382.4	1.13	199.2	37.8	0.18	52.7	116.7	158.6		17.8	48.5	125.2	21.8	98.6	4.93	7.59	393.2	15.08
103.3	117.5	96.7	170.6	19.8	94.4	263.9	1.09	228.5	72.8	0.18	53.7	100.8	109.9		17.6	20.8	169.2	20.3	91.6	4.87	1.19	267.3	13.99
107.0	100.7	99.4	171.9	19.6	85.8	254.9	1.06	226.4	70.3	0.18	54.4	103.1	90.6		17.3	22.3	169.0	20.6	83.1	3.56	1.28	255.0	13.96
132.9	85.9	107.0	195.5	19.8	80.2	148.2	1.13	238.9	78.4	0.17	55.7	133.8	83.2		19.2	3.9	201.3	21.4	82.5	3.60	0.36	156.5	13.55
54.0	95.9	105.4	167.9	24.2	90.2	285.5	1.25	307.7	52.9	0.20	54.4	56.8	75.0		18.8	25.0	149.3	24.2	94.1	4.10	1.27	295.8	15.85
78.0	133.6	103.9	161.4	23.2	106.5	292.7	1.27	219.9	42.9	0.17	51.4	86.1	131.1		19.3	54.9	164.3	24.0	109.8	5.55	3.43	313.1	17.11
79.3	127.5	109.2	164.9	23.4	110.0	299.9	1.27	216.9	50.0	0.19	52.7	84.0	126.7		18.4	35.6	142.6	23.5	109.1	5.49	2.18	309.7	16.77
94.4	161.0	113.5	172.4	24.6	121.1	329.9	1.38	201.8	30.6	0.18	55.4	93.5	160.7		19.1	38.3	172.5	25.2	123.5	6.28	2.37	339.1	19.64
97.7	144.3	115.1	186.7	25.9	126.1	268.4	1.41	202.8	32.4	0.18	53.9	97.4	132.5		18.9	36.3	180.4	25.2	123.4	6.33	2.09	271.1	19.25
90.5	148.1	111.3	142.0	25.0	106.9	246.1	1.37	212.6	32.6	0.19	55.3	99.4	158.7		19.3	28.2	127.4	26.0	106.6	5.01	2.13	256.3	19.47
90.5	149.3	110.9	166.7	24.3	116.9	403.1	1.33	205.6	32.3	0.17	53.6	95.4	161.9		18.7	53.1	147.9	24.3	115.0	5.84	4.31	410.4	18.29
107.0	125.9	95.3	175.2	20.8	101.8	364.5	1.18	207.7	38.2	0.19	55.7	117.4	124.6		18.5	65.2	179.4	21.7	103.7	5.13	0.74	383.7	14.09
51.8	134.0	122.0	224.5	31.8	168.6	447.3	1.74	225.3	15.3	0.19	51.2	52.6	125.6		21.0	49.1	227.4	32.0	166.1	7.99	4.75	446.0	30.52
97.2	151.9	106.0	242.2	22.4	118.6	419.0	1.30	201.4	30.7	0.19	57.3	96.5	152.2		18.8	28.4	249.1	23.2	119.7	5.93	2.28	424.4	19.51
133.9	114.7	131.4	245.9	21.3	107.8	528.2	1.26	271.2	79.3	0.18	62.8	134.7	115.6		19.2	19.2	257.6	21.8	108.3	5.32	1.18	567.4	15.27
135.8	112.2	129.4	241.7	22.5	111.0	471.7	1.24	297.5	86.3	0.20	62.3	137.4	103.0		19.4	25.2	257.2	23.6	110.8	5.15	1.46	500.3	15.16
48.2	145.7	146.5	321.7	31.5	196.6	397.0	1.73	244.7	16.8	0.17	47.9	76.8	140.7		20.7	76.7	315.7	31.3	181.7	7.54	8.07	384.7	28.25
34.9	105.9	165.0	225.5	35.7	224.7	519.8	2.18	283.7	7.9	0.17	47.1	38.9	94.6		22.2	62.0	234.0	35.6	225.8	9.86	4.81	511.8	36.00
46.2	104.6	150.9	261.7	37.1	235.5	487.3	2.20	283.3	13.2	0.17	47.4	81.0	100.6		22.8	59.1	261.1	37.0	234.2	9.70	2.63	513.6	39.73
173.2	209.5	126.9	244.6	21.0	105.0	229.2	1.18	211.7	32.9	0.17	68.4	189.3	223.3		17.6	37.7	233.3	20.5	104.2	4.24	2.59	254.0	14.15
88.0	168.9	153.1	320.0	29.1	159.2	646.8	1.71	298.3	13.4	0.18	56.3	89.6	161.4		20.2	45.1	324.1	28.8	152.7	6.42	3.19	636.8	23.81

105.6	112.5	116.9	259.4	22.7	106.3	289.3	1.18	242.8	53.8	0.19	57.3	107.9	114.5		18.4	31.7	268.4	22.3	104.6	4.26	6.33	292.3	14.93
65.6	140.4	154.8	213.2	33.6	191.0	429.6	1.94	242.7	9.8	0.19	53.1	69.0	152.2		21.4	40.1	223.1	33.5	195.0	8.30	3.54	432.1	32.82
219.9	151.0	314.1	235.7	19.2	108.7	250.0	1.16	205.2	30.9	0.18	64.1	203.0	161.2		18.7	23.6	237.7	19.6	95.3	4.11	1.21	250.1	13.78
78.6	146.2	131.6	228.9	25.5	139.2	235.7	1.40	238.4	34.5	0.19	54.9	78.3	149.3		19.6	54.0	226.5	25.3	128.3	5.53	4.21	235.9	18.97
126.1	102.8	125.8	243.0	22.2	108.7	268.3	1.21	279.1	51.1	0.20	68.0	133.9	95.3		20.2	24.0	259.4	23.3	112.3	5.43	3.01	278.2	15.38
73.6	50.3	44.4	168.7	10.9	28.7	255.7	0.43	84.9	104.9	0.09	20.3	76.7	57.8	49.4	17.6	170.4	173.1	9.7	29.1	1.57	3.65	273.1	3.07
123.5	116.2	83.9	124.1	27.1	76.3	62.7	1.15	265.6	199.0	0.17	43.9	130.0	106.3	84.7	16.6	12.6	117.5	24.0	70.8	3.29	0.43	65.1	6.39
107.6	98.9	72.0	206.2	23.8	74.3	313.4	0.85	198.2	187.5	0.18	45.0	117.9	101.8	78.3	16.8	103.5	210.0	22.0	71.4	3.03	2.37	308.4	5.83
69.3	52.4	42.9	177.2	12.0	32.0	60.4	0.46	102.7	75.1	0.09	20.8	63.6	63.1	45.5	17.3	9.7	167.9	11.5	27.2	1.31	2.80	64.5	2.89
79.9	64.5	52.7	202.8	11.8	31.7	169.6	0.45	104.0	88.3	0.10	23.1	84.8	75.2	54.6	18.3	51.1	215.0	10.8	31.1	1.42	5.63	164.9	3.00
110.8	86.5	64.9	147.9	20.2	48.8	94.9	0.76	149.3	92.4	0.14	29.7	108.2	90.6	66.6	15.1	11.3	134.8	18.2	44.1	1.89	1.57	90.7	4.25
144.4	115.6	93.1	129.7	25.9	78.5	101.0	0.99	240.8	191.5	0.19	47.8	150.9	106.3	88.7	16.7	14.2	127.2	22.7	74.3	3.02	1.09	100.6	6.39
82.9	51.5	31.4	196.7	8.9	23.3	61.3	0.36	89.0	75.7	0.07	18.7	80.6	54.2	32.7	17.9	19.0	199.6	8.0	23.5	1.10	6.19	68.6	2.61
42.2	53.0	43.1	226.8	12.3	49.1	100.6	0.55	107.1	149.2	0.08	20.5	38.6	70.7	43.0	17.4	19.3	219.0	11.3	38.8	1.43	0.54	97.5	5.08
25.6	22.9	32.5	297.2	7.5	24.0	99.7	0.35	63.3	52.6	0.06	13.3	22.2	22.4	29.5	17.0	34.0	293.8	6.9	24.9	0.88	1.35	101.4	4.46
59.4	38.6	42.7	227.8	10.8	32.8	52.3	0.50	101.8	59.0	0.08	23.0	57.3	35.0	41.6	16.9	9.3	216.0	10.1	31.4	1.29	0.32	49.8	4.03
81.1	58.8	62.9	187.3	16.1	45.7	147.4	0.71	141.4	77.2	0.12	32.1	74.6	61.2	58.0	16.6	8.9	169.8	14.9	43.3	1.92	0.22	137.3	8.24
178.8	64.0	109.0	171.0	16.1	52.9	98.2	0.79	163.4	206.9	0.12	33.7	194.1	75.7	107.0	17.7	39.5	183.2	16.5	55.9	2.59	0.47	93.3	9.26
348.5	64.2	87.0	185.0	17.5	56.4	128.8	0.81	158.3	202.6	0.12	41.1	338.4	86.1	86.5	16.7	59.5	187.3	17.1	56.0	2.53	0.21	123.8	5.07
109.8	99.7	103.6	115.1	29.4	83.1	73.4	1.20	229.6	232.9	0.18	50.5	99.7	98.0	106.9	16.4	14.3	111.2	27.5	84.9	3.59	0.53	66.6	9.52
106.1	102.6	117.2	110.9	28.1	88.9	104.1	1.19	229.1	231.1	0.19	55.2	102.8	107.3	126.2	16.2	14.4	108.6	27.3	84.6	3.64	0.46	97.0	8.07
125.7	83.1	84.5	118.1	25.2	74.7	109.7	1.01	211.9	256.2	0.16	48.7	121.2	80.8	85.7	15.6	22.4	118.1	24.2	74.4	3.06	0.73	105.7	10.33
109.0	80.9	84.9	122.2	23.5	81.1	59.4	1.03	220.5	337.5	0.18	47.5	108.6	77.6	99.4	16.2	15.6	121.7	23.3	77.7	3.20	0.70	57.9	8.08
24.6	31.4	53.7	500.8	89.5	378.9	431.7	1.23	90.3	65.4	0.08	12.2	19.2	12.1	56.6	23.4	13.7	454.7	85.8	363.9	21.98	0.06	415.1	131.44
43.6	39.4	95.3	715.7	92.5	453.5	515.9	1.36	134.3	217.5	0.09	16.7	40.6	37.2	106.1	25.9	30.9	699.4	93.0	440.8	22.64	0.13	507.3	144.63
59.5	44.2	72.8	697.9	85.9	344.3	654.6	1.31	116.2	55.5	0.08	16.9	53.8	47.8	75.1	24.9	26.4	672.1	83.9	328.9	19.29	0.05	621.4	127.95
54.3	75.2	159.6	239.7	30.5	116.7	122.7	1.26	314.9	85.9	0.22	55.3	52.4	88.8	0.30	19.6	29.2	239.2	30.3	114.3	5.34	0.93	117.6	12.45
26.5	57.0	171.2	144.4	45.1	188.5	311.1	1.70	349.0	21.5	0.20	51.0	27.0	54.1	0.48	19.7	31.4	141.5	43.5	183.7	9.85	0.87	311.1	21.35
50.4	61.8	139.1	143.0	43.1	187.0	327.2	1.66	350.4	21.3	0.21	51.8	46.2	58.9	0.54	20.5	32.1	139.3	43.7	190.1	9.88	0.85	309.9	21.76
48.4	46.7	141.3	152.3	30.1	108.8	202.1	1.37	334.9	88.8	0.20	58.3	49.4	47.4	0.46	20.5	19.2	159.0	32.3	112.9	5.40	0.63	205.1	12.73
57.3	49.9	164.0	158.6	30.8	106.7	199.7	1.30	319.2	88.1	0.21	55.4	58.3	45.9	0.38	19.6	18.5	155.2	31.0	104.6	5.28	0.57	198.8	12.32
119.5	65.1	158.3	131.2	30.2	102.6	137.7	1.24	304.7	140.9	0.24	50.6	99.5	69.0	0.22	18.3	9.9	129.1	29.6	102.6	5.62	0.20	124.4	10.17
49.3	47.5	138.2	125.4	27.9	95.0	113.3	1.19	296.6	141.2	0.19	49.1	51.5	51.2	0.16	17.6	9.5	123.2	28.3	95.3	5.73	0.19	112.8	9.29
53.1	102.5	167.7	119.5	35.2	126.5	216.7	1.36	334.2	91.3	0.20	56.7	54.1	110.2	0.43	20.0	25.7	122.4	36.0	133.8	7.52	0.72	215.0	15.09
85.3	53.3	159.3	134.9	38.1	133.2	144.4	1.65	373.6	106.7	0.21	86.5	81.6	58.0	0.89	21.0	17.4	133.0	38.5	133.6	8.02	0.60	144.5	11.78
35.3	52.7	159.5	132.3	36.8	129.2	142.6	1.59	365.3	103.0	0.23	51.7	35.7	58.4	0.30	20.6	16.6	128.2	37.2	131.7	6.75	0.56	141.0	11.57
105.2	50.0	124.0	131.0	25.0	80.1	76.3	1.19	300.2	231.1	0.20	56.7	95.3	47.4	0.33	19.3	8.2	131.1	25.4	80.7	4.55	0.45	75.1	7.12
104.0	49.4	127.2	136.9	26.3	82.9	77.2	1.22	310.1	238.8	0.21	84.1	101.1	51.8	0.64	19.6	8.5	134.8	26.4	85.8	5.70	0.52	74.0	7.32
11.5	80.2	175.9	119.8	38.2	119.9	97.0	1.75	397.9	9.0	0.21	58.7	19.0	80.0	0.35	20.0	7.1	116.8	38.7	125.5	7.64	0.53	95.1	10.96
5.2	58.5	179.3	121.1	45.6	162.8	226.4	1.85	358.2	7.7	0.30	50.0	8.1	56.2	0.51	20.7	20.1	131.5	45.9	172.3	9.66	1.32	220.5	17.41
52.3	85.6	150.6	140.3	34.2	119.1	134.5	1.47	359.8	59.2	0.20	54.3	51.4	92.4	0.22	20.1	11.7	137.0	34.1	114.6	6.75	1.08	134.3	10.94
58.7	54.3	152.2	165.8	29.1	102.0	207.1	1.11	284.8	109.1	0.21	105.9	60.5	61.0	1.40	18.7	17.9	156.9	27.7	98.0	6.17	1.28	217.9	12.12
19.8	61.3	182.3	174.3	42.3	172.2	261.3	1.80	411.2	18.0	0.21	57.7	27.8	62.8	0.57	21.9	44.2	185.8	44.8	190.3	9.59	2.19	271.6	20.67
22.7	63.3	191.9	184.8	43.0	169.5	264.0	1.74	386.4	17.3	0.24	53.5	26.6	72.4	0.47	21.0	42.1	181.0	43.8	177.0	9.31	2.35	268.5	20.20
14.8	66.9	166.6	147.9	43.7	171.3	329.3	1.75	368.1	27.9	0.24	53.2	20.4	65.1	1.43	21.1	26.2	149.8	43.3	170.1	9.70	1.06	301.6	20.70

23.7	74.5	165.1	135.7	31.6	104.6	157.0	1.34	344.2	59.6	0.23	50.9	24.3	76.5	0.33	18.7	39.6	133.4	30.8	109.1	5.97	13.28	152.4	10.51
14.7	62.5	147.3	143.0	44.8	163.5	160.1	1.72	368.7	34.2	0.21	50.1	18.9	62.3	0.55	22.8	39.2	153.1	48.8	185.9	8.64	6.06	162.7	15.92
62.2	59.5	129.1	147.8	25.8	97.1	224.0	0.96	264.1	105.0	0.19	50.1	57.9	66.7	0.25	17.2	17.5	147.5	25.7	100.8	4.76	1.01	209.6	11.30
86.8	49.6	120.2	164.9	33.7	109.4	216.7	1.28	312.3	13.3	0.25	40.5	80.0	49.7	0.25	17.4	22.2	164.2	32.6	113.5	5.51	1.11	206.7	12.94
68.0	97.8	143.4	149.0	28.5	103.4	232.9	1.17	279.0	94.3	0.05	63.2	61.5	95.4	0.37	18.5	21.0	148.2	28.5	93.6	4.10	0.98	225.1	12.59
55.1	59.6	139.8	145.9	33.8	119.5	176.5	1.33	315.7	75.3	0.20	109.5	54.8	65.1	1.09	19.5	18.5	139.8	34.0	121.8	8.46	0.69	181.4	13.19
48.8	51.5	154.5	144.0	33.6	123.9	186.8	1.30	327.2	79.6	0.21	54.8	48.0	58.6	0.43	19.6	18.9	138.7	34.1	126.4	6.91	0.67	190.2	13.40
80.6	54.0	127.7	134.5	24.8	82.8	122.8	1.00	276.7	180.8	0.17	57.1	70.1	54.6	0.26	17.8	18.8	135.7	25.0	76.8	4.10	2.87	117.1	8.18
71.4	148.6	122.7	214.5	32.0	105.8	318.2	1.20	333.3	149.1	0.25	53.8	71.6	146.5		18.5	88.6	210.4	32.8	112.5	5.49	0.64	325.2	10.52
66.8	176.9	137.0	201.0	31.0	95.8	154.2	1.37	353.4	100.7	0.25	51.1	76.0	177.3		19.5	37.3	201.0	31.6	99.6	4.68	2.31	156.7	9.34
38.2	133.6	182.6	195.0	48.0	168.9	206.7	1.71	306.3	68.6	0.26	43.8	37.1	233.6		21.0	52.7	192.5	48.7	175.3	9.10	0.72	207.0	14.89
69.6	150.6	146.7	186.3	35.7	111.5	301.8	1.48	375.1	79.0	0.24	55.1	71.9	146.6		20.3	78.8	181.5	35.5	119.4	5.07	0.84	306.8	12.04
62.7	135.7	152.3	129.7	40.9	111.2	172.7	1.37	343.6	70.9	0.22	52.7	61.5	126.5		18.2	32.0	126.1	40.9	115.3	5.60	0.15	170.7	13.62
173.8	133.8	157.8	140.2	43.0	156.8	247.6	1.42	369.4	67.5	0.24	54.8	185.6	121.0		19.4	30.1	144.2	44.7	164.2	7.84	0.81	247.6	16.84
77.6	152.7	834.1	147.6	39.4	126.1	135.2	1.60	387.1	123.5	0.19	50.0	79.0	171.5		21.5	4.6	147.6	39.6	126.2	6.73	0.20	136.1	11.20
66.4	163.9	159.6	241.6	33.0	98.1	172.3	1.28	351.4	141.0	0.23	56.7	74.2	178.9		18.8	44.9	246.7	32.9	97.4	4.92	0.77	170.1	10.34
75.2	151.6	218.5	120.5	29.5	99.4	112.5	1.11	335.2	104.5	0.21	60.4	85.2	165.8		19.2	10.9	121.6	30.6	103.9	4.55	1.26	111.5	8.97
159.8	82.4	91.2	144.0	25.1	93.3	193.5	0.87	230.2	380.6	0.17	53.0	162.4	72.9		17.5	16.4	144.0	25.9	93.3	4.29	1.80	198.7	14.52
170.4	122.5	90.1	145.1	20.6	74.1	193.3	0.74	216.3	507.5	0.20	55.8	163.6	136.5		15.6	24.8	144.8	21.8	76.2	3.53	1.14	193.8	11.90
9.4	65.3	181.5	155.3	41.9	163.6	296.0	1.67	361.4	12.4	0.23	53.1	11.9	57.7	0.44	20.6	27.1	153.8	42.1	164.7	7.32	1.49	285.4	19.32
50.9	55.7	139.6	143.1	30.4	114.6	134.9	1.32	318.2	100.6	0.23	50.0	47.7	54.4	0.23	18.9	20.4	143.1	30.0	108.3	5.71	1.20	122.3	9.73
15.3	56.4	136.4	62.4	39.3	145.2	88.0	1.71	337.9	14.7	0.22	56.6	15.8	55.6	0.33	18.7	4.7	62.5	40.5	154.6	8.10	0.72	86.0	18.36
58.8	159.4	142.7	129.1	36.2	113.7	128.2	1.35	341.8	90.0	0.22	56.1	60.7	169.1		18.3	16.2	128.2	37.3	116.5	5.66	1.49	126.0	11.54
39.4	66.5	136.1	156.7	29.1	100.7	183.6	1.19	312.1	70.8	0.21	54.5	35.5	73.0	0.30	18.3	21.9	154.4	29.5	98.7	5.24	2.06	176.4	10.69
84.1	127.1	111.6	196.2	24.6	92.0	267.3	1.02	282.9	83.3	0.19	51.9	81.4	124.5		16.9	74.1	183.9	23.5	83.4	3.39	2.21	250.1	13.26
69.8	68.9	70.8	215.8	16.7	52.1	277.4	0.65	200.1	118.7	0.16	42.1	68.3	61.5		16.6	20.5	211.1	15.9	46.8	1.74	0.19	255.1	7.70
16.1	80.1	151.5	112.8	48.4	188.9	144.0	1.95	313.6	4.2	0.23	35.3	13.6	81.4		19.9	8.9	108.3	48.6	183.5	10.33	0.34	144.0	18.05
107.7	101.2	96.9	183.1	40.4	169.5	534.2	1.37	275.9	116.6	0.16	39.3	86.1	117.6		17.8	57.1	169.5	39.8	163.6	7.38	3.74	520.6	22.44
50.8	155.2	94.4	156.6	33.5	111.0	168.7	1.29	281.7	124.4	0.17	46.6	47.4	155.2		16.9	11.0	142.3	32.9	103.9	5.65	0.72	164.0	11.94
65.7	110.8	90.1	146.7	29.0	102.3	46.9	1.12	266.4	85.4	0.18	45.1	66.2	112.7		16.0	4.3	137.1	28.8	96.0	4.00	0.23	42.4	10.27
20.3	63.6	170.7	163.0	41.9	136.4	192.5	1.74	363.0	16.1	0.26	50.2	23.6	59.9	0.43	20.7	23.5	163.6	42.3	133.2	8.03	1.90	181.4	14.78
35.6	54.6	139.5	154.0	31.8	111.7	223.3	1.32	320.0	44.5	0.18	48.9	36.4	53.0	0.29	19.8	20.1	154.0	31.0	109.3	5.12	0.95	207.4	12.16
44.7	46.8	122.8	140.2	25.5	80.7	165.6	0.99	284.7	140.8	0.21	49.4	39.4	42.2	0.15	16.9	11.7	141.5	25.1	77.7	3.61	0.46	156.3	8.68
15.3	63.6	171.5	127.8	39.2	138.2	174.6	1.53	367.0	32.5	0.20	51.2	17.3	65.8	0.38	19.4	15.9	125.4	38.1	140.0	7.41	1.71	163.9	13.27
81.8	46.7	151.1	147.9	37.6	132.5	216.8	1.48	304.5	57.6	0.20	87.2	76.8	45.8	0.95	19.9	23.5	146.0	36.6	227.9	9.05	0.81	216.7	15.12
18.1	52.4	227.1	104.8	34.5	154.5	53.2	1.79	374.4	16.8	0.17	48.1	19.5	59.1	0.42	25.8	7.0	110.9	38.2	174.4	8.09	0.48	55.9	13.54
21.4	62.1	169.9	155.6	45.2	199.6	335.1	1.80	378.8	16.6	0.21	51.8	19.5	55.0	0.51	21.1	30.4	152.3	46.2	200.7	10.66	0.96	332.2	23.33
7.9	30.4	136.6	167.8	24.1	178.2	297.5	1.43	291.3	1.6	0.15	44.8	7.6	5.7	0.37	22.7	14.6	166.7	25.6	187.0	8.71	0.26	295.6	32.49
181.5	59.9	153.6	173.2	36.2	129.3	305.8	1.56	383.5	142.9	0.21	55.5	170.7	65.7	0.34	20.5	77.5	168.8	36.7	135.0	7.43	15.92	325.6	10.86
96.9	198.9	155.0	398.3	23.6	143.7	441.8	1.80	431.6	341.0	0.20	63.0	98.6	216.7		22.9	29.3	405.5	24.6	143.7	6.42	1.25	455.8	22.35
816.9	153.1	677.1	245.7	29.9	191.5	699.2	1.59	367.3	6.7	0.24	37.7	796.3	183.9		24.3	79.0	247.9	30.0	195.4	9.16	1.02	683.2	29.15
806.1	95.8	158.0	6.7	10.0	41.2	14.4	0.28	104.4	4234.3	0.16	53.0	786.7	90.1	151.6	7.8	0.8	6.3	9.7	36.5	2.15	0.06	10.4	6.11
58.1	60.1	53.2	226.3	7.7	11.2	213.9	0.21	105.4	144.6	0.13	25.7	61.1	56.0	49.6	13.8	5.5	212.4	6.9	19.6	0.62	0.14	218.9	2.90
19.9	65.1	60.9	287.7	8.9	25.8	157.3	0.30	88.2	1.0	0.10	26.9	25.4	65.4	62.8	18.4	6.8	294.8	8.1	25.9	1.12	0.48	170.8	5.17
106.4	57.7	44.5	246.5	7.4	22.5	141.7	0.21	100.5	308.0	0.11	20.8	111.0	62.8	40.6	15.7	8.4	246.5	7.4	24.6	0.54	0.37	149.0	4.10

194.2	89.1	65.7	96.6	8.9	21.5	79.3	0.29	173.9	494.6	0.18	40.3	195.4	98.5	59.4	10.8	7.6	95.6	8.5	21.2	0.75	1.27	84.2	2.91
41.3	70.0	88.0	284.7	9.2	25.5	238.5	0.35	115.4	164.4	0.10	23.0	45.2	73.1	90.1	16.1	15.0	277.5	8.6	25.7	1.00	0.70	249.3	4.57
118.7	85.4	88.1	290.8	5.6	19.7	333.3	0.19	76.3	83.5	0.13	29.9	127.0	86.7	89.0	17.8	22.5	299.9	5.2	21.1	0.54	1.28	342.2	2.68
191.2	429.4	117.2	697.1	12.6	18.6	383.8	0.67	259.3	84.8	0.21	42.0	191.5	445.0	110.5	14.6	22.2	708.0	12.0	17.9	0.37	1.37	400.2	2.54
347.9	473.7	100.5	742.5	9.8	19.2	325.5	0.62	218.7	573.6	0.21	71.4	375.8	515.5	106.2	14.6	16.8	763.1	9.2	19.5	0.57	1.07	300.8	4.38
101.0	33.2	63.2	804.4	12.2	148.7	927.6	0.59	109.7	171.0	0.09	19.9	98.0	41.4	67.3	20.6	153.1	786.4	12.8	148.5	11.00	3.32	913.2	37.08
81.7	43.3	63.9	276.1	10.8	28.4	525.1	1.04	165.9	55.1	0.21	33.0	75.6	48.2	64.7	15.9	40.1	239.5	9.6	30.4	1.29	1.13	517.0	5.66
17.4	24.3	76.6	1838.4	20.6	216.5	2968.8	0.71	78.6	11.2	0.10	11.4	18.0	26.3	84.4	24.4	96.0	1813.2	19.8	226.5	5.15	0.52	2799.9	125.28
130.5	417.4	70.2	450.0	3.9	20.6	116.1	0.15	67.6	91.4	0.12	25.5	132.5	391.5	64.7	16.2	7.9	464.1	3.7	20.5	0.47	0.81	120.8	3.07
708.5	2911.8	115.4	450.6	6.5	30.4	269.1	0.19	66.2	141.1	0.14	43.7	695.7	2979.2	113.2	15.8	20.8	424.2	6.4	30.4	0.78	0.90	272.0	7.45
666.0	838.0	130.0	131.9	13.3	134.7	513.2	0.35	113.6	139.1	0.22	71.1	642.7	819.9	133.9	13.2	48.7	131.5	12.8	92.1	2.70	2.52	533.4	10.42
422.4	717.8	94.6	404.9	7.3	10.9	69.7	0.23	145.4	153.9	0.18	49.4	417.5	727.4	90.9	13.8	4.1	418.6	6.7	13.4	0.22	0.22	73.7	2.46
225.1	143.7	99.6	343.5	9.6	24.4	227.8	0.24	118.4	467.8	0.19	48.5	223.2	153.7	95.2	14.0	14.9	350.4	8.6	26.1	0.74	0.68	232.5	9.39
408.8	1465.4	144.6	32.4	17.8	45.5	581.5	0.61	230.4	224.0	0.27	70.2	420.0	1450.1	154.9	10.6	53.2	32.3	16.6	44.4	1.86	3.15	599.7	9.68
85.8	65.4	48.4	542.1	9.9	38.5	196.4	0.28	110.6	99.6	0.12	24.9	78.7	70.8	55.8	14.9	9.1	574.4	8.9	35.8	1.15	0.23	204.5	7.16
316.3	218.7	97.3	212.9	6.6	23.7	229.5	0.24	134.1	380.4	0.25	60.1	312.3	243.5	104.5	14.7	15.3	212.5	6.4	23.2	0.39	0.78	241.7	2.62
150.4	346.2	62.6	532.6	7.1	14.9	183.3	0.20	112.5	251.3	0.15	37.7	145.8	366.4	71.7	14.5	15.4	517.4	6.4	16.9	0.34	0.41	190.1	3.88
24.1	123.1	90.4	230.9	42.0	120.5	586.2	1.33	332.5	6.3	0.21	42.2	41.6	114.4	92.5	19.5	27.8	230.9	38.1	122.0	6.93	1.79	614.2	22.10
61.9	147.3	120.7	520.9	28.7	79.9	854.8	0.98	288.7	126.9	0.21	48.8	69.2	148.1	124.6	16.3	44.0	540.0	27.7	78.6	4.49	2.35	835.4	10.82
144.1	175.3	125.0	941.9	8.8	50.7	887.9	0.46	49.4	280.9	0.09	35.2	145.3	182.1	128.8	21.9	51.2	951.2	7.5	47.8	2.12	4.15	857.4	41.18
84	80	70																				80	21
88	32	90																				110	16
460	48	13																				130	
29	100	200														76	260	26	240	8.6		680	
51															15	10	355	13	90	3.35	0.42	59	14.28
150															17	5	80	27	87	4.1	0.95	93	3.76
21															15	40.2	242	13	106	4.1	2	722	15.67
21															15	40.2	242	13	106	4.1	2	722	15.67
9				14		12									22	106.9	123	58.33	584	14.84	1.87	1190	278.27
1															23	138	66	44	374	12.8	7.95	919	19.28
1															23	138	66	44	374	12.8	7.95	919	19.28
1															20	69	34	38	336	11.3	2.59	713	32.96
1															20	69	34	38	336	11.3	2.59	713	32.96
60															21	2.6	127	46.2	148	7.1	0.53	33.02	8.13
19	90	100														67	320	19	120	4.4		680	19
62	100	100														41	250	22	120	6.2		270	17
700	86	70														2.8	110	21	83	2.7		30	13
54	43	180														30	170	20	140	3.9		230	15
94	96	200														27	270	19	120	3.1		430	15
40	100	210														61	310	17	160	6		520	24
62															20	77	422	19	120	5.08	1.48	1397	26.39
51	40	110														54	240	24	120	3.3		820	21
106															18	1	225	31	110	7	0.01	57	13.42
116															19	9	159	32	107	5.05	0.17	285	13.48
12															24	106.9	278	63.15	513	30.75	2.68	2822	126.04

11			14	23	23	195.4	29	53.61	429	21.13	9.39	1125	18.51
10			14	11	21	104.1	250	52	615	32.1	2.51	3173	72.52

51	70	110				46	410	25	100	3		550	18
28	100	130				50	300	21	140	4.4		300	24

3				14	26	17	65.7	89	45.22	420	15.47	1.01	571	31.25
1						21	99.8	78	44.55	462	16.02	1.55	852	73.62
46						19	11	463	19	147	9.73	3.13	170	20.92
46						19	11	463	19	147	9.73	3.13	170	20.92
53						15	22	236	19	129	9.59	0.96	253	15.15
53						15	22	236	19	129	9.59	0.96	253	15.15
122						18	1.1	130	27.05	50	3.3	0.02	24	2.82
3						21	210.8	109	59.56	474	28.06	2.85	891	113.43
69						18	51	377	13	276	3.35	3.07	439	14.16
69						18	51	377	13	276	3.35	3.07	439	14.16
9						22	128.1	103	55	562	18.9	1.93	1683	119.77
9						22	128.1	103	55	562	18.9	1.93	1683	119.77
	53	73	220		148				11	40	2			6.04
	79	101	211		276						28			
	60	92	245		188				8	31	1.7			5.33
	45	69	222		146						39			
73	16	142			1857					126				
72	94	117			1262					124				
67	33	302			2942					123				
100	117	99			525					71				
49	57	117			273					109				
106	8	108	294.61	20.78	169		114.27			75	4	4		10.21
113	96	94	220.56	15.06	59		7.16			56	2.33	0.18		6.86
96	14	89	114.94	19.94	47		2.97			109	4.8	0.15		14.39
139	54	111	177.22	24.26	108		7.5			101	4.23	0.22		14.46
121	4	283	104.25	23.54	219		16.4			103	4.68	0.42		13.2
130	60	189	86.1	23.51	804		75.03			133	6.04	2.01		12.77
77	128	134	193.04	26.9	180		9.84			104	4.49	0.24		13.36
88	58	119	192.82	25.86	447		15.14			105	4.59	0.23		13.51
152	89	93	197.45	20.71	73		4.76			86	3.79	0.13		14.44
150	94	101	291.54	19.83	95		6.06			89	3.93	0.18		13.8
151	36	101	115.42	21.09	32		2.52			85	3.92	0.14		9.59
117	152	90	98.12	17.01	34		1.63			68	3.09	0.1		11.65
122	94	84	197.67	17.95	151		5.78			71	3.15	0.12		10.23
80	151	113	237.52	22.83	861		51.6			93	4.33	0.28		14.77
59	96	122	280.18	25.61	140		25.16			127	6.4	1.16		19.63
89	69	80			492					46				
53	393	94			493					133				
55	94	100			253					132				
111	186	172	203.32	25.56	271		26.57			100	4.72	0.76		12.6
80	115	159	266.01	32.39	89		8.24			108	5.13	0.37		18.04
83	77	138	171.84	23.53	64		3.51			111	5.51	0.16		19.24
105	172	120	163.16	24.09	103		13.91			101	4.58	0.47		13.49
115	74	151	154.27	18.57	168		18.15			109	5.68	2.94		9.2
140	54	109	212.88	21.34	355		29.84			81	3.68	0.41		11.87

73	137	107	279.3	30.7	18	1.67	100	4.58	0.13	13.45
133	110	98	399.54	14.68	353	15.32	69	3.56	0.14	10.78
134	39	98	221.15	14.02	161	15.43	84	4.74	0.1	12.97
143	248	86	165.46	24.04	107	3.98	157	14.74	0.1	24.49
103	152	90	467.51	25.67	1065	68.87	193	12.8	2.25	38.02
87	106	75	273.18	23.03	328	24.74	181	12.18	0.91	31.27
86	39	134	598.42	24.69	1001	69.83	184	12.17	2.3	35.52
101	185	107	415.21	26.05	710	34.12	201	13.63	1.01	40.38
88	90	115	560.02	24.28	536	29.63	181	12.37	1.03	35.77
79	114	96	647.91	22.05	1312	56.02	174	11.39	1.95	34.52
63	111	110	533.63	32.53	796	26.89	252	18.36	1.63	45.63
62	72	129	494.67	31.74	985	55.43	252	18.32	3.35	51.7
130	454	67			351		217			
97	145	123			832		169			
80	151	67			617		225			
1	0	198			511		311			
3	0	347			716		224			
10	27	135			699		260			
5	9	120			685		221			
14	62	80			958		207			
19	24	161			290		288			
15	35	103			327		213			
40	148	77			123		174			
221	60	129			1431		150			
10	52	94			426		240			
305	215	138	463.11	24.1	1038	26.16	185	19.23	0.48	39.76
95	47	89	481.7	21.69	166	11.83	151	12.12	0.51	27.38
135	32	100	530.2	21.96	559	28.69	167	12.68	1.25	27.25
29	90	49	408.48	22.52	1122	108.75	205	10.79	3.98	44.19
208	17	115	405.47	19.65	531	16.25	148	7.39	0.35	25.22
7	11	125	578.41	26.78	828	119.9	234	13.18	2.3	45.81
4	35	101	643.22	26.35	1046	144.46	232	13.07	2.97	50.5
41	111	111	209.84	24.19	97	10.72	150	8.52	0.18	32.07
115	123	117	598.83	27.92	1498	53.69	206	15.21	0.42	39.91
105	150	134			810		168			
346	154	123	235.66	22.19	466	20.56	139	13.39	0.17	22.09
320	113	97	114.3	21.14	121	11.67	132	12.81	0.49	17.45
320	57	126	151.14	21.85	406	20.65	134	13.22	0.24	22.03
352	111	110			320		139			
342	136	127			236		122			
328	27	107			346		139			
357	126	120			434		139			
63	111	111	216.47	24.04	73	3.11	124	7.37	0.11	20.64
78	8	124	262.44	27.15	167	18.68	124	7.62	0.64	40.26
67	9	120	195.94	22.55	1037	97.69	122	7.42	2.93	21.22

64	18	122	335.93	23.89		560		38.05	123	7.57	1.3		24.92
63	136	92	414.01	25.64		119		8.44	125	7.6	0.32		27.37
63	64	90	365.26	24.17		209		23.88	124	7.6	1.46		26.59
66	80	75	589.01	24		216		10.22	127	7.59	0.64		24.9
67	68	87	202.58	20.94		987		42.65	127	7.03	0.6		25.69
216			164	15.7	61	190		5		2.2			
119			165	16	63	197		8		2.2			7.75
106			172	16	64	180		7		2.2			
801			116	11.5	44	97		5		1.3			5.54
874			115	11	43	125		7		1.3			5.38
1138			90	8.7	34	95		4		1.1			4.27
952			109	10.1	40	123		9		1.3			5.05
68			164	17	64	180		6		2.6			
70			175	17	64	184		7		2.6			
61			176	17.5	66	190		4		2.6			
408			154	13.5	52	106		10		1.8			6.52
348			152	14.2	54	242		9		2			6.78
386			161	14.4	56	236		5		2			7.6
174			158	15.5	61	150		3		2.2			7.59
193			172	16.1	60	160		5		2.2			
112			171	16.5	63	205		5		2.2			
122			166	16	62	187		5		2.2			
54			169	17	66	190		8		2.2			
416	67	93	231	14	76	202		28				3.3	10.8
319	76	86	197	17	82	181	14	24				2.2	10.3
408	76	83	133	13	74	225	12	40				3	10.2
209	73	75	258	14	95	371	16	28				1.1	17
247	95	87	179	13	60	148	15	20				2	7.7
510	66	76	129	11	56	141	12	22				2.5	9

140Ce ppm	141Pr ppm	146Nd ppm	147Sm ppm	153Eu ppm	157Gd ppm	159Tb ppm	163Dy ppm	165Ho ppm	166Er ppm	169Tm ppm	172Yb ppm	175Lu ppm	178Hf ppm	181Ta ppm	208Pb ppm	232Th ppm	238U ppm	Os ppb	Ir ppb	Ru ppb	Rh ppb	Pt ppb	Pd ppb	Au ppb
7.69	0.97	3.99	0.97	0.51	0.93	0.15	0.98	0.20	0.58	0.09	0.60	0.10	0.40	0.05	7.76	0.53	0.13							
8.81	1.14	4.66	1.18	0.48	1.14	0.19	1.25	0.26	0.76	0.13	0.84	0.13	0.65	0.07	2.32	0.71	0.20							
9.47	1.23	5.06	1.23	0.50	1.24	0.21	1.40	0.28	0.82	0.13	0.89	0.13	1.15	0.10	5.12	0.78	0.22	0.91	0.17	0.29	0.58	21.9	9.90	1.25
9.49	1.24	5.14	1.26	0.67	1.22	0.19	1.24	0.24	0.70	0.11	0.77	0.12	0.65	0.07	13.34	0.51	0.18		0.50	0.68	1.96	24.3	33.7	0.34
17.58	2.31	9.64	2.41	0.78	2.46	0.43	2.75	0.55	1.57	0.25	1.74	0.26	1.50	0.16	4.01	1.53	0.34	0.18	0.93	2.98	0.79	8.81	6.56	1.17
12.53	1.68	7.23	1.92	0.76	2.00	0.36	2.38	0.48	1.40	0.23	1.58	0.25	1.05	0.08	2.74	0.92	0.24	0.16						
4.94	0.80	3.18	0.81	0.44	0.73	0.12	0.81	0.17	0.47	0.08	0.54	0.09	0.36	0.06	6.42	0.35	0.33	0.25	0.25	0.33	0.98	16.4	16.7	1.20
25.90	3.18	11.96	2.45	0.77	2.33	0.36	2.13	0.44	1.34	0.20	1.18	0.19	1.84	0.22	15.22	3.94	1.24							
25.97	3.14	11.86	2.61	0.84	2.41	0.38	2.23	0.45	1.35	0.21	1.29	0.20	1.90	0.34	17.11	3.98	1.29							
27.26	3.24	12.45	2.68	0.83	2.45	0.39	2.35	0.46	1.45	0.22	1.25	0.20	1.93	0.24	7.83	4.03	1.32							
38.46	4.64	17.42	3.70	0.96	3.37	0.53	2.99	0.58	1.81	0.29	1.64	0.25	2.66	0.38	10.45	6.55	1.82		1.13	4.65	0.68	1.98	2.75	0.32
29.34	3.58	13.58	2.97	0.85	2.66	0.44	2.44	0.50	1.48	0.24	1.38	0.21	2.18	0.29	9.09	4.72	1.41							
27.84	3.38	12.66	2.76	0.84	2.55	0.40	2.44	0.47	1.48	0.22	1.35	0.21	1.94	0.27	9.08	4.64	1.29							
33.77	4.11	15.43	3.44	1.03	3.13	0.49	2.87	0.55	1.71	0.26	1.65	0.27	2.74	0.35	10.68	6.19	1.70							
28.89	3.54	13.73	3.13	1.01	2.87	0.45	2.70	0.55	1.70	0.26	1.58	0.25	2.17	0.25	11.06	4.80	1.47							
38.42	4.75	17.88	3.82	1.17	3.56	0.55	3.34	0.67	1.98	0.31	1.92	0.29	3.12	0.35	11.19	6.51	1.64		1.48	6.28	0.94	2.09	2.74	0.15
32.08	4.07	14.85	3.40	1.01	3.03	0.46	2.88	0.54	1.70	0.25	1.58	0.24	1.62	0.31	10.15	5.38	1.46							
38.63	4.77	17.22	3.89	0.98	3.43	0.50	3.11	0.60	1.80	0.29	1.87	0.28	2.63	0.43	27.12	6.37	1.98							
53.45	7.00	25.50	5.79	1.29	5.36	0.79	4.88	0.90	2.82	0.43	2.68	0.42	2.90	0.66	9.65	6.29	1.84							
54.62	6.82	24.54	5.59	1.47	4.94	0.74	4.56	0.85	2.54	0.39	2.44	0.37	4.14	0.56	5.82	10.19	2.77							
64.14	7.94	28.12	6.03	1.72	5.35	0.76	4.70	0.90	2.75	0.42	2.58	0.39	4.86	0.61	7.52	10.35	3.23		1.15	3.01	0.62	3.16	3.25	0.88
52.15	6.37	22.39	4.97	1.10	4.28	0.63	3.88	0.72	2.18	0.35	2.08	0.33	4.66	0.45	10.85	9.87	2.77		0.15	0.21	0.43	2.66	3.51	0.84
68.85	8.04	28.75	5.96	1.21	5.47	0.85	4.62	0.90	2.60	0.38	2.49	0.40	6.46	0.80	12.94	11.53	3.35		3.61	0.60	0.90	1.37	0.18	
25.32	3.09	11.61	2.56	0.79	2.54	0.38	2.25	0.45	1.36	0.21	1.34	0.22	1.78	0.24	7.57	3.53	1.01							
25.37	3.10	11.47	2.52	0.91	2.43	0.38	2.19	0.43	1.29	0.19	1.24	0.20	1.99	0.26	7.61	4.11	1.21							
24.40	2.90	11.18	2.59	0.88	2.42	0.37	2.38	0.46	1.32	0.20	1.32	0.21	1.44	0.18	6.98	2.80	0.77							
28.03	3.43	12.99	3.02	0.78	2.77	0.42	2.60	0.51	1.47	0.22	1.41	0.22	1.99	0.27	9.99	3.73	0.98							
28.09	3.34	12.83	2.92	0.86	2.70	0.41	2.55	0.51	1.49	0.23	1.47	0.23	2.27	0.30	11.80	4.20	1.23							
32.10	3.98	15.50	3.68	1.07	3.23	0.51	3.08	0.62	1.78	0.28	1.71	0.26	1.61	0.32	7.93	4.06	1.05							
20.47	2.46	9.74	2.36	0.79	2.21	0.36	2.20	0.45	1.28	0.21	1.32	0.20	1.50	0.24	7.07	2.98	0.81							
24.77	2.99	11.69	2.78	0.84	2.49	0.40	2.38	0.48	1.38	0.20	1.35	0.21	1.49	0.18	7.61	3.15	0.86							
32.32	3.76	13.60	2.97	0.82	2.67	0.40	2.45	0.49	1.34	0.21	1.36	0.21	2.54	0.37	9.21	5.10	1.31							
25.60	3.10	11.87	2.83	0.82	2.69	0.42	2.56	0.51	1.45	0.21	1.46	0.22	1.75	0.26	9.30	3.49	0.91							
22.33	2.74	10.36	2.39	0.79	2.30	0.36	2.20	0.44	1.24	0.19	1.20	0.20	1.46	0.19	8.43	3.09	0.92							
26.36	3.29	12.33	2.77	0.78	2.18	0.40	2.54	0.49	1.45	0.23	1.47	0.21	1.81	0.29	5.95	3.60	0.95							
79.92	8.79	28.13	3.70	0.61	3.50	0.43	2.56	0.45	1.42	0.22	1.52	0.22	3.29	0.96	4.99	16.58	1.54							
17.91	2.18	8.53	1.75	0.46	1.86	0.29	1.84	0.34	1.01	0.15	0.94	0.14	1.55	0.17	3.53	2.51	0.57		0.08	0.42	0.42	3.47	8.16	1.17
11.84	1.47	5.71	1.09	0.30	1.18	0.18	1.17	0.21	0.65	0.10	0.65	0.09	0.84	0.12	5.95	1.72	0.28		0.53	2.06	1.03	3.97	5.97	0.48
5.22	0.58	2.48	0.59	0.19	0.62	0.10	0.70	0.13	0.39	0.06	0.40	0.05	0.49	0.06	2.60	0.92	0.26							
5.99	0.67	2.83	0.62	0.19	0.62	0.10	0.72	0.13	0.40	0.07	0.45	0.06	0.74	0.08	1.62	1.00	0.28							
5.85	0.65	2.63	0.60	0.16	0.57	0.10	0.66	0.12	0.38	0.06	0.38	0.06	0.45	0.07	2.01	0.92	0.25							
6.55	0.73	2.99	0.63	0.18	0.64	0.11	0.72	0.13	0.42	0.06	0.43	0.07	0.75	0.06	3.01	1.02	0.27							

5.64	0.61	2.31	0.47	0.13	0.46	0.08	0.48	0.09	0.27	0.04	0.29	0.04	0.37	0.05	1.24	0.83	0.15	0.12	0.43	0.36	1.54	2.95	0.57
5.23	0.55	2.25	0.52	0.14	0.47	0.08	0.49	0.09	0.25	0.04	0.30	0.04	0.37	0.04	2.14	0.69	0.18						
3.31	0.38	1.58	0.38	0.12	0.36	0.07	0.45	0.08	0.25	0.04	0.28	0.04	0.33	0.05	1.21	0.72	0.17						
4.19	0.46	1.86	0.45	0.13	0.41	0.07	0.49	0.09	0.25	0.04	0.27	0.04	0.82	0.05	1.18	0.66	0.17	0.11	0.27	0.35	3.22	3.93	0.69
3.13	0.31	1.36	0.39	0.11	0.39	0.07	0.44	0.08	0.25	0.04	0.27	0.03	0.27	0.02	1.17	0.58	0.14						
3.75	0.36	1.47	0.36	0.11	0.34	0.06	0.40	0.07	0.22	0.04	0.23	0.03	0.25	0.02	1.01	0.59	0.16						
6.24	0.63	2.48	0.51	0.16	0.46	0.08	0.49	0.09	0.28	0.05	0.31	0.04	0.40	0.04	0.60	0.78	0.16						
3.48	0.35	1.53	0.39	0.09	0.35	0.06	0.44	0.08	0.25	0.04	0.26	0.03	0.30	0.03	0.79	0.56	0.18						
6.84	0.89	3.78	1.00	0.34	1.03	0.18	1.26	0.24	0.71	0.12	0.71	0.10	0.57	0.05	1.60	0.92	0.24	0.35	0.83	1.73	9.16	24.3	2.32
6.17	0.82	3.50	0.89	0.27	1.02	0.17	1.16	0.23	0.67	0.11	0.69	0.10	0.49	0.05	0.94	0.86	0.21						
6.36	0.88	4.05	1.14	0.36	1.24	0.21	1.44	0.27	0.81	0.13	0.85	0.11	0.63	0.07	1.41	1.03	0.25						
7.44	0.93	3.94	1.02	0.21	1.05	0.19	1.31	0.24	0.72	0.12	0.77	0.10	0.53	0.06	5.02	1.09	0.27						
9.71	1.24	5.04	1.26	0.38	1.25	0.21	1.43	0.27	0.82	0.13	0.82	0.11	0.60	0.10	2.84	1.36	0.36						
18.69	2.46	9.16	2.05	0.60	2.08	0.34	2.11	0.39	1.15	0.16	1.13	0.17	1.44	0.19	8.42	2.97	0.78	0.13	0.51	0.63	5.23	3.52	2.49
18.07	2.43	9.05	2.04	0.61	2.03	0.32	2.09	0.39	1.13	0.17	1.12	0.17	1.39	0.20	6.66	2.90	0.74						
20.27	2.55	9.62	2.15	0.57	2.06	0.34	2.16	0.40	1.22	0.18	1.19	0.18	1.54	0.20	4.48	3.03	0.82						
4.63	0.53	2.60	0.84	0.30	0.86	0.15	1.01	0.20	0.62	0.10	0.69	0.10	0.63	0.08	2.44	1.30	0.35	0.37	0.69	0.61	3.51	2.74	0.51
25.32	3.18	11.60	2.46	0.79	2.57	0.39	2.44	0.45	1.41	0.22	1.40	0.20	2.24	0.26	4.08	3.70	0.91						
17.78	2.23	8.55	1.89	0.73	1.94	0.31	2.02	0.38	1.13	0.18	1.18	0.17	1.49	0.18	4.71	2.57	0.68						
5.61	0.74	3.45	1.18	0.44	1.46	0.26	1.74	0.34	1.05	0.17	1.14	0.16	1.05	0.11	0.28	1.52	0.49						
20.02	2.58	9.76	2.09	0.85	2.22	0.34	2.26	0.43	1.25	0.21	1.32	0.19	1.61	0.20	5.60	3.19	0.79	0.08	0.33	0.48	4.56	7.51	1.23
23.94	3.00	11.11	2.44	0.82	2.33	0.38	2.42	0.47	1.38	0.22	1.36	0.20	1.93	0.25	6.99	3.77	0.98						
25.81	3.10	11.74	2.53	0.72	2.44	0.37	2.28	0.44	1.31	0.21	1.30	0.19	2.03	0.29	10.07	4.49	1.09						
26.61	3.28	12.67	2.62	0.80	2.67	0.41	2.49	0.50	1.47	0.23	1.47	0.22	2.10	0.30	5.72	4.59	1.09						
26.26	3.29	12.39	2.53	0.77	2.53	0.40	2.41	0.48	1.40	0.22	1.40	0.21	1.89	0.28	8.64	4.11	1.02						
50.16	5.35	16.73	2.14	0.49	1.19	0.18	1.04	0.23	0.74	0.12	0.75	0.11	2.10	0.22	4.60	14.04	2.45						
32.32	3.91	14.56	2.86	0.87	2.89	0.42	2.49	0.52	1.46	0.24	1.44	0.21	2.33	0.36	18.61	5.61	1.43						
33.64	4.14	15.90	3.36	0.99	3.36	0.52	3.05	0.61	1.88	0.28	1.82	0.28	2.56	0.37	10.04	5.24	1.43						
32.90	4.13	15.34	3.30	0.94	3.37	0.51	2.97	0.59	1.81	0.27	1.76	0.26	2.47	0.34	11.56	5.19	1.45	0.03	0.08	0.38	5.72	3.04	3.02
35.88	4.36	16.69	3.37	1.20	3.56	0.54	3.21	0.67	1.95	0.32	1.98	0.29	3.47	0.44	5.90	7.23	1.95						
34.10	4.07	15.40	3.25	0.96	3.20	0.49	2.98	0.54	1.63	0.27	1.69	0.25	2.53	0.37	12.98	5.94	1.71						
73.02	8.25	30.21	5.95	1.39	6.03	0.90	5.11	0.93	2.88	0.48	2.91	0.43	4.46	0.80	14.69	11.91	2.96	0.10	0.42	0.60	8.02	6.05	0.95
41.03	4.61	15.88	2.59	0.30	2.30	0.20	0.97	0.17	0.46	0.07	0.47	0.07	1.65	0.54	5.18	6.62	0.63						
42.50	4.57	14.97	2.25	0.35	2.19	0.23	1.15	0.21	0.65	0.11	0.74	0.11	1.33	0.10	11.90	8.46	1.25	<0.03	<0.08	0.24	3.87	7.00	0.77
39.89	4.14	13.63	2.19	0.38	2.10	0.26	1.65	0.34	1.10	0.21	1.45	0.21	1.35	0.11	34.78	7.27	1.32						
41.80	4.62	16.06	2.99	0.52	2.77	0.30	1.32	0.22	0.56	0.09	0.56	0.08	2.35	0.22	17.22	7.25	1.10						
40.87	3.95	11.42	1.20	0.22	0.76	0.11	0.71	0.15	0.49	0.09	0.60	0.10	1.96	0.19	12.66	6.93	0.92	0.24	0.24	0.48	4.88	5.10	0.84
16.13	1.72	5.74	1.01	0.19	0.64	0.10	0.73	0.15	0.44	0.08	0.51	0.08	1.50	0.29	2.92	5.60	1.03	0.42	1.45	1.39	5.70	9.35	1.34
73.55	8.77	32.03	6.13	1.36	5.90	0.84	4.99	0.87	2.58	0.43	2.62	0.38	2.56	0.84	11.21	13.36	2.17						
77.15	8.69	31.39	6.23	1.42	6.17	0.92	5.32	1.04	3.16	0.50	2.89	0.44	9.19	0.82	21.38	16.78	4.24	0.23	0.28	0.45	7.03	7.46	1.00
23.45	2.55	9.57	2.11	0.60	2.11	0.36	2.34	0.46	1.44	0.24	1.46	0.22	2.27	0.31	5.49	4.50	0.99						
58.61	6.86	25.12	4.93	1.26	5.02	0.72	4.26	0.81	2.55	0.40	2.40	0.36	4.56	0.55	16.72	10.86	2.59	0.15	0.17	0.41	6.32	4.99	0.96
11.27	1.47	6.01	1.47	0.35	1.50	0.26	1.73	0.35	0.98	0.15	0.91	0.13	1.06	0.11	2.52	1.56	0.39						
7.68	0.99	4.12	0.98	0.32	0.98	0.16	1.12	0.23	0.63	0.11	0.64	0.10	0.66	0.07	2.88	1.06	0.27						
10.12	1.27	5.23	1.24	0.39	1.25	0.20	1.35	0.26	0.79	0.13	0.73	0.12	0.77	0.10	2.58	1.43	0.34						

11.14	1.41	5.62	1.25	0.52	1.27	0.20	1.36	0.27	0.80	0.13	0.79	0.13	0.87	0.10	2.90	1.52	0.37							
15.00	1.89	7.33	1.57	0.63	1.62	0.25	1.58	0.33	0.95	0.15	0.94	0.14	0.96	0.13	4.58	1.81	0.45		0.07	0.30	0.30	2.41	3.92	0.67
16.75	2.03	7.75	1.62	0.56	1.64	0.23	1.56	0.30	0.88	0.14	0.85	0.13	1.26	0.16	3.68	2.67	0.65		0.05	0.20	0.48	9.15	9.14	1.74
15.08	1.86	6.86	1.60	0.56	1.46	0.23	1.46	0.28	0.82	0.13	0.82	0.12	1.13	0.14	5.12	2.23	0.66							
17.85	2.21	8.62	1.85	0.62	1.80	0.27	1.73	0.35	1.03	0.16	0.98	0.15	1.25	0.17	4.86	2.88	0.71							
19.15	2.37	8.71	1.92	0.72	1.91	0.29	1.81	0.37	1.06	0.16	1.03	0.14	1.39	0.22	5.25	3.36	0.79							
11.49	1.54	6.05	1.64	0.44	1.56	0.29	1.88	0.38	1.11	0.18	1.18	0.16	1.37	0.18	2.39	3.20	0.68							
10.19	1.73	7.76	2.73	0.54	2.21	0.42	2.53	0.44	1.21	0.19	1.18	0.15	4.29	0.47	5.03	22.47	0.86		0.03	<0.08	0.15	1.64	1.91	0.31
12.81	1.31	4.51	0.72	0.17	0.46	0.05	0.40	0.08	0.23	0.03	0.21	0.04	0.91	0.18	2.74	2.47	0.71							
12.14	1.61	6.30	1.75	0.51	1.84	0.32	2.11	0.43	1.24	0.20	1.28	0.19	1.57	0.22	1.58	3.43	0.83		<0.03	<0.08	0.18	1.08	2.09	0.54
17.77	2.22	8.33	1.98	0.59	1.90	0.30	1.99	0.38	1.14	0.17	1.13	0.17	1.55	0.17	5.21	2.93	0.70							
19.14	2.41	9.30	1.98	0.59	1.95	0.32	2.07	0.40	1.17	0.18	1.17	0.19	1.67	0.22	5.50	3.41	0.78		0.06	0.30	3.89	14.4	59.5	2.34
12.89	1.59	6.22	1.38	0.46	1.32	0.23	1.46	0.29	0.82	0.13	0.85	0.13	1.01	0.13	5.42	2.20	0.55							
24.07	2.95	11.12	2.34	0.76	2.35	0.37	2.31	0.45	1.30	0.21	1.30	0.20	1.80	0.25	6.49	4.24	0.93							
18.43	2.27	8.92	1.95	0.77	1.96	0.32	2.01	0.38	1.12	0.19	1.16	0.18	1.44	0.18	14.46	2.70	0.72							
12.52	1.58	5.82	1.28	0.39	1.22	0.19	1.32	0.25	0.75	0.11	0.74	0.11	0.94	0.15	3.32	2.02	0.47							
14.52	1.83	6.89	1.49	0.55	1.47	0.23	1.51	0.28	0.83	0.12	0.82	0.13	0.90	0.14	3.92	2.07	0.53							
10.23	1.33	5.00	1.15	0.44	1.17	0.19	1.27	0.24	0.71	0.11	0.70	0.11	0.79	0.12	3.35	1.67	0.40							
11.98	2.34	11.31	3.76	2.41	3.42	0.63	3.94	0.68	1.89	0.27	1.71	0.24	1.80	0.22	6.80	2.43	0.60							
14.93	2.07	7.83	1.73	0.48	1.79	0.26	1.76	0.31	1.00	0.15	1.01	0.15	1.36	0.17	3.59	2.72	0.63							
10.48	1.37	5.35	1.41	0.45	1.52	0.24	1.67	0.30	0.96	0.14	0.93	0.14	1.14	0.18	2.24	2.28	0.58							
14.05	1.83	6.93	1.68	0.47	1.74	0.26	1.83	0.33	1.02	0.15	1.02	0.15	1.28	0.19	2.00	2.64	0.67							
3.51	0.47	1.71	0.37	0.15	0.31	0.04	0.26	0.05	0.17	0.02	0.19	0.04	1.84	0.22	2.46	9.00	0.88		<0.03	<0.08	0.04	0.71	2.10	0.65
24.22	3.03	11.17	2.36	0.77	2.35	0.34	2.22	0.40	1.23	0.18	1.18	0.18	1.82	0.23	6.99	3.93	1.18							
4.03	0.50	1.81	0.41	0.12	0.41	0.05	0.43	0.08	0.24	0.03	0.23	0.03	0.36	0.05	0.58	0.72	0.15	0.96						
23.05	2.92	12.10	2.96	0.82	2.89	0.51	3.21	0.65	1.86	0.30	1.94	0.30	1.94	0.20	6.19	1.92	0.48	0.24						
19.75	2.44	9.72	2.28	1.01	2.23	0.38	2.49	0.51	1.52	0.25	1.69	0.28	1.32	0.11	8.29	1.56	0.54	1.62						
6.00	0.81	3.65	1.06	0.45	1.05	0.19	1.38	0.29	0.87	0.15	1.00	0.16	0.51	0.02	2.51	0.28	0.09	0.09						
8.65	1.13	4.66	1.03	0.37	0.91	0.13	0.83	0.17	0.52	0.08	0.55	0.08	0.77	0.04	3.43	0.54	0.14		0.12	0.37	0.56	5.96	7.87	0.71
5.43	0.68	2.81	0.73	0.40	0.65	0.10	0.73	0.16	0.45	0.07	0.48	0.07	0.50	0.03	4.86	0.34	0.12		1.49	4.76	1.16	7.35	1.81	0.54
8.27	1.04	4.16	1.00	0.38	0.94	0.15	1.00	0.21	0.61	0.10	0.65	0.10	0.70	0.06	45.73	0.67	0.18		0.31	0.68	0.22	2.94	6.23	0.70
14.11	1.73	7.06	1.61	0.64	1.50	0.25	1.37	0.28	0.80	0.14	0.89	0.13	0.86	0.11	8.28	1.04	0.21	0.23	0.28	0.50	0.38	7.05	8.47	1.49
4.03	0.62	3.34	1.23	0.57	1.44	0.29	2.04	0.42	1.21	0.20	1.39	0.21	0.70	0.05	4.76	0.12	0.02							
7.24	1.16	6.18	2.20	0.80	2.59	0.52	3.71	0.75	2.20	0.36	2.47	0.39	1.64	0.16	3.63	0.20	0.06							
5.47	0.82	4.12	1.41	0.58	1.63	0.31	2.18	0.45	1.32	0.21	1.48	0.22	0.88	0.09	7.41	0.18	0.10							
4.73	0.78	4.16	1.50	0.54	1.81	0.36	2.56	0.53	1.54	0.26	1.81	0.28	1.06	0.08	4.34	0.16	0.09							
6.49	1.11	5.91	2.12	0.52	2.38	0.47	3.15	0.63	1.80	0.29	1.97	0.30	1.18	0.13	2.68	0.16	0.07							
11.01	1.90	10.13	3.44	1.06	3.58	0.70	4.65	0.92	2.66	0.43	2.68	0.40	1.81	0.15	8.80	0.26	0.09							
28.79	3.84	14.63	3.26	1.13	3.48	0.51	3.40	0.66	1.94	0.30	1.91	0.31	2.21	0.29	6.33	2.90	0.76							
34.00	4.50	17.06	3.89	1.25	3.83	0.59	3.83	0.74	2.14	0.35	2.20	0.34	2.53	0.36	7.82	3.18	1.03							
27.77	3.69	14.16	3.34	1.09	3.33	0.50	3.30	0.64	1.87	0.30	1.92	0.30	2.14	0.30	6.51	2.39	0.65							
28.81	3.79	14.62	3.27	0.98	3.27	0.51	3.31	0.65	1.85	0.31	1.92	0.30	1.96	0.30	5.82	2.76	0.79							
28.08	3.66	14.05	3.10	1.14	3.17	0.48	3.13	0.61	1.79	0.30	1.80	0.28	2.04	0.29	6.93	2.71	1.02							
46.63	6.10	23.43	5.15	1.51	5.02	0.75	4.70	0.90	2.59	0.43	2.63	0.41	3.55	0.50	10.09	4.81	1.36							
52.02	6.82	25.85	5.52	1.45	5.35	0.79	4.95	0.96	2.73	0.45	2.70	0.43	3.72	0.53	8.25	5.31	1.50							

47.39	6.13	23.04	4.98	1.44	4.85	0.71	4.43	0.86	2.49	0.40	2.45	0.39	3.48	0.43	8.44	4.69	1.21
29.03	3.81	14.32	3.14	1.06	3.29	0.48	3.18	0.62	1.79	0.29	1.82	0.29	2.21	0.30	8.37	3.07	1.17
28.93	3.85	14.56	3.30	1.14	3.42	0.50	3.41	0.66	1.95	0.31	1.93	0.31	2.38	0.30	8.16	2.81	1.10
28.49	3.76	14.29	3.21	1.13	3.31	0.49	3.28	0.64	1.91	0.31	1.88	0.30	2.24	0.30	7.13	2.77	0.87
27.76	3.65	13.88	3.08	1.02	3.19	0.47	3.16	0.61	1.80	0.28	1.82	0.29	2.06	0.28	4.81	2.70	0.80
26.21	3.56	13.46	3.09	1.13	3.26	0.49	3.29	0.65	1.93	0.31	1.90	0.31	2.05	0.27	5.97	2.23	0.75
31.28	4.08	15.39	3.43	1.15	3.62	0.53	3.68	0.72	2.14	0.35	2.15	0.34	2.48	0.29	8.02	2.99	0.65
23.71	3.16	12.17	2.85	1.05	3.07	0.48	3.27	0.66	1.92	0.31	1.93	0.32	1.90	0.23	7.83	2.06	0.49
47.39	6.16	22.63	4.82	1.41	4.77	0.69	4.43	0.85	2.46	0.40	2.45	0.39	3.03	0.45	11.30	4.92	1.37
44.54	5.75	21.09	4.56	1.35	4.56	0.65	4.15	0.81	2.33	0.39	2.32	0.37	2.95	0.44	11.39	4.66	1.27
59.14	7.61	28.39	5.94	1.66	5.81	0.83	5.11	1.01	2.92	0.46	2.99	0.45	4.31	0.56	13.14	6.58	1.72
61.17	7.86	29.37	6.21	1.69	5.97	0.85	5.24	1.01	3.02	0.46	3.03	0.46	4.47	0.59	13.63	6.91	1.80
52.18	6.80	25.87	5.68	1.67	5.55	0.83	5.22	1.02	3.01	0.47	3.02	0.46	3.90	0.57	12.42	5.45	1.53
52.27	6.84	26.15	5.63	1.64	5.55	0.83	5.20	1.02	3.01	0.47	3.05	0.46	3.80	0.58	11.07	5.36	1.65
51.03	6.71	25.20	5.47	1.65	5.43	0.81	5.11	1.00	2.95	0.46	3.04	0.46	3.99	0.58	14.43	5.46	1.61
36.91	4.85	18.43	4.08	1.21	4.13	0.62	3.99	0.77	2.30	0.36	2.33	0.34	2.65	0.37	6.24	3.27	0.92
31.65	4.20	15.99	3.54	1.16	3.56	0.53	3.42	0.68	1.99	0.31	2.02	0.31	2.37	0.33	7.19	2.93	0.77
30.18	3.99	15.32	3.42	1.23	3.51	0.51	3.31	0.66	1.96	0.30	2.01	0.30	2.30	0.31	7.35	2.85	0.81
53.76	7.01	26.08	5.47	1.48	5.38	0.77	4.82	0.94	2.74	0.42	2.79	0.42	3.33	0.52	6.08	5.60	1.55
27.00	3.57	13.92	3.18	1.08	3.22	0.49	3.12	0.63	1.86	0.29	1.92	0.30	2.13	0.28	6.11	2.59	0.72
33.37	4.38	16.80	3.73	1.15	3.63	0.55	3.53	0.71	2.09	0.33	2.17	0.32	2.53	0.34	7.29	3.45	1.01
33.14	4.35	16.75	3.72	1.23	3.67	0.55	3.54	0.70	2.04	0.32	2.15	0.32	2.54	0.33	8.39	3.20	0.88
29.82	3.93	14.99	3.34	1.15	3.26	0.50	3.27	0.63	1.88	0.29	1.89	0.30	2.43	0.31	6.30	2.96	0.81
30.05	3.94	15.10	3.38	1.14	3.37	0.52	3.40	0.67	1.98	0.30	1.97	0.31	2.25	0.31	7.26	3.17	0.90
30.47	3.99	15.34	3.43	1.19	3.40	0.53	3.48	0.68	2.00	0.31	2.03	0.33	2.42	0.32	7.93	3.24	0.99
28.77	3.82	14.82	3.28	1.11	3.28	0.50	3.30	0.64	1.90	0.29	1.85	0.30	2.27	0.30	5.92	2.65	0.67
28.61	3.74	14.67	3.31	1.10	3.22	0.50	3.32	0.64	1.87	0.29	1.85	0.29	2.11	0.30	5.97	2.67	0.72
28.39	3.76	14.81	3.33	1.14	3.32	0.52	3.43	0.66	1.96	0.30	1.92	0.31	2.09	0.29	8.08	2.48	0.75
33.19	4.33	16.89	3.87	1.29	3.84	0.61	3.90	0.78	2.27	0.36	2.26	0.37	2.44	0.34	7.56	3.09	0.82
34.78	4.56	17.29	3.85	1.25	3.79	0.59	3.79	0.75	2.18	0.34	2.20	0.36	2.72	0.36	9.13	3.63	1.05
33.95	4.42	17.04	3.77	1.23	3.75	0.57	3.70	0.73	2.13	0.34	2.15	0.35	2.69	0.35	8.07	3.52	0.97
40.00	5.19	19.78	4.29	1.42	4.21	0.64	4.05	0.80	2.33	0.36	2.35	0.38	3.07	0.40	9.95	3.98	1.06
39.02	5.07	19.42	4.21	1.36	4.12	0.63	4.00	0.79	2.26	0.36	2.31	0.36	2.99	0.40	8.05	3.85	1.04
39.62	5.17	19.90	4.44	1.36	4.30	0.65	4.18	0.83	2.39	0.37	2.33	0.38	2.70	0.41	5.64	4.11	1.16
37.17	4.83	18.69	4.11	1.33	3.97	0.60	3.87	0.76	2.22	0.35	2.25	0.36	2.84	0.39	6.42	3.89	1.09
29.72	3.92	15.17	3.44	1.23	3.42	0.53	3.50	0.69	2.01	0.31	2.02	0.33	2.48	0.31	8.23	2.97	0.85
60.56	7.70	28.67	5.98	1.67	5.70	0.84	5.21	1.00	2.90	0.45	2.78	0.45	3.97	0.57	11.77	6.76	1.77
39.12	4.99	18.81	4.03	1.39	3.85	0.58	3.73	0.72	2.12	0.33	2.16	0.34	2.90	0.39	9.26	4.08	1.09
31.79	4.21	17.04	3.62	1.19	3.58	0.60	3.51	0.71	2.11	0.33	1.90	0.33	2.74	0.36		3.06	0.60
32.77	4.35	17.66	3.88	1.26	3.78	0.64	3.85	0.78	2.28	0.37	2.13	0.37	2.85	0.36		3.18	0.68
60.46	7.81	30.40	6.00	1.64	5.69	0.91	5.12	1.00	2.93	0.46	2.75	0.45	4.52	0.57		6.68	1.39
75.37	9.74	37.28	7.14	1.86	6.73	1.06	5.85	1.12	3.29	0.51	3.00	0.52	5.51	0.71		8.70	1.76
78.98	10.32	39.43	7.79	1.96	7.09	1.10	6.25	1.21	3.46	0.55	3.35	0.52	5.70	0.74		8.96	1.85
28.68	3.89	15.69	3.40	1.10	3.24	0.56	3.27	0.66	1.93	0.30	1.89	0.31	2.42	0.31		2.61	1.71
48.55	6.44	25.56	5.22	1.63	5.00	0.80	4.81	0.95	2.74	0.45	2.72	0.43	3.92	0.48		5.28	1.20

30.95	4.18	16.73	3.62	1.18	3.56	0.59	3.72	0.75	2.19	0.36	2.10	0.35	2.67	0.30		3.26	0.55
65.63	8.64	33.07	6.53	1.73	6.13	0.96	5.54	1.08	3.13	0.50	3.04	0.48	4.78	0.65		7.99	1.66
28.54	3.84	15.34	3.34	1.13	3.26	0.54	3.27	0.65	1.89	0.31	1.87	0.30	2.32	0.30		3.00	0.63
38.27	5.11	20.30	4.26	1.33	4.09	0.67	4.07	0.80	2.32	0.38	2.27	0.37	3.07	0.40		4.30	1.01
33.29	4.44	17.93	3.83	1.25	3.83	0.64	3.82	0.76	2.23	0.36	2.14	0.36	2.85	0.38		3.13	0.68
7.07	1.01	4.31	1.20	0.55	1.09	0.21	1.53	0.31	0.97	0.16	0.98	0.15	0.78	0.09	3.20	1.73	0.15
15.61	2.23	9.68	2.75	0.87	2.79	0.53	3.56	0.76	2.29	0.37	2.41	0.37	1.85	0.23	3.15	1.82	0.34
14.03	2.06	8.60	2.50	0.86	2.55	0.50	3.27	0.68	2.09	0.34	2.16	0.33	1.75	0.19	6.76	1.51	0.34
6.65	0.96	4.04	1.19	0.50	1.06	0.20	1.50	0.32	0.97	0.16	0.98	0.15	0.66	0.09	2.81	0.75	0.15
7.07	1.03	4.42	1.27	0.58	1.19	0.24	1.70	0.35	1.07	0.18	1.11	0.18	0.81	0.09	4.01	0.73	0.17
9.72	1.42	6.07	1.74	0.64	1.75	0.34	2.34	0.50	1.52	0.25	1.57	0.23	1.06	0.14	3.28	1.00	0.23
14.72	2.16	9.20	2.60	0.86	2.71	0.52	3.49	0.73	2.23	0.36	2.36	0.35	1.83	0.20	3.02	1.39	0.34
5.69	0.82	3.53	0.95	0.47	0.88	0.18	1.30	0.27	0.83	0.13	0.87	0.13	0.61	0.08	3.12	0.56	0.12
8.49	1.20	5.14	1.43	0.61	1.51	0.28	1.83	0.38	1.11	0.18	1.19	0.18	1.02	0.12	6.25	0.68	0.21
5.00	0.68	3.07	0.93	0.48	0.91	0.16	1.16	0.23	0.69	0.11	0.75	0.12	0.66	0.07	4.14	0.36	0.13
7.00	0.96	4.43	1.29	0.55	1.32	0.24	1.67	0.34	1.00	0.16	1.10	0.17	0.87	0.10	3.65	0.54	0.18
9.22	1.31	5.93	1.73	0.66	1.83	0.34	2.32	0.47	1.35	0.22	1.49	0.23	1.20	0.15	4.31	0.72	0.25
10.80	1.42	6.48	1.86	0.71	2.06	0.37	2.49	0.51	1.47	0.24	1.62	0.25	1.40	0.17	4.85	1.08	0.29
10.86	1.45	6.60	2.00	0.72	2.11	0.39	2.72	0.54	1.57	0.27	1.78	0.27	1.49	0.18	4.00	0.94	0.29
15.96	2.22	10.06	3.06	0.95	3.33	0.65	4.31	0.86	2.49	0.42	2.78	0.43	2.37	0.28	2.55	1.35	0.46
15.67	2.13	9.83	2.99	0.95	3.34	0.62	4.10	0.83	2.39	0.40	2.70	0.41	2.25	0.27	2.38	1.37	0.42
14.46	1.99	9.09	2.73	0.88	3.01	0.58	3.87	0.78	2.24	0.38	2.49	0.39	2.11	0.24	3.86	1.20	0.41
13.53	1.86	8.59	2.60	0.86	2.85	0.54	3.71	0.73	2.15	0.35	2.35	0.36	2.16	0.24	4.11	1.14	0.39
268.85	31.47	118.03	22.52	3.10	19.60	2.82	15.13	2.64	7.26	1.09	6.88	0.97	9.91	1.35	9.44	28.12	1.75
290.73	33.36	125.58	23.58	3.72	20.81	2.98	15.90	2.78	7.69	1.12	7.12	1.01	11.47	1.29	45.55	30.38	1.89
260.48	29.78	112.02	21.27	3.24	19.12	2.70	14.45	2.55	6.95	1.00	6.48	0.89	8.91	1.39	19.98	26.60	1.63
28.31	3.80	15.52	3.97	1.17	4.28	0.73	5.03	0.98	3.00	0.48	3.10	0.45	2.97	0.33	6.98	2.45	0.64
48.15	6.33	25.14	6.07	1.63	6.29	1.05	7.24	1.41	4.38	0.70	4.49	0.67	4.77	0.66	7.84	4.20	1.02
46.41	6.06	24.23	5.82	1.60	6.12	1.04	6.98	1.36	4.28	0.68	4.33	0.65	4.41	0.57	7.11	4.10	1.00
29.27	3.97	16.24	4.14	1.26	4.49	0.77	5.34	1.02	3.13	0.51	3.17	0.48	2.87	0.22	5.41	2.32	0.55
27.91	3.79	15.53	4.16	1.23	4.41	0.74	5.25	1.00	3.14	0.48	3.23	0.46	2.81	0.36	4.18	2.27	0.53
23.21	3.19	13.37	3.52	1.13	3.74	0.67	4.76	0.95	2.89	0.47	2.90	0.45	2.56	0.34	18.20	1.38	0.41
21.41	3.03	12.68	3.32	1.04	3.69	0.63	4.63	0.91	2.73	0.44	2.97	0.43	2.51	0.39	2.01	1.30	0.36
33.17	4.41	17.08	4.42	1.28	4.76	0.83	5.85	1.15	3.52	0.58	3.61	0.56	3.29	0.43	5.62	3.22	0.76
27.29	3.82	16.25	4.50	1.42	4.93	0.87	6.10	1.20	3.67	0.59	3.65	0.58	3.37	0.48	3.31	1.90	0.47
26.60	3.73	15.81	4.36	1.34	4.70	0.85	5.98	1.18	3.60	0.58	3.58	0.55	3.30	0.45	3.21	1.82	0.47
16.96	2.47	10.54	3.07	1.01	3.30	0.60	4.23	0.82	2.53	0.40	2.54	0.38	2.06	0.27	2.34	0.89	0.23
17.17	2.45	10.65	2.98	1.04	3.39	0.60	4.25	0.84	2.54	0.39	2.52	0.38	2.16	0.34	1.90	0.90	0.23
26.03	3.76	16.34	4.41	1.45	5.07	0.89	6.39	1.23	3.76	0.61	3.76	0.59	3.15	0.52	2.41	1.28	0.35
37.68	5.14	21.40	5.29	1.54	5.94	1.03	7.18	1.42	4.27	0.71	4.47	0.66	4.18	0.53	4.84	2.73	0.68
24.64	3.41	14.26	3.79	1.23	4.19	0.75	5.43	1.06	3.22	0.51	3.27	0.50	2.85	0.43	2.83	1.55	0.38
26.19	3.47	13.87	3.44	1.07	3.73	0.65	4.53	0.89	2.74	0.44	2.74	0.43	2.49	0.40	5.32	2.55	0.60
44.90	6.03	23.78	5.80	1.62	6.30	1.05	7.32	1.38	4.30	0.71	4.42	0.69	4.44	0.54	6.41	3.96	0.95
43.29	5.81	23.16	5.54	1.64	5.96	1.03	6.98	1.37	4.17	0.67	4.19	0.66	4.26	0.63	5.79	3.81	0.94
47.01	6.31	24.92	6.01	1.76	6.26	1.08	7.19	1.44	4.43	0.71	4.34	0.68	4.24	0.54	6.49	3.58	0.95

23.53	3.27	13.48	3.64	1.18	3.86	0.69	4.88	1.00	2.95	0.48	3.00	0.48	2.72	0.32	4.48	1.66	0.43
36.11	5.03	20.88	5.68	1.72	6.13	1.12	7.78	1.53	4.63	0.77	4.87	0.73	4.39	0.46	3.98	2.56	0.65
24.94	3.30	13.31	3.32	1.01	3.57	0.61	4.23	0.84	2.60	0.42	2.67	0.41	2.62	0.25	4.90	2.56	0.60
29.94	4.06	16.82	4.21	1.33	4.62	0.75	5.40	1.05	3.21	0.52	3.42	0.51	2.96	0.29	4.39	1.81	0.47
28.41	3.81	15.20	3.80	1.15	4.10	0.69	4.77	0.94	2.91	0.47	3.00	0.46	2.35	0.21	5.75	2.50	0.58
28.71	3.90	15.83	4.02	1.22	4.48	0.76	5.45	1.05	3.21	0.53	3.25	0.50	3.06	0.53	3.99	2.37	0.61
30.12	4.08	16.47	4.23	1.27	4.68	0.80	5.62	1.10	3.39	0.56	3.43	0.54	3.29	0.48	5.16	2.48	0.64
18.40	2.57	10.72	2.91	0.92	3.17	0.58	4.12	0.79	2.50	0.40	2.61	0.40	1.96	0.24	3.04	1.29	0.32
24.87	3.28	13.62	3.65	1.11	3.72	0.68	4.93	1.01	3.03	0.50	3.09	0.47	3.00	0.36	8.25	1.90	0.56
23.94	3.20	13.26	3.71	1.18	3.60	0.67	4.77	0.98	2.92	0.48	3.05	0.48	2.78	0.37	3.57	1.53	1.33
38.21	5.15	20.73	5.74	1.61	5.63	1.03	7.39	1.51	4.46	0.73	4.59	0.71	4.69	0.60	16.14	2.50	0.71
29.50	3.88	15.97	4.28	1.38	4.15	0.75	5.32	1.09	3.22	0.53	3.39	0.53	3.05	0.38	4.40	2.42	0.73
34.17	4.43	17.88	4.97	1.32	4.73	0.88	6.04	1.25	3.78	0.63	3.95	0.61	3.23	0.45	4.43	2.45	1.67
40.88	5.17	20.71	5.40	1.47	5.42	0.95	6.61	1.38	4.13	0.68	4.36	0.68	4.56	0.56	6.94	4.37	1.26
28.54	3.86	15.94	4.61	1.39	4.47	0.83	5.89	1.21	3.59	0.60	3.76	0.57	3.35	0.45	32.95	1.63	0.45
25.02	3.29	13.30	3.68	1.12	3.74	0.68	4.80	1.02	2.95	0.50	3.11	0.48	2.64	0.37	6.43	1.83	0.53
22.27	2.92	12.07	3.30	1.02	3.42	0.62	4.54	0.94	2.82	0.46	2.94	0.46	2.79	0.30	44.58	1.80	0.54
32.70	3.89	14.35	3.49	1.00	3.59	0.57	3.88	0.80	2.41	0.39	2.45	0.37	2.56	0.32	11.06	4.71	1.22
26.19	3.12	11.38	2.84	0.83	2.93	0.47	3.27	0.68	1.99	0.33	2.11	0.32	2.09	0.25	5.42	3.76	0.94
43.26	5.75	23.24	5.79	1.70	5.82	1.04	6.89	1.38	4.19	0.67	4.16	0.64	4.04	0.38	6.19	2.90	0.69
22.61	3.12	13.15	3.50	1.19	3.96	0.69	4.80	0.98	2.97	0.47	2.93	0.45	2.66	0.32	2.92	1.37	0.37
42.35	5.73	22.93	5.68	1.05	5.95	0.99	6.71	1.32	4.05	0.65	4.10	0.64	3.76	0.43	4.88	2.53	0.58
28.83	3.81	15.31	4.26	1.22	4.21	0.78	5.53	1.17	3.40	0.57	3.45	0.55	3.19	0.40	2.45	2.06	0.60
23.80	3.18	13.00	3.45	1.05	3.68	0.67	4.70	0.93	2.91	0.48	3.17	0.46	2.63	0.32	4.18	2.22	0.54
24.69	3.12	12.86	3.18	1.02	3.29	0.56	3.57	0.72	2.09	0.35	2.30	0.36	2.17	0.25	6.54	2.34	0.61
13.13	1.71	7.31	1.98	0.75	2.08	0.37	2.41	0.49	1.42	0.23	1.58	0.24	1.26	0.14	5.94	1.14	0.32
41.12	5.37	22.71	5.76	1.39	6.10	1.08	6.93	1.43	4.27	0.72	4.86	0.76	4.82	0.76	2.24	3.79	1.12
42.39	5.30	21.62	5.25	1.44	5.43	0.93	5.77	1.15	3.37	0.55	3.70	0.57	4.12	0.53	6.88	4.50	1.19
23.62	3.22	13.91	3.84	1.18	4.20	0.76	4.92	1.00	2.87	0.47	3.22	0.50	2.73	0.40	6.88	1.69	0.50
20.14	2.72	11.89	3.36	1.00	3.60	0.66	4.28	0.87	2.54	0.42	2.78	0.44	2.47	0.30	1.90	2.01	0.54
33.34	4.62	19.39	5.06	1.56	5.52	1.00	6.75	1.38	4.12	0.67	4.08	0.63	3.41	0.42	5.65	2.15	0.54
28.17	3.89	15.52	4.06	1.29	4.34	0.74	5.12	1.04	3.18	0.51	3.14	0.49	2.73	0.27	4.93	2.34	0.58
20.26	2.81	11.81	3.08	1.06	3.36	0.59	4.11	0.84	2.53	0.41	2.49	0.40	2.09	0.21	3.59	1.22	0.30
30.97	4.24	17.48	4.67	1.37	5.14	0.89	6.31	1.25	3.83	0.63	4.05	0.61	3.60	0.46	5.79	2.38	0.59
33.97	4.57	18.67	4.64	1.41	5.02	0.85	5.72	1.16	3.51	0.55	3.45	0.53	5.38	0.57	4.83	2.48	0.64
31.90	4.29	16.83	4.31	0.90	4.69	0.87	6.24	1.24	3.79	0.63	3.96	0.62	4.33	0.46		4.10	1.01
50.86	6.73	26.02	6.31	1.72	6.80	1.13	7.53	1.49	4.66	0.76	4.76	0.71	4.90	0.58	9.34	4.47	1.05
60.40	8.65	32.04	6.58	1.79	5.79	0.77	4.37	0.78	2.29	0.33	2.12	0.30	4.27	0.47	3.15	5.42	1.10
25.72	3.63	15.26	4.18	1.11	4.61	0.84	5.93	1.16	3.57	0.57	3.52	0.57	3.33	0.48	3.57	2.02	0.49
53.28	6.63	25.07	5.49	1.71	5.43	0.76	4.16	0.77	2.26	0.34	2.04	0.30	3.83	0.40	10.42	3.80	0.86
68.60	8.48	31.68	6.95	1.94	5.96	0.90	4.74	0.88	2.58	0.37	2.31	0.33	5.05	0.62	49.50	7.04	1.88
11.49	1.48	6.01	1.41	0.27	1.29	0.23	1.37	0.29	0.88	0.15	1.01	0.14	0.84	0.15	3.61	1.89	0.40
5.36	0.74	3.14	0.88	0.43	0.83	0.16	1.08	0.22	0.65	0.10	0.76	0.11	0.33	0.04	13.97	0.40	0.07
9.37	1.17	4.99	1.13	0.62	1.20	0.20	1.23	0.27	0.81	0.13	0.93	0.13	0.58	0.07	4.07	0.57	0.10
7.70	0.99	3.99	0.96	0.49	1.05	0.19	1.12	0.24	0.70	0.10	0.79	0.11	0.48	0.04	5.51	0.49	0.08

5.92	0.76	3.30	0.99	0.34	0.99	0.20	1.26	0.28	0.90	0.13	1.01	0.13	0.46	0.06	8.10	0.63	0.18							
8.66	1.14	4.54	1.17	0.50	1.23	0.20	1.28	0.26	0.80	0.13	0.92	0.12	0.58	0.07	8.99	0.60	0.14	0.65	0.42	1.29	0.51	42.1	56.2	3.36
5.07	0.65	2.64	0.70	0.45	0.71	0.11	0.78	0.15	0.46	0.08	0.54	0.08	0.40	0.04	39.65	0.35	0.09							
5.77	0.89	4.25	1.36	0.63	1.43	0.30	1.82	0.38	1.20	0.17	1.41	0.20	0.36	0.03	6.04	0.18	0.07							
7.78	1.10	4.95	1.31	0.64	1.25	0.21	1.37	0.29	0.85	0.14	1.01	0.14	0.48	0.04	6.35	0.23	0.11							
76.46	7.93	27.48	4.37	1.11	3.08	0.36	1.83	0.41	1.23	0.22	1.56	0.22	4.76	0.72	18.51	10.33	0.76							
10.79	1.41	5.67	1.48	0.64	1.35	0.24	1.42	0.32	0.95	0.14	1.08	0.15	0.73	0.09	9.82	0.80	0.20							
225.83	25.90	90.15	14.14	3.53	10.26	0.98	3.85	0.67	1.76	0.22	1.46	0.22	6.32	0.25	19.37	11.80	1.02							
5.52	0.69	2.74	0.70	0.43	0.63	0.10	0.56	0.13	0.38	0.06	0.45	0.06	0.54	0.03	8.33	0.63	0.15							
13.53	1.57	5.78	1.11	0.67	0.91	0.16	0.95	0.20	0.62	0.09	0.80	0.13	0.82	0.12	6.95	1.97	0.95	3.71						
21.16	2.59	9.31	1.97	0.47	1.74	0.29	1.86	0.40	1.28	0.21	1.50	0.22	2.81	0.24	2.69	4.47	1.63	11.1	15.4	95.6	49.2	403	405	21.5
4.96	0.71	2.96	0.82	0.36	0.92	0.16	1.01	0.23	0.66	0.10	0.67	0.10	0.38	0.02	5.18	0.18	0.03							
18.46	2.36	9.52	2.10	0.79	1.74	0.26	1.45	0.29	0.84	0.12	0.83	0.13	0.66	0.09	8.24	1.48	0.75		16.2	9.10	58.2	941	2116	66.1
19.78	2.48	9.86	2.26	0.53	2.72	0.36	2.40	0.50	1.51	0.26	1.97	0.28	1.23	0.21	2.87	2.83	0.75							
13.92	1.77	7.02	1.56	0.56	1.42	0.23	1.39	0.28	0.83	0.14	0.96	0.14	0.92	0.12	7.40	1.92	0.80	0.09						
5.11	0.66	3.07	0.80	0.45	0.89	0.15	0.96	0.21	0.62	0.10	0.75	0.11	0.41	0.03	3.99	0.29	0.10							
6.78	0.93	3.86	0.91	0.54	0.93	0.16	0.91	0.19	0.60	0.10	0.70	0.10	0.30	0.03	7.54	0.45	0.13							
44.14	5.55	23.04	5.54	1.66	6.02	0.95	5.96	1.18	3.49	0.60	3.93	0.61	3.79	0.53	5.66	4.58	1.12		0.20	0.16	0.75	18.0	27.4	0.19
21.02	2.80	11.90	3.25	1.09	3.66	0.64	3.90	0.84	2.38	0.42	2.97	0.41	2.10	0.33	9.36	1.88	0.42							
68.30	7.52	26.63	4.07	2.57	3.30	0.32	1.35	0.24	0.69	0.10	0.66	0.12	1.18	0.19	16.13	1.68	1.27							
53		20	3.4	1	3.8				2.4		2				7									
43		17	3	1.5	3.8				2.4		2				19									
															4									
															53									
30.93	3.64	14.07	2.68	0.66	2.39	0.35	2.12	0.43	1.21	0.18	1.16	0.17	2.32	0.25		3.14	0.66							
11.05	1.7	8.71	3.07	0.71	3.77	0.7	4.51	0.96	2.64	0.39	2.45	0.36	2.36	0.29		1.04	0.25							
34.93	4.07	15.53	2.967	0.73	2.449	0.36	2.17	0.45	1.21	0.19	1.15	0.18	2.61	0.29		3.63	1.01							
34.93	4.07	15.53	2.967	0.73	2.449	0.36	2.17	0.45	1.21	0.19	1.15	0.18	2.61	0.29		3.63	1.01							
580.25	65.83	217.65	26.86	6.29	15.7	1.97	10.61	2.04	5	0.71	4.27	0.61	14.38	0.9		5.77	2.26							
52.53	7.42	32.51	7.33	1.38	6.74	1.09	6.79	1.46	4.31	0.67	4.34	0.67	9.73	0.97		6.55	1.95							
52.53	7.42	32.51	7.33	1.38	6.74	1.09	6.79	1.46	4.31	0.67	4.34	0.67	9.73	0.97		6.55	1.95							
75.64	9.59	39.42	7.83	1.41	6.82	1.04	6.21	1.27	3.59	0.54	3.35	0.49	8.57	0.94		6.39	1.68							
75.64	9.59	39.42	7.83	1.41	6.82	1.04	6.21	1.27	3.59	0.54	3.35	0.49	8.57	0.94		6.39	1.68							
22.74	3.49	16.89	5.12	1.8	6.47	1.14	7.48	1.65	4.75	0.725	4.51	0.68	4.07	0.55		0.87	0.2							
37			4.3	1		0.85					2	0.33	2.8	0.4	7									
28			4	0.88		0.52					1.3	0.23	3.7	0.4	7									
19			2.5	0.62		0.48					1.4	0.19	3	0.6	7									
31			2.9	0.77		0.53					1.9	0.25	3.9	0.5	40									
30			3.1	0.84		0.51					1.7	0.26	3	0.5	25									
50			4.5	0.99		0.75					1.9	0.3	3.7	0.4	40									
54.08	6.25	23.74	4.4	1.07	3.66	0.54	3.13	0.64	1.77	0.27	1.62	0.24	3.07	0.357		9.43	1.77							
42			3.6	0.95		0.77					1.9	0.3	2.3	0.4	13									
31.63	4.05	17.48	4.2	1.17	4.61	0.76	4.95	1.12	2.95	0.44	2.97	0.43	2.84	0.41		2.72	0.65							
30.7	3.94	16.95	4.1	1.16	4.39	0.73	4.93	1.13	3	0.45	2.95	0.43	2.85	0.23		2.7	0.64							
286.82	32.79	124.49	21.31	4.02	16.67	2.28	12.08	2.33	6.29	0.84	5.48	0.78	12.87	1.6		10.09	1.98							

38.75	5.97	29.15	10.29	1.12	11.83	1.7	9.36	1.91	4.77	0.69	4.44	0.69	11.61	1.3		8.45	2.35
182.74	21.18	84.23	14.56	2.72	11.16	1.56	8.98	1.9	5.38	0.79	5.18	0.77	14.91	1.65		7.7	1.59

34			3.7	0.79		0.69					1.9	0.27	3	0.4	6		
39			4.1	1		0.71					2	0.34	3.3	0.4	8		

81.63	10.17	39.9	9.51	1.89	8.57	1.31	7.54	1.5	4.15	0.63	4.02	0.63	10.8	1.06		9.84	2.38
160.45	19.4	74.4	13.13	2.08	9.44	1.33	7.52	1.51	4.31	0.67	4.25	0.64	11.64	1.19		7.5	1.36
48.45	6.18	25.49	5.28	1.6	4.4	0.64	3.57	0.69	1.8	0.26	1.562	0.23	3.88	0.79		3.33	0.87
48.45	6.18	25.49	5.28	1.6	4.4	0.64	3.57	0.69	1.8	0.26	1.562	0.23	3.88	0.79		3.33	0.87
35.56	4.5	18.42	4.03	1.2	3.7	0.57	3.3	0.66	1.81	0.27	1.566	0.23	3.43	0.59		2.81	0.45
35.56	4.5	18.42	4.03	1.2	3.7	0.57	3.3	0.66	1.81	0.27	1.566	0.23	3.43	0.59		2.81	0.45
7.62	1.24	6.75	2.31	0.63	2.97	0.57	3.56	0.86	2.45	0.35	1.99	0.29	0.22	0.17		0.21	0.07
253.66	29.65	103.35	17.72	1.6	11.97	1.8	10.32	2.05	5.87	0.93	6.22	0.92	13.92	2.35		21.45	4.85
29.34	3.97	13.8	2.8	0.84	2.15	0.37	2.07	0.57	1.37	0.18	1.29	0.21	8.15	0.28		3.52	0.93
29.34	3.97	13.8	2.8	0.84	2.15	0.37	2.07	0.57	1.37	0.18	1.29	0.21	8.15	0.28		3.52	0.93
245.14	28.26	101.48	17.41	2.99	12.29	1.76	9.65	1.87	5.04	0.75	4.73	0.7	14.07	1.24		9.43	1.77
245.14	28.26	101.48	17.41	2.99	12.29	1.76	9.65	1.87	5.04	0.75	4.73	0.7	14.07	1.24		9.43	1.77
12.54	1.58	6.57	1.54	0.69	1.74	0.28	1.86	0.42	1.08	0.18	1.13	0.17		0.18	3	0.91	0.19
11.44	1.48	5.93	1.41	0.67	1.54	0.24	1.59	0.33	0.96	0.14	0.96	0.15		0.110	3.9	0.82	0.18

22.68	2.93	12.91	3.19	1.31	4.02	0.64	4.15	0.88	2.45	0.34	2.21	0.33	1.25	0.69			
15.44	2.03	8.68	2.27	0.76	2.6	0.44	2.9	0.6	1.61	0.24	1.51	0.21	0.91	0.22			
32.24	4.04	15.92	3.49	0.61	3.58	0.6	3.87	0.85	2.24	0.36	2.32	0.36	2.92	0.43			
32.04	4.07	16.65	3.84	1.1	4.24	0.71	4.58	0.98	2.7	0.42	2.53	0.39	2.76	0.36			
29.21	3.5	14.18	3.27	1.13	3.65	0.64	4.4	0.96	2.63	0.39	2.46	0.34	1.8	0.39			
29.49	3.8	15.66	3.46	1.17	3.78	0.61	4.11	0.87	2.57	0.4	2.5	0.37	3.74	0.5			
34.46	4.38	17.81	4.14	1.33	4.57	0.76	5	1.07	3	0.45	2.76	0.41	2.43	0.36			
31.73	4.12	17.78	4.28	1.1	4.62	0.79	4.85	1.09	2.83	0.47	2.84	0.44	2.95	0.38			
31.34	3.8	14.58	3.54	1.02	3.38	0.6	3.55	0.8	2.38	0.35	2.2	0.33	1.83	0.35		2.69	0.6
30.73	3.95	15.16	3.69	1.06	3.69	0.65	3.83	0.82	2.27	0.33	2.12	0.3	1.75	0.33		2.45	0.53
23.64	3.1	12.52	3.21	0.99	3.57	0.62	3.75	0.85	2.41	0.33	1.99	0.27	1.37	0.36		2.38	0.55
24.77	3.06	11.62	2.76	0.87	2.98	0.51	3.03	0.65	1.86	0.26	1.6	0.22	1.03	0.37		1.86	0.45
23.12	2.92	11.37	2.78	0.85	2.99	0.52	3.19	0.7	1.98	0.28	1.68	0.25	1.21	0.48		1.9	0.45
33.07	4.1	16.38	3.89	1.37	4.14	0.67	4.2	0.89	2.48	0.35	2.1	0.3	2.15	0.46		2.42	0.59
45.38	5.66	21.95	4.93	1.39	5.2	0.8	4.78	1.01	2.78	0.4	2.55	0.38	3.29	0.5		3.99	0.97

30.32	3.94	15.64	3.76	0.87	4.1	0.72	4.53	0.99	2.95	0.45	2.89	0.45	2.99	0.39		2.81	0.58
38.32	4.91	19.38	4.77	1.51	5.38	0.89	5.71	1.22	3.29	0.46	2.66	0.37	2.41	0.42		3.15	0.73
41.78	5.08	19.67	4.33	1.24	4.37	0.72	4.32	0.91	2.55	0.37	2.35	0.34	2.94	0.62		4.4	1.16
29.69	3.76	14.58	3.6	0.79	3.98	0.69	4.39	0.96	2.78	0.42	2.75	0.42	2.86	0.41		2.58	0.55
22.52	2.95	11.42	2.8	0.67	2.96	0.5	3.26	0.71	2.13	0.34	2.17	0.36	3.44	0.51		4.65	1.1
26.82	3.39	13.14	3.26	0.73	3.44	0.59	3.71	0.82	2.38	0.34	2.21	0.33	2.29	0.34		2.25	0.5

32.3	4.14	16.56	4.35	1.77	5.21	0.87	5.48	1.15	3.2	0.48	2.96	0.44	2.58	0.47	2.68	0.63
24.12	3.18	12.98	3.1	1.05	3.05	0.5	2.86	0.58	1.53	0.2	1.12	0.16	1.56	0.39	1.4	0.32
29.97	3.8	15.06	3.35	0.89	3.26	0.5	2.74	0.55	1.44	0.2	1.19	0.18	2.31	0.36	2.48	0.29
53.19	6.94	28.15	5.96	1.77	5.51	0.85	4.56	0.92	2.53	0.34	2.15	0.3	4.22	1	2.75	0.44
87.55	11.31	43.97	9.13	2.61	7.84	1.07	5.53	1.03	2.56	0.35	2.06	0.31	5.16	0.86	5.21	1
71.22	9.16	35.54	7.31	1.76	6.13	0.9	4.81	0.91	2.35	0.31	1.81	0.26	4.81	0.72	3.74	0.62
81.12	10.36	41.22	8.56	2.46	7.28	1.03	5.18	0.95	2.45	0.31	1.84	0.27	4.59	0.74	3.8	0.66
91.27	11.7	46.11	9.53	2.52	7.95	1.1	5.59	1.02	2.7	0.37	2.15	0.32	5.62	0.84	5.3	1.04
80.44	10.41	41.4	8.59	2.4	7.28	1.03	5.24	0.95	2.34	0.31	1.8	0.27	4.61	0.78	3.76	0.64
77.13	9.7	38.33	7.77	2.32	6.69	0.93	4.72	0.88	2.25	0.31	1.76	0.26	4.28	0.76	3.54	0.59
106.91	14.19	55.49	11.6	2.91	9.67	1.33	6.86	1.26	3.17	0.42	2.39	0.35	5.09	1.14	3.54	0.55
110.91	14.16	55.9	11.15	3.2	9.4	1.31	6.54	1.25	3.09	0.43	2.42	0.34	4.94	1.1	3.48	0.55

83.01	10.24	40.09	7.94	2.08	7.18	1	5.33	1.02	2.54	0.36	2.12	0.29	4.15	1.26		
60.57	7.7	32.1	6.69	1.52	6.13	0.88	4.78	0.89	2.26	0.3	1.88	0.28	3.39	0.79		
59.66	7.34	30.56	6.48	1.92	6.03	0.86	4.71	0.92	2.21	0.31	1.88	0.27	3.42	0.84		
91.63	11.22	43.81	8.28	1.95	7.04	0.98	4.95	0.93	2.32	0.31	1.98	0.3	5.07	0.69		
54.16	6.82	26.99	5.38	1.75	4.89	0.71	4.14	0.77	2.08	0.29	1.75	0.26	3.7	0.46		
97.23	11.87	45.63	8.69	1.83	7.56	1.1	5.71	1.08	2.75	0.39	2.29	0.35	6.07	0.95		
103.21	12.7	48.94	9.17	2.41	7.85	1.07	5.69	1.09	2.69	0.39	2.38	0.34	6.02	0.97		
70.53	8.83	33.29	6.82	1.93	6.13	0.9	4.68	0.92	2.4	0.33	2.02	0.31	4.25	0.74	6.06	1.47
85.56	11.28	44.1	8.88	2.79	7.67	1.11	5.78	1.11	2.83	0.39	2.28	0.33	4.96	0.99	3.18	0.55

49.65	6.31	24.97	5.41	1.53	5.12	0.77	4.28	0.86	2.21	0.31	1.76	0.24	3.31	0.88	2.5	0.37
40.19	5.08	21.46	4.85	1.25	4.62	0.71	3.95	0.79	2.2	0.3	1.85	0.29	3.74	0.84	2.35	0.35
49.11	6.36	25.29	5.54	1.6	5.28	0.8	4.5	0.92	2.39	0.32	1.92	0.29	3.65	0.88	2.43	0.35

43.93	5.15	18.48	3.98	0.65	3.82	0.65	4.12	0.88	2.56	0.39	2.48	0.39	3.62	0.78	9.81	3.17
77.61	8.79	32.32	6.36	1.45	5.69	0.9	4.8	1.01	2.76	0.39	2.54	0.37	3.34	0.72	10.32	3.65
44.43	5.05	18.22	3.79	0.8	3.63	0.61	3.81	0.83	2.38	0.36	2.45	0.36	3.63	0.73	10.09	3.35

51.93	6.17	22.91	4.8	0.85	4.45	0.72	4.18	0.89	2.6	0.38	2.46	0.38	3.53	0.77		10.03	3.44
55.59	6.21	23.11	4.81	1.27	4.66	0.77	4.31	0.95	2.64	0.4	2.43	0.36	3.6	0.83		10.2	3.56
53.1	6.09	22.53	4.82	1.11	4.55	0.74	4.4	0.91	2.65	0.4	2.4	0.36	3.25	0.67		9.94	3.47
51.69	6.05	21.94	4.63	1.04	4.33	0.73	4.28	0.93	2.67	0.39	2.48	0.37	3.63	0.79		10.25	3.53
54.01	6.2	22.32	4.62	1.19	4.33	0.71	3.99	0.81	2.25	0.33	2.15	0.34	3.56	0.71		9.85	3.39
17.3		9.63	2.28	0.734	2.47		2.63		1.62		1.53						
12.3		6.91	1.65	0.533	1.75		1.88		1.15		1.11						
11.9		6.68	1.59	0.508	1.71		1.83		1.12		1.08						
9.5		5.3	1.26	0.404	1.36		1.46		0.896		0.865						
11.2		6.34	1.5	0.494	1.61		1.73		1.06		1.02						
14.5		8.24	1.94	0.634	2.13		2.26		1.37		1.32						
15.1		8.45	2.03	0.672	2.19		2.34		1.42		1.37						
16.6		9.09	2.1	0.646	2.21		2.32		1.42		1.35						
16.8		9.43	2.23	0.716	2.41		2.58		1.58		1.51						
23		11	2.29	0.89							1.4			0.2	3	2.5	0.41
22.9	2.9	12	2.9	0.95	3	0.5	3.3	0.65	1.8	0.27	1.7	0.29		0.2	9.2	1.4	0.3
19.5	2.6	9.6	2.2	0.8	2.9	0.4	2.4	0.5	1.4	0.2	1.3			0.2	4	2.1	0.5
34		15	2.77	0.96							1.25			0.1	2	2.8	0.4
18		8	1.97	0.66							1.42	0.23		0.1	2	1.4	0.1
17.5	2.2	9	2	0.7	2.5	0.3	2.2	0.4	1.2	0.2	1.2	0.2		0.2	4	1.7	0.3

Appendix C - Geochemical Standards

	ICP-OES	SiO2	TiO2	Al2O3	Fe2O3	MnO	MgO	CaO
Certified/Prefe	JB1a	52.16	1.30	14.51	9.10	0.15	7.75	9.23

Run	Certified/Prefe	SiO2	TiO2	Al2O3	Fe2O3	MnO	MgO	CaO
1	JB1a	52.31	1.29	14.36	9.55	0.15	7.77	9.36
	% Error	0.00	0.01	0.01	-0.05	-0.02	0.00	-0.01
2	JB1a	51.88	1.29	14.79	9.21	0.15	7.72	10.00
	% Error	0.01	0.00	-0.02	-0.01	-0.02	0.00	-0.08
3	JB1a	51.58	1.33	13.32	9.60	0.16	8.05	9.91
	% Error	0.01	-0.02	0.08	-0.05	-0.05	-0.04	-0.07
4	JB1a	52.32	1.32	15.43	9.28	0.15	7.92	9.29
	% Error	0.00	-0.01	-0.06	-0.02	0.00	-0.02	-0.01
5	JB1a	52.22	1.30	14.62	9.25	0.16	8.12	9.97
	% Error	0.00	0.00	-0.01	-0.02	-0.05	-0.05	-0.08
6	JB1a	51.91	1.28	14.09	9.08	0.15	7.88	9.85
	% Error	0.00	0.02	0.03	0.00	0.01	-0.02	-0.07
7	JB1a	51.93	1.31	14.59	9.09	0.15	7.69	10.35
	% Error	0.00	-0.01	-0.01	0.00	0.03	0.01	-0.12
8	JB1a	51.97	1.30	14.10	9.35	0.15	7.91	9.34
	% Error	0.00	0.00	0.03	-0.03	0.00	-0.02	-0.01
9	JB1a	52.82	1.32	13.99	8.98	0.16	8.02	9.36
	% Error	-0.01	-0.01	0.04	0.01	-0.08	-0.03	-0.01
10	JB1a	52.44	1.33	14.49	9.03	0.16	7.72	8.55
	% Error	-0.01	-0.02	0.00	0.01	-0.05	0.00	0.07

	SiO2	TiO2	Al2O3	Fe2O3	MnO	MgO	CaO
Average	52.14	1.31	14.38	9.24	0.15	7.88	9.60
STDEV	0.35	0.02	0.56	0.21	0.01	0.15	0.52
RSD	0.68	1.34	3.89	2.28	3.48	1.92	5.37

	ICP-OES	SiO2	TiO2	Al2O3	Fe2O3	MnO	MgO	CaO
Certified/Prefe	NIM-G	75.70	0.09	12.08	2.02	0.02	0.06	0.78

Run	Certified/Prefe	SiO2	TiO2	Al2O3	Fe2O3	MnO	MgO	CaO
1	NIM-G	76.58	0.09	12.16	2.12	0.02	0.03	0.77
	% Error	-0.01	-0.01	-0.01	-0.05	0.15	0.52	0.01
2	NIM-G	76.41	0.09	12.12	2.07	0.01	0.03	0.78
	% Error	-0.01	-0.04	0.00	-0.02	0.32	0.51	0.01
3	NIM-G	76.23	0.08	11.87	2.10	0.03	0.03	0.83
	% Error	-0.01	0.08	0.02	-0.04	-0.29	0.48	-0.07
4	NIM-G	75.11	0.09	13.25	2.00	0.02	0.18	0.67
	% Error	0.01	0.03	-0.10	0.01	0.26	-2.05	0.15
5	NIM-G	75.75	0.09	12.20	2.13	0.02	0.03	0.82
	% Error	0.00	-0.02	-0.01	-0.05	0.12	0.53	-0.05
6	NIM-G	75.99	0.09	12.07	2.04	0.02	0.05	0.77
	% Error	0.00	0.01	0.00	-0.01	-0.07	0.11	0.01
7	NIM-G	75.76	0.06	12.12	2.08	0.05	0.08	0.80
	% Error	0.00	0.28	0.00	-0.03	-1.54	-0.27	-0.02
8	NIM-G	75.69	0.10	11.83	2.00	0.02	0.04	0.79
	% Error	0.00	-0.06	0.02	0.01	0.21	0.32	0.00
9	NIM-G	76.06	0.10	10.94	2.04	0.02	0.03	0.79
	% Error	0.00	-0.13	0.09	-0.01	-0.02	0.44	-0.01
10	NIM-G	76.31	0.09	12.17	1.85	0.02	0.03	0.69
	% Error	-0.01	0.00	-0.01	0.09	0.19	0.50	0.11

	SiO2	TiO2	Al2O3	Fe2O3	MnO	MgO	CaO
Average	75.99	0.09	12.07	2.04	0.02	0.05	0.77
STDEV	0.43	0.01	0.56	0.08	0.01	0.05	0.05
RSD	0.57	11.03	4.63	4.05	51.23	89.94	6.87

	ICP-OES	Ir	Ru	Rh	Pt	Pd	Au
Certified/Prefe	TDB1	0.15	0.3	0.7	5.8	22.4	6.3

Run	Certified/Prefe	Ir	Ru	Rh	Pt	Pd	Au
1	TDB1	0.09	0.44	0.54	5.73	23.0	5.83
	% Error	1.00	0.66	0.96	0.37	-152.11	0.25
2	TDB1	0.10	0.24	0.47	6.22	26.1	7.19

% Error	1.00	0.82	0.97	0.32	-173.06	0.07

	Ir	**Ru**	**Rh**	**Pt**	**Pd**	**Au**
Average	0.10	0.34	0.50	5.97	24.54	6.51
STDEV	0.00	0.14	0.05	0.35	2.22	0.96
RSD	3.33	42.31	10.59	5.87	9.05	14.79

ICP-OES		**Ir**	**Ru**	**Rh**	**Pt**	**Pd**	**Au**
Certified/Pref	**WMG1**	**46**	**35**	**26**	**731**	**382**	**110**

Run	**Certified/Pref**	**Ir**	**Ru**	**Rh**	**Pt**	**Pd**	**Au**
1	**WMG1**	44.7	38.5	23.9	741	364	108
	% Error	-9249.66	-2181.52	-816.18	-331820.42	-30009.95	6225.35
2	**WMG1**	44.4	32.9	28.4	735	370	104
	% Error	-9181.07	-1862.43	-967.78	-329322.38	-30452.41	6006.41

	Ir	**Ru**	**Rh**	**Pt**	**Pd**	**Au**
Average	44.52	35.68	26.14	737.92	366.96	106.06
STDEV	0.23	3.98	3.14	3.94	3.80	2.69
RSD	0.53	11.15	12.00	0.53	1.03	2.53

Na2O	**K2O**	**P2O5**	**LOI**	**Total**	**Sc**	**V**	**Cr**
2.74	**1.42**	**0.25**	**0.78**	**99.39**	**27.9**	**206.0**	**415.0**

Na2O	**K2O**	**P2O5**	**LOI**	**Total**	**Sc**	**V**	**Cr**
2.70	1.43	0.25	0.78	99.95	28.6	214.3	414.9
0.01	-0.01	0.01	0.00	-0.01	-0.03	-0.04	0.00
2.78	1.49	0.25	0.78	100.36	30.3	243.8	405.1
-0.02	-0.05	-0.01	0.00	-0.01	-0.09	-0.18	0.02
2.55	1.35	0.24	0.78	98.87	28.3	211.8	414.1
0.07	0.05	0.04	0.00	0.01	-0.01	-0.03	0.00
2.65	1.43	0.27	0.78	100.84	28.4	212.9	399.6
0.03	-0.01	-0.07	0.00	-0.01	-0.02	-0.03	0.04
2.66	1.46	0.27	0.78	100.81	28.8	210.5	410.0
0.03	-0.03	-0.10	0.00	-0.01	-0.03	-0.02	0.01
2.64	1.39	0.25	0.78	99.29	29.7	202.7	432.6
0.04	0.02	-0.01	0.00	0.00	-0.06	0.02	-0.04
3.31	1.48	0.29	0.78	100.97	29.5	208.9	425.7
-0.21	-0.04	-0.15	0.00	-0.02	-0.06	-0.01	-0.03
2.65	1.47	0.26	0.78	99.29	29.9	212.6	424.1
0.03	-0.03	-0.03	0.00	0.00	-0.07	-0.03	-0.02
2.80	1.44	0.24	0.78	99.92	29.9	216.2	422.2
-0.02	-0.02	0.02	0.00	-0.01	-0.07	-0.05	-0.02
2.79	1.49	0.27	0.78	99.05	27.7	219.9	423.7
-0.02	-0.05	-0.07	0.00	0.00	0.01	-0.07	-0.02

Na2O	**K2O**	**P2O5**	**LOI**	**Total**	**Sc**	**V**	**Cr**
2.75	1.44	0.26	0.78	99.93	29.11	215.35	417.21
0.21	0.04	0.01	0.00	0.79	0.85	10.97	10.25
7.69	3.11	5.77	0.00	0.79	2.92	5.09	2.46

Na2O	**K2O**	**P2O5**	**LOI**	**Total**	**Sc**	**V**	**Cr**
3.36	**4.99**	**0.01**	**0.51**	**99.62**	**1.0**	**2.0**	**12.0**

Na2O	**K2O**	**P2O5**	**LOI**	**Total**	**Sc**	**V**	**Cr**
3.44	4.84	0.01	0.55	100.61	0.4	8.1	8.3
-0.02	0.03	0.45	-0.08	-0.01	0.59	-3.03	0.31
3.28	4.84	0.01	0.55	100.20	0.2	6.2	16.4
0.02	0.03	0.31	-0.08	-0.01	0.77	-2.12	-0.37
3.29	4.84	0.00	0.55	99.87	0.1	1.9	12.1
0.02	0.03	0.84	-0.08	0.00	0.88	0.03	-0.01
3.42	4.88	0.01	0.55	100.18	0.2	2.2	8.1
-0.02	0.02	-0.49	-0.08	-0.01	0.82	-0.11	0.32
3.20	4.81	0.01	0.55	99.62	0.3	5.2	4.4
0.05	0.04	-0.06	-0.08	0.00	0.74	-1.61	0.63
3.31	4.89	0.01	0.55	99.80	1.2	3.4	11.4
0.02	0.02	0.09	-0.08	0.00	-0.15	-0.69	0.05
3.26	4.87	0.02	0.55	99.64	8.5	1.5	9.0
0.03	0.03	-0.75	-0.08	0.00	-7.53	0.27	0.25
3.27	5.08	0.01	0.55	99.37	0.3	1.5	19.0
0.03	-0.02	-0.14	-0.08	0.00	0.70	0.26	-0.59
3.22	4.84	0.01	0.55	98.61	0.08	0.9	18.3
0.04	0.03	0.33	-0.08	0.01	0.92	0.54	-0.52
3.39	5.04	0.01	0.55	100.15	0.3	2.9	7.2
-0.01	-0.01	0.36	-0.08	-0.01	0.73	-0.45	0.40

Na2O	**K2O**	**P2O5**	**LOI**	**Total**	**Sc**	**V**	**Cr**
3.31	4.89	0.01	0.55	99.80	1.15	3.38	11.42
0.08	0.09	0.00	0.00	0.55	2.61	2.37	4.99
2.44	1.86	51.89	0.00	0.55	226.40	69.98	43.67

Co	Ni	Cu	Zn	Sr	Y	Zr	Ba	
39.5	134.0	55.0	82.0	443.0	24.0	146.0	497.0	Certified/Prefe

Co	Ni	Cu	Zn	Sr	Y	Zr	Ba	Run
37.1	136.2	16.3	86.7	449.9	23.2	139.1	493.9	1
0.06	-0.02	0.70	-0.06	-0.02	0.03	0.05	0.01	
39.1	129.5	53.2	82.6	450.3	23.4	140.4	500.1	2
0.01	0.03	0.03	-0.01	-0.02	0.03	0.04	-0.01	
38.3	145.3	56.5	81.6	444.5	23.3	138.8	489.4	3
0.03	-0.08	-0.03	0.00	0.00	0.03	0.05	0.02	
39.4	145.0	58.8	87.1	456.3	22.8	143.6	478.2	4
0.00	-0.08	-0.07	-0.06	-0.03	0.05	0.02	0.04	
41.5	130.7	55.1	86.4	449.8	23.2	142.6	501.6	5
-0.05	0.02	0.00	-0.05	-0.02	0.03	0.02	-0.01	
36.7	127.9	58.3	76.1	439.1	24.3	141.0	492.7	6
0.07	0.05	-0.06	0.07	0.01	-0.01	0.03	0.01	
37.2	135.7	47.6	79.5	431.4	23.7	139.5	490.0	7
0.06	-0.01	0.13	0.03	0.03	0.01	0.04	0.01	
37.5	140.1	53.6	73.3	434.1	24.5	143.8	485.6	8
0.05	-0.05	0.03	0.11	0.02	-0.02	0.01	0.02	
41.0	137.6	60.3	86.9	439.1	24.3	148.4	548.5	9
-0.04	-0.03	-0.10	-0.06	0.01	-0.01	-0.02	-0.10	
38.1	133.0	56.1	82.8	450.4	24.6	145.1	506.5	10
0.04	0.01	-0.02	-0.01	-0.02	-0.03	0.01	-0.02	

Co	Ni	Cu	Zn	Sr	Y	Zr	Ba
38.59	136.10	51.58	82.30	444.49	23.74	142.23	498.66
1.64	6.07	12.91	4.82	8.17	0.66	3.06	19.33
4.26	4.46	25.02	5.85	1.84	2.76	2.15	3.88

Co	Ni	Cu	Zn	Sr	Y	Zr	Ba
4.0	8.0	12.0	50.0	10.0	143.0	300.0	120.0

Co	Ni	Cu	Zn	Sr	Y	Zr	Ba	Run
2.7	2.2	982.3	50.5	9.8	145.2	309.9	115.7	1
0.34	0.72	-80.86	-0.01	0.02	-0.02	-0.03	0.04	
2.5	12.3	17.9	46.6	9.5	143.2	299.8	114.6	2
0.37	-0.53	-0.49	0.07	0.05	0.00	0.00	0.04	
3.7	12.7	28.2	56.9	8.7	149.6	306.9	107.2	3
0.07	-0.59	-1.35	-0.14	0.13	-0.05	-0.02	0.11	
0.6	4.2	27.0	59.2	8.9	144.4	310.4	104.8	4
0.84	0.48	-1.25	-0.18	0.11	-0.01	-0.03	0.13	
1.3	17.5	24.6	43.5	9.9	143.5	298.2	117.6	5
0.67	-1.18	-1.05	0.13	0.01	0.00	0.01	0.02	
4.2	12.3	126.1	50.4	9.8	147.1	303.2	112.2	6
-0.06	-0.54	-9.51	-0.01	0.02	-0.03	-0.01	0.06	
9.7	11.4	9.9	53.4	12.4	145.8	280.7	115.8	7
-1.42	-0.42	0.18	-0.07	-0.24	-0.02	0.06	0.03	
6.0	1.4	13.0	35.0	10.2	150.1	295.2	107.4	8
-0.50	0.83	-0.08	0.30	-0.02	-0.05	0.02	0.10	
9.1	10.0	16.8	59.2	10.6	151.7	308.5	119.1	9
-1.28	-0.26	-0.40	-0.18	-0.06	-0.06	-0.03	0.01	
2.5	39.0	15.3	49.6	8.4	150.5	319.4	107.9	10
0.38	-3.87	-0.28	0.01	0.16	-0.05	-0.06	0.10	

Co	Ni	Cu	Zn	Sr	Y	Zr	Ba
4.24	12.29	126.12	50.43	9.81	147.13	303.21	112.24
3.11	10.70	302.77	7.50	1.14	3.13	10.59	5.05
73.50	87.06	240.07	14.87	11.63	2.12	3.49	4.50

ICP-MS	49TiO2	51V	52Cr	55MnO	59Co	60Ni	65Cu	66Zn
JB1a	**1.30**	**206.0**	**415.0**	**0.15**	**39.5**	**140.0**	**55.0**	**82.0**

Certified/Prefe	49TiO2	51V	52Cr	55MnO	59Co	60Ni	65Cu	66Zn
JB1a	1.27	214.7	407.0	0.16	37.7	144.6	26.2	87.1
% Error	0.02	-0.04	0.02	-0.11	0.05	-0.03	0.52	-0.06
JB1a	1.28	216.0	419.9	0.15	38.9	140.9	49.5	78.5
% Error	0.01	-0.05	-0.01	0.01	0.01	-0.01	0.10	0.04
JB1a	1.27	212.2	400.2	0.15	38.5	131.1	54.2	80.7
% Error	0.02	-0.03	0.04	0.01	0.02	0.06	0.02	0.02
JB1a	1.30	217.7	399.2	0.14	38.5	144.1	58.6	81.5
% Error	0.00	-0.06	0.04	0.09	0.03	-0.03	-0.07	0.01
JB1a	1.30	206.8	390.1	0.15	37.5	129.2	55.6	79.2
% Error	0.00	0.00	0.06	0.00	0.05	0.08	-0.01	0.03
JB1a	1.30	209.8	432.0	0.16	38.0	131.2	53.6	81.0
% Error	0.00	-0.02	-0.04	-0.07	0.04	0.06	0.02	0.01
JB1a	1.33	213.8	430.1	0.15	38.9	157.3	52.7	81.8
% Error	-0.03	-0.04	-0.04	-0.01	0.02	-0.12	0.04	0.00
JB1a	1.33	227.5	414.5	0.15	39.3	138.9	64.9	88.2
% Error	-0.02	-0.10	0.00	0.01	0.01	0.01	-0.18	-0.08
JB1a	1.32	214.5	437.0	0.15	40.4	136.8	61.4	84.7
% Error	-0.02	-0.04	-0.05	-0.03	-0.02	0.02	-0.12	-0.03
JB1a	1.28	214.2	411.1	0.15	37.1	144.2	58.9	84.2
% Error	0.02	-0.04	0.01	-0.01	0.06	-0.03	-0.07	-0.03

	49TiO2	51V	52Cr	55MnO	59Co	60Ni	65Cu	66Zn
	1.30	214.71	414.10	0.15	38.49	139.84	53.57	82.69
	0.02	5.46	15.58	0.01	0.97	8.44	10.60	3.26
	1.89	2.54	3.76	5.08	2.51	6.03	19.79	3.94

ICP-MS	49TiO2	51V	52Cr	55MnO	59Co	60Ni	65Cu	66Zn
NIM-G	**0.09**	**2.0**	**12.0**	**0.02**	**4.0**	**8.0**	**12.0**	**50.0**

Certified/Prefe	49TiO2	51V	52Cr	55MnO	59Co	60Ni	65Cu	66Zn
NIM-G	0.09	9.7	8.4	0.03	2.6	1.3	213.3	57.1
% Error	-0.02	-3.87	0.30	-0.47	0.35	0.84	-16.77	-0.14
NIM-G	0.09	0.2	16.1	0.02	3.0	11.2	23.8	49.0
% Error	-0.01	0.89	-0.34	-0.18	0.25	-0.40	-0.99	0.02
NIM-G	0.08	1.5	13.9	0.04	2.0	13.7	17.6	53.4
% Error	0.02	0.25	-0.16	-0.86	0.49	-0.72	-0.46	-0.07
NIM-G	0.09	1.4	10.7	0.03	1.4	3.8	22.1	52.8
% Error	0.00	0.30	0.11	-0.74	0.65	0.53	-0.84	-0.06
NIM-G	0.09	8.5	14.9	0.03	0.4	8.2	27.2	48.7
% Error	-0.03	-3.26	-0.24	-0.74	0.91	-0.02	-1.26	0.03
NIM-G	0.09	3.1	12.0	0.02	2.1	9.5	40.3	50.0
% Error	-0.03	-0.57	0.00	-0.20	0.48	-0.19	-2.36	0.00
NIM-G	0.07	1.3	18.8	0.01	3.1	14.2	17.3	46.9
% Error	0.17	0.34	-0.56	0.35	0.23	-0.78	-0.44	0.06
NIM-G	0.09	1.3	10.0	0.02	0.8	1.8	15.4	37.7
% Error	-0.09	0.34	0.17	0.20	0.80	0.77	-0.28	0.25
NIM-G	0.10	0.0	7.6	0.01	3.0	17.1	11.4	50.1
% Error	-0.19	0.98	0.36	0.65	0.24	-1.14	0.05	0.00
NIM-G	0.09	4.3	7.2	0.02	2.2	14.2	14.5	54.2
% Error	-0.11	-1.13	0.40	0.00	0.44	-0.78	-0.21	-0.08

	49TiO2	51V	52Cr	55MnO	59Co	60Ni	65Cu	66Zn
	0.09	3.14	11.95	0.02	2.06	9.51	40.29	49.99
	0.01	3.40	3.87	0.01	0.94	5.62	61.35	5.28
	9.17	108.35	32.39	42.50	45.77	59.08	152.28	10.57

71Ga	**85Rb**	**88Sr**	**89Y**	**90Zr**	**93Nb**	**133Cs**	**137Ba**	**139La**
18.0	**42.0**	**443.0**	**24.0**	**146.0**	**27.00**	**1.20**	**497.0**	**38.10**

71Ga	**85Rb**	**88Sr**	**89Y**	**90Zr**	**93Nb**	**133Cs**	**137Ba**	**139La**
18.1	40.3	444.7	24.0	142.2	26.49	1.16	492.4	36.78
-0.01	0.04	0.00	0.00	0.03	0.02	0.03	0.01	0.03
17.3	36.9	441.7	23.7	139.8	26.60	1.18	491.0	38.50
0.04	0.12	0.00	0.01	0.04	0.01	0.02	0.01	-0.01
16.9	39.2	436.1	23.5	139.7	26.41	1.33	492.8	38.28
0.06	0.07	0.02	0.02	0.04	0.02	-0.11	0.01	0.00
17.6	40.9	444.8	23.8	143.9	26.44	1.23	496.9	39.02
0.02	0.03	0.00	0.01	0.01	0.02	-0.02	0.00	-0.02
17.8	40.1	442.0	23.1	138.4	26.78	1.29	489.0	39.27
0.01	0.05	0.00	0.04	0.05	0.01	-0.08	0.02	-0.03
17.8	43.2	449.5	25.0	145.8	27.08	1.11	513.0	38.26
0.01	-0.03	-0.01	-0.04	0.00	0.00	0.07	-0.03	0.00
18.0	39.9	444.3	24.7	140.8	28.61	1.23	493.6	38.40
0.00	0.05	0.00	-0.03	0.04	-0.06	-0.03	0.01	-0.01
17.7	39.4	441.0	24.5	141.0	26.20	1.18	487.3	37.64
0.02	0.06	0.00	-0.02	0.03	0.03	0.02	0.02	0.01
18.8	40.8	450.8	24.3	138.5	28.09	1.46	510.3	37.82
-0.04	0.03	-0.02	-0.01	0.05	-0.04	-0.21	-0.03	0.01
18.2	39.1	439.3	24.0	140.8	27.60	1.14	489.4	38.45
-0.01	0.07	0.01	0.00	0.04	-0.02	0.05	0.02	-0.01

71Ga	**85Rb**	**88Sr**	**89Y**	**90Zr**	**93Nb**	**133Cs**	**137Ba**	**139La**
17.83	39.98	443.42	24.05	141.08	27.03	1.23	495.56	38.24
0.53	1.60	4.44	0.57	2.34	0.81	0.10	8.91	0.71
2.95	4.00	1.00	2.39	1.66	3.00	8.40	1.80	1.84

71Ga	**85Rb**	**88Sr**	**89Y**	**90Zr**	**93Nb**	**133Cs**	**137Ba**	**139La**
27.0	**320.0**	**10.0**	**143.0**	**300.0**	**53.00**	**1.00**	**120**	**109.00**

71Ga	**85Rb**	**88Sr**	**89Y**	**90Zr**	**93Nb**	**133Cs**	**137Ba**	**139La**
31.1	337.0	9.6	145.3	306.5	44.42	0.90	115.0	110.64
-0.15	-0.05	0.04	-0.02	-0.02	0.16	0.10	0.04	-0.02
28.8	323.6	10.7	145.1	299.5	45.46	0.81	114.1	110.90
-0.07	-0.01	-0.07	-0.01	0.00	0.14	0.19	0.05	-0.02
28.3	315.6	9.8	144.7	310.1	51.67	0.99	109.8	107.63
-0.05	0.01	0.02	-0.01	-0.03	0.03	0.01	0.08	0.01
29.8	313.7	8.1	145.0	300.0	53.22	0.87	115.9	112.89
-0.10	0.02	0.19	-0.01	0.00	0.00	0.13	0.03	-0.04
29.1	319.6	6.6	139.3	299.7	45.00	0.95	112.0	111.90
-0.08	0.00	0.34	0.03	0.00	0.15	0.05	0.07	-0.03
29.4	329.4	8.5	144.3	302.8	50.7	0.93	114.1	110.74
-0.09	-0.03	0.15	-0.01	-0.01	0.04	0.07	0.05	-0.02
30.5	330.4	8.6	141.5	291.8	54.77	1.01	117.2	108.70
-0.13	-0.03	0.14	0.01	0.03	-0.03	-0.01	0.02	0.00
27.8	335.1	6.8	147.3	295.2	46.57	0.89	115.3	103.94
-0.03	-0.05	0.32	-0.03	0.02	0.12	0.11	0.04	0.05
28.7	372.1	8.3	144.7	313.7	59.87	1.09	120.0	116.63
-0.06	-0.16	0.17	-0.01	-0.05	-0.13	-0.09	0.00	-0.07
30.8	317.1	8.3	146.0	308.8	55.29	0.87	107.9	113.43
-0.14	0.01	0.17	-0.02	-0.03	-0.04	0.13	0.10	-0.04

71Ga	**85Rb**	**88Sr**	**89Y**	**90Zr**	**93Nb**	**133Cs**	**137Ba**	**139La**
29.44	329.36	8.55	144.33	302.83	50.69	0.93	114.13	110.74
1.11	17.09	1.26	2.29	6.91	5.22	0.08	3.51	3.46
3.78	5.19	14.75	1.58	2.28	10.30	8.92	3.07	3.13

140Ce	**141Pr**	**146Nd**	**147Sm**	**153Eu**	**157Gd**	**159Tb**	**163Dy**	**165Ho**
66.10	**7.30**	**25.50**	**5.02**	**1.47**	**4.54**	**0.69**	**4.19**	**0.72**

140Ce	**141Pr**	**146Nd**	**147Sm**	**153Eu**	**157Gd**	**159Tb**	**163Dy**	**165Ho**
65.80	7.16	25.68	5.17	1.47	4.86	0.70	4.16	0.75
0.00	0.02	-0.01	-0.03	0.00	-0.07	-0.02	0.01	-0.04
66.01	7.29	25.76	5.05	1.46	4.79	0.69	4.07	0.74
0.00	0.00	-0.01	-0.01	0.01	-0.05	0.00	0.03	-0.02
64.35	7.19	24.70	4.86	1.45	5.02	0.69	3.94	0.74
0.03	0.01	0.03	0.03	0.01	-0.10	0.00	0.06	-0.03
63.25	7.41	26.12	5.13	1.53	5.34	0.71	4.10	0.74
0.04	-0.02	-0.02	-0.02	-0.04	-0.18	-0.04	0.02	-0.03
64.56	7.38	25.39	5.06	1.47	4.68	0.68	4.13	0.74
0.02	-0.01	0.00	-0.01	0.00	-0.03	0.01	0.01	-0.03
69.61	7.38	25.36	5.18	1.57	4.70	0.72	4.06	0.75
-0.05	-0.01	0.01	-0.03	-0.07	-0.04	-0.05	0.03	-0.05
67.52	7.52	26.57	5.09	1.50	5.01	0.68	4.03	0.74
-0.02	-0.03	-0.04	-0.01	-0.02	-0.10	0.01	0.04	-0.03
67.18	7.14	26.07	5.12	1.50	4.73	0.69	4.05	0.73
-0.02	0.02	-0.02	-0.02	-0.02	-0.04	0.00	0.03	-0.01
65.37	7.14	25.84	5.05	1.47	4.83	0.69	3.99	0.72
0.01	0.02	-0.01	-0.01	0.00	-0.06	0.00	0.05	0.00
69.97	7.84	25.13	5.19	1.49	4.52	0.69	4.13	0.75
-0.06	-0.07	0.01	-0.03	-0.02	0.00	0.00	0.01	-0.04

140Ce	**141Pr**	**146Nd**	**147Sm**	**153Eu**	**157Gd**	**159Tb**	**163Dy**	**165Ho**
66.36	7.35	25.66	5.09	1.49	4.85	0.70	4.07	0.74
2.21	0.22	0.54	0.10	0.04	0.23	0.01	0.07	0.01
3.33	2.96	2.10	1.90	2.47	4.70	1.92	1.67	1.25

140Ce	**141Pr**	**146Nd**	**147Sm**	**153Eu**	**157Gd**	**159Tb**	**163Dy**	**165Ho**
195.00	**-**	**72.00**	**15.80**	**0.35**	**14.00**	**3.00**	**17.00**	**-**

140Ce	**141Pr**	**146Nd**	**147Sm**	**153Eu**	**157Gd**	**159Tb**	**163Dy**	**165Ho**
201.68	22.38	70.70	15.81	0.33	15.01	2.59	17.87	3.72
-0.03	-	0.02	0.00	0.06	-0.07	0.14	-0.05	-
211.78	22.60	70.81	14.55	0.34	15.25	2.71	18.42	3.80
-0.09	-	0.02	0.08	0.04	-0.09	0.10	-0.08	-
203.71	22.20	71.13	14.91	0.33	14.47	2.70	18.03	3.82
-0.04	-	0.01	0.06	0.06	-0.03	0.10	-0.06	-
205.50	22.77	74.03	15.25	0.36	16.90	2.73	19.00	3.87
-0.05	-	-0.03	0.03	-0.04	-0.21	0.09	-0.12	-
201.68	22.53	70.63	14.48	0.32	14.56	2.56	18.09	3.80
-0.03	-	0.02	0.08	0.08	-0.04	0.15	-0.06	-
202.56	22.39	71.35	14.91	0.33	14.93	2.67	17.96	3.79
-0.04	-	0.01	0.06	0.06	-0.07	0.11	-0.06	-
195.40	23.75	73.95	15.21	0.32	15.06	2.61	17.64	3.85
0.00	-	-0.03	0.04	0.07	-0.08	0.13	-0.04	-
191.08	19.94	66.84	13.80	0.30	14.26	2.55	17.17	3.52
0.02	-	0.07	0.13	0.15	-0.02	0.15	-0.01	-
200.67	22.19	72.50	15.18	0.33	14.80	2.85	17.38	3.94
-0.03	-	-0.01	0.04	0.05	-0.06	0.05	-0.02	-
211.54	23.14	71.54	14.96	0.33	14.07	2.71	18.05	3.82
-0.08	-	0.01	0.05	0.06	-0.01	0.10	-0.06	-

140Ce	**141Pr**	**146Nd**	**147Sm**	**153Eu**	**157Gd**	**159Tb**	**163Dy**	**165Ho**
202.56	22.39	71.35	14.91	0.33	14.93	2.67	17.96	3.79
6.36	0.98	2.03	0.54	0.02	0.79	0.09	0.52	0.11
3.14	4.39	2.84	3.63	4.83	5.26	3.42	2.87	2.95

166Er	169Tm	172Yb	175Lu	178Hf	181Ta	208Pb	232Th	238U
2.18	**0.31**	**2.10**	**0.32**	**3.48**	**1.60**	**7.20**	**8.80**	**1.60**

166Er	169Tm	172Yb	175Lu	178Hf	181Ta	208Pb	232Th	238U
2.19	0.35	2.07	0.32	3.38	1.61	7.04	8.80	1.67
0.00	-0.14	0.01	-0.01	0.03	-0.01	0.02	0.00	-0.04
2.09	0.33	2.07	0.32	3.35	1.65	7.70	8.78	1.61
0.04	-0.08	0.02	0.00	0.04	-0.03	-0.07	0.00	0.00
2.07	0.33	2.07	0.32	3.43	1.65	7.36	8.96	1.57
0.05	-0.06	0.01	0.01	0.02	-0.03	-0.02	-0.02	0.02
2.15	0.32	2.14	0.32	3.32	1.64	7.35	8.74	1.59
0.01	-0.05	-0.02	-0.01	0.04	-0.02	-0.02	0.01	0.01
2.16	0.34	2.07	0.31	3.43	1.67	7.77	8.69	1.56
0.01	-0.09	0.01	0.03	0.02	-0.04	-0.08	0.01	0.03
2.29	0.35	2.09	0.32	3.46	1.51	5.87	8.83	1.73
-0.05	-0.12	0.01	0.01	0.00	0.06	0.18	0.00	-0.08
2.13	0.32	2.05	0.31	3.47	1.65	7.27	8.61	1.67
0.02	-0.03	0.02	0.02	0.00	-0.03	-0.01	0.02	-0.05
2.01	0.32	2.01	0.31	3.34	1.61	7.02	8.70	1.61
0.08	-0.02	0.05	0.03	0.04	-0.01	0.02	0.01	-0.01
2.02	0.30	2.04	0.29	3.47	1.60	4.55	8.73	1.48
0.07	0.03	0.03	0.10	0.00	0.00	0.37	0.01	0.07
2.19	0.34	2.08	0.32	3.37	1.65	6.80	9.30	1.58
0.00	-0.10	0.01	0.00	0.03	-0.03	0.06	-0.06	0.01

166Er	169Tm	172Yb	175Lu	178Hf	181Ta	208Pb	232Th	238U
2.13	0.33	2.07	0.31	3.40	1.62	6.87	8.81	1.61
0.08	0.02	0.04	0.01	0.06	0.05	0.98	0.19	0.07
3.95	4.88	1.71	3.42	1.63	2.83	14.20	2.20	4.44

166Er	169Tm	172Yb	175Lu	178Hf	181Ta	208Pb	232Th	238U
-	**2.00**	**14.20**	**2.00**	**12.00**	**4.50**	**40.00**	**50.00**	**15.00**

166Er	169Tm	172Yb	175Lu	178Hf	181Ta	208Pb	232Th	238U
12.61	2.26	14.23	2.06	12.14	4.50	29.45	49.91	16.13
-	-0.13	0.00	-0.03	-0.01	0.00	0.26	0.00	-0.08
12.44	2.15	14.03	2.16	12.02	4.60	39.81	49.10	16.08
-	-0.08	0.01	-0.08	0.00	-0.02	0.00	0.02	-0.07
12.69	2.22	13.79	2.09	12.00	4.49	36.08	50.62	16.61
-	-0.11	0.03	-0.05	0.00	0.00	0.10	-0.01	-0.11
12.90	2.18	14.60	2.17	12.07	4.55	35.76	49.69	16.72
-	-0.09	-0.03	-0.09	-0.01	-0.01	0.11	0.01	-0.11
12.48	2.15	14.44	2.16	11.68	4.52	23.69	47.73	16.25
-	-0.07	-0.02	-0.08	0.03	0.00	0.41	0.05	-0.08
12.37	2.16	14.15	2.13	12.07	4.56	34.97	48.87	16.35
-	-0.08	0.00	-0.07	-0.01	-0.01	0.13	0.02	-0.09
12.46	2.13	13.91	2.16	12.37	4.37	37.83	48.74	16.84
-	-0.07	0.02	-0.08	-0.03	0.03	0.05	0.03	-0.12
11.02	1.99	13.44	2.01	11.45	4.61	42.15	47.01	16.47
-	0.01	0.05	0.00	0.05	-0.02	-0.05	0.06	-0.10
12.11	2.16	14.34	2.19	12.43	4.76	28.42	49.34	16.02
-	-0.08	-0.01	-0.10	-0.04	-0.06	0.29	0.01	-0.07
12.66	2.22	14.54	2.17	12.49	4.66	30.35	47.71	16.08
-	-0.11	-0.02	-0.08	-0.04	-0.04	0.24	0.05	-0.07

166Er	169Tm	172Yb	175Lu	178Hf	181Ta	208Pb	232Th	238U
12.37	2.16	14.15	2.13	12.07	4.56	33.85	48.87	16.35
0.52	0.07	0.36	0.06	0.32	0.11	5.72	1.12	0.29
4.21	3.36	2.56	2.71	2.69	2.32	16.90	2.28	1.78

Appendix D - Isotopic Data

Sample	Sm ppm	Nd ppm	147Sm/144Nd	143Nd/144Nd	±2SE	Luppm	Hf ppm	176Lu/177Hf	176Hf/177Hf	±2SE	87Sr/86Sr	±2SE	Pb64 corr	± 2SE Prop	Pb74 corr	± 2SE Prop
BD096	0.5469	1.7566	0.1882	0.511947	0.000008	0.10668	1.392865	0.0109	0.282261	0.000029	0.707820	0.000004	18.2781	0.0017	15.7938	0.0018
BD091	0.9348	3.5703	0.1583	0.511743	0.000007	0.13745	1.305238	0.0149	0.282154	0.000007	0.710585	0.000005	17.6057	0.0018	15.7502	0.0019
BD078	0.4847	1.1489	0.2550	0.512854	0.000009	0.10563	0.994113	0.0151	0.282707	0.000009	0.712903	0.000005	19.0274	0.0020	15.8522	0.0019
BD037	0.1078	0.5027	0.1296	0.511394	0.000027	0.02355	0.374686	0.0089	0.281975	0.000020	0.728534	0.000029	35.6411	0.0128	17.4838	0.0058
BD044	0.4104	0.9727	0.2551	0.512815	0.000009	0.06272	0.588738	0.0151	0.283396	0.000008	0.710054	0.000007	19.1223	0.0018	15.9297	0.0020
BD065	1.8622	8.7869	0.1281	0.511399	0.000009	0.21849	2.569987	0.0120	0.281706	0.000009	0.716918	0.000005	17.9006	0.0016	15.8272	0.0018
EB002	1.6083	7.2383	0.1343	0.511618	0.000010	0.24155	0.962565	0.0356	0.282670	0.000007	0.704678	0.000004	16.6625	0.0015	15.3370	0.0019
EB003	0.7141	2.1783	0.1982	0.512481	0.000009	0.15760	0.604891	0.0369	0.283127	0.000011	0.707692	0.000005	15.6634	0.0021	15.2529	0.0022
EB005	0.3768	1.5206	0.1498	0.511842	0.000009	0.07433	0.445016	0.0237	0.282415	0.000006	0.707081	0.000004	16.0123	0.0014	15.2664	0.0017
EB006	0.5462	2.1239	0.1554	0.511863	0.000009	0.12273	0.90894	0.0191	0.282172	0.000007	0.709568	0.000028	21.3550	0.0029	16.1902	0.0020
AG003	0.8942	3.5909	0.1505	0.511857	0.000009	0.13450	0.992307	0.0192	0.282212	0.000009	0.704965	0.000004	16.4079	0.0016	15.4043	0.0019
AG004	0.4725	1.8110	0.1577	0.511913	0.000010	0.11808	0.730749	0.0229	0.282448	0.000006	0.706368	0.000005	16.5215	0.0016	15.4524	0.0020
AG006	1.0675	4.0551	0.1591	0.511990	0.000007	0.21879	0.976316	0.0318	0.282791	0.000006	0.706171	0.000005	17.2635	0.0017	15.6495	0.0019
AG007	0.2856	0.7591	0.2274	0.512637	0.000008	0.08631	0.353912	0.0346	0.282922	0.000006	0.710113	0.000004	17.5924	0.0015	15.8578	0.0018
RV006	0.9246	3.7892	0.1475	0.511810	0.000009	0.14552	0.673958	0.0306	0.282732	0.000008	0.707949	0.000005	14.6991	0.0013	15.0410	0.0017
RV009	0.9185	3.4254	0.1621	0.512039	0.000008	0.16832	0.553768	0.0431	0.283386	0.000010	0.706268	0.000004	15.9882	0.0015	15.2959	0.0018
RV014	0.4960	2.4264	0.1235	0.511400	0.000008	0.11288	0.846103	0.0189	0.282171	0.000007	0.707090	0.000005	17.2368	0.0015	15.4873	0.0017
RV021	to be run	2.8975		0.511875	0.000007	0.09196	0.342398	0.0381	0.283136	0.000009	0.705460	0.000004	15.5461	0.0014	15.2371	0.0018
BCR-2	to be run	14.5434		0.512637	0.000008	0.49073	4.918704	0.0141	0.282864	0.000006	0.705093	0.000014	18.7246	0.0016	15.6302	0.0017

Pb84 corr	± 2SE Prop	Pb76 corr	± 2SE Prop	Pb86 corr	± 2SE Prop
36.4108	0.0052	0.86407	0.00004	1.99200	0.00018
36.2839	0.0050	0.89462	0.00001	2.06095	0.00014
37.2886	0.0053	0.83312	0.00003	1.95977	0.00014
60.2441	0.0231	0.49061	0.00002	1.69033	0.00013
37.7226	0.0056	0.83303	0.00002	1.97269	0.00013
36.3033	0.0048	0.88419	0.00002	2.02812	0.00013
35.2925	0.0053	0.92047	0.00002	2.11815	0.00015
35.3825	0.0060	0.97383	0.00005	2.25905	0.00018
35.3287	0.0048	0.95344	0.00002	2.20642	0.00016
40.7609	0.0062	0.75815	0.00005	1.90874	0.00015
35.4853	0.0053	0.93885	0.00003	2.16271	0.00016
36.4834	0.0057	0.93532	0.00003	2.20831	0.00017
35.5765	0.0050	0.90651	0.00002	2.06075	0.00014
35.0070	0.0047	0.90140	0.00002	1.98990	0.00013
34.5103	0.0047	1.02325	0.00002	2.34779	0.00015
34.7270	0.0049	0.95676	0.00002	2.17212	0.00014
35.0792	0.0047	0.89852	0.00002	2.03518	0.00013
34.7317	0.0050	0.98013	0.00002	2.23411	0.00016
38.6999	0.0050	0.83471	0.00002	2.06678	0.00013

Appendix E - Geochemical and location data for the Du Chef and Mistassini Dyke Swarms

Sample	**Easting**	**Northing**	**SiO2**	**TiO2**	**Al2O3**	**Fe2O3**	**MnO**	**MgO**
Number	UTM Zone	UTM Zone	wt%	wt%	wt%	wt%	wt%	wt%
DC001	550620	5497068	45.57	2.38	14.40	15.94	0.22	5.73
DC002	550653	5497125	47.40	1.62	14.35	14.88	0.20	6.04
DC003	560353	5479443	45.04	2.47	13.50	18.56	0.23	5.37
DC004	565583	5471571	47.88	1.54	14.70	14.38	0.19	6.39
DC005	573015	5467189	52.01	1.02	14.41	12.20	0.17	5.95
DC006	573462	5466863	47.13	1.66	15.65	14.16	0.17	7.23
DC007	548834	5463730	47.82	1.61	13.28	16.21	0.22	6.29
DC008	552965	5458295	47.43	1.33	15.69	12.03	0.15	7.87
DC009	552965	5458295	49.15	1.68	13.89	16.03	0.25	4.47
DC010	552965	5458295	45.90	1.30	15.52	12.32	0.18	8.04
DC011	585722	5459991	47.60	1.17	15.33	11.92	0.15	9.02
DC012	585759	5459971	52.93	1.00	12.95	13.03	0.14	6.35
DC013	584705	5460291	48.13	1.17	13.79	14.66	0.19	6.40
DC014	584680	5460299	46.15	1.58	14.56	16.56	0.20	6.76
DC015	581748	5468324	45.70	2.60	13.97	17.70	0.22	5.76
DC016	578738	5481228	45.32	2.69	12.34	19.68	0.23	7.13
DC017	578768	5481245	45.69	2.20	14.12	17.61	0.21	5.87
DC018	582583	5482545	48.03	1.11	15.25	14.00	0.18	8.88
DC019	582578	5482500	47.82	1.20	15.47	14.74	0.19	7.42
DC020	582595	5483019	48.06	1.46	15.69	13.01	0.16	6.82
DC021	582773	5487183	75.07	0.21	12.75	1.51	0.01	0.39
DC022	583726	5460595	53.02	1.17	14.64	15.14	0.21	5.14

Sample	**Longitude**	**Latitude**	**SiO2**	**TiO2**	**Al2O3**	**Fe2O3**	**MnO**	**MgO**
Number	(degrees E)	(degrees N)	wt%	wt%	wt%	wt%	wt%	wt%
98-JG-2101C	-76.641	53.625	52.8	2.68	13.0	13.6	0.20	3.07
99-JG-1190	-76.757	53.764	53.0	2.71	13.0	13.5	0.19	3.03
00-JG-1652	-75.346	53.722	53.6	2.39	12.5	12.1	0.14	3.02
00-JG-1655	-75.482	53.411	49.6	3.21	12.6	15.7	0.23	3.64
FA65-048-07	-73.908	51.651	52.9	2.55	13.4	12.5	0.23	3.20
FA65-048-08	-73.908	51.651	54.0	2.34	14.2	12.7	0.17	3.11
FA65-049-03	-73.978	51.703	54.7	2.46	13.8	13.1	0.22	3.21
FA65-055-06	-73.567	51.717	50.6	2.96	13.5	14.8	0.19	3.54
FA65-056-07	-73.554	51.548	53.2	2.49	13.4	13.6	0.20	2.72
FA65-056-08	-73.554	51.548	54.3	2.10	15.0	11.6	0.16	2.38
FA76-001-02	-73.85	51.83	53.5	2.19	14.9	11.7	0.16	2.43
FA76-004-08	-73.676	51.041	50.0	0.60	11.6	9.0	0.14	13.12
FA76-005-05	-73.773	51.073	49.0	0.60	12.0	9.8	0.15	12.75
FA76-007-01	-73.936	51.239	43.2	0.10	2.7	10.7	0.17	31.38
FA76-008-03	-73.922	51.242	48.0	2.76	14.6	13.4	0.20	4.46
FA76-009-06	-73.642	51.302	46.4	0.82	10.1	12.0	0.17	16.21
FA76-010-08	-73.374	51.403	52.8	2.45	13.1	13.8	0.21	2.73
FA76-011-01	-73.367	51.385	48.7	0.88	12.0	11.7	0.17	12.43
FA76-012-02	-73.362	51.388	50.8	0.63	15.2	9.5	0.15	6.67
FA76-013-03	-73.466	51.468	56.0	1.62	16.7	9.8	0.14	1.82
FA76-014-02	-73.862	51.607	53.2	2.43	13.8	12.6	0.19	2.66
FA76-015-05	-73.916	51.655	54.4	2.10	15.0	12.5	0.17	2.80

CaO	**Na2O**	**K2O**	**P2O5**	LOI	Total	**Sc**	**V**	**Cr**
wt%	wt%	wt%	wt%	wt%	wt%	ppm	ppm	ppm
9.92	2.38	1.21	0.31	1.58	99.64	37.3	325.6	97.9
9.63	2.14	1.10	0.30	1.48	99.12	39.2	262.1	106.9
8.55	2.75	1.20	0.27	1.27	99.21	40.9	398.1	42.6
9.45	2.55	0.85	0.19	0.89	99.01	39.5	225.9	118.3
9.81	2.46	0.91	0.07	0.82	99.84	41.0	241.4	153.1
9.85	3.25	0.58	0.22	1.21	101.13	29.7	203.8	89.5
8.99	2.78	0.95	0.38	0.57	99.09	35.2	161.2	117.4
10.34	2.53	0.70	0.15	1.66	99.88	26.1	177.0	186.6
9.42	2.36	1.10	0.14	1.88	100.38	41.4	283.0	59.0
10.50	2.42	1.26	0.15	2.21	99.80	25.5	180.1	179.3
11.66	2.26	0.35	0.14	1.36	100.95	27.5	177.7	228.1
9.67	1.61	0.47	0.07	1.05	99.27	37.1	244.9	204.5
10.38	2.45	0.64	0.17	0.71	98.69	46.0	202.7	134.3
9.40	2.37	0.67	0.21	0.93	99.40	35.9	232.5	76.0
9.27	2.19	0.92	0.42	1.54	100.29	35.8	256.4	168.9
9.99	2.18	0.56	0.21	0.42	100.74	49.2	391.5	205.5
9.24	2.23	0.63	0.28	1.93	100.03	32.5	221.2	70.5
10.05	2.17	0.36	0.10	0.25	100.38	35.0	203.6	202.6
10.10	2.20	0.34	0.12	0.47	100.05	36.9	226.0	108.7
9.65	2.64	0.55	0.18	0.55	98.76	27.0	219.2	95.2
2.93	5.74	0.05	0.07	0.21	98.93	3.1	19.6	7.7
8.81	0.64	0.14	0.08	0.45	99.45	43.8	324.1	50.2

CaO	**Na2O**	**K2O**	**P2O5**	LOI	Total	**Sc**	**V**	**Cr**
wt%	wt%	wt%	wt%	wt%	wt%	ppm	ppm	ppm
5.62	3.50	2.86	0.82	0.3	98.70	23.0	190	25
5.86	3.60	2.69	0.82	0.1	98.40	23.0	187	26
6.02	3.20	4.13	0.71	0.5	98.50	21.0	173	25
5.45	3.50	2.12	0.87	2.0	99.00	26.0	245	42
5.35	3.80	2.68	0.87	1.1	99.40	25.0	188	24
5.44	4.00	2.37	0.72	1.1	100.90	23.0	189	28
4.65	3.74	2.36	0.67	1.2	100.70	23.0	193	27
6.58	3.10	2.48	0.85	0.5	99.50	26.0	255	45
6.03	3.60	2.67	0.97	0.2	99.70	23.0	124	26
5.82	4.20	2.58	0.80	0.5	100.00	19.0	104	28
5.75	3.90	2.76	0.78	0.7	99.20	19.0	119	27
9.12	1.70	1.48	0.09	2.4	100.10	31.0	162	1570
9.25	1.50	1.26	0.07	2.2	99.30	32.0	171	1440
2.62	0.10	0.04	0.01	7.7	100.50	23.0	86	3280
7.89	3.10	1.87	0.67	2.3	100.10	26.0	194	43
6.92	1.50	0.64	0.08	3.8	99.70	25.0	168	1030
6.06	3.80	2.56	1.00	0.3	99.50	23.0	119	16
8.83	2.00	1.12	0.09	2.2	101.20	29.0	198	889
10.02	2.20	1.40	0.06	2.2	99.50	38.0	220	175
5.15	4.40	3.12	0.54	0.9	100.80	15.0	79	14
5.10	3.90	2.71	0.68	0.6	98.50	22.0	188	20
6.09	4.10	2.42	0.64	0.2	100.80	21.0	164	16

Co	**Ni**	**Cu**	**Zn**	**Sr**	**Y**	**Zr**	**Ba**	49Ti
ppm	ppm	ppm	ppm	ppm	ppm	ppm	ppm	%
52.4	72.3	92.0	131.4	260.5	31.8	156.1	367.5	2.33
49.9	81.4	80.9	139.4	217.9	27.2	135.9	397.0	1.64
56.5	109.7	106.6	253.9	242.9	31.9	131.5	304.2	2.51
50.4	137.3	88.8	211.0	298.6	26.4	67.7	140.7	1.49
41.3	121.5	94.5	227.3	173.0	22.2	54.6	150.0	0.97
57.1	121.9	77.3	137.4	325.8	23.9	89.0	215.6	1.56
52.2	78.1	78.4	172.9	258.4	40.1	161.7	400.5	1.60
50.0	171.8	74.0	183.1	306.1	20.0	82.1	91.4	1.29
44.5	56.2	99.1	159.5	144.7	40.5	109.9	88.9	1.73
46.0	185.5	57.6	238.1	233.6	20.5	88.4	60.5	1.28
47.0	186.5	55.9	119.6	293.0	17.2	67.3	139.0	1.12
44.0	391.0	72.2	109.9	116.4	22.1	61.6	96.0	1.01
53.0	52.3	75.7	121.1	246.7	24.1	69.0	257.6	1.17
61.5	92.6	85.2	141.0	257.3	26.2	64.7	204.6	1.58
52.6	411.9	88.1	166.8	236.6	43.4	148.9	280.7	2.50
61.3	133.1	109.5	195.5	234.4	29.1	87.9	256.7	2.55
54.7	81.3	88.4	169.2	260.1	33.1	115.4	293.7	2.16
59.8	430.4	82.4	127.4	225.5	18.7	50.7	152.7	1.08
54.3	116.0	99.4	235.4	228.7	20.1	49.7	8860.1	1.20
49.6	123.3	78.1	118.2	321.6	21.5	92.6	211.2	1.43
4.4	15.4	7.6	39.5	619.7	2.4	100.9	9.5	0.22
47.3	703.8	97.6	82.1	19.4	25.4	99.9	12.6	1.25

Co	**Ni**	**Cu**	**Zn**	**Sr**	**Y**	**Zr**	**Ba**	49Ti
ppm	ppm	ppm	ppm	ppm	ppm	ppm	ppm	%
44	15	18	132	366	22.00	122	1600	2.68
42	14	18	132	366	23.00	121	1500	2.71
35	14	10	115	279	22.00	123	1700	2.39
49	25	22	146	241	35.00	211	830	3.21
44	12	20	137	310	23.00	117	1900	2.55
42	17	23	129	394	23.00	124	1500	2.34
42	18	24	131	372	23.00	132	1630	2.46
53	27	24	174	381	34.00	203	1200	2.96
39	15	23	147	336	26.00	124	1300	2.49
34	15	23	130	409	22.00	111	1300	2.10
35	15	20	129	398	22.00	116	1400	2.19
56	471	79	58	175	16.00	85	290	0.60
60	467	73	69	246	13.00	64	220	0.60
98	895	-10	54	-10	2.60	7.2	20	0.10
49	42	44	110	426	23.00	103	1000	2.76
77	762	93	89	160	14.00	78	180	0.82
38	13	27	144	328	27.00	114	1300	2.45
60	476	93	84	175	17.00	82	250	0.88
41	85	95	76	170	16.00	48	260	0.63
20	-10	17	74	437	18.00	107	1500	1.62
42	16	24	120	332	24.00	113	1600	2.43
39	14	20	124	467	20.00	107	1300	2.10

51V ppm	52Cr ppm	55Mn %	59Co ppm	60Ni ppm	65Cu ppm	66Zn ppm	71Ga ppm	85Rb ppm
343.2	113.1	0.23	49.0	68.6	96.6	138.1	20.5	30.1
265.6	122.2	0.21	50.9	74.6	77.4	139.2	18.3	25.9
389.6	48.1	0.24	57.9	104.4	107.6	273.3	21.9	20.0
240.4	127.8	0.19	53.8	127.3	85.2	208.1	18.0	7.1
246.4	198.3	0.17	41.1	110.3	97.4	217.9	15.8	19.7
210.0	89.5	0.16	53.9	121.2	76.2	120.6	18.1	9.5
162.1	122.4	0.21	53.0	77.4	71.1	163.2	18.9	15.9
210.0	200.7	0.15	49.1	167.9	73.1	174.8	17.7	5.5
293.7	63.0	0.25	46.3	64.0	94.9	160.8	19.4	11.5
200.6	200.6	0.17	45.5	194.5	55.4	233.9	16.5	18.5
191.5	232.6	0.14	49.8	188.9	66.0	110.9	16.2	9.9
240.2	220.3	0.14	44.4	413.2	74.4	103.0	14.5	11.7
228.0	152.9	0.19	52.3	58.9	80.8	120.3	17.5	8.3
245.0	82.1	0.19	57.8	91.6	84.7	130.1	18.0	5.7
263.4	179.4	0.21	50.2	393.8	98.4	178.0	20.2	14.5
362.7	209.5	0.22	59.1	126.1	99.4	187.2	19.3	7.9
235.3	76.0	0.21	55.1	77.0	84.0	164.0	20.7	9.7
206.1	218.6	0.17	60.9	415.1	73.1	112.7	15.6	5.6
236.4	122.3	0.19	59.0	116.3	94.0	230.7	17.2	4.8
212.8	105.2	0.16	49.8	120.9	74.9	109.2	18.6	10.0
21.8	7.0	0.01	5.5	9.0	6.2	37.2	14.9	0.5
313.5	52.0	0.22	45.2	747.9	99.4	78.3	14.9	2.7

51V ppm	52Cr ppm	55Mn %	59Co ppm	60Ni ppm	65Cu ppm	66Zn ppm	71Ga ppm	85Rb ppm
190	25	0.20	44	15	18	132	20.0	43.0
187	26	0.19	42	14	18	132	20.0	42.0
173	25	0.14	35	14	10	115	17.0	140.0
245	42	0.23	49	25	22	146	22.0	43.0
188	24	0.23	44	12	20	137	20.0	66.0
189	28	0.17	42	17	23	129	20.0	39.0
193	27	0.22	42	18	24	131	21.0	39.0
255	45	0.19	53	27	24	174	22.0	65.0
124	26	0.20	39	15	23	147	20.0	44.0
104	28	0.16	34	15	23	130	20.0	43.0
119	27	0.16	35	15	20	129	20.0	52.0
162	1570	0.14	56	471	79	58	13.0	48.0
171	1440	0.15	60	467	73	69	13.0	54.0
86	3280	0.17	98	895	-10	54	2.6	3.0
194	43	0.20	49	42	44	110	21.0	28.0
168	1030	0.17	77	762	93	89	14.0	45.0
119	16	0.21	38	13	27	144	20.0	17.0
198	889	0.17	60	476	93	84	15.0	56.0
220	175	0.15	41	85	95	76	15.0	33.0
79	14	0.14	20	-10	17	74	20.0	21.0
188	20	0.19	42	16	24	120	21.0	32.0
164	16	0.17	39	14	20	124	20.0	42.0

88Sr ppm	89Y ppm	90Zr ppm	93Nb ppm	133Cs ppm	137Ba ppm	139La ppm	140Ce ppm	141Pr ppm
249.7	31.7	163.6	9.47	3.46	365.9	17.12	38.44	5.15
204.5	27.3	138.5	5.33	1.48	381.2	12.29	27.68	3.82
222.6	31.8	129.8	9.48	2.85	306.5	14.11	30.87	4.31
276.9	24.1	68.7	4.55	0.05	142.8	8.24	17.48	2.56
170.8	20.1	53.3	3.40	0.47	144.7	5.81	10.59	1.59
306.6	21.8	88.3	7.15	0.18	222.5	10.51	23.69	3.32
249.4	39.0	155.4	11.54	0.19	413.4	19.61	43.00	5.86
304.4	18.7	81.7	5.89	0.02	87.5	10.31	19.72	2.74
143.3	40.4	113.1	5.11	0.01	84.7	8.74	17.46	2.63
234.6	20.5	82.4	5.70	1.30	52.9	7.90	18.22	2.52
287.5	16.2	66.1	4.73	0.02	127.9	7.56	15.80	2.23
119.6	22.3	56.3	1.92	0.06	90.1	2.89	6.74	1.12
247.0	23.7	69.1	3.59	0.05	255.2	7.82	17.48	2.47
254.1	25.1	64.7	3.49	-0.04	196.2	9.42	18.75	2.71
230.1	41.3	153.9	12.93	0.09	264.1	20.10	38.29	5.23
224.8	27.4	86.3	6.43	0.10	235.5	9.16	21.22	3.04
258.5	32.3	115.7	8.90	0.08	286.0	12.89	29.56	4.12
225.5	17.7	55.1	3.34	-0.01	139.5	5.67	12.22	1.71
235.2	20.3	49.9	3.29	0.18	9065.2	6.30	12.88	1.84
325.6	21.5	86.7	6.45	0.16	204.4	11.14	22.23	3.02
628.4	2.3	96.5	1.74	-0.02	4.5	7.98	14.49	1.62
19.4	27.1	91.4	2.77	0.10	5.6	3.84	9.79	1.49

88Sr ppm	89Y ppm	90Zr ppm	93Nb ppm	133Cs ppm	137Ba ppm	139La ppm	140Ce ppm	141Pr ppm
-0.2	22.00	122	13	25	1600	31.0	70.0	8.90
0.4	23.00	121	13	26	1500	31.0	69.0	8.90
-0.2	22.00	123	12	25	1700	31.0	70.0	8.90
0.4	35.00	211	15	42	830	38.0	84.0	11.00
-0.2	23.00	117	13	24	1900	33.0	68.0	9.10
-0.2	23.00	124	13	28	1500	32.0	66.0	8.70
-0.2	23.00	132	14	27	1630	32.0	68.0	8.70
-0.2	34.00	203	14	45	1200	38.0	80.0	11.00
-0.2	26.00	124	17	26	1300	38.0	80.0	11.00
-0.2	22.00	111	15	28	1300	32.0	68.0	9.00
-0.2	22.00	116	16	27	1400	32.0	67.0	8.90
-0.2	16.00	85	9.4	1570	290	17.0	36.0	4.20
-0.2	13.00	64	7.1	1440	220	13.0	28.0	3.30
0.4	2.60	7.2	0.23	3280	20	0.4	1.0	0.13
-0.2	23.00	103	19	43	1000	25.0	55.0	7.30
0.4	14.00	78	12	1030	180	16.0	34.0	4.10
-0.2	27.00	114	17	16	1300	38.0	83.0	11.00
13	17.00	82	12	889	250	15.0	33.0	4.00
0.3	16.00	48	2.6	175	260	6.0	14.0	1.70
-0.2	18.00	107	15	14	1500	25.0	55.0	7.20
0.2	24.00	113	15	20	1600	30.0	67.0	8.80
-0.2	20.00	107	12	16	1300	27.0	60.0	7.60

146Nd ppm	147Sm ppm	153Eu ppm	157Gd ppm	159Tb ppm	163Dy ppm	165Ho ppm	166Er ppm	169Tm ppm
22.39	5.23	1.76	5.29	0.86	5.19	0.99	2.72	0.43
17.01	4.07	1.60	4.20	0.70	4.41	0.85	2.39	0.38
19.10	4.79	1.76	4.92	0.83	5.14	0.98	2.73	0.43
11.59	3.06	1.23	3.29	0.59	3.88	0.77	2.16	0.35
7.41	2.32	0.86	2.57	0.48	3.19	0.63	1.78	0.30
14.64	3.59	1.32	3.69	0.60	3.68	0.69	1.93	0.30
25.68	6.25	2.07	6.30	1.05	6.36	1.22	3.34	0.54
11.99	3.11	1.11	3.16	0.53	3.21	0.60	1.64	0.26
13.08	4.12	1.29	4.61	0.90	6.02	1.21	3.58	0.59
11.55	3.05	1.06	3.11	0.55	3.43	0.63	1.74	0.27
10.15	2.67	0.94	2.66	0.46	2.74	0.52	1.45	0.22
5.96	2.12	0.74	2.39	0.48	3.37	0.68	2.02	0.34
11.55	3.18	1.22	3.28	0.58	3.76	0.74	2.12	0.34
12.59	3.37	1.31	3.45	0.62	3.94	0.77	2.21	0.35
23.28	5.83	1.91	6.01	1.05	6.59	1.29	3.67	0.59
14.17	3.76	1.49	3.98	0.70	4.44	0.86	2.46	0.38
18.32	4.66	1.72	4.73	0.82	5.16	0.99	2.86	0.45
7.93	2.22	0.89	2.36	0.43	2.89	0.57	1.65	0.27
8.70	2.53	2.90	2.64	0.48	3.07	0.61	1.78	0.29
13.57	3.49	1.24	3.46	0.59	3.60	0.67	1.84	0.29
5.96	1.10	0.37	0.79	0.08	0.44	0.08	0.23	0.03
7.63	2.60	0.92	2.95	0.59	3.98	0.81	2.38	0.40

146Nd ppm	147Sm ppm	153Eu ppm	157Gd ppm	159Tb ppm	163Dy ppm	165Ho ppm	166Er ppm	169Tm ppm
37.0	7.50	3.10	6.30	0.83	4.40	0.82	1.90	0.29
37.0	7.10	3.10	6.10	0.80	4.20	0.79	1.90	0.28
36.0	7.10	2.90	5.90	0.79	4.00	0.76	1.90	0.29
45.0	9.40	3.20	8.20	1.20	6.20	1.20	3.20	0.48
38.0	7.70	3.30	6.50	0.86	4.40	0.85	2.10	0.29
36.0	7.00	2.90	6.00	0.82	4.30	0.84	2.10	0.30
36.0	6.90	2.90	6.10	0.81	4.30	0.84	2.10	0.29
44.0	8.80	3.00	8.10	1.10	6.10	1.20	3.30	0.46
44.0	8.80	3.20	7.30	0.98	5.10	0.95	2.40	0.33
37.0	7.20	2.80	6.20	0.79	4.20	0.81	2.10	0.28
36.0	7.00	2.80	6.00	0.80	4.10	0.79	2.00	0.28
16.0	3.20	0.83	2.90	0.47	2.80	0.57	1.40	0.24
12.0	2.50	0.75	2.40	0.39	2.30	0.48	1.20	0.20
0.5	0.16	0.06	0.26	0.05	0.38	0.09	0.26	0.05
31.0	6.20	2.60	5.60	0.80	4.30	0.82	1.90	0.30
15.0	3.10	0.96	2.90	0.45	2.60	0.51	1.20	0.20
46.0	9.20	3.30	7.50	1.00	5.30	0.99	2.30	0.35
16.0	3.20	1.00	3.10	0.52	3.00	0.62	1.50	0.25
7.3	1.90	0.67	2.40	0.43	2.60	0.57	1.50	0.24
29.0	5.70	2.60	4.50	0.65	3.40	0.66	1.50	0.25
37.0	7.10	3.10	5.70	0.83	4.40	0.86	1.90	0.31
33.0	6.20	2.70	5.10	0.73	3.70	0.73	1.70	0.26

172Yb ppm	175Lu ppm	178Hf ppm	181Ta ppm	208Pb ppm	232Th ppm	238U ppm
2.91	0.44	3.72	0.68	4.11	1.16	0.29
2.59	0.41	3.14	0.36	4.57	0.72	0.20
2.94	0.45	3.18	0.62	10.32	0.60	0.22
2.37	0.37	1.85	0.32	4.12	0.33	0.18
2.02	0.30	1.54	0.23	4.07	0.38	0.18
1.98	0.30	2.27	0.48	5.44	0.59	0.15
3.57	0.54	3.77	0.81	4.82	0.83	0.24
1.67	0.25	2.17	0.41	5.58	0.58	0.16
3.94	0.60	3.07	0.36	1.73	0.57	0.21
1.74	0.25	2.11	0.40	7.76	0.51	0.16
1.43	0.21	1.74	0.33	2.20	0.41	0.12
2.26	0.34	1.51	0.14	0.31	0.11	0.03
2.22	0.33	1.93	0.24	2.22	0.30	0.08
2.33	0.35	1.78	0.23	3.06	0.23	0.07
3.87	0.59	3.94	0.88	4.31	1.19	0.31
2.55	0.38	2.35	0.44	2.60	0.43	0.10
2.96	0.44	3.08	0.60	2.20	0.73	0.18
1.76	0.27	1.47	0.22	0.64	0.27	0.07
1.96	0.30	1.41	0.23	31.91	0.22	0.12
1.91	0.29	2.27	0.46	1.52	0.61	0.17
0.21	0.03	2.27	0.11	0.82	2.54	0.08
2.73	0.42	2.29	0.18	0.11	0.33	0.08

172Yb ppm	175Lu ppm	178Hf ppm	181Ta ppm	208Pb ppm	232Th ppm	238U ppm
1.90	0.31	3.0	0.7	10	2.30	0.38
1.90	0.29	3.0	0.7	6	2.30	0.38
1.80	0.29	3.1	0.6	14	2.40	1.30
3.20	0.50	5.1	0.8	8	2.40	0.50
1.90	0.31	3.2	0.7	6	2.50	0.46
2.00	0.32	3.2	0.8	6	2.40	0.39
1.90	0.31	3.3	0.8	8	2.40	0.42
3.10	0.49	5.2	0.7	9	2.40	0.52
2.20	0.35	3.4	1.0	7	2.70	0.51
1.90	0.30	3.0	0.9	7	2.30	0.42
1.80	0.30	3.0	0.9	7	2.30	0.46
1.60	0.23	2.3	0.6	2	4.20	0.72
1.30	0.20	1.7	0.5	2	3.20	0.53
0.34	0.06	0.2	-0.1	-1	0.09	0.03
1.90	0.29	2.7	1.1	3	1.80	0.43
1.30	0.18	2.2	0.7	2	3.40	0.56
2.20	0.35	3.2	1.0	5	2.40	0.47
1.60	0.23	2.3	0.7	4	2.80	0.73
1.60	0.25	1.4	0.2	3	1.60	0.50
1.60	0.24	2.7	0.9	5	2.20	0.80
1.90	0.30	3.1	0.8	8	2.10	0.35
1.80	0.28	2.9	0.7	5	2.00	0.37

APPENDIX F – GEOLOGICAL OVERIEW OF THE MISTASSINI AND DU CHEF DYKE SWARMS

F1. Mistassini dyke swarm

F.1.1. Geology

The Mistassini dykes are found to the north of Mistassini Lake in central Quebec, approximately 250 km east of James Bay and cover an area of ~100,000 km^2. The dykes vary from small discontinuous lenses approximately 1 m thick to sheets ~100 m thick which can be traced for ~150 km on aeromagnetic maps (Fahrig et al. 1986). The dykes are close to vertical and have been described as a subparrallel swarm with a dominant northwest strike (Fahrig et al. 1986) or as a giant radiating swarm with a fan angle of ~35° (Ernst and Buchan 2001) which cuts across the east-northeast strike of the Archaean terranes in the region.

Based on their geochemistry, Fahrig et al. (1986) divided the Mistassini swarm into a tholeiitic suite and a komatiitic suite with most dykes falling in the tholeiitic field on a Jensen plot (Jensen 1976). The tholeiitic suite dykes are locally porphyritic with plagioclase phenocrysts up to ~6cm in length concentrated into bands within the dyke. The plagioclase phenocrysts are slightly zoned and are saussuritised. The groundmass is composed of plagioclase, clinopyroxene (commonly altered to uralite) and minor opaque phases, biotite and apatite. The komatiitic suite dykes are composed of plagioclase, clinopyroxene and olivine. Plagioclase and olivine are altered to saussurite and serpentine + talc + magnetite + amphibole respectively. Clinopyroxene is partly altered to uralite. Minor phases include apatite and opaques. The metamorphic assemblages of the Mistassini dykes suggest the dykes experienced, at most, greenschist facies metamorphism.

F.1.2. Age

Establishing an absolute age for the Mistassini dyke swarm has not been the sole aim any published work, and so ages quoted by others who mention the swarm are variable and not particularly robust. Prior to 1986, the dating of the Mistassini swarm is noted to have been ‘not entirely satisfactory’ with K-Ar ages for individual dykes ranging from 1220-1925Ma being reported (Fahrig et al. 1986). Since 1986, the ages reported for the Mistassini dykes have become progressively older. Guha et al.

(1991) reports that the Mistassini swarm is 1960 Ma, however, does not cite any study or data to support this. Hamilton et al. (2001) states that the Mistassini dykes were emplaced at ca. 2475 Ma, but like Guha et al. (1991), does do not present any data to support this. Buchan et al. (2007) and Bleeker et al. (2008) report the Mistassini dykes as having been emplaced between 2500-2510 Ma, the date being cited from a one-age abstract (Heaman 2004) which does not present any actual data or methodology. Maurice et al. (2009) and Maurice and Francis (2010) quote an age of 2515±3 Ma for the swarm, which is taken from an unpublished report by Mike Hamilton of the Jack Satterly Geochronology Laboratory. The most recent literature which mentions the Mistassini dykes state that the dykes were intruded at 2510 Ma (Ernst and Bleeker 2010; Söderlund et al. 2010). The Irsuaq and Ptarmigan dykes which have been argued to be distal parts of the Mistassini swarm by Ernst and Bleeker (2010) have been dated as 2508±6 Ma and 2505±2 Ma respectively (Buchan et al. 1998; Maurice et al. 2009).

F.1.3. Tectonic Setting

Fahrig et al. (1986), first suggested that the Mistassini dyke swarm is a linear swarm, the geometry of which suggests that the dykes are the product of failed arm tensional tectonics formed during the early stages of ocean-spreading. The Mistassini dyke swarms were later reinterpreted as a giant radiating swarm with a fan angle of ~35° which defines a focus within the Grenville Front just to the north of the Gulf of Saint Lawrence (Ernst and Buchan 2001; Ernst et al. 2001; Ernst and Buchan 2002; Ernst and Bleeker 2010; Nilsson et al. 2010). Similar to the conclusions reached for the more obviously radiating Matachewan dyke swarm, workers argue that the intrusion of a dyke swarm with radiating geometry like that exhibited by the Mistassini swarm can only be adequately explained by intrusion of magma into crust which is subject to a radial stress regime related to crustal doming directly above a buoyant mantle plume head (Ernst and Buchan 2001; Phinney and Halls 2001; Ernst and Bleeker 2010).

F.1.4. Ni-Cu-PGE Mineralisation

Ni-Cu-PGE sulphide mineralisation has not been observed in the Mistassini dyke swarm and the swarm is not the subject the of any past or present exploration projects. No layered intrusions coeval with the Mistassini dyke swarm have been categorically identified on the Superior craton. However, grass-roots exploration carried out in 2002 by Bitterroot Resources in the area intruded by the Mistassini dykes, established the potential for unexposed Ni-Cu-PGE bearing mafic layered intrusions in the subsurface (Greig and Billard 2003). Further work, including airborne geophysics and diamond drilling were recommended but not carried out.

F.2. Du Chef Dyke Swarm

F.2.1. Geology

The geology of the Du Chef dykes is poorly described and understudied. Ciesielski (1991) supplies a map of the area to the southeast of Val d'Or, Quebec which delineates dozens of northeast-trending diabase dykes that crop out over an area of ~10,000 km^2 within the Grenville Front. Ernst and Buchan (2002), suggest that these dykes constitute a northeast-trending linear swarm, which they call the Du Chef dykes.

F.2.2. Age

Those who study the Du Chef dykes as part of Large Igneous Province reconstructions quote the age of the dykes as 2408±3 Ma (Ernst and Buchan 2002; Söderlund et al. 2010). This age is reported by Krogh et al. (1994) who carried out U-Pb analysis on two samples of magmatic zircons obtained from a 'primary magmatic pegmatic patch in a coronitic metadiabase' dyke which cuts the general structural trends in the area. Interestingly, Krogh et al. (1994) never mentions the Du Chef dykes by name. The naming of the dykes appears to have come much later than the U-Pb dating work (Ernst and Buchan 2002).

A sample from a Du Chef dyke was collected in 2010 by Jake Ciborowski and Richard Ernst from a ~20 m thick, northeast-trending, coarse grained diabase dyke exposed ~50 km south of Chibougamau, Quebec (Sample DC016). This sample is currently being dated by Ulf Söderlund at Lund University.

F.2.3. Tectonic Setting

Söderlund et al. (2010) suggested, based on coeval intrusion ages, that the Du 2408±3 Ma Du Chef dykes are cogenetic with the 2408±2 Ma Sebanga dyke swarm (Zimbabwe Craton) and 2403±3 Ma Ringvassøy dykes (Kola Peninsula). Söderlund et al. (2010) suggests that reconstruction of these dykes into a now-dissected giant radiating swarm indicted that the Du Chef dykes formed in response to a mantle plume beneath a supercontinent composed of the Superior, Kola and Zimbabwe cratons at ~2.41 Ma.

F.2.4. Ni-Cu-PGE mineralisation

Ni-Cu-PGE sulphide mineralisation has not been reported in the Du Chef dyke swarm and the dykes are not the subject the of any past or present exploration projects. No layered intrusions coeval with the Du Chef swarm have been identified on the Superior craton.

F.3. References

Bleeker, W., Hamilton, M. A., Ernst, R. E. and Kulikov, V. S. 2008. The search for Archean-Paleoproterozoic supercratons: New constraints on Superior-Karelia-Kola correlations within supercraton Superia, including the first ca. 2504 Ma (Mistassini) ages from Karelia. In *International Geological Congress*. Oslo.

Buchan, K. L., Goutier, J., Hamilton, M. A., Ernst, R. E. and Matthews, W. A. 2007. Paleomagnetism, U-Pb geochronology, and geochemistry of Lac Esprit and other dyke swarms, James Bay area, Quebec, and implications for Paleoproterozoic deformation of the Superior Province. *Canadian Journal of Earth Sciences,* 44**,** 643-664.

Buchan, K. L., Mortensen, J. K., Card, K. D. and Percival, J. A. 1998. Paleomagnetism and U-Pb geochronology of diabase dyke swarms of Minto block, Superior Province, Quebec, Canada. *Canadian Journal of Earth Sciences,* 35**,** 1054-1069.

Ciesielski, A. 1991. Litho-tectonic map of the Grenville Front, southeast of Val d'Or, Quebec. In *Open File*. Geological Survey of Canada.

Ernst, R. E. and Bleeker, W. 2010. Large igneous provinces (LIPs), giant dyke swarms, and mantle plumes: significance for breakup events within Canada and adjacent regions from 2.5 Ga to the Present. *Canadian Journal of Earth Sciences,* 47**,** 695-739.

Ernst, R. E. and Buchan, K. L. 2001. The use of mafic dike swarms in identifying and locating mantle plumes. *Geological Society of America Special Papers,* 352**,** 247-265.

Ernst, R. E. and Buchan, K. L. 2002. Maximum size and distribution in time and space of mantle plumes: evidence from large igneous provinces. *Journal of Geodynamics*, 34 309-342.

Ernst, R. E., Grosfils, E. B. and Mège, D. 2001. Giant Dyke Swarms: Earth, Venus, and Mars. *Annual review of Earth and planetary sciences,* 29**,** 489-534.

Fahrig, W. F., Christie, K. W., Chown, E. H., Janes, D. and Machado, N. 1986. The tectonic significance of some basic dyke swarms in the Canadian Superior Province with special reference to the geochemistry and paleomagnetism of the Mistassini swarm, Quebec, Canada. *Canadian Journal of Earth Sciences,* 23**,** 238-253.

Greig, C. J. and Billard, D. 2003. Geological report on the Mistassini project, Northern Quebec. Bitterroot Resources.

Guha, J., Chown, E. H. and Daigneault, R. 1991. Litho-tectonicframewrk and associated mineralization of the eastern extremity of the Abitibi Greenstone Belt, Quebec (Fild Trip 3). In *Open File Report*. Geological Survey of Canada.

Hamilton, M. A., Goutier, J. and Matthews, W. 2001. U-Pb baddeleyite age for the Paleoproterozoic Lac Esprit dyke swarm, James Bay region, Quebec; Radiogenic Age and Isotopic Studies. In *Current Research*, 6. Geological Survey of Canada.

Heaman, L. M. 2004. 2.5-2.4 Ga global magmatism: Remnants or supercontinents or products of superplumes. . *Geological Society of America, Abstracts with Programs,* 36**,** 255.

Jensen, L. S. 1976. A new cation plot for classifying subalkaline volcanic rocks. *Ontario Division of Mines,* Misc. Pap. 66.

Krogh, T. E., Kamo, S. L. and Bohor, B. F. 1996. Shock metamorphosed zircons with correlated U-Pb discordance and melt rocks with concordant protolith ages indicate an impact origin for the Sudbury Structure. In *Earth Processes: Reading the Isotopic Code,* 343-352. American Geophysical Union.

Maurice, C., David, J., O'Neil, J. and Francis, D. 2009. Age and tectonic implications of Paleoproterozoic mafic dyke swarms for the origin of 2.2 Ga enriched lithosphere beneath the Ungava Peninsula, Canada. *Precambrian Research,* 174**,** 163-180.

Maurice, C. and Francis, D. 2010. Enriched crustal and mantle components and the role of the lithosphere in generating Paleoproterozoic dyke swarms of the Ungava Peninsula, Canada. *Lithos,* 114**,** 95-108.

Nilsson, M. K. M., Söderlund, U., Ernst, R. E., Hamilton, M. A., Scherstén, A. and Armitage, P. E. B. 2010. Precise U–Pb baddeleyite ages of mafic dykes and intrusions in southern West Greenland and implications for a possible reconstruction with the Superior craton. *Precambrian Research,* 183**,** 399-415.

Phinney, W. C. and Halls, H. C. 2001. Petrogenesis of the Early Proterozoic Matachewan dyke swarm, Canada, and implications for magma emplacement and subsequent deformation. *Canadian Journal of Earth Sciences,* 38**,** 1541-1563.

Söderlund, U., Hofmann, A., Klausen, M. B., Olsson, J. R., Ernst, R. E. and Persson, P.-O. 2010. Towards a complete magmatic barcode for the Zimbabwe craton: Baddeleyite U–Pb dating of regional dolerite dyke swarms and sill complexes. *Precambrian Research,* 183**,** 388-398.

Lithos xxx (2012) xxx–xxx

Contents lists available at SciVerse ScienceDirect

Lithos

journal homepage: www.elsevier.com/locate/lithos

The geochemistry and petrogenesis of the Blue Draw Metagabbro

T. Jake R. Ciborowski [a,*], Andrew C. Kerr [a], Iain McDonald [a], Richard E. Ernst [b], Matthew J. Minifie [a]

[a] *School of Earth and Ocean Sciences, Cardiff University, Park Place, Cardiff, Wales, CF10 3AT, UK*
[b] *Department of Earth Sciences, Carleton University, 1125 Colonel By Drive, Ottawa, Ontario, K1S 5B6, Canada & Ernst Geosciences, 43 Margrave Ave. Ottawa, Ontario, Canada K1T 3Y2*

ARTICLE INFO

Article history:
Received 16 April 2012
Accepted 30 June 2012
Available online xxxx

Keywords:
Large Igneous Provinces
Layered intrusions
Blue Draw Metagabbro
Ni–Cu–PGE mineralisation

ABSTRACT

The Blue Draw Metagabbro (BDM) in western South Dakota, is an 800 m thick, layered intrusion, which is interpreted to have been intruded as a rift-related subvolcanic sill during the Palaeoproterozoic. The age and tectonic setting of the BDM are similar to those recorded by the East Bull Lake Suite of layered intrusions in Southern Ontario. These similarities have led previous authors to suggest that the two sets of intrusions are cogenetic. The East Bull Lake Suite intrusions are relatively well studied and are known to host significant contact-type Ni–Cu–PGE sulphide mineralisation, however, prior to this work, relatively little was known of BDM both in terms of its geochemistry and mineralisation potential. Chemostratigraphic profiles through the BDM show that the intrusion is the product of at least two magma pulses which fractionated to produce a sequence of rocks which grade from peridotitic at the base of the intrusion to gabbronoritic at the upper margin. Closed-system fractionation following the intrusion of the second magma pulse caused the magma to become saturated in sulphur and precipitate Ni–Cu–PGE bearing sulphides—now preserved in a low-grade 50 m thick zone near the top of the intrusion. Petrological modelling shows that the parental melt of the BDM was a low-Ti tholeiite, with a trace element chemistry defined by enrichments in large-ion lithophile and light rare-earth elements and prominent negative Nb, Ta, and Ti anomalies. This 'arc-like' geochemistry recorded by the BDM parent magma is shared with parent magmas of the East Bull Lake Suite and may suggest that the BDM and its potential Canadian relatives share a common magmatic source. However, the relative ubiquity of such geochemical signatures in Archaean–Palaeoproterozoic intracontinental magmatic rocks coeval with the BDM suggests that the geochemical similarities recorded by the BDM and East Bull Lake Suite are non-unique and hence, are not definitive evidence of a genetic link between the two sets of intrusions. Instead, this geochemical signature that is common to many ancient igneous provinces may indicate the presence of a transient and (currently) poorly understood Archaean–Palaeoproterozoic mantle reservoir which was a globally significant magma source.

1. Introduction

The Blue Draw Metagabbro (BDM) is an 800 m thick (~6 km^2 outcrop area) layered gabbroic sill which crops out in the Black Hills, South Dakota, immediately west of Nemo township (Fig. 1). The BDM is one of several Archaean–Palaeoproterozoic metamorphosed mafic intrusions preserved within the Black Hills, but is significant in that it is the only one for which a reliable date has been obtained. The best age estimate for the intrusion of the BDM is a $^{207}Pb/^{206}Pb$ titanite age of 2480 ± 6 Ma from a dioritic pegmatite near the stratigraphic top of the sill (Dahl et al., 2006).

The age recorded by the BDM shows that the intrusion is coeval with the East Bull Lake Suite (EBLS) of layered intrusions preserved on the Superior craton near Sudbury, Ontario. The coeval nature of the EBLS and BDM as well as similar tectonic relationships (Vogel et al., 1998b), consistent palaeomagnetic properties of coeval mafic dyke swarms (Harlan, 2005) and stratigraphic similarities of associated sedimentary packages (Bekker et al., 2005; Roscoe and Card, 1993) have led previous authors to suggest a cogenetic origin for these intrusions (Bleeker and Ernst, 2006; Dahl et al., 2006; Ernst and Bleeker, 2010).

While the data described above allow the possibility of a genetic link between the BDM and EBLS, preliminary geochemical studies (Van Boening, 2007; Van Boening and Nabelek, 2008) indicated that the BDM was emplaced in a continental arc setting, rather than the widely accepted plume-driven continental rift setting invoked for other 2.5–2.45 Ga intrusions, including the EBLS (Easton et al., 2010; Ernst, 2007; Heaman, 1997).

Several of the EBLS intrusions are known to host significant contact-type Ni–Cu–PGE mineralisation (James et al., 2002; Peck et al., 2001; Vogel et al., 1999). Prior to this work, little was known of the BDM in terms of its geochemistry and economic potential. Given its proposed genetic link with metalliferous intrusions preserved on other cratons, the BDM may represent a potential target for Ni–Cu–PGE mineral exploration.

This paper presents whole-rock major, trace and platinum-group element (PGE) data for samples collected from throughout the

---

* Corresponding author. Tel.: +44 2920 876420.
E-mail address: jake.ciborowski@live.co.uk (T.J.R. Ciborowski).

0024-4937/$ – see front matter © 2012 Elsevier B.V. All rights reserved.
doi:10.1016/j.lithos.2012.06.035

Please cite this article as: Ciborowski, T.J.R., et al., The geochemistry and petrogenesis of the Blue Draw Metagabbro, Lithos (2012), doi:10.1016/j.lithos.2012.06.035

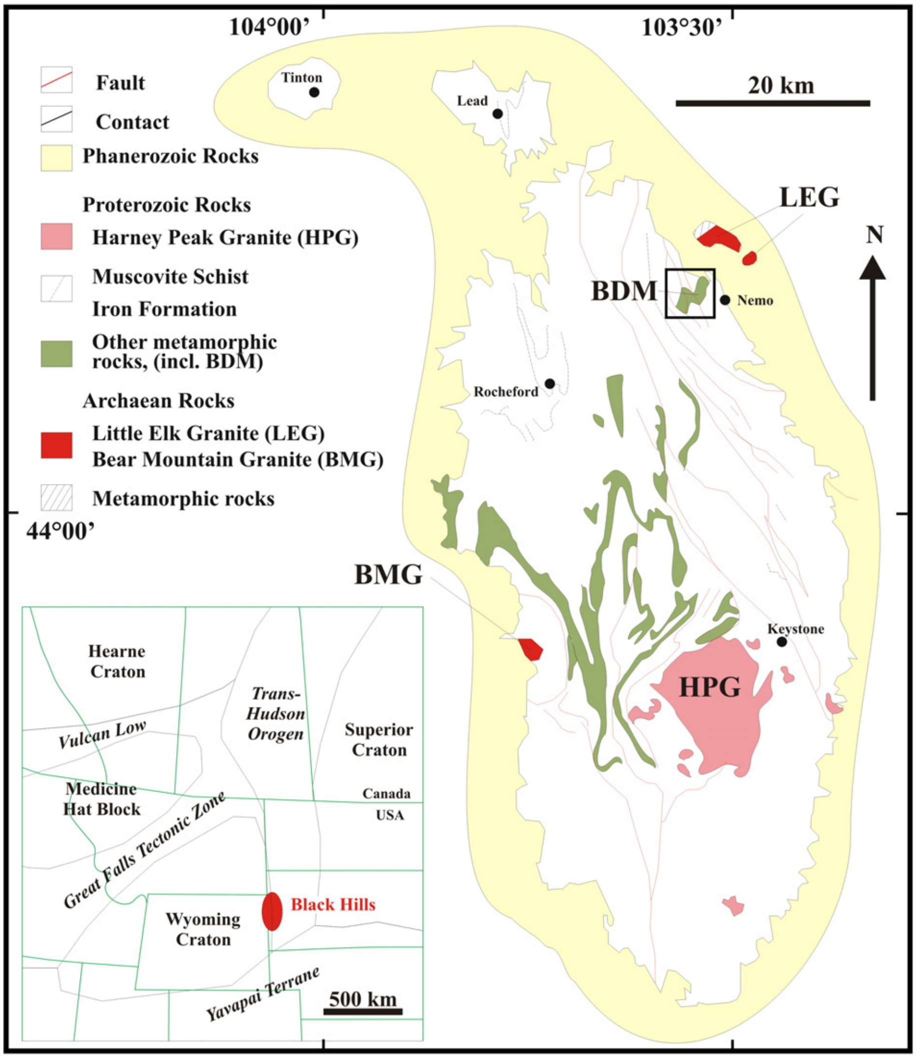

Fig. 1. Generalised geologic map of the Black Hills uplift, South Dakota. Map is modified after Dahl et al. (2006).

stratigraphy of the intrusion. These data are used to; characterise the petrogenetic evolution of the BDM; estimate the composition of the parental melt; deduce the level of in-situ contamination experienced by the crystallising magma; and decipher the nature of the mantle sources for the intrusion. The potential for Ni–Cu–PGE mineralisation within the intrusion is explored and geochemical comparisons between the BDM and its proposed cogenetic intrusions in the EBLS are discussed. Finally, we review the implications of our study for proposed continental reconstructions at 2.5–2.45 Ga.

2. Geology

The Wyoming Province is a distinct Archaean cratonic block which underlies much of the north-western United States (Fig. 1). The province is subdivided into the Montana Sedimentary Province, the Beartooth-Bighorn Magmatic Zone and the Southern Accreted Terranes (Foster et al., 2006), which were amalgamated, accreted and cratonised by the late Archaean (Mueller and Frost, 2006). The Wyoming Province is bounded on its northern, eastern and southern margins by ~1.9–1.7 Ga orogenic belts formed during the assembly of Laurentia (Chamberlain et al., 2003).

The ~7000 km^2 Black Hills Uplift (Fig. 1) lies along the eastern margin of the Wyoming Province and is one of only a few areas which expose the Precambrian basement of the province. The rocks preserved in the Black Hills were uplifted during the ~75–35 Ma Laramide orogen and consist of Archaean gneisses intruded by ~2.56 Ga granitoids which are overlain by, or in fault-contact with, complex sequences of Palaeoproterozoic metaconglomerates, quartzites, graywackes, iron formations, metavolcanics, gabbros, schists, phyllites and slates which record at least three to five separate deformation events (Gosselin et al., 1990; Hill, 2006; Redden et al., 1990).

The BDM (Fig. 2) intrudes the Boxelder Creek Quartzite which is the oldest recognised sedimentary sequence to have been deposited on the Archaean Little Elk granitoid-gneiss terrane in the northeast Black Hills. The ~3300 m thick Boxelder Creek Quartzite is composed of a basal assemblage of taconite-bearing and chloritic conglomerates, laterally changing to phyllites and dolomitic marbles which are overlain by granular quartzites, iron formations and fluvially deposited metaconglomerates (Hill, 2006; Lee, 1996). The Boxelder Creek Quartzite, along with correlative units in the Huronian Supergroup (Superior Province) and Snowy Pass Supergroup (Wyoming Province) have been interpreted to have formed in an intracratonic rift environment between ~2.55 and 2.48 Ga in response to mantle-plume-driven continental break-up (Heaman, 1997; James et al., 2002; Roscoe and Card, 1993).

Initial work on the BDM by Woo (1952) described the intrusion as a 1 km thick layered sill which exposes a fractionated sequence of serpentenite at the base which grades into hornblendite, plagioclase gabbro-diorite, biotite granodiorite and discontinuous dioritic pegmatite. The margins of the intrusion are concordant with bedding in

Please cite this article as: Ciborowski, T.J.R., et al., The geochemistry and petrogenesis of the Blue Draw Metagabbro, Lithos (2012), doi:10.1016/j.lithos.2012.06.035

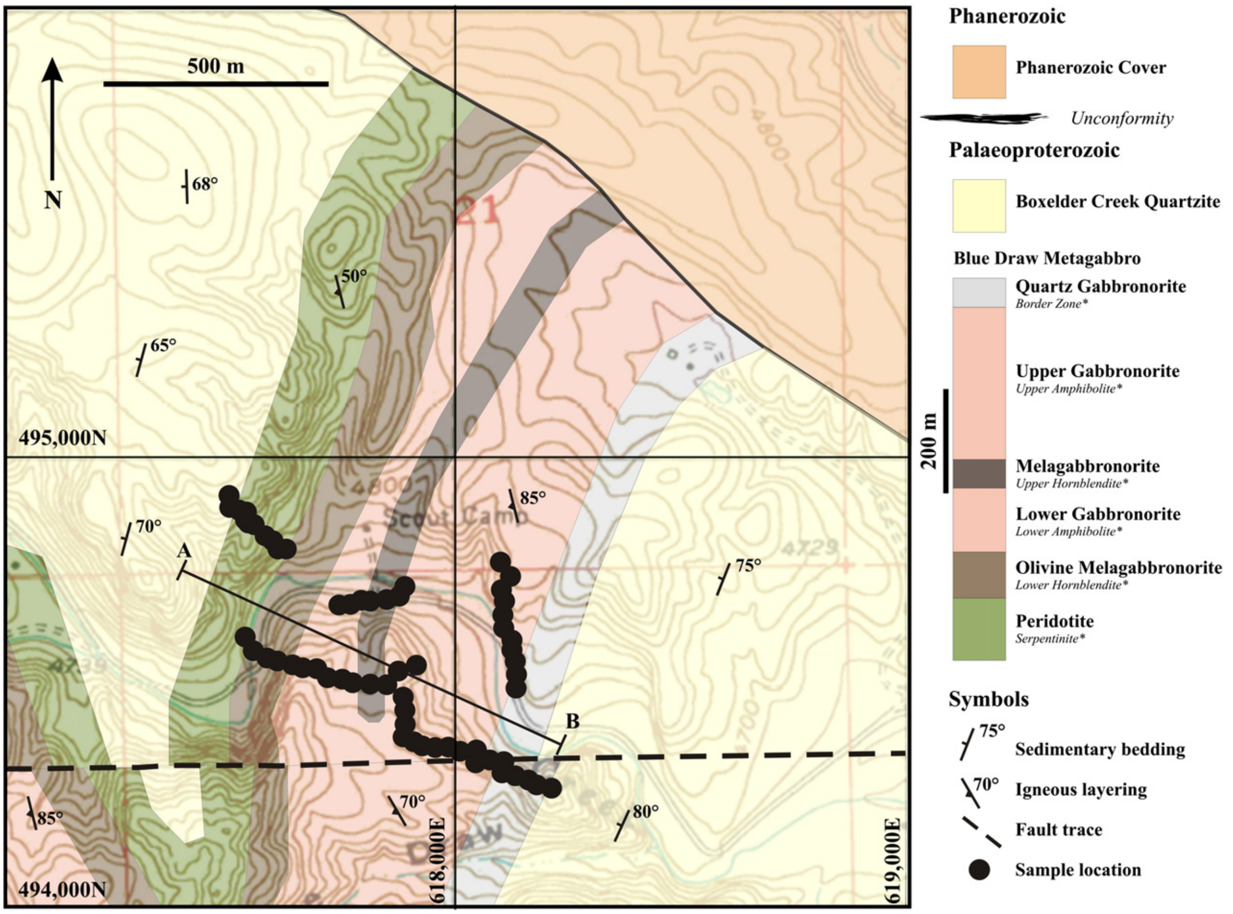

Fig. 2. Geologic map and stratigraphic column of the northern limb of the BDM showing sample locations of this study. Coordinate system is UTM Zone 13T. * denotes stratigraphic nomenclature used by Maranate (1979). Map is modified after Maranate (1979).

the Boxelder Creek Quartzite which, in the study area, dips 70–80° towards the northwest. A series of dominantly NW-SE trending faults have removed the side-wall contacts of the intrusion and have otherwise dismembered the BDM such that slivers of metamorphosed gabbro thought to be correlative with the BDM crop out at several locations throughout the area (Dahl et al., 2006).

Previous studies of Palaeoproterozoic mafic rocks in the Black Hills (Redden et al., 1990; Van Boening and Nabelek, 2008) suggest that post-crystallisation metamorphic events do not appear to have exceeded greenschist facies conditions.

3. Igneous stratigraphy: field relations and petrography

Maranate (1979) produced the first map of the BDM and based on metamorphic mineral assemblages, divided the BDM into a ~130 m thick serpentinite unit which is successively overlain by the ~100 m thick lower hornblendite unit and the ~250 m thick amphibolite which is separated into lower and upper units by the ~50 m thick upper hornblendite unit which crops out discontinuously at ~380 m from the base of the intrusion. The upper amphibolite unit is overlain by a ~60 m thick border zone of biotite- and quartz-rich rocks which, close to the margin of the intrusion, contain xenoliths of the Boxelder Creek Quartzite.

The stratigraphic nomenclature produced by Maranate (1979) described above is unsuitable, partly because the metamorphic terms used to describe the lithologies are at odds with the igneous nature of the BDM, and also as the slight differences in modal mineral abundances between rocks classed as Amphibolites and others which are classed as Hornblendites (the latter being more melanocratic) do not adequately reflect variation of lithology within the intrusion.

Therefore, the CIPW normative mineralogy for samples from the stratigraphic units mapped by Maranate (1979) were calculated and classified using the IUGS Plagioclase-Olivine-Pyroxene classification scheme (Le Maitre, 2002). This classification allows new lithological names for the different units of the BDM to be assigned (Fig. 3). Most samples from the rock units described by Maranate (1979) fall within discrete areas within the IUGS plagioclase-olivine-pyroxene classification scheme. Using this classification, the serpentinite, lower hornblendite, lower amphibolite, upper hornblendite, upper amphibolite and border zone units of Maranate (1979) have been reclassified into the peridotite, olivine melagabbronorite, lower gabbronorite, melagabbronorite, upper gabbronorite and quartz gabbronorite units respectively.

3.1. Peridotite unit

The peridotite unit at the base of the intrusion is dominated by serpentinised olivine (~90%) and chrome spinel (~10%) though some samples can contain up to ~40% altered pyroxene. The unit ranges from equigranular nearer the base, with samples showing cumulate textures, to porphyritic, in which megacrysts of serpentinised olivine are enclosed by finer grained crystals of the same material (Fig. 4A and B). Serpentinisation of the olivine in this unit is complete and manifests itself as radial to randomly aligned masses of very fine grained crystals of serpentine which pseudomorph the primary olivine crystals and largely preserve primary igneous textures.

Towards the top of the peridotite unit, serpentinised olivine occurs as both a megacryst phase and groundmass phase. In the megacrysts, talc and magnesite alteration is aligned in bands across the megacrysts giving the megacrysts an apparent fabric which is not shared with the groundmass.

Please cite this article as: Ciborowski, T.J.R., et al., The geochemistry and petrogenesis of the Blue Draw Metagabbro, Lithos (2012), doi:10.1016/j.lithos.2012.06.035

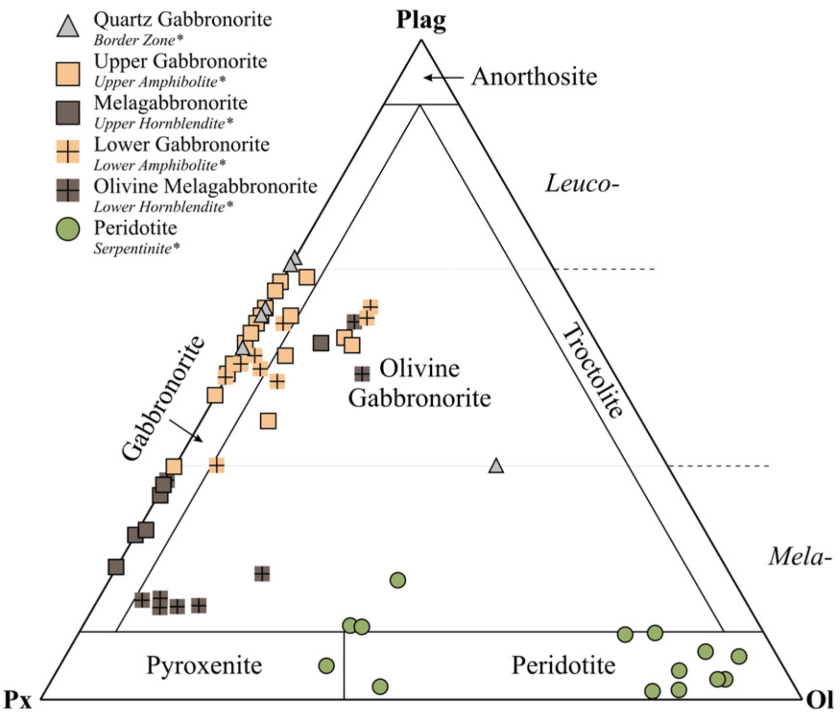

Fig. 3. Classification of the rocks from the BDM based on norm calculations and IUGS classification. Diagram is modified after Le Maitre (2002) and Barnes and Gomwe (2011). * denotes stratigraphic nomenclature used by Maranate (1979).

In the intrusion as a whole, chrome spinel is most abundant in the peridotite unit where it occurs as fine grained euhedral–subhedral prismatic crystals which are disseminated evenly through the rock. Where the peridotite unit is megacrystic, chrome spinel is present both as inclusions in the serpentinised olivine megacrysts and disseminated through the groundmass. The grain boundaries of chrome spinel crystals in the equigranular serpentinites are irregular and show evidence of alteration and recrystallisation. This effect is less visible in spinel crystals included in serpentinised olivine megacrysts.

3.2. Olivine melagabbronorite unit

The olivine melagabbronorite unit is composed primarily of altered pyroxene and plagioclase. At the base of the unit, altered pyroxene accounts for ~80% of the rock volume, while altered plagioclase and very minor amounts of serpentinised olivine accounts for the rest. At the top of the unit, altered pyroxene decreases to <50% of the rock volume and altered plagioclase becomes dominant. The altered pyroxenes in the olivine melagabbronorite unit are primarily clinopyroxene (which, in less altered samples, preserve primary, euhedral lath-shaped habits) with lesser amounts of orthopyroxene. The alteration of the pyroxenes manifests itself as either fine grained cross-cutting bladed crystals of amphibole and patchy calcite in pyroxene interiors and grain boundaries, to total pseudomorphic replacements (Fig. 4C). The alteration of the plagioclase is similar to that observed elsewhere in the intrusion and is dominated by very fine grained replacements of sericite and quartz.

3.3. Lower gabbronorite unit

The lower gabbronorite unit is predominantly (50–60%) composed of plagioclase showing moderate-advanced sericite alteration. Approximately 35% of the rock is made up of altered pyroxenes, dominated by pale green clinopyroxene which shows moderate-advanced alteration to amphibole, biotite, calcite and quartz. The biotite alteration primarily occurs at grain boundaries where it pseudomorphically replaces the pyroxene while the quartz occurs as amorphous patches in the middle of crystals. Trace amounts of magnetite showing partial alteration to secondary iron oxides (likely haematite) are present.

3.4. Melagabbronorite unit

The melagabbronorite unit is similar in mineralogy to the olivine melagabbronorite unit in that it is dominated by altered pyroxene (60–80%) with lesser amounts of moderately sericitised plagioclase, serpentinised olivine and contains trace amounts (<2%) of an opaque phase, potentially chromite or magnetite which has been altered to iron oxide phases along grain boundaries.

3.5. Upper gabbronorite unit

The rocks at the base of the upper gabbronorite are predominantly made up of variably sericitised plagioclase (~55%). Approximately 40% of the rock is composed of altered pyroxene with clinopyroxene being dominant. The pyroxenes are moderately-completely altered to amphibole and calcite. Some samples contain minor amounts (<5%) of quartz which occasionally displays granophyric texture (Fig. 4D). Trace amounts of fine grained, euhedral, partially oxidised magnetite are also present.

Towards the top of the upper gabbronorite unit, partially sericitised plagioclase and quartz become more abundant and collectively constitute approximately 60–70% of the rock volume. In the uppermost samples from the upper gabbronorite unit, biotite (with minor amounts of chlorite), which can constitute up to 20% of the rock, occurs as fine grained aggregates of randomly aligned minerals that appear to form networks around larger (usually plagioclase) crystals. Clinopyroxene is largely absent from the rocks near the top of the upper gabbronorite unit, but orthopyroxene remains, constituting ~10% of the rock volume and is moderately–completely altered to green amphibole, biotite, calcite and quartz.

3.6. Quartz gabbronorite unit

The quartz gabbronorite unit of the intrusion is composed of silicic rocks which become extremely quartz-rich at the top of the zone. In

Please cite this article as: Ciborowski, T.J.R., et al., The geochemistry and petrogenesis of the Blue Draw Metagabbro, Lithos (2012), doi:10.1016/j.lithos.2012.06.035

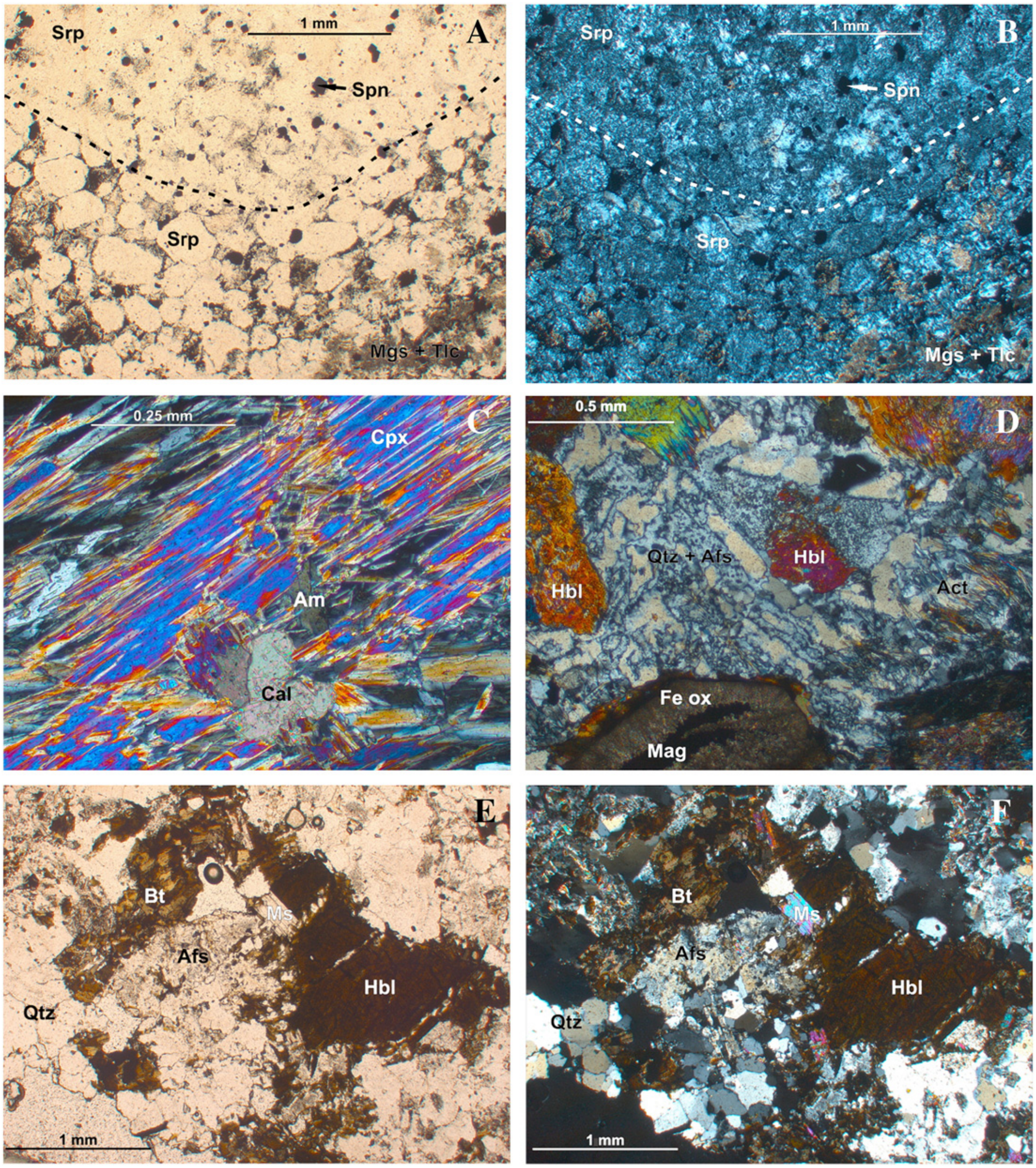

Fig. 4. Optical micrographs of; A) serpentinised olivine phenocrysts in the Peridotite unit in PPL; B) XPL image of view in A); C) XPL image of typical alteration of clinopyroxene to amphibole and calcite; D) XPL image of granophyric texture in upper gabbronorite unit; E) PPL image of typical texture in the quartz gabbronorite unit; F) XPL image of view in E).

the quartz gabbronorite unit, quartz occurs both as a primary phase and as fine grained inclusions in sericitised plagioclase crystals. Primary quartz occurs as granular masses of fine grained equant crystals which exhibit irregular grain boundaries both within the masses and with adjacent plagioclase which occurs in minor amounts and is weakly-moderately sericitised. Biotite (and minor chlorite) is the most common mica in the quartz gabbronorite unit and occurs as very fine grained granular masses of randomly aligned euhedral laths. Muscovite is also present in this unit but in minor amounts and is intergrown with biotite. Iron-rich amphibole (hornblende) is also present in minor amounts and forms anhedral crystals which fill the space between the abundant quartz (Fig. 4E and F). The grain boundaries of the hornblende are altered to biotite with minor muscovite.

3.7. Boxelder Creek Quartzite

The Boxelder Creek Quartzite is made up almost entirely of poorly sorted, fine-medium grained, sub-rounded quartz with minor amounts of muscovite. Microscopic layering of the Boxelder Creek Quartzite is preserved and defined by interlaying of more micaceous bands within the quartzite. In hand specimen, samples from the Boxelder Creek Quartzite appear more psammitic than as true quartzites.

3.8. Summary

In summary, the BDM records a primary igneous stratigraphy which shows a general evolution from mafic cumulates rich in olivine and pyroxene at the base to more evolved, mafic mineral-poor, feldspar-rich rocks with increasing stratigraphic height. This general trend is interrupted at the base of the melagabbronorite unit which contains a much greater proportion of mafic minerals than the underlying lower gabbronorite unit, which may suggest that the BDM was recharged during fractionation. The likelihood of this is explored later (see Section 5.2). At the uppermost levels of the intrusion, the rocks are extremely evolved and contain high percentages of primary quartz and mica. At the lowest levels of the intrusion, serpentinised olivine is present in two size populations (Fig. 4A) which suggests that the BDM parental magma was intruded as a melt + olivine crystal mixture. Following crystallisation, the dominant primary magmatic minerals in

Please cite this article as: Ciborowski, T.J.R., et al., The geochemistry and petrogenesis of the Blue Draw Metagabbro, Lithos (2012), doi:10.1016/j.lithos.2012.06.035

Table 1
Whole-rock major element, trace element, rare earth element (REE) for 19 representative samples from the BDM. Unit abbreviations: QG — quartz gabbronorite, UG — upper gabbronorite, MG — melagabbronorite, LG — lower gabbronorite, OMG — olivine melagabbro, P — peridotite.

Sample	BD073	BD065	BD008	BD058	BD056	BD050	BD049	BD092	BD091	BD100	BD087	BD097	BD082	BD080	BD046	BD040	BD037	BD032	BD030
Height (m)	773	720	680	600	555	510	480	438	410	385	348	300	240	208	155	95	65	23	0
Unit	QG	QG	UG	UG	UG	UG	UG	UG	MG	MG	LG	LG	LG	OMG	OMG	P	P	P	P
Majors (wt.%)																			
SiO_2	69.84	55.06	53.64	52.28	51.07	51.40	52.01	51.09	52.75	52.09	50.89	49.93	51.06	48.14	50.08	36.76	37.45	36.74	41.61
TiO_2	1.05	0.62	0.63	0.59	0.53	0.47	0.45	0.45	0.37	0.39	0.45	0.33	0.35	0.31	0.29	0.11	0.12	0.17	0.28
Al_2O_3	11.29	13.89	13.73	12.07	13.49	10.89	13.58	8.46	8.40	5.77	9.12	16.72	14.33	13.69	3.81	1.99	2.43	3.16	4.83
Fe_2O_3	7.59	10.71	12.61	10.08	10.52	10.86	9.53	10.38	10.74	11.49	11.33	9.09	8.59	7.92	9.92	11.60	10.84	10.90	12.13
MnO	0.20	0.17	0.17	0.16	0.15	0.17	0.16	0.17	0.18	0.21	0.18	0.16	0.16	0.12	0.20	0.14	0.13	0.14	0.18
MgO	1.37	6.15	5.31	6.44	7.79	11.85	9.91	12.31	13.38	17.09	15.34	9.25	8.39	9.46	19.03	38.52	38.94	34.80	32.30
CaO	1.26	9.42	9.20	8.08	9.39	10.30	8.84	9.30	10.22	9.65	7.63	11.17	13.08	8.28	12.27	0.19	0.10	2.06	0.30
Na_2O	2.23	2.82	2.64	3.04	3.52	2.56	3.75	2.00	1.64	0.79	1.99	2.56	2.25	3.32	0.69	0.00	0.01	0.00	0.01
K_2O	3.42	1.31	1.07	1.26	0.75	0.12	0.16	0.05	0.45	0.21	0.05	0.42	0.39	0.12	0.03	0.00	0.00	0.00	0.01
P_2O_5	0.18	0.08	0.08	0.04	0.06	0.06	0.06	0.05	0.03	0.05	0.05	0.06	0.03	0.02	0.02	0.01	0.01	0.02	0.03
LOI	1.27	0.63	0.61	7.13	2.31	1.40	1.60	4.95	1.98	2.18	2.78	1.45	1.58	8.56	3.15	11.04	11.18	12.45	8.37
Total	99.70	100.86	99.68	101.18	99.59	100.08	100.04	99.21	100.14	99.92	99.80	101.12	100.21	99.93	99.48	100.35	101.20	100.44	100.03
Traces (ppm)																			
Sc	13	29	32	31	32	40	36	36	34	37	33	29	31	34	55	8	9	11	16
Zr	100.9	97.7	78.3	76.5	69.6	65.4	63.3	57.8	47.7	61.1	50.9	37.1	39.6	33.4	21.5	11.0	14.6	30.5	37.1
V	97	208	198	219	195	253	232	232	227	242	206	169	161	180	264	40	44	50	69
Cr	14	106	124	283	306	1102	615	547	605	2874	682	160	188	242	884	2702	3131	2507	2364
Co	15.6	46.2	44.4	44.9	44.0	51.7	45.0	47.7	59.6	68.5	55.4	42.6	41.9	42.7	70.0	134.7	133.7	112.7	97.0
Ni	20	171	13	143	89	199	148	272	189	1357	193	117	109	117	258	1155	1204	983	879
Cu	23	45	375	66	96	46	53	31	44	32	39	103	62	19	179	8	38	66	106
Ga	16.3	16.6	15.9	14.2	15.5	11.9	13.2	10.2	10.3	7.8	11.0	13.8	13.6	12.3	6.1	3.1	3.7	4.7	6.9
Rb	99.4	46.9	33.9	38.3	21.1	1.4	2.4	0.9	13.9	5.9	0.4	11.8	17.3	15.8	0.1	0.2	0.3	0.6	1.1
Sr	135	217	221	102	277	144	193	76	133	41	80	184	188	221	20	1	1	23	5
Y	28.6	17.2	16.8	16.1	14.1	13.6	12.9	12.1	11.5	10.9	11.5	8.9	9.7	8.3	7.3	2.0	2.5	3.8	6.7
Nb	9.02	4.45	3.32	4.02	3.64	2.64	2.62	2.69	1.98	2.17	2.17	1.73	2.23	1.23	0.66	0.33	0.59	1.05	1.55
La	37.43	16.46	17.35	13.71	12.27	10.21	9.68	9.47	8.16	8.61	4.79	7.30	7.94	5.38	3.74	3.13	2.08	3.07	6.41
Ce	73.55	34.10	28.89	26.61	23.94	20.27	18.07	19.14	17.77	14.93	11.49	14.52	16.75	11.14	7.44	3.75	3.31	5.99	11.84
Pr	8.77	4.07	3.54	3.28	3.00	2.55	2.43	2.41	2.22	2.07	1.54	1.83	2.03	1.41	0.93	0.36	0.38	0.67	1.47
Nd	32.03	15.40	13.73	12.67	11.11	9.62	9.05	9.30	8.33	7.83	6.05	6.89	7.75	5.62	3.94	1.47	1.58	2.83	5.71
Sm	6.13	3.25	3.13	2.62	2.44	2.15	2.04	1.98	1.98	1.73	1.64	1.49	1.62	1.25	1.02	0.36	0.38	0.62	1.09
Eu	1.36	0.96	1.01	0.80	0.82	0.57	0.61	0.59	0.59	0.48	0.44	0.55	0.56	0.52	0.21	0.11	0.12	0.19	0.30
Gd	5.90	3.20	2.87	2.67	2.33	2.06	2.03	1.95	1.90	1.79	1.56	1.47	1.64	1.27	1.05	0.34	0.36	0.62	1.18
Tb	0.84	0.49	0.45	0.41	0.38	0.34	0.32	0.32	0.30	0.26	0.29	0.23	0.23	0.20	0.19	0.06	0.07	0.10	0.18
Dy	4.99	2.98	2.70	2.49	2.42	2.16	2.09	2.07	1.99	1.76	1.88	1.51	1.56	1.36	1.31	0.40	0.45	0.72	1.17
Ho	0.87	0.54	0.55	0.50	0.47	0.40	0.39	0.40	0.38	0.31	0.38	0.28	0.30	0.27	0.24	0.07	0.08	0.13	0.21
Er	2.58	1.63	1.70	1.47	1.38	1.22	1.13	1.17	1.14	1.00	1.11	0.83	0.88	0.80	0.72	0.22	0.25	0.40	0.65
Tm	0.43	0.27	0.26	0.23	0.22	0.18	0.17	0.18	0.17	0.15	0.18	0.12	0.14	0.13	0.12	0.04	0.04	0.07	0.10
Yb	2.62	1.69	1.58	1.47	1.36	1.19	1.12	1.17	1.13	1.01	1.18	0.82	0.85	0.79	0.77	0.23	0.28	0.45	0.65
Lu	0.38	0.25	0.25	0.22	0.20	0.18	0.17	0.19	0.17	0.15	0.16	0.13	0.13	0.13	0.10	0.03	0.04	0.06	0.09
Hf	2.56	2.53	2.17	2.10	1.93	1.54	1.39	1.67	1.55	1.36	1.37	0.90	1.26	0.87	0.53	0.25	0.33	0.74	0.84
Ta	0.84	0.37	0.25	0.30	0.25	0.20	0.20	0.22	0.17	0.17	0.18	0.14	0.16	0.10	0.06	0.02	0.05	0.08	0.12
Pb	11.21	12.98	11.06	5.72	6.99	4.48	6.66	5.50	5.21	3.59	2.39	3.92	3.68	2.90	5.02	1.01	1.21	1.62	5.95
Th	13.36	5.94	4.80	4.59	3.77	3.03	2.90	3.41	2.93	2.72	3.20	2.07	2.67	1.52	1.09	0.59	0.72	1.00	1.72
U	2.17	1.71	1.47	1.09	0.98	0.82	0.74	0.78	0.70	0.63	0.68	0.53	0.65	0.37	0.27	0.16	0.17	0.28	0.28

Please cite this article as: Ciborowski, T.J.R., et al., The geochemistry and petrogenesis of the Blue Draw Metagabbro, Lithos (2012), doi:10.1016/j.lithos.2012.06.035

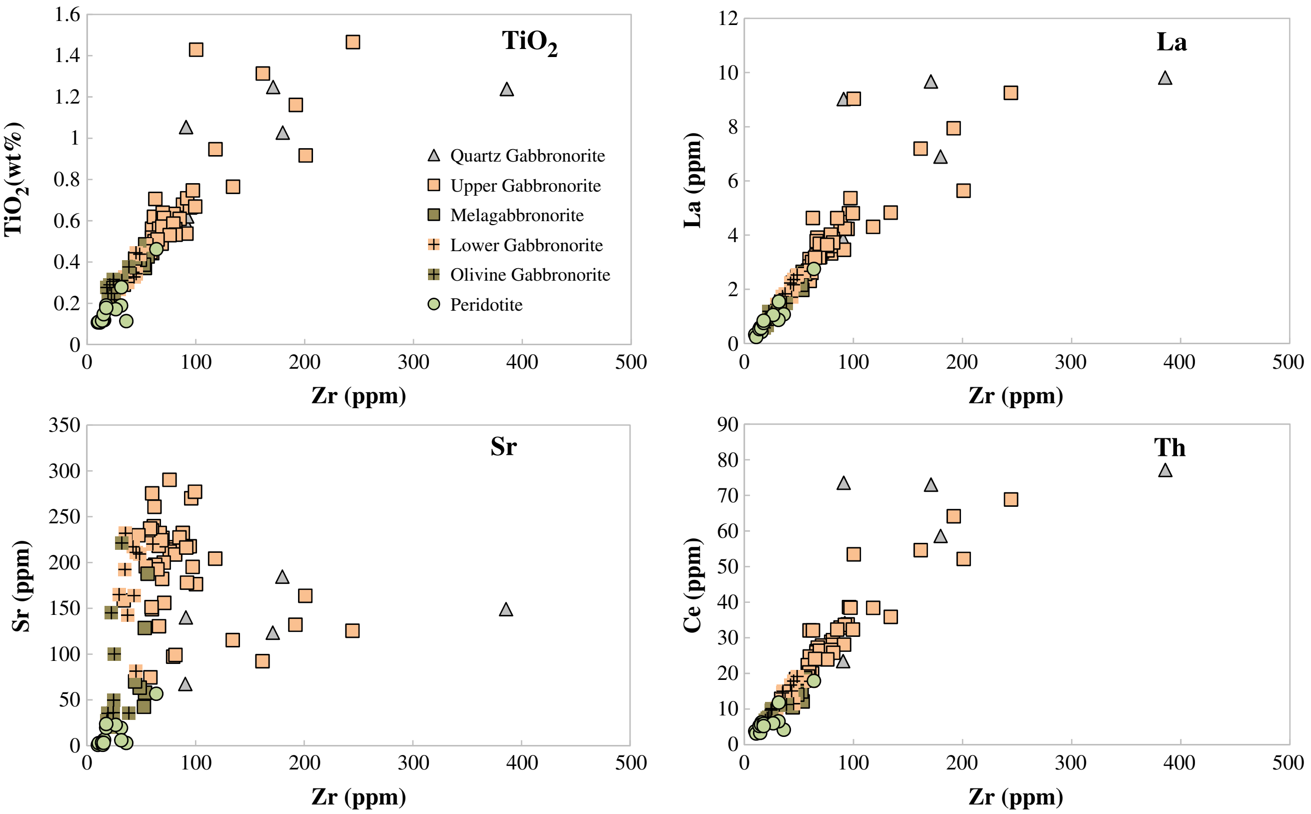

Fig. 5. Bivariate diagrams of selected elements plotted against Zr.

the intrusion were olivine, pyroxene and plagioclase. These have subsequently been moderately-completely replaced by serpentine, amphibole, calcite, sericite and quartz which is characteristic of greenschist–amphibolite facies metamorphism.

4. Geochemistry

4.1. Analytical procedures

Sample preparation and analysis was carried out at Cardiff University. Prior to analysis, weathered surfaces and infilled fractures were removed with a rock saw. The samples were then crushed into ~5 mm chips using a steel jaw crusher. Approximately 80 ml of this material was then powdered in an agate planetary ball mill. Approximately 2 g of the resulting powder was ignited in a furnace at 900 °C for two hours in order to determine loss on ignition values.

Whole-rock major element, trace element and rare earth element (REE) data were obtained following Li metaborate fusion (McDonald and Viljoen, 2006). Major element and Sc abundances were determined using a JY Horiba Ultima 2 Inductively Coupled Plasma Optical Emission Spectrometer (ICP-OES). Trace elements were analysed by a Thermo X Series 2 Inductively Coupled Plasma Mass Spectrometer (ICP-MS). The internationally recognised standard JB-1A was run with each sample batch. Relative standard deviations show precision of 1–5% for most major and trace elements for JB-1A. 2σ values encompass certified values for the vast majority of elements. Full analytical results including repeat runs of standard basalt JB-1A can be found in the Supplementary Information.

PGE and Au data were obtained by Ni sulphide fire assay followed by ICP-MS (Huber et al., 2001; McDonald and Viljoen, 2006). The resulting sulphide buttons were dissolved in concentrated HCl. Following dissolution, noble metals were co-precipitated with Te using $SnCl_2$ as a reductant. The liquid-precipitate mixture was filtered under vacuum then dissolved in a 7 ml solution of aqua regia with a Tl spike as an internal standard to monitor for instrumental drift. After digestion was complete, the resulting solution was diluted to 50 ml with deionised water before being analysed by ICP-MS.

4.2. Element mobility

Whole-rock major element, trace element and rare earth element (REE) data for 19 representative samples from the BDM are presented in Table 1. As the BDM has undergone at least greenschist facies metamorphism and samples show abundant alteration (Fig. 4) the effects of secondary element remobilisation must be considered.

The high field strength elements (HFSE) are thought to be relatively immobile under greenschist facies metamorphism (Pearce, 1996). As the HFSE are incompatible in the main rock forming minerals, they should plot on linear arrays when plotted against each other for a suite of rocks formed from a common fractionating magma. Secondary remobilisation of elements can result in a scattered trend.

Good linear correlations are observed between Zr and the REE and other HFSE, indicating that secondary remobilisation of these elements was very limited. Conversely, the incompatible large ion lithophile elements (LILE) generally show a more scattered correlation with Zr which indicates that these elements have been remobilised. A subset of these graphs is shown in (Fig. 5).

The abundance of the chalcophile elements, Cu, Ni and PGE in magmatic systems are largely influenced by the presence of sulphur (Naldrett, 1999) and so their potential for remobilisation cannot be assessed in the same way as other trace elements.

4.3. Classification

The total alkali vs. silica (TAS) diagram (LeBas et al., 1986) classifies the BDM samples as a continuum of tholeiitic foidites, picrobasalts, basalts, basalts, basaltic andesites, andesites and dacites (Fig. 6A). The continuum defined by the analyses also crudely reflects the igneous

Please cite this article as: Ciborowski, T.J.R., et al., The geochemistry and petrogenesis of the Blue Draw Metagabbro, Lithos (2012), doi:10.1016/j.lithos.2012.06.035

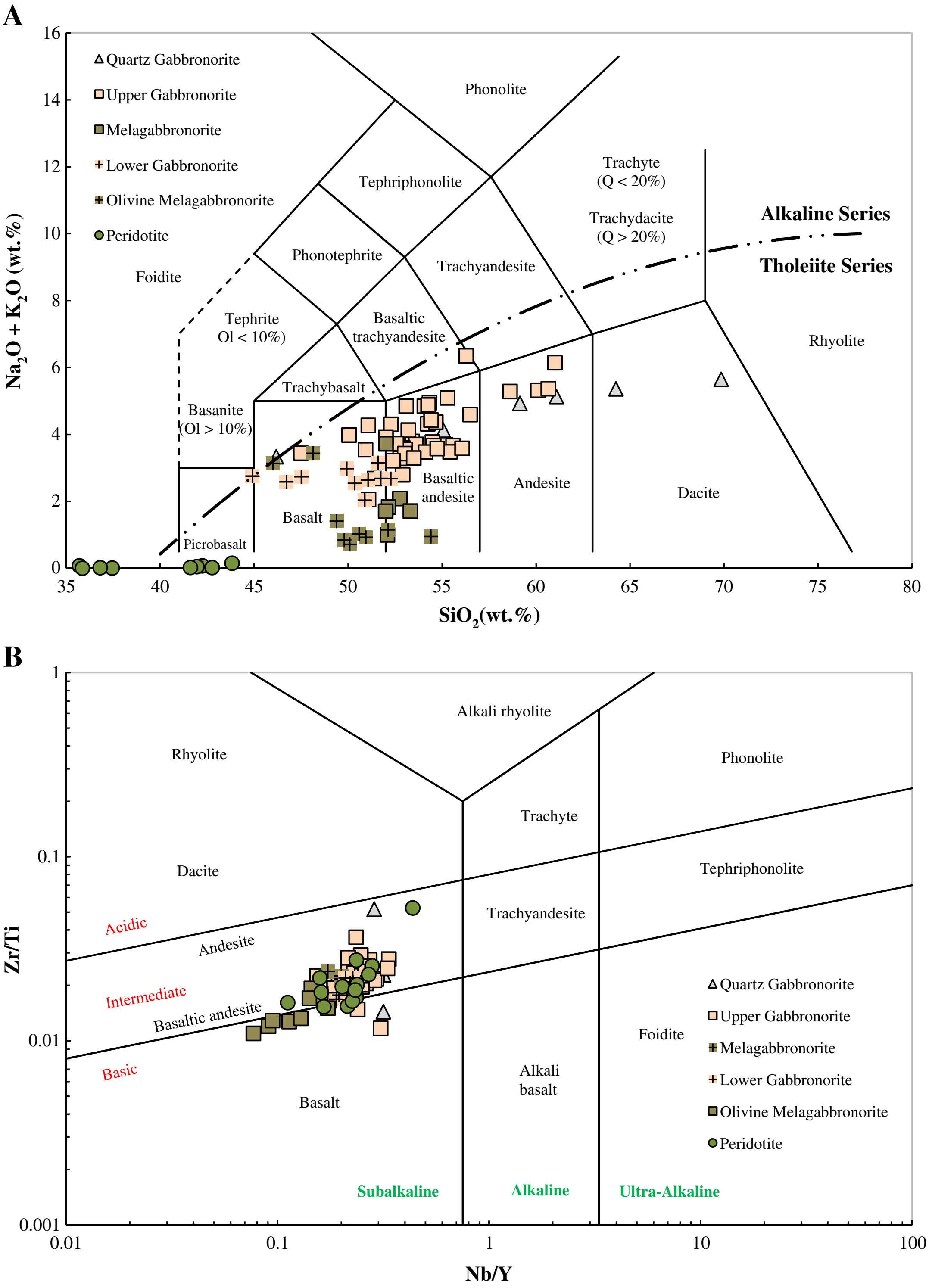

Fig. 6. Classification diagrams for the BDM: A) Total alkali vs. silica diagram (LeBas et al., 1986). Alkaline–Tholeiite line from Irvine and Baragar (1971). B) Zr/Ti vs. Nb/Yb diagram (Pearce, 1996).

stratigraphy in the intrusion, in that the peridotite unit and olivine melagabbronorite unit from near the base of the intrusion plot as picrobasalts and basalts, while the upper gabbronorite unit and quartz gabbronorite unit rocks from near the top of the intrusion plot as basaltic andesites to dacites. This trend may be an effect of fractional crystallisation of the BDM parent magma.

The TAS diagram relies on Na and K to classify igneous rocks, so consequently the applicability of the TAS diagram for classifying BDM rocks is questionable, as these elements have been remobilised in the intrusion. Instead, the Zr/Ti vs. Nb/Y diagram (Fig. 6B) is more useful as the elements used in the classification have been shown to be immobile during greenschist facies metamorphism (Pearce, 1996). On this diagram the majority of the BDM rocks plot as a cluster of points which overlap the basaltic and basaltic andesite fields, suggesting that they may be derived from a common parent magma. There does not appear to be a trend associated with stratigraphic height in these data as the different stratigraphic units largely overlap in Zr/Ti-Nb/Y space.

Please cite this article as: Ciborowski, T.J.R., et al., The geochemistry and petrogenesis of the Blue Draw Metagabbro, Lithos (2012), doi:10.1016/j.lithos.2012.06.035

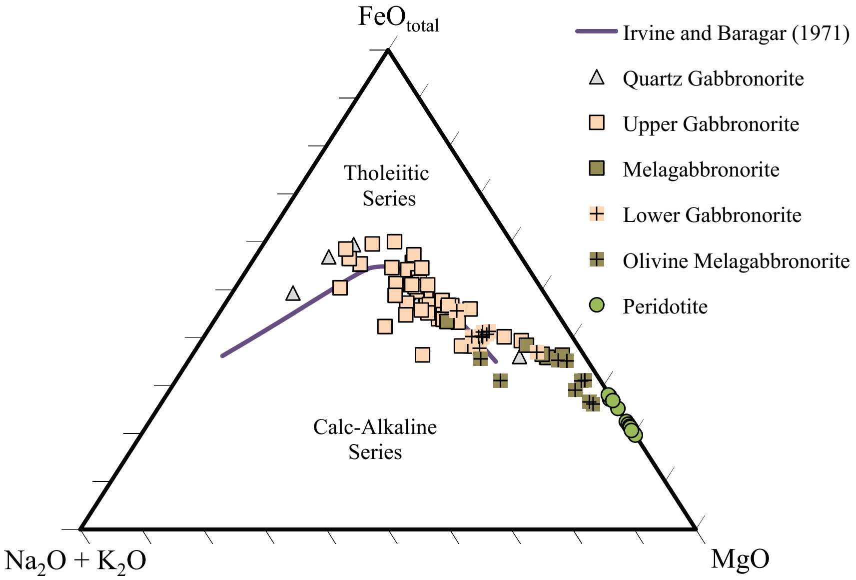

Fig. 7. AFM diagram showing Fe-enrichment trend of the BDM. Boundary between calc-alkaline field and tholeiitic field after Irvine and Baragar (1971).

On the AFM diagram (Fig. 7), the BDM define a trend of moderate Fe-enrichment with stratigraphic height. This trend is characteristic of fractionation of tholeiitic rocks and is also found in the EBLS as typified by the Agnew intrusion (Vogel, 1996).

4.4. Stratigraphic geochemical profiles

The concentrations of the majority of elements in the BDM have been shown to be largely unaffected by secondary mobility (Fig. 5). Consequently, their recorded concentrations can be assumed to be primary and they can be used with confidence in discussions regarding the petrogenesis of the intrusion.

Representative major and trace elements are plotted against stratigraphic height in (Fig. 8). This approach is made possible by the sampling strategy shown in (Fig. 2). A series of strike-normal traverses permitted collection of samples from throughout the stratigraphy of the intrusion. By projecting the sample locations along strike to the cross section line, chemostratigraphic profiles for the Blue Draw intrusion can be constructed. These chemostratigraphic profiles better demonstrate geochemical trends through the intrusion and help define the mineralisation potential of the intrusion.

4.4.1. Major elements

Stratigraphic geochemical profiles for the major elements show that generally, the BDM trends from Mg- and Fe-rich rocks at the base of the intrusion to more Si- and Al-rich rocks at the top. Throughout the peridotite unit, SiO_2, MgO and Fe_2O_3 concentrations remain largely constant at ~37 wt.%, 38 wt.% and 11 wt.% respectively. At the base of the olivine melagabbronorite unit (~125 m), the SiO_2 concentration jumps to ~52 wt.% and remains constant until ~700 m, at which point SiO_2 increases with stratigraphic height to ~70 wt.% at the top of the intrusion. Conversely to SiO_2, MgO begins to decrease in concentration above the peridotite unit to reach ~1 wt.% at the top of the intrusion. This decrease in MgO is mirrored by CaO and a concomitant increase in Al_2O_3.

These general trends described above are interrupted by a partial resetting of compositions at the base of the melagabbronorite unit (~370 m) where the whole-rocks become more basic before evolving to more acidic compositions with increasing stratigraphic height.

4.4.2. Incompatible trace elements

Chemostratigraphic profiles for incompatible elements including the REE, HFSE, K_2O, TiO_2, Na_2O and P_2O_5 show common trends through the BDM. Incompatible element concentrations are lowest in the peridotite unit at the base of the intrusion and remain constantly low throughout the unit. At the base of the olivine melagabbronorite unit (~125 m), incompatible element concentrations begin to increase with stratigraphic height. This increase is interrupted at ~300 m by a sharp fall in incompatible element concentrations after which, concentrations begin to increase again at a similar rate to that observed between 125–300 m. This increase in incompatible element concentration with stratigraphic height continues uniformly until ~700 m (near the top of the upper gabbronorite unit), at which point, the rate of incompatible element concentration increase becomes an order of magnitude greater than that observed lower in the intrusion.

4.4.3. Compatible trace elements

Compatible trace element (Ni, Co, Cr, Sc and V) concentrations in the BDM are linked to modal mineral proportions in the rock. Stratigraphic geochemical profiles for these elements (Fig. 8) define two often complimentary trends in the BDM. The first trend is defined by Ni, Co and Cr, the highest concentrations of which are recorded in the peridotite unit at the base of the intrusion, probably as a consequence of the high proportion of olivine and spinel in these units, within which Ni, Co and Cr are compatible. At the base of the olivine melagabbronorite unit (~125 m), concentrations of Ni, Co and Cr decrease exponentially with stratigraphic height before stabilising at low levels which remain low through the lower gabbronorite unit until they peak again at the base of the melagabbronorite unit at ~370 m. Following this peak at ~370 m, concentrations of Ni, Co and Cr decrease rapidly in a similar way to that observed in the olivine melagabbronorite and lower gabbronorite units.

The second trend is defined by Sc and V, the lowest concentrations of which are recorded in the peridotite unit. Concentrations of Sc and V peak at the base of the olivine melagabbronorite unit before decreasing rapidly in a similar manner to Ni, Co and Cr. Concentrations in Sc and V peak again at the base of the melagabbronorite unit before either decreasing with increasing stratigraphic height (Sc) or showing no readily discernable trend with increasing stratigraphic height

Please cite this article as: Ciborowski, T.J.R., et al., The geochemistry and petrogenesis of the Blue Draw Metagabbro, Lithos (2012), doi:10.1016/j.lithos.2012.06.035

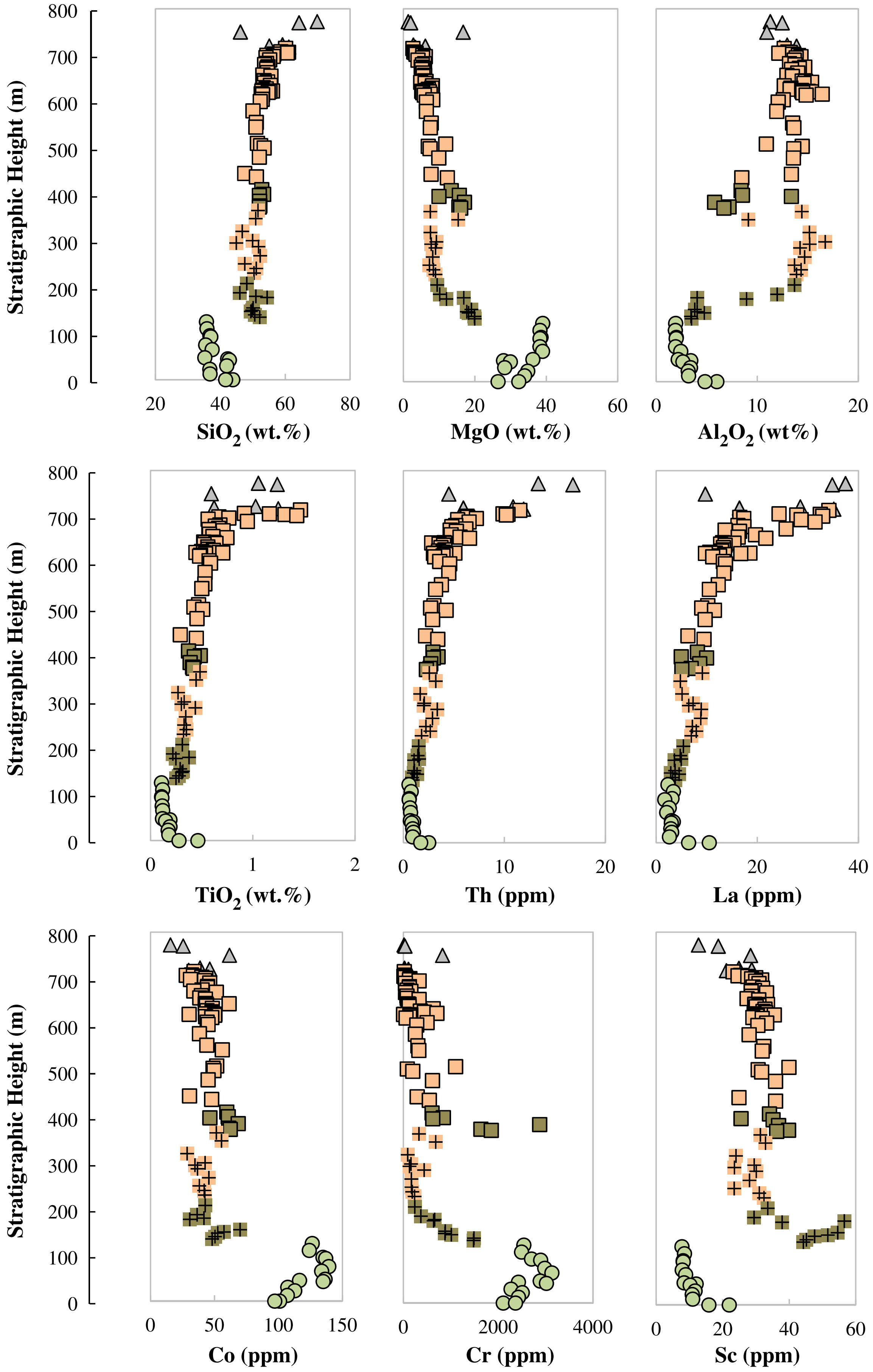

Fig. 8. Chemostratigraphic profiles through the BDM for selected elements. Symbols the same as in Fig. 7.

Please cite this article as: Ciborowski, T.J.R., et al., The geochemistry and petrogenesis of the Blue Draw Metagabbro, Lithos (2012), doi:10.1016/j.lithos.2012.06.035

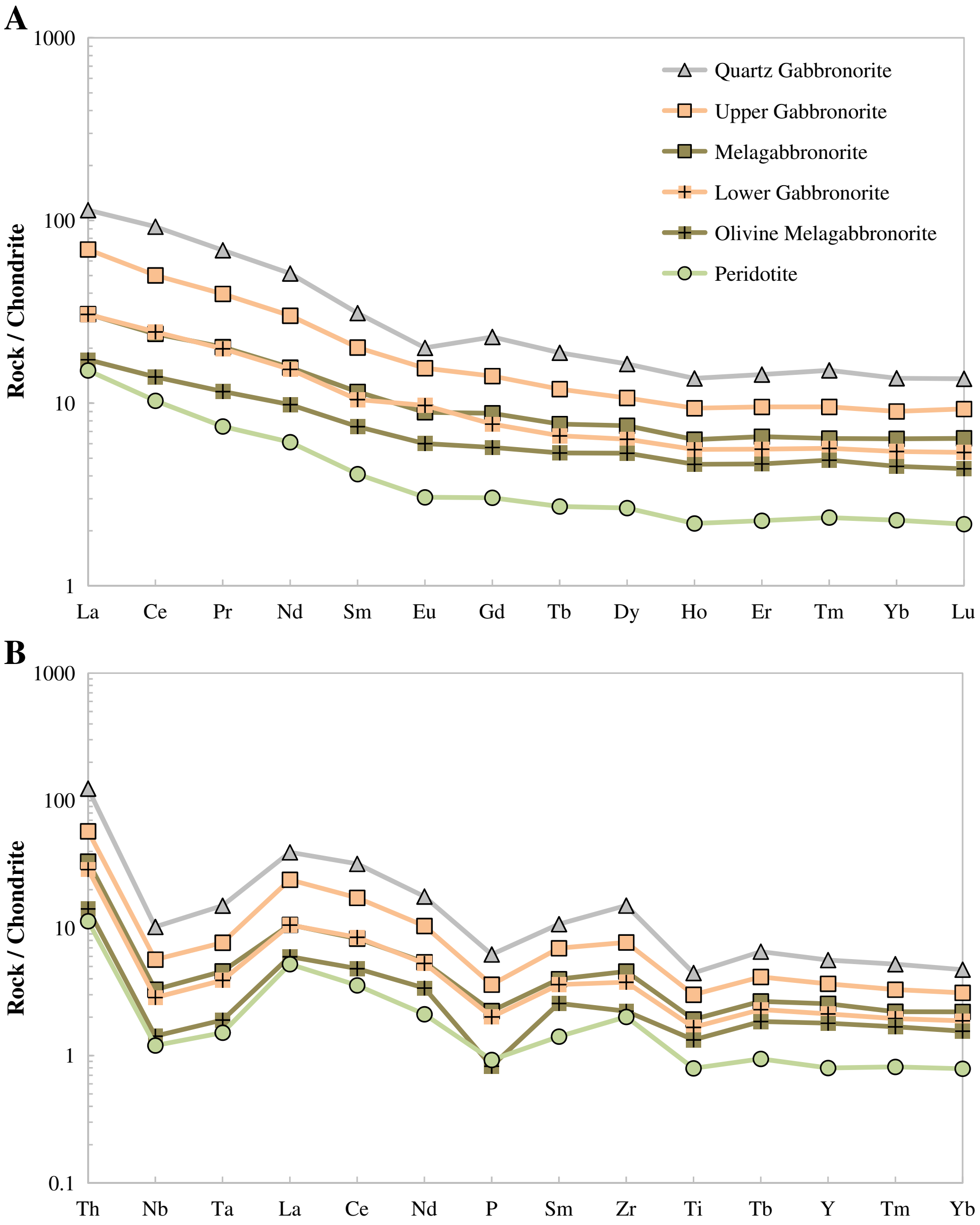

Fig. 9. Normalised trace element plots of average values of stratigraphic units in the BDM: A) Chondrite-normalised REE plot; B) Primitive mantle-normalised trace element plot. Normalising factors from McDonough and Sun (1995).

(V). These peaks in Sc and V are likely due to the dominance of pyroxene in these units, within which Sc and V are compatible.

4.4.4. Rare earth and multi-element profiles

Fig. 9A shows average chondrite-normalised REE profiles for the different stratigraphic units in the BDM with salient features from the whole data set shown in Table 2. Total abundance of REE is linked to stratigraphic height with the lowermost peridotite unit containing $\sum$REE 6.5 times chondritic values increasing with each stratigraphic unit to the most evolved rocks of the Border Zone which have $\sum$REE of 53 times chondritic values. All BDM rocks have a concave-up pattern of light-REE (LREE) enrichment with a range in $(La/Yb)_N$ (subscript N denotes chondrite normalised) of 2.4–13.0. Each stratigraphic unit in the intrusion has a sub-parallel REE pattern with slight differences in slope being explained by differences in modal mineral compositions. For example, the peridotite unit at the base of the intrusion is dominated (~90%) by altered olivine and has an average $(La/Yb)_N$ ratio of 6.6 while the immediately overlying olivine melagabbronorite unit which is dominated by altered pyroxene and subordinate amounts of altered plagioclase has an average $(La/Yb)_N$ ratio of 3.8. The difference in $(La/Yb)_N$ ratios between these two units may be explained by the greater compatibility of the heavy-REE (HREE) relative to the LREE in pyroxene compared to olivine (Bédard, 2005; 2007) thus giving the pyroxene dominated olivine melagabbronorite unit a lower $(La/Yb)_N$ ratio than the olivine dominated peridotite unit.

Consistent Eu anomalies are observed in the lower gabbronorite unit and quartz gabbronorite unit. The anomaly in the lower gabbronorite unit is slightly positive ($Eu/Eu^* = 1.07$) [$Eu/Eu^* = Eu_N/((Sm_N + Gd_N)/2)$] which likely reflects an accumulation of plagioclase in the unit after the crystallisation and removal of olivine and pyroxene to form the underlying peridotite and olivine melagabbronorite units. The quartz gabbronorite unit is the only unit in the BDM to record a sizeable negative Eu anomaly ($Eu/Eu^* = 0.74$) and this is most likely due to plagioclase fractionation.

Please cite this article as: Ciborowski, T.J.R., et al., The geochemistry and petrogenesis of the Blue Draw Metagabbro, Lithos (2012), doi:10.1016/j.lithos.2012.06.035

Table 2
Rare earth element (REE) data for each stratigraphic unit in the BDM. Unit abbreviations as in Table 1.

Unit	*n*	$(\mathrm{La/Sm})_N$ average	$(\mathrm{La/Sm})_N$ range	$(\mathrm{Gd/Yb})_N$ average	$(\mathrm{Gd/Yb})_N$ range	$\mathrm{Eu/Eu}^*$ average	$\mathrm{Eu/Eu}^*$ range	∑REE (x Chon)	∑REE range (x Chon)
QG	6	3.66	2.97–3.94	1.68	1.19–1.86	0.74	0.68–0.90	53	22–70
UG	44	3.44	2.66–5.44	1.56	1.23–1.82	0.91	0.63–1.20	31	13–64
MG	6	2.66	1.83–3.22	1.38	1.18–1.52	0.88	0.83–0.93	16	12–20
LG	10	2.93	1.88–3.26	1.41	1.09–1.60	1.07	0.84–1.20	15	11–19
OMG	9	2.33	1.63–2.78	1.27	1.13–1.40	0.91	0.63–1.23	10	7–12
P	14	3.69	2.84–5.60	1.33	1.09–1.63	0.86	0.74–0.99	7	3–19

Primitive-mantle normalised multi-element profiles (Fig. 9B) additionally reveal that all the BDM rocks have pronounced negative anomalies in Nb, Ta and Ti.

4.4.5. Platinum group elements

PGE data collected for the BDM are presented in Table 3. The PGE can be split into two subgroups (IPGE: Ru, Os, Ir; and PPGE: Pd, Pt, Rh) based on their differing behaviour during fractionation (Barnes et al., 1985; Tredoux et al., 1995). These groupings are evident in the PGE depth profiles for the BDM (Fig. 10 and Table 3) in that the IPGEs (Ir and Ru) show similar trends to each other and which are different to those of the PPGEs.

The IPGEs record their highest concentrations in the peridotite unit (up to ~6 ppb Ru and ~1.5 ppb Ir) and decrease rapidly above the peridotite unit, levelling off at ~0.3 ppb Ru and ~0.1 ppb Ir between 200 and 400 m. A second Ir-Ru peak is observed in two samples between ~400 and 500 m, above which IPGE concentrations in the BDM decrease towards detection limit (0.03 ppb) with increasing stratigraphic height.

In contrast, the PPGEs (Pt, Pd) from the peridotite unit record some of the lowest concentrations in the intrusion (~2.5 ppb Pt, 2.7 ppb Pd and 0.5 ppb Au). Above the peridotite unit, PPGE concentrations remain scattered, but low, throughout the intrusion until ~650–700 m where the Pt, Pd and Au concentrations spike up to ~14 ppb, ~60 ppb and ~3 ppb respectively. Above this zone, PPGE concentrations decrease towards 1.64 ppb Pt and 1.91 ppb Pd with increasing stratigraphic height. Rhodium shows intermediate behaviour between the IPGE and other PPGE in the BDM in that it is relatively abundant in the peridotite unit (similar to the IPGE) but also has a spike in concentration at ~650–700 m (similar to the PPGE).

The shape of primitive mantle normalised PGE patterns in BDM rocks changes with stratigraphic height (Fig. 11). The peridotite unit has relatively flat PGE patterns ($(\mathrm{(Ir/Pt)}_N = 1.18)$) while the upper gabbronorite unit and quartz gabbronorite unit rocks show more fractionated patterns [$(\mathrm{Ir/Pt})_N = 0.01$]. All BDM samples show a marked depletion in Ni and Cu relative to Ir and Pt respectively.

5. Discussion

5.1. Parental magma

Fieldwork in 2010 failed to identify potential feeder dykes to the BDM or definite chilled margin material which would record the composition of the BDM parental magma. Furthermore, scanning electron microscopy (SEM) observations have revealed that the early-formed spinels (which might have contained melt inclusions with remnants of the unfractionated parent magma) are altered and show evidence of significant recrystallisation.

We have therefore estimated the parental melt composition of the BDM by summing the compositions of each stratigraphic unit into a weighted average for the whole intrusion (e.g., James et al., 2002; Polat et al., 2011). This method is only applicable to layered intrusions that have experienced limited contamination by host rocks and have not lost evolved melts during crystallisation. There is good evidence that contamination of the BDM by the Boxelder Creek Quartzite host rocks is limited (see Section 5.3), while the evolved nature of the BDM, the presence of pegmatites (Dahl et al., 2006) and the lack of coeval volcanic material in the Boxelder Creek Quartzite or overlying Benchmark Iron Formation (Hill, 2006; Lee, 1996) suggests that the BDM did not undergo significant melt extraction and eruption.

Table 3
Platinum group element (PGE) for samples collected from the BDM. Unit abbreviations as in Table 1.

Sample	Height (m)	Unit	Ir (ppb)	Ru (ppb)	Rh (ppb)	Pt (ppb)	Pd (ppb)	Au (ppb)	Ni (ppm)	Cu (ppm)
BD076	723	QG	0.03	0.08	0.15	1.64	1.91	0.31	19	101
BD065	720	QG	0.06	0.30	0.89	14.44	59.52	2.34	168	47
BD013	705	UG	0.03	0.08	0.18	1.81	2.09	0.54	16	825
BD011	700	UG	0.24	0.24	0.48	4.88	5.10	0.84	13	543
BD008	680	UG	0.10	0.42	0.40	8.02	6.05	0.95	10	405
BD007	675	UG	0.15	0.17	0.41	6.32	4.99	0.96	48	819
BD005	663	UG	0.23	0.28	0.45	7.03	7.46	1.00	13	1125
BD004	655	UG	0.05	0.20	0.48	9.15	9.14	1.74	18	1021
BD019	645	UG	0.03	0.08	0.38	5.72	3.04	3.02	59	147
BD020	635	UG	0.07	0.30	0.30	2.41	3.92	0.67	202	65
BD025	628	UG	0.03	0.08	0.24	3.87	7.00	0.77	859	231
BD001	625	UG	0.09	0.34	0.47	4.56	7.65	1.42	459	2452
BD058	600	UG	0.13	0.51	0.63	5.23	3.52	2.49	126	69
BD056	555	UG	0.12	0.43	0.26	1.54	2.95	0.57	82	101
BD049	480	UG	0.35	0.83	0.73	9.16	24.32	2.32	139	48
BD091	410	MG	0.37	0.69	0.61	3.51	2.74	0.51	200	40
BD053	365	LG	0.11	0.27	0.35	3.22	3.93	0.69	337	45
BD096	295	LG	0.15	0.21	0.43	2.66	3.51	0.84	131	28
BD081	230	LG	0.08	0.42	0.42	3.47	8.16	1.17	115	16
BD078	178	OMG	0.42	1.45	0.49	5.70	9.35	1.34	161	91
BD044	140	OMG	0.53	2.06	1.03	3.97	5.97	0.48	365	38
BD041	110	P	1.11	3.78	0.64	2.06	2.58	0.28	877	47
BD037	65	P	1.48	6.28	0.94	2.09	2.74	0.15	1237	35
BD029	0	P	1.15	3.01	0.62	3.16	3.25	0.88	834	90

Please cite this article as: Ciborowski, T.J.R., et al., The geochemistry and petrogenesis of the Blue Draw Metagabbro, Lithos (2012), doi:10.1016/j.lithos.2012.06.035

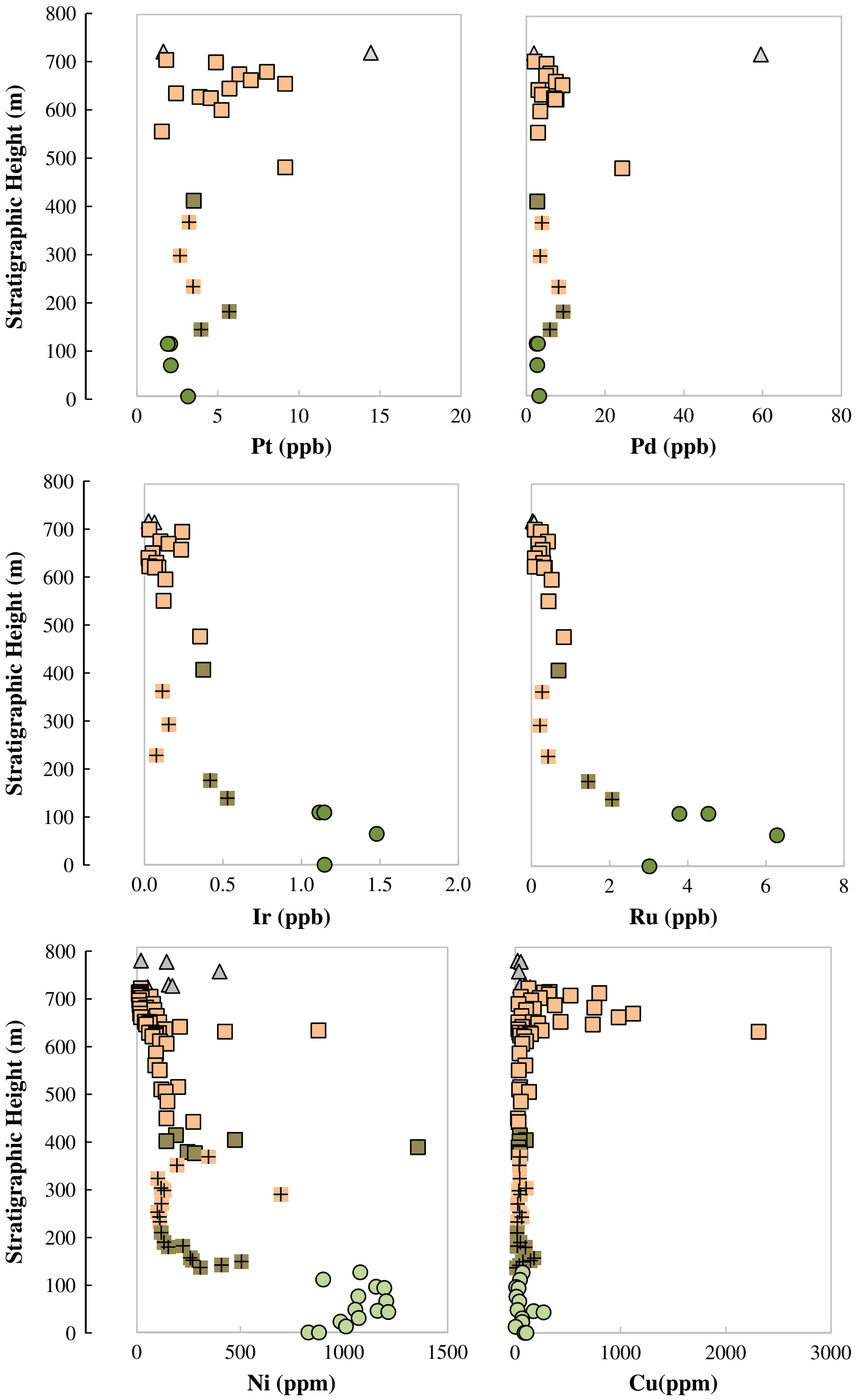

Fig. 10. Chemostratigraphic profiles through the BDM for chalcophile elements. Symbols the same as in Fig. 7.

Therefore, following a recharge of the system (see Section 5.2), the chamber appears to have crystallised under near-closed system conditions.

When calculated using the weighted-average method, the BDM parent magma is estimated to have been a basaltic magma containing ~12.7 wt.% MgO with a primitive mantle-normalised trace element pattern which shows LREE and LILE enrichment and significant negative Nb–Ta and Ti anomalies, but no significant Eu anomaly, similar to the bulk of the samples shown in Fig. 9 (see online appendix for full parental melt composition).

Fractional crystallisation of this melt was modelled using the petrogenetic software PELE (Boudreau, 1999) which is based on the Java-supported MELTS software (Ghiorso and Sack, 1995) to determine if this magma is capable of producing a bulk mineralogy similar to that observed in the BDM. The crystallisation model calculated by PELE for fractionation of the BDM parent magma uses a quartz–fayalite–magnetite (QFM) oxygen buffer at 3 kbar predicts initial crystallisation of olivine + spinel until ~15% crystallisation, at which point clinopyroxene joins the assemblage followed by plagioclase at ~22% crystallisation. The model predicts that olivine stops crystallising at ~53% which coincides

Please cite this article as: Ciborowski, T.J.R., et al., The geochemistry and petrogenesis of the Blue Draw Metagabbro, Lithos (2012), doi:10.1016/j.lithos.2012.06.035

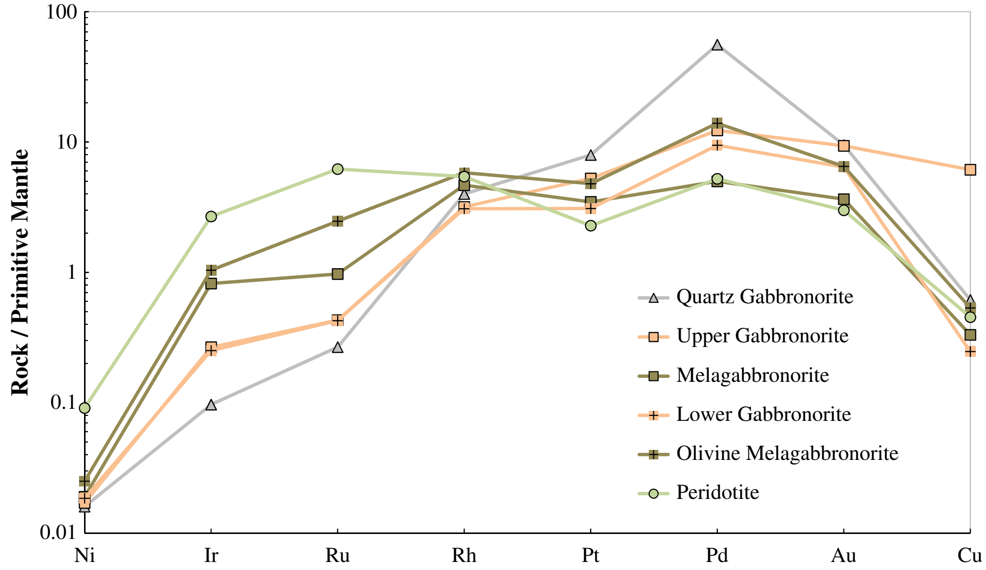

Fig. 11. Primitive mantle-normalised PGE plots for average values of stratigraphic units in the BDM. Normalising factors from McDonough and Sun (1995).

with the onset of orthopyroxene crystallisation which continues to crystallise until ~74% crystallisation. Quartz and alkali feldspar are last to form, appearing after approximately 80% of the original magma has crystallised. The crystallisation sequence predicted to form from fractionation of the proposed parental melt is in good agreement with that observed in thin section of samples from the stratigraphy of the BDM (see Section 3).

To further test the validity of the estimated parent melt, the chemistry of the cumulates predicted to form during fractional crystallisation of the melt was modelled at 5% intervals using the mineral assemblages predicted by PELE and then compared to the composition of the cumulates in the intrusion. The model predicts the first cumulates to form in the intrusion are olivine-dominated and are MgO rich (40–50 wt.%), Al_2O_3 poor (0–4 wt.%) and contain ~40 wt.% SiO_2. Crystallisation of these olivine-dominated cumulates is followed by crystallisation of clinopyroxene + plagioclase-rich rocks which are much lower in MgO (~10 wt.%), higher in Al_2O_3 (~16 wt.%) and contain ~50 wt.% SiO_2. Comparison of these modelled cumulates with the stratigraphic geochemical profiles for cumulate rocks near the base of the BDM show that the two are in good agreement (Fig. 12A and B) in terms of cumulate composition. Moreover, the model predicts that the significant compositional change between the olivine and clinopyroxene + plagioclase rich rocks occurs over a relatively short (5–10%) crystallisation interval. In this, the model is again in good agreement with the stratigraphic geochemical profiles of the intrusion which show the same stark change in cumulate chemistry occurring over

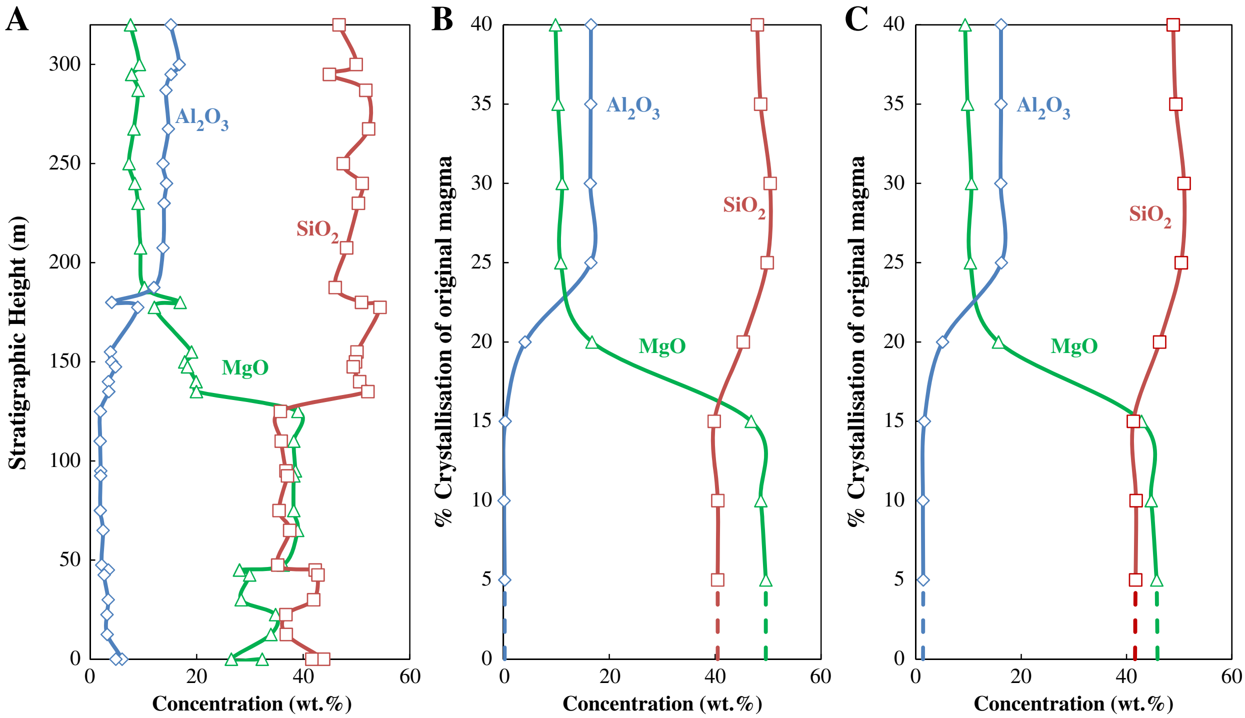

Fig. 12. Major element geochemistry of cumulate rocks from the lower half of the BDM (A). Chemistry of cumulates predicted to form at 5% intervals of crystallisation from estimated parental melt with no trapped melt fraction (B) and 10% trapped melt fraction (C). Dashed line between 0% and 5% in B and C denotes extrapolation from first data point at 5%.

Please cite this article as: Ciborowski, T.J.R., et al., The geochemistry and petrogenesis of the Blue Draw Metagabbro, Lithos (2012), doi:10.1016/j.lithos.2012.06.035

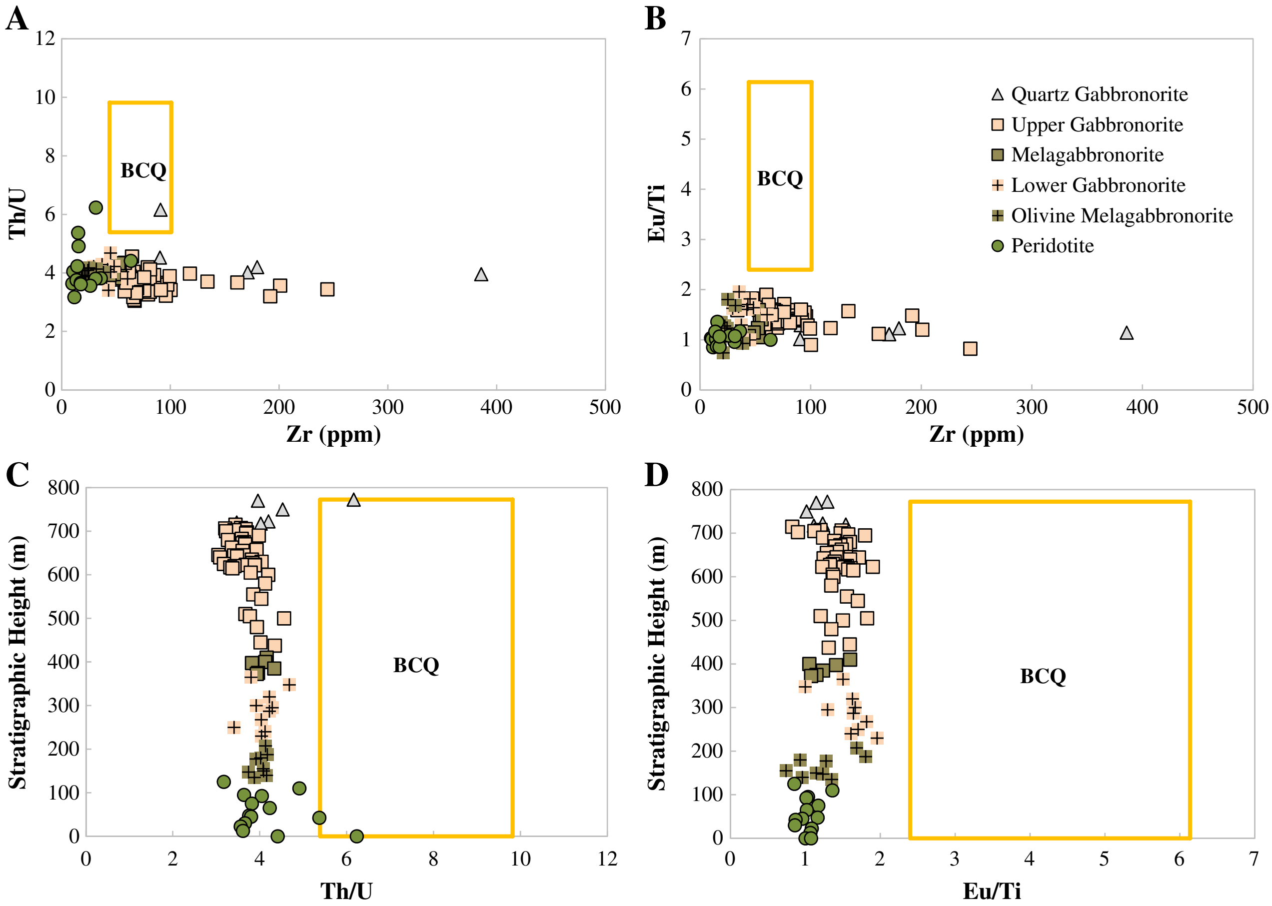

Fig. 13. Ratios of element pairs with similar bulk partition coefficients plotted against Zr (A and B) and stratigraphic height (C and D). BCQ = Boxelder Creek Quartzite. See text for determination of field size.

~10 m. The fit of the model with the data can be greatly improved by including a 10% trapped melt fraction (Fig. 12C). While these models predict much of the compositional trends in the lower portion of the BDM, the models do not perfectly predict the compositional variability of the cumulates close to the basal margin of the intrusion (between 0–40 m). However, as Section 5.3 discusses, these samples are also variable in their trace element composition and may indicate that these samples have been contaminated by the country rock hosting the intrusion.

While estimating the parental magma of layered intrusions using this method has been shown to be successful with layered intrusions similar to the BDM, (e.g., James et al., 2002; Polat et al., 2011), its applicability to the BDM is questionable. Firstly, while the evolved nature of the intrusion, presence of pegmatites and its lack of extrusive equivalents suggest that the intrusion evolved as a closed system, the possibility of the intrusion having had material extracted during eruptive episodes cannot be ruled out as any such material may have been lost during an period of erosion marked by the angular Estes unconformity which separates the Boxelder Creek Quartzite and overlying <1.89 Ga Montana Mine Formation (Frei et al., 2008).

The second issue to note is that the bimodal distribution of olivine in the peridotite unit (Fig. 4A) suggests that the BDM parent magma was intruded as a mixture of magma and olivine crystals rather

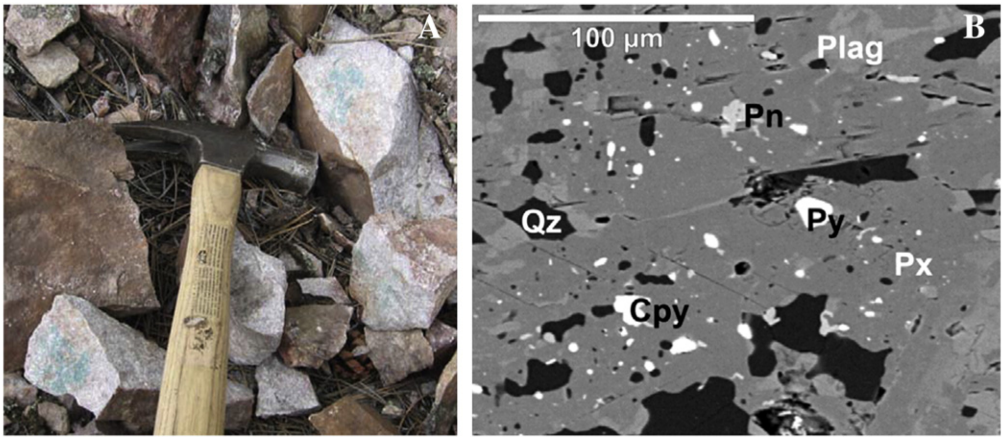

Fig. 14. Photograph (A) and SEM micrograph (B) of Cu and Ni-bearing mineralisation in the upper gabbronorite unit.

Please cite this article as: Ciborowski, T.J.R., et al., The geochemistry and petrogenesis of the Blue Draw Metagabbro, Lithos (2012), doi:10.1016/j.lithos.2012.06.035

than as a homogenous liquid. If this is the case, the composition of the olivine crystal phases injected with the melt would be erroneously included in the whole-intrusion average calculation. To address this issue, 2.64 volume % of olivine was subtracted from the weighted average to account for the estimated volume % of the peridotite unit made up of megacrystic olivine.

Despite these potential issues, given the lack of other suitable material which may be used to estimate the composition of the BDM parent magma described above, it is the opinion of the authors than the weighted-average calculation presented in this paper currently represents the best estimate of the parental magma of the BDM intrusion.

5.2. Recharge

Chemostratigraphic profiles for the BDM show a significant and ubiquitous change in composition at ~300–350 m from the base of the intrusion to less evolved compositions, most obviously signified by spikes in the concentration of compatible elements (Fig. 8). These geochemical trends coincide with a return of olivine to the normative mineralogy and suggest that after ~300 m of cumulates had formed, the system was recharged by a less fractionated magma which mixed with the residual melt fraction retained in the chamber before the resulting hybrid melt fractionated again.

The sub-parallel nature of the REE and trace element patterns (Fig. 9) show that the rocks above and below the postulated recharge event have indistinguishable incompatible trace element ratios. This indicates that the parental melts from which these cumulates crystallised were likewise compositionally indistinguishable and that the recharging magma was simply a second batch of the initial, less-fractionated BDM magma.

Although the trace element data appear to record the recharge event at ~370 m (Fig. 8), the major element and compatible trace element data suggest recharge occurs at ~350 m. Two possible reasons for this are: (1) Melt trapping: The recharging melt is injected through the permeable gabbroic crystal mush near the cumulate-melt interface at ~350–370 m. Small quantities of the recharging magma are trapped as interstitial networks within the crystal mush which, on crystallisation, alter the whole-rock trace element chemistry of the rock, but do not significantly affect the major element chemistry. Above the crystal mush, olivine fractionates from the hybrid melt and forms MgO-rich cumulates above ~370 m. (2) Crystal settling: The recharging magma is injected into the BDM after ~350 m of cumulates have formed and mixes with the remaining melt fraction. Plagioclase and pyroxene crystals near to the cumulate/melt interface continue to grow in equilibrium with the new hybrid melt and record more primitive trace element chemistry while MgO-bearing minerals crystallising from the melt take time to form and settle into a cumulate horizon causing the MgO concentration spike observed in the depth profiles to appear higher up in the stratigraphy.

5.3. In-situ contamination

Assimilation of country rock by a magma undergoing fractional crystallisation (AFC) is a common process in the petrogenesis of layered intrusions (e.g., Amelin et al., 1996; Maier et al., 2000; Palacz, 1985). Crustal assimilation is also important from an economic perspective as it is thought to be a key prerequisite in the formation of Ni–Cu–PGE deposits (Maier, 2005; Naldrett, 1999).

The importance of assimilation of country rock during fractionation of the BDM can be investigated using the trace element chemistry of the intrusion. As the BDM intrudes (and is entirely hosted by) the Boxelder Creek Quartzite (Fig. 2), the Boxelder Creek Quartzite represents the most obvious crustal contaminant of the BDM. To test whether AFC operated during crystallisation of the BDM, trace element ratios which are insensitive to fractional crystallisation are plotted for both the BDM and Boxelder Creek Quartzite against Zr (used as a fractionation index) and stratigraphic height (Fig. 13). In these diagrams, the Boxelder Creek Quartzite (BCQ) is plotted as a field defined by the average value of the Boxelder Creek Quartzite ($n=6$) ± one standard deviation in an attempt to display the variable trace element composition of the unit.

When plotted against fractionation indices (Fig. 13A and B), the trace element ratios exhibited by the BDM remain largely constant, i.e., the trace element composition of the BDM magma does not change as fractional crystallisation progresses and does not appear to trend towards the discrete fields of the Boxelder Creek Quartzite as would be expected if AFC were to have operated during the evolution of the BDM. As the BDM shows general trends of increased fractionation with increasing stratigraphic height (Fig. 8), it would be expected that the rocks near the top of the intrusion would be the most contaminated with the Boxelder Creek Quartzite host rock if AFC had occurred. However, as Fig. 13C and D show, there is no systematic change in contaminant-sensitive trace element ratios towards the top of the intrusion, nor is there a change in the Nb/Nb* anomaly [$\mathrm{Nb/Nb^* = Nb_N/((Th_N + La_N)/2)}$] in any but the most evolved rocks in the Quartz Gabbronorite (Fig. 9B), which suggests that assimilation of the host Boxelder Creek Quartzite occurred on an insignificant scale during crystallisation of the intrusion and may only be limited to rocks crystallising very close to the intrusion margins, as indicated by the slight variation in trace element composition of rocks sampled from these areas.

The data therefore demonstrate that the trace element chemistry of the BDM did not change to increasingly resemble that of the hosting Boxelder Creek Quartzite during fractional crystallisation of the parent magma. This suggests that AFC did not operate during the evolution of the BDM, and that if any contamination of the BDM parent magma occurred, then it must have happened prior to the emplacement of the BDM, potentially during fractionation of the BDM in a deeper crustal chamber.

5.4. Mineralisation

Intrusions genetically linked to the BDM, including the EBLS, host significant contact-type Ni–Cu–PGE sulphide mineralisation (James et al., 2002; Peck et al., 1995; Vogel et al., 1999), the economic potential of which is currently being explored. If the proposed genetic link between the BDM and EBLS exists, then we need to ask the question why significant economic Ni–Cu–PGE mineralisation of the type observed in the EBLS is not present in BDM.

Primary sulphides are not observed in BDM outcrops in the study area, however, abundant malachite staining is present in outcrops near the upper contact of the intrusion (Fig. 14A) and very fine grained disseminated Cu- and Ni-bearing sulphides are present in the most evolved BDM rocks (Fig. 14B). In order to better constrain where any potential Ni–Cu–PGE mineralisation may be present in the BDM, chemostratigraphic profiles of Ni, Cu, the PGE and other associated elements can be used to identify prospective horizons (Fig. 10). The chemostratigraphic profile of Ni shows three conspicuous peaks in concentration at ~50, ~370 and ~650 m, of which the two lowest peaks correspond to the highest concentrations in MgO (Fig. 8) which indicates that the Ni concentration peaks at ~50 and ~370 m are caused by the presence of olivine-rich cumulates in which Ni is compatible.

The lowermost of these peaks also corresponds to the highest IPGE concentrations but the lowest PPGE concentrations (Fig. 10), which suggests that during accumulation of the olivine-rich Peridotite unit, the IPGE have behaved compatibly while the PPGE have behaved incompatibly. This decoupling of the PGE in fractionated systems is commonly observed and has been explained either by the IPGE being compatible during olivine and/or chrome spinel fractionation (Brenan et al., 2003; Capobianco and Drake, 1990) or by the

Please cite this article as: Ciborowski, T.J.R., et al., The geochemistry and petrogenesis of the Blue Draw Metagabbro, Lithos (2012), doi:10.1016/j.lithos.2012.06.035

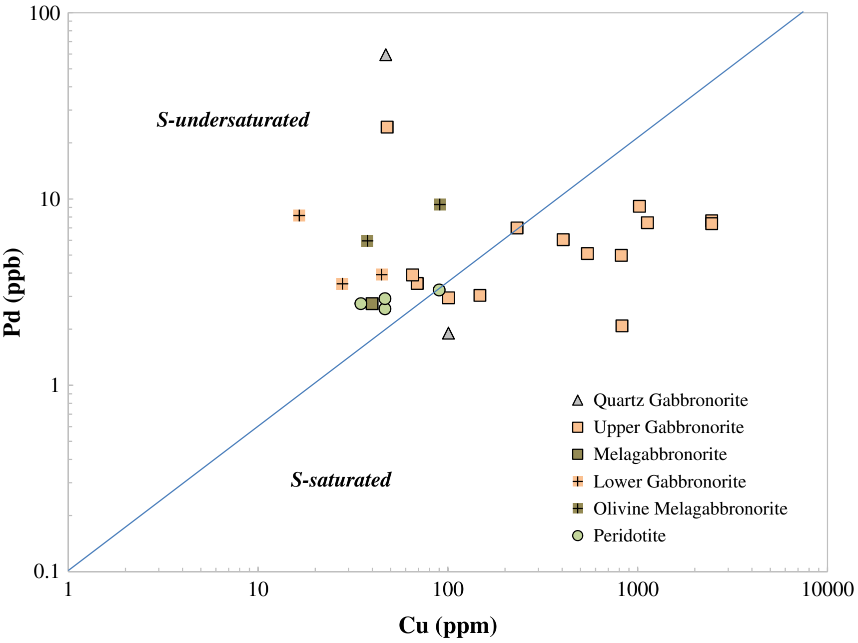

Fig. 15. Cu vs. Pd diagram (Vogel and Keays, 1997) for discriminating between sulphur saturated and sulphur undersaturated BDM rocks.

precipitation of IPGE (but not PPGE) alloys directly from the magma (Tredoux et al., 1995) or in local reduction fronts at chromite grain boundaries (Finnigan et al., 2008). The uppermost peak in Ni at ~650 m coincides with a conspicuous spike in Cu and highest Pd(+Pt) and Au concentrations in the intrusion (Fig. 10). These associations suggest that these chalcophile elements are present together in sulphide phases. SEM imaging of rocks from this stratigraphic height has confirmed the presence of very fine grained (≤ 12 μm) disseminated sulphides, dominated by pyrite and chalcopyrite (Fig. 14B). The presence of these minerals indicates that through fractional crystallisation, the BDM magma attained sulphur saturation and precipitated Ni–Cu–PGE-bearing sulphides — a key prerequisite in Ni–Cu–PGE deposit formation (Naldrett, 1999). Despite this, the BDM contains decidedly uneconomic concentrations of PGE (Pt + Pd + Au < 80 ppb). These concentrations of precious metals are in stark contrast to those recorded by other tholeiitic layered intrusions (e.g. Skaergaard and Sonju Lake) which preserve well defined, stratiform zones of significant PGE-bearing sulphide mineralisation, which (in the case of Skaergaard) can contain up to 5.5 ppm Pt + Pd (Andersen et al., 1998; Miller, 1999).

In order for a mafic-ultramafic magma to form an economic Ni–Cu–PGE deposit, the magma must first precipitate an immiscible sulphide liquid through crystallisation and/or interaction with crustal rocks (e.g., (Arndt et al., 2005; Maier, 2005; Naldrett, 2011)). This sulphide liquid must then raise its PGE tenor by scavenging chalcophile elements from chalcophile element-bearing silicate magma, either through interaction with magma already in the chamber (e.g., Andersen et al., 1998) or through interaction with recharging pulses of sulphur-undersaturated magma (e.g., Kerr and Leitch, 2005; Peck et al., 2001). However, data from the BDM suggest that the intrusion lacks some of these crucial steps. First, trace element data (Fig. 13 and Section 5.3) indicate that no appreciable in-situ contamination of the BDM occurred during fractionation of the magma. With no additional sulphur assimilated from the potential sedimentary contaminant with which to trigger sulphur saturation of the magma, the BDM was limited to reaching sulphur saturation through fractional crystallisation of Fe-bearing silicate minerals. Secondly, while there is good evidence of the BDM having undergone magma recharge during crystallisation (Fig. 8 and Section 5.2), geochemical evidence suggests that recharge of the system occurred prior to sulphide saturation, meaning that there was no immiscible sulphide liquid present to scavenge chalcophile elements from the recharging magma. Thirdly, incompatible element trends through the intrusion (Fig. 8) suggest that the BDM formed through fractional crystallisation and gravity settling to build an igneous stratigraphy upwards from the base of the intrusion. If this interpretation is correct, then sulphur saturation of the magma occurred after most (~75%) of the intrusion had crystallised. The immiscible sulphide liquid would thus have been restricted to concentrate the Ni–Cu–PGE budget of a relatively small amount of magma which had already seen extensive removal of Ni + IPGE by silicate fractionation.

These data suggest that the BDM parent magma was metal-bearing and sulphur-undersaturated when it was injected into the Boxelder Creek Quartzite. The melt reached sulphur saturation through fractional crystallisation of silicates to produce a low-grade (Pt + Pd + Au < 80 ppb) disseminated sulphide zone near the top of the upper gabbronorite unit. This interpretation is strengthened when the data from the BDM is plotted on the Cu vs. Pd sulphur-saturation discrimination diagram (Fig. 15) of (Vogel and Keays, 1997). On this diagram, the peridotite, olivine melagabbronorite, lower gabbronorite and melagabbronorite units plot inside the sulphur-undersaturated field indicating that they formed from a sulphur-undersaturated magma, while samples from the quartz gabbronorite and upper gabbronorite units mainly plot in the sulphur-saturated field, which indicates that during fractional crystallisation to form the upper gabbronorite unit, the BDM magma reached sulphur saturation.

5.5. Magma source

Based on coeval geochronology of intrusive units (Dahl et al., 2006), similar tectonic relationships (Vogel et al., 1998b), stratigraphic similarities in associated sedimentary sequences (Roscoe and Card, 1993) and consistent palaeomagnetic properties of coeval mafic dyke swarms (Harlan, 2005), the BDM has been genetically linked to the East Bull Lake Suite of layered intrusions. The East Bull Lake Suite along with the Matachewan radiating dyke swarm and the Elliot Lake flood basalt province are all preserved on the Superior craton and have been interpreted as the remnants of the Matachewan Large Igneous Province (LIP) which formed from mantle melting initiated during plume-driven continental break-up (Bryan and Ernst, 2008; Ernst, 2007; Heaman, 1997; James et al., 2002; Phinney and Halls, 2001). Paradoxically, the

Please cite this article as: Ciborowski, T.J.R., et al., The geochemistry and petrogenesis of the Blue Draw Metagabbro, Lithos (2012), doi:10.1016/j.lithos.2012.06.035

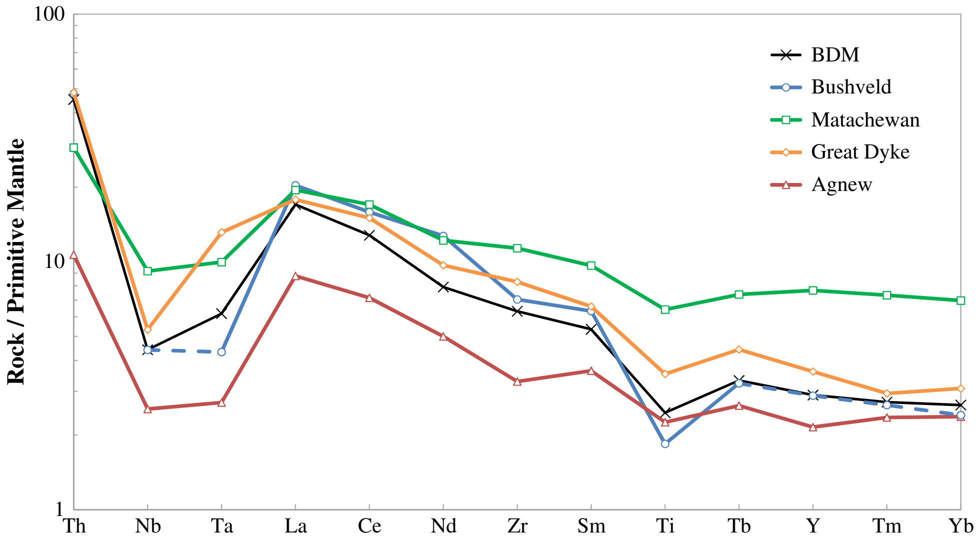

Fig. 16. Primitive-mantle normalised trace element plots of different Archaean–Palaeoproterozoic magmatic rocks. BDM = parent magma composition of the BDM as calculated by this study. Bushveld = Basaltic andesite parent magma (Barnes and Maier, 2002). Matachewan = Average composition of Matachewan dykes (Halls et al., 2005). Great dyke = Average composition of satellite dyke samples (Stubbs et al., 1999). Agnew = Streich dyke composition (Vogel, 1996). Normalising factors from McDonough and Sun (1995).

trace element geochemistry of these different LIP units (as well as the BDM) do not record a typical "mantle plume-like" OIB signature and instead display signatures which are characterised by negative anomalies in Nb, Ta, Ti and P (Halls et al., 2005; James et al., 2002; Jolly, 1987a; Phinney and Halls, 2001; Vogel, 1996). These trace element signatures are typical in igneous rocks formed in modern volcanic arc settings (Pearce and Peate, 1995) and thus, previous studies have interpreted the trace element chemistry recorded by the BDM to be evidence of formation in such an environment (Van Boening, 2007; Van Boening and Nabelek, 2008).

However, the arc-like trace element compositions shown by the BDM are shared by other ~2.48 Ga rocks which preserve field evidence that precludes them having formed in an arc environment, including the Agnew intrusion, Matachewan radiating dyke swarm (Phinney and Halls, 2001), and flood basalts from within the Huronian Supergroup (Jolly, 1987b) which suggests that using geochemistry alone to determine the tectonic settings of igneous rocks (especially ones as ancient as the BDM) is inadvisable (see Wang and Glover, 1992). Furthermore, field and geochronological evidence suggest that the BDM was intruded into the Boxelder Creek Quartzite, which is stratigraphically and temporally linked to equivalent units in the Snowy Pass and Huronian Supergroups widely interpreted to have formed during extension and continental rifting between 2.5 and 2.45 Ga (Bekker et al., 2005; Heaman, 1997; Roscoe and Card, 1993). Therefore, an alternative mechanism for the generation of negative Nb–Ta and Ti anomalies is required in order to explain the trace element geochemistry of the BDM. Such alternative explanations which have been proposed to explain similar geochemistry in other ~2.48 Ga rocks include: the contamination of mantle melts by crustal material in deep-mid level crustal chambers (e.g., Nelson et al., 1990); partial melting of sub-continental lithospheric mantle (SCLM) which has previously been modified by subduction-related fluids (Sandeman and Ryan, 2008); or the existence of a fundamental difference in the geochemistry of the ancient mantle compared to the modern mantle, imposed during early differentiation of the Earth (Vogel et al., 1998a).

The bimodal distribution of olivine present in the peridotite unit (Fig. 3A) suggests that the BDM was intruded as a melt + olivine crystal mush indicating that prior to its intrusion into the Boxelder Creek Quartzite, the BDM parent magma was stored in a deeper crustal chamber where it began to fractionate olivine. It is possible that during this period of storage and fractionation, the BDM magma assimilated and was contaminated by Archaean host rocks which imbued the magma with its significant Nb–Ta and Ti anomalies. Comparing the trace element chemistry of rocks formed prior to and following the recharge event, however, indicates that the trace element geochemistry of the two magma pulses is very similar (Fig. 9). If we assume that the recharging magma is sourced from the same deeper crustal chamber undergoing AFC as the original pulse, then in order to maintain such a consistent trace element chemistry between the two magma pulses, the contaminant affecting the magma stored in the deeper crustal chamber would have to have a trace element chemistry very similar to the BDM magma, or, for assimilation in the deeper chamber to have ceased following the extraction of the first BDM magma pulse. Neither of these potential explanations appear likely and instead, the data are better explained by assuming that crustal contamination of the BDM parent magma while it was stored in the deeper magma chamber was insignificant, just as it has been shown to be during fractionation of the BDM itself.

The geochemical anomalies described above are quite common in Archaean–Palaeoproterozoic intracontinental magmatic rocks coeval with the BDM (Vogel et al., 1998a) and the debate regarding the magmatic source of such widespread rocks which retain signatures more associated with modern subduction-related rocks is ongoing (Baker et al., 1996; Gallagher and Hawkesworth, 1992; Sandeman and Ryan, 2008; Vogel et al., 1998a; Xie et al., 1993) and not something this study aims to resolve. However, as crustal contamination is deemed an unlikely mechanism for generating the Nb–Ta and Ti anomalies observed in the BDM (see Section 5.3), we interpret these anomalies to have been inherited from the BDM parent magma's mantle source, either through mixing of partial melts of a subduction-modified SCLM with partial melts of other mantle reservoirs, including depleted mid-ocean ridge mantle (DMM), enriched mid-ocean ridge mantle (E-MORB) or deeper, undepleted primitive mantle (e.g., Sandeman and Ryan, 2008) or by partial melting of a poorly understood Archaean–Palaeoproterozoic reservoir defined by higher LILE and LREE concentrations relative to HFSE and HREE, (e.g., Vogel et al., 1998a).

5.6. Tectonic setting of the BDM

Previous geochemical studies of the BDM by Van Boening (2007) and Van Boening and Nabelek (2008) conclude that the BDM formed in a volcanic arc environment as opposed to the more widely accepted continental rift setting (Bleeker and Ernst, 2006; Dahl et al., 2006;

Please cite this article as: Ciborowski, T.J.R., et al., The geochemistry and petrogenesis of the Blue Draw Metagabbro, Lithos (2012), doi:10.1016/j.lithos.2012.06.035

Ernst and Bleeker, 2010; Heaman, 1997). Van Boening (2007) and Van Boening and Nabelek (2008) based much of their interpretation on tectonic discrimination diagrams which assign magmatic rocks to tectonic environments solely based on their geochemistry. However, in suites of altered rocks as old as the BDM, this approach is overly simplistic and does not provide sufficient evidence for the original tectonomagmatic setting of these rocks (see discussion in Duncan, 1987 and Wang and Glover, 1992), particularly where other information regarding their formation is lacking or equivocal and especially as fundamental questions regarding the chemistry and structure of the Archaean–Palaeoproterozoic mantle remain.

While the BDM records a similar chemistry to the EBLS and other associated rocks preserved on the Superior craton, it also records a geochemical signature very similar to other entirely unrelated Palaeoproterozoic magmatic rocks (Fig. 16). The ubiquitous nature of the geochemistry recorded by these ancient magmatic rocks makes it difficult to use the geochemistry of the BDM as presented in this paper to definitively test the continental reconstructions presented by others, (e.g., Bleeker, 2004; Dahl et al., 2006; Ernst and Bleeker, 2010; Heaman, 1997). Instead, future work should use geochemistry in tandem with high-precision U-Pb geochronology and palaeomagnetic studies to fully constrain continental reconstructions involving such ancient magmatic systems. Our understanding of the petrogenesis of the BDM and its relationship to the coeval EBLS will be aided by studying mafic dyke swarms preserved in Laramide uplifts of Archaean–Palaeoproterozoic crust in the Wyoming craton (e.g., Harlan, 2005). This approach will better place the BDM in both space and time and allow more rigorous comparisons of its geochemistry with other, potentially related rocks.

6. Summary and conclusions

1. The parental magma of the BDM is a sulphur-undersaturated basalt, formed from partial melting of a mantle source enriched in the LILE and LREE relative to the HFSE and HREE.
2. Prior to its intrusion into the Boxelder Creek Quartzite, the BDM parent melt ponded in a mid-deep level crustal chamber where it began to fractionate olivine with insignificant assimilation of host rocks. This mid-deep level crustal chamber was periodically tapped, with melt fractions migrating from the chamber and intruding into the Boxelder Creek Quartzite as a melt + olivine crystal mush through a currently unexposed or eroded system of feeder dykes.
3. After intrusion into the Boxelder Creek Quartzite, the BDM parental magma fractionated cumulate sequences of olivine + spinel, followed by clinopyroxene, plagioclase, orthoclase and quartz with insignificant assimilation of the Boxelder Creek Quartzite host rock. After ~50% of the original parent magma had fractionated, the system was recharged by a more primitive batch of magma before fractionating again under closed system conditions.
4. Fractional crystallisation of silicates caused the BDM parent magma to reach sulphur saturation late in its evolution which produced a ~50 m thick zone of very low-grade, disseminated Cu-Ni-PGE mineralisation near the top of the intrusion.

Acknowledgements

This study forms part of a Ph.D. dissertation undertaken by T.J.R.C. at the University of Cardiff, United Kingdom. P. Dahl's assistance in planning the 2010 field season is greatly appreciated. L. Badham, A. Oldroyd, L. Woolley and P. Fisher are thanked for their help in preparation and analysis of samples. Discussions with A. Hastie regarding the Blue Draw were invaluable. Troy and Willie Saye, and the staff of Nemo Guest Ranch are very much thanked for their hospitality and logistical support during the 2010 field season. This manuscript benefited greatly from reviews by Jean Bédard and an anonymous reviewer.

Appendix A. Supplementary data

Supplementary data to this article can be found online at http://dx.doi.org/10.1016/j.lithos.2012.06.035.

References

Amelin, Y.V., Neymark, L.A., Ritsk, E.Y., Nemchin, A.A., 1996. Enriched Nd–Sr–Pb isotopic signatures in the Dovyren layered intrusion (eastern Siberia, Russia): evidence for source contamination by ancient upper-crustal material. Chemical Geology 129, 39–69.

Andersen, J.C.O., Rasmussen, H., Nielsen, T.F.D., Ronsbo, J.G., 1998. The Triple Group and the Platinova gold and palladium reefs in the Skaergaard Intrusion; stratigraphic and petrographic relations. Economic Geology 93, 488–509.

Arndt, N.T., Lesher, C.M., Czamanske, G.K., 2005. Mantle-derived magmas and magmatic Ni–Cu–(PGE) deposits. Economic Geology 100th Anniversary Volume, pp. 5–23.

Baker, J.A., Thirlwall, M.F., Menzies, M.A., 1996. Sr–Nd–Pb isotopic and trace element evidence for crustal contamination of plume-derived flood basalts: Oligocene flood volcanism in western Yemen. Geochimica et Cosmochimica Acta 60, 2559–2581.

Barnes, S.-J., Gomwe, T.S., 2011. The Pd deposits of the Lac des Iles Complex, Northwestern Ontario. In: Li, C., Ripley, E.M. (Eds.), Magmatic Ni–Cu and PGE deposits: Geology, Geochemistry, and Genesis. Society of Economic Geologists, Denver, Colorado, pp. 351–370.

Barnes, S.-J., Maier, W.D., 2002. Platinum-group element distributions in the Rustenberg Layered Suite of the Bushveld Complex, South Africa. In: Cabri, L.J. (Ed.), The Geology, Geochemistry, Mineralogy and Mineral Beneficiation of Platinum-Group Elements. Canadian Institute of Mining, Metallurgy and Petroleum, Special Volume 54, pp. 431–458.

Barnes, S.-J., Naldrett, A.J., Gorton, M.P., 1985. The origin of platinum-group elements in terrestrial magmas. Chemical Geology 53, 303–323.

Bédard, J.H., 2005. Partitioning coefficients between olivine and silicate melts. Lithos 83, 394–419.

Bédard, J.H., 2007. Trace element partitioning coefficients between silicate melts and orthopyroxene: parameterizations of D variations. Chemical Geology 244, 263–303.

Bekker, A., Kaufman, A.J., Karhu, J.A., Eriksson, K.A., 2005. Evidence for Paleoproterozoic cap carbonates in North America. Precambrian Research 137, 167–206.

Bleeker, W., 2004. Taking the pulse of planet Earth: a proposal for a new multi-disciplinary flagship project in Canadian solid earth sciences. Geoscience Canada 31, 179–190.

Bleeker, W., Ernst, R., 2006. Short-lived mantle generated magmatic events and their dyke swarms: the key unlocking Earth's paleogeographic record back to 2.6 Ga. In: Hanski, E., Mertanen, S., Rämö, T., Vuollo, T., Taylor, J. (Eds.), Dyke Swarms — Time Markers of Crustal Evolution. Balkema Publishers, Rotterdam, pp. 3–26.

Boudreau, A.E., 1999. PELE-a version of the MELTS software program for the PC platform. Computers and Geosciences 25, 201–203.

Brenan, J.M., McDonough, W.F., Dalpé, C., 2003. Experimental constraints on the partitioning of rhenium and some platinum-group elements between olivine and silicate melt. Earth and Planetary Science Letters 212, 135–150.

Bryan, S.E., Ernst, R.E., 2008. Revised definition of large igneous provinces (LIPs). Earth-Science Reviews 86, 175–202.

Capobianco, C.J., Drake, M.J., 1990. Partitioning of ruthenium, rhodium, and palladium between spinel and silicate melt and implications for platinum group element fractionation trends. Geochimica et Cosmochimica Acta 54, 869–874.

Chamberlain, K.R., Frost, C.D., Frost, B.R., 2003. Early Archean to Mesoproterozoic evolution of the Wyoming Province: Archean origins to modern lithospheric architecture. Canadian Journal of Earth Sciences 40, 1357–1374.

Dahl, P.S., Hamilton, M.A., Wooden, J.L., Foland, K.A., Frei, R., McCombs, J.A., Holm, D.K., 2006. 2480 Ma mafic magmatism in the northern Black Hills, South Dakota: a new link connecting the Wyoming and Superior cratons. Canadian Journal of Earth Sciences 1579–1600.

Duncan, A.R., 1987. The Karoo igneous province — a problem area for inferring tectonic setting from basalt geochemistry. Journal of Volcanology and Geothermal Research 32, 13–34.

Easton, R.M., James, R.S., Jobin-Bevans, L.S., 2010. Geological guidebook to the Paleoproterozoic East Bull Lake intrusive suite plutons at East Bull Lake, Agnew Lake and River Valley. Ontario Geological Survey, Open File Report 6253. . 108 pp.

Ernst, R.E., 2007. Large igneous provinces in Canada through time and their metallogenic potential. In: Goodfellow, W.D. (Ed.), Mineral Deposits of Canada: A Synthesis of Major Deposit-Types, District Metallogeny, the Evolution of Geological Provinces, and Exploration Methods: Special Publication- Geological Association of Canada, Mineral Deposits Division, vol. 5, pp. 929–937.

Ernst, R.E., Bleeker, W., 2010. Large igneous provinces (LIPs), giant dyke swarms, and mantle plumes: significance for breakup events within Canada and adjacent regions from 2.5 Ga to the Present. Canadian Journal of Earth Sciences 47, 695–739.

Finnigan, C.S., Brenan, J.M., Mungall, J.E., McDonough, W.F., 2008. Experiments and models bearing on the role of chromite as a collector of platinum group minerals by local reduction. Journal of Petrology 49, 1647–1665.

Foster, D.A., Mueller, P.A., Mogk, D.W., Wooden, J.L., Vogl, J.J., 2006. Proterozoic evolution of the western margin of the Wyoming craton: implications for the tectonic

Please cite this article as: Ciborowski, T.J.R., et al., The geochemistry and petrogenesis of the Blue Draw Metagabbro, Lithos (2012), doi:10.1016/j.lithos.2012.06.035

and magmatic evolution of the northern Rocky Mountains. Canadian Journal of Earth Sciences 43, 1601–1619.

Frei, R., Dahl, P.S., Duke, E.F., Frei, K.M., Hansen, T.R., Frandsson, M.M., Jensen, L.A., 2008. Trace element and isotopic characterization of Neoarchean and Paleoproterozoic iron formations in the Black Hills (South Dakota, USA): assessment of chemical change during 2.9–1.9 Ga deposition bracketing the 2.4–2.2 Ga first rise of atmospheric oxygen. Precambrian Research 162, 441–474.

Gallagher, K., Hawkesworth, C., 1992. Dehydration melting and the generation of continental flood basalts. Nature 358, 57–59.

Ghiorso, M.S., Sack, R.O., 1995. Chemical mass transfer in magmatic processes IV. A revised and internally consistent thermodynamic model for the interpolation and extrapolation of liquid–solid equilibria in magmatic systems at elevated temperatures and pressures. Contributions to Mineralogy and Petrology 119, 197–212.

Gosselin, D.C., Papike, J.J., Shearer, C.K., Peterman, Z.E., Laul, J.C., 1990. Geochemistry and origin of Archean granites from the Black Hills, South Dakota. Canadian Journal of Earth Sciences 27, 57–71.

Halls, H.C., Stott, G.M., Davis, D.W., 2005. Paleomagnetism, geochronology and geochemistry of several Proterozoic mafic dike swarms in northwestern Ontario. Ontario Geological Survey, Open File Report 6171. . 59 pp.

Harlan, S.S., 2005. The Paleoproterozoic Leopard Dikes of Montana and Wyoming: A Dismembered fragment of the 2.45Ga Hearst-Matachewan giant radiating dike swarm of the Superior Craton? Geological Society of America Abstracts with Programs 37, 50.

Heaman, L.M., 1997. Global mafic magmatism at 2.45 Ga: remnants of an ancient large igneous province? Geology 25, 299–302.

Hill, J. C., 2006. Structural geology and tectonics of the paleoproterozoic rocks of the Mount Rushmore quadrangle, Black Hills, South Dakota. PhD thesis. University of Missouri, Missouri.

Huber, H., Koeberl, C., McDonald, I., Reimold, W.U., 2001. Geochemistry and petrology of Witwatersrand and Dwyka diamictites from South Africa: search for an extraterrestrial component. Geochimica et Cosmochimica Acta 65, 2007–2016.

Irvine, T.N., Baragar, W.R.A., 1971. A guide to the chemical classification of the common volcanic rocks. Canadian Journal of Earth Sciences 8, 523–548.

James, R.S., Easton, R.M., Peck, D.C., Hrominchuk, J.L., 2002. The East Bull Lake Intrusive Suite: remnants of a 2.48 Ga large igneous and metallogenic province in the Sudbury area of the Canadian Shield. Economic Geology 97, 1577–1606.

Jolly, W.T., 1987a. Geology and geochemistry of Huronian rhyolites and low-Ti continental tholeiites from the Thessalon region, central Ontario. Canadian Journal of Earth Sciences 24, 1360–1385.

Jolly, W.T., 1987b. Lithophile elements in Huronian low-Ti continental tholeiites from Canada, and evolution of the Precambrian Mantle. Earth and Planetary Science Letters 85, 401–415.

Kerr, A., Leitch, A.M., 2005. Self-destructive sulfide segregation systems and the formation of high-grade magmatic ore deposits. Economic Geology 100, 311–332.

Le Maitre, R.W., 2002. Igneous Rocks: A Classification and Glossary of Terms, Recommendations of the International Union of Geological Sciences Subcommission on the Systematics of Igneous Rocks. Cambridge University Press, Cambridge, p. 236.

LeBas, M.J., LeMaitre, R.W., Streckeisen, A., Zanettin, B., 1986. A chemical classification of volcanic rocks based on the total alkali-silica diagram. Journal of Petrology 27, 745–750.

Lee, K. H., 1996. Structure and geochemistry of the Nemo area Black Hills, South Dakota, United States of America. PhD thesis. University of Nebraska, Lincoln.

Maier, W.D., 2005. Platinum-group element (PGE) deposits and occurrences: mineralization styles, genetic concepts, and exploration criteria. Journal of African Earth Sciences 41, 165–191.

Maier, W.D., Arndt, N.T., Curl, E.A., 2000. Progressive crustal contamination of the Bushveld Complex: evidence from Nd isotopic analyses of the cumulate rocks. Contributions to Mineralogy and Petrology 140, 316–327.

Maranate, S., 1979. Petrogenesis of a layered amphibolite sill in the Nemo district, Black Hills, South Dakota. MSc thesis. South Dakota School of Mines and Technology, Rapid City.

McDonald, I., Viljoen, K.S., 2006. Platinum-group element geochemistry of mantle eclogites: a reconnaissance study of xenoliths from the Orapa kimberlite, Botswana. Transactions of the Institutions of Mining and Metallurgy, Section B 115, 81–91.

McDonough, W.F., Sun, S.S., 1995. The composition of the Earth. Chemical Geology 120, 223–253.

Miller, J.D., 1999. Geochemical evaluation of platinum group element (PGE) mineralization in the Sonju Lake Intrusion, Finland, Minnesota. Minnesota Geological Survey Information Circular, p. 31.

Mueller, P.A., Frost, C.D., 2006. The Wyoming Province: a distinctive Archaen craton in Laurentian North America. Canadian Journal of Earth Sciences 43, 1391–1397.

Naldrett, A.J., 1999. World-class Ni–Cu–PGE deposits: key factors in their genesis. Mineralium Deposita 34, 227–240.

Naldrett, A.J., 2011. Fundamentals of Magmatic Sulfide Deposits. In: Li, C., Ripley, E.M. (Eds.), Magmatic Ni–Cu and PGE deposits: Geology, Geochemistry, and Genesis. Society of Economic Geologists, Denver, pp. 1–50.

Nelson, D.O., Morrison, D.A., Phinney, W.C., 1990. Open-system evolution versus source control in basaltic magmas: Matachewan–Hearst dike swarm, Superior Province, Canada. Canadian Journal of Earth Sciences 27, 767–783.

Palacz, Z.A., 1985. Sr–Nd–Pb isotopic evidence for crustal contamination in the Rhum intrusion. Earth and Planetary Science Letters 74, 35–44.

Pearce, J.A., 1996. A user's guide to basalt discrimination diagrams. In: Wyman, D. (Ed.), Trace element geochemistry of volcanic rocks: application for massive sulphide exploration: Geological Association of Canada, Short Course Notes, 12, pp. 79–113.

Pearce, J.A., Peate, D.W., 1995. Tectonic implications of the composition of volcanic arc magmas. Annual Review of Earth and Planetary Sciences 23, 251–285.

Peck, D.C., James, R.S., Chubb, P.T., Keays, R.R., 1995. Geology, metallogeny and petrogenesis of the East Bull Lake intrusion, Ontario. Ontario Geological Survey, Open File Report 5923. . 117 pp.

Peck, D.C., Keays, R.R., James, R.S., Chubb, P.T., Reeves, S.J., 2001. Controls on the Formation of Contact-Type Platinum-Group Element Mineralization in the East Bull Lake Intrusion. Economic Geology 96, 559–581.

Phinney, W.C., Halls, H.C., 2001. Petrogenesis of the Early Proterozoic Matachewan dyke swarm, Canada, and implications for magma emplacement and subsequent deformation. Canadian Journal of Earth Sciences 38, 1541–1563.

Polat, A., Fryer, B.J., Appel, P.W.U., Kalvig, P., Kerrich, R., Dilek, Y., Yang, Z., 2011. Geochemistry of anorthositic differentiated sills in the Archean (2970 Ma) Fiskenæsset Complex, SW Greenland: implications for parental magma compositions, geodynamic setting, and secular heat flow in arcs. Lithos 123, 50–72.

Redden, J.A., Peterman, Z.E., Zartman, R.E., DeWitt, E.R., 1990. U-Th-Pb geochronology and preliminary interpretation of Precambrian events in the Black Hills, South Dakota. In: Lewry, J.F., Stauffer, M.R. (Eds.), The Trans-Hudson orogen: Geological Association of Canada, Special Paper, 37, pp. 229–251.

Roscoe, S.M., Card, K.D., 1993. The reappearance of the Huronian in Wyoming: rifting and drifting of ancient continents. Canadian Journal of Earth Sciences 30, 2475–2480.

Sandeman, H.A., Ryan, J.J., 2008. The Spi Lake Formation of the central Hearne domain, western Churchill Province, Canada: an axial intracratonic continental tholeiite trough above the cogenetic Kaminak dyke swarm. Canadian Journal of Earth Sciences 45, 745–767.

Stubbs, H.M., Hall, R.P., Hughes, D.J., Nesbitt, R.W., 1999. Evidence for a high Mg andesitic parental magma to the East and West satellite dykes of the Great Dyke, Zimbabwe: a comparison with the continental tholeiitic Mashonaland sills. Journal of African Earth Sciences 28, 325–336.

Tredoux, M., Lindsay, N.M., Davies, G., McDonald, I., 1995. The fractionation of platinum-group elements in magmatic systems, with the suggestion of a novel causal mechanism. South African Journal of Geology 98, 157–167.

Van Boening, A. M., 2007. Petrogenesis and Tectonic Implications of Mafic Rocks in the Precambrian Core of the Black Hills, South Dakota. MSc thesis. University of Missouri, Missouri.

Van Boening, A.M., Nabelek, P.I., 2008. Petrogenesis and tectonic implications of paleoproterozoic mafic rocks in the Black Hills, South Dakota. Precambrian Research 167, 363–376.

Vogel, D. C., 1996. The geology and geochemistry of the Agnew intrusion: implications for the petrogenesis of early Huronian mafic igneous rocks in central Ontario, Canada. PhD thesis, University of Melbourne, Victoria.

Vogel, D.C., Keays, R.R., 1997. The petrogenesis and platinum-group element geochemistry of the Newer Volcanic Province, Victoria, Australia. Chemical Geology 136, 181–204.

Vogel, D.C., James, R.S., Keays, R.R., 1998a. The early tectono-magmatic evolution of the Southern Province: implications from the Agnew Intrusion, central Ontario, Canada. Canadian Journal of Earth Sciences 35, 854–870.

Vogel, D.C., Vuollo, J.I., Alapieti, T.T., James, R.S., 1998b. Tectonic, stratigraphic, and geochemical comparisons between ca. 2500–2440 Ma mafic igneous events in the Canadian and Fennoscandian Shields. Precambrian Research 92, 89–116.

Vogel, D.C., Keays, R.R., James, R.S., Reeves, S.J., 1999. The geochemistry and petrogenesis of the Agnew Intrusion, Canada: a product of S-undersaturated, high-Al and low-Ti tholeiitic magmas. Journal of Petrology 40, 423–450.

Wang, P., Glover, L.I., 1992. A tectonics test of the most commonly used geochemical discriminant diagrams and patterns. Earth-Science Reviews 33, 111–131.

Woo, C. C., 1952. The Pre-Cambrian geology and amphibolites of the Nemo district, Black Hills, South Dakota. PhD thesis. University of Chicago, Chicago.

Xie, Q., Kerrich, R., Fan, J., 1993. HFSE/REE fractionations recorded in three komatiite-basalt sequences, Archean Abitibi greenstone belt: implications for multiple plume sources and depths. Geochimica et Cosmochimica Acta 57, 4111–4118.

Please cite this article as: Ciborowski, T.J.R., et al., The geochemistry and petrogenesis of the Blue Draw Metagabbro, Lithos (2012), doi:10.1016/j.lithos.2012.06.035

Appendix H - Parental Magam Estimation of Blue Draw Metagabbro

SiO2		Start Height (	End Height (	Median Height (	Thickness (	**gradient**	**y**	**c**	**x**		
	3	677.5	760	718.75	82.5	4.766	718.75	422.71	62.11498	6.74274	
	2	112.5	677.5	395	565	54.298	395	-2379.8	51.10317	37.9912	
	1	0	112.5	56.25	112.5				36	5.32895	
										50.0629	**SiO2**

TiO2		Start Height (	End Height (	Median Height (	Thickness (	**gradient**	**y**	**c**	**x**		
	3	600	760	680	160	104.29	680	581.54	0.944098	0.19876	
	2	112.5	600	356.25	487.5	1262.5	356.25	-157.37	0.406828	0.26096	
	1	0	112.5	56.25	112.5	-862.39	56.25	171.16	0.133246	0.01972	
										0.47944	**TiO2**

Al2O3		Start Height (	End Height (	Median Height (	Thickness (	**gradient**	**y**	**c**	**x**		
	4	600	760	680	160	-28.532	680	1051.9	13.03449	2.7441	
	3	300	600	450	300				12	4.73684	
	2	112.5	300	206.25	187.5	9.2002	206.25	99.457	11.60768	2.86374	
	1	0	112.5	56.25	112.5	-48.789	56.25	173.38	2.400746	0.35537	
										10.7001	**Al2O3**

Fe2O3		Start Height (	End Height (	Median Height (	Thickness (	**gradient**	**y**	**c**	**x**		
	3	600	760	680	160	16.821	680	470.14	12.47607	2.62654	
	2	300	600	450	300				10.5	4.14474	
	1	0	300	150	300	-43.992	150	565.82	9.452173	3.73112	
										10.5024	**Fe2O3**

MnO		Start Height (	End Height (	Median Height (	Thickness (	**gradient**	**y**	**c**	**x**		
	1	0	760	380	760				0.17	0.17	
										0.17	**MnO**

MgO		Start Height (	End Height (	Median Height (	Thickness (	**gradient**	**y**	**c**	**x**		
	3	300	760	530	460	-29.152	530	780.15	8.580886	5.19369	
	2	112.5	300	206.25	187.5	-9.0204	206.25	303.72	10.80551	2.66583	
	1	0	112.5	56.25	112.5	5.8441	56.25	-154.68	36.09281	5.34269	
										13.2022	**MgO**

CaO		Start Height (	End Height (	Median Height (	Thickness (	**gradient**	**y**	**c**	**x**		
	3	600	760	680	160	-13.989	680	770.97	6.502967	1.36905	
	2	112.5	600	356.25	487.5	-48.952	356.25	857.52	10.24003	6.56844	

	1	0	112.5	56.25	112.5	-22.478	56.25	77.928	0.96441	0.14276	
										8.08024	**CaO**
Na2O		Start Height (	End Height (	Median Height (	Thickness (	**gradient**	**y**	**c**	**x**		
	1	0	760	380	760				3	3	
										3	**Na2O**
K2O		Start Height (	End Height (	Median Height (	Thickness (	**gradient**	**y**	**c**	**x**		
	4	600	760	680	160	55.731	680	586.23	1.682547	0.35422	
	3	274.5	600	437.25	325.5	162.83	437.25	357.17	0.491801	0.21063	
	2	112.5	274.5	193.5	162	183.7	193.5	140.18	0.290256	0.06187	
	1	0	112.5	56.25	112.5				0	0	
										0.62672	**K2O**
P2O5		Start Height (	End Height (	Median Height (	Thickness (	**gradient**	**y**	**c**	**x**		
	4	600	760	680	160	766.72	680	587.76	0.120305	0.02533	
	3	300	600	450	300	13477	450	-302.04	0.055802	0.02203	
	2	112.5	300	206.25	187.5	3496.5	206.25	95.815	0.031584	0.00779	
	1	0	112.5	56.25	112.5	-1929.2	56.25	82.669	0.013694	0.00203	
										0.05717	**P2O5**
Cr (ppm)		Start Height (	End Height (	Median Height (	Thickness (	**gradient**	**y**	**c**	**x**		
	4	600	760	680	160				300	63.1579	
	3	300	600	450	300				500	197.368	
	2	112.5	300	206.25	187.5	-0.0793	206.25	238.01	400.5044	98.8087	
	1	0	112.5	56.25	112.5				3100	458.882	
										818.217	**Cr (ppm)**

	SiO2	**TiO2**	**Al2O3**	**FeO**	**Fe2O3**	**MnO**	**MgO**	**CaO**	**Na2O**	**K2O**	**P2O5**	**Cr2O3**
Whole Intrusion	51.61	0.49	11.03	9.74	1.08	0.18	13.61	8.33	3.09	0.65	0.06	0.12
Parent Liquid	51.87	0.51	11.31	9.40	1.46	0.18	12.71	8.54	3.17	0.66	0.06	0.13

La		Start Height (	End Height (	Median Height (	Thickness (	**gradient**	**y**	**c**	**x**	
	4	600	760	680	160	3.7291	680	586.08	25.1857	5.30225
	3	300	600	450	300	28.978	450	171.86	9.598316	3.78881
	2	112.5	300	206.25	187.5	23.148	206.25	57.466	6.42751	1.58573
	1	0	112.5	56.25	112.5	-16.314	56.25	96.215	2.449736	0.36263

									11.0394	**La**
Ce	Start Height (	End Height (	Median Height (	Thickness (	**gradient**	**y**	**c**	**x**		
4	600	760	680	160	2.0765	680	582	47.1948	9.93575	
3	300	600	450	300	16.141	450	143.47	18.99077	7.49636	
2	112.5	300	206.25	187.5	10.777	206.25	60.654	13.50988	3.33303	
1	0	112.5	56.25	112.5	-15.868	56.25	128.51	4.553819	0.67409	
									21.4392	**Ce**
Pr	Start Height (	End Height (	Median Height (	Thickness (	**gradient**	**y**	**c**	**x**		
4	600	760	680	160	17.575	680	580.31	5.672262	1.19416	
3	300	600	450	300	136.29	450	123.01	2.399222	0.94706	
2	112.5	300	206.25	187.5	90.804	206.25	52.813	1.68976	0.41688	
1	0	112.5	56.25	112.5	-163.93	56.25	136.61	0.490209	0.07256	
									2.63067	**Pr**
Nd	Start Height (	End Height (	Median Height (	Thickness (	**gradient**	**y**	**c**	**x**		
4	600	760	680	160	5.0272	680	575.49	20.78891	4.37661	
3	300	600	450	300	37.013	450	113.4	9.094102	3.58978	
2	112.5	300	206.25	187.5	26.253	206.25	33.209	6.591285	1.62614	
1	0	112.5	56.25	112.5	-43.281	56.25	143.95	2.026293	0.29994	
									9.89247	**Nd**
Sm	Start Height (	End Height (	Median Height (	Thickness (	**gradient**	**y**	**c**	**x**		
4	600	760	680	160	24.696	680	570.63	4.428652	0.93235	
3	300	600	450	300	194.3	450	55.955	2.028024	0.80054	
2	112.5	300	206.25	187.5	139.86	206.25	-3.5863	1.500331	0.37015	
1	0	112.5	56.25	112.5	-286.53	56.25	183.62	0.444526	0.0658	
									2.16883	**Sm**
Eu	Start Height (	End Height (	Median Height (	Thickness (	**gradient**	**y**	**c**	**x**		
4	600	760	680	160	117.24	680	542.29	1.174599	0.24728	
3	300	600	450	300	530.23	450	107.08	0.646738	0.25529	
2	112.5	300	206.25	187.5	301.28	206.25	50.069	0.518392	0.12789	
1	0	112.5	56.25	112.5	-806.43	56.25	166.38	0.136565	0.02022	
									0.65068	**Eu**
Gd	Start Height (	End Height (	Median Height (	Thickness (	**gradient**	**y**	**c**	**x**		
4	600	760	680	160	27.197	680	567.26	4.14531	0.8727	

	3	300	600	450	300	203.87	450	43.012	1.996311	0.78802	
	2	112.5	300	206.25	187.5	148.72	206.25	-17.785	1.506421	0.37165	
	1	0	112.5	56.25	112.5	-252.9	56.25	171.05	0.453934	0.06719	
										2.09956	**Gd**
Tb		Start Height (	End Height (	Median Height (	Thickness (	**gradient**	**y**	**c**	**x**		
	4	600	760	680	160	193.69	680	559.57	0.621767	0.1309	
	3	300	600	450	300	1317.5	450	26.726	0.321271	0.12682	
	2	112.5	300	206.25	187.5	1009.1	206.25	-36.731	0.24079	0.05941	
	1	0	112.5	56.25	112.5	-1642.6	56.25	181.89	0.076488	0.01132	
										0.32844	**Tb**
Dy		Start Height (	End Height (	Median Height (	Thickness (	**gradient**	**y**	**c**	**x**		
	4	600	760	680	160	34.364	680	553.4	3.684088	0.7756	
	3	300	600	450	300	224.65	450	-15.06	2.070154	0.81717	
	2	112.5	300	206.25	187.5	170.14	206.25	-62.376	1.578853	0.38952	
	1	0	112.5	56.25	112.5	-228.58	56.25	174.29	0.516406	0.07644	
										2.05872	**Dy**
Ho		Start Height (	End Height (	Median Height (	Thickness (	**gradient**	**y**	**c**	**x**		
	4	600	760	680	160	189.49	680	545.83	0.708058	0.14906	
	3	300	600	450	300	1077.7	450	23.016	0.396199	0.15639	
	2	112.5	300	206.25	187.5	812.12	206.25	-47.112	0.311976	0.07697	
	1	0	112.5	56.25	112.5	-1261.3	56.25	176.49	0.09533	0.01411	
										0.39654	**Ho**
Er		Start Height (	End Height (	Median Height (	Thickness (	**gradient**	**y**	**c**	**x**		
	4	600	760	680	160	62.336	680	547.4	2.127182	0.44783	
	3	300	600	450	300	381.53	450	1.8724	1.174554	0.46364	
	2	112.5	300	206.25	187.5	286.06	206.25	-54.185	0.910421	0.22461	
	1	0	112.5	56.25	112.5	-358.37	56.25	158.74	0.285989	0.04233	
										1.17841	**Er**
Tm		Start Height (	End Height (	Median Height (	Thickness (	**gradient**	**y**	**c**	**x**		
	4	600	760	680	160	397.36	680	548.63	0.330607	0.0696	
	3	300	600	450	300	2176.4	450	49.968	0.183804	0.07255	
	2	112.5	300	206.25	187.5	2067.9	206.25	-90.103	0.143311	0.03536	
	1	0	112.5	56.25	112.5	-2574.5	56.25	178.64	0.047539	0.00704	

										0.18455	**Tm**
Yb		Start Height (	End Height (	Median Height (	Thickness (	**gradient**	**y**	**c**	**x**		
	4	600	760	680	160	66.543	680	543.9	2.045294	0.43059	
	3	300	600	450	300	362.4	450	20.449	1.185295	0.46788	
	2	112.5	300	206.25	187.5	318.06	206.25	-77.578	0.892373	0.22016	
	1	0	112.5	56.25	112.5	-371.16	56.25	170.08	0.306687	0.0454	
										1.16402	**Yb**
Lu		Start Height (	End Height (	Median Height (	Thickness (	**gradient**	**y**	**c**	**x**		
	4	600	760	680	160	439.27	680	542.03	0.314089	0.06612	
	3	300	600	450	300	2635.3	450	-13.679	0.175949	0.06945	
	2	112.5	300	206.25	187.5	2389.6	206.25	-102.61	0.129252	0.03189	
	1	0	112.5	56.25	112.5	-1804.9	56.25	132.76	0.04239	0.00627	
										0.17374	**Lu**
Th		Start Height (	End Height (	Median Height (	Thickness (	**gradient**	**y**	**c**	**x**		
	4	600	760	680	160	10.821	680	592.74	8.06395	1.69767	
	3	300	600	450	300	95.726	450	139.95	3.238932	1.27853	
	2	112.5	300	206.25	187.5	60.322	206.25	81.772	2.063559	0.5091	
	1	0	112.5	56.25	112.5	-174.1	56.25	185.24	0.740896	0.10967	
										3.59497	**Th**
Nb		Start Height (	End Height (	Median Height (	Thickness (	**gradient**	**y**	**c**	**x**		
	4	600	760	680	160	14.82	680	587.87	6.216599	1.30876	
	3	300	600	450	300	112.58	450	138.19	2.769675	1.09329	
	2	112.5	300	206.25	187.5	75.475	206.25	78.501	1.6926	0.41758	
	1	0	112.5	56.25	112.5	-86.55	56.25	106.42	0.579665	0.08581	
										2.90544	**Nb**
Ta		Start Height (	End Height (	Median Height (	Thickness (	**gradient**	**y**	**c**	**x**		
	4	600	760	680	160	181.55	680	589.45	0.498761	0.105	
	3	300	600	450	300	1569.9	450	114.35	0.213803	0.0844	
	2	112.5	300	206.25	187.5	939.45	206.25	81.92	0.132343	0.03265	
	1	0	112.5	56.25	112.5	-1503.6	56.25	123.35	0.044626	0.00661	
										0.22865	**Ta**
Zr		Start Height (	End Height (	Median Height (	Thickness (	**gradient**	**y**	**c**	**x**		
	4	600	760	680	160	0.4378	680	613.05	152.9237	32.1945	

3	300	600	450	300	5.5288	450	128.38	58.17176	22.9625	
2	112.5	300	206.25	187.5	4.4564	206.25	44.477	36.30127	8.95591	
1	0	112.5	56.25	112.5	-1.5391	56.25	79.286	14.96719	2.21554	
									66.3284	**Zr**

Y	Start Height (	End Height (	Median Height (	Thickness (	**gradient**	**y**	**c**	**x**		
4	600	760	680	160	5.6734	680	551.72	22.61078	4.76016	
3	300	600	450	300	35.648	450	3.9807	12.51176	4.93885	
2	112.5	300	206.25	187.5	26.623	206.25	-48.17	9.556399	2.35766	
1	0	112.5	56.25	112.5	-40.868	56.25	166.93	2.708231	0.40089	
									12.4576	**Y**

Hf	Start Height (	End Height (	Median Height (	Thickness (	**gradient**	**y**	**c**	**x**		
4	600	760	680	160	18.937	680	607.11	3.849079	0.81033	
3	300	600	450	300	223.46	450	103.04	1.552672	0.6129	
2	112.5	300	206.25	187.5	154.81	206.25	49.795	1.010626	0.24933	
1	0	112.5	56.25	112.5	-81.083	56.25	88.557	0.398444	0.05898	
									1.73154	**Hf**

U	Start Height (	End Height (	Median Height (	Thickness (	**gradient**	**y**	**c**	**x**		
4	600	760	680	160	18.937	680	607.11	3.849079	0.81033	
3	300	600	450	300	223.46	450	103.04	1.552672	0.6129	
2	112.5	300	206.25	187.5	154.81	206.25	49.795	1.010626	0.24933	
1	0	125	62.5	125	-81.083	62.5	88.557	0.321362	0.05286	
									1.72542	**U**

	Th	**Nb**	**Ta**	**La**	**Ce**	**Pr**	**Nd**	**Zr**	**Hf**	**Sm**	**Eu**
Whole Intrusion	3.59	2.91	0.23	11.04	21.44	2.63	9.89	66	1.73	2.17	0.65
	Ti	**Gd**	**Tb**	**Dy**	**Y**	**Ho**	**Er**	**Tm**	**Yb**	**Lu**	
	2997	2.10	0.33	2.06	12.46	0.40	1.18	0.18	1.16	0.17	

Appendix I - Geochemical Reservoirs used in Modelling

Mantle	**Th**	**Nb**	**Ta**	**La**	**Ce**	**Pr**	**Nd**	**Zr**	**Hf**	**Sm**	**Eu**	**Ti**	**Gd**	**Tb**	**Dy**	**Y**	**Ho**	**Er**	**Tm**	**Yb**	**Lu**	**Reference**
DMM	0.01	0.15	0.01	0.19	0.55	0.11	0.58	5.08	0.16	0.24	0.10	716	0.36	0.07	0.51	3.33	0.12	0.35	0.05	0.37	0.06	**9**
EM1	0.03	0.38	0.03	0.60	1.75	0.29	1.47	12.56	0.36	0.52	0.20	1433	0.72	0.13	0.92	5.77	0.20	0.60	0.09	0.62	0.10	**8**
EM2	0.04	0.37	0.03	0.61	1.77	0.29	1.48	12.91	0.37	0.52	0.20	1457	0.73	0.14	0.94	5.88	0.21	0.61	0.09	0.63	0.10	**8**
HIMU	0.04	0.69	0.04	0.77	2.29	0.41	2.26	22.31	0.63	0.84	0.33	2437	1.19	0.22	1.52	9.50	0.34	1.00	0.15	1.04	0.16	**1**
Primitive Mantle	0.09	0.71	0.04	0.69	1.78	0.28	1.35	11.20	0.31	0.44	0.17	1300	0.60	0.11	0.74	4.55	0.16	0.48	0.07	0.49	0.07	**5**
Archaean SCLM	23.57	13.09	0.98	73.63	147.08	15.94	62.28	242.98	6.04	10.57	2.62	3513	7.17	0.82	4.05	18.79	0.64	1.75	0.22	1.39	0.20	**2**

Crust	**Th**	**Nb**	**Ta**	**La**	**Ce**	**Pr**	**Nd**	**Zr**	**Hf**	**Sm**	**Eu**	**Ti**	**Gd**	**Tb**	**Dy**	**Y**	**Ho**	**Er**	**Tm**	**Yb**	**Lu**	**Reference**
Lower Cont. Crust	1.20	5.00	0.27	8.00	20.00	2.40	11.00	68.00	1.90	2.80	1.10	4916	3.10	0.48	3.10	16.00	0.68	1.90	0.24	1.50	0.25	**6**
Upper Cont. Crust	10.50	12.00	0.90	31.00	63.00	7.10	27.00	193.00	5.30	4.70	1.00	3837	4.00	0.70	3.90	21.00	0.83	2.30	0.30	1.96	0.31	**6**
Average Cont. Crust	5.60	8.00	0.70	20.00	43.00	4.90	20.00	132.00	3.70	3.90	1.10	4316	3.70	0.60	3.60	19.00	0.77	2.10	0.28	1.90	0.30	**6**
N-MORB	0.12	2.33	0.13	2.50	7.50	1.32	7.30	74.00	2.05	2.63	1.02	7600	3.68	0.67	4.55	28.00	1.01	2.97	0.46	3.05	0.46	**7**
Altered MORB	0.19	3.56	0.25	4.18	13.08	2.31	12.24	127.43	3.33	4.44	1.53	11498	6.28	1.05	7.00	44.13	1.57	4.38	0.66	4.24	0.68	**4**
Oceanic Crust Gabbro	0.08	1.70	0.19	4.79	14.89	2.20	10.22	77.60	2.12	3.09	1.15	8045	3.86	0.73	4.67	26.89	0.96	2.77	0.42	2.77	0.40	**3**
Average Ocean Crust	0.11	2.14	0.17	3.81	11.75	1.86	9.25	81.14	2.21	3.04	1.13	8212	4.03	0.74	4.85	29.06	1.04	3.01	0.46	3.03	0.45	**8**

Reference

1. Chauvel, C., Hofmann, A. W. and Vidal, P., 1992. HIMU-EM: The French Polynesian connection. Earth and Planetary Science Letters, 110, 99-119.

2. Cousens, B. L., Aspler, L. B., Chiarenzelli, J. R., Donaldson, J. A., Sandeman, H., Peterson, T. D. and LeCheminant, A. N., 2001. Enriched Archean lithospheric mantle beneath western Churchill Province tapped during Paleoproterozoic orogenesis. Geology, 29, 827-830.

3. Hart, S. R., Blusztajn, J., Dick, H. J. B., Meyer, P. S. and Muehlenbachs, K., 1999. The fingerprint of seawater circulation in a 500-meter section of ocean crust gabbros. Geochimica et Cosmochimica Acta, 63, 4059-4080.

4. Kelley, K. A., Plank, T., Ludden, J. and Staudigel, H., 2003. Composition of altered oceanic crust at ODP Sites 801 and 1149. Geochem. Geophys. Geosyst., 4, 8910.

5. McDonough, W. F. and Sun, S. S., 1995. The composition of the Earth. Chemical Geology, 120, 223-253.

6. Rudnick, R. L. and Gao, S., 2003. 3.01 - Composition of the Continental Crust. In Treatise on Geochemistry, eds. D. H. Editors-in-Chief: Heinrich and K. T. Karl, 1-64. Oxford: Pergamon.

7. Sun, S. s. and McDonough, W. F., 1989. Chemical and isotopic systematics of oceanic basalts: implications for mantle composition and processes. Geological Society, London, Special Publications, 42, 313-345.

8. Willbold, M. and Stracke, A., 2006. Trace element composition of mantle end-members: Implications for recycling of oceanic and upper and lower continental crust. Geochem. Geophys. Geosyst., 7, Q04004.

9. Workman, R. K. and Hart, S. R., 2005. Major and trace element composition of the depleted MORB mantle (DMM). Earth and Planetary Science Letters, 231, 53-72.

Phenocryst Composition	Phenocryst Proportion (est. from hand sample)	Anorthite proportion (est. from CIPW norm)	Albite proportion (est. from CIPW norm)	SiO2 (wt.%)	TiO2 (wt.%)	Al2O3 (wt.%)	Fe2O3 (wt.%)	MnO (wt.%)	MgO (wt.%)	CaO (wt.%)	Na2O (wt.%)	K2O (wt.%)	P2O5 (wt.%)
NBH13FA	0.3	0.8	0.2	49.46	0.00	32.43	0.00	0.00	0.00	15.21	2.90	0.00	0.00
BR6A	0.3	0.8	0.3	50.15	0.00	31.97	0.00	0.00	0.00	14.67	3.22	0.00	0.00
BR4C	0.3	0.7	0.3	50.38	0.00	31.81	0.00	0.00	0.00	14.49	3.32	0.00	0.00
BR1K	0.3	0.8	0.2	48.54	0.00	33.05	0.00	0.00	0.00	15.94	2.47	0.00	0.00
BR4I	0.3	0.7	0.3	50.38	0.00	31.81	0.00	0.00	0.00	14.49	3.32	0.00	0.00
NBH13KA	0.3	0.8	0.3	50.15	0.00	31.97	0.00	0.00	0.00	14.67	3.22	0.00	0.00
NBH13A	0.3	0.7	0.3	50.38	0.00	31.81	0.00	0.00	0.00	14.49	3.32	0.00	0.00
NBH13UNOR	0.3	0.7	0.3	50.61	0.00	31.66	0.00	0.00	0.00	14.30	3.43	0.00	0.00
BR5	0.0	0.7	0.3	51.99	0.00	30.73	0.00	0.00	0.00	13.22	4.07	0.00	0.00
NBH1CB	0.2	0.7	0.3	50.38	0.00	31.81	0.00	0.00	0.00	14.49	3.32	0.00	0.00
NBH2KA	0.3	0.8	0.3	50.15	0.00	31.97	0.00	0.00	0.00	14.67	3.22	0.00	0.00
BR3A	0.0	0.7	0.3	51.99	0.00	30.73	0.00	0.00	0.00	13.22	4.07	0.00	0.00
NBH7HB	0.1	0.6	0.4	52.91	0.00	30.11	0.00	0.00	0.00	12.49	4.49	0.00	0.00
BR5K	0.0	0.6	0.4	54.29	0.00	29.18	0.00	0.00	0.00	11.40	5.13	0.00	0.00
NBH6A	0.0	0.6	0.4	52.91	0.00	30.11	0.00	0.00	0.00	12.49	4.49	0.00	0.00
BR3	0.0	0.6	0.4	53.37	0.00	29.80	0.00	0.00	0.00	12.13	4.71	0.00	0.00
NBH3UNOR	0.0	0.6	0.4	53.37	0.00	29.80	0.00	0.00	0.00	12.13	4.71	0.00	0.00
NBH3D	0.0	0.6	0.4	53.37	0.00	29.80	0.00	0.00	0.00	12.13	4.71	0.00	0.00

	SiO2 (wt.%)	TiO2 (wt.%)	Al2O3 (wt.%)	Fe2O3 (wt.%)	MnO (wt.%)	MgO (wt.%)	CaO (wt.%)	Na2O (wt.%)	K2O (wt.%)	P2O5 (wt.%)
Albite	67.39	0.00	20.35	0.00	0.00	0.00	1.07	11.19	0.00	0.00
Anorthite	44.40	0.00	35.84	0.00	0.00	0.00	19.20	0.56	0.00	0.00

Groundmass Compostion	Phenocryst Proportion (est. from hand sample)	SiO2 (wt.%)	TiO2 (wt.%)	Al2O3 (wt.%)	Fe2O3 (wt.%)	MnO (wt.%)	MgO (wt.%)	CaO (wt.%)	Na2O (wt.%)	K2O (wt.%)	P2O5 (wt.%)	Total
NBH13FA	0.3	47.1	0.5	26.7	5.7	0.1	2.3	11.6	1.6	2.4	0.0	97.9
BR6A	0.3	45.9	0.5	25.1	6.6	0.1	3.4	11.8	1.9	0.9	0.0	96.2

BR4C	0.3	48.2	0.7	24.5	8.0	0.1	4.1	13.1	2.0	0.5	0.0	101.3
BR1K	0.3	46.8	0.6	24.4	7.2	0.1	3.4	7.4	1.5	5.5	0.0	97.0
BR4I	0.3	47.8	0.7	23.4	8.2	0.1	4.3	11.0	1.8	2.4	0.1	99.7
NBH13KA	0.3	47.6	0.6	23.0	8.3	0.1	3.7	12.2	1.8	0.7	0.1	98.2
NBH13A	0.3	48.0	0.7	23.3	8.0	0.1	3.2	12.8	1.8	1.1	0.1	99.1
NBH13UNOR	0.3	46.8	1.0	18.0	13.2	0.2	6.2	10.0	1.5	0.5	0.1	97.4
BR5	0.0	49.5	0.8	20.6	8.8	0.1	4.5	11.1	2.5	0.4	0.1	98.4
NBH1CB	0.2	47.6	0.9	18.6	10.3	0.1	4.6	11.3	1.5	1.1	0.1	96.1
NBH2KA	0.3	47.0	1.1	15.8	12.8	0.2	6.1	10.2	1.0	1.8	0.1	96.2
BR3A	0.0	48.5	0.9	18.8	9.4	0.2	5.5	11.2	2.2	2.2	0.1	98.9
NBH7HB	0.1	49.0	1.1	13.5	14.0	0.2	7.7	10.0	1.8	0.4	0.1	97.9
BR5K	0.0	50.5	1.0	15.7	12.4	0.2	6.9	10.3	2.6	0.4	0.1	100.2
NBH6A	0.0	50.0	1.0	14.6	12.9	0.2	6.6	9.9	2.0	0.4	0.1	97.6
BR3	0.0	49.5	1.2	16.5	11.8	0.2	6.1	10.0	2.4	0.4	0.1	98.1
NBH3UNOR	0.0	49.4	1.2	14.2	14.3	0.2	6.7	9.9	2.0	0.3	0.1	98.4
NBH3D	0.0	50.2	1.3	14.8	14.6	0.2	6.7	10.0	2.1	0.3	0.1	100.3